Oxidative Medicine and Cellular Longevity

Reactive Oxygen Species in Inflammation and Tissue Injury

Lead Guest Editor: Chaoliang Tang
Guest Editors: Peilin Yu, Xiaoyuan Zhou, Xin Luo, and Xiuyun Liu

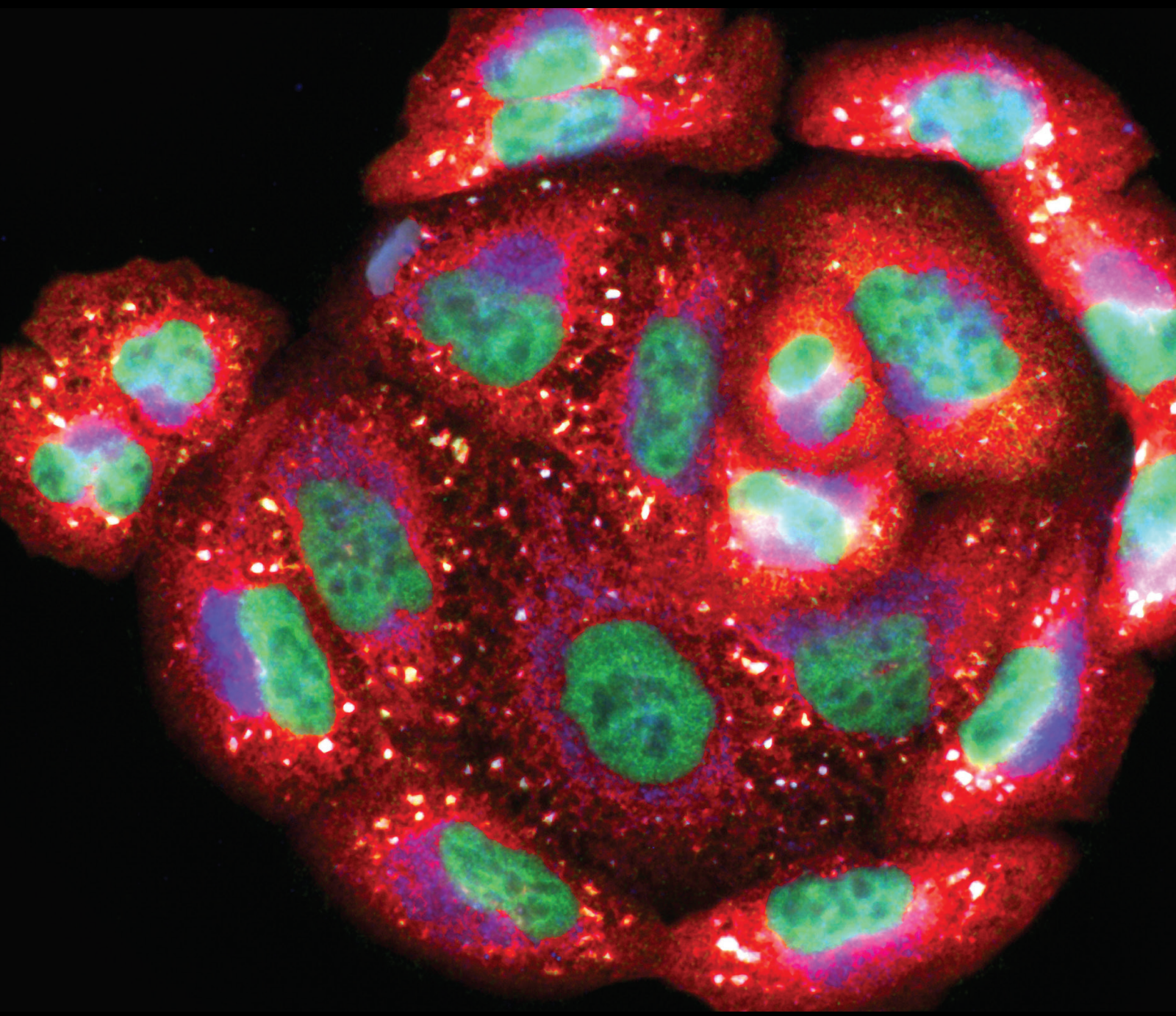

Reactive Oxygen Species in Inflammation and Tissue Injury

Oxidative Medicine and Cellular Longevity

Reactive Oxygen Species in Inflammation and Tissue Injury

Lead Guest Editor: Chaoliang Tang
Guest Editors: Peilin Yu, Xiaoyuan Zhou, Xin Luo, and Xiuyun Liu

Chief Editor

Jeannette Vasquez-Vivar, USA

Associate Editors

Amjad Islam Aqib, Pakistan
Angel Catalá, Argentina
Cinzia Domenicotti, Italy
Janusz Gebicki, Australia
Aldrin V. Gomes, USA
Vladimir Jakovljevic, Serbia
Thomas Kietzmann, Finland
Juan C. Mayo, Spain
Ryuichi Morishita, Japan
Claudia Penna, Italy
Sachchida Nand Rai, India
Paola Rizzo, Italy
Mithun Sinha, USA
Daniele Vergara, Italy
Victor M. Victor, Spain

Academic Editors

Ammar AL-Farga, Saudi Arabia
Mohd Adnan, Saudi Arabia
Ivanov Alexander, Russia
Fabio Altieri, Italy
Daniel Dias Rufino Arcanjo, Brazil
Peter Backx, Canada
Amira Badr, Egypt
Damian Bailey, United Kingdom
Rengasamy Balakrishnan, Republic of Korea
Jiaolin Bao, China
Ji C. Bihl, USA
Hareram Birla, India
Abdelhakim Bouyahya, Morocco
Ralf Braun, Austria
Laura Bravo, Spain
Matt Brody, USA
Amadou Camara, USA
Marcio Carocho, Portugal
Peter Celec, Slovakia
Giselle Cerchiaro, Brazil
Arpita Chatterjee, USA
Shao-Yu Chen, USA
Yujie Chen, China
Deepak Chhangani, USA
Ferdinando Chiaradonna, Italy
Zhao Zhong Chong, USA
Fabio Ciccarone, Italy
Alin Ciobica, Romania
Ana Cipak Gasparovic, Croatia
Giuseppe Cirillo, Italy
Maria R. Ciriolo, Italy
Massimo Collino, Italy
Manuela Corte-Real, Portugal
Manuela Curcio, Italy
Domenico D'Arca, Italy
Francesca Danesi, Italy
Claudio De Lucia, USA
Damião De Sousa, Brazil
Enrico Desideri , Italy
Francesca Diomede, Italy
Raul Dominguez-Perles, Spain
Joël R. Drevet, France
Grégory Durand, France
Alessandra Durazzo, Italy
Javier Egea, Spain
Pablo A. Evelson, Argentina
Mohd Farhan, USA
Ioannis G. Fatouros, Greece
Gianna Ferretti, Italy
Swaran J. S. Flora, India
Maurizio Forte, Italy
Teresa I. Fortoul, Mexico
Anna Fracassi , USA
Rodrigo Franco, USA
Juan Gambini, Spain
Gerardo García-Rivas, Mexico
Husam Ghanim, USA
Jayeeta Ghose, USA
Rajeshwary Ghosh, USA
Lucia Gimeno-Mallench , Spain
Anna M. Giudetti, Italy
Daniela Giustarini, Italy
José Rodrigo Godoy, USA
Saeid Golbidi, Canada
Guohua Gong, China
Tilman Grune, Germany
Solomon Habtemariam, United Kingdom
Eva-Maria Hanschmann, Germany
Md Saquib Hasnain, India
Md Hassan, India

Contents

Contents

Hindawi
Oxidative Medicine and Cellular Longevity
Volume 2022, Article ID 9407927, 12 pages
https://doi.org/10.1155/2022/9407927

Research Article

The Protective Role of Hydrogen Sulfide and Its Impact on Gene Expression Profiling in Rat Model of COPD

Yanjing He,[1,2] **Yun Sun**,[1] **Chengcheng Liao**,[1] **Fan Lin**,[1] **Zhengyuan Xia**,[2,3,4] **Yongfen Qi**,[5] **and Yahong Chen**[1]

[1]*Department of Pulmonary and Critical Care Medicine, Peking University Third Hospital, Beijing, China*
[2]*Department of Anesthesiology, The University of Hong Kong, Hong Kong, China*
[3]*State Key Laboratory of Pharmaceutical Biotechnology, Department of Medicine, The University of Hong Kong, Hong Kong, China*
[4]*Department of Anesthesiology, Affiliated Hospital of Guangdong Medical University, Zhanjiang, China*
[5]*Key Laboratory of Molecular Cardiovascular Science, Ministry of Education, Beijing, China*

Correspondence should be addressed to Yongfen Qi; yongfenqi@163.com and Yahong Chen; chenyahong@vip.sina.com

Received 27 August 2021; Accepted 27 January 2022; Published 18 March 2022

Academic Editor: Alin Ciobica

Chronic obstructive pulmonary disease (COPD) is a leading cause of death worldwide, which is usually caused by exposure to noxious particles or gases. Hydrogen sulfide (H_2S), as an endogenous gasotransmitter, is involved in the pathogenesis of COPD, but its role in COPD is little known. To investigate the role of H_2S in COPD, a rat model of COPD was established by cigarette smoking (CS) and intratracheal instillation of lipopolysaccharide (LPS). Rats were randomly divided into 4 groups: control, CS + LPS, CS + LPS + sodium hydrosulfide (NaHS, H_2S donor), and CS + LPS + propargylglycine (PPG, inhibitor of cystathionine-γ-lyase, and CTH). Lung function *in vivo*, histology analysis of lung sections, malondialdehyde (MDA) concentration, CTH protein, total superoxide dismutase (T-SOD), and catalase (CAT) activity in lung tissues were assessed. Gene expression profiling of lung was assessed by microarray analysis. The results showed that rats in the CS + LPS group had lower body weight and lung function but higher lung pathological scores, MDA concentration, CTH protein, T-SOD, and CAT activity compared with the control. Compared with CS + LPS group, NaHS treatment decreased lung pathological scores and MDA concentration, while PPG treatment decreased body weight of rats and T-SOD activity, and no significant differences were detected in pathological scores by PPG treatment. Microarray analysis identified multiple differentially expressed genes, and some genes regulated by H_2S were involved in oxidative stress, apoptosis, and inflammation pathways. It indicates that H_2S may play a protective role in COPD via antioxidative stress and antiapoptosis pathway.

1. Introduction

Chronic obstructive pulmonary disease (COPD) is a preventable and chronic airway disease, which is characterized by airflow limitation that is not fully reversible and persistent respiratory symptoms, and it is usually caused by exposure to noxious particles or gases. Currently, COPD is the third leading cause of death worldwide and causes great burden to the society [1, 2]. Nowadays, it is well-known that cigarette smoking is the commonest risk factor for COPD; however, not all smokers get COPD in their lifetime [3]. In contrast, nonsmokers may develop COPD [4], and it indicates that genetic susceptibility may exist in this complex disease. Other risk factors, such as infections [5], genetic factors (alpha-1 antitrypsin deficiency) [6], and age [7], also influence the development of COPD, while the mechanisms of those risk factors leading to the development of COPD are poorly understood. Oxidative stress [8], apoptosis [9], inflammation [10], and the imbalance of protease and antiprotease [11], all contribute to COPD, and it seems promising to develop an effective antioxidative stress or antiapoptosis intervention as therapies for COPD.

Hydrogen sulfide (H_2S) was considered as a toxic gas once time, it was discovered as the third endogenous gasotransmitter after nitric oxide (NO) and carbon monoxide (CO) in recent decades [12], and it can be catalyzed and

generated in mammalian cells by three enzymes, namely cystathionine-γ-lyase (CTH), cystathionine-β-synthase (CBS), and 3-mercaptopyruvate sulphurtransferase (3-MST) [13, 14], and the 3-MST is identified in brain and blood vessel wall, this enzyme cooperates with cysteine aminotransferase to produce H_2S [15]. Accumulated evidence shows that H_2S is implicated in respiratory diseases, such as COPD, asthma, pulmonary fibrosis, and pulmonary arterial hypertension [16–21]. As an endogenous gasotransmitter, H_2S is involved in physiological and pathological processes, such as tracheal tone [22], pulmonary fibrosis [20], oxidative stress [23], apoptosis, and inflammation [24]. Our previous study showed that serum H_2S level was higher in patients with stable COPD than that in healthy control subjects or patients with acute exacerbation of COPD (5), and other study reported that H_2S protected against tobacco smoke-induced emphysema in mice [25]. However, the underling molecular mechanism of H_2S in regulating COPD is largely unknown.

In the present study, we established a rat model of COPD and applied microarray analysis to explore potential candidate genes mediated by H_2S in this model. The potential differentially expressed (DE) genes were screened among the control group, rat model of COPD, and rat model treated with sodium hydrosulfide (NaHS) or propargylglycine (PPG). We hypothesized that H_2S may play a protective role in COPD by antioxidative stress and antiapoptosis pathways. We further applied Gene Ontology (GO) and Kyoto Encyclopedia of Genes and Genomes (KEGG) enrichment analysis to investigate the signaling pathways which the genes were involved in.

2. Materials and Methods

2.1. Rat Model of COPD. Animal care and experimental protocols were in compliance with the PR China Animal Management Rule (documentation 55, 2001, Ministry of Health of PR China).

Male Sprague–Dawley (SD) rats (210–250 g) were supplied by the Animal Center, Health Science Center, Peking University, and housed on a 12 h light/dark cycle in a temperature-controlled room ($25 \pm 2^{\circ}C$) with free access to water and food. The rats were randomly divided into four groups: control, cigarette smoking (CS) + lipopolysaccharide (LPS, Sigma), CS + LPS + NaHS (Sigma), and CS + LPS + PPG (Sigma) groups. The rat model of COPD was established with minor modification as previously described [22, 26]. Briefly, rats were exposed to cigarette smoking in a dynamic smoke box (Tianjin Hope Corp., Tianjin, China) on days 1-4, 6-18, and 20-30, respectively, 2 times/day, 1.5 h/time. In addition, LPS solution (500 μg/ml, 200 μl/animal/time) was instilled into exposed trachea with 1 ml syringe on days 5 and 19. Freshly prepared NaHS (14 μmol/kg) or PPG (37.5 mg/kg) was injected intraperitoneally 2 h before CS or LPS exposure in NaHS or PPG treatment group, respectively. The control group underwent an identical schedule but received air or saline instead. Rats were anesthetized by intraperitoneal injection of 20% (w/v) urethane (5 ml/kg) 24 h later after the last CS exposure and processed to lung function test. The rats were sacrificed by exsanguination from abdominal artery.

2.2. Lung Function Test and Histological Analysis. Lung function was tested as previously described [18]. Peak expiratory flow (PEF), peak inspiratory flow (PIF), intrapressure (IP), and maximum rising slope of IP (IP slope) were analyzed using Chart 4.1 software (AD Instruments, Australia).

Histological analysis of rat lung and pathological scores was performed as previously described [22]. Briefly, the left lung tissue was fixed in 4% paraformaldehyde solution and embedded in paraffin. The lung tissue slices (5 μm) were stained with hematoxylin and eosin (H&E), periodic acid-schiff (PAS), and Masson trichrome separately. The pathological scores were evaluated according to the following nine parameters with mild modification, namely constriction or occlusion of the small airway lumen, abscission or ulceration, squamous cell metaplasia, goblet cell proliferation of epithelium, inflammatory cell infiltration, pigment deposits, proliferation of fibrous tissue, smooth muscle hypertrophy in the airway wall, and emphysema of lung tissue. Three membranous bronchioles of each rat were selected for evaluation at random. Score for each parameter was ranged from 0 (normal) to 3 (abnormal). A total pathological score is calculated by summing the scores to all nine parameters in each rat. Scoring was performed in a blinded test.

2.3. MDA Concentration, Total SOD Activity, and CAT Activity. Rat lung tissues stored in -80°C fridge were homogenized in cold sterile saline on ice. Malondialdehyde (MDA) concentration, total superoxide dismutase (T-SOD), and catalase (CAT) activity were measured by spectrophotometry according to manufacturer's instructions (Jiancheng Bioengineering Institute, Nanjing, China) as previously described [27]. The MDA concentration was expressed as $nmol.mg^{-1}$ protein. The T-SOD and CAT activity were expressed as $units.mg^{-1}$ protein.

2.4. Western Blotting Analysis. The protein extraction of lung tissue was boiled with gel-loading buffer for 10 min at 100°C, resolved on 12% SDS-PAGE, and transferred to nitrocellulose membranes. The membranes were probed with CTH antibody (1 : 2000, Abnova, Taiwan) or β-actin antibody (Santa Cruz Biotechnology) and visualized with enhanced chemiluminescence (Applygen Technologies; Beijing). The protein levels were quantified by Image J software and normalized to β-actin as an internal control.

2.5. RNA Extraction and Microarray Analysis. Total RNA was extracted from the left upper lobe of rat lungs using Trizol reagent (Invitrogen, Carlsbad, CA) according to the manufacturer's instructions. The purity and concentration of RNA was detected using NanoDrop 2000 spectrophotometer. The quality of RNA was assessed using Agilent 2100 Bioanalyzer, and samples with a RIN (RNA integrity number) of >7.0 were used in this study. cRNA was hybridized against Agilent G4853A GeneChips. Microarray experiments were performed following manufacturer's instructions. The raw data was analyzed using GeneSpring version 12.0 software. The screened differentially expressed DE

genes were processed to cluster analysis, GO, and KEGG enrichment analysis using Funnet (http://www.funnet.info).

2.6. Statistical Analysis. Data are expressed as mean ± standard deviation (SD) or mean ± standard error of mean (SEM). Statistical significance in pathological scores among groups is tested with Kruskal-Wallis test followed by Dunn's post test. Other comparisons among groups are tested with one-way analysis of variance followed by Turkey test. Unpaired *t*-test is used between the two groups (GraphPad prism version 5). To derive DE genes, the fold change ≧2 is considered as upregulation or downregulation. A value of $P < 0.05$ is considered statistically significant.

3. Results

3.1. Body Weight and Lung Function. The COPD rat model was established by continuous cigarette smoking and intratracheal instillation of lipopolysaccharide (LPS) for 2 times. The body weight of each rat was monitored each day before the administration of NaHS or PPG.

Before experiment, there was no significant difference in body weight of rats among the groups. By the end of the experiment, the body weight in the CS + LPS group was decreased significantly compared with the control. Compared with the CS + LPS group, there was no significance in body weight of rats by NaHS treatment, but PPG treatment decreased body weight markedly (Table 1).

For lung function, The peak expiratory flow (PEF) was significantly lower in the CS + LPS group than that in the control group, whereas intrapressure (IP) was 66% higher (all $P < 0.01$) (Table 2). No significant differences were detected in lung function after NaHS or PPG treatment compared with the CS + LPS group (Table 2).

Data are expressed as mean ± SD, $n = 7$/group; $^{*}P < 0.05$ vs. control, $^{***}P < 0.001$ vs. CS + LPS group.

PIF, peak inspiratory flow; PEF, peak expiratory flow; IP, intrapressure; IP slope, maximum rising slope of IP. Data are expressed as mean ± SD, $n = 7$/group, $^{**}P < 0.01$, and $^{***}P < 0.001$ vs. control.

3.2. NaHS Treatment Alleviated Lung Injury in Rats Exposed to CS Combined with LPS. In CS + LPS group, represented COPD rat model, the lung sections by histological analysis showed the following pathological features: airway mucus secretion and inflammatory cell obstruction, necrosis and erosion of bronchial epithelium, metaplasia of airway goblet cells, airway inflammatory cell infiltration, proliferation of fibrous tissues in airway wall, and emphysema, and each features was shown in different degrees. Chronic bronchitis was the main feature of this model. The lung pathological injury scores in the CS + LPS group were increased significantly compared with that in the control group ($P < 0.01$) (Figures 1(a), 1(b), 1(c), and 1(d)), whereas the scores were decreased by NaHS treatment ($P < 0.01$). No significant difference was detected in pathological scores between CS + LPS and CS + LPS + PPG group. The raw histological images were provided in supplementary files (SF1).

Table 1: The body weight of rats in each group before and after experiment.

Group	Preexperiment (g)	Postexperiment (g)
Control	246.4 ± 6.4	436.7 ± 34.88
CS + LPS	241.5 ± 15.1	384.4 ± 18.36*
CS + LPS + NaHS	241.9 ± 6.1	394.0 ± 24.1
CS + LPS + PPG	239.4 ± 9.4	305.2 ± 37.7***

3.3. Oxidant/Antioxidant Stress Imbalance. MDA, SOD, and CAT activities were selected to act as markers of oxidative stress. Compared with the control, in the CS + LPS group, the MDA concentration in lung tissues was increased by 24% ($P < 0.05$) (Figure 2(a)); compared with the CS + LPS group, NaHS treatment decreased MDA concentration by 21% ($P < 0.05$), whereas there is no significant difference for MDA concentration after the blockade of endogenous CTH with PPG; compared with the control group, the T-SOD and CAT activity in the CS + LPS group were increased by 47% and 52% ($P < 0.01$), respectively; However, compared with the CS + LPS group, after the administration of NaHS or PPG, there is no significantly difference for CAT activity among the groups, but the T-SOD activity was decreased by 33% in the CS + LPS + PPG group compared with the CS + LPS group ($P < 0.05$) (Figures 2(b) and 2(c)).

3.4. Chronic Exposure to CS Combined with LPS Increased CTH Protein Expression Level. CTH protein expression level in lung tissue was increased in the CS + LPS group compared with the control group ($P < 0.01$) (Figure 3); however, after the administration of NaHS or PPG, there was no statistical significance for CTH protein level compared with CS + LPS group.

3.5. DE Genes Screened by Microarray Analysis. There were total 30507 genes on gene chips, of which 20726 genes were detected and 9781 genes were not detected. Genes with fold change (FC) ≥ 2 and $P < 0.05$ were accepted as DE genes. The gene expression data was deposited in Gene Expression Omnibus (GEO), and the GEO accession number is GSE184693 (https://www.ncbi.nlm.nih.gov/geo/info/linking.html). Comparing the CS + LPS group with control, 341 DE genes were identified, of these 341 genes, 108 genes were downregulated, and 233 genes upregulated; comparing the CS + LPS + NaHS or CS + LPS + PPG group with the control group, 241 and 448 DE genes were identified, respectively; comparing the CS + LPS + NaHS group with the CS + LPS group, 191 DE genes were identified, of these 191 genes, 40 genes were downregulated, and 151 genes upregulated; comparing the CS + LPS + PPG group with the CS + LPS group, 217 DE genes were identified, of these 217 genes, 56 genes were downregulated, and 161 genes upregulated (Table 3).

3.6. Cluster Analysis. The genes were processed to unsupervised hierarchical cluster analysis. Generally, subjects with similar characteristics will cluster together into the same cluster, and the DE genes with similar expression patterns

Table 2: Lung function.

Group	PIF(L/S)	PEF(L/S)	IP(mmHg)	IPslope(mmHg/s)
Control	3.09 ± 0.19	6.13 ± 0.99	0.90 ± 0.42	91.99 ± 16.26
CS + LPS	2.97 ± 0.12	4.68 ± 0.16***	1.49 ± 0.16**	95.52 ± 8.23
CS + LPS + NaHS	2.96 ± 0.10	4.93 ± 0.13	1.33 ± 0.20	91.07 ± 4.92
CS + LPS + PPG	2.96 ± 0.10	4.80 ± 0.27	1.45 ± 0.18	87.67 ± 3.42

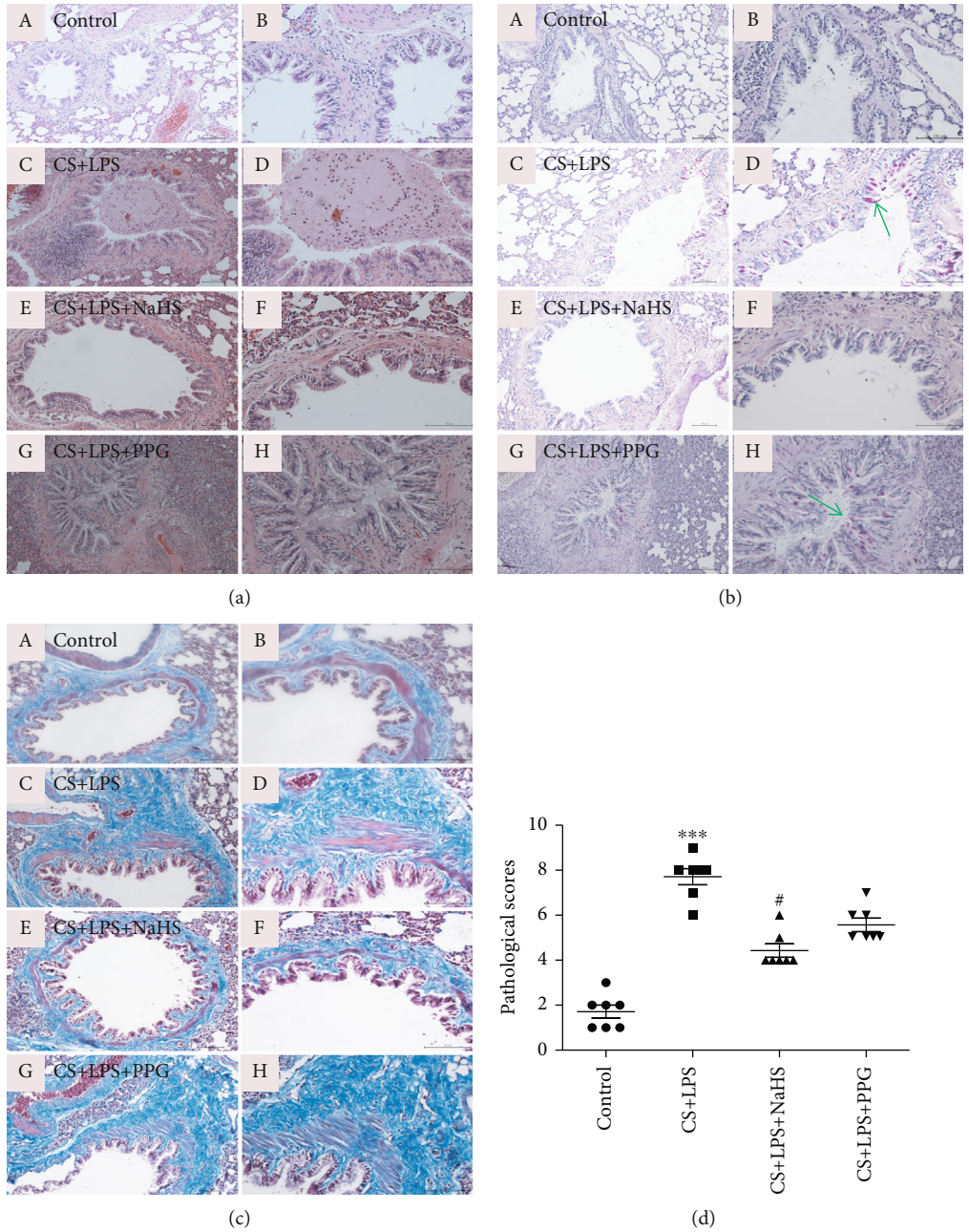

Figure 1: Histological analysis of lung tissue section. (a) H&E staining. (b) PAS staining, arrows indicate positive staining. (c) Masson trichrome staining. (A) and (B): control group; (C) and (D): CS + LPS group; (E) and (F): CS + LPS + NaHS group; (G), (H): CS + LPS + PPG group. (A), (C), (E), and (G) (magnification ×100); (B), (D), (F), and (H) (magnification ×200). (d) Pathological scores of rat lung tissues. Data are expressed as mean ± SEM ($n = 7$/group), $^{***}P < 0.001$ vs. control; $^{\#}P < 0.05$ vs. CS + LPS group.

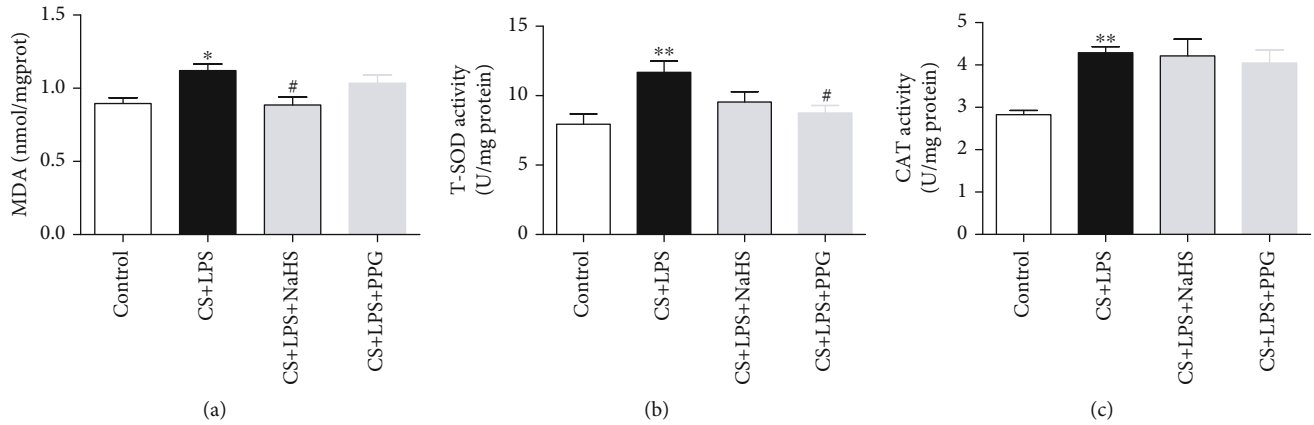

Figure 2: MDA concentration and T-SOD and CAT activities in rat lung tissues. (a) MDA concentration; (b) T-SOD activity; (c) CAT activity. Data are expressed as mean ± SEM ($n = 7$/group), $^{*}P < 0.05$, $^{**}P < 0.01$ vs. control, and $^{\#}P < 0.05$ vs. CS + LPS group.

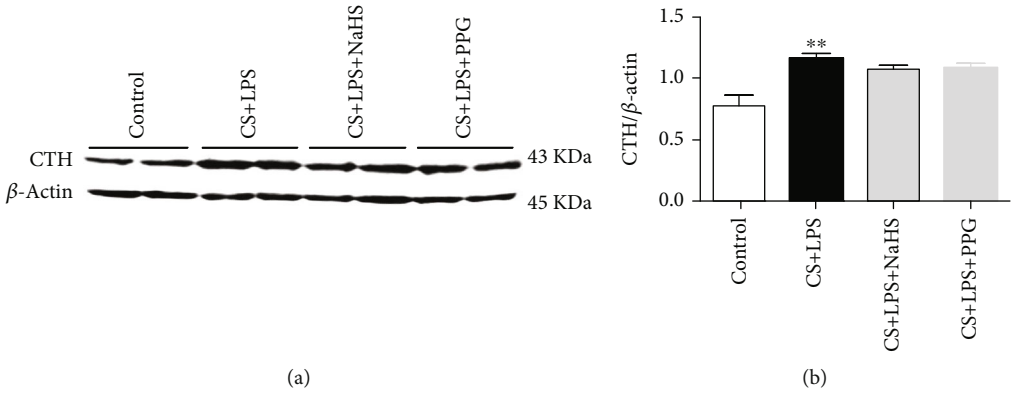

Figure 3: CTH protein in rat lung tissues. (a) Representative band of western blotting. β-Actin was reference control. (b) Quantification of CTH protein level by Image J software. Data are expressed as mean ± SEM ($n = 4$/group), $^{**}P < 0.01$ vs. control.

Table 3: The number of DE Genes.

Comparison group	Reference group	Upregulated	Downregulated	Total
CS + LPS	Control	233	108	341
CS + LPS + NaHS	Control	127	114	241
CS + LPS + PPG	Control	287	161	448
CS + LPS + NaHS	CS + LPS	151	40	191
CS + LPS + PPG	CS + LPS	161	56	217

$^{*}n = 3$/group.

will cluster together, and we found the subjects in the same group were clustered together. Thereafter, all the DE genes were annotated by GO and KEGG enrichment analysis (in the following sections), 27 DE genes involved in apoptosis, oxidative stress, and inflammation, and engulfment pathways were selected to cluster again with unsupervised hierarchical cluster analysis; it showed that subjects in the same group clustered together, the gene expression profiling between the CS + LPS and control group has big difference, and the gene expression profiling in theCS + LPS + NaHS group was close to the control group (Figure 4).

3.7. GO Enrichment Analysis. The GO enrichment analysis includes biological process category, molecular function category, and cellular component category. All the DE genes were annotated by GO enrichment analysis.

Between CS + LPS group and control group, 163 DE genes were annotated in GO biological processes. According to the number of DE genes annotated by the considered GO biological process category, the top 5 signaling pathways were shown as follows: response to drug (12 genes), multicellular organismal development (11 genes), positive regulation of apoptosis (9 genes), immune response (9 genes), and inflammatory response (8 genes) (Figure 5(a)). The DE genes involved in positive regulation of apoptosis pathway are *Itga6* (integrin, alpha6), *C6* (complement component 6), *Igfbp3* (insulin-like growth factor binding protein 3), *Itgb1* (integrin, beta1), *Jun* (Jun oncogene), *Tnfrsf8* (tumor

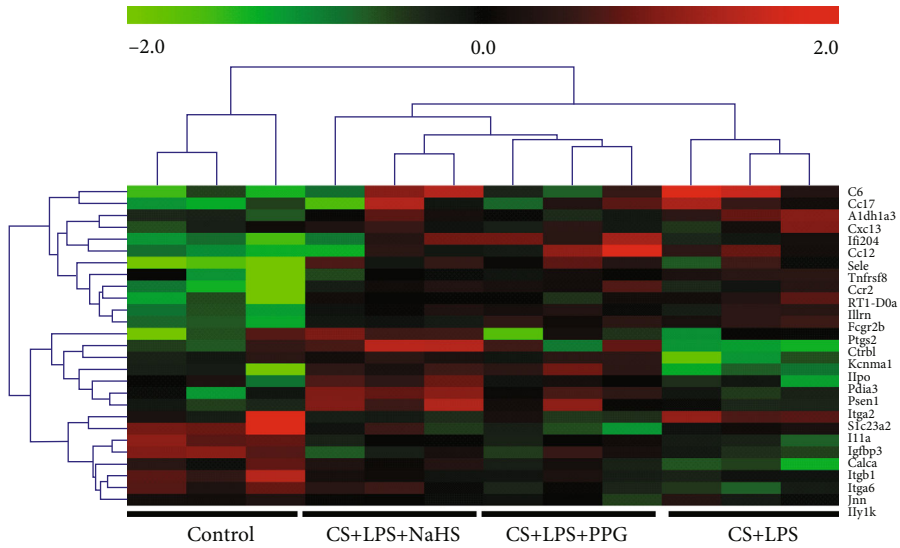

Figure 4: Heat map of unsupervised hierarchical cluster analysis of representative genes. Data from individual subjects and individual genes are shown in columns and rows separately. The color represents the intensity of the signal ($n = 3$/group). Green bars represent low expression levels, red bars represent high expression levels, and black bars represent no change relative to normalized median gene expression values.

necrosis factor receptor superfamily, member 8), *Aldh1a3* (aldehyde dehydrogenase 1 family, member A3), *Ifi204* (interferon activated gene 204), and *Kcnma1* (potassium large conductance calcium-activated channel, subfamily M, alpha member1) (Table 4).

Between CS + LPS + NaHS group and CS + LPS group, 92 DE genes were annotated in GO biological process, and the top 5 signaling pathways were shown as follows: nervous system development (7 genes), positive regulation of apoptosis (6 genes), transmembrane transport (6 genes), cell proliferation (5 genes), and negative regulation of cell proliferation (5 genes) (Figure 5(b)). The DE genes involved in positive regulation of apoptosis pathway are *Itgb1*, *Kcnma1*, *Psen1* (presenilin 1), *Pdia3* (protein disulfide isomerase family A member 3), *Ptgs2* (prostaglandin-endoperoxide synthase 2), and *Ctrb1* (chymotrypsinogen B1) (Table 4). Notably, *Itgb1* and *Kcnma1* were downregulated in the CL + LPS group compared with the control group but upregulated in the NaHS-treated group compared with the CL + LPS group. Between CS + LPS + NaHS group and CS + LPS group, there were 4 genes involved in response to oxidative stress pathway, namely *Psen1*, *Ptgs2* (prostaglandin endoperoxide synthase 2), *Mpo* (myeloperoxidase), and *Slc23a2* (solute carrier family 23 member 2), the former three genes were upregulated in the NaHS treatment group compared with the CS + LPS group, and the latter one was downregulated. The gene *Ppargc1a* (peroxisome proliferator-activated receptor gamma, coactivator 1 alpha) is involved in the regulation of cell death, positive regulation of gluconeogenesis, positive regulation of fatty acid oxidation, negative regulation of neuron apoptosis, and neuron death, and it was upregulated in the NaHS treatment group compared with the CS + LPS group.

Between CS + LPS + PPG group and CS + LPS group, 98 DE genes were annotated in GO biological process, and the top 5 signaling pathways were shown as follows: immune response (10 genes), antigen processing and presentation (8 genes), cell adhesion (7 genes), antigen processing and presentation of peptide antigen via MHC class I (7 genes), and positive regulation of cell proliferation (6 genes) (Figure 5(c)).

The detailed DE genes annotated by considered GO biological process category, GO molecular function category, and cellular component category were in supplementary data online (File S2).

3.8. KEGG Enrichment Analysis. All the DE genes were also annotated by the considered KEGG category.

Between CS + LPS group and control group, 85 DE genes were annotated by the considered KEGG category. According to the number of DE genes annotated by the considered KEGG category, the top 5 signaling pathways were shown as follows: cell adhesion molecules (9 genes), leishmaniasis (8 genes), phagosome (8 genes), toxoplasmosis (7 genes), and systemic lupus erythematosus (7 genes) (Figure 6(a)).

Between CS + LPS + NaHS group and CS + LPS group, 39 DE genes were annotated by the considered KEGG category, and the top 5 signaling pathways were shown as follows: phagosome (4 genes), focal adhesion (4 genes), regulation of actin cytoskeleton (4 genes), small cell lung cancer (3 genes), and leukocyte transendothelial migration (3 genes) (Figure 6(b)).

Between CS + LPS + PPG group and CS + LPS group, 52 DE genes were annotated by the considered KEGG category, and the top 5 signaling pathways were shown as follows: phagosome (9 genes), cell adhesion molecules (9 genes), endocytosis (8 genes), antigen processing and presentation (8 genes), and type 1 diabetes mellitus (8 genes) (Figure 6(c)).

The detailed DE genes annotated by considered KEGG enrichment analysis were in supplementary data online (File S3).

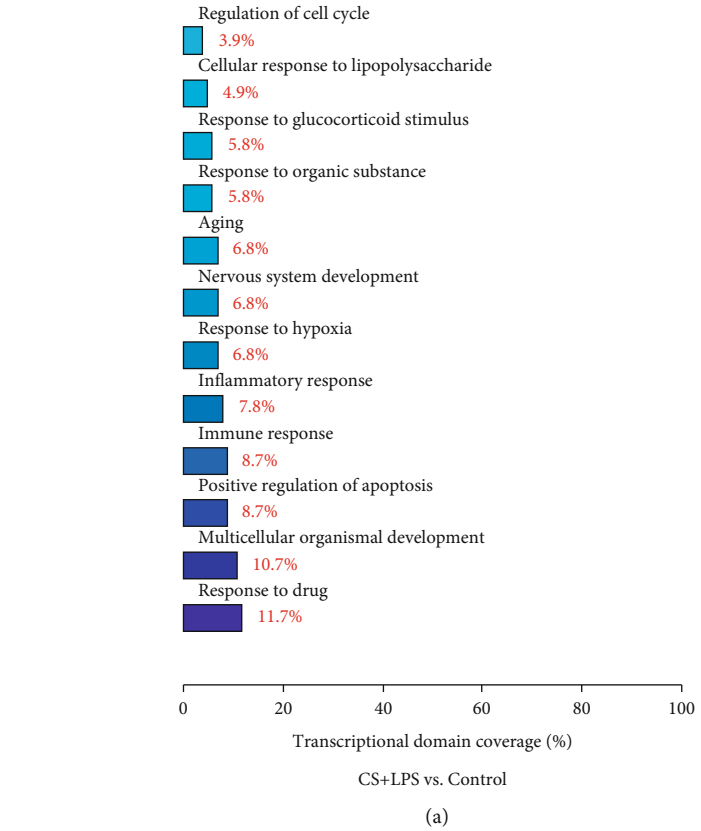

(a)

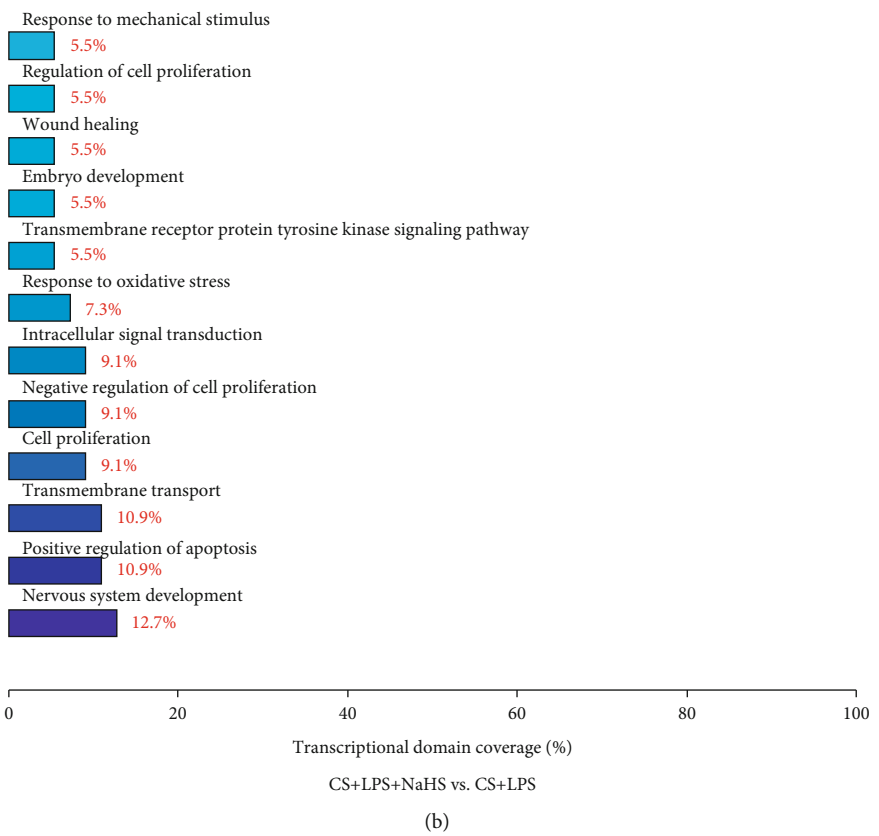

(b)

Figure 5: Continued.

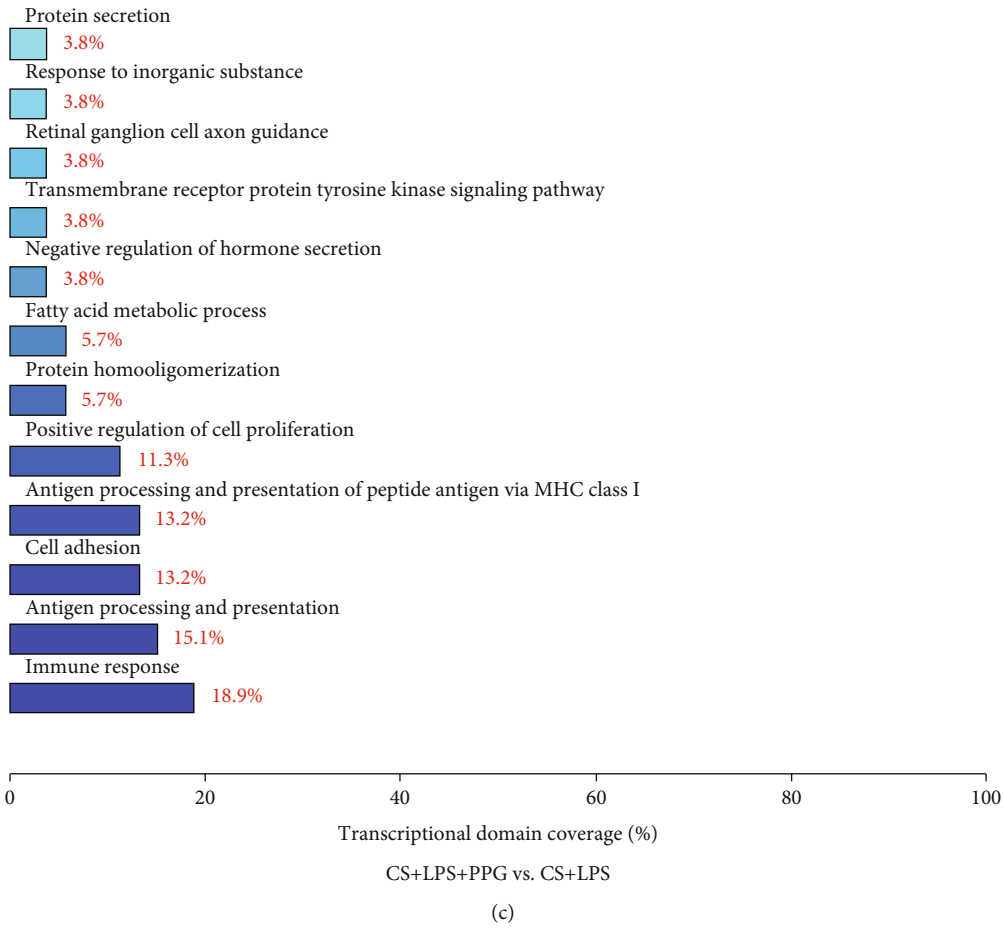

Figure 5: DE genes annotated by the considered GO biological process category. The DE genes between CS + LPS and control group (a), between CS + LPS + NaHS and CS + LPS group (b), and between CS + LPS + PPG and CS + LPS group (c), respectively. (n = 3/group).

Table 4: The DE Genes involved in positive regulation of apoptosis or response to oxidative stress.

GO biological process		
Positive regulation of apoptosis		Response to oxidative stress
CS + LPS/control	CS + LPS + NaHS/CS + LPS	CS + LPS + NaHS/CS + LPS
Itgb1↓	*Itgb1*↑	*Slc23a2*↓
Kcnma1↓	*Kcnma1*↑	*Mpo*↑
Igfbp3↓	*Ctrb1*↑	*Psen1*↑
Itga6↓	*Pdia3*↑	*Ptgs2*↑
Jun↓	*Psen1*↑	–
Aldh1a3↑	*Ptgs2*↑	–
C6↑	–	–
Ifi204↑	–	–
Tnfrsf8↑	–	–

"↓":downregulated; "↑": upregulated.

4. Discussion

In the present study, in order to shorten the induction of COPD rat model, we established the model by exposure to CS and LPS, and histological analysis of lung has shown some pathological features of COPD, such as airway mucus and inflammatory cells obstruction, airway inflammatory cell infiltration, and proliferation of fibrous connective tissues in airway wall, and this model showed the main features of chronic bronchitis. Our findings showed that the pathological scores in the COPD rat model and the lipid peroxidation product MDA were increased significantly compared

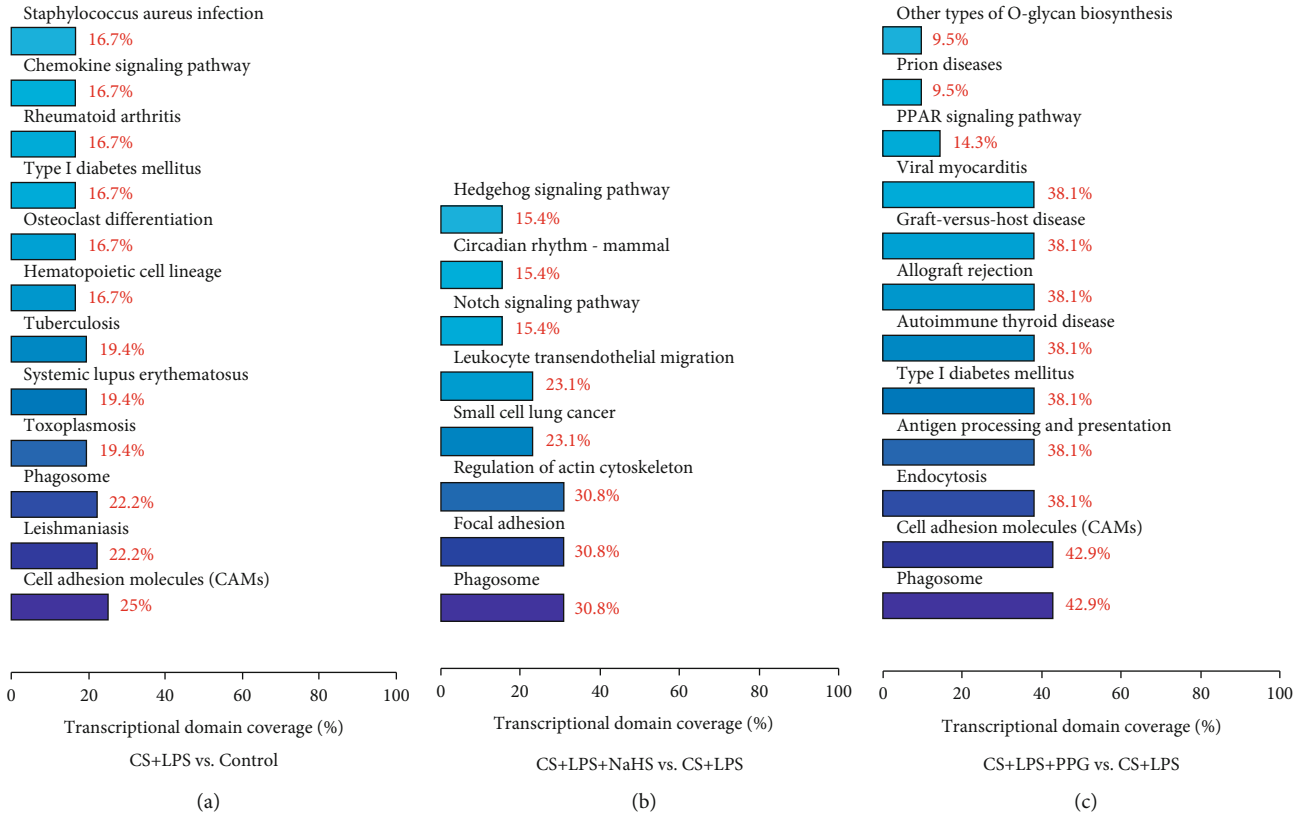

Figure 6: DE genes annotated by the considered KEGG category. The DE genes between CS + LPS and control group (a), between CS + LPS + NaHS and CS + LPS group (b), and between CS + LPS + PPG and CS + LPS group (c), respectively. ($n = 3$/group).

with the control and reduced by NaHS treatment. The activities of antioxidant enzymes T-SOD and CAT were also increased significantly in the rat model of COPD, and the PPG treatment reduced the activity of T-SOD and body weight. Furthermore, with microarray analysis, we found lots of DE genes were implicated in multiple biological pathways, such as response to oxidative stress and regulation of apoptosis pathways, and some DE genes, such as *Ppargcla*, *Itgb1*, *Kcnma*, *Ptgs2*, and *Psen1*, may play the role of antioxidative stress and antiapoptosis in the rat model of COPD.

Oxidative stress is one of critical mechanisms in the development of COPD [8]. As a lipid peroxidation product, serum MDA concentration was higher in patients with COPD compared with healthy people [28], consistent with previous study, MDA concentration in lung tissue of COPD rat model was higher compared with the control in our study. SOD enzymes include CuZnSOD, MnSOD (SOD2), and SOD3, SOD3 levels in induced sputum supernatants of COPD patients were higher compared to nonsmokers [29], and in our study, both total SOD and CAT activity were increased in COPD rat model, it may be a compensatory mechanism to counteract the acceleration of oxidative stress. H_2S, as a gasotranmitter following NO and CO, has its own antioxidant features. H_2S scavenged peroxynitrite and inhibited peroxynitrite-induced tyrosine nitration [30], it enhanced glutathione production in cells and alleviated cell injury induced by oxidative stress [31], and it also alleviated cigarette smoke extraction or LPS-induced oxidative stress [32, 33]. Our study demonstrated that the NaHS treatment reduced the pathological injury scores and MDA concentration compared to the COPD rat model, and the PPG treatment reduced the activity of T-SOD and body weight of rats. It is suggested that H_2S acts as an antioxidant to protect against oxidative stress in this COPD rat model. The CAT activity was not changed by NaHS or PPG treatment, and the mechanism needs to be investigated in future study.

COPD is a progressive and irreversible disorder, whichever genes involved in its pathogenesis is incompletely understood. The present study applied microarray analysis to investigate the impact of H_2S on gene expression profiling in COPD. Our study has found some DE genes between NaHS treatment group and CS + LPS group, such as *Psen1*, *Ptgs2*, *Mpo*, and *Slc23a2*, were involved in oxidative stress pathway, and *Ppargc1a* was upregulated by NaHS treatment. The protein encoded by *Ppargc1a* gene (also known as PGC-1α in human) is peroxisome proliferator-activated receptor gamma coactivator 1α (PGC-1α), as a transcriptional coactivator, it is an important regulator of energy metabolism [34], overexpressed PGC-1α alleviates oxidative stress and decreases apoptotic cell death in endothelial cells [34], and upregulation of PGC-1α is associated with reduction of oxidative stress and inflammation in diabetic myocardium [35] and attenuation of COPD in mice [36]. PGC-1α is essential for the induction of ROS-detoxifying enzymes such as glutathione peroxidase and SOD2 under oxidative stress, PGC-1α null mice were sensitive to oxidative stress [37]; PGC-1α inhibited mitochondrial oxidative stress by facilitating Nrf2

binding to antioxidant response element promoter site and inducing SOD2 expression in sepsis [38]. It is suggested that the upregulation of PGC-1α by H_2S is one of the mechanisms for antioxidative stress and for the treatment of COPD.

Apoptosis is one kind of regulated cell death [9], many studies have shown that apoptotic cells are increased in the lungs of COPD patients [39], and apoptosis of epithelial and endothelial lung cells led to lung parenchyma destruction and emphysema; animal experiments have also proven that apoptosis is involved in the pathogenesis of COPD [40]. In the present study, 6 differential expressed genes between NaHS treatment group and CS + LPS group were involved in the positive regulation of apoptosis pathway (Table 4), such as *Ptgs2* and *Itgb1*, and these two genes were upregulated by NaHS treatment. *Ptgs2* encodes protein prostaglandin-endoperoxide synthase 2 is also known as cyclooxygenase 2 (COX-2). COX-2 is an enzyme that catalyzes the production of thromboxanes and prostaglandins from arachidonic acid, it is related with tumorigenesis, and the overexpression of COX-2 inhibits apoptosis [41]. In contrast, inhibition of COX-2 promoted TGF-β-induced apoptosis and aortic valve calcification [42]. In addition, *Itgb1* encodes protein β1 integrin, which is one subunit of integrins. Integrins are membrane receptors that mediate cell adhesion and migration. Cultured pancreatic acinar cells from β1 integrin-deficient mice showed an increase of cell apoptosis [43]; β1 integrin is important for the survival of vascular smooth muscle cells, the conditional deletion of *Itgb1* in adult mice resulted in vascular smooth muscle cell apoptosis and vascular fibrosis [44]; edothelial β1 integrin is indispensable for embryonic liver growth, deletion of *Itgb1* in endothelial cells results in smaller liver size and more apoptotic cells in liver [45]. Our previous study has shown that H_2S attenuated cigarette smoke-induced apoptosis in rat lung [46], and the upregulation of gene *Ptgs2* and *Itgb1* by H_2S may contribute to attenuate apoptosis in the lungs of COPD rat model. It needs further validation in vitro in future study.

The novelty of the present study is that we screened many DE genes regulated by H_2S in COPD rat model, and by bioinformatic analysis, we found that the DE genes were involved in multiple signaling pathways, such as oxidative stress, apoptosis, immune response, and inflammation response pathways, and several genes were upregulated by H_2S treatment. However, there are several drawbacks in this study. The first drawback is that we did not further verify the interesting DE genes by quantitative real-time polymerase chain reaction (qRT-PCR). Another drawback is that we did not detect markers of apoptosis in lung tissues, while our previous study has demonstrated that H_2S alleviated cigarette smoke-induced apoptosis *in vivo* [46], and the present work has proven the successful COPD rat model induced by cigarette smoking and LPS and detected the markers of oxidative stress.

Future studies are needed to confirm the DE genes regulated by H_2S in the development of COPD, such as *Ppargc1a, Ptgs2*, and *Itgb1*. It is indispensable to prove the function of these genes *in vivo* and *in vitro*. As microarray analysis screens thousands of genes and gives us too much information, it is meaningful to explore other interesting genes from the data. We afforded preliminary data of DE genes in this study, and the findings will give insight into future study for the mechanisms of H_2S in COPD.

Data Availability

The gene expression data used to support the findings of this study are deposited in the database Gene Expression Omnibus (GEO) (GEO accession number: GSE184693). Other data are included within the article and supplementary information files.

Conflicts of Interest

The authors declare no conflict of interest.

Authors' Contributions

He YJ, Sun Y, and Chen YH contributed to the conceptualization; He YJ and Sun Y contributed to the investigation; He YJ, Liao CC, Lin F, Xia ZY, and Qi YF contributed to the methodology; Chen YH and Qi YF contributed to the resources; He YJ and Sun Y contributed to the writing-original draft; He YJ, Sun Y, Xia ZY, and Chen YH contributed to the writing-review and editing of this study. All authors have read and agreed to the version of this manuscript.

Acknowledgments

The authors thank Jingrui Chang, Xiaohui Duan, Lei Zhao, and Yajing Han for technical assistance. This work was supported by National Natural Science Foundation of China (Nos. 82090014 and 81970037).

Supplementary Materials

File S1: the raw histological images. File S2: the DE genes annotated by considered GO enrichment analysis between CS + LPS and control group, between CS + LPS + NaHS and CS + LPS group, and between CS + LPS + PPG and CS + LPS group. File S3: the DE genes annotated by considered KEGG enrichment analysis between CS + LPS and control group, between CS + LPS + NaHS and CS + LPS group, and between CS + LPS + PPG and CS + LPS group. *(Supplementary Materials)*

References

[1] D. M. Mannino and A. S. Buist, "Global burden of COPD: risk factors, prevalence, and future trends," *Lancet*, vol. 370, no. 9589, pp. 765–773, 2007.

[2] R. Lozano, M. Naghavi, K. Foreman et al., "Global and regional mortality from 235 causes of death for 20 age groups in 1990 and 2010: a systematic analysis for the global burden of disease study 2010," *Lancet*, vol. 380, no. 9859, pp. 2095–2128, 2012.

[3] S. I. Rennard and J. Vestbo, "COPD: the dangerous underestimate of 15," *Lancet*, vol. 367, no. 9518, pp. 1216–1219, 2006.

[4] B. Lamprecht, M. A. McBurnie, W. M. Vollmer et al., "COPD in never smokers: results from the population-based burden of obstructive lung disease study," *Chest*, vol. 139, no. 4, pp. 752–763, 2011.

[5] R. De Marco, S. Accordini, A. Marcon et al., "Risk factors for chronic obstructive pulmonary disease in a European cohort of young adults," *American Journal of Respiratory and Critical Care Medicine*, vol. 183, no. 7, pp. 891–897, 2011.

[6] P. Strnad, N. G. McElvaney, and D. A. Lomas, "Alpha1-antitrypsin deficiency," *The New England Journal of Medicine*, vol. 382, no. 15, pp. 1443–1455, 2020.

[7] N. Mercado, K. Ito, and P. J. Barnes, "Accelerated ageing of the lung in COPD: new concepts," *Thorax*, vol. 70, no. 5, pp. 482–489, 2015.

[8] P. J. Barnes, "Oxidative stress-based therapeutics in COPD," *Redox Biology*, vol. 33, pp. 101544–101544, 2020.

[9] I. S. B. Maor Sauler and P. J. Lee, "Cell death in the lung: the apoptosis-necroptosis axis," *Annual Review of Physiology*, vol. 81, no. 1, pp. 375–402, 2019.

[10] P. J. Barnes, "Inflammatory mechanisms in patients with chronic obstructive pulmonary disease," *The Journal of Allergy and Clinical Immunology*, vol. 138, no. 1, pp. 16–27, 2016.

[11] K. C. Pandey, S. De, and P. K. Mishra, "Role of proteases in chronic obstructive pulmonary disease," *Frontiers in Pharmacology*, vol. 8, pp. 512–512, 2017.

[12] R. Wang, "Two's company, three's a crowd: can H2S be the third endogenous gaseous transmitter?," *The FASEB Journal*, vol. 16, no. 13, pp. 1792–1798, 2002.

[13] M. H. Stipanuk and P. W. Beck, "Characterization of the enzymic capacity for cysteine desulphhydration in liver and kidney of the rat," *Biochemical Journal*, vol. 206, no. 2, pp. 267–277, 1982.

[14] R. De Marco, S. Accordini, A. Marcon et al., "3-Mercaptopyruvate sulfurtransferase produces hydrogen sulfide and bound sulfane sulfur in the brain," *Antioxidants & Redox Signaling*, vol. 11, no. 4, pp. 703–714, 2009.

[15] R. Wang, "Hydrogen sulfide: the third Gasotransmitter in biology and medicine," *Antioxidants and Redox Signaling*, vol. 12, no. 9, pp. 1061–1064, 2010.

[16] Y. H. Chen, W. Z. Yao, B. Geng et al., "Endogenous hydrogen sulfide in patients with COPD," *Chest Journal*, vol. 128, no. 5, pp. 3205–3211, 2005.

[17] Y. He, S. Liu, Z. Zhang et al., "Imbalance of endogenous hydrogen sulfide and homocysteine in chronic obstructive pulmonary disease combined with cardiovascular disease," *Frontiers in Pharmacology*, vol. 8, pp. 624–624, 2017.

[18] Y. H. Chen, R. Wu, B. Geng et al., "Endogenous hydrogen sulfide reduces airway inflammation and remodeling in a rat model of asthma," *Cytokine*, vol. 45, no. 2, pp. 117–123, 2009.

[19] K. F. Chung, "Hydrogen sulfide as a potential biomarker of asthma," *Expert Review of Respiratory Medicine*, vol. 8, no. 1, pp. 5–13, 2014.

[20] X. Zhou, G. An, and J. Chen, "Inhibitory effects of hydrogen sulphide on pulmonary fibrosis in smoking rats via attenuation of oxidative stress and inflammation," *Journal of Cellular and Molecular Medicine*, vol. 18, no. 6, pp. 1098–1103, 2014.

[21] L. Xiaohui, D. Junbao, S. Lin et al., "Down-regulation of endogenous hydrogen sulfide pathway in pulmonary hypertension and pulmonary vascular structural remodeling induced by high pulmonary blood flow in rats," *Circulation Journal*, vol. 69, no. 11, pp. 1418–1424, 2005.

[22] Y. H. Chen, P. P. Wang, X. M. Wang et al., "Involvement of endogenous hydrogen sulfide in cigarette smoke-induced changes in airway responsiveness and inflammation of rat lung," *Cytokine*, vol. 53, no. 3, pp. 334–341, 2011.

[23] J. W. Calvert, S. Jha, S. Gundewar et al., "Hydrogen sulfide mediates cardioprotection through Nrf2 signaling," *Circulation Research*, vol. 105, no. 4, pp. 365–374, 2009.

[24] A. Sivarajah, M. Collino, M. Yasin et al., "Anti-apoptotic and anti-inflammatory effects of hydrogen sulfide in a rat model of regional myocardial I/R," *Shock*, vol. 31, no. 3, pp. 267–274, 2009.

[25] W. Han, Z. Dong, C. Dimitropoulou, and Y. Su, "Hydrogen sulfide ameliorates tobacco smoke-induced oxidative stress and emphysema in mice," *Antioxidants & Redox Signaling*, vol. 15, no. 8, pp. 2121–2134, 2011.

[26] N. Mizutani, J. I. Fuchikami, M. Takahashi, T. Nabe, S. Yoshino, and S. Kohno, "Pulmonary emphysema induced by cigarette smoke solution and lipopolysaccharide in Guinea pigs," *Biological & Pharmaceutical Bulletin*, vol. 32, no. 9, pp. 1559–1564, 2009.

[27] G. J. Xu, H. Li, M. G. Irwin et al., "Propofol ameliorates hyperglycemia-induced cardiac hypertrophy and dysfunction via heme oxygenase-1/signal transducer and activator of transcription 3 signaling pathway in rats," *Critical Care Medicine*, vol. 42, no. 8, pp. e583–e594, 2014.

[28] P. Joppa, D. Petrášová, B. Stančák, Z. Dorková, and R. Tkáčová, "Oxidative stress in patients with COPD and pulmonary hypertension," *Wiener Klinische Wochenschrift*, vol. 119, no. 13-14, pp. 428–434, 2007.

[29] E. A. Regan, W. Mazur, E. Meoni et al., "Smoking and COPD increase sputum levels of extracellular superoxide dismutase," *Free Radical Biology & Medicine*, vol. 51, no. 3, pp. 726–732, 2011.

[30] M. Whiteman, J. S. Armstrong, S. H. Chu et al., "The novel neuromodulator hydrogen sulfide: an endogenous peroxynitrite 'scavenger'?," *Journal of Neurochemistry*, vol. 90, no. 3, pp. 765–768, 2004.

[31] Y. Kimura, Y.-I. Goto, and H. Kimura, "Hydrogen sulfide increases glutathione production and suppresses oxidative stress in mitochondria," *Antioxidants & Redox Signaling*, vol. 12, no. 1, pp. 1–13, 2010.

[32] R. Guan, Z. Cai, J. Wang et al., "Hydrogen sulfide attenuates mitochondrial dysfunction-induced cellular senescence and apoptosis in alveolar epithelial cells by upregulating sirtuin 1," *Aging (Albany NY)*, vol. 11, no. 24, pp. 11844–11864, 2019.

[33] K. K. Zimmermann, S. G. Spassov, K. M. Strosing et al., "Hydrogen sulfide exerts anti-oxidative and anti-inflammatory effects in acute lung injury," *Inflammation*, vol. 41, no. 1, pp. 249–259, 2018.

[34] I. Valle, A. Álvarez-Barrientos, E. Arza, S. Lamas, and M. Monsalve, "PGC-1α regulates the mitochondrial antioxidant defense system in vascular endothelial cells," *Cardiovascular Research*, vol. 66, no. 3, pp. 562–573, 2005.

[35] R. Kosuru, V. Kandula, U. Rai, S. Prakash, Z. Xia, and S. Singh, "Pterostilbene decreases cardiac oxidative stress and inflammation via activation of AMPK/Nrf2/HO-1 pathway in fructose-fed diabetic rats," *Cardiovascular Drugs and Therapy*, vol. 32, no. 2, pp. 147–163, 2018.

[36] A. Miyamoto, K. Asai, H. Kadotani et al., "Ninjin'yoeito ameliorates skeletal muscle complications in COPD model mice by

upregulating peroxisome proliferator-activated receptor γ coactivator-1α expression," *International Journal of Chronic Obstructive Pulmonary Disease*, vol. Volume 15, pp. 3063–3077, 2020.

[37] J. St-Pierre, S. Drori, M. Uldry et al., "Suppression of reactive oxygen species and neurodegeneration by the PGC-1 transcriptional coactivators," *Cell*, vol. 127, no. 2, pp. 397–408, 2006.

[38] A. D. Cherry, H. B. Suliman, R. R. Bartz, and C. A. Piantadosi, "Peroxisome proliferator-activated receptor γ co-activator 1-α as a critical co-activator of the murine hepatic oxidative stress response and mitochondrial biogenesis in Staphylococcus aureus sepsis," *The Journal of Biological Chemistry*, vol. 289, no. 1, pp. 41–52, 2014.

[39] Y. A. S. U. N. O. R. I. Kasahara, R. M. Tuder, C. D. Cool, D. A. Lynch, S. C. Flores, and N. F. Voelkel, "Endothelial cell death and decreased expression of vascular endothelial growth factor and vascular endothelial growth factor receptor 2 in emphysema," *American Journal of Respiratory and Critical Care Medicine*, vol. 163, no. 3, pp. 737–744, 2001.

[40] B. Bartalesi, E. Cavarra, S. Fineschi et al., "Different lung responses to cigarette smoke in two strains of mice sensitive to oxidants," *The European Respiratory Journal*, vol. 25, no. 1, pp. 15–22, 2005.

[41] Y. Zhang, S. Tighe, and Y.-T. Zhu, "COX-2 signaling in the tumor microenvironment," in *Tumor Microenvironment : Molecular Players – Part B*, A. Birbrair, Ed., pp. 87–104, Springer International Publishing, Cham, 2020.

[42] F. Vieceli Dalla Sega, F. Fortini, P. Cimaglia et al., "COX-2 is downregulated in human stenotic aortic valves and its inhibition promotes dystrophic calcification," *International Journal of Molecular Sciences*, vol. 21, no. 23, p. 8917, 2020.

[43] M. M. Riopel, J. Li, S. Liu, A. Leask, and R. Wang, "β1 integrin-extracellular matrix interactions are essential for maintaining exocrine pancreas architecture and function," *Laboratory Investigation*, vol. 93, no. 1, pp. 31–40, 2013.

[44] K. A. Turlo, J. Scapa, P. Bagher et al., "β1-integrin is essential for vasoregulation and smooth muscle survival in vivo," *Arteriosclerosis, Thrombosis, and Vascular Biology*, vol. 33, no. 10, pp. 2325–2335, 2013.

[45] L. Lorenz, J. Axnick, T. Buschmann et al., "Mechanosensing by β1 integrin induces angiocrine signals for liver growth and survival," *Nature*, vol. 562, no. 7725, pp. 128–132, 2018.

[46] F. Lin, C. Liao, Y. Sun et al., "Hydrogen sulfide inhibits cigarette smoke-induced endoplasmic reticulum stress and apoptosis in bronchial epithelial cells," *Frontiers in Pharmacology*, vol. 8, pp. 675–675, 2017.

Hindawi
Oxidative Medicine and Cellular Longevity
Volume 2022, Article ID 9771743, 17 pages
https://doi.org/10.1155/2022/9771743

Research Article

Sevoflurane Improves Hemorrhagic Shock and Resuscitation-Induced Cognitive Impairments and Mitochondrial Dysfunctions through SIRT1-Mediated Autophagy

Jianwei Shu,[1,2,3] **Xiaotong Huang**,[1,2,3] **Qizhi Liao**,[1,2,3] **Jianan Wang**,[1,2,3] **Yuqi Zhou**,[4] **Yihuan Chen**,[4] **Ming Chen**,[4] **Cheng Qian**,[5] **Ye Zhang**,[1,2] **Xianwen Hu**,[1,2] **and Chunxia Huang**[1,2]

[1]*Department of Anesthesiology, The Second Affiliated Hospital of Anhui Medical University, Hefei City, Anhui Province, China*
[2]*Key Laboratory of Anesthesiology and Perioperative Medicine of Anhui Higher Education Institutes, Anhui Medical University, Hefei City, Anhui Province, China*
[3]*Scientific Research and Experiment Center of the Second Affiliated Hospital of Anhui Medical University, Hefei City, Anhui Province, China*
[4]*The Second Clinical Medical College of Anhui Medical University, Hefei City, Anhui Province, China*
[5]*Center for Scientific Research of Anhui Medical University, Hefei City, Anhui Province, China*

Correspondence should be addressed to Xianwen Hu; huxianwen001@163.com
and Chunxia Huang; huangchunxia@ahmu.edu.cn

Received 6 August 2021; Revised 25 January 2022; Accepted 10 February 2022; Published 11 March 2022

Academic Editor: Anwen Shao

Cerebral ischemia reperfusion injury (IRI) induced by hemorrhagic shock and reperfusion (HSR) is the main cause of death following trauma. Previous studies indicated the neuroprotective effect of sevoflurane postconditioning (SP) in cerebral IRI. However, the mechanisms still remain elusive. Cerebral IRI models with SP were established by using HSR with C57BL/6 mice (male, 3-month-old) *in vivo* and by using oxygen glucose deprivation and reoxygenation (OGD/R) with HT22 cells *in vitro*. Postoperative cognition was evaluated by the Morris water maze, novel object recognition, and elevated plus maze tests. The role of SIRT1 was determined by using siRNA, a sensitive inhibitor (EX527), or an overexpression shRNA-GFP lentivirus. IRI caused significant disabilities of spatial learning and memory associated with enhanced cerebral infarct and neuronal apoptosis, which were effectively attenuated by SP. IRI also made a significant decrease of SIRT1 accompanied by oxidative stress, mitochondria dysfunction, and inactivated autophagy. SP or genetically overexpressing SIRT1 significantly suppressed defective autophagy, mitochondrial oxidative injury, and neuronal death caused by HSR or OGD/R. However, genetic suppression or pharmacological inhibition of SIRT1 significantly reversed the impact of SP treatment on mitochondrial DNA transcription ability and autophagy. Our results demonstrate that the loss of SIRT1 causes a sequential chain of mitochondrial dysfunction, defective autophagy, and neuronal apoptosis after IRI in the preclinical stroke models. Sevoflurane postconditioning treatment could effectively attenuate pathophysiological signatures induced by noxious stimuli, which maybe mediated by SIRT1.

1. Introduction

Approximately 1.9 million people die of hemorrhagic shock every year in the world [1]. Hemorrhagic shock reperfusion (HSR) injury occurs when restoring circulating blood volume with diluted hemoglobin concentration, which further reduced oxygen supply and aggravated tissue damage [2]. As a scenario of ischemia-reperfusion injury (IRI), HSR increases the long-term mortality, leaves serious sequelae [3, 4], such as cognitive dysfunction [5], and causes serious burden to patients' families and the society. Although early mortality is low after severe trauma, chronic critical illness

is a common trajectory in survivors and is associated with poor long-term outcomes. Advancing age, shock severity, and persistent organ dysfunction are predictive variables of chronic critical illness [4]. Therefore, early identification may facilitate targeted interventions to change the trajectory of this morbid phenotype.

Silent information regulator-1 (SIRT1) is a nicotinamide adenine dinucleotide- (NAD+) dependent histone deacetylase, which can catalyze the deacetylation of acetyl lysine of histone and nonhistone substrates (such as p53 and FOXO). SIRT1 participates in the regulation of glucose and lipid metabolism, inflammation, cell aging and apoptosis, oxidative stress, and tumor formation. Numbers of studies reported that SIRT1 was downregulated in the IRI models, such as middle cerebral artery occlusion (MCAO) and reperfusion, oxygen glucose deprivation and reoxygenation (OGD/R). And it was also associated with multiple biocellular processes, including the activation of apoptosis and neuroinflammation [6], the suppression of angiogenesis [7], and mitochondrial oxidative stress and dysfunction [8]. In $SIRT1^{-/-}$ animals, the area of cerebral infarction was significantly increased following focal cerebral ischemia [9]. SIRT1 gene overexpression significantly alleviated hippocampal damage, including less cerebral infarction, and reduced neuronal degeneration and cognition improvement [10]. It has been regarded that SIRT1 elicits neuroprotective effect in decreasing apoptosis and neuronal damage through regulating autophagy [11]. Autophagy is a cellular homeostatic program for the turnover of cellular organelles and proteins. Emerging evidence indicates autophagy as a critical modulator for cerebral IRI [12]. However, the association between SIRT1 and autophagy in IRI is still not fully understood.

In addition to anesthesia, sevoflurane can also alleviate cerebral IRI. In the early phase after transient global cerebral IRI, the activation of antioxidant enzymes (Nrf2/HO-1) may contribute to the neuroprotection of SP [13]. Furthermore, SP alleviates neuronal death and axon demyelination in neonatal rats by regulating microglia autophagy. Therefore, SP provides long-term cognitive, learning, and memory protection [14]. In our previous study, SP improved the impairments of spatial learning and memory induced by HSR in rats [15]. SP remarkably reduced the apoptosis of hippocampal neurons through reducing the endoplasmic reticulum stress. Moreover, SP stabilized the integrity of mitochondrial structure and function via preventing the opening of the mitochondrial mPTP channel [16]. However, the role of SIRT1 in the neuroprotective impact of SP has not been clearly illustrated.

In the present study, we aimed to investigate the mechanism by which SP potentially improved the cognitive deficits following HSR in mice. The cognition and anxiety-like behaviors were evaluated following SP without or with the SIRT1 inhibitor in HSR mice. The characteristics of mitochondrial morphology and function were indicated in OGD/R with either SP or SIRT1 siRNA transfection in HT22 cells. The association between SIRT1 and autophagy in the IRI was demonstrated in both HSR and OGD/R without or with SP.

2. Materials and Methods

2.1. Animals. Male C57BL/6 mice weighing 25-30 g were provided by Laboratory Animal Center in Anhui Medical University. All experimental procedures were performed in accordance with the NIH Guide for the Care and Use of Laboratory Animals and approved by the Ethics Committee for the use of experimental animals in Anhui Medical University (reference number LLSC20190765, date of approval 26/10/2019). Animals were randomly divided into specific groups depending on the different purposes. Mice were bred and housed in a temperature- and humidity-controlled room with a 12/12 h light/dark cycle. All animals had access to food and water ad libitum. One-week acclimatization period was applied before experiment employment. All behavioral tests have been performed during the light phase.

2.2. Hemorrhagic Shock and Resuscitation Mouse Model. Mice were fasted for 12 h before surgery and free to drink water. Hemorrhagic shock and resuscitation (HSR) were performed as described previously [17]. Polyethylene catheters were inserted into the right carotid artery and left jugular vein for blood extraction and infusion, respectively. Approximately 50% of the total blood volume (total blood volume [18] = weight (g) × 7%) were continuously extracted within 30 min through a two-way automatic infusion pump (Genie Touch, Kent Scientific Corporation, USA). After 1 hour, the collected blood was infused within 30 min at a constant speed. Rectal temperature was maintained at 37.0 ± 0.5 °C by using a heating blanket. Finally, all catheters were removed, and the mouse was returned to its cage for recovery. The sham operation was only catheter intubation in the right carotid artery and left jugular vein without withdrawing or transfusing blood.

2.3. Intracerebroventricular Lentivirus Injection. To determine if the supplement of SIRT1 could reverse the impact of HSR, SIRT1 overexpression shRNA-GFP lentivirus (titer: 2.0×10^9 TU/ml) and control lentiviral vector (LV-CTR) (titer: 1.5×10^9 TU/ml) were purchased from GeneChem Company (Shanghai, China). After anesthesia, total 3 μl control lentiviral vector or SIRT1 overexpression shRNA-GFP lentivirus was injected in the right lateral ventricle at the rate of 0.5 μl/min. The following coordinates (relative to bregma) were used, -0.2 mm AP, -1 mm ML, and -2.5 mm DV according to the stereotaxic atlas of Paxinos and Franklin (Third edition, 2007) by using a stereotaxic apparatus (RWD Life Science Co., Ltd., China). To prevent reflux or backflow, the needle was slowly removed at 10 min after the injection. Seven days after lentivirus injection, mice were subjected to HSR.

To downregulate SIRT1, the inhibitor EX527 (i.p., 10 mg/kg) was administrated at 30 min before catheter intubation [19].

2.4. Behavioral Tests

2.4.1. Morris Water Maze Test. According to the previous report [20], the apparatus (Zhenghua Biologic, China) was consisted of a circular swimming pool (120 cm diameter

and 50 cm height), a depth of 30 cm covering black platform (10 cm diameter), and a camera with a video recording system on the ceiling to capture the movement of animals in the tank. The pool was divided into four quadrants with specific conspicuous visual cues. The platform was fixed in the center of the southwest and submerged approximately 0.7 cm below the water surface.

The spatial acquisition training was started on the 3rd day after HSR and carried out for 6 successive days. For each trial, mice randomly entered into each quadrant facing the wall. If the mouse failed to find the platform within 60 sec, it was guided to the platform and allowed to stay for 10 sec. The escape latency was recorded. To evaluate memory capability, the probe test was given at 24 hours of the last training trial. After removing the platform, mice were placed in the opposite quadrant searching for 60 sec [21]. The swimming distance (cm) and the proportion of time spent in the target quadrant (%) were documented through the computer image analyzer.

2.4.2. Open Field Test. In an empty and light grey square arena (40 cm × 40 cm × 40 cm) (RWD Life Science, China), mice were placed in the center, and its behavior was recorded from 3 to 15 min [22]. The distance and the time spent in the center area were analyzed by PanLab Smart 3 software (Harvard, USA).

2.4.3. Novel Object Recognition Test. The novel object recognition test consists of three phases with 24-hour interval: habituation, familiarization, and test phase. In our experience, the habituation phase is equal to the open field test. During the familiarization phase, a single mouse was placed in the open field arena containing two identical objects (A+A) for 10 min. During the test phase, the mouse was returned to the arena with two different objects: one is identical to the old and the other one is novel (A+B) [23]. The total exploration time and the exploration time of each object were recorded by PanLab Smart 3 software.

2.4.4. Elevated plus Maze Test. To evaluate the changes of anxiety-related behaviors in mice, elevated plus maze (EPM) test was conducted on the 14th day after HSR. The apparatus consisted of plastic open and closed arms (5 cm width and 35 cm length). The closed arm was about 15 cm height, and the height of the maze from the ground was about 40-55 cm. The animals moved freely in the elevated cross maze (RWD Life Science, China) for 10 min. The moving distance and residence time in the arms were recorded and analyzed by PanLab Smart 3 software.

2.5. Infarct Volume Assessment. After EPM test, the animals were sacrificed, and the entire brain was fast frozen at -20°C for 20 min. Then, 1 mm thick coronal sections were continuously segmented and incubated in 2% 2,3,5-tribenzene tetrachloride (TTC) for 30 min at 37°C. Brain slices were further fixed in 4% polyformaldehyde for 24 hours and then digitally scanned to a computer for analysis using ImageJ software (National Institutes of Health, USA): Infarction volume% = (infarction area × 1 mm)/(whole brain area × 1 mm) × 100%.

2.6. Oxygen and Glucose Deprivation/Reoxygenation Protocol. The mouse hippocampal neuronal cell line (HT22) (Jennio Biotech Co., Ltd., Guangzhou, China) was cultured in Dulbecco's modified Eagle's medium (DMEM) (HyClone, USA) with 10% fetal bovine serum (FBS) at 37°C in a humidified atmosphere containing 5% CO_2. When reaching 70-80% confluency, cells were subjected to OGD/R. Briefly, oxygen and glucose deprivation (OGD) was carried out in an anaerobic chamber (Stem Cell, USA) containing 95% N_2 and 5% CO_2. Cells were incubated with glucose-free DMEM and FBS for 4 hours at 37°C. After replacing the medium to the ordinary DMEM containing 10% FBS, cells were further cultured in the CO_2 incubator for 4 hours.

To genetically inhibit the expression of SIRT1, siRNA transfection was introduced 24 hours before OGD/R without or with sevoflurane postconditioning. Nonsense sequence for the SIRT1 negative control (SIRT1-NC) and siRNA against SIRT1 (si-SIRT1) were purchased from GenePharma (Shanghai, China). According to the manufacturers' instructions, HT22 cells were seeded into 6-well plates and cultured to 50-60% confluence. Then transfection was performed with 20 μM siRNA using 4 μl of jetPRIME Transfection Reagent (Polyplus-Transfection®) in 200 μl jetPRIME buffer. After 10 min, 2 ml fresh medium was added for further incubation. No-load siRNA plasmid was used as a control. The efficiency of SIRT1 intervention was confirmed by RT-PCR.

2.7. Sevoflurane Postconditioning In Vivo and In Vitro. At the onset of blood refusion, mouse was stabilized in a gas-tight anesthesia chamber with sevoflurane inhalation for 1 hour. Sevoflurane (Sevofrane®, AbbVie, Japan) was delivered by the carrier gases (5% CO_2 and 95% O_2, 3.5 l/min total gas flow) through the sevoflurane volatilizer (Vapor 2000, Germany). The concentration was maintained at 2.4% and measured by an anesthetic monitor (Mindray Bene View T8, Shenzhen, China). In the sham operation or HSR, mice were only exposed to the mixed gas (95% O_2 and 5% CO_2) for 1 hour.

For HT22 cells, at the beginning of reoxygenation with ordinary DMEM containing 10% FBS, cells were incubated in the gas-tight anesthesia chamber (Modular Incubator Chamber, Billups Rothenberg, USA) with 5% CO_2 and 95% air. The percentage of sevoflurane in the chamber was maintained at 2 for 1 hour.

2.8. Evaluation of Cell Viability and Apoptosis. MTT (Beyotime Biotechnology, China) and CCK-8 (7-Seabiotech, China) assays were used to determine the viability of HT22 cells according to the manufacturer's instructions. Optical density was calculated with the absorbance measuring by Varioskan LUX microplate reader (Thermo Fisher Scientific, USA). The results were expressed as the ratio to the control values.

To detect apoptosis, HT22 cells were immunolabeled with cleaved caspase 3 (Cell Signaling Technology, USA) and identified with TdT-mediated dUTP nick-end labeling (TUNEL) (In Situ Cell Death Detection Kit TMR red, Roche, USA) according to the manufacturer's instructions. After fixation with 4% paraformaldehyde, HT22 cells were

permeabilized with 0.1% Triton X-100 and then blocked with 10% normal goat serum for 2 hours at room temperature. HT22 cells were further incubated with primary antibody against cleaved caspase 3 overnight at 4°C and subsequent Alexa Fluor 488 secondary antibody (Invitrogen, USA) for 2 hours at room temperature. Finally, HT22 cells were exposed to TUNEL reagent for 1 hour at 37°C. The nucleus was recognized by DAPI (Sigma-Aldrich, USA), and the apoptotic cells were examined under a laser scanning confocal fluorescent microscope (Carl Zeiss LSM 880, Germany).

2.9. Assessment of Oxidative Stress and Mitochondrial Transmembrane Potential. Oxidative stress in the HT22 cells was measured using MDA and SOD assays (Nanjing Jiancheng, China) according to the manufacturer's recommendations. ATP content was also evaluated (Nanjing Jiancheng, China) according to the manufacturer's recommendations. MitoSOX Red (Invitrogen, USA) was used to measure the accumulation of mitochondrial ROS. JC-1 Mitochondrial Membrane Potential Dye (Invitrogen, USA) was used to evaluate mitochondrial transmembrane potential in HT22 cells. Briefly, HT22 cells were treated with MitoSOX Red or JC-1 solution at 37°C for 10-20 min and then detected by the fluorescent microscope (Axio Vert. A1, ZEISS, Germany). According the manufacturer's instructions, the average fluorescent intensities at 488 nm and 590 nm were determined by ImageJ software (National Institutes of Health, USA) and then analyzed as the red/green ratio.

2.10. Quantitative Real-Time Polymerase Chain Reaction. According to the manufacturer's protocol, total RNA from HT22 cells was extracted using TRIzol reagent (TAKARA, Japan). After reverse transcription with HiScript® III RT SuperMix (Vazyme, China), PCR was performed with StepOnePlus™ Real-Time PCR system (Applied Biosystems, USA) with the AceQ®qPCR SYBR Green Master Mix Kit (Vazyme, China). NADH dehydrogenase subunits 1 (ND1) and cytochrome c oxidase subunit 3 (COX3) were used to reflect the transcript level of mtDNA. Primers of SIRT1, ND1, and COX3 were purchased from Genepharma (Shanghai, China), and sequences were as follows: SIRT1 (F: 5′-GCAGGTTGCAGGAATCCAAA-3′, R: 5′-GGCAAGATGCTGTTGCAAAG-3′), ND1 (F: 5′-GGATCCGAGCATCTTATCCA-3′, R: 5′-GGTGGTACTCCCTCTGTAAA-3′), and COX3 (F: 5′- CGTGAAGGAAACTACCCAGG-3′, R: 5′-CGCTCAGAAGAATCCTGCAA-3′). The relative levels of SIRT1, ND1, and COX3 were normalized to internal control GAPDH with $2^{-\Delta\Delta Ct}$ method. The relative mRNA level of SIRT1 was shown in the SFig. 3.

2.11. SDS-PAGE and Western Blot Analysis. Total proteins were extracted and subjected to 10% or 15% polyacrylamide gels electrophoresis. Nonspecific binding sites were blocked with 5% nonfat dry milk for 1 hour at room temperature. Then, membranes were incubated with specific primary antibodies overnight at 4°C, including SIRT1 (Cell Signaling Technology, USA), Bax (CST, USA), Bcl-2 (CST, USA), Pink1 (CST, USA), Parkin (CST, USA), LC3B (CST, USA), mtTFA (NOVUS, USA), and GAPDH (Sigma-Aldrich, USA). After the incubation with horseradish peroxidase-conjugated secondary antibodies (ZSGB-BIO, Beijing, China) for 2 hours at room temperature, the immunoreactive band signal intensity was subsequently visualized by chemiluminescence (SuperSignal™ West Femto Maximum Sensitivity Substrate) (Thermo Fisher Scientific, USA). All immunoblots were normalized for gel loading with GAPDH (Sigma-Aldrich, USA) antibody. The intensities of chemiluminescent bands were measured by ImageJ software (National Institutes of Health, USA).

2.12. Deacetylase Assay. Nuclear proteins from the cells were firstly extracted using a nuclear and cytoplasmic protein extraction kit (Beyotime, Shanghai, China). Then, the NAD+-dependent deacetylase activity was evaluated by using a SIRT1/Sir2 deacetylase fluorometric assay kit Ver.2 (CycLex, Medical & Biological Laboratories Co., Ltd., Japan). According to the manufacturers' instructions and the preliminary experiments, the SIRT1 activity was expressed as the rate of reaction for the first 30 min, when there was a good linear correlation between the fluorescence and the reaction time.

2.13. Transmission Electron Microscopy. After specific treatments, HT22 cells were collected by centrifugation and then fixed overnight with 2.5% glutaraldehyde at 4°C. After rinse in PBS (0.01 M, PH 7.2) for 6 hours at 4°C, samples were further fixed in 1% osmium tetroxide for 1 hour at 4°C. Following dehydration with gradient alcohol, samples were incubated in propylene oxide and epoxy resin for 2 hours at room temperature and then embedded in epoxy resin for further ultramicrosectioning (70 nm in thickness, Leica UC-7 microtome). The area of mitochondria (10000x) was analyzed by using ImageJ software. The number of mitochondria autophagy bodies (10000×) was observed in at least 10 visual fields (including intact neuronal bodies) by a JEM1400 electron microscope (JEOL, Japan).

2.14. Immunofluorescence Staining. After the behavioral observation, the mouse was deeply anesthetized, and the brain was removed and postfixed in 4% paraformaldehyde for 72 hours. Following the dehydration by using graded series of saccharose and embedding with OCT, coronal 16 μm thick sections (from -1.46 mm to -2.46 mm posterior to bregma) were made. Nonspecific binding was blocked by 10% normal goat serum. Sections were incubated with primary antibodies against SIRT1 (CST, USA), LC3B (CST, USA), TOM20 (CST, USA), 8-OHdG (Santa Cruz Biotechnology, USA), and VDAC (CST, USA) overnight at 4°C. Alexa Fluor 568 or 488 secondary antibodies (Invitrogen, USA) were further incubated for 2 hours at room temperature. The nucleus was identified with DAPI. *Z*-stack images were acquired by using a laser scanning confocal fluorescent microscope (20x, 40x oil, and 63x oil immersion objectives) (Carl Zeiss LSM 880, Germany) equipped with ZEN light software at 1,024 × 1,024 resolution. All quantitative

analyses were performed from at least three independent experiments. Data were analyzed with ImageJ software.

2.15. Statistical Analysis. The data of the Morris water maze were analyzed by two-way analysis of variance (ANOVA) followed by the Tukey *post hoc* test for repeated measures, using the statistic software GraphPad Prism 8.0 (Graph Pad Software Inc., USA). Other data, such as elevated plus maze test, normalized band intensities in western blot, and quantification of immunoreactivity, were analyzed by one-way ANOVA followed by the Tukey *post hoc* test. Normality of the data and homogeneity of group variances were assessed using the D'Agostino-Pearson omnibus normality test, Shapiro-Wilk normality test, and Kolmogorov-Smirnov test, respectively. Statistical significance was determined if $p < 0.05$. Data are represented as the mean ± SD in the context.

3. Results

3.1. Sevoflurane Postconditioning Improved Cognitive Deficits and Anxiety Induced by Hemorrhagic Shock and Resuscitation. We firstly established and tested the animal model of ischemia-reperfusion injury (IRI) in mice. On postoperative day 14, hemorrhagic shock and resuscitation (HSR) caused severe cerebral infarct. The introduction of sevoflurane postconditioning (SP) at the beginning of reperfusion significantly reduced cerebral infarct size. However, when pretreated with EX527 before SP, the infarct size was significantly stronger than SPm group ($F = 33.82$, Figures 1(a) and 1(b)).

To evaluate the impact of HSR on the spatial learning and memory, the Morris water maze (MWM) test was performed from postoperative day 3 to 9. Especially on 6th training day, mice in the HSR group acquired longer escape latency than mice in the sham group. After SPm treatment, the escape latency was remarkably shortened. Nevertheless, mice with EX527 pretreatment needed longer time to find the platform ($p_{\text{time}} < 0.0001$, $p_{\text{group}} = 0.0104$, and $p_{\text{time*group}} = 0.0189$; Figure 1(c)). In the probe test for spatial memory determination, comparing with the sham group, mice after HSR swam less time (19.4 ± 9.6 sec vs. 29.0 ± 8.4 sec) and shorter distance (180.8 ± 131.7 cm vs. 287.4 ± 111.0 cm) in the target quadrant. SP significantly improved animal's spatial memory, which was indicated by swimming longer and farther. However, this improvement was effectively reversed by a single preadministration of EX527 (Figures 1(d)–1(f)).

In the novel object recognition (NOR) test, the discrimination index (DI) of mice after HSR (0.51 ± 0.17) suggested that mice spent equal time on exploring two different objects. Higher DI following SPm implied that it strengthened animals' discrimination ability to two different objects (0.70 ± 0.14). However, the addition of EX527 to SPm made a significant DI decline ($F = 5.825$, Figures 1(g) and 1(h)).

To investigate the impact of SP on anxiety-like behaviors, open field test (OFT) and elevated plus maze (EPM) test were initiated in HSR mice without or with SP. In the OFT, mice following HSR were less active, evidenced by shorter moving distance and less residence time in the center area. In the SPm group, there were more spontaneous activities in the center area compared with the HSR group. When mice received EX527, they performed significantly inactive in the center area (Figures 2(a)–2(c)). In the EPM test, mice in the HSR group performed anxiety-like behaviors, such as fewer entries and less residence time in the open arms. The addition of SPm significantly relieved anxiety, which indicated by higher entry frequency (Figures 2(d) and 2(e)) and longer duration (Figure 2(f)) in the open arms. However, significant less open arm entries and duration were observed in the mice with EX527 pretreatment ($F = 4.008$, $F = 4.624$).

3.2. Sevoflurane Postconditioning Reversed SIRT1 Loss and Cell Apoptosis Caused by IRI In Vivo and In Vitro. By using western blot analysis, consistent loss of SIRT1 was observed in IRI models *in vivo* and *in vitro*, including HSR, oxygen glucose deprivation, and reoxygenation (OGD/R) (0.59 ± 0.09-fold of Ctrl in mice; 0.46 ± 0.07-fold of Ctrl in HT22 cell, Figures 3(a) and 3(b)). Meanwhile, significant apoptosis was also observed with the increase in Bax expression and decrease in BCL2 expression (Figures 3(a) and 3(b)). After SP, changes of SIRT1, Bax, and BCL2 induced by HSR or ODG/R were significantly reversed. In addition, the deposition and distribution of SIRT1, as well as the deacetylation activity of SIRT1, were varied following OGD/R without or with SP (SFig. 1, SFig. 2). Either EX527 or si-SIRT1 significantly reduced SIRT1 expression accompanying with distinct more apoptosis (Figures 3(a) and 3(b), SFig. 3). When overexpressing SIRT1 by using lentivirus transfection before HSR, SIRT1 loss and apoptosis were significantly eliminated (Figure 3(c)).

Consistent with the distinct apoptosis, cell viability was remarkably dropped after OGD/R (0.49 ± 0.03-fold of Ctrl, SFig. 4). In addition to promoting cell survival, SP prevented apoptosis and DNA damage, which was evidenced with the decreased immunoreactivities of cleaved caspase 3, TUNEL, and 8-OHdG (Figures 3(d) and 3(e), SFig. 5 & 6). However, these decreases were significantly reversed after SIRT 1 gene silencing by using si-SIRT1 transfection in HT22 cells. When HSR mice were preinjected with SIRT1 overexpression lentivirus, less distributions of cleaved caspase 3^+ and TUNEL^+ immuno-signals were observed in the hippocampal CA1 region.

3.3. Sevoflurane Postconditioning Improved Oxidative Stress and Mitochondrial Dysfunction Caused by IRI In Vitro. By using CCK8 assay, more survived cells were observed after SPc treatment than OGD/R (Figure 4(a)). In the HT22 cells, OGD/R made a remarkable oxidative stress, signed by the decrease of SOD production, increase of MDA accumulation (Figure 4(b)), and increase of MitoSOX immunoreactivity (Figure 4(c)). In addition, OGD/R dramatically reduced ATP production and disrupted mitochondrial membrane potentiation (MMP) determined by JC-1 assay (Figures 4(d) and 4(e)). SPc significantly alleviated oxidative stress with the evidence including more SOD yields, less MDA release, and less MitoSOX toxicity. SPc also promoted ATP production and improved mitochondrial damage

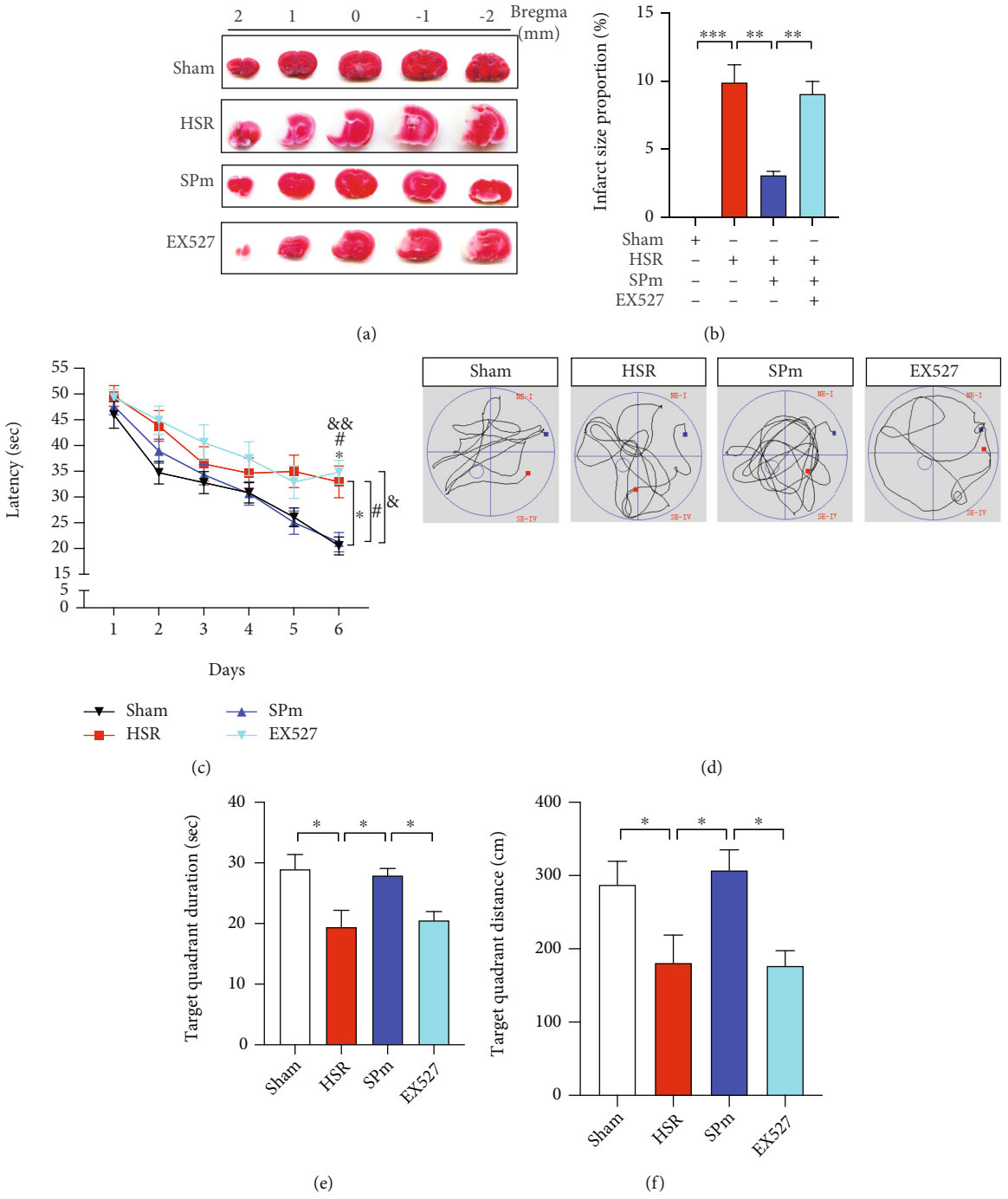

Figure 1: Continued.

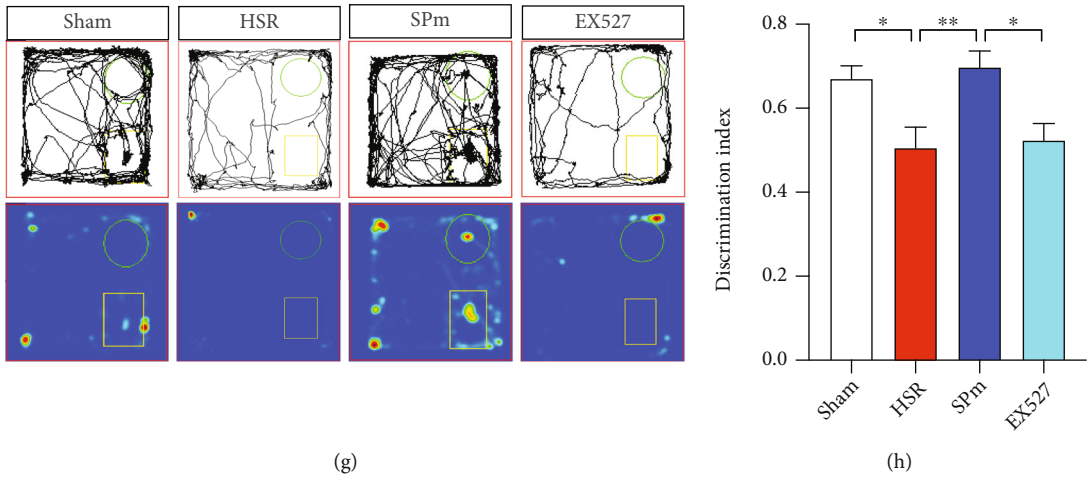

Figure 1: Sevoflurane postconditioning improved cognitive impairments induced by hemorrhagic shock and resuscitation (HSR). (a, b) Representative cerebral TTC staining photographs and the calculation of infarct size were made after HSR without or with sevoflurane postconditioning (SPm). EX527 (SIRT1 inhibitor) (i.p., 10 mg/kg) was administrated at 30 min before catheter intubation; then, mice were exposed to HSR with SPm. Infarct size of coronal brain sections was determined by TTC staining on postoperative day 14. HSR caused a significant cerebral infarction (white area). (c) A learning curve was made in the training session for spatial acquisition in the Morris water maze (MWM) test from postoperative day 3 to 8. (d–f) In the MWM test, the performance in the probe test included swimming route, duration, and distance in the target quadrant in the probe test. (g, h) Representative exploration route for two different objects, heat map, and discrimination index were recorded in the novel object recognition (NOR) test. The discrimination index was calculated by the ratio of time exploring the new object versus two different objects. All values are represented as mean ± SEM. $n = 12$ per group; $^{*}p < 0.05$, $^{**}p < 0.01$, and $^{***}p < 0.001$, the HSR group vs. sham group; $^{\#}p < 0.05$, the SPm group vs. HSR group; and $^{\&}p < 0.05$, the EX527 group vs. SPm group.

through enhancing MMP. Otherwise, the effects of SPc on oxidative stress and MMP were completely reversed by genetic silence of SIRT1 with si-SIRT1.

To further investigate the transcript level of mtDNA during IRI without or with SPc, mitochondrial copy number including NADH dehydrogenase subunits 1 (ND1) and cytochrome c oxidase subunit 3 (COX3) was determined. OGD/R strikingly suppressed mitochondrial DNA transcript ability, which was boosted by SPc (Figure 4(f)). Additionally, both OGD/R and HSR decreased the expression of mitochondria transcription factor A (mtTFA). After SP, the increases of mtTFA were noted in both HT22 cells and mouse hippocampi. However, there was a prominent drop of mtTFA after SIRT1 gene silencing. The overexpression of SIRT1 by lentivirus transfection made a comparable level of mtTFA to SPm (Figures 4(g) and 4(h)).

3.4. Sevoflurane Postconditioning Reversed Autophagy Caused by IRI In Vitro. Under TEM observation, OGD/R made mitochondria swelling and hypertrophy, as well as mitochondrial ridge disruption (Figure 5(a)). Meanwhile, less mitophagy events were noted (Figure 5(b)). The effect of SPc or si-SIRT1 on autophagy was further determined by immunofluorescent staining of LC3B (Figures 5(c)–5(e)). Furthermore, the levels of autophagy markers, such as LC3B, PINK1, Parkin, and P62, were significantly reduced following OGD/R in HT22 cells (Figure 5(f)). SPc successfully prevented mitochondria against swelling, ridge disruption, and vacuolization. SPc also improved the suppression of LC3B, PINK1, and Parkin induced by OGD/R. Otherwise, all these changes were reversed after the introduction of si-SIRT1 to SPc.

3.5. Sevoflurane Postconditioning Manipulated Autophagy through SIRT1 Intervention with Pharmacological Inhibition or Genetic Overexpression In Vivo. Firstly, the impact of SP on autophagy in IRI was consistently demonstrated in the animal model of HSR (Figures 6(a) and 6(b)). After the systemic administration of EX527, there were noted decreases of LC3B, PINK1, and Parkin (Figure 6(a)). The effect of SPm without or with SIRT1 intervention on autophagy was also presented by the varied distributions of LC3B in the hippocampal CA1 region (Figure 6(c)).

To further investigate the effect of SIRT1 on autophagy, SIRT1 overexpression lentivirus was ventricularly injected one week before HSR. SPm and LV-SIRT1 comparably increased the protein expressions of LC3B, PINK1, and Parkin, as well as the distribution of LC3B in the hippocampal CA1 region (Figures 6(b) and 6(d)). Furthermore, significant deposition of SIRT1 was noted in the same region, associated with remarkable colocalization with TOM20 (Figures 6(e)–6(g)).

4. Discussion

We successfully demonstrated the neuroprotective effect of sevoflurane postconditioning (SP) in two ischemia reperfusion injury (IRI) models, hemorrhagic shock and

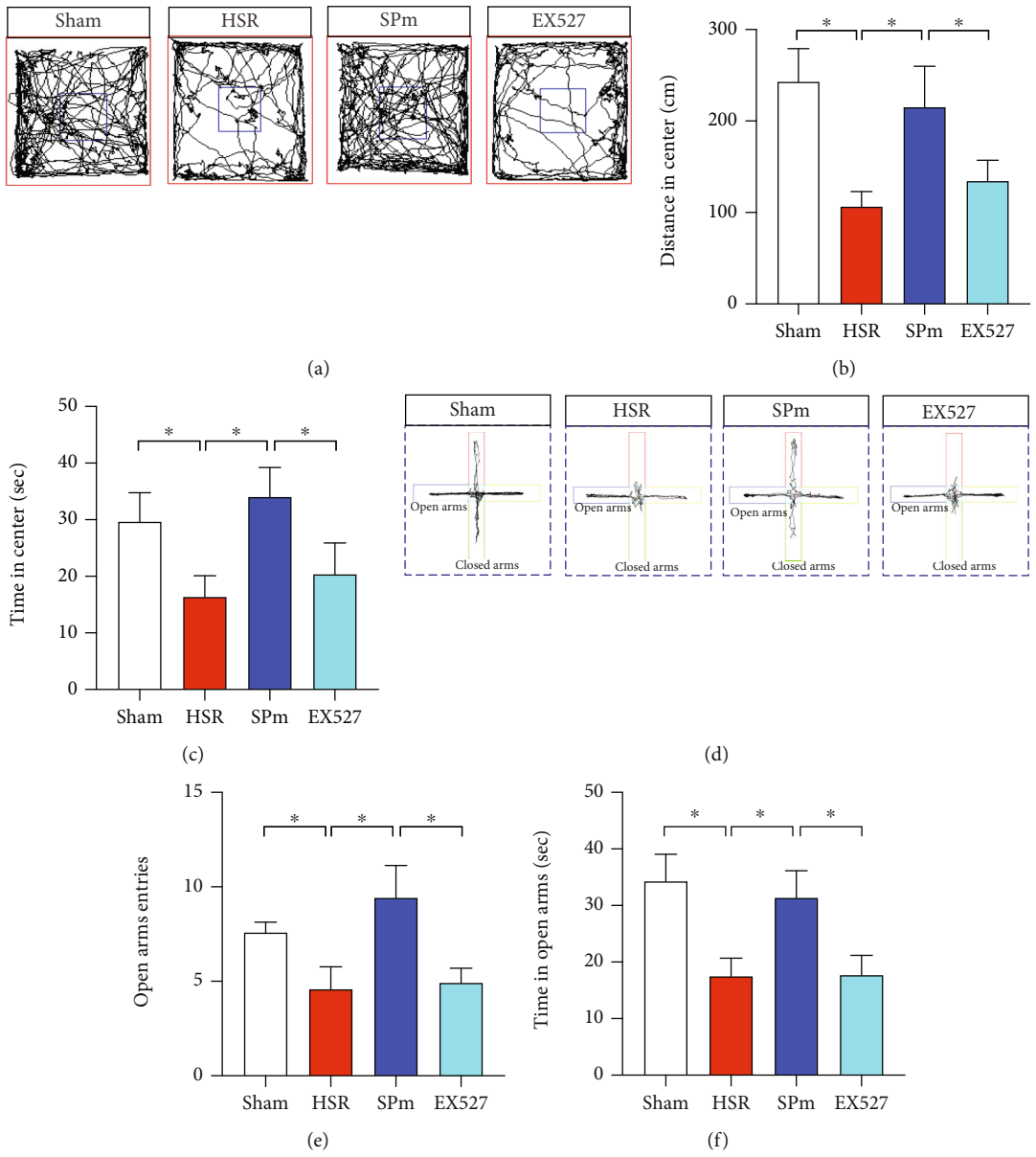

Figure 2: Sevoflurane postconditioning improved anxiety-like behaviors caused by HSR. (a–c) In the open field test (OFT), representative moving tracks in the arena were traced and descripted during their spontaneous activities. Particularly, moving distance and duration in the center area were further calculated as the signatures of anxiety. (d–f) In the elevated plus maze (EPM) test, representative moving tracks in both open and closed arms were traced and descripted within 10 min. To determine the anxious reactions, the entry frequency and the duration in the open arms were calculated. All values are represented as mean ± SEM. $n = 12$ per group, $^*p < 0.05$.

resuscitation (HSR), and oxygen and glucose deprivation (OGD/R). SP significantly prevented the impairments of spatial learning and memory, as well as anxiety-like behaviors. It also improved the oxidative damage, mitochondrial dysfunction, and defective autophagy induced by IRI. However, the impact of SP on IRI was consistently reversed by the posttranslational modification of SIRT1 by pharmacological inhibitor or gene silencing.

The mechanisms of IRI are mainly related to oxidative stress, calcium imbalance, mitochondrial injury, excessive inflammatory response, endoplasmic reticulum stress, and programmed cell death. In the common animal model of cerebral IRI, such as middle cerebral artery occlusion (MCAO), distinct cerebral infarction and cognitive dysfunction are usually presented with apoptosis, neuroinflammation, oxidative stress, and mitochondrial dysfunction [8–11, 24]. In this study, HSR was used as another mouse model of IRI. It caused significant cerebral infarctions, spatial learning, and memory deficits, as well as object recognition disability. Meanwhile, mice after HSR also performed anxiety-like behaviors, including less active and more anxiety.

On the other hand, oxygen glucose deprivation and reoxygenation (OGD/R), as an *in vitro* model of IRI, suppressed cell viability with increased oxidative stress injury in HT22 cells. Mitochondria are a major target in hypoxic/

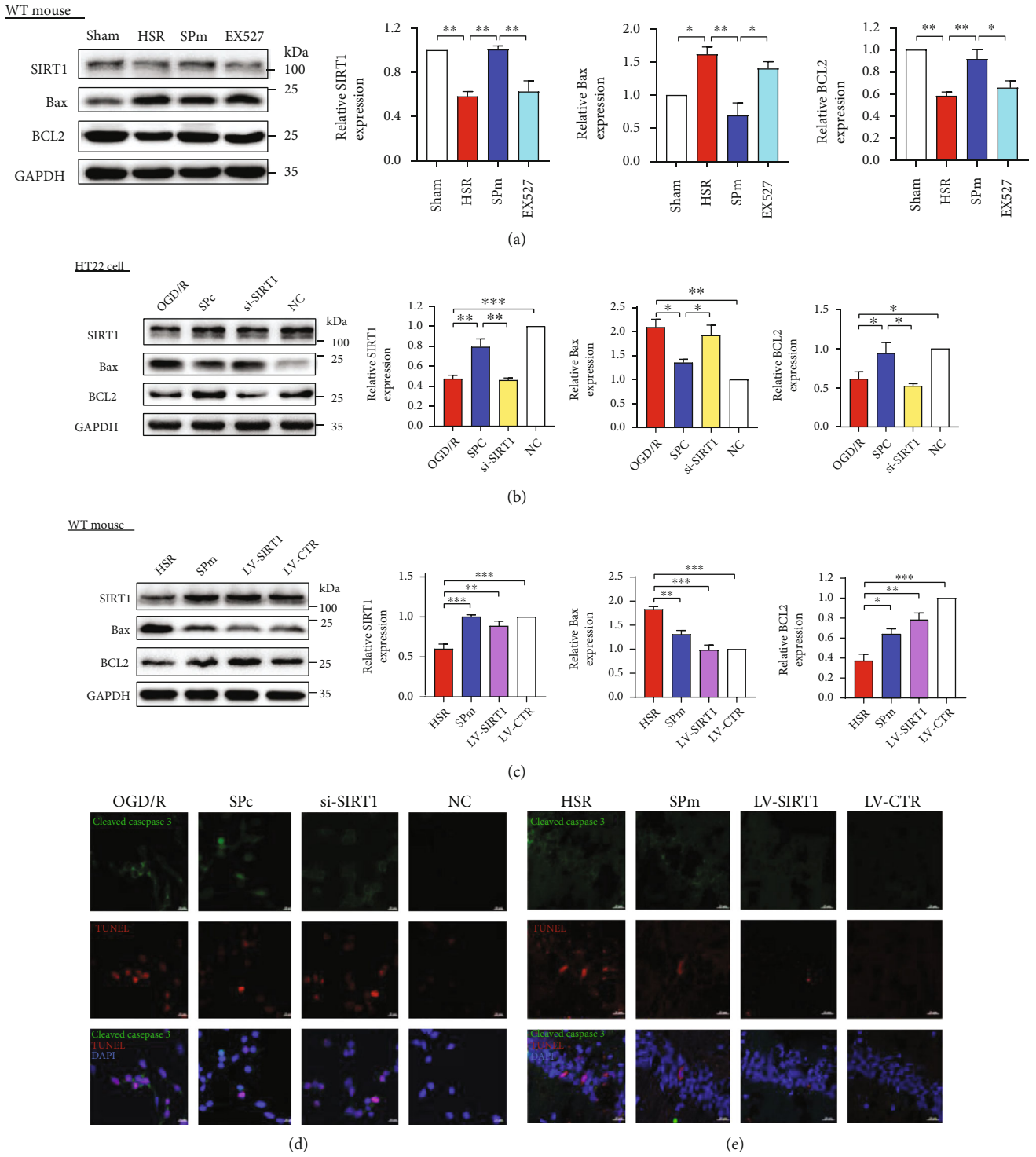

Figure 3: Sevoflurane postconditioning attenuated SIRT1 loss and cell apoptosis induced by ischemia-reperfusion injury in both *in vivo* and *in vitro* models. (a, b) By using western blotting analysis, protein expression levels of SIRT1, proapoptotic Bax, and antiapoptotic BCL2 were demonstrated following HSR or oxygen glucose deprivation and reoxygenation (OGD/R) with or without sevoflurane postconditioning (SP). After pretreatment with SIRT1 selective inhibitor EX527 or si-SIRT1 before SP, the levels of SIRT1 and apoptosis-related proteins were also measured. Nonsense sequence for SIRT1 was the negative control (NC). (c) After overexpressing SIRT1 through lentivirus transfection, protein levels of SIRT1, Bax, and BCL2 were evaluated in mice following HSR without SP. Control lentiviral vector (LV-CTR) was cerebrally injected without or with HSR or SPm. (d, e) Apoptotic cells induced by HSR or OGD/R were presented by double labelling with cleaved caspase 3 and TUNEL. All values are represented as mean ± SEM. $n = 4$-6 per group; $^{*}p < 0.05$, $^{**}p < 0.01$, $^{***}p < 0.001$, and $^{****}p < 0.0001$. Scale bar = 20 μm.

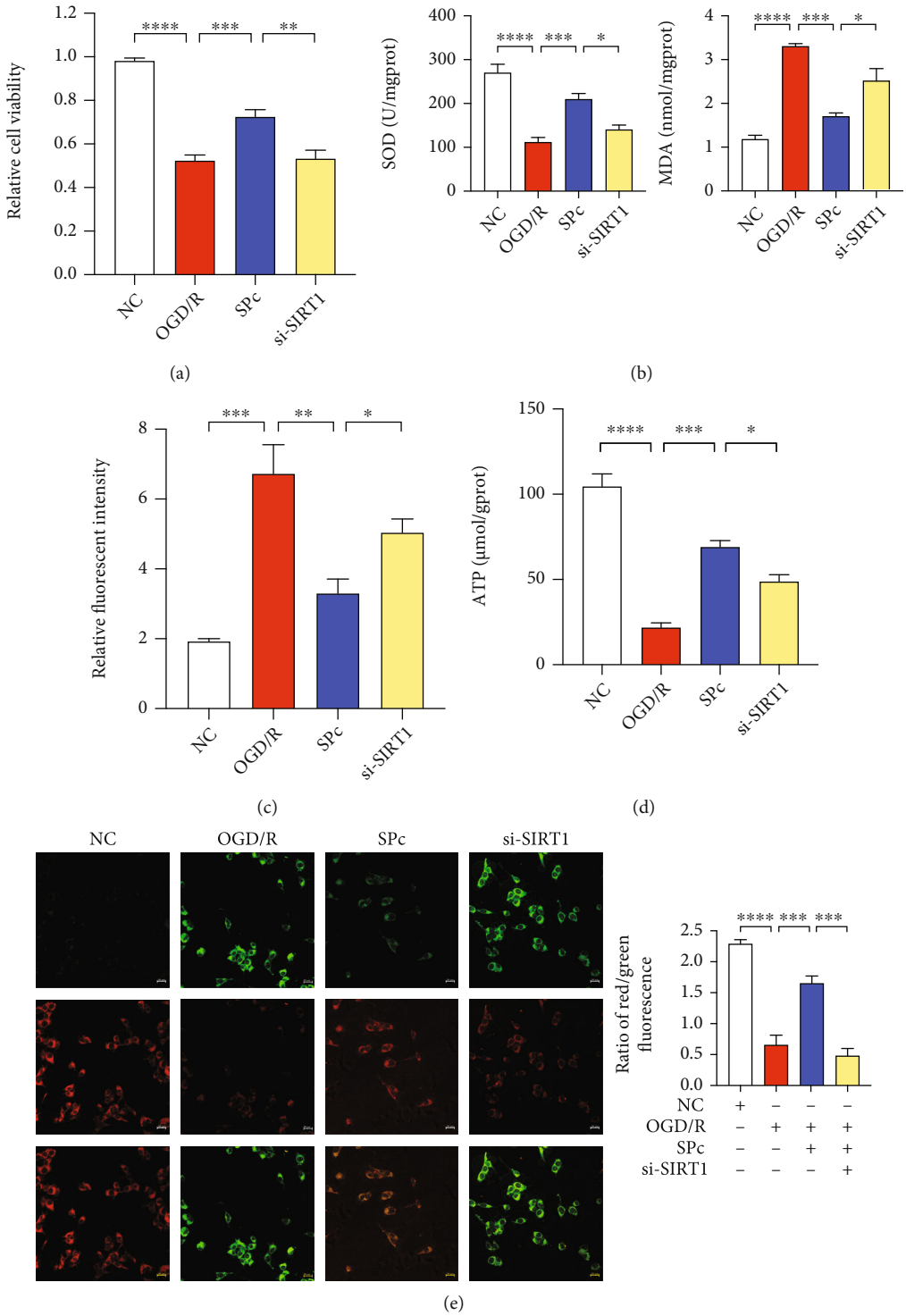

Figure 4: Continued.

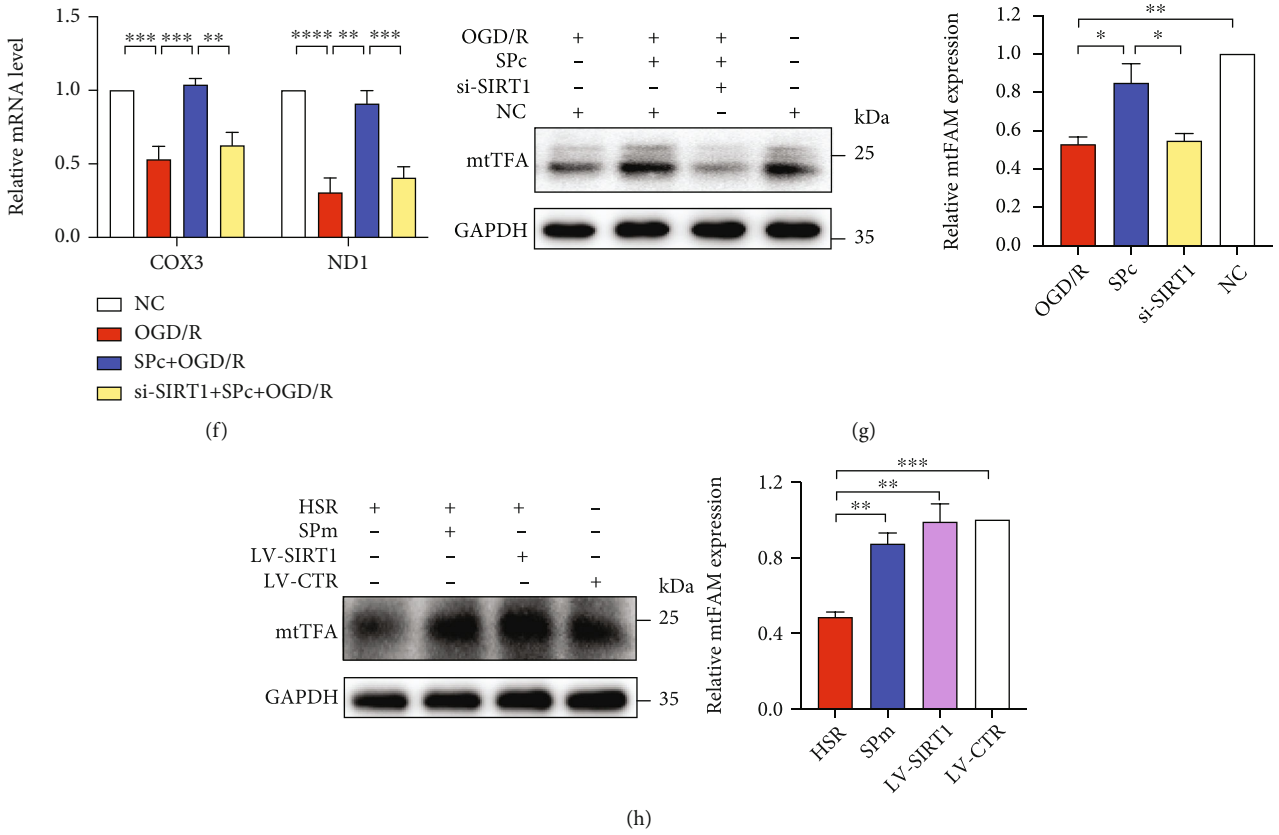

Figure 4: Sevoflurane postconditioning alleviated oxidative stress and mitochondrial dysfunction caused by OGD/R. (a) During OGD/R, sevoflurane postconditioning (SPc) increased cell viability in the CCK8 assays. Transfection of siRNA against SIRT1 (si-SIRT1) was introduced 24 hours before OGD/R with SPc. Nonsense sequence for SIRT1 was the negative control (NC). (b–d) SPc relieved oxidative stress with more SOD, less burdens of MDA and MitoSOX, and more ATP production. (e) Representative photographs and the quantification of mitochondria membrane potentiation (MMP) was determined by JC-1 assay in HT22 cells following OGD/R with SP treatment. Scale bar = 20 μm. (f) Relative mitochondria DNA copy numbers of COX3 and ND1 were quantified by RT-qPCR after SPc with si-SIRT1 treatments. (g, h) Relative mitochondrial transcription factor A (mtTFA) protein expressions in HT22 cells and hippocampi following IRI with SIRT1 down- and upregulation. All values are represented as mean ± SEM. n = 4-6 per group; $^{*}p < 0.05$, $^{**}p < 0.01$, $^{***}p < 0.001$, and $^{****}p < 0.0001$.

ischemic injury. At the early stage of reperfusion, there is a promotion in the opening of mitochondrial membrane permeability transition pore (mPTP) [25] and increases in the releases of cytochrome c and apoptosis inducing factor. At a long period following ischemia-reperfusion, a large number of ROS interrupts the activities of respiratory chain complexes I, II, III, and IV. And the dysfunction of mitochondrial respiratory chain further increases the production and accumulation of ROS, triggering a series of cell damage [26], such as mitochondrial DNA (mtDNA) oxidative damage [27]. The mtDNA damage directly decreased the encoding of respiratory chain related proteins, which contributed to the dysfunctions of oxidative respiratory chain and ATP production. Consequently, ROS were further increased, so that oxidative damage was aggravated [28].

Disturbance of mitochondria function resulted in neuronal apoptosis and neurological dysfunction after cerebral infarction. In this study, consistent cell apoptosis was observed in HT22 cells after OGD/R and in the hippocampal CA1 region after HSR, respectively. In addition to the disrupted mitochondrial membrane potentiation and ATP generation, OGD/R also interrupted mitochondrial DNA (mtDNA) transcription. Because mtDNA is close to the respiratory chain and lacks histone protection, it is more vulnerable to the oxidative stress [29, 30]. Consistent to the findings in the aging process [27], we found that cerebral IRI made mtDNA oxidative damage, such as decreases in NADH dehydrogenase subunits 1 (ND1) and cytochrome c oxidase subunit 3 (COX3). Studies have shown that mtDNA oxidative damage can be detected 1 hour after IR, and cell death can be observed 6 hours later [31], suggesting that mtDNA oxidative damage may be one of the factors leading to early IR injury. Mitochondrial transcription factor A (mtTFA) is essential for mitochondrial biogenesis and plays a critical role in the maintenance of mitochondrial DNA replication and transcription [32]. However, mtTFA expression was consistently decreased in both HSR and OGD/R.

SIRTs are class III histone deacetylases and sorted into groups I–IV (SIRT1–3, SIRT4, SIRT5, and SIRT6/7). SIRT1 impacts multiple processes including chromatin remodeling, DNA repair, cell survival, and neurogenesis. It is essential for

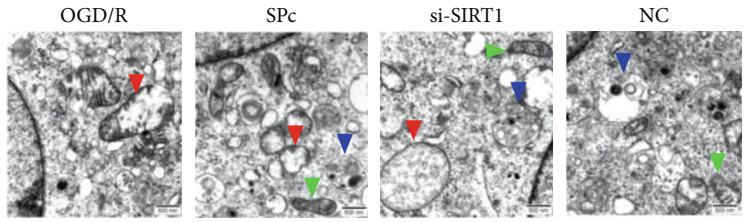

(a)

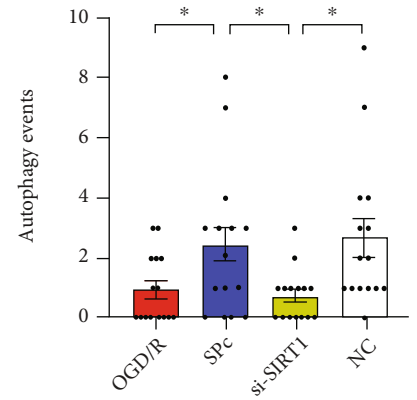

(b)

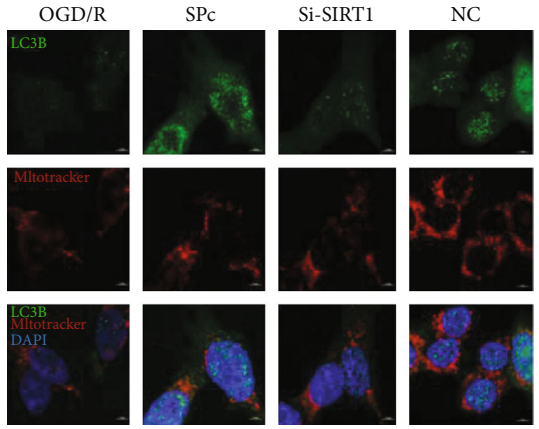

(c)

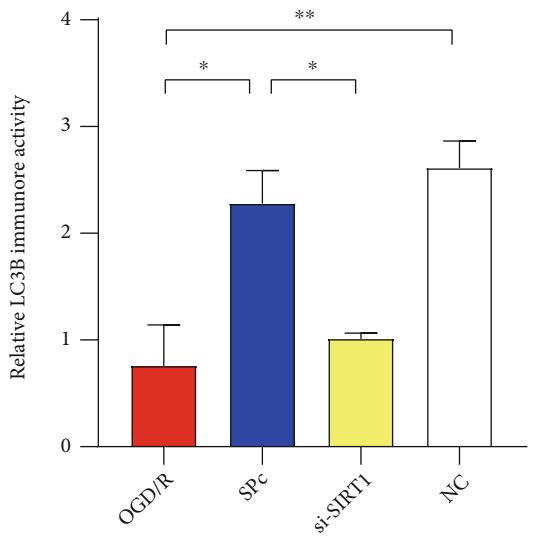

(d)

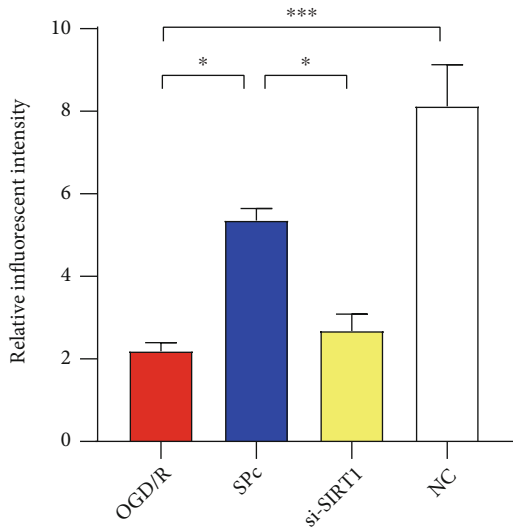

(e)

Figure 5: Continued.

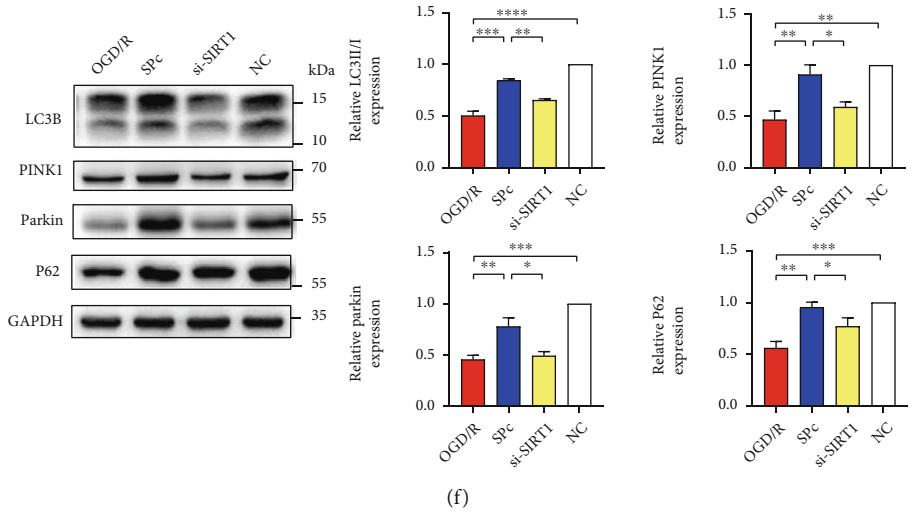

(f)

Figure 5: SIRT1 silence reversed the effect of sevoflurane postconditioning on autophagy during OGD/R. (a) Mitochondrial morphological changes under TEM following OGD/R and SPc. Green arrow, healthy mitochondria; red arrow, injured mitochondria; blue arrow, mitophagy. Scale bar = 500 nm. Sevoflurane postconditioning was performed at the beginning of reoxygenation in HT22 cells (SPc). During OGD/R, transfection of siRNA against SIRT1 (si-SIRT1) was introduced 24 hours before OGD/R with SPc. Nonsense sequence for SIRT1 was the negative control (NC). (b) By using electron microscopy images, autophagy-like events were quantified in HT22 cells after OGD/R and SPc, $n = 4$ neurons from 3 mice per each group. (c–e) The deposition and distribution of LC3B in HT22 cells were quantified after OGD/R and SPc. Scale bar = 5 μm. Mitochondria were labelled with MitoTracker. The relative fluorescent intensity of MitoTracker was quantified. (f) Relative levels of autophagy-related proteins were determined in HT22 cells after OGD/R with SPc. All values are represented as mean ± SEM. $n = 4$-6 per group; $^{*}p < 0.05$, $^{**}p < 0.01$, $^{***}p < 0.001$, and $^{****}p < 0.0001$.

the maintenance of brain integrity, normal learning, memory, and synaptic plasticity in animals [33]. At 48 hours after focal ischemia, larger infarct volumes were displayed in SIRT1$^{-/-}$ mice than the wild-type counterparts [9]. In contrast to SIRT1, SIRT2 and SIRT3 show diverse force in IR. At the early phase of ischemic stroke, SIRT2 mediates myelin-dependent neuronal dysfunction. In both mild and severe MCAO, there were no significant differences in neither infarct volumes nor inflammatory cell count between SIRT2$^{-/-}$ and wild-type mice. Especially at 48 hours after reperfusion, SIRT2$^{-/-}$ mice showed less neurological damage in the experimental stroke models [34]. It also reported that a compensatory rise in SIRT1 rather than the loss of SIRT3 after stroke contributed to the significant neuroprotective effect against IR or stroke injury in SIRT3$^{-/-}$ mice [35]. By using two experimental IRI models (HSR and OGD/R), we found a significant decrease of SRIT1 associated with cell apoptosis and mitochondrial oxidative damage, which were strikingly improved after SIRT1 genetic overexpression or SP treatment.

In response to hypoxic-ischemic conditions, SIRT1 has a pivotal role in maintaining mitochondrial homeostasis by activating many downstream targets, such as regulating peroxisome proliferator-activated receptor γ coactivator α (PGC-1α) for mitochondrial biosynthesis, increasing the expression of ROS degrading enzymes [36], inhibiting p53 induced apoptosis through deacetylation [37], and regulating molecular mediators such as hypoxia-inducible factor 1α (HIF-1α), c-MYC, and AMPK [38], as well as SIRT1/2/3-Foxo3a-MnSOD/PGC-1 signaling pathways [39]. SIRT1 also plays a critical role in the turnover of defective mitochondria through mitophagy [40]. To promote neuronal survival in cerebral ischemia, mitophagy is initiated to eliminate damaged mitochondria through autophagy [12]. SIRT1 activation and autophagy induction contribute to the anti-inflammatory and neuroprotective activities of urolithin A in brain cells (BV2 microglia and APPSwe-transfected ReNcell VM human neural cells) exposing to lipopolysaccharide. Those changes are reversed in the presence of EX527 (SIRT1 inhibitor) and chloroquine (autophagy inhibitor) [41]. In our study, both SIRT1 and autophagy were suppressed by HSR and OGD/R and associated with cognitive dysfunction, mitochondrial dysfunction, and neuronal apoptosis. The overexpression of SIRT1 by shRNA-GFP lentivirus successfully improved the pathological disruptions induced by HSR.

During starvation, LC3 cycles between nucleus and cytoplasm depending on its nuclear deacetylation by SIRT1. Consistent to other cases [42, 43], we also found the dominant distribution of LC3 in the nucleus of intact hippocampal neuronal cells. However, IR suppressed the redistribution of LC3, which was partially attributed to SIRT1 loss. In addition to senescence and aging [44], translocation of SIRT1 from its original nuclear resides to cytosolic puncta was also found in IR in this study. The colocalization of SIRT1 and LC3 supports the new identify of SIRT1 as a new substrate of nuclear autophagy. SIRT1 degradation is mediated by LC3 with the involvement of nucleus-to-cytoplasm shuttling of SIRT1 and

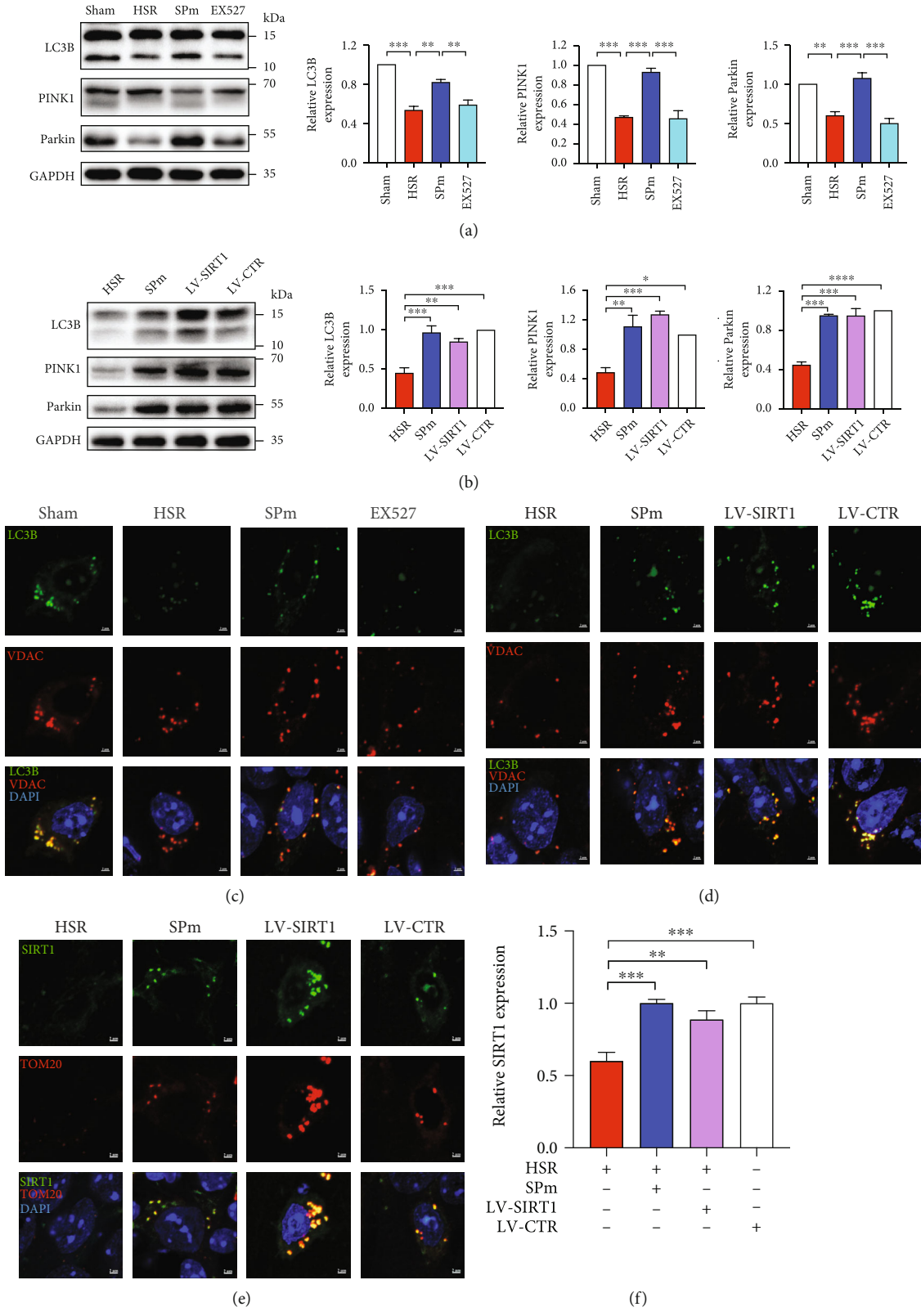

Figure 6: Continued.

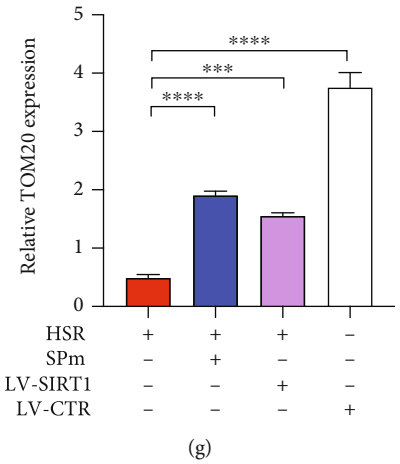

Figure 6: Regulation of autophagy and SIRT1 manipulation by sevoflurane postconditioning during HSR. (a, b) By using western blot analysis, relative levels of autophagy-related proteins were quantified in the hippocampi after HSR with SPm. Sevoflurane postconditioning was performed at the onset of blood refusion in mice (SPm). EX527 (SIRT1 inhibitor) (i.p., 10 mg/kg) was administrated at 30 min before catheters intubation; then, mice were exposed to HSR with SPm. After overexpressing SIRT1 through lentivirus transfection, mice were exposed to HSR without SPm. Control lentiviral vector (LV-CTR) was cerebrally injected without HSR or SPm. (c, d) The localization of LC3B was presented in the hippocampal CA1 region following SPm with pharmacological inhibition or genetic overexpression of SIRT1. (e–g) The quantification of SRIT1 and TOM20 in the hippocampus was presented following HSR without and with genetic overexpression of SIRT1. All values are represented as the mean ± SEM. $n = 4$-6 per group. $^{*}p < 0.05$, $^{**}p < 0.01$, $^{***}p < 0.001$, and $^{****}p < 0.0001$.

autophagosome-lysosome degradation [43, 45]. Interestingly, although SIRT1 prevents DNA damage and oxidative stress through the induction of autophagy, SIRT inhibits corticosterone-induced autophagy with subsequent enforced cell apoptosis [46]. Therefore, a further study is needed to clarify the relationship between SIRT1 and LC3 in the development of IRI.

Even though the effect of sevoflurane on cognition were controversial, such as the deleterious impact of sevoflurane exposure in the neonatal period [47], numbers of studies reported the protective effect of SP in varied IRI models. In myocardial IRI, SP reduces the production of mitochondrial ROS, increases the content of mitochondrial ATP, and thus reduces apoptosis through activating the JAK2-STAT3 pathway [48]. For transient global cerebral ischemia in rats, SP plays an anti-inflammatory role by blocking the TLR-4/NF-κB pathway [49]. SP also attenuates OGD/R-induced autophagosome accumulation in the SHSY-5Y cell line [50]. Our previous studies demonstrated that SP prevented cerebral damage against HSR in rats [15, 16]. SP efficiently improved the spatial learning and memory ability by stabilizing the integrity of mitochondrial structure and function. Furthermore, the downregulation of endoplasmic reticulum stress also involved in the attenuated hippocampal neuronal apoptosis induced by SP through the IRE1α/caspase-12 pathway [16]. In this study, the employment of 1-hour SP dramatically prevented the cognitive and mental disorders induced by HSR in mice, as well as mitochondrial dysfunction and neuronal apoptosis attributed to OGD/R in HT22 cells. Pharmacological inhibition with EX527 or genetic suppression with siRNA effectively reversed the neuroprotective actions of SP in cognitive dysfunction, mitochondrial oxidative damage, and autophagy disturbance. Otherwise, it is notable to investigate if SP-induced neuroprotection could be overturned when autophagy was suppressed with specific inhibitors.

5. Conclusions

In this study, we showed that SP prevented the cognitive dysfunction and anxiety caused by HSR. SP improved neuronal apoptosis by attenuating mitochondrial oxidative stress and improving autophagy. SIRT1 potentially plays an essential role in the neuroprotective effect of SP against IRI. Our findings suggest that SIRT1 may be a functional target in modulating the oxidative stress and autophagy in IRI.

Data Availability

The data used to support the findings of this study are available from the corresponding authors upon request.

Conflicts of Interest

The authors declare no conflicts of interest.

Authors' Contributions

J.S., X.H., and Q.L. performed the experiment. J.W., Y.Z., Y.C., M.C., and C.Q. analyzed the data. Y.Z. revised the manuscript. X.H. and C.H. designed the experiments and then drafted and revised the manuscript. All authors have read and approved the final manuscript. Jianwei Shu,

Xiaotong Huang, and Qizhi Liao contributed equally to this work.

Acknowledgments

This study was supported by the National Natural Science Foundation of China (NSFC 81801050), Basic and clinical cooperative research promotion program of Anhui Medical University (2019xkjT026), and Anhui Medical University promotion program of scientific research platform and base construction (2020xkjT060). We thank the technical support from the center for Scientific Research of Anhui Medical University. We thank Dr. Chanjuan Chen for revising the entire manuscript.

Supplementary Materials

Figure S1: sevoflurane postconditioning varied the deposition and distribution of SIRT1 following IRI. Figure S2: relative deacetylation activity of SIRT1 after sevoflurane postconditioning in HT22 cells. Figure S3: relative mRNA level of SIRT1 after siRNA transfection in HT22 cells. Figure S4: sevoflurane postconditioning promoted the cell viability following OGD/R. Figure S5: sevoflurane postconditioning attenuated the apoptosis induced by OGD/R. Figure S6: sevoflurane postconditioning attenuated DNA damage induced by OGD/R. *(Supplementary Materials)*

References

[1] R. Lozano, M. Naghavi, K. Foreman et al., "Global and regional mortality from 235 causes of death for 20 age groups in 1990 and 2010: a systematic analysis for the Global Burden of Disease Study 2010," *Lancet*, vol. 380, no. 9859, pp. 2095–2128, 2012.

[2] J. W. Cannon, "Hemorrhagic shock," *The New England journal of medicine.*, vol. 378, no. 4, pp. 370–379, 2018.

[3] B. Mitra, B. J. Gabbe, K. M. Kaukonen, A. Olaussen, D. J. Cooper, and P. A. Cameron, "Long-term outcomes of patients receiving a massive transfusion after trauma," *Shock (Augusta, Ga)*, vol. 42, no. 4, pp. 307–312, 2014.

[4] J. C. Mira, J. Cuschieri, T. Ozrazgat-Baslanti et al., "The epidemiology of chronic critical illness after severe traumatic injury at two level-one trauma centers," *Critical Care Medicine*, vol. 45, no. 12, pp. 1989–1996, 2017.

[5] C. G. Hughes, A. Morandi, T. D. Girard et al., "Association between endothelial dysfunction and acute brain dysfunction during critical illness," *Anesthesiology*, vol. 118, no. 3, pp. 631–639, 2013.

[6] M. Li, S. C. Li, B. K. Dou et al., "Cycloastragenol upregulates SIRT1 expression, attenuates apoptosis and suppresses neuroinflammation after brain ischemia," *Acta Pharmacologica Sinica*, vol. 41, no. 8, pp. 1025–1032, 2020.

[7] X. W. Zheng, C. S. Shan, Q. Q. Xu et al., "Buyang Huanwu decoction targets SIRT1/VEGF pathway to promote angiogenesis after cerebral ischemia/reperfusion injury," *Frontiers in Neuroscience*, vol. 12, p. 911, 2018.

[8] J. Duan, J. Cui, H. Zheng et al., "Aralia taibaiensis protects against I/R-induced brain cell injury through the Akt/SIRT1/FOXO3a pathway," *Oxidative Medicine and Cellular Longevity*, vol. 2019, Article ID 7609765, 18 pages, 2019.

[9] M. Hernandez-Jimenez, O. Hurtado, M. I. Cuartero et al., "Silent information regulator 1 protects the brain against cerebral ischemic damage," *Stroke; a Journal of Cerebral Circulation*, vol. 44, no. 8, pp. 2333–2337, 2013.

[10] W. Xian, T. Li, L. Li, L. Hu, and J. Cao, "Maresin 1 attenuates the inflammatory response and mitochondrial damage in mice with cerebral ischemia/reperfusion in a SIRT1-dependent manner," *Brain Research*, vol. 1711, pp. 83–90, 2019.

[11] W. Chen, H. Wang, Z. Zhu, J. Feng, and L. Chen, "Exosome-shuttled circSHOC2 from IPASs regulates neuronal autophagy and ameliorates ischemic brain injury via the miR-7670-3p/SIRT1 axis," *Molecular Therapy–Nucleic Acids*, vol. 22, pp. 657–672, 2020.

[12] H. Yan, X. Zhang, W. Hu et al., "Histamine H3 receptors aggravate cerebral ischaemic injury by histamine- independent mechanisms," *Nature Communications*, vol. 5, no. 1, p. 3334, 2014.

[13] H. Lee, Y. H. Park, Y. T. Jeon et al., "Sevoflurane postconditioning increases nuclear factor erythroid 2-related factor and haemoxygenase-1 expression via protein kinase C pathway in a rat model of transient global cerebral ischaemia," *British Journal of Anaesthesia*, vol. 114, no. 2, pp. 307–318, 2015.

[14] H. Xue, Y. H. Zhang, Q. S. Gao et al., "Sevoflurane postconditioning ameliorates neuronal deficits and axon demyelination after neonatal hypoxic ischemic brain injury: role of microglia/macrophage," *Cellular and Molecular Neurobiology*, vol. 41, no. 8, pp. 1801–1816, 2021.

[15] X. Hu, M. Zhang, X. Duan et al., "Sevoflurane postconditioning improves the spatial learning and memory impairments induced by hemorrhagic shock and resuscitation through suppressing IRE1α-caspase-12-mediated endoplasmic reticulum stress pathway," *Neuroscience Letters*, vol. 685, pp. 160–166, 2018.

[16] X. Hu, J. Wang, L. Zhang, Q. Zhang, X. Duan, and Y. Zhang, "Postconditioning with sevoflurane ameliorates spatial learning and memory deficit via attenuating endoplasmic reticulum stress induced neuron apoptosis in a rat model of hemorrhage shock and resuscitation," *Brain Research*, vol. 1696, pp. 49–55, 2018.

[17] Y. Tang, X. F. Xia, Y. Zhang et al., "Establishment of an experimental mouse model of trauma-hemorrhagic shock," *Experimental Animals*, vol. 61, no. 4, pp. 417–425, 2012.

[18] M. C. de Waard, I. van der Pluijm, N. Zuiderveen Borgesius et al., "Age-related motor neuron degeneration in DNA repair-deficient Ercc1 mice," *Acta Neuropathologica*, vol. 120, no. 4, pp. 461–475, 2010.

[19] H. Li, L. Shen, T. Lv et al., "Salidroside attenuates dextran sulfate sodium-induced colitis in mice via SIRT1/FoxOs signaling pathway," *European Journal of Pharmacology*, vol. 861, p. 172591, 2019.

[20] J. Wang, S. Zhu, W. Lu et al., "Varenicline improved laparotomy-induced cognitive impairment by restoring mitophagy in aged mice," *European Journal of Pharmacology*, vol. 916, p. 174524, 2022.

[21] D. Li, Y. Huang, B. Cheng, J. Su, W. X. Zhou, and Y. X. Zhang, "Streptozotocin induces mild cognitive impairment at appropriate doses in mice as determined by long-term potentiation and the Morris water maze," *Journal of Alzheimer's disease : JAD.*, vol. 54, no. 1, pp. 89–98, 2016.

[22] A. K. Kraeuter, P. C. Guest, and Z. Sarnyai, "The open field test for measuring locomotor activity and anxiety-like behavior," *Methods in Molecular Biology*, vol. 1916, pp. 99–103, 2019.

[23] A. Wolf, B. Bauer, E. L. Abner, T. Ashkenazy-Frolinger, and A. M. Hartz, "A comprehensive behavioral test battery to assess learning and memory in 129S6/Tg2576 mice," *PLoS One*, vol. 11, no. 1, article e0147733, 2016.

[24] Z. T. Zhang, C. Y. Hu, F. B. Dai, F. Tang, and C. L. Tang, "Mechanisms and status of research on the protective effects of traditional Chinese medicine against ischemic brain injury," *Tradit Med Res.*, vol. 7, no. 1, p. 6, 2022.

[25] X. R. Wang, R. Ding, T. Q. Tao et al., "Myofibrillogenesis regulator 1 rescues Renal ischemia/reperfusion injury by recruitment of PI3K-dependent P-AKT to mitochondria," *Shock (Augusta, Ga)*, vol. 46, no. 5, pp. 531–540, 2016.

[26] J. Qu, W. Chen, R. Hu, and H. Feng, "The injury and therapy of reactive oxygen species in intracerebral hemorrhage looking at mitochondria," *Oxidative Medicine and Cellular Longevity*, vol. 2016, Article ID 2592935, 9 pages, 2016.

[27] M. Pinto, A. M. Pickrell, X. Wang et al., "Transient mitochondrial DNA double strand breaks in mice cause accelerated aging phenotypes in a ROS-dependent but p53/p21-independent manner," *Cell Death and Differentiation*, vol. 24, no. 2, pp. 288–299, 2017.

[28] Q. Hu, J. Ren, G. Li et al., "The mitochondrially targeted antioxidant MitoQ protects the intestinal barrier by ameliorating mitochondrial DNA damage via the Nrf2/ARE signaling pathway," *Cell Death & Disease*, vol. 9, no. 3, p. 403, 2018.

[29] Q. Hu, Q. Zhou, J. Wu, X. Wu, and J. Ren, "The role of mitochondrial DNA in the development of ischemia reperfusion injury," *Shock (Augusta, Ga)*, vol. 51, no. 1, pp. 52–59, 2019.

[30] A. P. West and G. S. Shadel, "Mitochondrial DNA in innate immune responses and inflammatory pathology," *Nature Reviews. Immunology*, vol. 17, no. 6, pp. 363–375, 2017.

[31] X. Tan, L. Zhang, Y. Jiang et al., "Postconditioning ameliorates mitochondrial DNA damage and deletion after renal ischemic injury," *Nephrology, Dialysis, Transplantation*, vol. 28, no. 11, pp. 2754–2765, 2013.

[32] K. B. Busch, A. Kowald, and J. N. Spelbrink, "Quality matters: how does mitochondrial network dynamics and quality control impact on mtDNA integrity?," *Philosophical Transactions of the Royal Society of London. Series B, Biological Sciences*, vol. 369, no. 1646, p. 20130442, 2014.

[33] S. Michan, Y. Li, M. M. Chou et al., "SIRT1 is essential for normal cognitive function and synaptic plasticity," *The Journal of neuroscience : the official journal of the Society for Neuroscience.*, vol. 30, no. 29, pp. 9695–9707, 2010.

[34] L. Krey, F. Lühder, K. Kusch et al., "Knockout of silent information regulator 2 (SIRT2) preserves neurological function after experimental stroke in mice," *Journal of Cerebral Blood Flow and Metabolism: Official Journal of the International Society of Cerebral Blood Flow and Metabolism*, vol. 35, no. 12, pp. 2080–2088, 2015.

[35] R. Verma, R. M. Ritzel, J. Crapser, B. D. Friedler, and L. D. McCullough, "Evaluation of the neuroprotective effect of Sirt3 in experimental stroke," *Translational Stroke Research*, vol. 10, no. 1, pp. 57–66, 2019.

[36] H. Huang, A. Aminian, M. Hassan et al., "Gastric bypass surgery improves the skeletal muscle ceramide/S1P ratio and upregulates the AMPK/ SIRT1/ PGC-1α pathway in Zucker diabetic fatty rats," *Obesity Surgery*, vol. 29, no. 7, pp. 2158–2165, 2019.

[37] S. Carloni, G. Riparini, G. Buonocore, and W. Balduini, "Rapid modulation of the silent information regulator 1 by melatonin after hypoxia-ischemia in the neonatal rat brain," *Journal of Pineal Research*, vol. 63, no. 3, p. e12434, 2017.

[38] P. B. Ham 3rd and R. Raju, "Mitochondrial function in hypoxic ischemic injury and influence of aging," *Progress in Neurobiology*, vol. 157, pp. 92–116, 2017.

[39] W. Xie, T. Zhu, P. Zhou et al., "Notoginseng leaf triterpenes ameliorates OGD/R-induced neuronal injury via SIRT1/2/3-Foxo3a-MnSOD/PGC-1α signaling pathways mediated by the NAMPT-NAD pathway," *Oxidative Medicine and Cellular Longevity*, vol. 2020, Article ID 7308386, 15 pages, 2020.

[40] B. L. Tang, "Sirt1 and the mitochondria," *Molecules and Cells*, vol. 39, no. 2, pp. 87–95, 2016.

[41] R. Velagapudi, I. Lepiarz, A. El-Bakoush et al., "Induction of autophagy and activation of SIRT-1 deacetylation mechanisms mediate neuroprotection by the pomegranate metabolite urolithin A in BV2 microglia and differentiated 3D human neural progenitor cells," *Molecular Nutrition & Food Research*, vol. 63, no. 10, article e1801237, 2019.

[42] R. Huang, Y. Xu, W. Wan et al., "Deacetylation of nuclear LC3 drives autophagy initiation under starvation," *Molecular Cell*, vol. 57, no. 3, pp. 456–466, 2015.

[43] J. X. Tan and T. Finkel, "Autophagy goes nuclear," *Nature Cell Biology*, vol. 22, no. 10, pp. 1159–1161, 2020.

[44] C. Xu, L. Wang, P. Fozouni et al., "SIRT1 is downregulated by autophagy in senescence and ageing," *Nature Cell Biology*, vol. 22, no. 10, pp. 1170–1179, 2020.

[45] L. Wang, C. Xu, T. Johansen, S. L. Berger, and Z. Dou, "SIRT1 - a new mammalian substrate of nuclear autophagy," *Autophagy*, vol. 17, no. 2, pp. 593–595, 2021.

[46] Y. Jiang, B. O. A. Botchway, Z. Hu, and M. Fang, "Overexpression of SIRT1 inhibits corticosterone-induced autophagy," *Neuroscience*, vol. 411, pp. 11–22, 2019.

[47] S. Y. Song, X. W. Meng, Z. Xia et al., "Cognitive impairment and transcriptomic profile in hippocampus of young mice after multiple neonatal exposures to sevoflurane," *Aging*, vol. 11, no. 19, pp. 8386–8417, 2019.

[48] J. Wu, J. Yu, P. Xie et al., "Sevoflurane postconditioning protects the myocardium against ischemia/reperfusion injury via activation of the JAK2-STAT3 pathway," *PeerJ*, vol. 5, article e3196, 2017.

[49] J. W. Hwang, Y. T. Jeon, Y. J. Lim, and H. P. Park, "Sevoflurane postconditioning-induced anti-inflammation via inhibition of the Toll-like receptor-4/nuclear factor kappa B pathway contributes to neuroprotection against transient global cerebral ischemia in rats," *International Journal of Molecular Sciences*, vol. 18, no. 11, p. 2347, 2017.

[50] A. Cheng, Y. Lu, Q. Huang, and Z. Zuo, "Attenuating oxygen-glucose deprivation-caused autophagosome accumulation may be involved in sevoflurane postconditioning-induced protection in human neuron-like cells," *European Journal of Pharmacology*, vol. 849, pp. 84–95, 2019.

Hindawi
Oxidative Medicine and Cellular Longevity
Volume 2022, Article ID 8188404, 26 pages
https://doi.org/10.1155/2022/8188404

Research Article

The lncRNA-AK046375 Upregulates Metallothionein-2 by Sequestering miR-491-5p to Relieve the Brain Oxidative Stress Burden after Traumatic Brain Injury

Wei Tang, Weina Chai, Donglin Du, Yongzhi Xia, Yifan Wu, Li Jiang, Chongjie Cheng, Zongduo Guo, Xiaochuan Sun, Zhijian Huang, and Jianjun Zhong

Department of Neurosurgery, The First Affiliated Hospital of Chongqing Medical University, Chongqing, China 400016

Correspondence should be addressed to Zhijian Huang; zhijian@cqmu.edu.cn and Jianjun Zhong; jianjun@hospital.cqmu.edu.cn

Received 25 July 2021; Revised 8 December 2021; Accepted 27 December 2021; Published 16 February 2022

Academic Editor: Xin Luo

We previously discovered that traumatic brain injury (TBI) induces significant perturbations in long noncoding RNA (lncRNA) levels in the mouse cerebral cortex, and lncRNA-AK046375 is one of the most significantly changed lncRNAs after TBI. lncRNA-AK046375 overexpression and knockdown models were successfully constructed both *in vitro* and *in vivo*. In cultured primary cortical neurons and astrocytes, lncRNA-AK046375 sequestered miR-491-5p, thereby enhancing the expression of metallothionein-2 (MT2), which ameliorated oxidative-induced cell injury. In addition, upregulated lncRNA-AK046375 promoted the recovery of motor, learning, and memory functions after TBI in C57BL/6 mice, and the underlying mechanism may be related to ameliorated apoptosis, inhibited oxidative stress, reduced brain edema, and relieved loss of tight junction proteins at the blood-brain barrier in the mouse brain. Therefore, we conclude that lncRNA-AK046375 enhances MT2 expression by sequestering miR-491-5p, ultimately strengthening antioxidant activity, which ameliorates neurological deficits post-TBI.

1. Introduction

Traumatic brain injury (TBI) is a significant cause of morbidity and mortality worldwide [1, 2]. According to its pathophysiological process, TBI can be divided into primary injury and secondary injury. The secondary injury, such as oxidative stress, mitochondrial dysfunction, calcium overloading, and neuroinflammation, strongly influences the outcomes of TBI, which to some degree are reversible and can be mitigated by therapeutics [3–5]. Although there have been many studies seeking to develop TBI therapies in recent years, no available therapeutic method has been confirmed to convey significant improvement for TBI patients in clinical practice.

Long noncoding RNAs (lncRNAs) are defined as RNAs with >200 nucleotides in length without protein-coding ability. lncRNAs have been found to regulate gene expression at the epigenetic, transcriptional, and posttranscriptional levels and actively participate in various physiological and pathological processes [6]. Increasing evidence has shown that lncRNAs participate in the modulation of central nervous system (CNS) development and disease [7]. Several studies have demonstrated that TBI induces perturbations of lncRNA levels in the mouse brain, but few studies have probed the possible roles of lncRNAs in the pathological progression of TBI. We previously reported significant upregulation of lncRNA-AK046375 levels (~4-fold compared to preinjury levels) in the mouse cortex around the injury site after TBI [8], and the present study is aimed at further interrogating whether and how lncRNA-AK046375 is involved in post-TBI pathology. lncRNA-AK046375, with a clone number of "B230377K03" in the GenBank database, has 2,662 nucleotide bps and has not been described by its biological functions. In our lncRNA-AK046375 overexpressing cell model, next-generation sequencing results revealed that lncRNA-AK046375 might be involved in cellular antioxidation activity.

Excessive production of oxidants and free radicals is a common feature in the injured cortex after TBI, and relieving oxidative stress burden is expected to be neuroprotective and to ameliorate neurological deficits after TBI.

In this study, lncRNA-AK046375 was found to function as an antioxidative factor, conveying neuroprotection through inhibiting apoptosis, maintaining the integrity of the blood brain barrier (BBB), and relieving brain edema in the mouse brain after TBI. Moreover, the mechanism underlying the antioxidative effects of lncRNA-AK046375 is likely related to its sequestering miR-491-5p and enhancing MT2 expression.

2. Materials and Methods

2.1. Ethics Statement. All procedures strictly followed the institutional guidelines of Chongqing Medical University and complied with the Guide for the Care and Use of Laboratory Animals issued by the Ministry of Science and Technology of the People's Republic of China. Animal experiments complied with the ARRIVE (Animal Research: Reporting *In Vivo* Experiments) ethical guidelines and were confirmed by the Institutional Animal Care and Use Committee (IACUC) of Chongqing Medical University (approving number: 20141011).

2.2. Recombinant Overexpression and Knockdown lncRNA-AK046375 Adenovirus. The lncRNA-AK046375 overexpression adenovirus (1.0×10^{11} pfu/ml), overexpression control adenovirus (5.5×10^{10} pfu/ml), lncRNA-AK046375 knockdown adenovirus (1.0×10^{11} pfu/ml), and knockdown control adenovirus (1.0×10^{11} pfu/ml) were produced by Sangon Biotech Co., Ltd. (Shanghai, China). The overexpression of adenovirus constructs is pADV-mCMV-MCS, and the knockdown of adenovirus constructs is pAVsiRNA1.1.

2.3. Animals. Adult male C57BL/6 mice ($n = 270$) were purchased from the animal experimental center of Chongqing Medical University (Chongqing, China). Mice were randomly divided into 6 groups: (1) sham (received only craniotomy, but no TBI or any treatment, $n = 45$), (2) TBI (received only TBI, $n = 45$), (3) AK046375 overexpression (received TBI and AK046375-overexpression adenovirus, $n = 45$), (4) vector overexpression (received TBI and AK046375 overexpression control adenovirus, $n = 45$), (5) AK046375 knockdown (received TBI and AK046375 knockdown adenovirus, $n = 45$), and (6) vector knockdown (received TBI and AK046375 knockdown control adenovirus, $n = 45$). All mice were housed in the experimental animal center of Chongqing Medical University (Chongqing, China) in a 12/12 dark and light environment. Methods of anesthesia induction were followed as in our previously published study [9]. Newborn mice ($n = 120$) were used to extract and culture primary cortical neurons and astrocytes.

2.4. Intracerebroventricular Injection. The adenovirus was cranially injected into the lateral ventricles in a stereotaxic device under general anesthesia based on protocols described in our previously published study [9]. Briefly, once achieving an appropriate level of anesthesia (the mice in this study were anesthetized induction with 3% isoflurane in a 67% N_2O/30% O_2, and maintained by 5% isoflurane), 3 μl diluted adenovirus were injected into the right cerebral lateral ventricle at the following coordinates (mm from the bregma) under stereotaxic apparatus guidance: AP+1.5, ML+1, and DV-2.

2.5. Controlled Cortical Injury (CCI). A CCI model was exploited to mimic TBI in mice under appropriate general anesthesia on 7 days after adenovirus injection using our previously reported parameters: (1) velocity: 5.0 m/s, [2] depth: 2.0 mm, and [3] dwelling time: 100 ms. The sham group received only a craniotomy, but no CCI impact [9].

2.6. Neurobehavioral Tests. We evaluated neurobehaviors in mice according to our previously published protocols [9, 10]. Briefly, neurological severity scores (NSS), wire-gripping scores, and rotarod test were used to evaluate neurological function in mice on the preoperative, 1, 3, 7, and 14 days after CCI. Cued learning ability was assessed using the Morris water maze test on 15 to 19 days after CCI. The spatial memory was evaluated by Morris water maze test on 20 days after CCI when the hiding platform was removed. The platform was located in quadrant 4.

2.7. Cell Culture

2.7.1. HT22 Cell Culture. The immortalized mouse hippocampal cell line (HT22) was provided by JENNIO Biological Technology (Guangzhou, China) and cultured in DMEM (Gibco, Carlsbad, USA) with 10% fetal bovine serum (FBS) (Wisent Biotechnology Co. Ltd., Nanjing, China) and 1% penicillin and streptomycin (Gibco, Carlsbad, USA). And the culture media was regularly replaced every 3 days.

2.7.2. Primary Cortical Neuron Culture. Primary cortical neurons were harvested from newborn mice (C57BL/6, postnatal 24 h) as described in previous studies [11]. Briefly, the newborn mice were disinfected with 75% ethanol and euthanized by decapitation, and the meninges were removed out and the cerebral cortex was made into single suspended cells with digesting buffer (papain (2 mg/ml)) (Worthington, America)/DNase I (Solarbio life science, Beijing, China) (10 mg/ml) = 1/100). The cells were seeded into the plates coated with polylysine (Solarbio Life Science, Beijing, China). Culture media (Neurobasal-A (Gibco, Carlsbad, USA) containing 2% B27 (Invitrogen, America) and 2 Mm glutamine (Gibco, Carlsbad, USA)) were regularly replaced every 3 days, and adenovirus were used to infect neurons at a MOI = 50 for 8 h.

2.7.3. Primary Cortical Astrocyte Culture. Primary cortical astrocytes were harvested using previously described protocols [12, 13]. Briefly, the newborn mice were disinfected with 75% ethanol and euthanized by decapitation, and the meninges were removed out, and the cerebral cortex was made into single suspended cells with digesting buffer (0.025%Tyrisin/DNase I (10 mg/ml) = 1/100). Adenovirus was used to infect the astrocytes under an MOI = 20 for 6 h. Media was replaced with complete medium

(DMEM/F12 : FBS = 10 : 1) after miR-491-5p mimics, miR-491-5p inhibitor, mimics-NC, and inhibitor-NC (Gene Pharma, Shanghai, China) were diluted in DMEM/F12 medium to transfect astrocytes for 7 h. To investigate how AK046375 regulates MT2 expression, miR-491-5p mimic or inhibitor was administered for 48 h starting on the 3rd day after virus infection.

2.8. Cell Counting Kit 8 (CCK8) Assay. The CCK8 assay (Dojindo Laboratories, Japan) was performed per the instructions. In brief, primary cortical neurons and astrocytes were washed with PBS after received H_2O_2 treatments (supplementary fig. 3); 100 μl of serum-free medium containing 10% CCK8 working buffer was added to each well and maintained (neuron for 4 h, astrocyte for 2 h) at 37°C. A microplate reader (Thermo Fisher, America) was used to detect the absorbance at the 550 nm. The cell vitality was calculated by the ratio of (sample group – blank group)/(nontreated group – blank group).

2.9. LDH Assay. Lactate dehydrogenase (LDH) released into the medium from cells was measured using the LDH release assay kit (Beyotime biotechnology, Shanghai, China) as described in instructions. The LDH releasing rate was calculated by the ratio of (sample group – blank group)/(nontreated group – blank group).

2.10. Quantitative Real-Time Polymerase Chain Reaction (qRT-PCR) Assay. TRIzol reagent (Takara, Japan) was applied to extract total cellular or tissue RNA. qRT-PCR was applied on an Applied Biosystems® 7500 Fast system. mRNA primers (AK046375: forward: GCTCAAGGGAT ATGGCCAGC, reverse: CGCTCAGCTCCTTTGCTCTC; MT2: forward: CAGATATACCAGCCCAGTGAAC, reverse: GAG- TGTACTTGGTAGAGGTGAC; miR-491-5p: forward AGTGGGGAACCCTTCCATGAG) were synthesized by Sangon Biotech (Shanghai, China) and normalized to actin and U6, respectively. The quantification of genes was carried out per the formula $2^{-(\Delta Ct-\bar{\Delta} Ct)}$.

2.11. Western Blotting Assay. Tissue and cell lysates were separated, transferred to 0.45 μm PVDF membranes (Millipore, America), blocked and incubated in primary antibodies (metallothionein 2, MT2, 1 : 200, Immunoclone, America, ICA868Hu01). BCL2(1 : 1000, 15071), cleaved-caspase 3 (1 : 1000, 9661S), SOD2(1 : 1000, 13194), CAT (1 : 1000, 12980) (CST, America). cytochrome C (1 : 500, Abcam, Britain, ab133504). Bax (1 : 1000, 60267-1-Ig), VDAC1(1 : 1000, 66345-1-Ig) (Proteintech, Wuhan, China), malondialdehyde (MDA) (1 : 1000, Novus, America, NBP2-59366). claudin 5 (1 : 1000, #AF5216), ZO1 (1 : 1000, #AF5145), occludin (1 : 1000, #DF7504) (Affinity, Jiangsu, China), and β-actin (1 : 800, Boster, Wuhan, China, BA2305), and followed by incubation in HRP-conjugated secondary antibodies (Proteintech, Wuhan, China, SA00001-1 and SA00001-2). The membranes were visualized by the ECL system (Thermo, America, 32132), and the quantification of the band intensity were calculated by the ImageJ software [14, 15].

2.12. GSH and GSSG Assays. The total glutathione/oxidized glutathione assay kit (Nanjing JianCheng, Nanjing, China) was used to detect expression GSSG (oxidized glutathione, GSSG), GSH (reduced glutathione), and the GSH/GSSG ratio per the manufacturer's protocol.

2.13. MitoSOX™ Assay. The MitoSOX™ red mitochondrial superoxide indicator (Invitrogen, America) was used to determine mitochondrial superoxide expression in neurons and astrocytes as previously described [16]. Briefly, the live cells were incubated with 5 μM of MitoSOX™ Red at 37°C for 10 min after received the treatments and then washed 3 times in Hank's solution; the stained cells were imaged by confocal microscopy with analysis using Image-Pro Plus.

2.14. Immunofluorescence Assay. Immunofluorescence staining was performed as described in previous protocols [15]. Brain sections, primary cortical neurons, and astrocytes were fixed in 4% paraformaldehyde, blocked in 5% goat serum, and then incubated in primary antibody β3 tubulin (1 : 50, 4466), GFAP (1 : 400, 3670), NeuN (1 : 400, #243075), (CST, America), and MT2 (1 : 25) at 4°C overnight, followed by incubation with secondary antibody (dylight 650 goat anti-mouse IgG (A23610), dylight 594 goat anti-rabbit IgG (A23420)) (Abbkine, America) at 37°C for 60 min. Images were taken by confocal microscopy.

2.15. TUNEL Assay. Apoptotic cells were detected as in previously published protocols [17]. Briefly, the one step TUNEL apoptosis assay kit (Beyotime, Shanghai, China) was performed per the manufacturer's instructions, and images were taken by confocal microscopy.

2.16. Brain Water Content Assay. Brain water content was assessed on 7 days after CCI as previously described and calculated as $[(\text{wet weight} - \text{dry weight})/\text{wet weight}] \times 100\%^2$.

2.17. Evans Blue Fluorescence and Extravasation of Evans Blue In Vivo. Evans blue fluorescence and the content of Evans blue in brain tissue on 7 days after TBI were performed as in previous protocols [2, 18]. Briefly, mice were injected with 2% Evans blue (5 ml/kg) via the tail vein 1 h before brain removal, and the brain was snap frozen right after removal and sectioned and visualized by confocal microscopy. Besides, we also detected the content of Evans blue in brain tissue which exuated from the injury vascellum. The brain supernatants were made with 0.9% saline after perfusion with 0.9% saline; the contents of Evans blue in mice were detected by spectrophotometer.

2.18. Dual-Luciferase Reporter Assay. The dual-luciferase reporter assay was performed as previously published to determine whether miRNAs directly bind to their target gene. Briefly, to verify whether miR-491-5p and/or miR-505-3p could bind to the 3′-UTRs of MT2-mRNA and AK046375, the predicted 3′-UTRs wild-type or mutant binding sequence of MT2 or AK046375 were designed and predicted using the databases "miRanda," "PITA," and "RNAhybrid." Binding sequences (wild-type or mutant binding sequences) were cloned into the pmirGLO vector. Firstly, the pGL3-MT2-WT

vector, pGL3-MT2-MUT vector, miR-491-5p/miR-505-3p mimics, and its negative controls were randomly cotransfected into 293T cells to verify whether miR-491-5p and/or miR-505-3p could bind to the 3′-UTRs of MT2-mRNA. Secondly, the pGL3-AK046375-WT vector, pGL3-AK046375-MUT vector, miR-491-5p mimics, and its negative control were randomly cotransfected into 293T cells to verify whether AK046375 could sequester miR-491-5p. And then, a chemiluminescent analyzer (Biosino, Beijing, China) was used to detected luciferase activity.

2.19. RNA Immunoprecipitation (RIP) Assay. The RIP assay was performed per the manufacturer's instructions. In brief, HT22 cells were lysed in 500 μl RIP lysis buffer (Thermo Fisher, America). Normal mouse IgG was regarded as a negative control and was separately added into the RIP buffer. Dynabeads® protein G (Thermo, America) were then added into the buffer, collected, and divided into two parts, one for detecting the content of AGO2 (CST, America) by western blotting and the remaining for detecting the expression levels of AK046375 and miR-491-5p by qRT-PCR.

2.20. Statistical Analysis. All experimental data were analyzed by SPSS 19.0 software and are expressed as the mean ± standard deviation (SD). NSS scoring and water maze test (latency and time spent in the correct quadrant (%)) were analyzed by two-way ANOVA followed by Tukey's post hoc test [9]. The remaining data were analyzed using t-test or one-way ANOVA followed by Tukey's post hoc test. All statistical plots were created using GraphPad Prism V5.0, and $P < 0.05$ was considered statistically significant.

3. Results

3.1. AK046375 Overexpression Induces Significantly Increased MT2 Expression. We used 5′- and 3′-RACE analyses to identify a 2581 bp full-length transcript of AK046375 (supplementary figure 1) and performed RNA-seq followed by bioinformatics analysis to determine whether overexpression of lncRNA-AK046375 induced alterations in mRNAs. Our next-generation sequencing results revealed that 1342 mRNAs were significantly altered in response to increased AK046375 overexpression (supplementary fig. 2A). These raw data were all submitted to the GEO database (ID number: GSE103353). Among the most significantly changed genes, we noticed that MT2 mRNA level was significantly elevated (~6-fold) by AK046375 overexpression (supplementary table 1). In addition to upregulation of MT2 mRNA, MT2 protein levels were also significantly increased in HT22 cells by AK046375 overexpression (supplementary fig. 2B). To further prove that AK046375 could upregulate the expression of MT2, we also tested whether AK046375 could upregulate the MT2 expression in primary cortical neurons and astrocytes. Firstly, we succeeded to transfect the AK046375 overexpression and knockdown adenovirus into the primary cortical neurons and astrocytes (Figures 1(a) and 1(e)). Secondly, it was interesting to found that AK046375 overexpression could also significantly increase the expression of MT2 compared to the nontreated group, by qRT-PCR, western blotting, and immunofluorescence in primary cortical neurons ($P < 0.05$, Figures 1(b)–1(d)) and astrocytes ($P < 0.05$, Figures 1(f)–1(h), and downregulation of AK046375 could significantly decrease the MT2 expression compared to the nontreated group in primary cortical neurons ($P < 0.05$, Figures 1(b)–1(d)) and astrocytes ($P < 0.05$, Figures 1(f)–1(h)). Therefore, these results proved that AK046375 overexpression resulted in upregulation of MT2 expression, suggesting that MT2 might be involved in the biological functions of AK046375. MT2 is a special protein with low molecular weight and high cysteine that binds a large number of heavy metal ions, which grant it strong antioxidant activity [19, 20].

Given these results, we hypothesized that upregulated AK046375 in the cerebral cortex after TBI might be involved in cellular antioxidation activity. Therefore, we investigated the antioxidation effects of AK046375 and the underlying mechanism.

3.2. Potential Mechanisms by which AK046375 Increases MT2 Expression

3.2.1. miR-491-5p Decreases MT2 Expression and Exaggerates H_2O_2-Induced Oxidative Stress in Astrocytes. miRNAs are small noncoding RNAs (18-23 bp) that inhibit the translation of their target mRNAs by binding to the 3′-UTR of mRNA. Both AK046375 and MT2 mRNA were predicted to possess common binding sites for miR-491-5p and miR-505-3p. However, in our dual-luciferase reporter assay, only miR-491-5p, not miR-505-3p, decreased MT2 wild-type fluorescence intensity ($P < 0.05$, Figure 2(a)), indicating that miR-491-5p does indeed bind to the 3′-UTR of MT2 mRNA directly. We also found that MT2 mRNA and protein expression levels were higher in the miR-491-5p inhibitor group ($P < 0.05$, Figures 2(b) and 2(c)) and lower in the miR-491-5p mimics group ($P < 0.05$, Figures 2(b) and 2(c)) compared to their respective control groups, indicating that miR-491-5P indeed decreases the expression of MT2.

When H_2O_2 treatment was applied in primary astrocytes, cell vitality was reduced in the miR-491-5p mimics +H_2O_2group ($P < 0.05$, Figure 2(d)) but was enhanced in the miR-491-5p inhibitor+H_2O_2 group ($P < 0.05$, Figure 2(d)) compared to the inhibitor-NC+H_2O_2 group and the mimics-NC+H_2O_2 group, respectively. The content of LDH and fluorescence intensity of MitoSOX^{red} were higher in the miR-491-5p mimics+H_2O_2 group ($P < 0.05$, Figures 2(e) and 2(f)) compared to the mimics-NC+H_2O_2 group, but lower in the miR-491-5p inhibitor+H_2O_2 group ($P < 0.05$, Figures 2(e) and 2(f)) compared to the inhibitor-NC+H_2O_2 group. These results indicate that miR-491-5p exaggerates H_2O_2-induced injury in astrocytes by inhibiting the expression of MT2.

3.2.2. AK046375 Enhances MT2 Expression by Sequestering miR-491-5p. To confirm that AK046375 upregulated MT2 expression by competitively sequestering miR-491-5p, we performed a dual-luciferase reporter assay and found that miR-491-5p decreased the fluorescence intensity of the

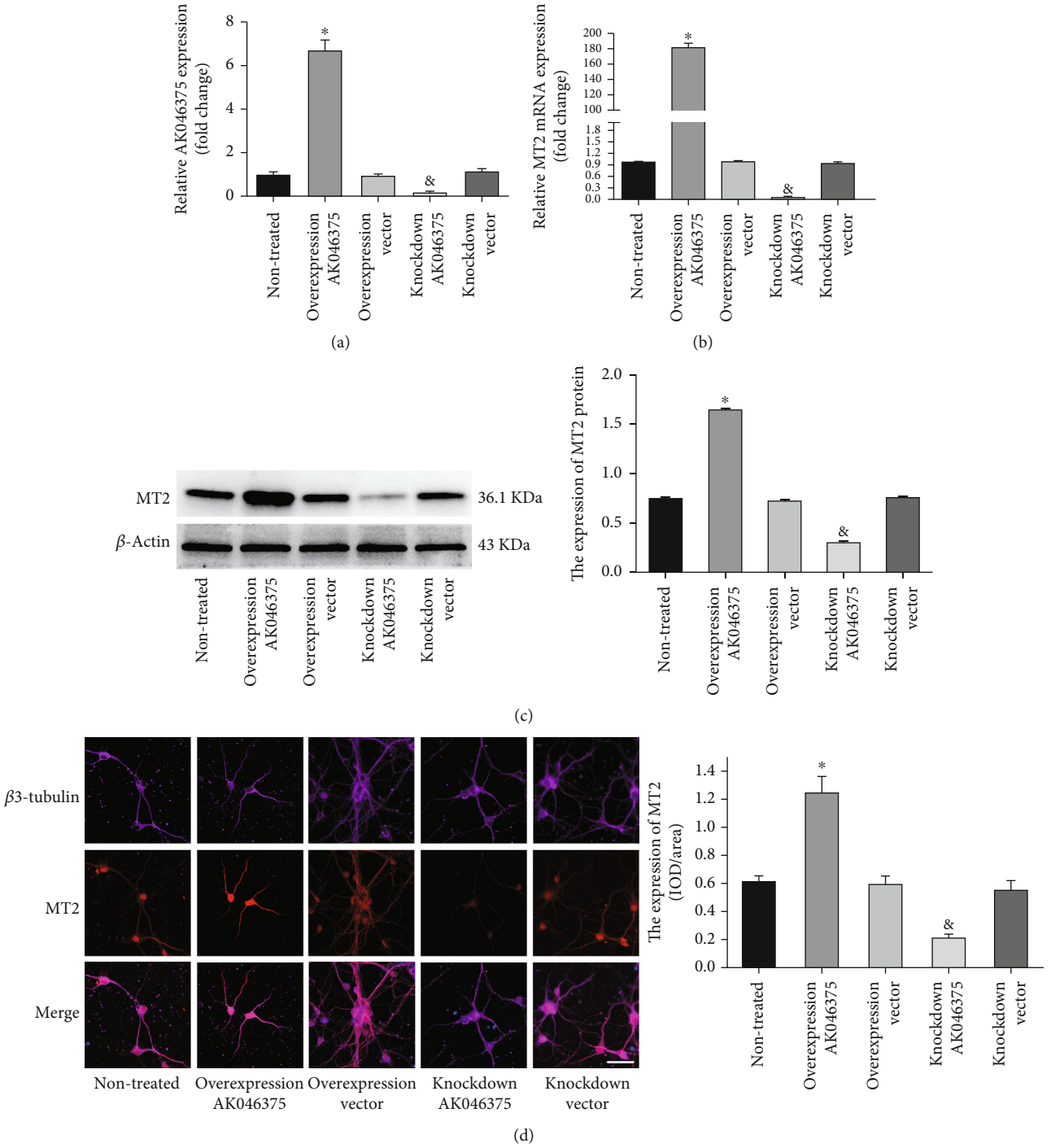

Figure 1: Continued.

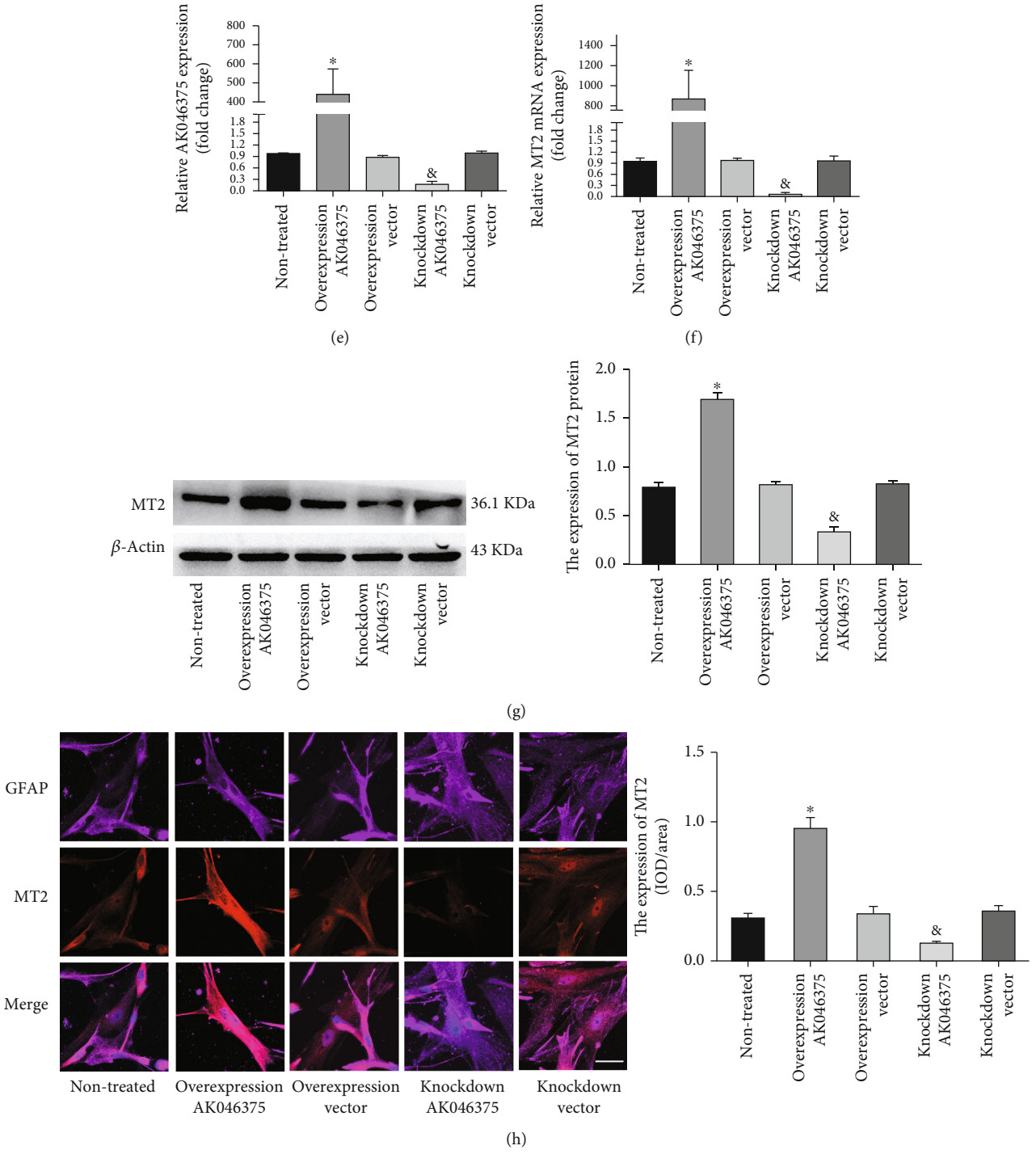

Figure 1: AK046375 significantly upregulates the expression of MT2 in primary cortical neurons and astrocytes. (1) Quantitative PCR analysis of AK046375 levels in mouse primary cortical neurons (a) and astrocytes (e) after transfection with either overexpression or knockdown AK046375 adenovirus or their responding control vector viruses. (2) Quantitative PCR analysis of MT2-mRNA levels and western blotting results of MT2 in mouse primary cortical neurons (b, c) and astrocytes (f, g) after transfection with either overexpression or knockdown AK046375 adenovirus or their corresponding vector viruses. (3) Immunofluorescence images of MT2 in primary neurons (d) and astrocytes (h) with different AK046375 levels and their quantification. β3-Tubulin is a neuronal marker, and glial fibrillary acidic protein (GFAP) is an astrocytic marker ($n = 6$/group, mean ± SD, $^{*}P < 0.05$ vs. the overexpression vector group, $^{\&}P < 0.05$ vs. the knockdown vector group by one-way ANOVA; scale bar = 50 μm, 400x).

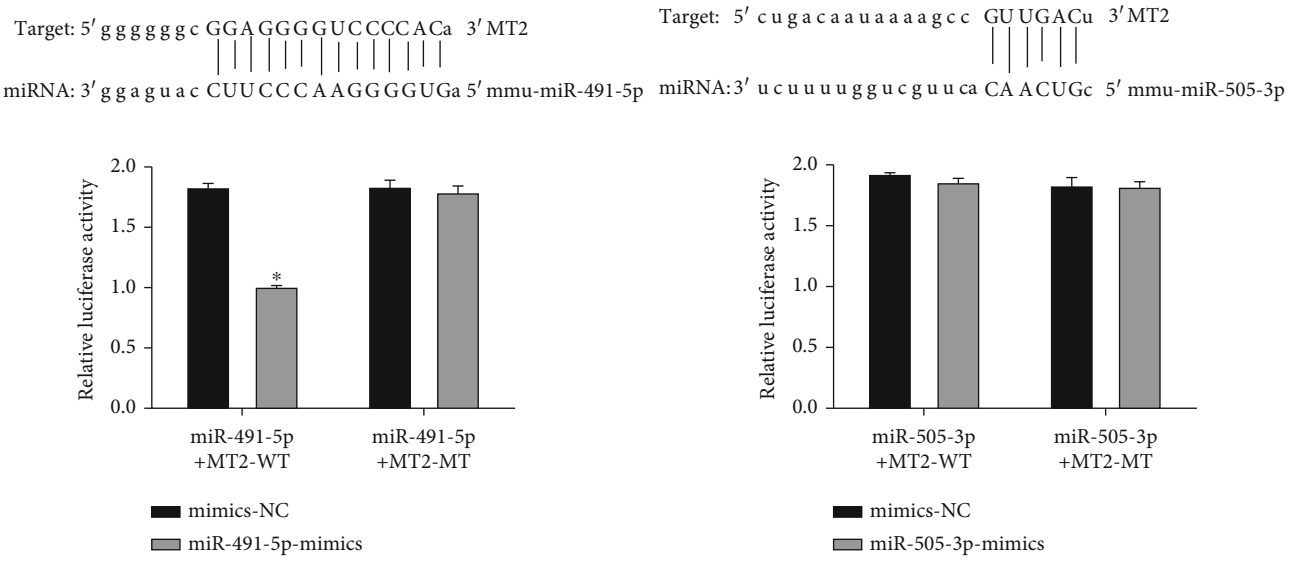

(a)

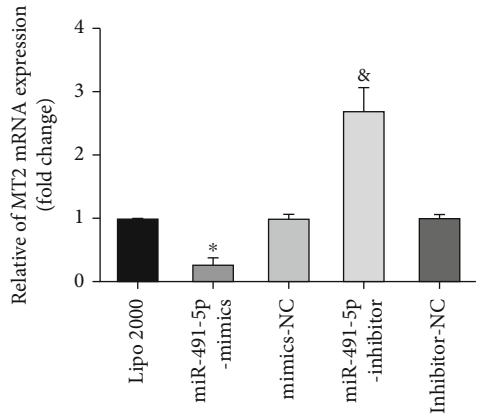

(b)

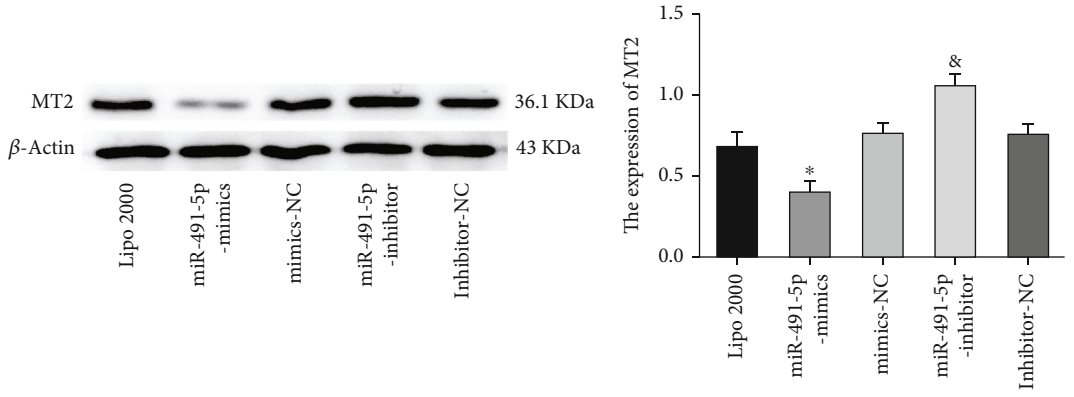

(c)

Figure 2: Continued.

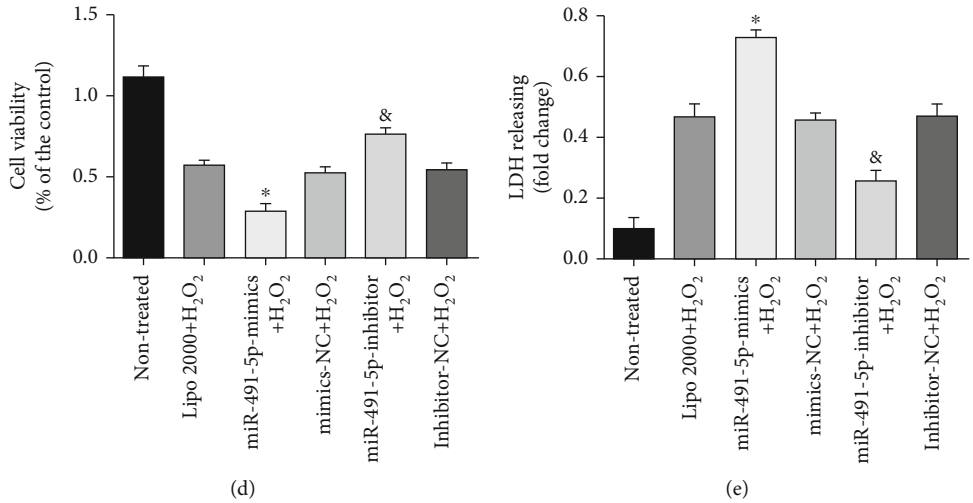

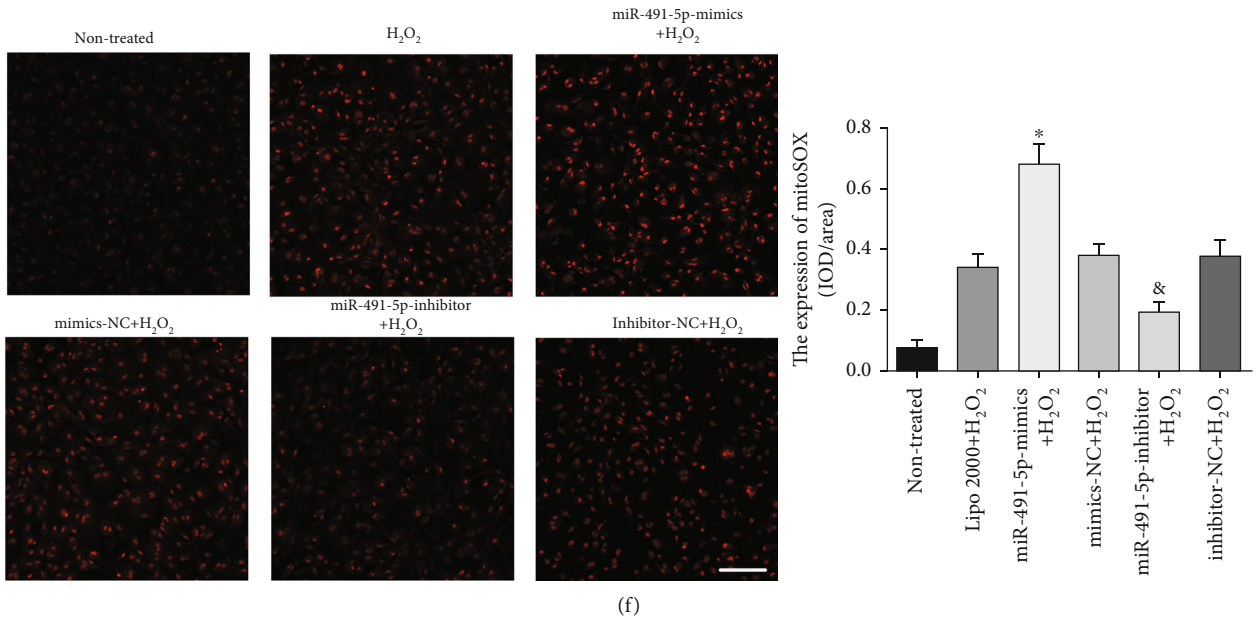

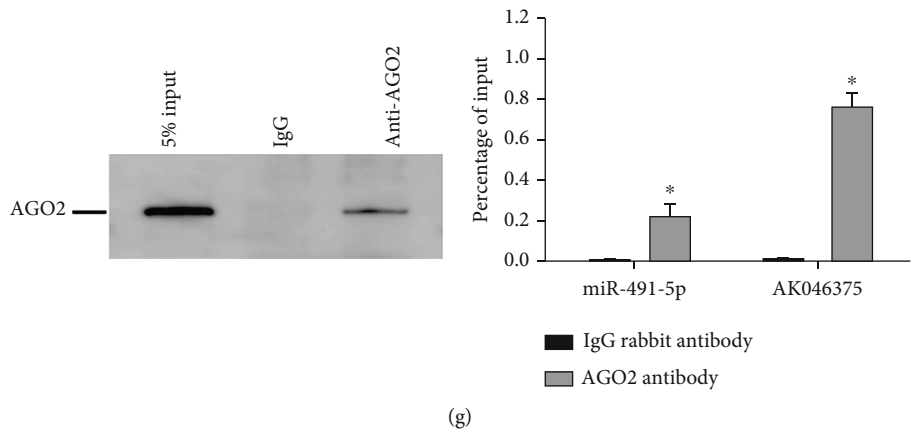

Figure 2: Continued.

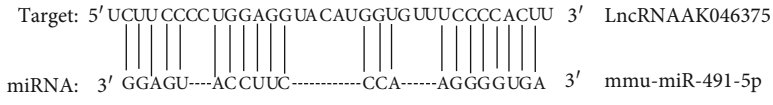

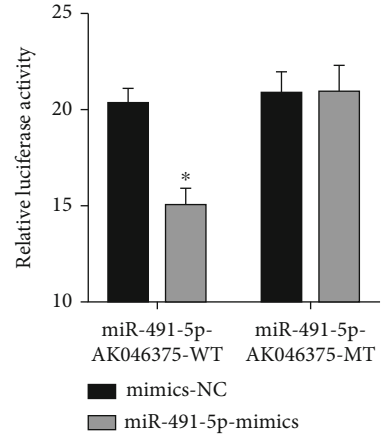

(h)

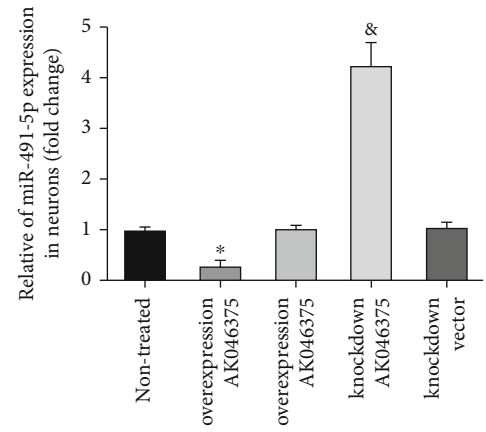

(i)

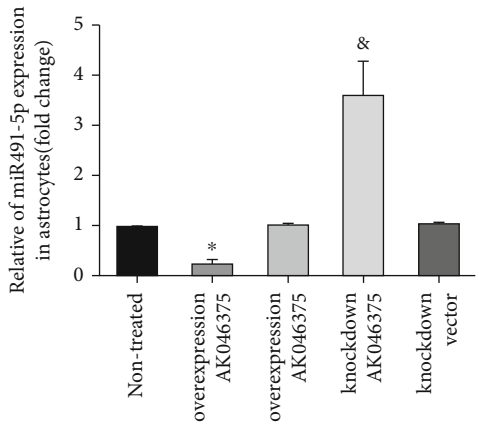

(j)

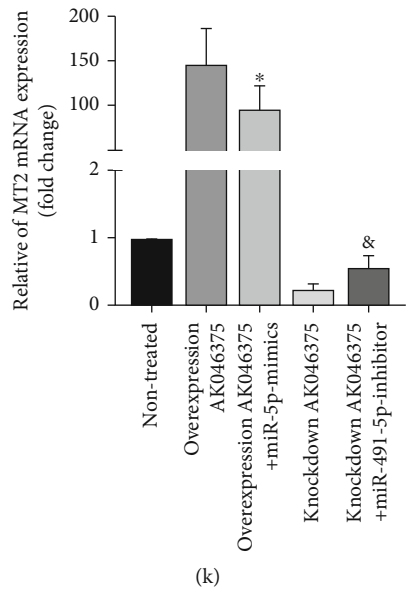

(k)

Figure 2: Continued.

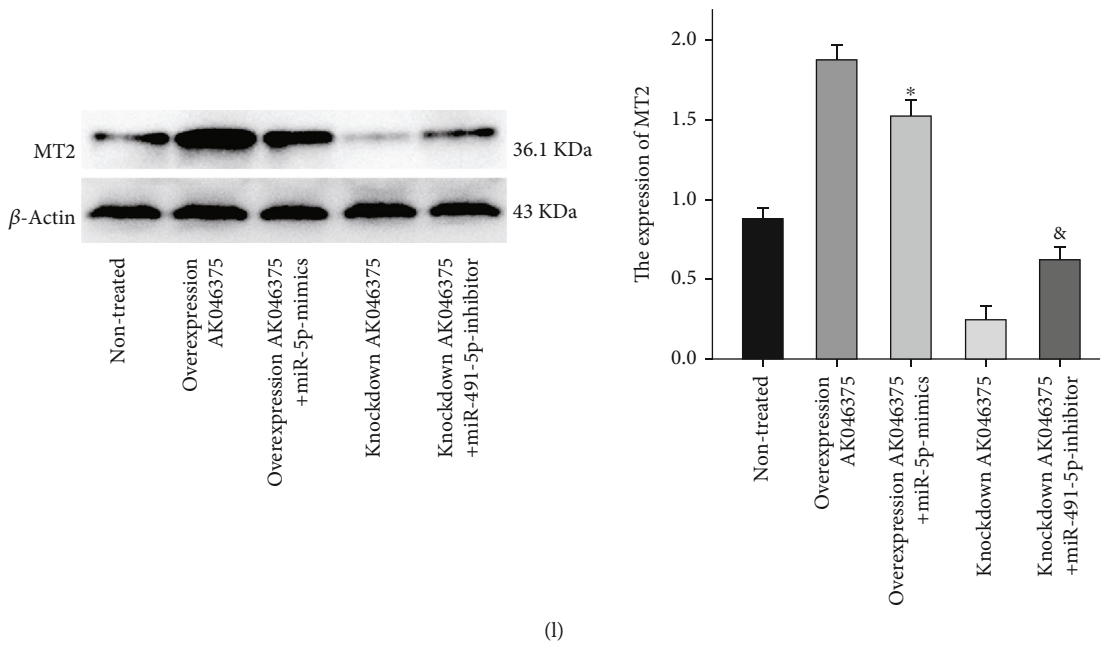

(l)

Figure 2: AK046375 upregulates MT2 expression by acting as a "sponge" for miR-491-5p. (a) Predicted binding sites of miR-491-5p and miR-505-3p with MT2-mRNA-3′-UTR and dual-luciferase reporter gene assay results verifying their binding activity ($n = 5$/group, mean ± SD, $^{*}P < 0.05$ vs. the mimics-NC group by t-test). (b) Expression of MT2 mRNA and MT2 protein levels in response to miR-491-5p-mimics or miR-491-5p-inhibitors in primary astrocytes ($n = 6$/group, mean ± SD, $^{*}P < 0.05$ vs. the mimics-NC group, $^{\&}P < 0.05$ vs. the inhibitors-NC group by one-way ANOVA). (d–f) Cell viability, membrane damage, and oxidative burden in astrocytes of each group ($n = 6$/group, mean ± SD, $^{*}P < 0.05$ vs. the mimics-NC+H_2O_2 group, $^{\&}P < 0.05$ vs. the inhibitors-NC+H_2O_2 group by one-way ANOVA, scale bar = 50 μm, 200x). (g) Ago2 protein level detected by western blot analysis. Quantitative PCR analysis of AK046375 and miR-491-5p levels compared to the input ($n = 3$/group, mean ± SD, $^{*}P < 0.05$ vs. the IgG group by t-test). (h) Potential binding sites of miR-491-5p with AK046375 (up), and luciferase activity of the wild-type and mutant AK046375 groups with miR-491-5p in 293T cells (down) ($n = 5$/group, mean ± SD, $^{*}P < 0.05$ vs. the mimics-NC group by t-test). (i, j) Quantitative PCR analysis of miR-491-5p levels in primary neurons and astrocytes after transfection with either overexpression or knockdown AK046375 adenovirus or their corresponding vector viruses ($n = 6$/group, mean ± SD, $^{*}P < 0.05$ vs. the overexpression vector group, $^{\&}P < 0.05$ vs. the AK046375 overexpression group by one-way ANOVA). (k, l) Quantitative PCR analysis of MT2 mRNA levels and western blotting results of MT2 in astrocytes from each group after transfection with AK046375 overexpression or knockdown adenovirus, miRN-491-5p-mimics, and miR-491-5p-inhibitor and their quantification ($n = 4$/group, mean ± SD, $^{*}P < 0.05$ vs. the AK046375 overexpression group, $^{\&}P < 0.05$ vs. the AK046375 knockdown group by one-way ANOVA).

AK046375 wild-type group significantly ($P < 0.05$, Figure 2(h)), indicating that miR-491-5p can bind to the AK046375. miRNAs have been found to perform their functions through forming ribonucleoprotein complexes (miRNPs) in which AGO2 is involved as a core component [21]. An RIP assay was performed in HT22 cells and demonstrated that both AK046375 and miR-491-5p were pulled down by the AGO2 antibody (Figure 2(g)), Furthermore, AK046375 overexpression could also inhibit the expression of miR-491-5p ($P < 0.05$, Figures 2(i) and 2(j)) in primary cortical neurons and astrocytes compared to their respective control groups.

To further investigate the relationship of AK046375 and miR-491-5p in the regulation of MT2 expression, we found that the expression of MT2 was lower in the AK046375 overexpression+miR-491-5p mimics group ($P < 0.05$, Figures 2(k) and 2(l)) compared to the AK046375 overexpression group and was higher in the AK046375 knockdown+miR-491-5p inhibitor group ($P < 0.05$, Figures 2(k) and 2(l)) compared to the AK046375 knockdown group, indicating that miR-491-5p is involved in the modulation of AK046375 on the MT2 expression. Based on AK046375 being simultaneously pulled down with miR-491-5p and miR-491-5p imposing a direct mediating effect on AK046375 for MT2 regulation, we inferred that AK046375 might upregulate MT2 expression by sequestering miR-491-5p.

3.3. AK046375 Alleviates H_2O_2-Induced Injury in Primary Cortical Neurons and Astrocytes

3.3.1. AK046375 Alleviates H_2O_2-Induced Oxidative Stress in Primary Cortical Neurons and Astrocytes. We measured oxidative stress in cells in response to H_2O_2 treatment. MitoSOX^{red} staining was applied to specifically detect reactive oxygen species in mitochondria. CAT, GSH, and SOD2 play important roles in cellular against the oxidative injury, MDA play a vital role in cellular oxidative injury. To explore whether the AK046375 decreased the oxidative stress level in cellular under H_2O_2 treatment, we detected the expression of CAT, SOD2, GSH, GSH/GSSG, MDA, GSSG and the MitoSOX red staining fluorescence intensity in cellular. H_2O_2 led the decrease expression of CAT, GSH, and SOD2 and increased the production of MDA compared to the

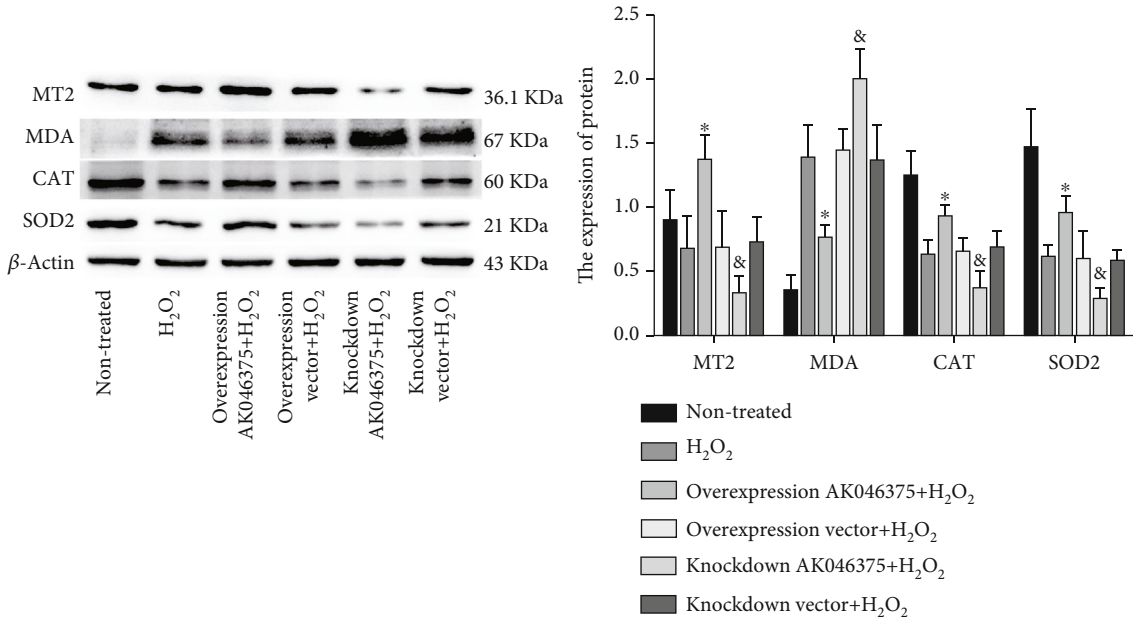

(a)

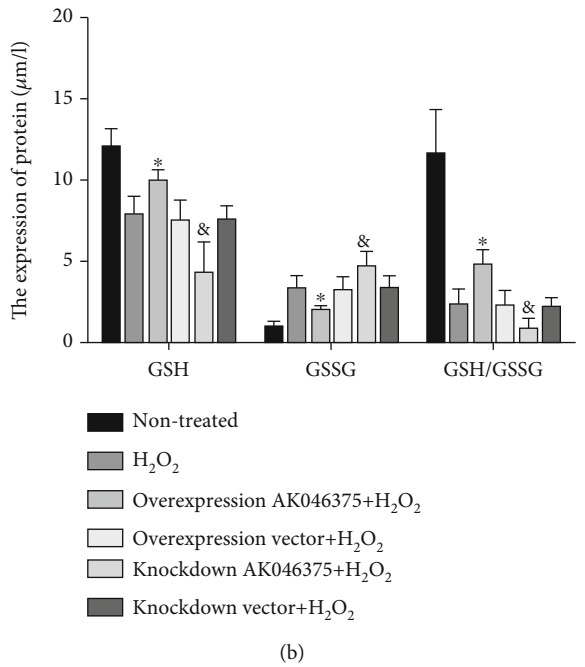

(b)

Figure 3: Continued.

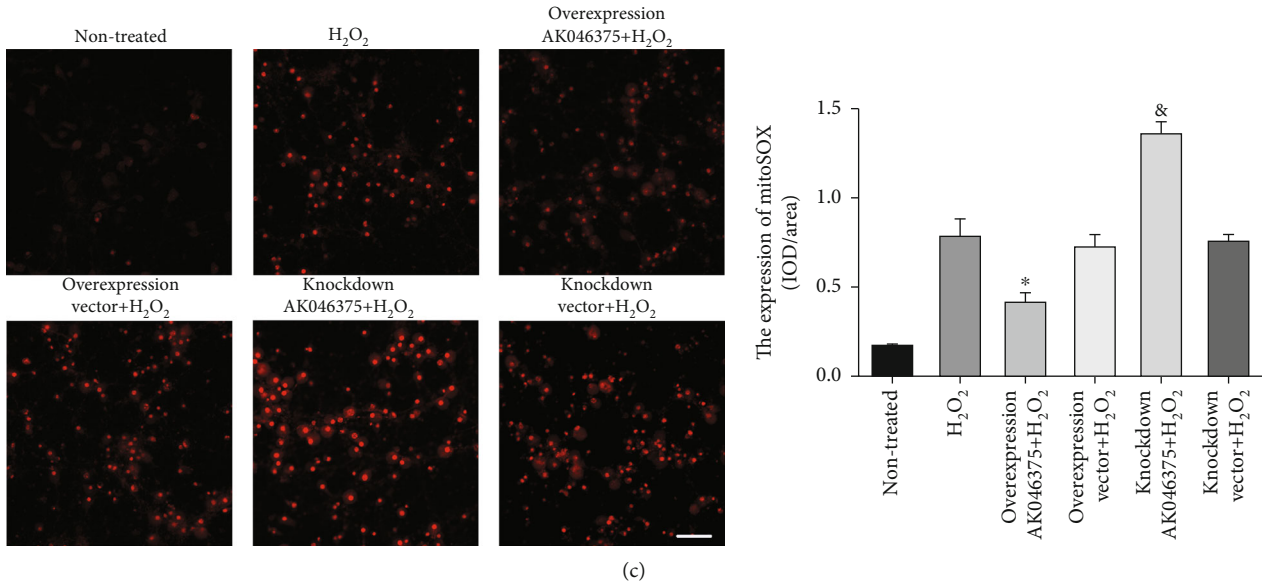

(c)

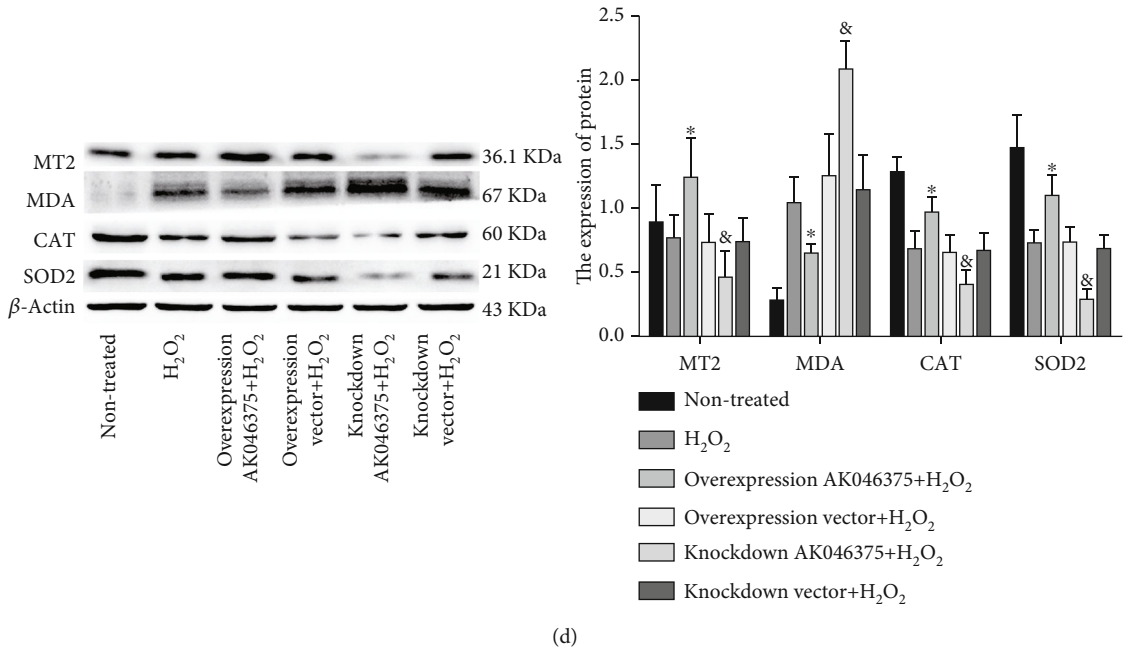

(d)

Figure 3: Continued.

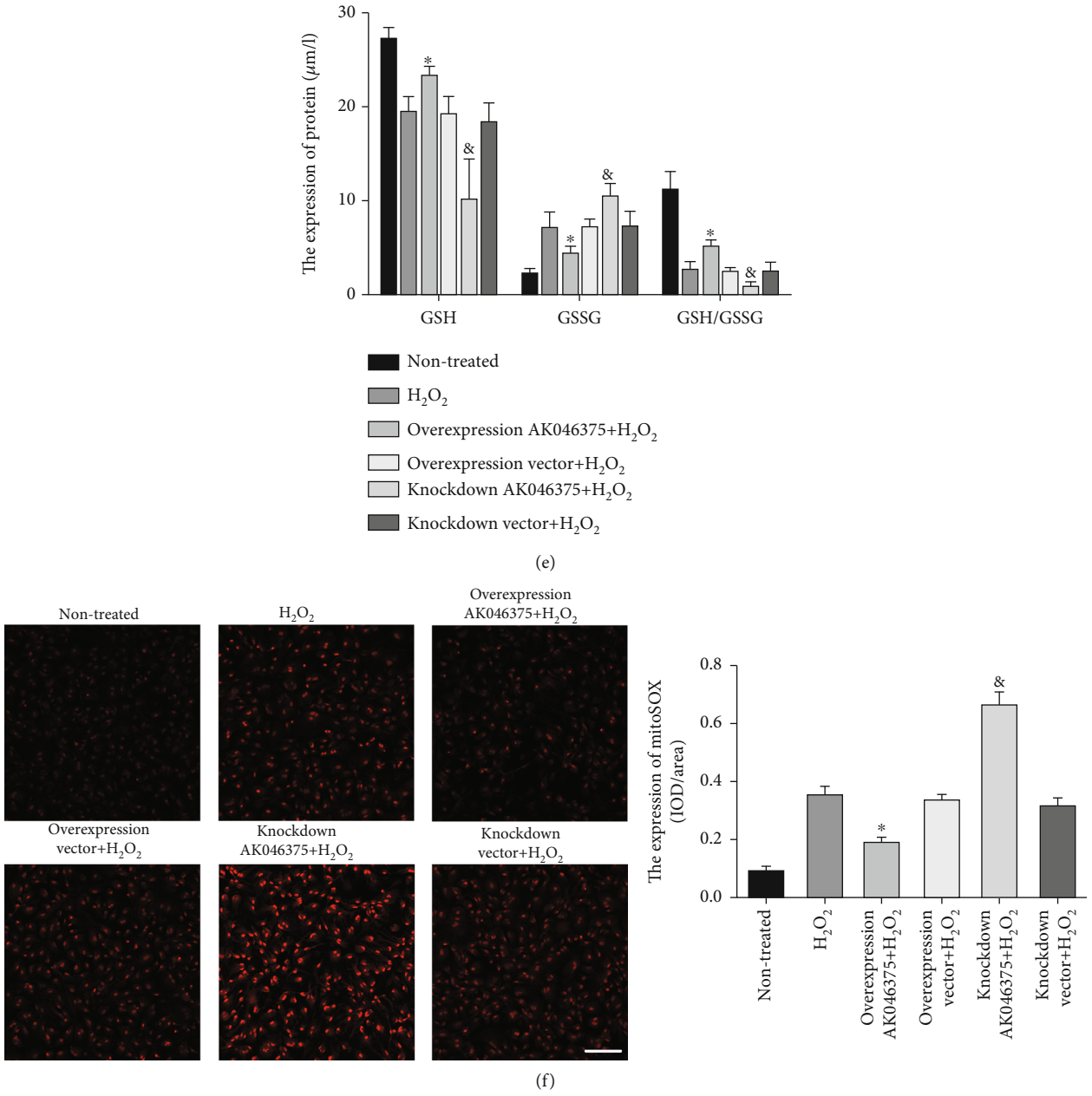

Figure 3: AK046375 alleviates H2O2-induced oxidative stress in primary neurons and astrocytes. (1) Western blotting images of MT2, MDA, CAT, and SOD2 in neurons (a) and astrocytes (d) for each group, and the content of GSH, GSSG, and GSH/GSSG in neurons (b) and astrocytes (e) with quantification. (2) Fluorescence of MitoSOX^{red} in neurons (c) and astrocytes (f) and quantification (scale bar = 50 μm, 400x for neurons; scale bar = 50 μm, 200x for astrocytes) (n = 6/group, mean ± SD, $^{*}P < 0.05$ vs. the overexpression vector+H_2O_2 group, $^{\&}P < 0.05$ vs. the knockdown vector+H_2O_2 group by one-way ANOVA).

nontreated group ($P < 0.05$, Figures 3(a) and 3(d)). There was no significant difference in the expression of CAT, SOD2, MT2, GSH, GSH/GSSG, MDA, GSSG, or the MitoSOX^{red} staining fluorescence intensity among the H_2O_2, overexpression vector, and knockdown vector groups ($P > 0.05$, Figure 3). The expressions of CAT, SOD2, MT2, GSH, and GSH/GSSG were higher in the AK046375 overexpression group ($P < 0.05$, Figures 3(a), 3(b), 3(d), and 3(e)) but lower in the AK046375 knockdown group ($P < 0.05$, Figures 3(a), 3(b), 3(d), and 3(e)) compared to their respective control groups. Expression of MDA, GSSG, and MitoSOX^{red} staining fluorescence intensity were lower in the AK046375 overexpression group ($P < 0.05$, Figure 3) and higher in the AK046375 knockdown group ($P < 0.05$, Figure 3) compared to their respective control groups. These results indicate that AK046375 alleviates H_2O_2-induced oxidative stress in primary neurons and astrocytes.

3.3.2. AK046375 Decreases H_2O_2-Induced Apoptosis in Primary Cortical Neurons and Astrocytes. The proteins of

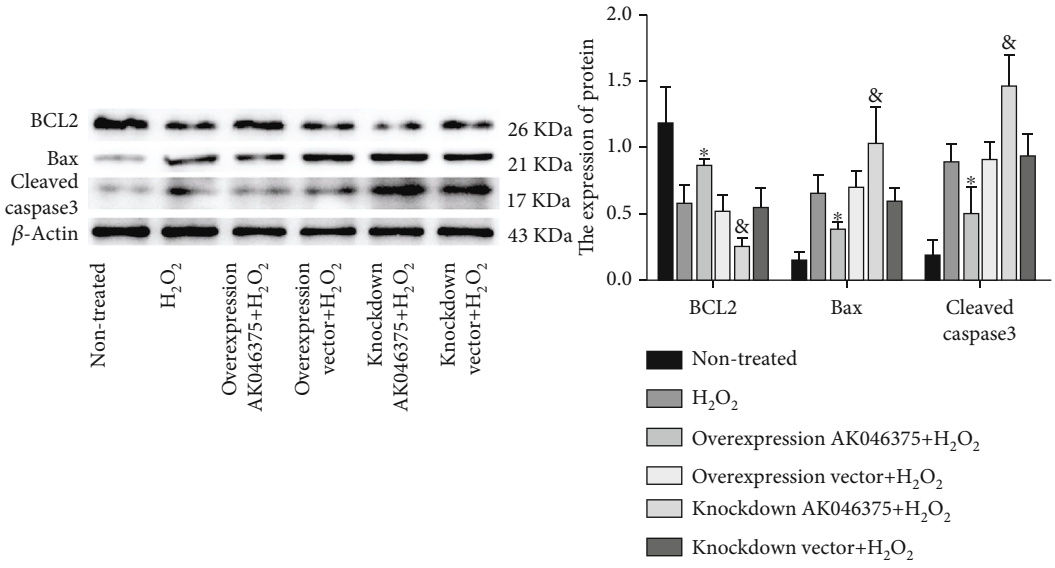

(a)

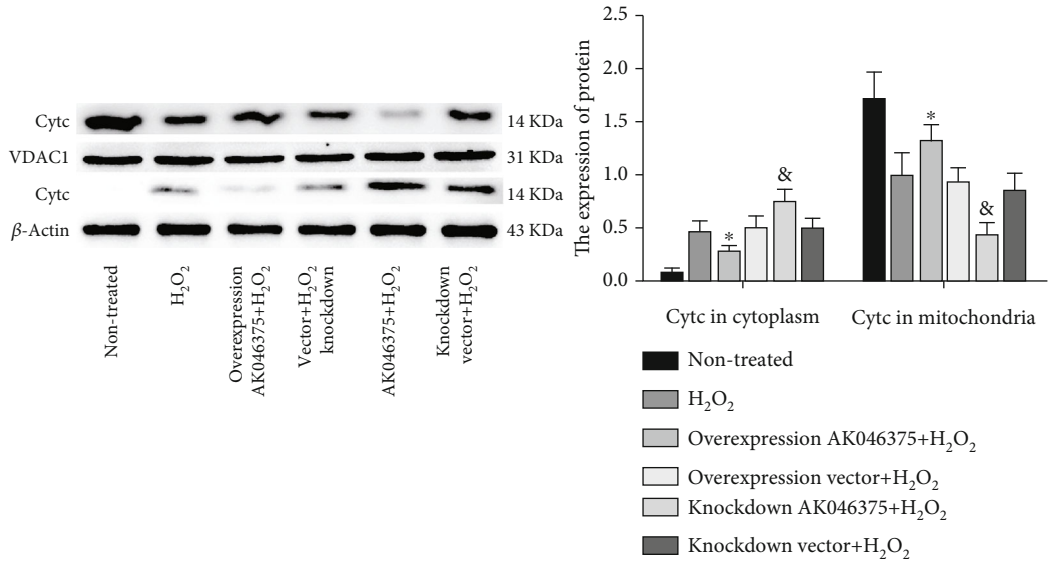

(b)

Figure 4: Continued.

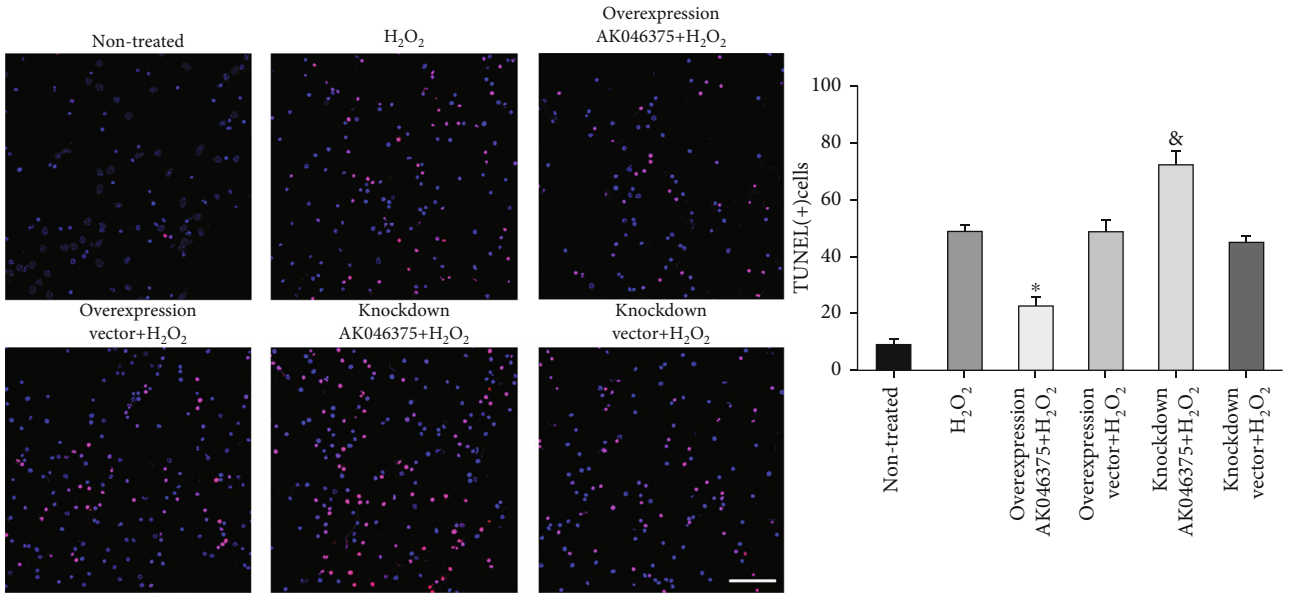

(c)

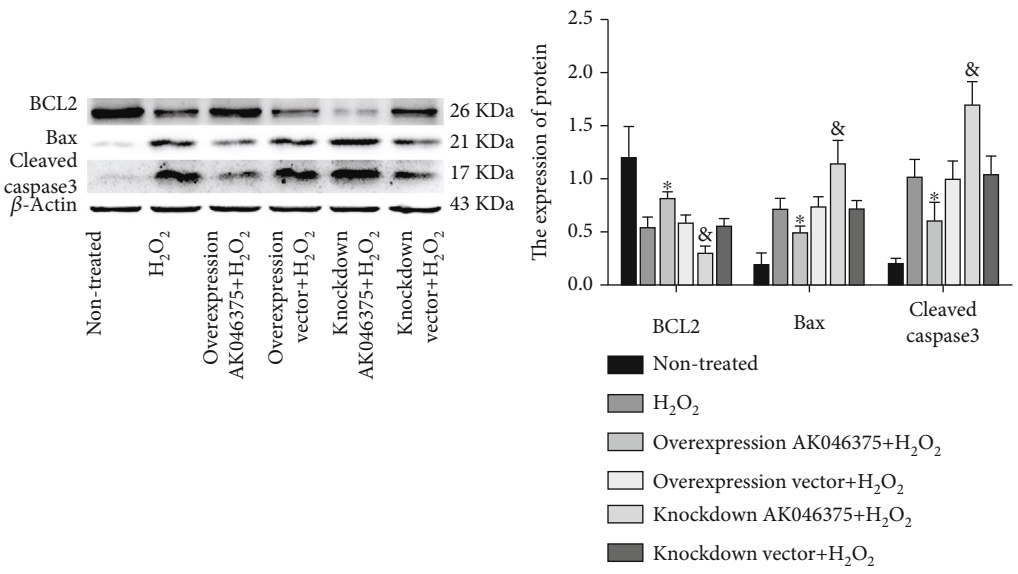

(d)

Figure 4: Continued.

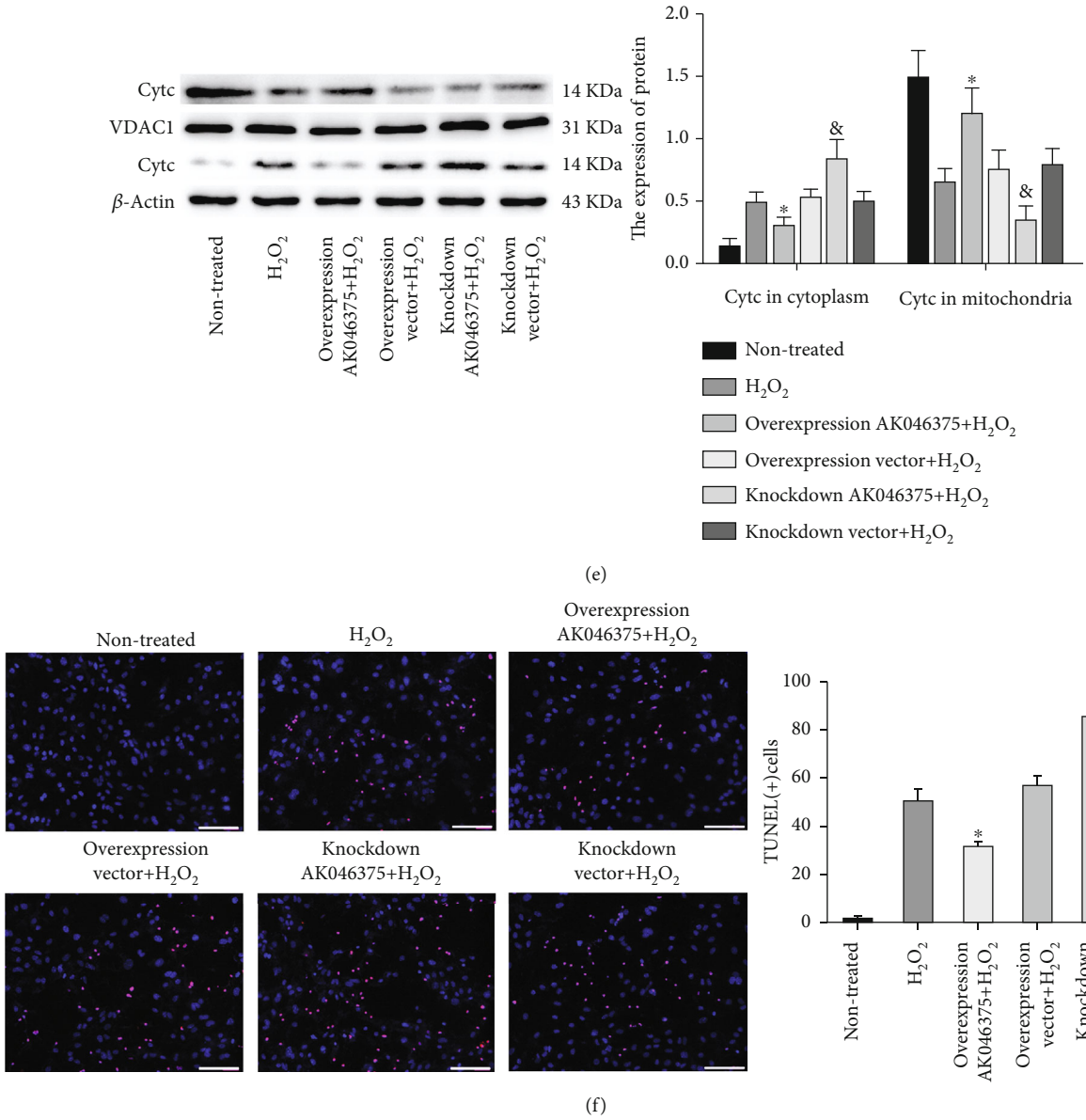

Figure 4: AK046375 decreased the H_2O_2-induced apoptosis on primary cortical neurons and astrocytes. (1) BCL2, Bax, and cleaved-caspase-3 in neurons (a) and astrocytes (d) detected by western blotting and quantification. (2) Cytochrome C (Cytc) in cytoplasm and mitochondria in neurons (b) and astrocytes (e) and quantification (VDAC1 was used as a loading control for mitochondrial proteins.). (3) TUNEL-positive cells in neurons (c) and astrocytes (f) and quantification (scale bar = 50 μm, 400x for neurons; scale bar = 50 μm, 200x for astrocytes) ($n = 6$/group, mean ± SD, $^*P < 0.05$ vs. the overexpression vector group, $^{\&}P < 0.05$ vs. the knockdown vector group by one-way ANOVA).

the BCL-2 family are the most important regulators of mitochondria-related apoptosis. The ratio of pro- and antiapoptotic proteins (BCL2 and Bax) determines whether mitochondria initiate the cell death program by releasing cytochrome C and other proapoptotic factors [22]. There was no significant difference in the number of TUNEL-positive cells or in the expression of BCL2, Bax, and cleaved-caspase-3 between the H_2O_2, overexpression vector, and knockdown vector groups ($P > 0.05$, Figure 4). The number of TUNEL-positive cells and expression of cleaved-caspase-3 and Bax were significantly lower in the AK046375 overexpression group and higher in the AK046375 knockdown group ($P < 0.05$, Figure 4) compared to their respective control groups. The expression of BCL2 was significantly higher in the AK046375 overexpression group and lower in the AK046375 knockdown group ($P < 0.05$, Figures 4(a) and 4(d)) compared to their respective control groups. Moreover, mitochondrial membrane damage induced the release of cytochrome C from the mitochondria to the cytoplasm and decreased the release inhibited apoptosis [23]. No significant differences were found in mitochondrial or cytoplasmic cytochrome C levels among the H_2O_2, overexpression vector, and knockdown vector groups ($P > 0.05$, Figures 4(b) and 4(e)). Expression of

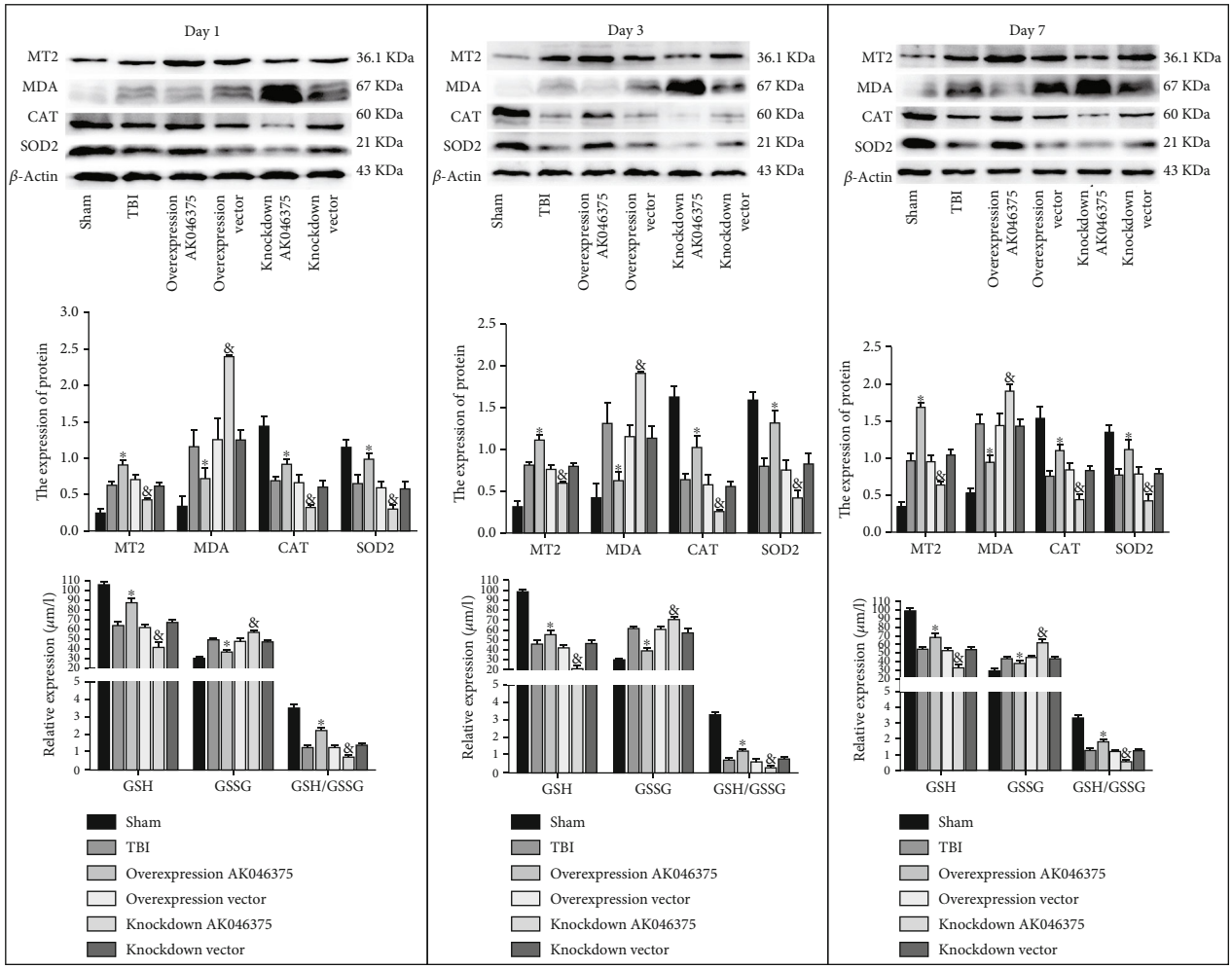

Figure 5: AK046375 alleviates oxidative stress on 1, 3, and 7 days after TBI. Western blotting results of MT2, MDA, CAT, SOD2, and GSSG, GSH, and GSH/GSSG content in each group and quantification after TBI ($n = 4$/group, mean ± SD, $^{*}P < 0.05$ vs. the overexpression vector group, $^{\&}P < 0.05$ vs. the knockdown vector group by one-way ANOVA).

cytochrome C in mitochondria was higher in the AK046375 overexpression group and lower in the AK046375 knockdown group ($P < 0.05$, Figures 4(b) and 4(e)) compared to their respective control groups. In addition, cytoplasmic cytochrome C was decreased in the AK046375 overexpression group ($P < 0.05$, Figures 4(b) and 4(e)) and increased in the AK046375 knockdown group ($P < 0.05$, Figures 4(b) and 4(e)) compared to their respective control groups. Besides, we also found that AK046375 could improve the cell survival under the H_2O_2 treatment (supplementary fig. 5). These results indicate that AK046375 relieves H_2O_2-induced apoptosis in neurons and astrocytes.

3.4. AK046375 Exerts Neuroprotective Effects in Mice after TBI

3.4.1. AK046375 Alleviates Oxidative Stress in Mice after TBI. In these *in vivo* experiments, AK046375 overexpression and knockdown adenoviruses were found to efficiently up- and downregulate AK046375 levels in the mouse brain, respectively (supplementary fig. 6A). MT2 mRNA and protein levels were upregulated and downregulated in response to AK046375 overexpression and knockdown groups, compared to their respective control groups (supplementary fig. 6B and C). Expression of GSH, GSSG, GSH/GSSG, MDA, MT2, SOD2, and CAT was not significantly different among the TBI, overexpression vector, and knockdown vector groups ($P > 0.05$, Figure 5). Expression of GSSG and MDA was significantly increased in the AK046375 knockdown group ($P < 0.05$, Figure 5) and decreased in the AK046375 overexpression group ($P < 0.05$, Figure 5) compared to their respective control groups. Expression of GSH, GSH/GSSG, SOD2, MT2, and CAT were significantly decreased in the AK046375 knockdown group ($P < 0.05$, Figure 5) and increased in the AK046375 overexpression group ($P < 0.05$, Figure 5) compared to their respective control groups. These results show that AK046375 alleviates the oxidative stress in the cerebral cortex around the injury focus after TBI.

3.4.2. AK046375 Significantly Decreases Apoptosis and Promotes the Neuron Survival in the Cerebral Cortex of Mice after TBI. We also detected apoptosis in the cerebral

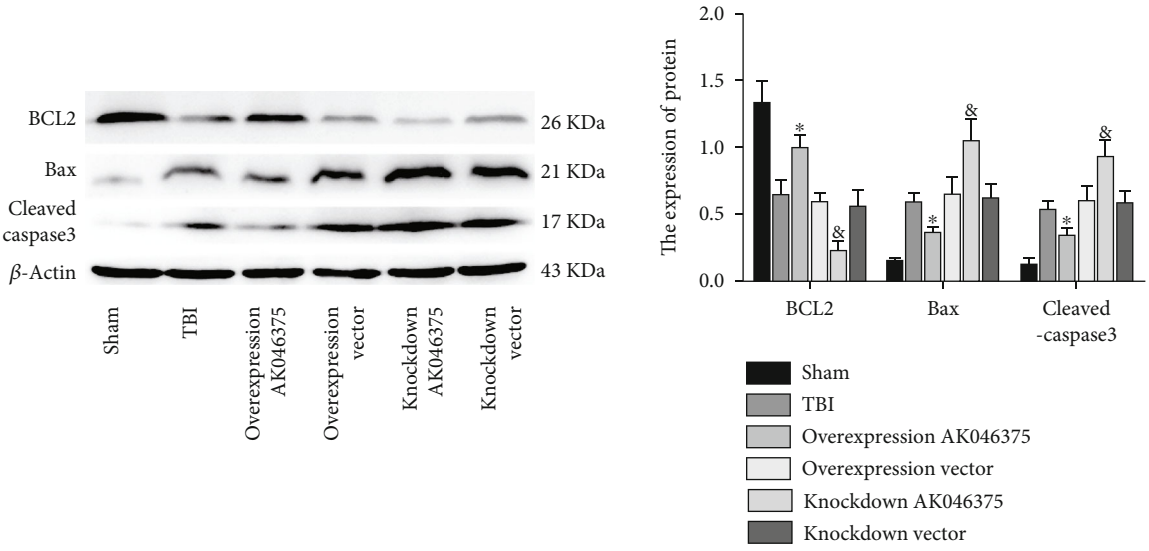

(a)

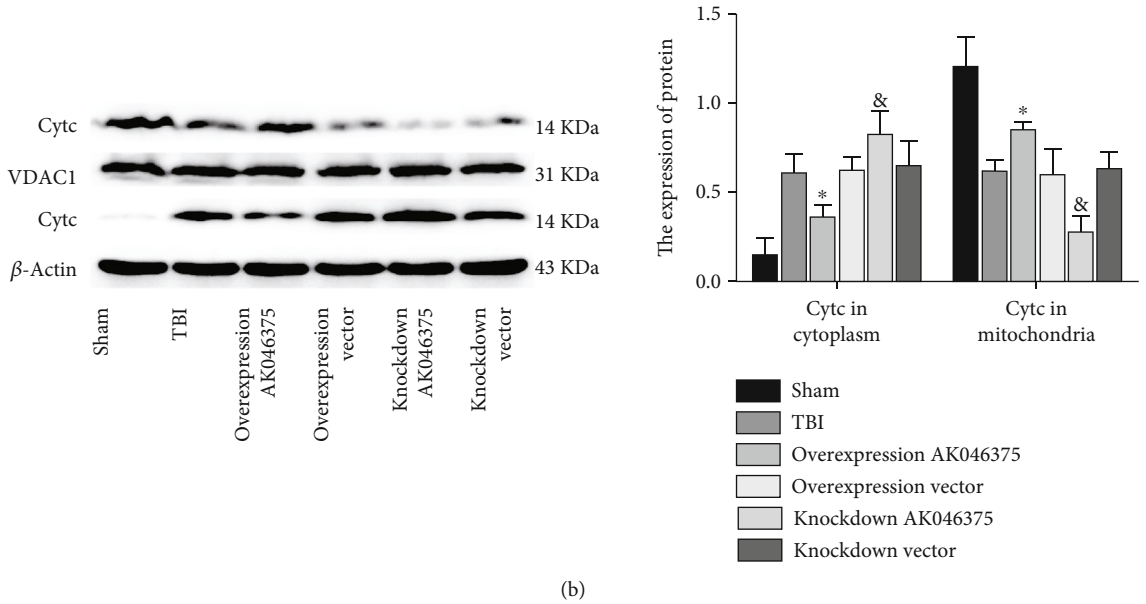

(b)

Figure 6: Continued.

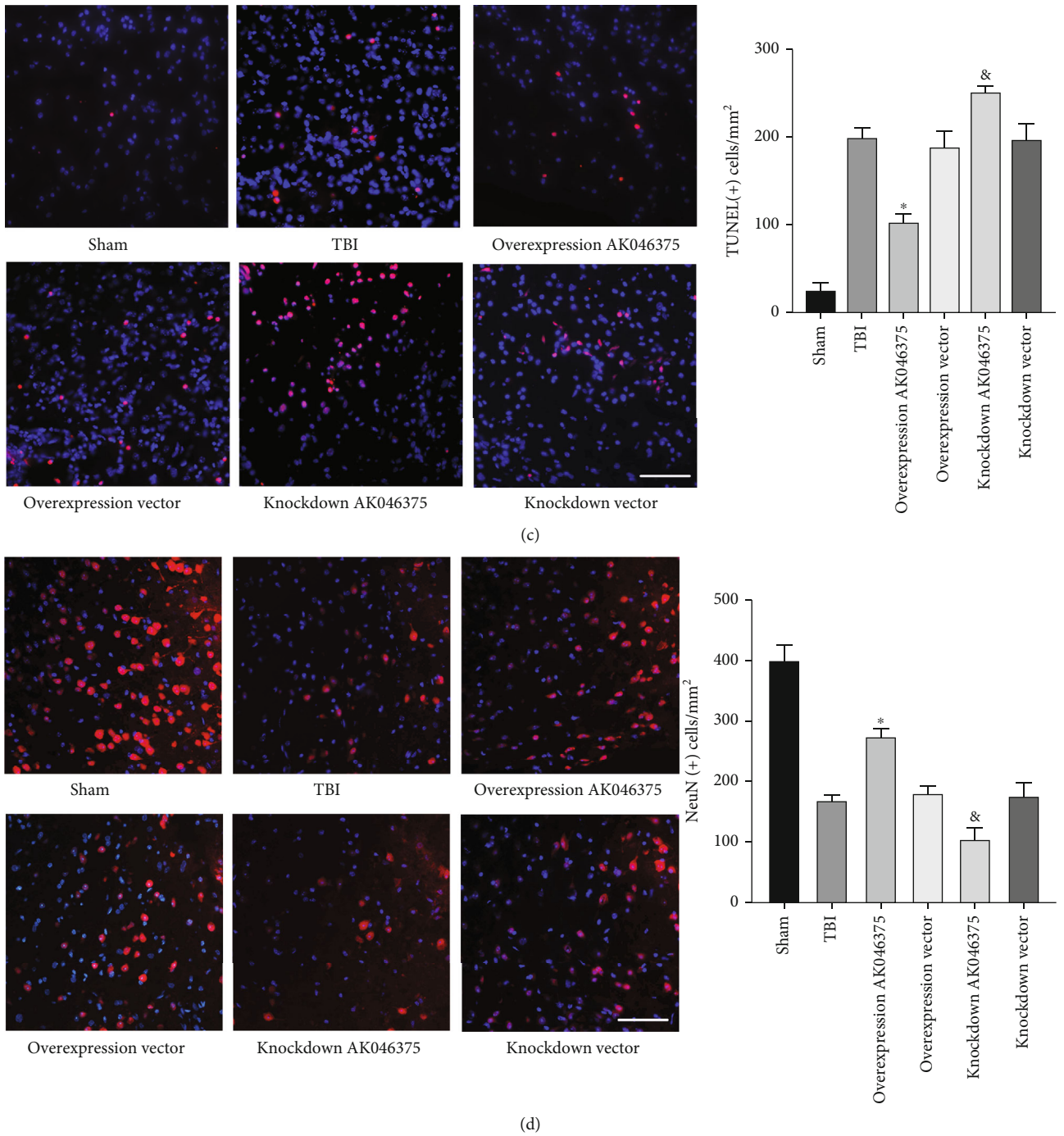

Figure 6: AK046375 inhibits apoptosis on 7 days after TBI. (a) Western blotting results of BCL2, Bax, and cleaved-caspase-3 in each group and quantification. (b) Western blotting results of cytochrome C (Cytc) in cytoplasm (up) and mitochondria (down) and quantification. (c) TUNEL-positive cells in the mouse cortex around the injury site and quantification (scale bar = 50 μm, 400x). (d) NeuN-positive cells in the mouse cortex around the injury site and quantification (scale bar = 50 μm, 400x). NeuN is a neuronal marker. (n = 5/group, mean ± SD, $^{*}P < 0.05$ vs. the overexpression vector group, $^{\&}P < 0.05$ vs. the knockdown vector group by one-way ANOVA).

cortex around the injury site 7 days after TBI. The expression of BCL2 was decreased; the Bax, cleaved-caspase-3, and the TUNEL-positive cells were increased in the TBI group compared with the sham group ($P < 0.05$, Figures 6(a) and 6(c)). The expression of BCL2, Bax, cleaved-caspase-3, and the TUNEL-positive cells showed no significant differences among the TBI, overexpression vector, and knockdown vector groups ($P > 0.05$, Figures 6(a) and 6(c)). The expression of BCL2 was significantly increased in the AK046375 overexpression group and decreased in the knockdown group ($P < 0.05$, Figure 6(a)) compared to their respective control groups. The expressions of Bax and cleaved-caspase-3 and TUNEL-positive cells in the overexpression AK046375

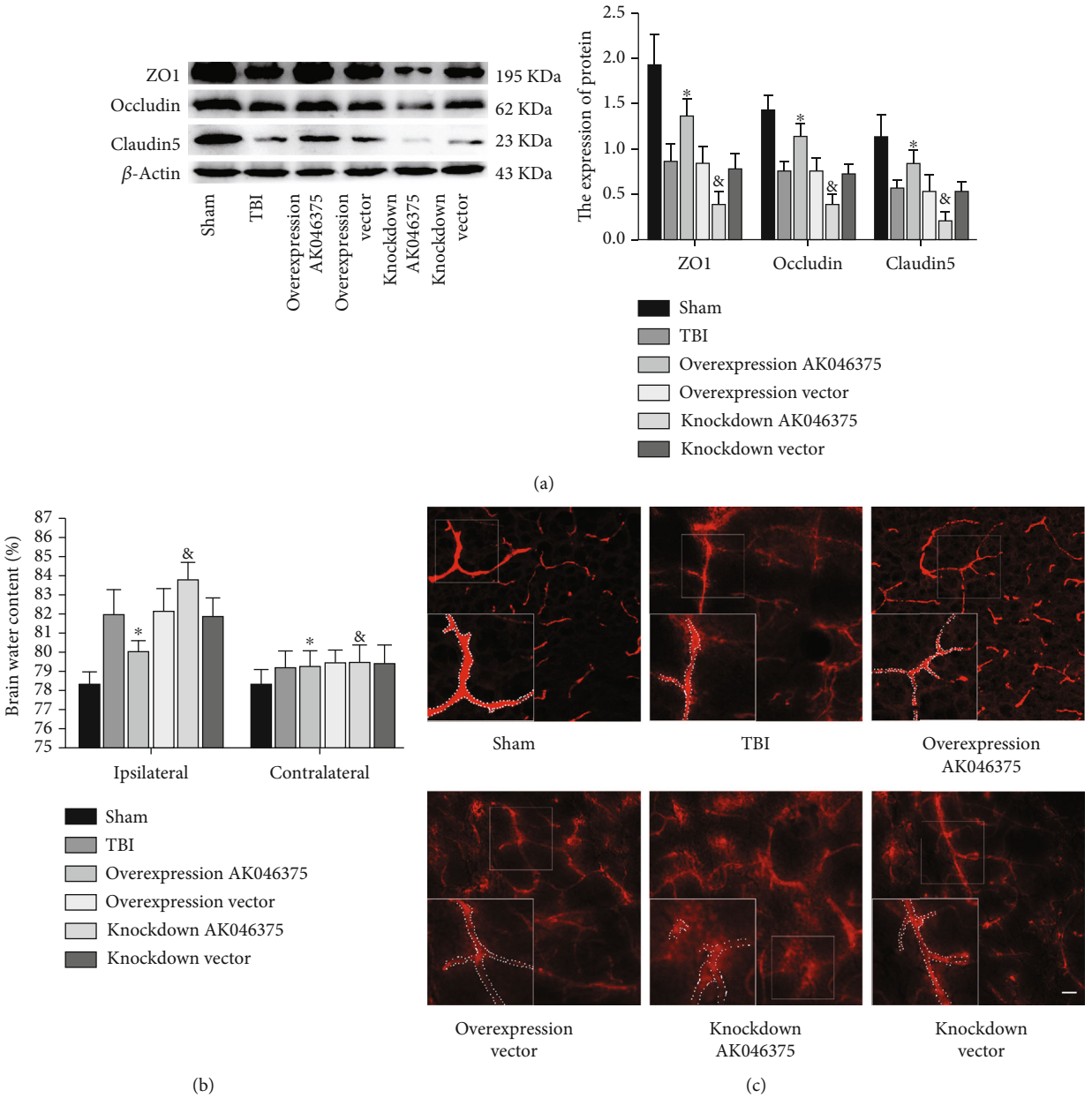

Figure 7: Continued.

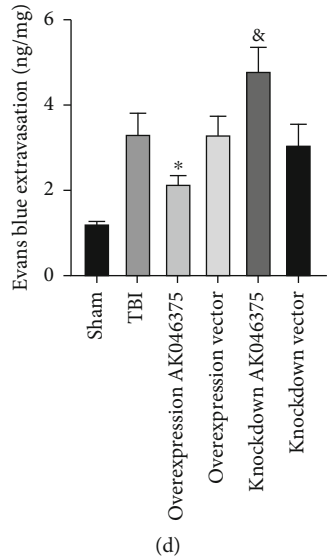

FIGURE 7: AK046375 maintains BBB integrity and decreases brain water content in mice on 7 days after TBI. (a) Western blotting results of ZO1, occludin, and claudin-5 in each group and quantification ($n = 6$/group, mean ± SD). (b) Brain water content in each group after TBI ($n = 6$/group, mean ± SD). (c, d) Fluorescence of Evans blue and Evans blue extravasation in each group around the injury site ($n = 12$/group, mean ± SD) (scale bar = 50 μm, 200x) ($^{*}P < 0.05$ vs. the overexpression vector group, $^{\&}P < 0.05$ vs. the knockdown vector group by one-way ANOVA).

group were reduced ($P < 0.05$, Figures 6(a) and 6(c)) compared to the overexpression vector group, and expressions of Bax and cleaved-caspase-3 in the AK046375 knockdown group were increased ($P < 0.05$, Figures 6(a) and 6(c)) compared to the knockdown vector group. TBI caused the release of cytochrome C from mitochondria to the cytoplasm compared to the sham group ($P < 0.05$, Figures 6(a) and 6(c)). The cytochrome C in the mitochondria and cytoplasm showed no significant difference among the TBI, overexpression vector, and knockdown vector groups ($P > 0.05$, Figure 6(b)). AK046375 overexpression significantly decreased cytochrome C release from the mitochondria into the cytoplasm ($P < 0.05$, Figure 6(b)) but AK046375 knockdown significantly increased the release ($P < 0.05$, Figure 6(b)) compared to their respective control groups.

To further confirm the *in vivo* antiapoptosis effect of AK046375, we also quantified the remaining neurons in the cerebral cortex around the injury site on 7 days after TBI. The number of NeuN-positive cells in the TBI group was decreased compared to the sham group ($P < 0.05$, Figure 6(d)). There was no significant difference in the number of NeuN-positive cells between the TBI, overexpression vector, and knockdown vector groups ($P < 0.05$, Figure 6(d)). The number of NeuN-positive cells were higher in the AK046375 overexpression group ($P < 0.05$, Figure 6(d)) and lower in the AK046375 knockdown group ($P < 0.05$, Figure 6(d)) compared to their respective control groups. These results suggest that AK046375 significantly decreases apoptosis and promotes the neuronal survival in the cerebral cortex around the injury site after TBI.

3.4.3. AK046375 Maintains BBB Integrity and Decreases Brain Edema after TBI. Occludin, claudin-5, and ZO-1 are the primary protein components of the BBB, and in our previous studies, we found that TBI induced significant loss of tight junction proteins. In the current study, we found that loss of occludin, claudin-5, and ZO-1 induced by TBI were attenuated by AK046375 overexpression ($P < 0.05$, Figure 7(a)) and were aggravated by AK046375 knockdown ($P < 0.05$, Figure 7(a)).

The dry/wet weight and Evans blue methods were performed to measure BBB permeability. There was no significant difference in brain water content or the content of Evans blue in the brain among the TBI, overexpression vector, and knockdown vector groups ($P > 0.05$, Figures 7(b) and 7(d)). Brain water content and the exudation of Evans blue were reduced in the AK046375 overexpression group ($P < 0.05$, Figures 7(b) and 7(d)) but increased in the AK046375 knockdown group ($P < 0.05$, Figures 7(b) and 7(d)) compared to their respective control groups. Additionally, the fluorescence of Evans blue showed that AK046375 overexpression decreased the exudation of Evans blue from the vasculum, but AK046375 knockdown deteriorated the exudation of Evans blue ($P < 0.05$, Figure 7(c)) compared to their control groups. These results prove that AK046375 maintains the integrity of the BBB and decreases brain edema after TBI.

3.4.4. AK046375 Significantly Improves Motor Function, Learning Ability, and Spatial Memory in Mice after TBI. The NSS and water maze tests were used to evaluate whether AK046375 influenced the recovery of motor function, learning abilities, and spatial memory in mice after TBI, respectively. One, 3, 7, and 14 days after TBI, there was no significant difference in NSS scores, wire-gripping scores, and rotarod test among the TBI, overexpression vector, and knockdown vector groups ($P > 0.05$, Figures 8(a)–8(c)). NSS scores were significantly higher in the AK046375 knockdown

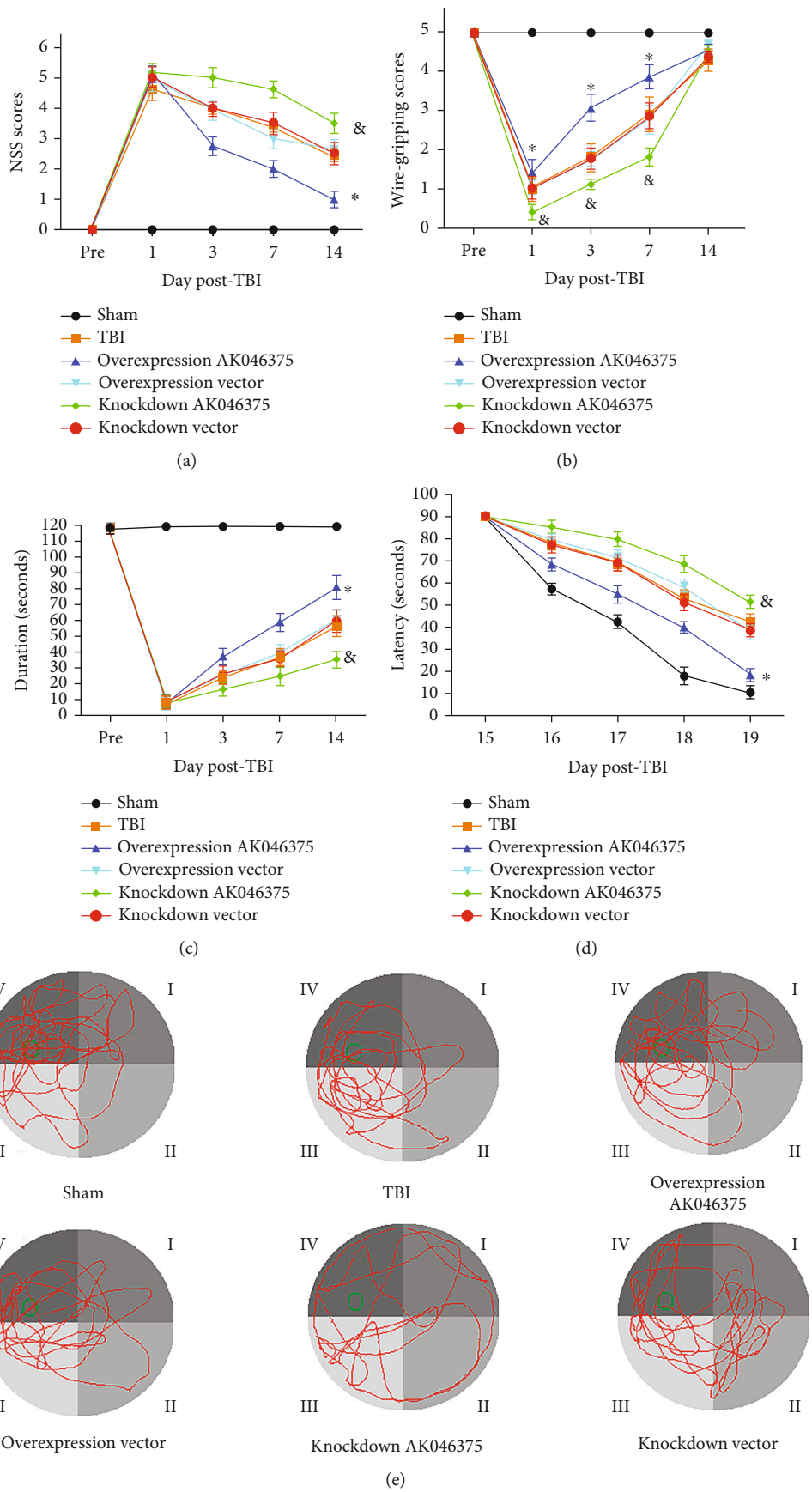

Figure 8: Continued.

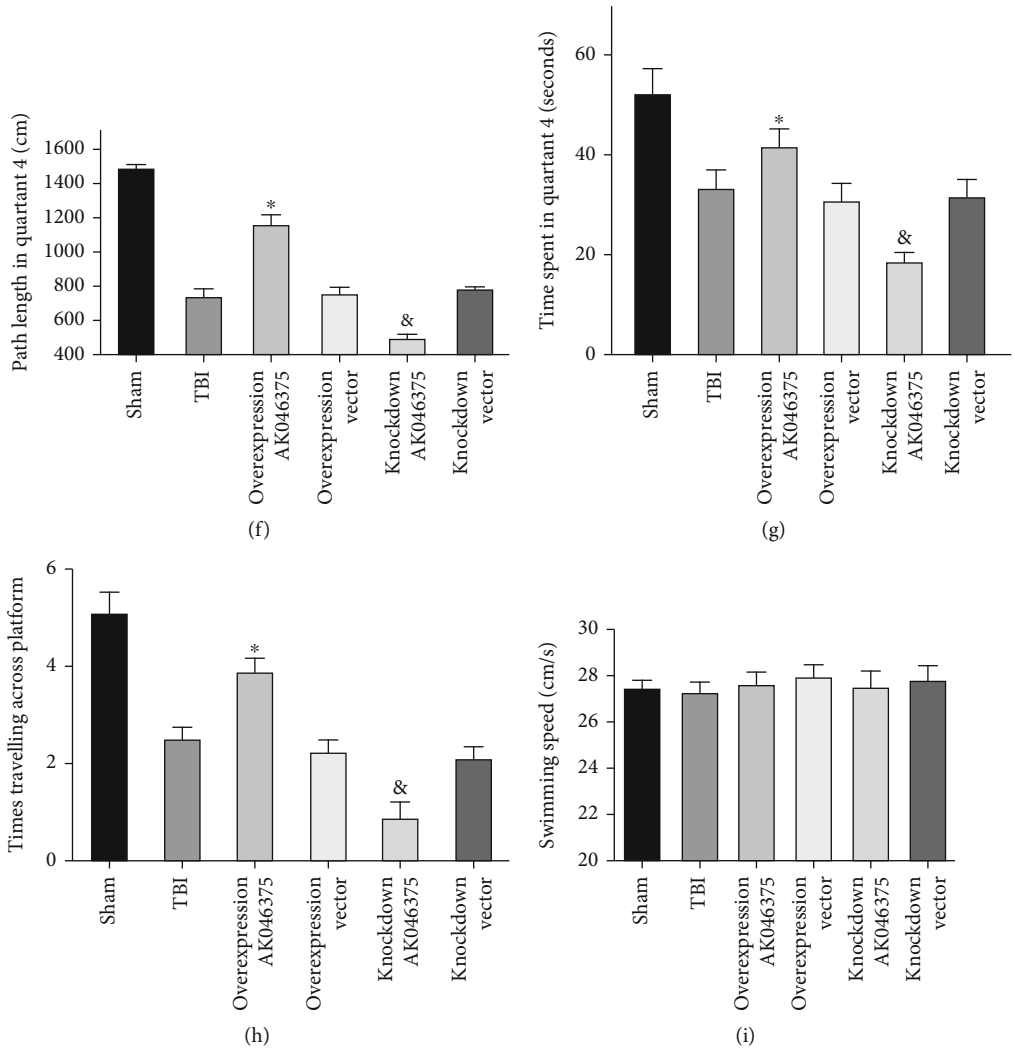

Figure 8: AK046375 improves motor function, learning ability, and spatial memory in mice after TBI. (a) NSS scores were detected on preoperative, 1, 3, 7, and 14 days after TBI. (b) Wire-gripping scores in each group on preoperative, 1, 3, 7, and 14 days after TBI. (c) The duration of rotarod test in each group on preoperative, 1, 3, 7, and 14 days after TBI. (d) Latency spent in quadrant 4 in cued learning performance in the Morris Water Maze (MWM) test on 15 to 19 days after TBI. (e) Swimming tracks in MWM test on 20 days after TBI. (f) Length of the swimming tracks in quadrant 4 on 20 days after TBI. (g) Time in quadrant 4 in MWM test on 20 days after TBI. (h) Times traveling across the platform in MWM test on 20 days after TBI. (i) Swimming speed in MWM test on 20 days after TBI ($n = 8$/group, mean ± SD) ($^{*}P < 0.05$ vs. the overexpression vector group, $^{\&}P < 0.05$ vs. the knockdown vector group by two-way ANOVA test for NSS scores, wire-gripping scores, rotarod test, and latency spent in quadrant 4. One-way ANOVA for length of the swimming tracks in quadrant 4, time in quadrant 4, and the number of times the mice crossed over the original location of the platform on 20 days after TBI).

group and lower in the AK046375 overexpression group ($P < 0.05$, Figure 8(a)) compared to their respective control groups on 3, 7, and 14 days after TBI. The wire-gripping scores and the duration of rotarod were significantly higher in AK046375 overexpression group ($P < 0.05$, Figures 8(b) and 8(c)) but lower in the AK046375 knockdown group ($P < 0.05$, Figures 8(b) and 8(c)) compared to their respective control groups. In the Morris water maze test, there was no significant difference in the latency to navigate the hidden platform on 15, 16, 17, 18, and 19 days after TBI between the TBI, overexpression vector, and knockdown vector groups ($P > 0.05$, Figure 8(d)). Besides, there was also no significant difference in swimming distance spent in quadrant 4, the time spent in quadrant 4, and the times passed over the platform location on 20 days after TBI between the TBI, overexpression vector, and knockdown vector groups ($P > 0.05$, Figures 8(f)–8(h)). Sixteen, 17, 18, and 19 days after TBI, latency was significantly decreased in the AK046375 overexpression group ($P < 0.05$, Figure 8(d)) and increased in the knockdown group ($P < 0.05$, Figure 8(d)) compared to their respective control groups. The hidden platform was removed on 20 days after TBI, the time and swimming distance spent in quadrant 4, and the times passed over the platform location were also significantly increased in the AK046375 overexpression group ($P < 0.05$, Figures 8(f)–8(h)) and decreased in the knockdown group ($P < 0.05$, Figures 8(f)–8(h)) compared to their

respective control groups; there was no significant difference in the swimming speed between the TBI, overexpression vector, and knockdown vector groups (Figure 8(i)). These results demonstrated that AK046375 promotes motor function, learning ability, and spatial memory recovery in mice after TBI.

4. Discussion

lncRNAs are reported to regulate gene expression and chromatin structure via the decoy, scaffold and posttranscriptional effects [24]. Our pervious study demonstrated that AK046375, which is abundantly expressed in the brain, was significantly upregulated in the cerebral cortex around the TBI focus (~4-fold in contrast to preinjury levels) [8]. Our present study is aimed at interrogating the implications of increased AK046375 expression in the injured brain after TBI.

First, we applied the *in situ* hybridization to confirm the existence and subcellular location of lncRNA AK046375 in neurons and astrocytes, the most common cell types in the mammalian brain, and found that AK046375 was expressed in both the nucleus and cytoplasm but was concentrated primarily in the cytoplasm (Supplementary fig. 4). Owing to the development of RNA-seq, we observed that the MT2 gene was the most significantly altered among all differentially expressed genes in response to AK046375 overexpression. To further confirm that MT2 was significantly increased in response to AK046375 overexpression, primary neurons and astrocytes were transfected with overexpression or knockdown viruses, and we found that both MT2 mRNA and protein levels were significantly increased or decreased, respectively, illustrating that MT2 is a downstream factor in the AK046375 pathway. MT2 is a special protein with low molecular weight and high cysteine content that binds a large number of heavy metals ions [25, 26], giving it a stronger ability to scavenge free radicals than either SOD or GSH. [27–29] MT2 is highly expressed in the CNS [20] and plays a neuroprotective role against brain injury through its antioxidative effect [30, 31]. In the current study, we demonstrate that the upregulated expression of lncRNA AK046375 can significantly inhibit the overoxidative response in vitro and in vivo.

Oxidative stress, neuroinflammation, and apoptosis are common features that occur after TBI, which, in turn, compromise normal cellular functions [32]. Overloading of intracellular oxidative stress leads to mitochondrial dysfunction and activation of the mitochondria-related apoptosis pathway [33]. Once cytochrome C is released from mitochondria, caspase-3 is activated and irreversibly leads to apoptosis [34], but BCL2 inhibits activation of caspase-3 by inhibiting the release of cytochrome C from the mitochondria to the cytoplasm [35]. In our present study, the decrease of antiapoptotic proteins (BCL2) and the increase of proapoptotic proteins (Bax, cleaved-caspase-3) induced by either TBI *in vivo* or H_2O_2*in vitro* were partially but still significantly reversed by AK046375 overexpression treatment, which was accompanied by less TUNEL-positive staining cells, suggesting an antiapoptic effect of lncRNA AK046375. Moreover, overloading oxidative stress is one of the causes of BBB disruption [36], which, in turn, deteriorates neurological function in mice after TBI. Previous research indicated that maintaining BBB integrity after TBI improved prognosis [2, 37]. In this study, we confirmed that AK046375 overexpression attenuated the loss of tight junction proteins, brain water content, and exudation of Evans blue, all of which could be attributed to reduced oxidation levels from AK046375 treatment. Most importantly, deficits in motor function, learning ability, and spatial memory in mice after TBI were significantly attenuated by AK046375 overexpression, suggesting that AK046375 may represent a potential target that deserves more attention in TBI therapeutic research.

Here, we also go further to elucidate the possible modulating mechanism of AK046375 on MT2. It is well known that lncRNA exerts its biological functions by serving as a "sponge" for miRNA, which negatively regulate targeted mRNA expression [28]. Interestingly, bioinformatics predictions indicated that AK046375 might upregulate MT2 translation through sequestering miR-491-5p or/and miR-505-3p. Our dual-luciferase reporter assay demonstrated that only miR-491-5p directly binds to the 3′-UTR MT2 mRNA and inhibits its translation. Previous studies on miR-491-5p have primarily focused on its roles in tumor pathology, such as inhibiting tumor proliferation, motility, and metastasis by posttranscriptionally modulating target genes [31, 38, 39]. There is no evidence regarding the interaction between miR-491-5p and MT2 that could be found, and here, for the first time, we showed that miR-491-5p negatively regulates the expression of MT2 and, in turn, exacerbates oxidative stress and cellular injury induced by H_2O_2 treatment. Of note, due to the primary neurons being unable to endure the lipo2000 cytotoxicity, we only transfected miR-491-5p mimics and inhibitor into the primary cortical astrocytes.

To further interrogate the potential relationship between miR-491-5p and AK046375, we measured miR-491-5p expression in response to different AK046375 levels. Results revealed that miR-491-5p expression was significantly up- and downregulated when AK046375 levels were decreased and increased, respectively, suggesting that there exists a mechanism that may mediate the regulation of AK046375 on miR-491-5p. A recent theory on competing endogenous RNAs (ceRNAs) proposes that lncRNAs modulate expression of other genes by forming microRNA response elements (MREs) [40]. Given the capability of AK046375 to capture miR-491-5p and the direct binding of miR-491-5p with the 3′-UTR MT2 mRNA, we propose that AK046375 may function as an endogenous "sponge" to attract endogenous miR-491-5p, which in turn relieves the inhibition of miR-491-5p on MT2-mRNA translation and promotes more MT2 protein production. Therefore, elevated levels of AK046375 in the injured brain tissue after TBI may effectively enhance MT2 expression through inhibiting the blocking of miR-491-5p on MT2-mRNA and ameliorating oxidative stress-related injury, which would certainly inhibit apoptosis and BBB damage, promoting neuronal survival and facilitating neurological function recovery. Of note, in our current study, we only explored the binding possibility of AK046375 interacting with miR-491-5p and miR-505-3p. However, we believe, in addition to miR-491-5p, there

are probably other miRNAs that are be directly captured by AK046375, and the RIP-seq method could be helpful to discern all other AK046375-binding miRNAs. Moreover, in addition to MT2, other genes may also be involved in the neuroprotective functions of AK046375. For example, mRNA levels of mt-Nd1, 3, 4, and mt-Adp8 genes were also found to be significantly altered in response to AK046375 overexpression, which also suggests a potential relationship between AK046375 and those genes. mt-Nd1, 3, 4, and mt-Adp8 are mitochondrial ATP-producing pathway-related genes, suggesting that AK046375 might also be involved in ATP production in mitochondria.

Collectively, our present study demonstrated that the increased endogenous lncRNA-AK046375 plays antioxidation roles in the injured cerebral cortex after TBI, suggesting it may represent a therapeutic target for TBI treatment. The mechanism underlying the antioxidant effect of AK046375 is likely based on enhancing MT2 expression through sequestering miR-491-5p.

Data Availability

The data used to support the findings of this study are available from the corresponding author upon request.

Conflicts of Interest

The authors declare that they have no conflict of interest.

Authors' Contributions

Z.J. directed the overall project. Z.J. and S.X. designed the study. T.W., D.D., W.Y., and C.W. performed the experiments. T.W. analyzed the data and wrote the main manuscript. Z.J. and X.Y. amended the manuscript. All authors reviewed the manuscript. H.Z. was responsible for western blotting assay. C.C was charged for RNA synthesis assay. G.Z. was responsible for immunofluorescence assay. Z.J is responsible for the supplementary and interpretation of the data.

Acknowledgments

This project was funded by grants of the National Natural Science Foundation of China (grant numbers: 82071397 and 82071332), youth fund of National Natural Science Foundation of China (grant number: 81801230), Chongqing Natural Science Foundation (grant number: cstc2019jcyj-msxmX0830), and the Excellent Scientific Research Talent's Fund of the First affiliated hospital of Chongqing Medical University.

Supplementary Materials

We had acquired the full length of AK046375, and AK046375 is primarily localized in the cytoplasm; we also obtained the concentrations of H_2O_2 used to establish the oxidative model in primary cortical neurons and astrocytes. MT2 was the most significantly altered mRNA following AK046375 overexpression which was proved *in vivo* and *in vitro*. AK046375 could improve the primary cortical neurons and astrocytes survival under the H_2O_2 treatment. *(Supplementary Materials)*

References

[1] C. A. Taylor, J. M. Bell, M. J. Breiding, and L. Xu, "Traumatic brain injury-related emergency department visits, hospitalizations, and deaths - United States, 2007 and 2013," *MMWR Surveillance Summaries*, vol. 66, no. 9, pp. 1–16, 2017.

[2] Z. Teng, Z. Guo, J. Zhong et al., "ApoE influences the blood-brain barrier through the NF- κB/MMP-9 pathway after traumatic brain injury∗∗," *Scientific Reports*, vol. 7, no. 1, p. 6649, 2017.

[3] S. Gyoneva and R. M. Ransohoff, "Inflammatory reaction after traumatic brain injury: therapeutic potential of targeting cell-cell communication by chemokines," *Trends in Pharmacological Sciences*, vol. 36, no. 7, pp. 471–480, 2015.

[4] E. D. Hall, J. A. Wang, and D. M. Miller, "Relationship of nitric oxide synthase induction to peroxynitrite-mediated oxidative damage during the first week after experimental traumatic brain injury," *Experimental Neurology*, vol. 238, no. 2, pp. 176–182, 2012.

[5] K. W. McConeghy, J. Hatton, L. Hughes, and A. M. Cook, "A review of neuroprotection pharmacology and therapies in patients with acute traumatic brain injury," *CNS Drugs*, vol. 26, no. 7, pp. 613–636, 2012.

[6] V. A. Moran, R. J. Perera, and A. M. Khalil, "Emerging functional and mechanistic paradigms of mammalian long non-coding RNAs," *Nucleic Acids Research*, vol. 40, no. 14, pp. 6391–6400, 2012.

[7] R. Cuevas-Diaz Duran, H. Wei, D. H. Kim, and J. Q. Wu, "Invited review: long non-codingRNAs: important regulators in the development, function and disorders of the central nervous system," *Neuropathology and Applied Neurobiology*, vol. 45, no. 6, pp. 538–556, 2019.

[8] J. Zhong, L. Jiang, C. Cheng et al., "Altered expression of long non-coding RNA and mRNA in mouse cortex after traumatic brain injury," *Brain Research*, vol. 1646, pp. 589–600, 2016.

[9] J. Zhong, L. Jiang, Z. Huang et al., "The long non-coding RNA Neat1 is an important mediator of the therapeutic effect of bexarotene on traumatic brain injury in mice," *Brain, Behavior, and Immunity*, vol. 65, pp. 183–194, 2017.

[10] C. Zhou, H. Chen, J. F. Zheng et al., "Pentraxin 3 contributes to neurogenesis after traumatic brain injury in mice," *Neural Regeneration Research*, vol. 15, no. 12, pp. 2318–2326, 2020.

[11] Y. H. Hung, S. H. Chang, C. T. Huang et al., "Inhibitor of differentiation-1 and hypoxia-inducible factor-1 mediate sonic hedgehog induction by amyloid beta-peptide in rat cortical neurons," *Molecular Neurobiology*, vol. 53, no. 2, pp. 793–809, 2016.

[12] N. Daschil, S. Geisler, G. J. Obermair, and C. Humpel, "Short- and long-term treatment of mouse cortical primary astrocytes with beta-amyloid differentially regulates the mRNA expression of L-type calcium channels," *Pharmacology*, vol. 93, no. 1-2, pp. 24–31, 2014.

[13] S. R. Oliveira, C. Figueiredo-Pereira, C. B. Duarte, and H. L. A. Vieira, "P2X7 receptors mediate CO-induced alterations in gene expression in cultured cortical astrocytes-transcriptomic study," *Molecular Neurobiology*, vol. 56, no. 5, pp. 3159–3174, 2019.

[14] J. Sun, J. Zheng, Y. Li, M. Yan, P. Li, and L. Ma, "LncRNA EPIC1 downregulation mediates hydrogen peroxide-induced neuronal cell injury," *Aging*, vol. 11, no. 23, 2019LncRNA EPIC1 downregulation mediates hydrogen peroxide-induced.pdf.

[15] J. Zhong, C. Cheng, H. Liu et al., "Bexarotene protects against traumatic brain injury in mice partially through apolipoprotein E," *Neuroscience*, vol. 343, pp. 434–448, 2017.

[16] Y. R. Tsai, C. F. Chang, J. H. Lai et al., "Pomalidomide ameliorates H_2O_2-induced oxidative stress injury and cell death in rat primary cortical neuronal cultures by inducing anti-oxidative and anti-apoptosis effects," *International Journal of Molecular Sciences*, vol. 19, no. 10, p. 3252, 2018.

[17] J. He, H. Liu, J. Zhong et al., "Bexarotene protects against neurotoxicity partially through a PPARγ-dependent mechanism in mice following traumatic brain injury," *Neurobiology of Disease*, vol. 117, pp. 114–124, 2018.

[18] Q. Tan, Q. Chen, Y. Niu et al., "Urokinase, a promising candidate for fibrinolytic therapy for intracerebral hemorrhage," *Journal of Neurosurgery*, vol. 126, no. 2, pp. 548–557, 2017.

[19] K. Nakajima, T. Tanaka, Y. Masubuchi et al., "Developmental exposure of mice to T-2 toxin increases astrocytes and hippocampal neural stem cells expressing metallothionein," *Neurotoxicity Research*, vol. 35, no. 3, pp. 668–683, 2019.

[20] W. R. Swindell, "Metallothionein and the biology of aging," *Ageing Research Reviews*, vol. 10, no. 1, pp. 132–145, 2011.

[21] X. Kong, C. X. Liu, G. D. Wang et al., "LncRNA LEGLTBC functions as a ceRNA to antagonize the effects of miR-34a on the downregulation of SIRT1 in glucolipotoxicity-induced INS-1 beta cell oxidative stress and apoptosis," *Oxidative Medicine and Cellular Longevity*, vol. 2019, Article ID 4010764, 16 pages, 2019.

[22] L. V. Bayunova, I. I. Zorina, I. O. Zakharova, and N. F. Avrova, "Insulin increases viability of neurons in rat cerebral cortex and normalizes Bax/Bcl-2 ratio under conditions of oxidative stress," *Bulletin of Experimental Biology and Medicine*, vol. 165, no. 1, pp. 14–17, 2018.

[23] H. Jaeschke, A. Ramachandran, X. Chao, and W. X. Ding, "Emerging and established modes of cell death during acetaminophen-induced liver injury," *Archives of Toxicology*, vol. 93, no. 12, pp. 3491–3502, 2019.

[24] T. Derrien, R. Johnson, G. Bussotti et al., "The GENCODE v7 catalog of human long noncoding RNAs: analysis of their gene structure, evolution, and expression," *Genome Research*, vol. 22, no. 9, pp. 1775–1789, 2012.

[25] M. A. Lynes, J. Hidalgo, Y. Manso, L. Devisscher, D. Laukens, and D. A. Lawrence, "Metallothionein and stress combine to affect multiple organ systems," *Cell Stress & Chaperones*, vol. 19, no. 5, pp. 605–611, 2014.

[26] S. Takahashi, "Positive and negative regulators of the metallothionein gene (review)," *Molecular Medicine Reports*, vol. 12, no. 1, pp. 795–799, 2015.

[27] K. Wakida, N. Morimoto, M. Shimazawa et al., "Cilostazol reduces ischemic brain damage partly by inducing metallothionein-1 and -2," *Brain Research*, vol. 1116, no. 1, pp. 187–193, 2006.

[28] X. Bai, J. Geng, X. Li et al., "Long noncoding RNA LINC01619 regulates microRNA-27a/forkhead box protein O1 and endoplasmic reticulum stress-mediated podocyte injury in diabetic nephropathy," *Antioxidants & Redox Signaling*, vol. 29, no. 4, pp. 355–376, 2018.

[29] R. Li, F. Yin, Y. Y. Guo, K. C. Zhao, Q. Ruan, and Y. M. Qi, "Knockdown of ANRIL aggravates H_2O_2-induced injury in PC-12 cells by targeting microRNA-125a," *Biomedicine & pharmacotherapy = Biomedecine & pharmacotherapie*, vol. 92, pp. 952–961, 2017.

[30] T. Cheng, M. Xu, B. Qin et al., "lncRNA H19 contributes to oxidative damage repair in the early age-related cataract by regulating miR-29a/TDG axis," *Journal of Cellular and Molecular Medicine*, vol. 23, no. 9, pp. 6131–6139, 2019.

[31] T. Chen, Y. Li, W. Cao, and Y. Liu, "miR-491-5p inhibits osteosarcoma cell proliferation by targeting PKM2," *Oncology Letters*, vol. 16, no. 5, pp. 6472–6478, 2018.

[32] S. U. Rehman, M. Ikram, N. Ullah et al., "Neurological enhancement effects of melatonin against brain injury-induced oxidative stress, neuroinflammation, and neurodegeneration via AMPK/CREB signaling," *Cell*, vol. 8, no. 7, p. 760, 2019.

[33] J. Jia, L. Ma, M. Wu et al., "Anandamide protects HT22 cells exposed to hydrogen peroxide by inhibiting CB1 receptor-mediated type 2 NADPH oxidase," *Oxidative Medicine and Cellular Longevity*, vol. 2014, Article ID 893516, 16 pages, 2014.

[34] M. Shafagh, F. Rahmani, and N. Delirezh, "CuO nanoparticles induce cytotoxicity and apoptosis in human K562 cancer cell line via mitochondrial pathway, through reactive oxygen species and P53," *Iranian Journal of Basic Medical Sciences*, vol. 18, no. 10, pp. 993–1000, 2015.

[35] A. Das, S. Chakrabarty, D. Choudhury, and G. Chakrabarti, "1,4-Benzoquinone (PBQ) induced toxicity in lung epithelial cells is mediated by the disruption of the microtubule network and activation of caspase-3," *Chemical Research in Toxicology*, vol. 23, no. 6, pp. 1054–1066, 2010.

[36] X. Lu, J. Dong, D. Zheng, X. Li, D. Ding, and H. Xu, "Reperfusion combined with intraarterial administration of resveratrol-loaded nanoparticles improved cerebral ischemia-reperfusion injury in rats," *Nanomedicine: Nanotechnology, Biology, and Medicine*, vol. 28, article 102208, 2020.

[37] Q. Rui, H. Ni, X. Lin et al., "Astrocyte-derived fatty acid-binding protein 7 protects blood-brain barrier integrity through a caveolin-1/MMP signaling pathway following traumatic brain injury," *Experimental Neurology*, vol. 322, article 113044, 2019.

[38] L. Lu, M. Cai, M. Peng, F. Wang, and X. Zhai, "miR-491-5p functions as a tumor suppressor by targeting IGF2 in colorectal cancer," *Cancer Management and Research*, vol. 11, pp. 1805–1816, 2019.

[39] T. Yu, L. N. Wang, W. Li et al., "Downregulation of miR-491-5p promotes gastric cancer metastasis by regulating SNAIL and FGFR4," *Cancer Science*, vol. 109, no. 5, pp. 1393–1403, 2018.

[40] L. Salmena, L. Poliseno, Y. Tay, L. Kats, and P. P. Pandolfi, "A *ceRNA* Hypothesis: The Rosetta Stone of a Hidden RNA Language?," *Cell*, vol. 146, no. 3, pp. 353–358, 2011.

Hindawi
Oxidative Medicine and Cellular Longevity
Volume 2022, Article ID 8622388, 23 pages
https://doi.org/10.1155/2022/8622388

Research Article

miRNA-22 Upregulates *Mtf1* in Dorsal Horn Neurons and Is Essential for Inflammatory Pain

Ling-Yun Hao,[1,2,3] Ming Zhang,[1,2,3] Yang Tao,[1,2,3] Hengjun Xu,[1,2,3] Qiaoqiao Liu,[1,2,3] Kehui Yang,[1,2,3] Runa Wei,[1,2,3] Huimin Zhou,[1,2,3] Tong Jin,[4] Xiao-Dan Liu,[1,2,3] Zhouya Xue,[1,2,3] Wen Shen,[5] Jun-Li Cao,[1,2,3,6] and Zhiqiang Pan[1,2,3]

[1]*Jiangsu Province Key Laboratory of Anesthesiology, Xuzhou Medical University, Xuzhou 221004, China*
[2]*Jiangsu Province Key Laboratory of Anesthesia and Analgesia Application Technology, Xuzhou Medical University, Xuzhou 221004, China*
[3]*NMPA Key Laboratory for Research and Evaluation of Narcotic and Psychotropic Drugs, Xuzhou 221004, China*
[4]*Department of Pain, Shanghai Tenth People's Hospital, Tongji University, Shanghai 200072, China*
[5]*Department of Pain, The Affiliated Hospital of Xuzhou Medical University, Xuzhou 221002, China*
[6]*Department of Anesthesiology, The Affiliated Hospital of Xuzhou Medical University, Xuzhou 221002, China*

Correspondence should be addressed to Zhiqiang Pan; 307577660@qq.com

Received 26 July 2021; Revised 5 December 2021; Accepted 14 December 2021; Published 10 February 2022

Academic Editor: Chaoliang Tang

Chronic inflammatory pain seriously affects patients' quality of life because of a paucity of effective clinical treatments caused, at least in part, by lack of full understanding of the underlying mechanisms. miRNAs are known to be involved in inflammatory pain via silencing or degrading of target mRNA in the cytoplasm. The present study provides a novel mechanism by which miRNA-22 positively regulates metal-regulatory transcription factor 1 (*Mtf1*) in the nuclei of neurons in the dorsal horn of the spinal cord. We found that miRNA-22 was significantly increased in the dorsal horn of mice with either inflammatory pain induced by plantar injection of complete Freund's adjuvant (CFA) or neuropathic pain induced by unilateral sciatic nerve chronic constrictive injury (CCI). Knocking down or blocking miRNA-22 alleviated CFA-induced mechanical allodynia and heat hyperalgesia, whereas overexpressing miRNA-22 produced pain-like behaviors. Mechanistically, the increased miRNA-22 binds directly to the *Mtf1* promoter to recruit RNA polymerase II and elevate *Mtf1* expression. The increased *Mtf1* subsequently enhances spinal central sensitization, as evidenced by increased expression of p-ERK1/2, GFAP, and c-Fos in the dorsal horn. Our findings suggest that the miRNA-22–*Mtf1* signaling axis in the dorsal horn plays a critical role in the induction and maintenance of inflammatory pain. This signaling pathway may be a promising therapeutic target in inflammatory pain.

1. Introduction

Epigenetic mechanisms play a critical role in the development and maintenance of chronic pain [1–5]. microRNAs (miRNAs), a class of non-coding RNAs 20–25 nucleotides in length, are highly conserved and stable, and recent studies have shown a strong connection between miRNAs and various diseases of the nervous system. Altered miRNA expression in primary sensory neurons after nerve injury was first observed in 2010 [6]; since then, a large body of research has demonstrated the essential regulatory function of miRNAs in the initiation and progression of pain signals in primary afferent nociceptors, dorsal root ganglia (DRG), spinal cord, and various brain areas. Manipulating miRNA expression can efficiently prevent or reverse persistent inflammatory, neuropathic, and cancer pain behavior [7, 8].

Previous reports on the role of miRNAs in pain have generally focused on negative regulatory mechanisms, by which miRNAs silence or degrade mRNA when the miRNA seed region matches the 3'-UTR fragment of mRNA in the neuronal cytoplasm [9]. However, several mature miRNAs have recently been found to transfer from the cytoplasm to

the nucleus, where they subsequently regulate the transcription of target genes [10]. For example, miRNA-1224, located mainly in the nuclei of spinal neurons, is downregulated by peripheral inflammation; rescuing this downregulation attenuates inflammation-induced nociceptive hypersensitivity by reducing the level of ciRNA-Filip1 in the dorsal horn [5], suggesting that nuclear miRNAs can play an important role in the pathological processes underlying inflammatory pain. Thus, understanding the role of nuclear miRNAs in pain may provide a novel approach for the management of inflammatory pain.

In previous work, we profiled miRNA expression in the dorsal horn of the spinal cord in mice and found that peripheral inflammation significantly upregulated expression of miRNA-22 [11]. Given that miRNA-22 is highly conserved across mouse and human and participates in several diseases, including Alzheimer's disease, glioma, and hepatocellular carcinoma [12–14], it is likely to be a player in the physiological and pathological processes of multiple peripheral and central nervous diseases. However, whether miRNA-22 is involved in inflammatory pain remains unknown.

In the current work, we report that miRNA-22 was enriched in neuronal nuclei in mouse dorsal horn. Upregulation of miRNA-22 in the dorsal horn was required for the development and maintenance of inflammatory pain through its positive regulation of *Mtf1* protein. Nuclear miRNA-22 in dorsal horn neurons may therefore play a critical role in the pathological processes underlying inflammatory pain.

2. Materials and Methods

2.1. Animals. Adult male Kunming mice (20-25 g) used in this study were provided by the Experimental Animal Center of Xuzhou Medical University. All animal experimental protocols were approved by the animal protection committee of Xuzhou Medical University. Every effort was made to reduce the animal's pain and the number of used animals. The animals were kept in a standard cage in a controlled environment (temperature: 23°C ± 3°C, relative humidity: 25% and 45%) and light period is maintained from 6 : 00 to 18 : 00, and food and water are freely available.

2.2. Pain Model. Inflammatory pain model: inflammatory pain model was implemented following the method described by Larson et al. [15]. CFA (complete Freund's adjuvant) (40 μl; F5881, Sigma-Aldrich, St. Louis, MO, USA) was injected into the surface of left hindpaw plantar, or the same volume of saline was used as control. Neuropathic pain model: unilateral sciatic nerve chronic constrictive injury (CCI) model was performed as described previously [5]. Mice were anesthetized with isoflurane inhalation. Skin preparation and disinfection were performed in the operating area. The sciatic nerve was exposed by blunt dissection. About 7 mm of nerve was freed adhering tissue in proximal to the sciatic trifurcation. The sciatic nerve trunk was loosely ligated with 7-0 gut, with 3 channels spaced 1 mm apart. In sham animals, sciatic nerve was exposed without ligated. The wound was sutured in layers and treated with penicillin.

2.3. Behavioral Test. Paw withdrawal latencies (PWL) corresponding to thermal hyperalgesia were detected by the IITC Plantar Analgesia Meter (IITC Model 336 Analgesia Meter, Series 8; IITC Life Science, USA) as described previously [16]. Double-blind detection was performed. The mice were placed in the plexiglass box on a 3 mm thick glass plate and adapted for 1 h. The movable thermal radiation device was placed under glass panels to focus onto the plantar surface of the mice left hindpaw. The time from the start of irradiation heat to elicit withdraw of the left hindpaw was defined as heat shrinkable foot the incubation period. At the beginning, the radiant heat intensity was adjusted so that the base value of the incubation period remained at 12-15 s and an automatic cut-off time is 25 s to avoid tissue damage. The left hindpaw of each animal was thermally stimulated for 6 times at interval of 5 min and the mean value was calculated.

Paw withdrawal threshold (PWT) corresponding to mechanical allodynia was detected by using von Frey filaments by up-down method. The mice were placed in the plexiglass box on a metal mesh floor and adapted for 1 h. Starting with a 0.16 g and ending with a 6.0 g filament in ascending order. The filaments vertically stimulated the plantar surface with sufficient force to cause slight bending against the paw for 5 times at 5 min interval. A brisk withdrawal or flinching of the paw was regarded as a positive response as described previously [16]. Double-blind detection was performed.

2.4. Spinal/DRG Tissue Collection. Mice were anesthetized with isoflurane inhalation, then the dorsal horn of lumbar spinal cord (L3-L4) was rapidly resected, and the ipsilateral and contralateral dorsal spinal horn and the DRG were separated and then put into liquid nitrogen immediately and stored at -80°C or directly used.

2.5. miRNA, mRNA Extraction and Reverse Transcription-Quantitative PCR (RT-qPCR). Total RNA extraction was performed according to the instructions of Trizol (15596–026, Invitrogen, Carlsbad, CA, USA) and the quality and quantity of total RNAs were evaluated with the NanoDrop ND-2000 (Thermo Scientific, Waltham, MA, USA). RNA (0.5 μg) was reverse-transcribed into single stranded cDNA using oligo $(dT)_{18}$ (for *Mtf1*, U6 and Gapdh gene) or specific primer (5'-TTAACTGGATACGAAGGGTCCGAACACCG GTCGTATCCAGTTAAACAGTTCT-3' for miRNA-22) with reverse transcriptase M-MLV (2641, Takara, Japan). The reverse transcription of *Mtf1*, *U6 snRNA* and *Gapdh* gene was performed at 37°C for 30 min, 42°C for 30 min and 75°C for 5 min; or miRNA-22 at 16°C for 30 min and 37°C for 30 min and 75°C for 5 min. The cDNA template (1 μl) was amplified by real-time quantitative PCR with the PCR primers (miRNA-22, F: 5'-TGCGGTAAGCTGCCAG TTGAAG-3', R: 5'-TACGAA GGGTCCGAACAC-3'; *Mtf1,* F: 5'-ACACCTTCGTCTGTAATCAGGA-3', R: 5'-CTGC ACGTC ACACTCAAATGG-3'; *Gapdh*, F: 5'-GGTGAAGG TCGGTGTGAACG-3', R: 5'-CTCGCTCCTGGAAGATGG

TG-3'; *U6 snRNA,* F: 5'-CTCGCTTCGGCAGCAC ATAT ACT-3'; R, 5'-ACGCT TCACGAATTTGCGTGTC-3').

Signal of each sample was determined in triplicate using SYBR Premix ExTaqII (RR820A; Takara). Reactions were carried out in a Roche Light Cycler 480 system. The expression levels of the target genes were quantified relative to *Gapdh* (an internal control of *Mtf1*) or U6 snRNA (an internal control of miRNA-22) expression (cycle threshold [Ct]) using the $2^{-(\Delta\Delta CT)}$ methods [17]. Any value among triplicates that had a marked difference (≥1.00) compared with the average of the other two was discarded.

2.6. Fluorescence in Suit Hybridization (FISH). The experiment was performed as the described previously [11]. Briefly, anesthetized mice were subjected to sternotomy followed by intracardial perfusion with saline and 4% ice-cold paraformaldehyde phosphate buffer, and spinal cord (L3-L4) was rapidly dissected and post fixed in 4% paraformaldehyde overnight. The tissue was dehydrated in 30% sucrose solution overnight and then transversely sectioned at the thickness of 30 μm. Hybridization process was carried out according to the instructions of FISH kit (Guangzhou Exon Co, China). miRNA-22 probe labeled with digoxin (5'-Dig-ACAGTTCTTCAACTGGCAGCTT-Dig-3') was hybridized in spinal section at 37°C for 16 h-72 h and subjected to wash in buffer, and was incubated in fluorescent-conjugated digoxin secondary antibody (Sangon Biotech, Shanghai, China) at 37°C for 1 h, then washed at room temperature for 10 min/time, 3 times. All solutions were prepared with nuclease-free water. Images were captured by a high-resolution digital confocal microscope (Olympus FV1000, Japan).

2.7. miRNA-22 Target Construction and Luciferase Reporter Assay. The identified region of *Mtf1* promoter from a mouse genomic DNA was amplified using primer pairs (F, 5'-ACGCTCGAGGGTGCGCCAGAGTCACTTAT-3' and R, 5'-AATAAGCTTTCTCAACCTGGT TCTGCACT-3'), and cloned into pGL6 plasmid (Beyotime, Shanghai, China) via XhoI and HindIII (NEB, USA) digestion. Empty pGL6 vector was used as control plasmid.

HEK293T cells were incubated in DMEM (Gibco BRL,Grand Island, NY, USA) containing 10% FBS (Gibco BRL) and 1×10^5 cells per well were seeded into 24-well plates before transfection. The reporter plasmids pGL6 or pGL6-*Mtf1* were co-transfected with miRNA-22 mimics or miRNA-22 inhibitor into 293 cells using Lipofectamine 2000 (11668-027, Invitrogen). After 48 h of incubation, the cells were collected to detect luciferase activity assays using the Double luciferase reporter kit (E1910, Promega, Madison, WI, USA) in accordance with the manufacturer's instruction. The ratio of firefly luciferase activity to Renilla luciferase activity in each group (Renilla luciferase activity as an internal reference) was used as the reporter gene activity.

2.8. Overexpression and Knockdown Plasmid Construction. To construct miRNA-22 (Lenti-22) and *Mtf1* overexpression vector (Lenti-*Mtf1*): one insert for miRNA-22 was prepared by PCR primer pairs (F: 5'-TGCGTTTAAACATTCAAGA ACCCCTCATTAGA-3', R: 5'-TTTGACGCGTCCCCA-GAGGACCAGGGTT-3') or for Mtf1 by PCR primer pairs (F: 5'-TGCGTTTAAACATGGGGGAACACAGTCCAGA-3', R: 5'-TTTGACGCGTCTAGGGTGGCACGCAGG-3'); PCR products and pWPXL vector were digested by restriction endonucleases PmeI and MluI and ligated with T4 ligase. To construct miRNA-22 knockdown (LV-miRNA-22-sponge) or Mtf1 knockdown vector (LV-Mtf1-shRNA), two oligos for LV-miRNA-22-sponge (F: 5'-CGCGtACAG TTCTTCAACTGGCAGCTTgctaAC AGTTCTT-CAACTGGCAGCTTgctaACAGTTCTTCAACTGGCAGC TTttttat-3', R: 5'-CGaTaaaAAAGCTGCCAAACTGAAGAA CTGTtagcAAGCTGCCAAACTAAGAACTGTtagcAAGCT GCCAAACTGAAGAACTGTa-3') or two oligos for LV-Mtf1-shRNA (F: 5'-CGCGtGGAGGATGATGAAGAC-GATGGAACGCCATCGTCTTCATCATCCTCCTTTTT Tta-3', R: 5'-CGatAAAAAAGGAGGATGATGAAGAC-GATGGCGTTCCATCGTCTTCATCATCCTCCa-3') were annealed and ligated to the digested PLVTHM plasmid with MluI and ClaI (NEB), respectively. All constructs were produced by the use of standard molecular methods and confirmed by DNA sequencing.

2.9. Lentivirus Production and Verification. The constructed core plasmid (16 μg) and two envelope plasmids, PSPAX2 (12 μg) and PMD2G (4.8 μg), were cotransfected into HEK293T cells in a 6-well plate according to the manufacturer's instructions of Lipofectamine 2000 (11668-027, Invitrogen). The supernatant was collected at 48 h after transfection and concentrated by using a Centricon Plus-70 filter unit (UFC910096, Millipore, MA, USA). Lentivirus with titers 10^8 TU/ml was used in the experiment. The assays of lentivirus in vitro and in vivo infection were performed according to a previous study [11]. Briefly, 20 μl lentivirus and 1.5 μl polybrene (1.4 μg/μl; H9268, Sigma-Aldrich) were added in a 24-well plate containing 1×10^5 HEK293T cells and DMEM without FBS; after 24 h, the transduction medium was replaced with 500 μl fresh complete medium containing 10% FBS; cells were collected at 48 h after transduction.

2.10. siRNA, Mimics, Inhibitor, and Lentivirus Delivery. 5 μl of 20 μM miRNA-22 mimics, inhibitor and *Mtf1* siRNA and 1 μl Lentivirus and their respective controls scrambled siRNA or an empty vector were intrathecally injected. The method of intrathecal injection was performed according to the previous study [5]. In brief, the mouse was held firmly by the pelvic girdle and then the needle of a 10 μl microsyringe was punctured into L5 and L6 vertebrae of the mouse. Proper insertion of the needle into the subarachnoid space was verified by a slight flick of the tail after a sudden advancement of the needle. The sequence of mimics, inhibitor/siRNA were as follow: miRNA-22 mimics (5'-AAGCUGCCAGUUG AAGAAC UGU-3'), miRNA-2 inhibitor (5'-ACAGUUCUUCAACU GGCAGCUU-3'), *Mtf1* siRNA (sense: 5'-AAGAAACAUUG AAGGUGCAACUCUUTT-3', antisense: 5'-AAGAGUUG CACC UUCAAUGUUUCUUTT-3').

2.11. Antibody Immunoprecipitation (ChIP). Immunoprecipitation was carried out according to EZ CHIP

Immunoprecipitation kit (17-371, Millipore) with minor modification. Briefly, spinal cord tissues were fragmented for chromatin cross-linking, followed by homogenization and ultrasound. We added 60 μl protein G agarose beads in each tube to incubate with rotation for 1 h at 4°C. Then centrifuged 4000 g for 1 min at 4°C to obtain the supernatant. The supernatant was divided into two parts, in which 10 μl was used as input and the remaining part (1 ml) was transferred to the new centrifuge tube. Subsequently 2 μg Anti-RNA Polymerase II/IgG was added to the supernatant to incubate along with rotation overnight at 4°C. Another 60 μl protein G agarose beads were added to the mixture to incubate with rotation for 1 h at 4°C and the chromatin was pulled down by magnetic beads. Finally, we digested the protein with proteinase K. Each sample was divided into two parts to undergo the extraction of RNA for miRNA-22 and DNA for *Mtf1* promoter detection.

2.12. RNA-DNA Immunoprecipitation. Referring the previously described [5, 18], some experimental procedures were modified. Biotin-labeled miRNA-22 probe (5'-Bio-ACAGTT CTTCAACTGGCAGCTT-3') was used to bind the *Mtf1* promoter via recognizing the target DNA regions. Spinal cord tissues were homogenized and fragmented by ultrasound. After centrifugation, 50 μl of the supernatant was retained as input, and the remaining part was incubated with miRNA-22 probes or Scrambled probes (0.5 μl, 50 μM) overnight with rotation at 4°C. 50 μl The Dyna-beads M-280 Streptavidin (11205D, Thermo Fisher Scientific, Waltham, MA, USA) was added into mixture and incubated at 4°C for 1 h. The mixture of beads-probes-DNAs was washed and NaCl (8 μl, 5 M) was added into it to incubate overnight at 65°C to reverse the formaldehyde crosslinking. Finally, DNA was extracted by the use of Mag-MK Animal Genomic DNA Extraction Kit (B518721, Sangon Biotech) for *Mtf1* promoter detection.

2.13. Protein Extraction and Western Blot Analysis. The spinal cord tissues (L3-L4) were homogenized in a lysis buffer containing Protease Inhibitor Cocktail (p8340, Sigma-Aldrich) [19]. The protein concentration was confirmed with BCA protein concentration determination assay kit (P0010, Beyotime, Shanghai, China). The protein samples were separated by SDS-PAGE gels and transferred onto polyvinylidene fluoride membrane (IPVH00010, Millipore). The membrane was sealed with 5% skim milk for 2 h at room temperature, subsequently incubated at 4°C overnight with the primary antibodies: *Mtf1* (1 : 500; Santa Cruz Biotechnology, CA, USA), p-ERK1/2 (1 : 5000; Sigma), ERK1/2 (1 : 1000; Santa Cruz Biotechnology), GFAP (1 : 1000; Cell Signaling Technology, Danvers, MA, USA) and β-actin (1 : 2000; Santa Cruz Biotechnology). The membrane was washed for 5 min/time 3 times at room temperature, incubated for 2 h in the corresponding secondary antibody: HRP-labeled goat anti-mouse IgG (1 : 1000; Beyotime), HRP-labeled goat anti-rabbit IgG (1 : 1000; Beyotime) and HRP-labeled donkey anti-goat IgG (1 : 1000; Beyotime) at room temperature. The membrane was then washed for 5 min/time 6 times, the immune complexes were detected by ECL chemiluminescent assay kit (Biosharp, Guangzhou, China). Signal intensity of band analyses was conducted with ImageJ software (Alliance Q9).

2.14. Spinal Neuron Culture. The primary culture of spinal neurons was conducted according to the previous study [20]. The newborn mice within 24 h were directly severed heads after disinfected with 70% alcohol. The tissue fragments were digested for 45 min at 37°C with the preheated papain (20 U/ml, Sigma-Aldrich) in oxygenated divalent-free EBSS (14155063, Life Technologies, Carlsbad, CA, USA). The enzymatic digestion reaction is terminated by using 3 ml EBSS solution containing bovine serum albumin (1 mg/ml; A1933, Sigma-Aldrich), trypsin inhibitor (10 mg/ml; T6522, Sigma-Aldrich), and DNase (0.01%; D5025, Sigma-Aldrich), and mechanical separation was operated using sterile Pasteur pipettes. The homogenate was deposited on top of 4 ml of a solution of composition similar to that used above, except that the concentration of bovine serum albumin was increased to 10 mg/ml. And then the cell solution was centrifuged at 500 rpm for 5 min, and the supernatant was discarded and instead by 5 ml of culture medium. The composition of medium was as follows: MEM-α (Invitrogen), FCS (5% v/v; Invitrogen), heat-inactivated horse serum (5% v/v; Invitrogen), penicillin and streptomycin (50 IU/ml for each; Invitrogen), transferrin (10 mg/ml; Sigma-Aldrich), insulin (5 mg/ml; Sigma-Aldrich), putrescine (100 nM; Sigma-Aldrich), and progesterone (20 nM; Sigma-Aldrich). After trituration using sterile Pasteur pipettes, the cells were plated on 35 mm collagen-coated plastic culture dishes. Cultures were maintained in a water-saturated atmosphere (95% air, 5% CO_2) at 37°C until use (10–15 d). Two days after the cells were seeded, cytosine arabinoside (10 μM) was added to the culture medium for 24 h to inhibit glial proliferation.

2.15. Cellular Fraction and RNA Isolation. PARIS Kit (AM1921, Invitrogen) was used to separately isolate nuclear and cytoplasmic RNA from cultured mouse spinal neurons following the manufacturer instructions.

2.16. Locomotor Function. Three reflex tests were performed according to previously described procedures [5]. To test the grasping reflex, climbing tests were performed. A metal wire-mesh (0.5 mm diameter, 5 mm wide grid) was placed vertically 30 cm above the table. Each mouse started from the bottom of the mesh with its head facing downwards. After the mouse was released, the time required for it to climb all the way to the top was recorded. A maximum time of 60 s was applied for animals that could not successfully complete this task. Two sessions were performed for each mouse with a 30-min interval, and the shorter time was recorded. To test the placing reflex, we held the mouse with the hind limbs slightly lower than the forelimbs and brought the dorsal surfaces of the hindpaws into contact with the edge of a table. The experimenter recorded whether the hindpaws were placed on the table surface reflexively. To test the righting reflex, we placed the mouse on its back on a flat surface; the experimenter noted whether it immediately

assumed the normal upright position. Scores for placing, grasping, and righting reflexes were based on the counts of each normal reflex exhibited in five trials.

2.17. Statistical Analysis. All data were presented as mean ± SEM. The data were analyzed with a one-way or two-way ANOVA or paired or unpaired Student's t test. When ANOVA was statistically significant, pairwise comparisons between means were performed by a post hoc Tukey's test. Statistical analyses of data were performed with GraphPad Prism 5. $p < 0.05$ was considered statistically significant in all analyses.

3. Results

3.1. miRNA-22 Is Increased in Mouse Dorsal Horn after Nociception. Our previous miRNA profiling showed that peripheral inflammation caused by intraplantar injection of complete Freund's adjuvant (CFA) induced an increase in miRNA-22 in mouse dorsal horn [11]. To investigate the role of miRNA-22 in chronic pain further, we examined the time course of miRNA expression in both an inflammatory pain model (intraplantar injection of CFA) and a neuropathic pain model (chronic constriction injury (CCI) of the sciatic nerve). Consistent with previous studies [5, 21], CFA injection led to heat hyperalgesia (Figure 1(a)) and mechanical allodynia (Figure 1(b)) in mice from day 2 to day 7; similarly, peripheral nerve injury resulted in heat hyperalgesia (Figure 1(c)) and mechanical allodynia (Figure 1(d)) from day 3 to day 21 post-CCI surgery. Next, we examined the level of dorsal horn miRNA-22 at different time points after CFA injection or CCI surgery. The level of miRNA-22 in the ipsilateral dorsal horn increased by 59.78% on day 2 after CFA injection, by 87.53% on day 3, by 36.47% on day 5, and by 29.57% on day 7, but was not increased at 2 hours, on day 1, or on day 14 (Figure 1(e)); no increases were observed in the contralateral dorsal horn (Figure 1(f)). Similarly, increased levels of miRNA-22 were observed in the ipsilateral dorsal horn from day 7 to day 21 after CCI surgery (Figure 1(g)), but there were no increases in the contralateral dorsal horn (Figure 1(h)). Interestingly, CFA contributed to a transient increase in the level of miRNA-22 in the ipsilateral dorsal root ganglion (DRG) on only day 3 post-CFA injection (Figure 1(i)), with no changes in the contralateral DRG (Figure 1(j)). These results suggest that both peripheral inflammation and peripheral nerve injury cause upregulation of miRNA-22 in the ipsilateral dorsal horn. To further determine the distribution of miRNA-22 in spinal neurons, we conducted miRNA-22 fluorescence in situ hybridization (FISH) and found that miRNA-22 was co-expressed with NeuN (a neuronal marker) in dorsal spinal horn (Figure 1(k)). Furthermore, we measured the cytoplasmic and nuclear RNA from spinal neurons cultured from three-week-old mice. The subcellular analysis showed that the level of nuclear miRNA-22 was 267.15% greater than the level of cytoplasmic miRNA-22 (Figure 1(l)). These data indicate that miRNA-22 is distributed predominantly in the nucleus of spinal neurons.

3.2. Blocking the miRNA-22 Increase in Dorsal Horn Mitigates Inflammatory Pain. Next, we examined whether miRNA-22 regulates inflammatory pain (Figure 2(a)–2(h)). We used two manipulation tools to reduce the binding of miRNA-22 to its downstream genes in dorsal horn: (i) 22-Ih, a synthesized miRNA-22 inhibitor (a small RNA with reverse complementary sequence to miRNA-22) and (ii) LV-22, an LV-miRNA-22-sponge (lentivirus-expressed RNA with the ability to absorb miRNA-22). As expected, CFA-induced thermal hyperalgesia and mechanical allodynia were markedly alleviated after intrathecal injection of 22-Ih on two consecutive days, but the scrambled control (Scr) had no effect (Figure 2(a), 2(b)). The therapeutic effect lasted for 4 days for thermal hyperalgesia and 2 days for mechanical allodynia. Similarly, inhibition of miRNA-22 by intrathecal injection of LV-22, but not the vector control group, significantly ameliorated pain hypersensitivity, as indicated by an increase in paw withdrawal threshold to heat and mechanical stimulation (Figure 2(e), 2(f)). Neither 22-Ih nor LV-22 changed the basal responses on the contralateral side of CFA-injected mice (Figure 2(c), 2(d) and 2(g), 2(h)), the basal responses on the ipsilateral and contralateral sides of saline-injected mice, or the animals' locomotor functions (Table S1). Collectively, these data strongly suggest that increased miRNA-22 in the dorsal horn is required for the development and maintenance of inflammatory pain.

3.3. Mimicking the Increase in miRNA-22 Produces Pain Hypersensitivity. We next explored whether increased miRNA-22 in dorsal horn is sufficient for inflammatory pain. We intrathecally injected a mimic of miRNA-22 (22-mics; synthesized small RNA with the same sequence as miRNA-22) or Lenti-22 (lentivirus-expressed small RNA with the same sequence as miRNA-22) in naïve adult mice. Scrambled miRNA (Scr) and lentivirus vector (Vector) were used as the respective controls. Intrathecal injection of 22-mics induced mechanical allodynia and heat hyperalgesia, as evidenced by decreases in the paw withdrawal threshold in response to mechanical stimulation and decreases in the paw withdrawal latency in response to heat stimuli (Figure 2(i), 2(j)); these decreases occurred 1 day after injection of 22-mics. Pain hypersensitivity was not observed in the scrambled control group. As expected, a significant increase in miRNA-22 was detected 2 days after injection of 22-mics, relative to the Scr group (Figure 2(k)). Similarly, intrathecal injection of Lenti-22, but not its vector control, produced pain hypersensitivity to mechanical and heat stimulation on day 2 after injection (Figure 2(l), 2(m)), with the hypersensitivity lasting at least 5 weeks (Supplementary Figure 1). Intrathecal injection of Lenti-22 also increased the level of miRNA-22 on day 2 after injection (Figure 2(n)). None of the intrathecally injected mice displayed any locomotor impairments (Table S1). Thus, our findings indicate that miRNA-22 upregulation leads to inflammatory-pain-like symptoms.

3.4. miRNA-22 Positively Regulates Mtf1 Expression in Inflammatory Pain. How does the increase in miRNA-22 regulate inflammatory pain? Growing evidence suggests that

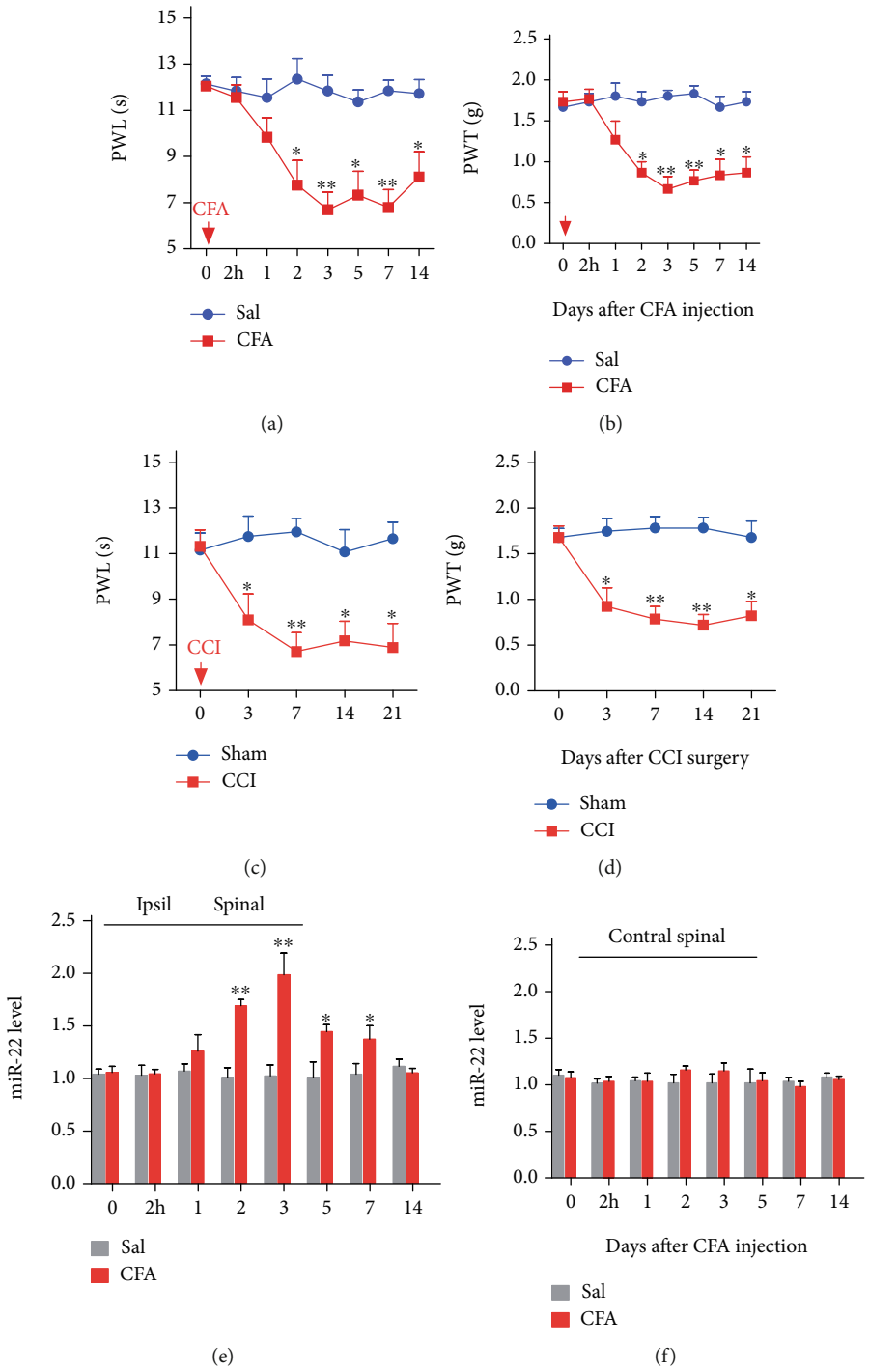

Figure 1: Continued.

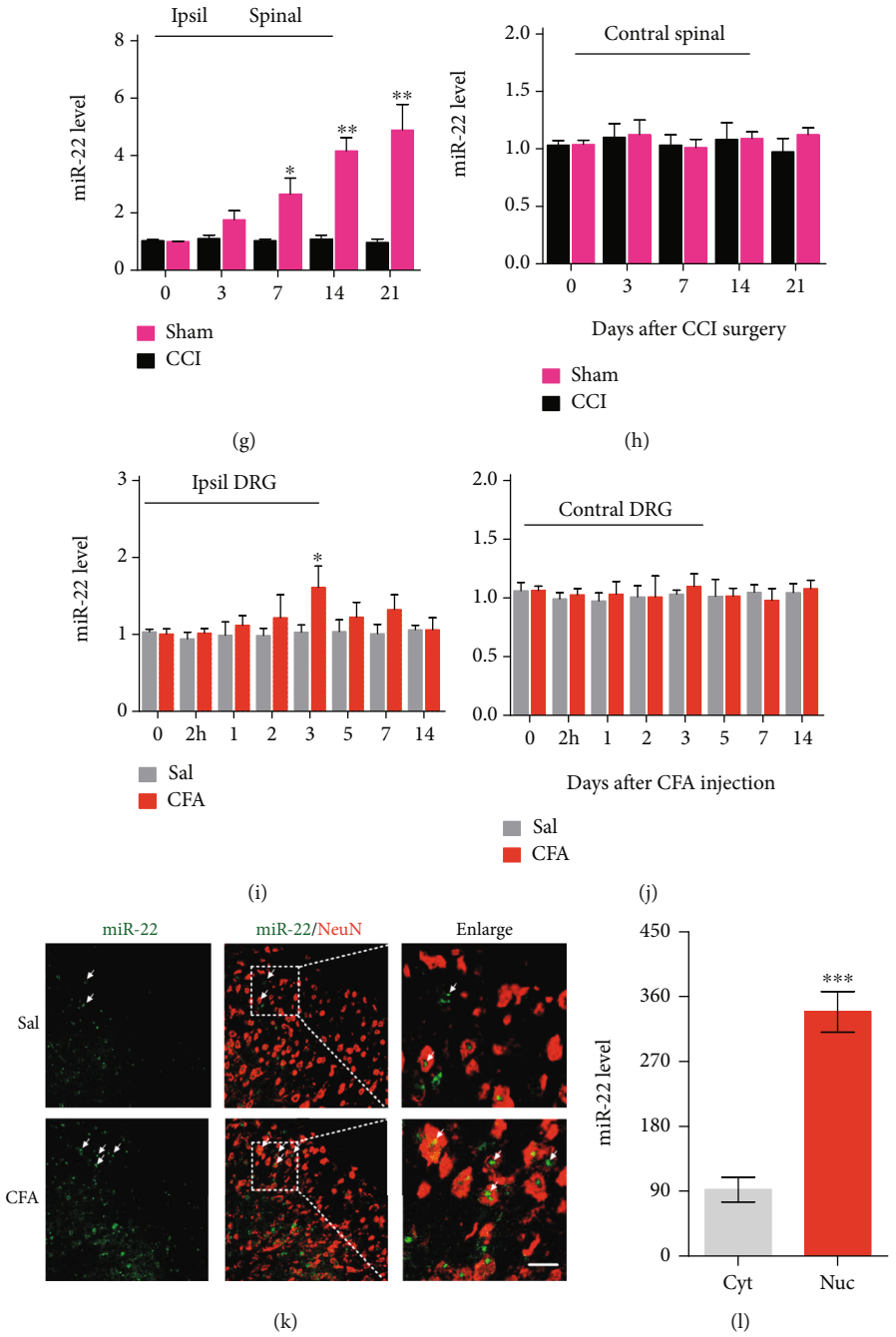

Figure 1: Inflammatory pain increased the expression of miRNA-22 in mouse dorsal horn. (a, b) Intraplantar injection of complete Freund's adjuvant (CFA) induced thermal hyperalgesia (a) and mechanical allodynia (b). n = 6. Red arrow indicates CFA or saline (Sal) injection. 2 h represents 2 hours after CFA injection. $*p < 0.05$; $**p < 0.01$ versus Sal. Data were analyzed with a two-way repeated-measures ANOVA followed by post hoc Tukey test. (c, d) Chronic constriction injury (CCI) of unilateral sciatic nerve caused hypersensitivity to heat (c) and mechanical (d) stimuli. $*p < 0.05$; $**p < 0.01$ versus Sham. n = 6. Data were analyzed with a two-way repeated-measures ANOVA followed by post hoc Tukey test. (e, f) Expression of miRNA-22 at different time points in ipsilateral (Ipsil) (e) or contralateral (Contral) (f) dorsal horn of mice with CFA-induced inflammatory pain. $*p < 0.05$, $**p < 0.01$ versus day 0. n = 5. 2 h represents 2 hours after CFA injection. Data were analyzed with a two-way ANOVA followed by post hoc Tukey test. (g, h) Expression of miRNA-22 at different time points in the ipsilateral (g) or contralateral (h) dorsal horn of mice with neuropathic pain after chronic constriction injury (CCI). $*p < 0.05$, $**p < 0.01$ versus day 0. n = 5. Data were analyzed with a two-way ANOVA followed by post hoc Tukey test. (i, j) Inflammatory pain slightly increased the expression of miRNA-22 in ipsilateral dorsal root ganglion (DRG) of mice (i), but not contralateral DRG (j), on only day 3 after CFA injection. $*p < 0.05$ versus 0 day. n = 5. Data were analyzed with a two-way ANOVA followed by post hoc Tukey test. (k) Co-staining of miRNA-22 *FISH* (green) and NeuN (a neuronal marker, red) immunofluorescence in dorsal horn on day 3 after CFA or saline injection. Scale bar, 50 μm. Arrows represent the location of the miRNA-22 signal in spinal neurons and the dotted lines indicate the region enlarged in the right-hand panel. (l) Distribution of miRNA-22 in the nucleus (Nuc) and cytoplasm (Cyt) of neurons cultured *in vitro*. Neurons were cultured *in vitro* for 48 h followed by separation of cytoplasmic and nuclear RNA. $***p < 0.001$ compared with Cyt group. n = 4. Data were analyzed with a Student's t test.

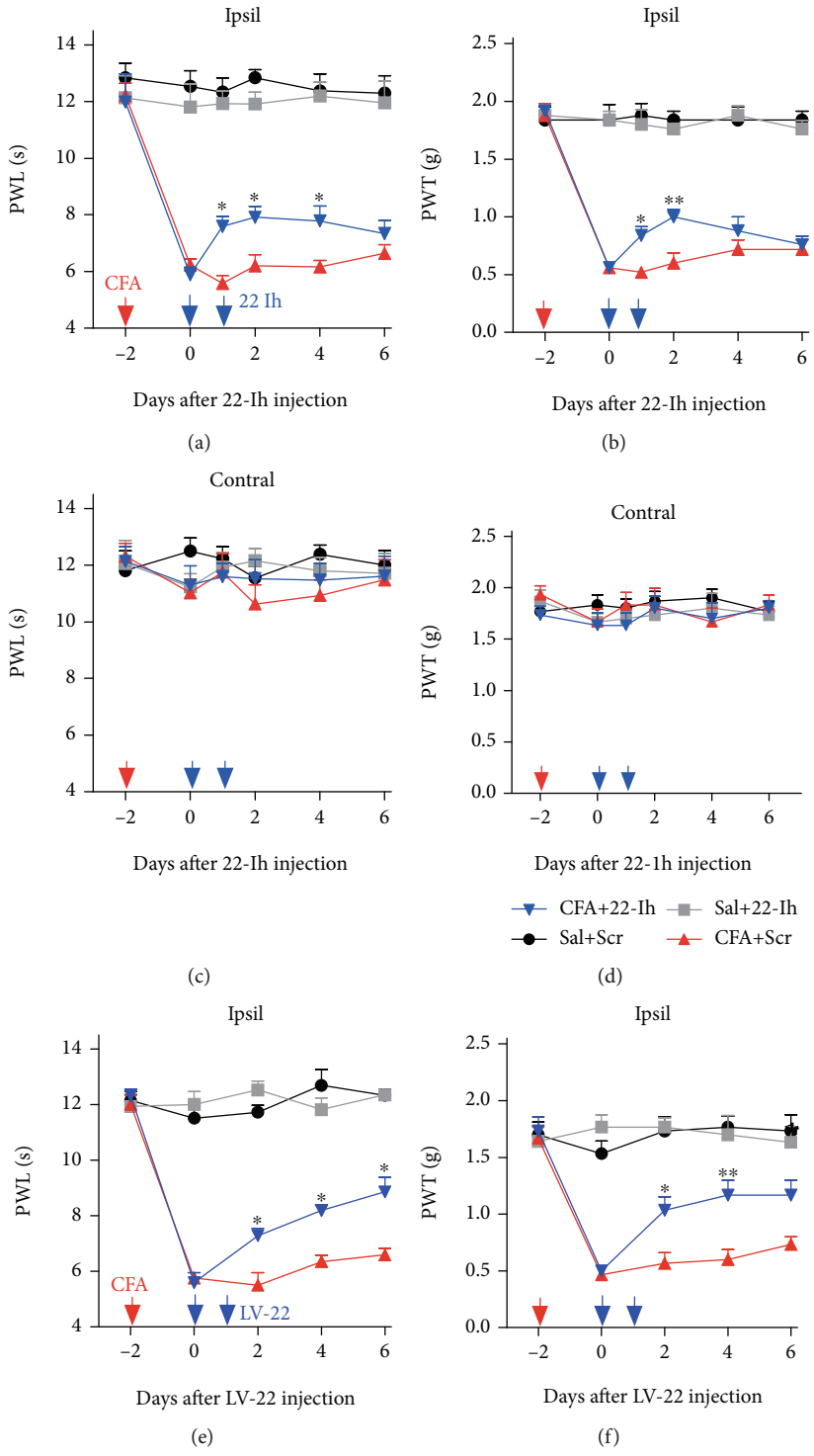

Figure 2: Continued.

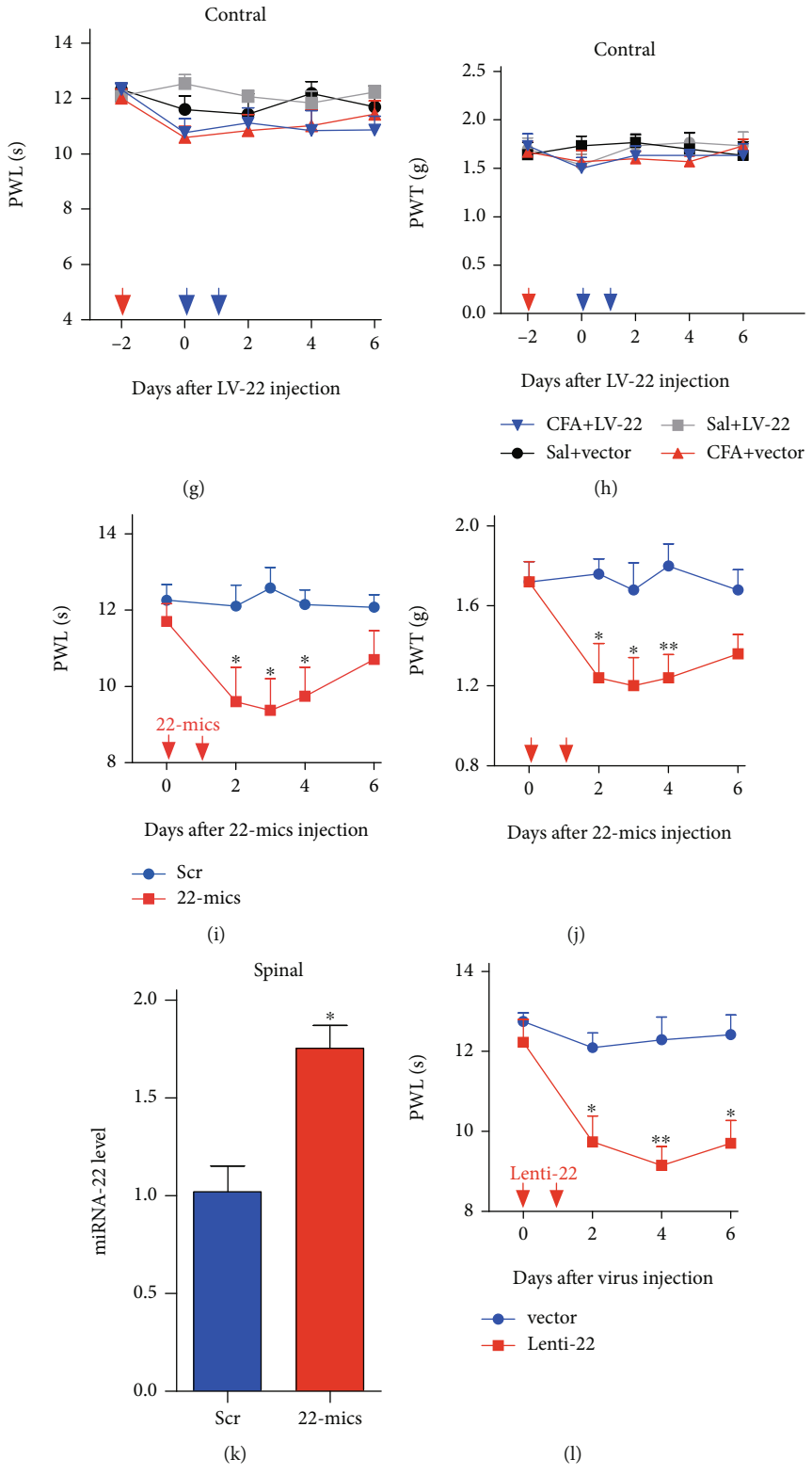

Figure 2: Continued.

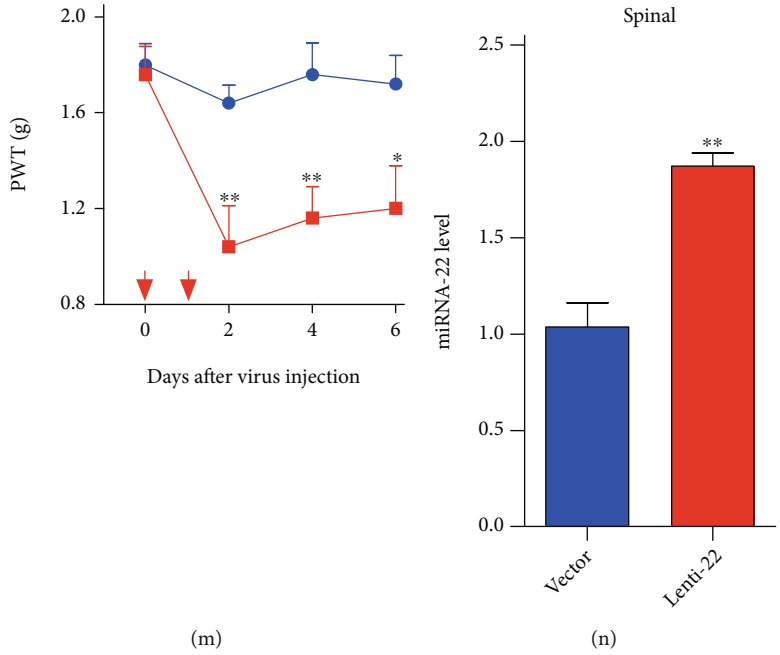

Figure 2: Increased miRNA-22 levels contribute to inflammatory pain behavior. (a) -(d) Intrathecal injection of miRNA-22 inhibitor for 2 consecutive days reversed CFA-induced hypersensitivity to thermal (a) and mechanical (b) stimuli on the ipsilateral paw, but did not change the sensitivity to thermal (c) and mechanical (d) stimuli in the contralateral paw in CFA-injected mice. $*p<0.05$, $**p<0.01$ versus CFA + Scrambled control (Scr), n = 6. Red arrow represents CFA or saline injection. Blue arrows represent injection of miRNA-22 Inhibitor (22-Ih) or the scrambled control (Scr). Data were analyzed with a two-way repeated-measures ANOVA followed by post hoc Tukey test. (e)-(h) Intrathecal injection of LV-miRNA-22-sponge (LV-22) for 2 consecutive days reversed the hypersensitivity to thermal (e) and mechanical (f) stimuli in the ipsilateral paw, but did not change the sensitivity to thermal (g) or mechanical (h) stimuli in the contralateral paw in CFA mice. $*p<0.05$, $**p<0.01$ versus CFA + Vector. n = 6. Red arrow represents CFA or saline injection. Blue arrows represent LV-22 or vector injection. Data were analyzed with a two-way repeated-measures ANOVA followed by post hoc Tukey test. (i)-(j) Intrathecal injection of an miRNA-22 mimic (22-mics) for 2 consecutive days led to the thermal (i) and mechanical (j) hypersensitivity. $*p<0.05$, $**p<0.01$ versus Scr. n = 6. Red arrows represent 22-mics or Scr injection. Data were analyzed with a two-way repeated-measures ANOVA followed by post hoc Tukey test. (k) Intrathecal injection of 22-mics for 2 consecutive days increased the miRNA-22 level in naïve mice. n = 4. $*p<0.05$, $**p<0.01$ versus Scr. Data were analyzed with a Student's t test. (l)-(m) miRNA-22 overexpression by intrathecal injection of Lenti-22 for 2 consecutive days increased the sensitivity to thermal (l) and mechanical (m) stimuli. $*p<0.05$, $**p<0.01$ versus Vector. n = 6. Red arrows represent Lenti-22 or vector control injection. Data were analyzed with a two-way repeated-measures ANOVA followed by post hoc Tukey test. (n) Intrathecal injection of Lenti-22 for 2 consecutive days increased the level of miRNA-22 in naïve mice. n = 6. $**p<0.01$ versus Vector. Data were analyzed with a Student's t test.

miRNAs can regulate gene expression in multiple ways. For example, miRNA can silence genes by binding to the 3' untranslated region (UTR) of mRNA [10]. Additionally, miRNA can enhance gene transcription via binding to the gene promoter [22]. Because metal-regulatory transcription factor 1 (*Mtf1*) was increased in mouse spinal cord after plantar CFA injection (Figure 3(c), 3(f), 3(g)), we hypothesized that nuclear miRNA-22 in spinal neurons increases *Mtf1* expression by binding to the *Mtf1* promoter to recruit RNA polymerase II. Our informatics analysis shows that the *Mtf1* promoter contains 12 potential binding sites spanning 1157 bp from −516 ~ +640 bp region (transcription start site denoted as +1). A chromatin immunoprecipitation (ChIP) assay revealed that an *Mtf1* promoter fragment containing binding sites could be pulled down by a bio-labeled miRNA-22 probe in dorsal horn nuclear fractions from saline control mice using a PCR test and DNA agarose gel electrophoresis. This amplification did not occur with the scrambled control probe, indicating specific binding of miRNA-22 to the *Mtf1* promoter (Figure 3(a)). Furthermore, CFA injection dramatically elevated the degree of miRNA-22–promoter binding, evidenced by a 71.25% increase in band intensity in the CFA group compared with the saline group on day 3 after CFA injection (Figure 3(a)). These results suggest that chromatin in the *Mtf1* promoter region is more open when the animal is in an inflammatory pain state.

Does the increased open region bound by miRNA-22 enhance the recruitment of RNA polymerase II? As expected, in a ChIP test with anti-RNA polymerase II (Anti-RPII), CFA injection increased the binding activity of RNA polymerase II in the promoter region bound by miRNA-22: activity was elevated by 146.42% in CFA-injected mice compared with saline mice (Figure 3(b)). IgG amplification did not occur in either saline or CFA-injected mice (Figure 3(b)). Additionally, in CFA-injected mice, pull-down of the miRNA-22-bound fragment in the *Mtf1* promoter by anti-RPII was 1.5 times that of saline mice; the bound fragment was undetected in the control IgG for both groups (Figure 3(c)). To further demonstrate

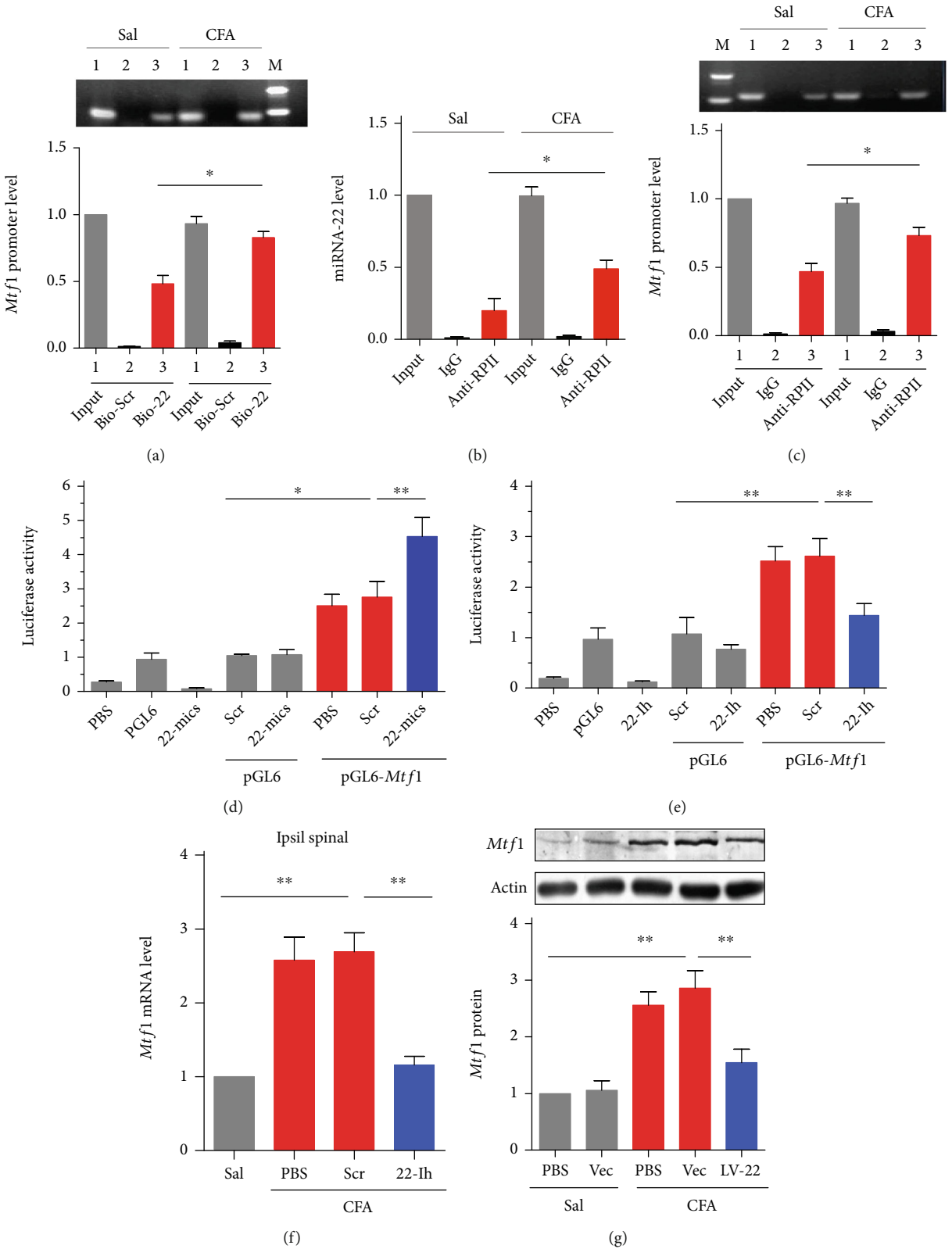

Figure 3: Continued.

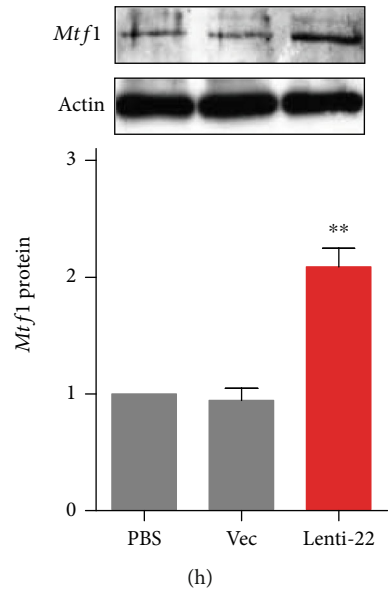

Figure 3: miRNA-22 positively regulates *Mtf1* expression by targeting the *Mtf1* promoter. (a) miRNA-22 binding to *Mtf1* promoter fragment evaluated by chromatin immunoprecipitation of bio-labeled miRNA-22 probes. $*p<0.05$ versus saline group. n = 4. Bio-miRNA-22 probes (Bio-22) or Bio-scrambled probes (Bio-Scr) were used to pull down the *Mtf1* promoter in dorsal horn homogenate. PCR and DNA gel electrophoresis were used to test the binding accounts. Data were analyzed with a one-way ANOVA followed by post hoc Tukey test. (b) Immunoprecipitation of RNA polymerase II and miRNA-22. The complex of miRNA-22 and RNA polymerase II was pulled down with an antibody against RNA polymerase II (anti-RP II) in dorsal horn tissue collected on day 3 after CFA injection. $*p<0.05$ versus saline group. n = 4. Data were analyzed with a one-way ANOVA followed by post hoc Tukey test. (c) Analysis of RNA polymerase II binding to *Mtf1* promoter in a chromatin immunoprecipitation complex by anti-RP II. $*p<0.05$ versus saline group. n = 4. Data were analyzed with a one-way ANOVA followed by post hoc Tukey test. (d), (e) Luciferase reporter analysis of miRNA-22 positive regulation of the transcription of *Mtf1* with co-transfection of the reporter plasmid and an miRNA-22 mimic (22-mics) (d) or miRNA-22 inhibitor (22-Ih) (e). $*p<0.05$, $**p<0.01$ versus the corresponding groups. n = 5. The *Mtf1* promoter bound by miRNA-22 was inserted into the luciferase promoter in the pGL6 vector. The constructed or empty pGL6 and *Mtf1* overexpression plasmid pcDNA3.1-*Mtf1* and miRNA-22 mimic or inhibitor were co-transfected into HEK293 cells and harvested 48 h after co-transfection. PBS (phosphate buffer saline) was used as the solvent control. Data were analyzed with a one-way ANOVA followed by post hoc Tukey test. (f) Intrathecal injection of miRNA-22 inhibitor weakened the increase in *Mtf1* mRNA in the spinal cord of CFA-injected mice. $**p<0.01$ versus the corresponding groups. n = 5. Tissues were collected on day 2 after injection. Data were analyzed with a two-way ANOVA followed by post hoc Tukey test. (g) Blocking miRNA-22 with LV-22 inhibited the increase in *Mtf1* protein in the spinal cord of CFA-injected mice, as measured by western blotting. The vector (Vec) was used as a control for LV-22. $**p<0.01$ versus the corresponding groups. n = 5. Data were analyzed with a one-way ANOVA followed by post hoc Tukey test. (h) Overexpression of miRNA-22 with Lenti-22 increased the expression of *Mtf1* protein in the dorsal horn of naïve mice, as measured by western blotting. Vec was used as a control for Lenti-22. $**p<0.01$ versus Vec. n = 5. Data were analyzed with a one-way ANOVA followed by post hoc Tukey test.

the role of miRNA-22 in the regulation of *Mtf1* transcription, we designed *in vitro* and *in vivo* tests. First, *in vitro*, we inserted the *Mtf1* promoter containing the regions bound by miRNA-22 upstream of the luciferase gene in the pGL6 plasmid (pGL6-*Mtf1*). We then co-transfected this reporter construct and 22-mics (the miRNA-22 mimic) in HEK293 cells, which express miRNA-22 endogenously. Reporter activity showed an increase with the empty pGL6 vector (Figure 3(d)), indicating that endogenous miRNA-22 may have activated luciferase expression. miRNA-22 overexpression (22-mics) elevated reporter activity by 64.14% compared with the pGL6-*Mtf1* plus scrambled miRNA group (Figure 3(d)). By contrast, blocking miRNA-22 with its inhibitor (22-Ih) significantly reduced reporter activity relative to the scrambled control (Figure 3(e)). These *in vitro* data indicate that miRNA-22 promotes gene expression via binding to the *Mtf1* promoter.

Next, we examined whether miRNA-22 positively regulates *Mtf1* expression *in vivo*. Blocking miRNA-22 by intrathecal injection of 22-Ih markedly inhibited the increase in *Mtf1* mRNA (Figure 3(f)) in CFA-injected mice, but the scrambled control did not. Similar results were seen with LV-22 treatment compared with the vector control (Figure 3(g)). Lenti-22-mediated overexpression of miRNA-22 increased the expression level of *Mtf1* protein (Figure 3(h)). These findings support the hypothesis that miRNA-22 participates in the increased expression of spinal *Mtf1* in CFA-induced inflammatory pain.

3.5. miRNA-22 Modulates Inflammatory Pain via Mediation of Mtf1. Given that increased spinal miRNA-22 is responsible for *Mtf1* upregulation during inflammatory pain, we wondered whether miRNA-22 regulates pain hypersensitivity via its effects on *Mtf1*. To test this, we first injected

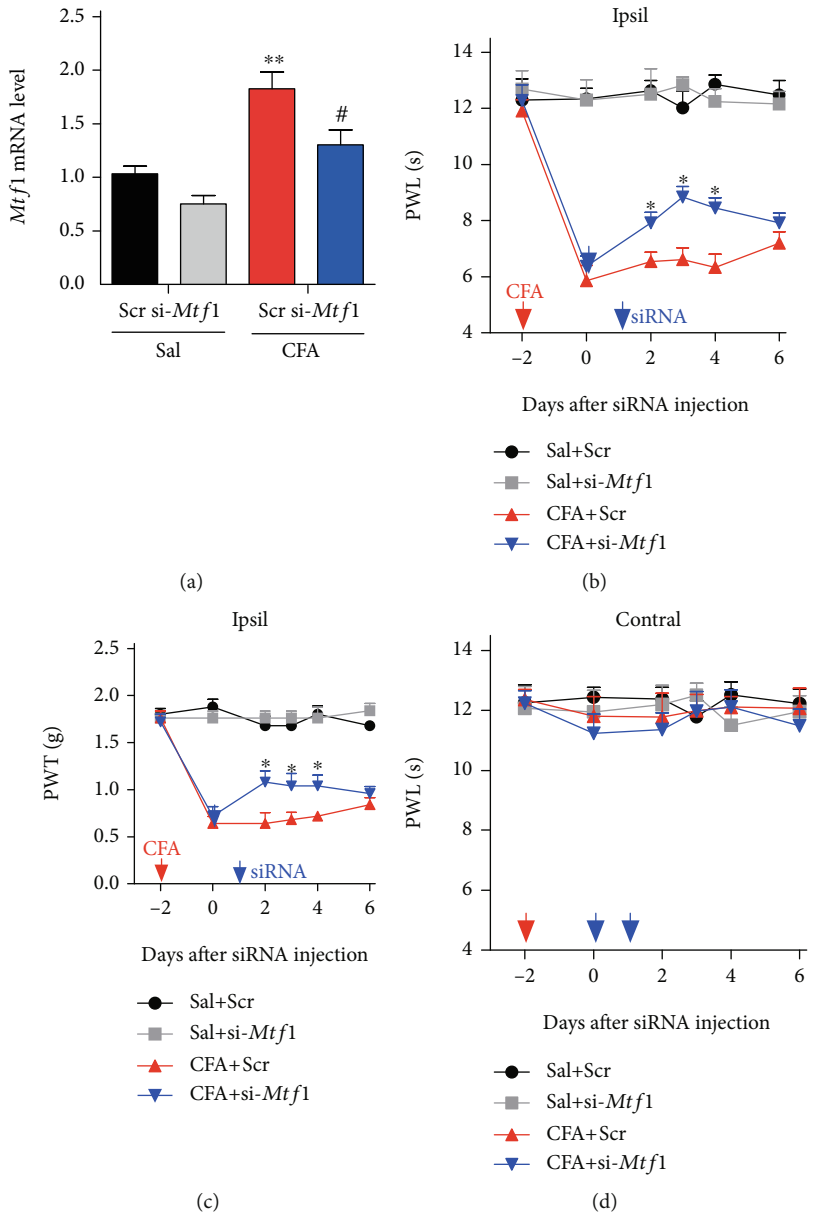

Figure 4: Continued.

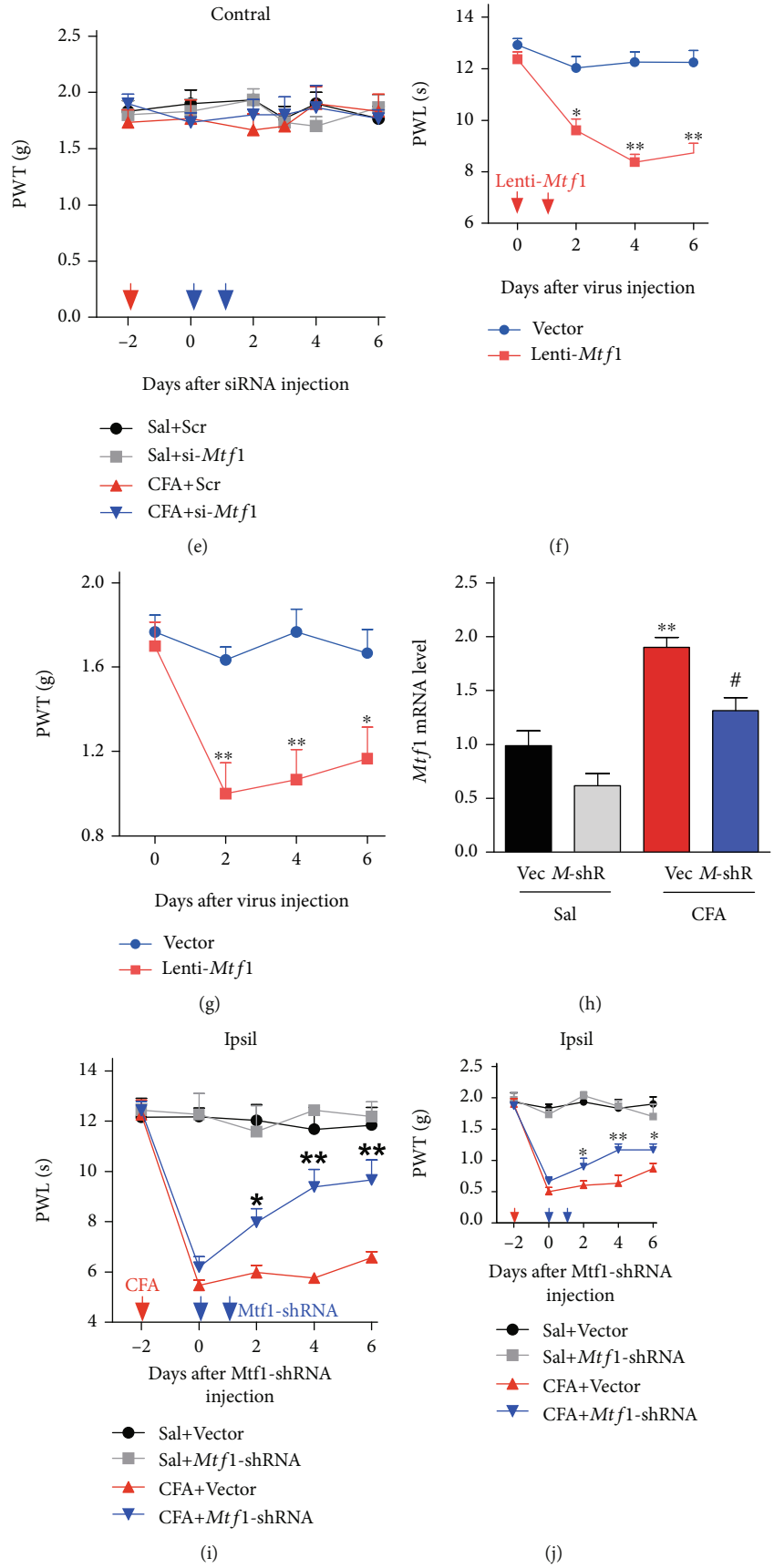

Figure 4: Continued.

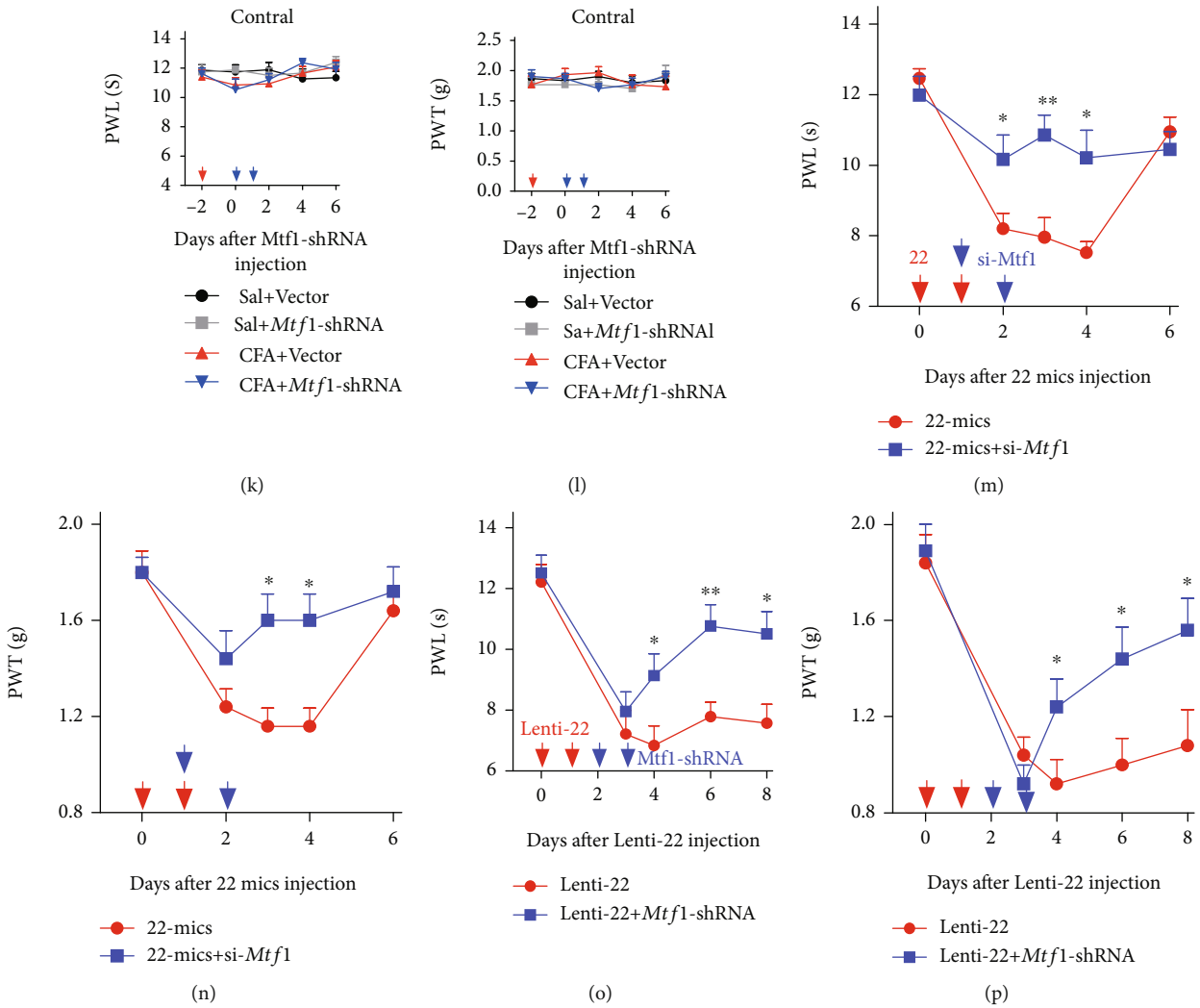

FIGURE 4: miRNA-22 mediates inflammatory pain behavior via the regulation of *Mtf1*. (a) Intrathecal injection of *Mtf1*-siRNA (si-*Mtf1*) for two consecutive days reversed the CFA-induced increase in *Mtf1* mRNA. $**p<0.01$ versus Sal+Scr. $^{\#}p<0.05$ versus CFA + Scr. n =6. Data were analyzed with a two-way ANOVA followed by post hoc Tukey test. (b)-(e) Intrathecal injection of si-*Mtf1* for two consecutive days reduced thermal hyperalgesia (b) and mechanical allodynia (c) on the ipsilateral paw of CFA-injected mice, but did not affect sensitivity to thermal (d) or mechanical (e) stimuli on the contralateral paw. $*p<0.05$ versus CFA + Scr. n =6. Red arrow, CFA or saline injection. Blue arrows, si-*Mtf1* or Scr injection. Data were analyzed with a two-way repeated-measures ANOVA followed by post hoc Tukey test. (f)-(g) *Mtf1* overexpression induced by intrathecal injection of Lenti-*Mtf1* for two consecutive days induced hypersensitivity to thermal (f) and mechanical (g) stimuli. $*p<0.05$, $**p<0.01$ versus Vector. n =6. Red arrows indicate Lenti-*Mtf1* or the control vector injection. Data were analyzed with a two-way repeated-measures ANOVA followed by post hoc Tukey test. (h) Intrathecal injection of Lenti-*Mtf1*-shRNA (*M*-shR) for two consecutive days inhibited the increase in *Mtf1* mRNA in CFA-injected mice. $**p<0.01$ versus Sal+Vec. $^{\#}p<0.05$ versus CFA + Vec. n =6. Data were analyzed with a two-way ANOVA followed by post hoc Tukey test. (i)-(l) Intrathecal injection of Lenti-*Mtf1*-shRNA (*Mtf1*-shRNA) for two consecutive days alleviated thermal hyperalgesia (i) and mechanical allodynia (j) induced by CFA injection in the ipsilateral paw, but sensitivity was unchanged in the contralateral paw (k)-(l). $*p<0.05$, $**p<0.01$ versus CFA + Vector. n =6. Red arrow, CFA or saline. Blue arrows, *Mtf1*-shRNA or Vector. Data were analyzed with a two-way repeated-measures ANOVA followed by post hoc Tukey test. (m)-(n) Intrathecal injection of si-*Mtf1* inhibited the pain hypersensitivity induced by miRNA-22 overexpression by its mimic (22-mics). $*p<0.05$, $**p<0.01$ versus 22-mics. n =6. Red arrow, 22-mics injection. Blue arrows, si-*Mtf1* injection. Data were analyzed with a two-way repeated-measures ANOVA followed by post hoc Tukey test. (o), (p) Intrathecal injection of *Mtf1*-shRNA attenuated the thermal hyperalgesia (o) and mechanical allodynia (p) induced by Lenti-22. $*p<0.05$, $**p<0.01$ versus Lenti-22. n =6. Red arrow, Lenti-22. Blue arrows, *Mtf1*-shRNA. Data were analyzed with a two-way repeated-measures ANOVA followed by post hoc Tukey test.

Mtf1-siRNA (si-*Mtf1*) intrathecally in the dorsal horn of CFA-injected mice to downregulate *Mtf1* expression. As expected, this manipulation (but not the scrambled siRNA control) led to a reduction in *Mtf1* expression 2 days after the intrathecal injection, and inhibited the increase in dorsal horn *Mtf1* mRNA in CFA-injected mice (Figure 4(a)). *Mtf1*-siRNA injection relieved CFA-induced pain hypersensitivity, as evidenced by a decrease in both heat hyperalgesia and

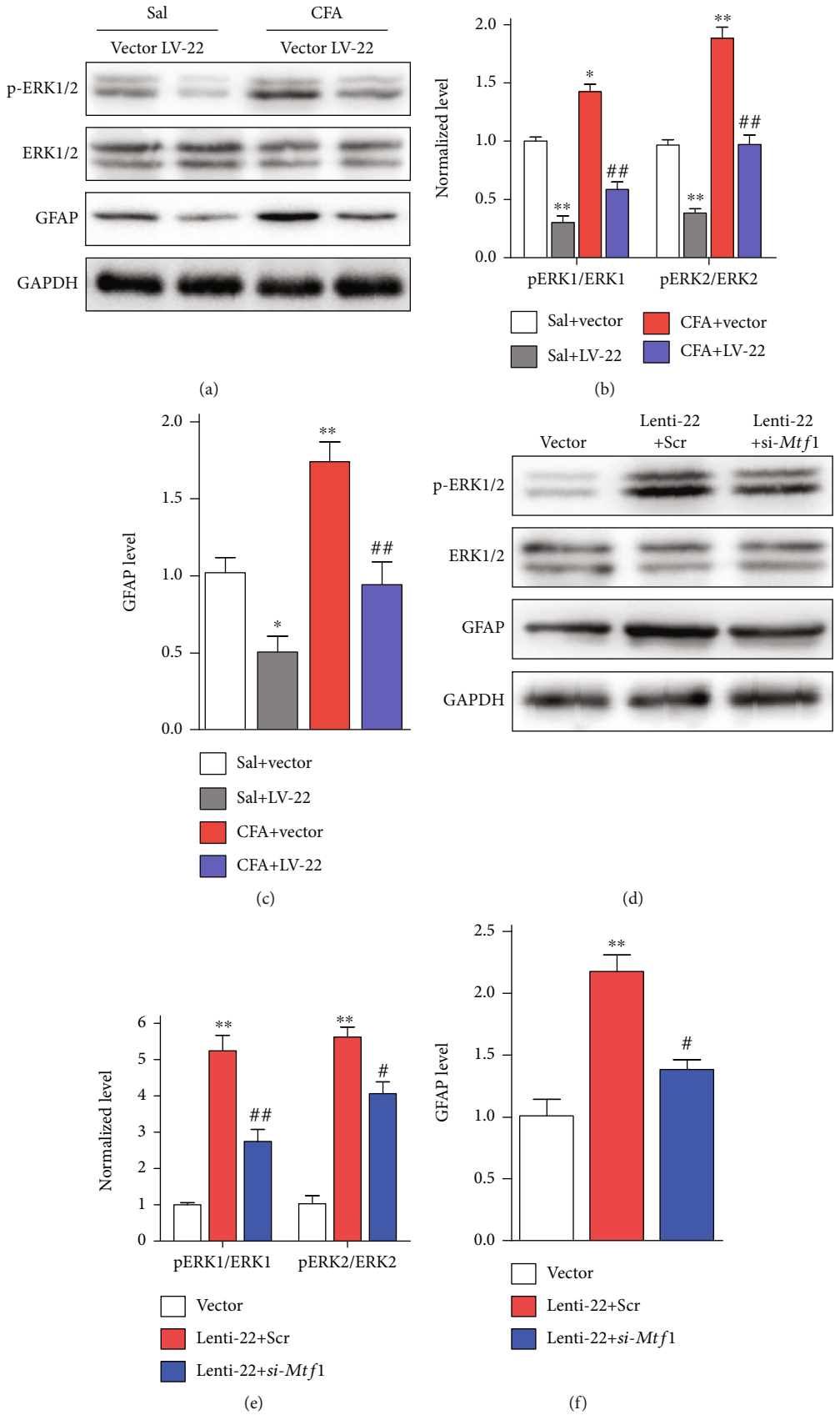

Figure 5: Continued.

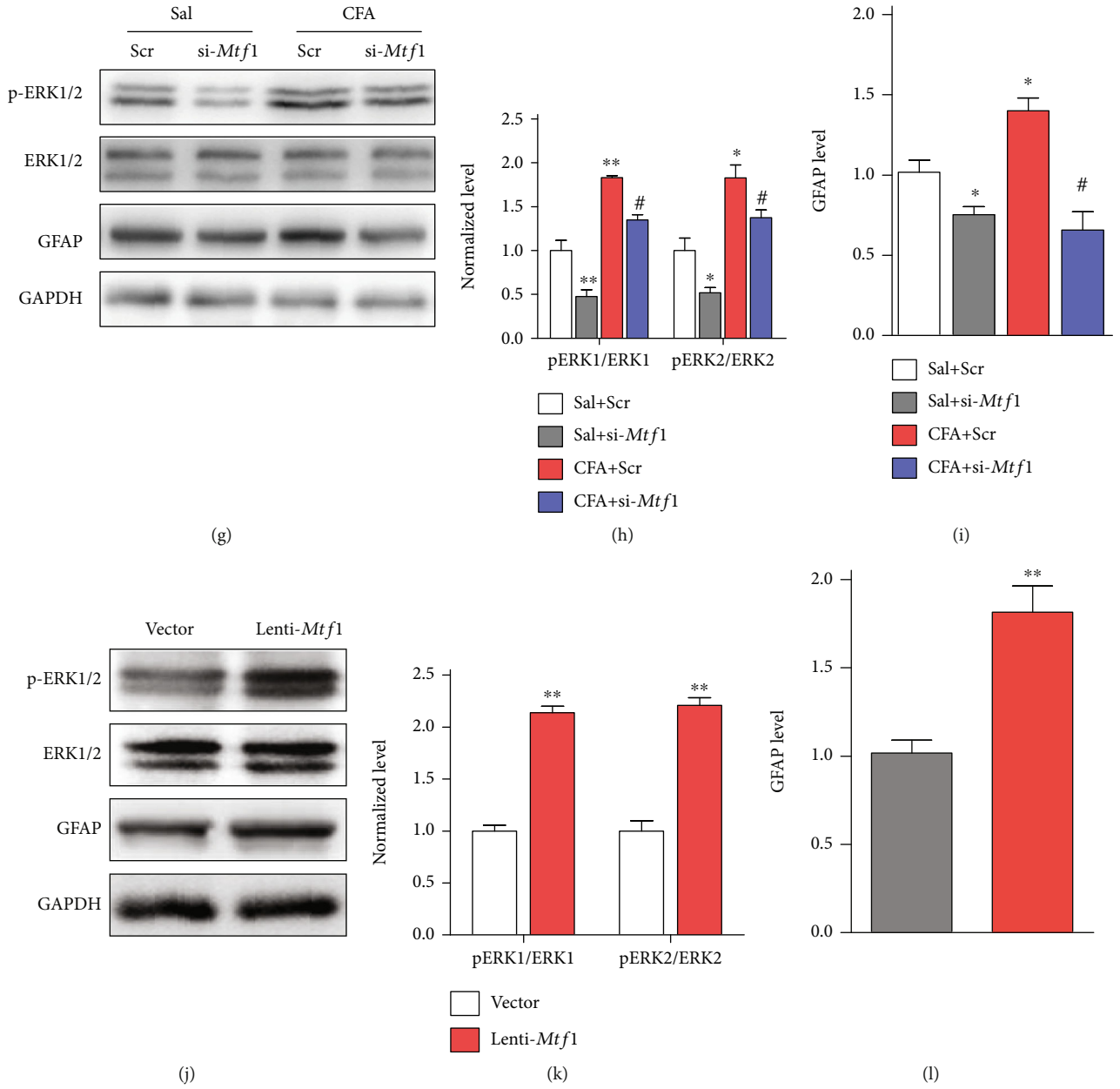

Figure 5: miRNA-22 activates ERK1/2 via regulation of *Mtf1*. (a)-(c) Knockdown of miRNA-22 with LV-22 reversed the CFA-induced increase in p-ERK1/2 (a, b) and GFAP protein (c) in the dorsal horn. $*p<0.05$, $**p<0.01$ versus Saline+Vector. n = 5. $^{\#\#}p<0.01$ versus CFA + Vector. n = 5. Data were analyzed with a two-way ANOVA followed by post hoc Tukey test. (d)-(f) miRNA-22 overexpression induced by Lenti-22 enhanced the protein levels of p-ERK1/2 (d, e) and GFAP (f) in naïve mice, and this increase was inhibited by *Mtf1* knockdown with si-*Mtf1*. Tissues were harvested on day 2 after si-*Mtf1* following intrathecal injection of Lenti-22. $**p<0.01$ versus Vector. $^{\#}p<0.05$, $^{\#\#}p<0.01$ versus Lenti-22 + Scr. n = 5. Data were analyzed with a one-way ANOVA followed by post hoc Tukey test. (g)-(i) siRNA-induced *Mtf1* knockdown weakened the CFA-induced increase in p-ERK1/2 (g, h) and GFAP (i) protein. $*p<0.05$, $**p<0.01$ versus Sal+Scr. n = 5. $^{\#}p<0.05$ versus CFA + Scr. n = 5. Data were analyzed with a two-way ANOVA followed by post hoc Tukey test. (j)-(l) Intrathecal injection of Lenti-*Mtf1* increased the expression of p-ERK1/2 (j, k) and GFAP (l) protein in naïve mice. $**p<0.01$ versus Vector. n = 5. Data were analyzed with a Student's t test.

mechanical allodynia from day 2 to day 4 after siRNA injection, but not the scrambled control (Figure 4(b), 4(c)). Neither *Mtf1*-siRNA nor the scrambled control had an effect on the contralateral side in CFA-injected mice (Figure 4(d), 4(e)), or on locomotor function (Table S1). Then, we examined whether *Mtf1* upregulation by Lenti-*Mtf1* increases pain thresholds in naïve mice. Intrathecal injection of Lenti-*Mtf1*, but not the vector control, produced pain hypersensitivity to mechanical and heat stimulation on day 2 after injection (Figure 4(f), 4(g)). Next, we injected Lentivirus-*Mtf1*-shRNA (*Mtf1*-shRNA) intrathecally to knockdown *Mtf1*. As expected, we observed a decrease in *Mtf1* mRNA on day 4 post injection of *Mtf1*-shRNA, but not the vector control, in saline-injected mice,

and the increase in *Mtf1* mRNA in CFA-injected mice was significantly inhibited by *Mtf1*-shRNA (Figure 4(h)). Additionally, when *Mtf1*-shRNA was injected for two consecutive days, it alleviated pain hypersensitivity (Figure 4(i), 4(j)). Neither *Mtf1*-shRNA nor the vector control had an effect on the contralateral side in CFA-injected mice (Figure 4(k), 4(l)), or on locomotor functions (Table S1).

Next, we tested whether blocking the *Mtf1* increase could ameliorate the pain hypersensitivity caused by miRNA-22 overexpression in naïve mice. Consistent with the above observations, marked pain hypersensitivity was induced by intrathecal injection of an miRNA-22 mimic on two consecutive days; these pain-like behaviors were rescued on day 1 after intrathecal injection of *Mtf1*-siNRA, but not its control, and the analgesic effect lasted for 3 days (Figure 4(m), 4(n)). Similarly, intrathecal injection of Lenti-22 over two consecutive days to upregulate dorsal horn miRNA-22 in naïve mice (Figure 2(n)) produced heat hyperalgesia and mechanical allodynia, and these pain hypersensitivities were inhibited by *Mtf1* knockdown with *Mtf1*-shRNA (injections on two consecutive days); this analgesic effect persisted for 8 days (Figure 4(o), 4(p)). Moreover, these treatments did not influence the normal locomotor activity of the mice (Table S1). Collectively, these results suggest that an increase in miRNA-22 leads to thermal hyperalgesia and mechanical allodynia via its effects on *Mtf1*.

3.6. miRNA-22 Regulates Central Sensitization in the Spinal Cord by Targeting Mtf1. We also tested whether increased miRNA-22 in the dorsal horn is associated with central sensitization under inflammatory pain conditions. Changes in the levels of phosphorylated extracellular signal-regulated kinase 1/2 (p-ERK1/2, a marker of neuronal activation) and glial fibrillary acidic protein (GFAP, a marker of astrocyte activation) were evaluated in the ipsilateral dorsal horn of mice subjected to manipulation by our miRNA-22 or *Mtf1* tools. We found that the levels of p-ERK1/2 and GFAP were significantly increased in the ipsilateral dorsal horn on day 3 after CFA injection and that these increases were reversed by LV-22 injections once daily for 2 days starting on day 3 after CFA injection. However, unlike p-ERK1/2, the level of total ERK1/2 did not vary among the treated groups (Figure 5(a)–5(c)). By contrast, miRNA-22 overexpression with Lenti-22, but not the control vector, augmented the levels of p-ERK1/2 and GFAP in the dorsal horn on day 4 after intrathecal injection once daily for 2 days (Figure 5(d)–5(f), Vector and Lenti-22 group), indicating that miRNA-22 positively regulates spinal sensitization. As *Mtf1* is positively involved in pain behavior, we further examined whether *Mtf1* could regulate the levels of spinal p-ERK1/2 and GFAP. *Mtf1* knockdown with siRNA, but not the scrambled control, inhibited the CFA-induced increases in p-ERK1/2 and GFAP (Figure 5(g)–5(i)) and upregulation of *Mtf1* increased the levels of p-ERK1/2 and GFAP in naïve mice (Figure 5(j)–5(l)). Furthermore, to determine whether *Mtf1* mediates the changes in sensitization produced by miRNA-22, we injected Lenti-22 intrathecally prior to the intrathecal injection of *Mtf1* siRNA. As anticipated, *Mtf1* siRNA, but not scrambled siRNA, blocked the increases in p-ERK1/2 and GFAP caused by Lenti-22. Consistent with the results above, there were no detectable changes in the level of total ERK1/2 protein with miRNA-22 overexpression (Figure 5(d)–5(f), Lenti-22 and Lenti-22 plus si-*Mtf1* groups).

Central sensitization is characterized by an increase in the activity of excitatory neurons during the pathogenesis of chronic pain. Therefore, we measured the level of c-Fos (a widely used marker of neuronal activity) in the dorsal horn. Immunohistochemical staining showed that downregulation of miRNA-22 by an inhibitor (22-Ih; Figure 6(a), 6(b)) or lentivirus (LV-22; Figure 6(c), 6(d)) reduced the CFA-induced increase in c-Fos expression in the dorsal horn, compared with the scrambled and vector controls. Upregulation of miRNA-22 by a mimic (22-mics; Figure 6(e), 6(f)) or Lenti-22 (Figure 6(g), 6(h)) led to a significant elevation of c-Fos expression in naïve mice. Together, these findings support the behavioral observations described above—miRNA-22 contributes to spinal sensitization through its effects on *Mtf1*.

4. Discussion

Chronic inflammatory pain is a complex, multi-dimensional disease. The pathogenesis of chronic inflammatory pain involves peripheral and/or central sensitization and activation of glial cells: these changes are attributed to aberrant neurotransmitter release and activity in intracellular signaling pathways at various levels in the nervous system, including the DRG, spinal cord, and brain [23–27]. The dorsal horn of the spinal cord links the peripheral nervous system to the central nervous system and is thus is a critical component in the transmission of nociception information; as such, it is a key target in the development of analgesic therapeutics and diagnostic strategies for pain. Recent reports have established a strong connection between epigenetic modifications and pain-related gene dysfunction in spinal cord neurons [3, 5, 11, 16, 28]. In this study, we provide the first evidence, to our knowledge, that peripheral inflammation leads to an increase in miRNA-22 expression in neuronal nuclei in the dorsal horn of the spinal cord. This increase is positively correlated with enhanced recruitment of RNA polymerase II to the *Mtf1* promoter and elevation of *Mtf1* mRNA and protein in spinal cord, resulting in inflammatory pain symptoms. Blocking this increase reverses the increase in RNA polymerase II recruitment, destabilizes the inflammation-induced upregulation of *Mtf1* in the spinal cord, and alleviates inflammation-associated pain hypersensitivities. Thus, our work demonstrates that miRNA-22 likely contributes to the mechanisms underlying inflammatory pain through its enhancement of *Mtf1* expression.

miRNAs are noncoding RNA species and have been well-studied in terms of their biogenesis and functions. Experiments with a variety of different pain models have linked miRNAs to multiple components at different stages within the nociceptive pathways, including ion channels [3, 29], membrane receptors [30, 31], transcription factors

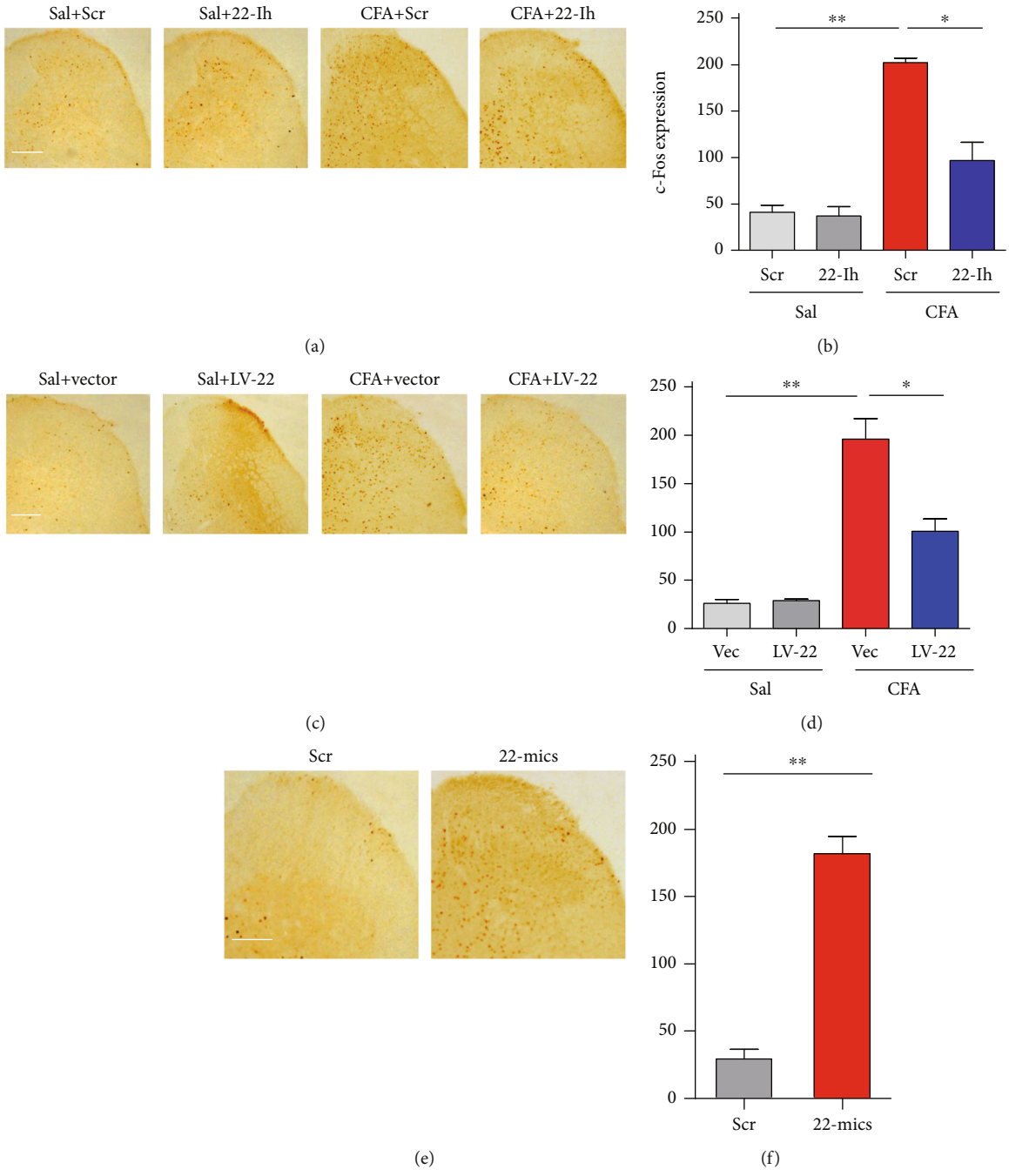

Figure 6: Continued.

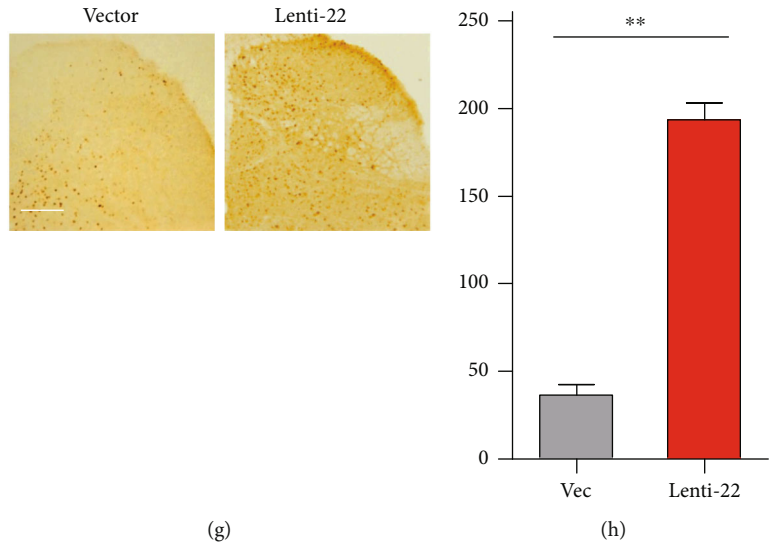

Figure 6: Spinal c-Fos is activated by the increase in miRNA-22 during inflammatory pain. (a)-(b) Blocking miRNA-22 with its inhibitor (22-Ih) reduced the CFA-induced increase in c-Fos expression in the ipsilateral dorsal horn. $*p < 0.05$, $**p < 0.01$ versus the corresponding groups. n = 5. Data were analyzed with a two-way ANOVA followed by post hoc Tukey test. (c)-(d) Inhibiting miRNA-22 by LV-22 reduced the CFA-induced increase in c-Fos expression in the ipsilateral dorsal horn. $*p < 0.05$, $**p < 0.01$ versus the corresponding groups. n = 5. Data were analyzed with a two-way ANOVA followed by post hoc Tukey test. (e)-(h) Overexpression of miRNA-22 by its mimic (22-mics, (e)-(f)) or Lenti-22 ((g)-(h)) augmented the level of c-Fos expression in the dorsal horn of naïve mice. $**p < 0.01$ versus the corresponding groups. n = 5. Scale bar, 50 μm. Data were analyzed with a Student's t test.

[32], translation factors [33], and other intracellular signals [34], in primary afferent nociceptors, DRGs, spinal cord, and brain areas. Nuclear miRNAs are known to have important functions in mRNA splicing and transcription [35, 36]. Our recent study uncovered the rich distribution of miRNA-1224 in the nuclei of spinal neurons and showed that mature circRNA-Filip1l expression is negatively regulated by miRNA-1224 via binding and splicing of the precursor to circRNA-Filip1l (pre-circRNA-Filip1l) in the spinal cord of mice with inflammatory pain. Moreover, we found that Ago2 is involved in the regulation of physiological and pathological nociception via miRNA-1224-dependent cleavage of circRNA-Filip1l [5]. However, the study of pain-related nuclear miRNAs is still in its infancy and there is currently limited molecular and functional data to support the potential regulatory role of nuclear miRNA in chronic pain. Our current work describes a novel mechanism by which miRNA-22 positively regulates *Mtf1* expression by promoting the transcription of *Mtf1* in the nucleus of spinal cord neurons.

miRNA-22 is highly conserved from fruit flies to humans and is broadly expressed in various tissues, including nervous system tissue [37]. Furthermore, miRNA-22 is associated with diabesity, glioma and hepatocellular carcinoma [13, 14, 38], dyslipidemia [39], muscle lipid metabolism [40], cardiac hypertrophy [41], rheumatoid arthritis [42], and HIV infection [43]. Recent findings show that hippocampal miRNA-22 is involved in epileptogenic focus formation [44], striatal and cortical miRNA-22 are involved in Huntington's disease [37], and peripheral blood miRNA-22 is decreased in Alzheimer's patients [12]. Although cytoplasmic miRNA-22 is closely linked to these various diseases, until now, little attention has been paid to: [1] the functional role of miRNA-22 in pain and [2] the neuronal nucleus as a locus of mechanism for miRNA-22 in the regulation of pain. In this work, we provide the first evidence that miRNA-22 is enriched in the nuclei of mouse spinal neurons. Furthermore, we revealed a novel role for miRNA-22 in the inflammatory pain process through its positive regulation of *Mtf1* in an RNA polymerase II-dependent manner. Since nuclear miRNA was first identified in HeLa cells, the existence of nuclear miRNAs has been confirmed and hundreds of nucleus-enriched miRNAs have been identified in a variety of cells [45]. Interestingly, the nuclear: cytoplasmic ratio varies across different cell lines [46]. In the present study, we found that miRNA-22 displayed the nuclear enrihment in the dorsal horn of the spinal cord, and was upregulated in the dorsal horn in mice with inflammatory or neuropathic pain, indicating that nuclear miRNA-22 in spinal neurons is closely associated with both pain models. Blocking spinal miRNA-22 markedly attenuated inflammation-induced pain behavior, and mimicking the increase in miRNA-22 induced pain hypersensitivity. However, mouse locomotor behavior was not affected by these manipulations. Our data support the hypothesis that spinal miRNA-22 contributes to the development and maintenance of inflammatory pain, but is not involved in motor function. We observed only a slight increase in miRNA-22 in the ipsilateral DRG on day 3 after CFA injection and thus excluded the possibility that DRG miRNA-22 regulates inflammatory pain. However, nociceptive information is transmitted from small DRG neurons to superficial dorsal horn neurons. Therefore, future studies should investigate whether and how miRNA-22 is involved in the transmission of nocicieptive signals between neurons

in the DRG and the dorsal horn. It also remains to be seen whether miRNA-22 is enriched in the nuclei of DRG cells. In addition, the mechanism that transports miRNA-22 between the cytoplasm and the nucleus remains elusive.

In a non-classic pathway, miRNA enhances transcription through its interactions with gene promoters to recruit transcription factors or RNA polymerase [47, 48]. Because miRNA-22 is enriched in the nucleus, we speculate that miRNA-22, similarly to protein transcription factors, may regulate gene transcription through binding to the gene promoter (after unraveling of double DNA to single DNA) to enhance recruitment of RNA polymerase. Additionally, *Mtf1* was increased in the spinal cord of mice with inflammatory pain, and knockdown of spinal miRNA-22 blocked the increase in *Mtf1* mRNA and protein expression. Therefore, we wondered whether miRNA-22 regulates *Mtf1* via binding to the *Mtf1* promoter. We analyzed the possible binding sites of miRNA-22 in *Mtf1* promoter regions and found 12 binding sites spanning 1157 bp from -516 ~ +640 bp region in *Mtf1* promoter. Our data show that miRNA-22 binding to the *Mtf1* promoter in the nuclei of spinal neurons was augmented in CFA-injected mice in an RNA polymerase II-dependent manner; further *in vitro* reporter and *in vivo* Western-blot assays demonstrated that blocking miRNA-22 reduced reporter activity in HEK293 cells and *Mtf1* protein levels in ipsilateral spinal cord of CFA-injected mice. Conversely, upregulating miRNA-22 increased reporter activity and *Mtf1* protein levels in naïve mice. These results suggest that nuclear miRNA-22 positively regulates *Mtf1* expression in an RNA polymerase II-dependent manner. Our findings provide the first evidence that miRNA contributes in a positive manner to gene transcription in the dorsal horn under pain conditions. Interestingly, miRNA-30 can repress gene transcription by inhibiting binding of the transcription factor TFEB to the gene promoter [49]. Whether miRNA-22 also recruits transcription factors to increase *Mtf1* expression during inflammatory pain remains to be investigated.

Mtf1, a Zn^{2+}-dependent transcription factor, is highly conserved in mammals, including human, mouse, and rat. It contains six zinc-finger motifs, three transactivation domains, and one cysteine-rich cluster, and this pseudotetrahedral geometry facilitates the binding with Zn^{2+} [50]. Recent limited evidence confirms the involvement of *Mtf1* in nervous system diseases, including pain. Although *Mtf1* is not required for neural differentiation after neural grafting in mice [51], it is involved in regulatory functions in various nervous tissues, such as the cortex, hippocampus, and motor neurons, via stabilizing Zn^{2+} metabolism [52] [53]. The concentration of Zn^{2+} markedly affects the threshold for visceral pain [54], suggesting that *Mtf1* may be associated with visceral nociception. In particular, deletion of *Mtf1* upregulates KLF4 expression in the ERK1/2 and AKT pathways [55], and Zn^{2+} is closely linked to activation of Cav3.2 T-channels, which shapes excitability in spinal neurons, as evidenced by the phosphorylation of ERK in the spinal cord [54]. Therefore, *Mtf1* likely regulates inflammatory pain by modulating sensitization within the spinal cord. This may explain why we detected p-ERK1/2 activity in mice with inflammatory pain. Central sensitization is caused by increased activity in excitatory spinal neurons (and/or decreased activity in inhibitory spinal neurons) and enhanced astrocytic activity. Therefore, in this study, we examined whether miRNA-22 is involved in regulating the expression of p-ERK1/2 and GFAP, which represent neuronal and astrocytic activity, respectively [56, 57]. Our results show that ERK1/2 was activated in CFA-injected mice and that inhibiting *Mtf1* abolished this activity, indicating that miRNA-22 regulates ERK1/2 activity via effects on *Mtf1*. However, it remains unclear whether miRNA-22 regulates GFAP directly or indirectly, and how *Mtf1* regulates ERK1/2 activity through intracellular Zn^{2+}–Cav3.2 interactions. These underlying mechanisms need to be examined in future studies. Moreover, central sensitization can be characterized as an increase in the excitability of dorsal horn excitatory neurons or a decrease in the excitability of dorsal horn inhibitory neurons. The specific subtypes of dorsal horn neurons that participate in the antinociception mediated by knockdown of miRNA-22 remain to be determined.

Taken together, our results demonstrate that analgesic effects are achieved by inhibiting the expression of miRNA-22 in the dorsal horn of spinal cord, and that miRNA-22 regulates *Mtf1* to, in turn, influence the ERK1/2 signaling pathway. Our results provide insights into the mechanisms underlying inflammatory pain. miRNA-22 appears to be a novel mediator of inflammatory pain in the dorsal horn and may be a promising potential therapeutic target for inflammatory pain.

Data Availability

All data supporting the findings of this study can be available from the corresponding authors upon reasonable request.

Conflicts of Interest

The authors declare that there are no conflicts of interest regarding the publication of this paper.

Authors' Contributions

These authors contributed equally: L-Y H. and M. Z.. Z. P. and J-L C. designed the research; L-Y H., M. Z., H-M Z., T. J., Y. T., H-J X., X-D L., Q-Q L., K-H Y. and R-N W., performed the research; L-Y H., M. Z., H-M Z., X-D L., T. J., H-J X., Z-Y X., and W. S. analyzed the data; Z. P. and L-Y H. wrote the paper.

Acknowledgments

The study was supported by grants from the National Natural Science Foundation of China (81701107 to L-Y Hao, 82171234, 81971041 to Z. Pan, 31771161, 81720108013 to J.-L. Cao, 81901132 to Z-Y, Xue); Jiang Su-Specially Appointed Professor Project, Natural Science Foundation of Jiangsu Province (BK20201460); Social Development Projects of Jiangsu Nature Science Foundation (BE2015626).

Supplementary Materials

Supplementary 1. The descriptions of supplementary Table 1. The locomotor functions including grasping, placing and righting reflex were measured on the corresponding days after the intrathecal injection of manipulation tools. Data are mean (SEM). n =5/group; five trials. No significance; one-way ANOVA (response time vs treated groups) followed by post hoc Tukey test.

Supplementary 2. Supplementary Figure 1a-1b: miRNA-22 overexpression by intrathecal injection of Lenti-22 for 2 consecutive days increased the sensitivity to thermal (a) and mechanical (b) stimuli in week 5 after injection. n =6. ∗ $p < 0.05$, versus Vec. Data were analyzed with a using Student's t test.

References

[1] S. Imai, D. Ikegami, A. Yamashita et al., "Epigenetic transcriptional activation of monocyte chemotactic protein 3 contributes to long-lasting neuropathic pain," *Brain: A Journal of Neurology*, vol. 136, no. 3, pp. 828–843, 2013.

[2] R. R. Ji, A. Chamessian, and Y. Q. Zhang, "Pain regulation by non-neuronal cells and inflammation," *Science*, vol. 354, no. 6312, pp. 572–577, 2016.

[3] Z. Pan, M. Zhang, T. Ma et al., "Hydroxymethylation of microRNA-365-3p regulates nociceptive behaviors via Kcnh2," *The Journal of Neuroscience: The Official Journal of the Society for Neuroscience*, vol. 36, no. 9, pp. 2769–2781, 2016.

[4] B. C. Jiang, L. N. He, X. B. Wu et al., "Promoted interaction of C/EBPα with DemethylatedCxcr3Gene promoter contributes to neuropathic pain in mice," *The Journal of Neuroscience: The Official Journal of the Society for Neuroscience*, vol. 37, no. 3, pp. 685–700, 2017.

[5] Z. Pan, G. F. Li, M. L. Sun et al., "MicroRNA-1224 splicing CircularRNA-Filip1l in an Ago2-dependent manner regulates chronic inflammatory pain via targeting Ubr5," *The Journal of Neuroscience: The Official Journal of the Society for Neuroscience*, vol. 39, no. 11, pp. 2125–2143, 2019.

[6] J. Zhao, M. C. Lee, A. Momin et al., "Small RNAs control sodium channel expression, nociceptor excitability, and pain thresholds," *The Journal of Neuroscience: The Official Journal of the Society for Neuroscience*, vol. 30, no. 32, pp. 10860–10871, 2010.

[7] A. Favereaux, O. Thoumine, R. Bouali-Benazzouz et al., "Bidirectional Integrative Regulation Of Cav1.2 Calcium Channel By Microrna Mir-103: Role In Pain," *The EMBO Journal*, vol. 30, no. 18, pp. 3830–3841, 2011.

[8] S. Imai, M. Saeki, M. Yanase et al., "Change in microRNAs associated with neuronal adaptive responses in the nucleus accumbens under neuropathic pain," *The Journal of Neuroscience: The Official Journal of the Society for Neuroscience*, vol. 31, no. 43, pp. 15294–15299, 2011.

[9] E. M. Small and E. N. Olson, "Pervasive roles of microRNAs in cardiovascular biology," *Nature*, vol. 469, no. 7330, pp. 336–342, 2011.

[10] K. Oura, A. Morishita, and T. Masaki, "Molecular and functional roles of MicroRNAs in the progression of hepatocellular carcinoma-a review," *International Journal of Molecular Sciences*, vol. 21, no. 21, p. 8362, 2020.

[11] Z. Pan, L. J. Zhu, Y. Q. Li et al., "Epigenetic modification of spinal miR-219 expression regulates chronic inflammation pain by targeting CaMKII," *The Journal of Neuroscience: The Official Journal of the Society for Neuroscience*, vol. 34, no. 29, pp. 9476–9483, 2014.

[12] C. Han, L. Guo, Y. Yang et al., "Mechanism of microRNA-22 in regulating neuroinflammation in Alzheimer's disease," *Brain and behavior*, vol. 10, no. 6, article e01627, 2020.

[13] Y. Zhang, L. Tu, X. Zhou, and B. Li, "MicroRNA-22 regulates the proliferation, drug sensitivity and metastasis of human glioma cells by targeting SNAIL1. Journal of B.U.ON. : Official journal of the Balkan union of," *Oncology*, vol. 25, pp. 491–496, 2020.

[14] Z. Zeng, J. Dong, Y. Li et al., "The expression level and diagnostic value of microRNA-22 in HCC patients," *Artificial cells, nanomedicine, and biotechnology*, vol. 48, no. 1, pp. 683–686, 2020.

[15] A. A. Larson, D. R. Brown, S. el-Atrash, and M. M. Walser, "Pain threshold changes in adjuvant-induced inflammation: a possible model of chronic pain in the mouse," *Pharmacology, Biochemistry, and Behavior*, vol. 24, no. 1, pp. 49–53, 1986.

[16] Z. Q. Pan, Z. Y. Xue, G. F. Li et al., "DNA Hydroxymethylation by ten-eleven translocation Methylcytosine dioxygenase 1 and 3 regulates nociceptive sensitization in a chronic inflammatory pain model," *Anesthesiology*, vol. 127, no. 1, pp. 147–163, 2017.

[17] K. J. Livak and T. D. Schmittgen, "Analysis of Relative Gene Expression Data Using Real-Time Quantitative PCR and the $2^{-\Delta\Delta C_T}$ Method," *Methods*, vol. 25, no. 4, pp. 402–408, 2001.

[18] X. Su, H. Wang, W. Ge et al., "An in vivo method to identify microRNA targets not predicted by computation algorithms: p21 targeting by miR-92a in cancer," *Cancer Research*, vol. 75, no. 14, pp. 2875–2885, 2015.

[19] N. Sun, J. R. Hao, X. Y. Li et al., "GluR6-FasL-Trx2 mediates denitrosylation and activation of procaspase-3 in cerebral ischemia/reperfusion in rats," *Cell Death & Disease*, vol. 4, no. 8, 2013.

[20] S. Hugel and R. Schlichter, "Presynaptic P2X receptors facilitate inhibitory GABAergic transmission between cultured rat spinal cord dorsal horn neurons," *The Journal of Neuroscience: The Official Journal of the Society for Neuroscience*, vol. 20, no. 6, pp. 2121–2130, 2000.

[21] J. X. Yang, L. Hua, Y. Q. Li et al., "Caveolin-1 in the anterior cingulate cortex modulates chronic neuropathic pain via regulation of NMDA receptor 2B subunit," *The Journal of Neuroscience: The Official Journal of the Society for Neuroscience*, vol. 35, no. 1, pp. 36–52, 2015.

[22] C. Catalanotto, C. Cogoni, and G. Zardo, "MicroRNA in control of gene expression: an overview of nuclear functions," *International Journal of Molecular Sciences*, vol. 17, no. 10, p. 1712, 2016.

[23] S. G. Wu, B. Marie Lutz, X. Miao et al., "Dorsal root ganglion transcriptome analysis following peripheral nerve injury in mice," *Molecular Pain*, vol. 12, article 174480691662904, 2016.

[24] V. Fernandes, D. Sharma, S. Vaidya, Y. Guan, K. Kalia, and V. Tiwari, "Cellular and molecular mechanisms driving neuropathic pain: recent advancements and challenges," *Expert Opinion on Therapeutic Targets*, vol. 22, no. 2, pp. 131–142, 2018.

[25] R. E. Andersen and D. A. Lim, "Forging our understanding of lncRNAs in the brain," *Cell and Tissue Research*, vol. 371, no. 1, pp. 55–71, 2018.

[26] E. S. J. Smith, "Advances in understanding nociception and neuropathic pain," *Journal of Neurology*, vol. 265, no. 2, pp. 231–238, 2018.

[27] S. M. Tang, J. Zhou, H. Jing et al., "Functional roles of lncRNAs and its potential mechanisms in neuropathic pain," *Clinical Epigenetics*, vol. 11, no. 1, p. 78, 2019.

[28] Z. Pan, Q. Zhang, X. Liu et al., "Methyltransferase-like 3 contributes to inflammatory pain by targeting TET1 in YTHDF2-dependent manner," *Pain*, vol. 162, no. 7, pp. 1960–1976, 2021.

[29] C. Peng, L. Li, M. D. Zhang et al., "miR-183 cluster scales mechanical pain sensitivity by regulating basal and neuropathic pain genes," *Science*, vol. 356, no. 6343, pp. 1168–1171, 2017.

[30] C. K. Park, Z. Z. Xu, T. Berta et al., "Extracellular microRNAs activate nociceptor neurons to elicit pain via TLR7 and TRPA1," *Neuron*, vol. 82, no. 1, pp. 47–54, 2014.

[31] P. Jiangpan, M. Qingsheng, Y. Zhiwen, and Z. Tao, "Emerging role of microRNA in neuropathic pain," *Current Drug Metabolism*, vol. 17, no. 4, pp. 336–344, 2016.

[32] H. L. D. M. Willemen, X. J. Huo, Q. L. Mao-Ying, J. Zijlstra, C. J. Heijnen, and A. Kavelaars, "MicroRNA-124 as a novel treatment for persistent hyperalgesia," *Journal of Neuroinflammation*, vol. 9, no. 1, 2012.

[33] Y. Sun, X. Q. Li, P. Sahbaie et al., "miR-203 regulates nociceptive sensitization after incision by controlling phospholipase A2 activating protein expression," *Anesthesiology*, vol. 117, no. 3, pp. 626–638, 2012.

[34] Y. Zhou, M. Lu, R. H. du et al., "MicroRNA-7 targets nod-like receptor protein 3 inflammasome to modulate neuroinflammation in the pathogenesis of Parkinson's disease," *Molecular Neurodegeneration*, vol. 11, no. 1, p. 28, 2016.

[35] J. Y. Liao, L. M. Ma, Y. H. Guo et al., "Deep sequencing of human nuclear and cytoplasmic small RNAs reveals an unexpectedly complex subcellular distribution of miRNAs and tRNA 3' trailers," *PLoS One*, vol. 5, no. 5, article e10563, 2010.

[36] T. B. Hansen, E. D. Wiklund, J. B. Bramsen et al., "miRNA-dependent gene silencing involving Ago2-mediated cleavage of a circular antisense RNA," *The EMBO Journal*, vol. 30, no. 21, pp. 4414–4422, 2011.

[37] A. Jovicic, J. F. Zaldivar Jolissaint, R. Moser, M. . F. Silva Santos, and R. Luthi-Carter, "MicroRNA-22 (miR-22) overexpression is neuroprotective via general anti-apoptotic effects and may also target specific Huntington's disease-related mechanisms," *PLoS One*, vol. 8, no. 1, article e54222, 2013.

[38] M. Thibonnier and C. Esau, "Metabolic benefits of MicroRNA-22 inhibition," *Nucleic Acid Therapeutics*, vol. 30, no. 2, pp. 104–116, 2020.

[39] G. P. Diniz, Z. P. Huang, J. Liu et al., "Loss of microRNA-22 prevents high-fat diet induced dyslipidemia and increases energy expenditure without affecting cardiac hypertrophy," *Clinical Science*, vol. 131, no. 24, pp. 2885–2900, 2017.

[40] J. Schweisgut, C. Schutt, S. Wüst et al., "Sex-specific, reciprocal regulation ofERα and miR-22 controls muscle lipid metabolism in male mice," *The EMBO Journal*, vol. 36, no. 9, pp. 1199–1214, 2017.

[41] Y. Tu, L. Wan, L. Bu et al., "MicroRNA-22 downregulation by atorvastatin in a mouse model of cardiac hypertrophy: a new mechanism for antihypertrophic intervention," *Cellular Physiology and Biochemistry: International Journal of Experimental Cellular Physiology, Biochemistry, and Pharmacology*, vol. 31, no. 6, pp. 997–1008, 2013.

[42] J. Lin, R. Huo, L. Xiao et al., "A novel p53/microRNA-22/Cyr61 axis in synovial cells regulates inflammation in rheumatoid arthritis," *Arthritis & rheumatology*, vol. 66, no. 1, pp. 49–59, 2014.

[43] E. Anadol, R. Schierwagen, N. Elfimova et al., "Circulating microRNAs as a marker for liver injury in human immunodeficiency virus patients," *Hepatology*, vol. 61, no. 1, pp. 46–55, 2015.

[44] E. M. Jimenez-Mateos, M. Arribas-Blazquez, A. Sanz-Rodriguez et al., "microRNA targeting of the P2X7 purinoceptor opposes a contralateral epileptogenic focus in the hippocampus," *Scientific Reports*, vol. 5, no. 1, 2015.

[45] G. Meister, M. Landthaler, A. Patkaniowska, Y. Dorsett, G. Teng, and T. Tuschl, "Human Argonaute2 mediates RNA cleavage targeted by miRNAs and siRNAs," *Molecular Cell*, vol. 15, no. 2, pp. 185–197, 2004.

[46] Y. L. Weng, X. Wang, R. An et al., "Epitranscriptomic m^6A Regulation of Axon Regeneration in the Adult Mammalian Nervous System," *Neuron*, vol. 97, no. 2, pp. 313–325.e6, 2018.

[47] S. S. Ajay, B. D. Athey, and I. Lee, "Unified translation repression mechanism for microRNAs and upstream AUGs," *BMC Genomics*, vol. 11, no. 1, 2010.

[48] L. C. Li, "Chromatin remodeling by the small RNA machinery in mammalian cells," *Epigenetics*, vol. 9, no. 1, pp. 45–52, 2014.

[49] H. Guo, M. Pu, Y. Tai et al., "Nuclear miR-30b-5p suppresses TFEB-mediated lysosomal biogenesis and autophagy," *Cell Death and Differentiation*, vol. 28, no. 1, pp. 320–336, 2021.

[50] V. Gunther, A. M. Davis, O. Georgiev, and W. Schaffner, "A conserved cysteine cluster, essential for transcriptional activity, mediates homodimerization of human metal-responsive transcription factor-1 (MTF-1)," *Biochimica et Biophysica Acta*, vol. 1823, no. 2, pp. 476–483, 2012.

[51] P. Lichtlen, O. Georgiev, W. Schaffner, A. Aguzzi, and S. Brandner, "The heavy metal-responsive transcription factor-1 (MTF-1) is not required for neural differentiation," *Biological Chemistry*, vol. 380, no. 6, pp. 711–715, 1999.

[52] L. A. Lichten, M. S. Ryu, L. Guo, J. Embury, and R. J. Cousins, "MTF-1-mediated repression of the zinc transporter Zip10 is alleviated by zinc restriction," *PLoS One*, vol. 6, no. 6, article e21526, 2011.

[53] S. Bahadorani, S. Mukai, D. Egli, and A. J. Hilliker, "Overexpression of metal-responsive transcription factor (MTF-1) in _Drosophila melanogaster_ ameliorates life-span reductions associated with oxidative stress and metal toxicity," *Neurobiology of Aging*, vol. 31, no. 7, pp. 1215–1226, 2010.

[54] M. Matsunami, S. Kirishi, T. Okui, and A. Kawabata, "Chelating luminal zinc mimics hydrogen sulfide-evoked colonic pain in mice: possible involvement of T-type calcium channels," *Neuroscience*, vol. 181, pp. 257–264, 2011.

[55] L. Ji, G. Zhao, P. Zhang et al., "Knockout of MTF1 inhibits the epithelial to mesenchymal transition in ovarian cancer cells," *Journal of Cancer*, vol. 9, no. 24, pp. 4578–4585, 2018.

[56] Y. J. Gao and R. R. Ji, "C-Fos and pERK, which is a better marker for neuronal activation and central sensitization after noxious stimulation and tissue injury?," *The open pain journal*, vol. 2, no. 1, pp. 11–17, 2009.

[57] Y. J. Gao and R. R. Ji, "Chemokines, neuronal-glial interactions, and central processing of neuropathic pain," *Pharmacology & Therapeutics*, vol. 126, no. 1, pp. 56–68, 2010.

Hindawi
Oxidative Medicine and Cellular Longevity
Volume 2022, Article ID 9927602, 11 pages
https://doi.org/10.1155/2022/9927602

Research Article

Changes of Functional, Morphological, and Inflammatory Reactions in Spontaneous Peripheral Nerve Reinnervation after Thermal Injury

Xing Yu,[1] Chang Liu,[2] Caihong Ji,[3] Cameron Lenahan,[4,5] Yuanjian Fang,[6] Yong Wang,[1] and Anwen Shao[6]

[1]*Department of Surgery, The Second Affiliated Hospital, Zhejiang University School of Medicine, Hangzhou, China*
[2]*College of Medicine, Zhejiang University, Hangzhou, China*
[3]*Department of Neurology, The First Affiliated Hospital, College of Medicine, Zhejiang University, Hangzhou, China*
[4]*Center for Neuroscience Research, Loma Linda University School of Medicine, Loma Linda, CA, USA*
[5]*Burrell College of Osteopathic Medicine, Las Cruces, NM, USA*
[6]*Department of Neurosurgery, The Second Affiliated Hospital, Zhejiang University School of Medicine, Hangzhou, China*

Correspondence should be addressed to Yong Wang; surgwy@zju.edu.cn and Anwen Shao; 21118116@zju.edu.cn

Received 18 March 2021; Revised 25 July 2021; Accepted 4 January 2022; Published 1 February 2022

Academic Editor: Xiaoyuan Zhou

In recent decades, the use of energy-based devices has substantially increased the incidence of iatrogenic thermal injury to nerves (cauterization, etc.). While recovery of the nerve after thermal injury is important, the changes in neural structure, function, and peripheral inflammatory reactions postinjury remain unclear. This study is aimed at demonstrating the changes mentioned above during the acute, subacute, and chronic stages of nerve reinnervation after thermal injury. Spontaneous reinnervation was evaluated, including the neural structures, nerve conduction abilities, and muscle regeneration. These effects vary depending on the severity of thermal injury (slight, moderate, and severe). Peripheral inflammatory reactions, as impediments to reinnervation, were found in significant numbers 3 days after thermal injury, exhibiting high expression of IL-1β and TNF-α, but low expression of IL-10. Our findings reveal the pathogenesis of peripheral nerve reinnervation after thermal injury, which will assist in selecting appropriate treatments in further research.

1. Introduction

Energy-based devices (EBDs) have been widely adopted for hemostasis in recent decades due to the easy application and effective reduction in blood loss [1, 2]. However, the use of EBDs is also controversial due to the high temperature of the head and the lateral thermal spread during activation. The incidence of iatrogenic thermal injury has reportedly increased, and the heat has gradually become a common cause of peripheral nerve injury [3].

Nerve thermal injury, as a less reversible type, was associated with obvious histologic damage [4–6]. It has been revealed that the peripheral nerves manifest as a reversible conduction block when exposed to lower-grade thermal injury but manifest with axonal degeneration at higher temperatures [7]. What is more, there is a decrease in the manifestation of electromyographic (EMG) changes in amplitude with a concomitant increase in latency during acute thermal nerve damage [8]. However, it is unclear whether peripheral nerves could develop spontaneous reinnervation after thermal injury. It is also unclear how the functional recovery differs when considering the severity or the time of recovery after thermal injury.

It has been demonstrated that nerve reinnervation is evaluated by assessing not only the reconstruction of the neural and muscular complex but also the improvement of conductive function [9]. EMG and the number of neuromuscular junctions (NMJ) in the skeletal muscles are critical indices in evaluating the recovery of nerve conduction abilities [10, 11]. Furthermore, the role of peripheral

inflammation and cytokine release was found and is reportedly active during nerve regeneration [12, 13].

This study aimed at elucidating the nerve's morphological and functional changes, as well as the peripheral inflammatory reactions that occur during spontaneous reinnervation following thermal injury in a rat model. We hypothesize that the consequence of reinnervation differs from the severity of thermal injury, presents in a time-dependent manner, and may be regulated by peripheral inflammatory reactions.

2. Methods

2.1. Surgical Procedures. The study involved 48 Sprague-Dawley (SD) male rats weighing 200-220 g. As described in the previous study, all rats were anesthetized with intraperitoneal injection of pentobarbital (40–80 mg/kg, 10 times dilution by physiological saline) and maintained on spontaneous ventilation [14]. As described in the previous study, each sciatic nerve was exposed via separation of the biceps femoris and the tensor fascia latae [9]. The right sciatic nerve was exposed to slight, moderate, and severe thermal injury, while a sham operation was performed on the right limb without any thermal injury as the control. The harmonic scalpel (HS; Ethicon Endo-Surgery, Inc.), as one of the EBDs, was activated for 10 seconds at power setting of 5. The head of the HS touched the nerve directly as the severe injury group, whereas the distances between the nerve and HS were controlled 1 and 3 mm in the moderate and slight injury groups, respectively. An infrared camera was used to improve the validity of the experimental model, quantifying the temperature based on infrared images so as to classify the thermal injury delivery as slight, moderate, and severe. Two surgeons performed the operation. While one of them used millimeter paper to verify that the distances between nerve and HS were consistent with the expectation, another surgeon manipulated the dissection part.

2.2. Schematic Diagram of Experimental Design. The functional, morphological, and peripheral inflammatory changes were recorded at the acute (3 hours and 1 day), subacute (3 and 7 days), and chronic (15 and 30 days) stages after thermal injury. Functional changes of the nerve were evaluated via EMG, including signal amplitude, latency, and nerve conduction velocity (NCV). The transversely morphological changes, including the structures of the sciatic nerve and gastrocnemius muscle, were recorded by using a light scope of hematoxylin and eosin (H&E) staining, immunofluorescent (IF) staining, and transmission electron microscopy (TEM). The changes in serum cytokine levels (TNF-α, IL-1β, and IL-10) were analyzed via the enzyme-linked immunosorbent assay (ELISA) to assess the peripheral inflammatory reactions of the nerve. Animals were sacrificed via intracardiac injection of potassium chloride solution at 3 days (representing subacute evidence) and 30 days (chronic evidence) after thermal injury (Figure 1).

2.3. Experimental Group Division. The rats were divided randomly into four groups according to the severity of the thermal injury. The severity was dependent on the parallel distance from the nerves to HS. For instance, in the severe injury group, the head of the HS touched the nerve directly (the distance is 0 mm), whereas the distances between the nerve and HS were 1 and 3 mm in the moderate and slight injury groups, respectively. Sham operation was designed as nerve exposure, but without thermal injury as the control group. The results of the EMG changes (detected immediately and retested at 3 hours after thermal injury) were recorded to verify the severity of nerve thermal injury (the control, slight, moderate, and severe groups) (Figure 2). These procedures were reviewed and approved by the Institutional Review Board (Ethics Committee, the Second Affiliated Hospital of Zhejiang University, School of Medicine) (approval number 2019-393).

2.4. EMG Analysis. As described previously in the protocol, the sciatic nerves were exposed in the anesthetized animal for electrophysiological testing [15]. The stimulating cathode, composed of a stainless-steel monopolar needle, was placed at the sciatic nerve trunk, and the parallel distance was 10 mm between the two cathodes. The motor response was recorded continuously and distally using a unipolar steel needle electrode inserted into the gastrocnemius muscle. Additionally, NCV, amplitude, and latency were recorded using a digital neurophysiological system (Neuro-MEP-Micro, Neurosoft Ltd., 5, Voronin Str., Ivanovo, 153032, Russia). The time for the electrical impulse to travel from the stimulation to the recording site was measured as the latency. Amplitude was calculated as the areas from baseline to the maximal negative peak. NCV was obtained by dividing the distance of 10 mm by the difference in the latency time.

2.5. Transmission Electron Microscopy (TEM). TEM was conducted to record structural changes in the nerve, particularly the morphological characteristics of myelinated axons and myelinated sheaths. A portion of the nerve was removed, fixed in 2.5% glutaraldehyde overnight in the refrigerator, and then washed in phosphate-buffered saline (pH 7.2) for 3 times at 15 min each. Then, it was placed in 1% osmium tetroxide and washed 3 times for 1 h each. After, the samples were stained with 4% uranyl acetate for 30 min, dehydrated by a series concentration of ethanol, and then embedded in resin mixture (70, 80, 90, and 95% ethanol, 10 min each). This was sectioned and observed under a TECNAI-10 transmission electron microscope (Phillips) [16].

2.6. Immunofluorescent (IF) Staining. Tissue samples were sectioned (4 μm thickness, CM1850, LEICA, Germany), stained using IF markers, and observed under a fluorescence microscope (ECLIPSE 80i, Nikon, Japan). Nuclei were stained blue using 4,6-diamidino-2-phenylindole (DAPI, Biosynthesis Biotechnology, China). Primary antibodies against the neurofilament (GT114, mouse anti-rat, GeneTex, Texas, USA) were used to identify axons and NMJ in the nerves and gastrocnemius muscles, respectively. Goat anti-mouse (red, Thermo Fisher Scientific, USA) was used as the secondary antibody.

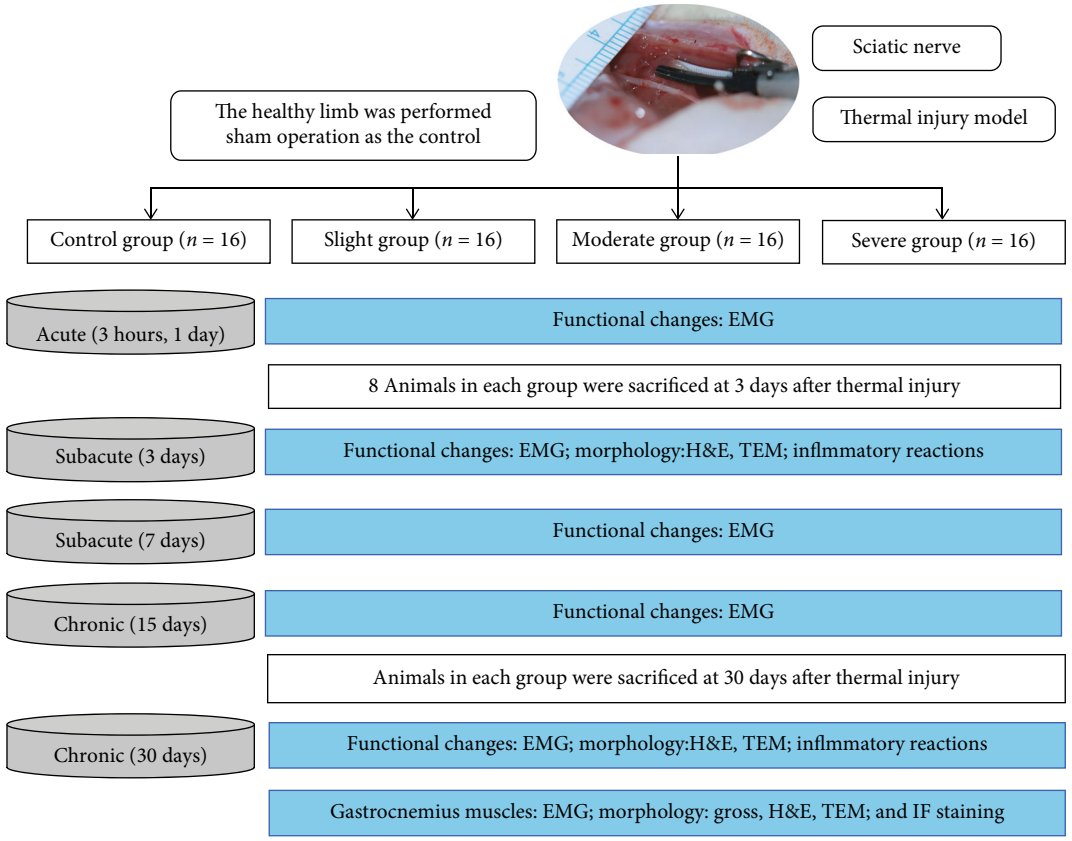

Figure 1: Schematic diagram of experimental design and animal group classification. EMG: electromyographic analysis; TEM: transmission electron microscopy; H&E: hematoxylin and eosin staining.

2.7. Enzyme-Linked Immunosorbent Assay (ELISA). Productions of TNF-α, IL-1β, and IL-10 were quantified using ELISA kits (Yili Biology, Shanghai, China) following the manufacturer's instructions. Briefly, a total of 5 mL of blood was collected from the exposed heart of the deeply anesthetized animals and incubated at room temperature for 30 min. The serum was obtained after centrifuging the whole blood at 2000 rpm at 4°C for 15 min and then analyzed using an ELISA kit. The concentrations of TNF-α, IL-1β, and IL-10 were measured through correlation with a standard curve. Blank disks were used as the control.

2.8. Statistical Analysis. Data were expressed as mean ± standard error, and statistical analysis was performed by Student's t-test, Kruskal-Wallis test, Fisher's precise test, and one-way analysis of variance (ANOVA) using the SPSS software (IBM SPSS Statistics, USA). Data were illustrated using the GraphPad Prism (GraphPad Software Inc., San Diego, CA, USA).

3. Results

3.1. Nerve Electrophysiological Changes after Thermal Injury. Nerve electrophysiological changes, such as NCV, amplitude, and latency, were recorded via EMG to evaluate the nerve conductive abilities. The nerve conductive abilities were destroyed, which was exhibited as the decrease in NCV and amplitude, as well as latency prolongation after thermal injury. The NCV and amplitude indices vary from 0 to 1, with 0 and 1 corresponding to complete dysfunction and normal function, respectively. The NCV index was measured in each time point (acute, subacute, and chronic) after thermal injury to assess spontaneous nerve reinnervation recovery. In the slight group, the NCV index was impaired immediately but began to recover 3 hours after thermal injury. However, the NCV index decreased immediately after thermal injury in the moderate group and continued to decline over the following 3 days. It should be noted that the NCV index began to increase from the 3rd to 30th day after thermal injury. In the severe group, the NCV index was also significantly decreased but could not recover until 30 days after thermal injury. As depicted in Figure 3, the NCV index was significantly decreased at 3 hours after thermal injury, exhibited as 0.85 ± 0.04, 0.23 ± 0.04, and 0.06 ± 0.07 in the slight, moderate, and severe groups, respectively. The NCV index was recorded at 30 days after thermal injury to evaluate the recovery of spontaneous nerve reinnervation, presenting as 0.97 ± 0.05, 0.45 ± 0.04, and 0.06 ± 0.08 in slight, moderate, and severe groups, respectively, with significant difference. There was no significant difference in the comparison of EMG changes within groups between 3 hours and 30 days after thermal injury.

3.2. Nerve Pathological Changes after Thermal Injury. Nerve pathological changes were recorded via light and electron microscopy at 3 days after slight, moderate, and severe

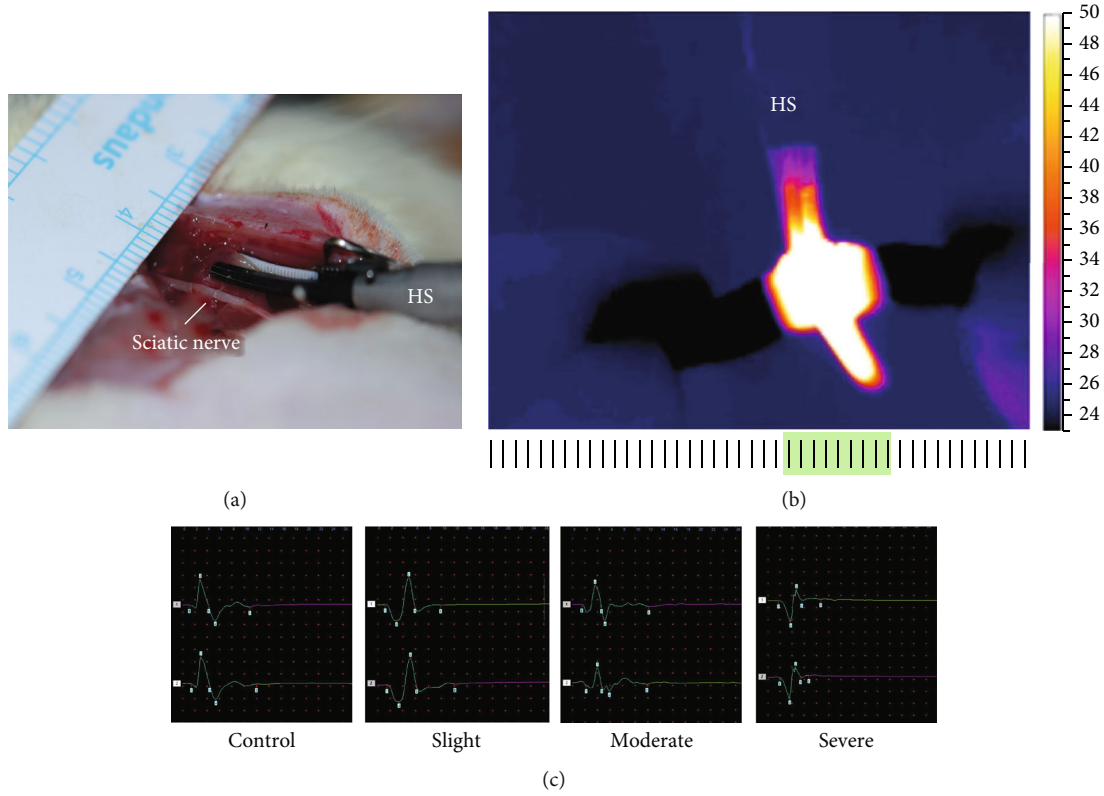

Figure 2: Establish the different degrees of severity of peripheral nerve thermal injury. (a) HS is activated parallel to the sciatic nerve to modify acute thermal injury. (b) Tissue heat map during HS activation based on infrared images with an infrared camera. (c) Features of EMG changes after thermal injury show that the amplitude decreased (order: severe > moderate > slight ≥ control) and the latency was prolonged (severe > moderate > slight ≥ control). Green band in (b) indicates the lateral thermal spread. HS: harmonic scalpel.

thermal injury (Figure 4). In subjective evaluation, there was no difference in neural appearance between the slight thermal injury group and the control group. Under light microscopy, the axons were frequently concentrically wrapped by the Schwann cells. TEM showed myelinated axons and a thick myelin sheath, in which numerous anchoring particles were observed maintaining the integrity of the myelin sheath. However, in the moderate thermal injury group, the neural appearance showed that myelin sheaths were loose and accompanied by lessened anchoring particles. The membrane of the myelin sheaths demonstrated effusion, which was considered a result of inflammatory reactions. The number of macrophages was increased, and they showed a tendency to be near the myelin sheath. In the severe thermal injury group, neural features of coagulation and homogenization, accompanied by peripheral inflammatory reactions, were observed by light microscopy. The TEM revealed that the number of intact axon fibers was significantly decreased in the same magnification. Multiple bubbles were detected in the myelin sheaths, and these bubbles destroyed the compact structure of the myelin sheath. The number of anchoring particles was significantly decreased in the same magnification, and the myelin sheath became loose and irregular. It can be speculated from the exhibitions above that these damaged structures impair the transport of neural signals (Table 1). The exhibitions of nerve pathological changes at 30 days were consistent with the results at 3 days after slight, moderate, and severe thermal injury.

3.3. Morphological Changes of the Gastrocnemius Muscle at 30 Days after Thermal Injury. The macro- and micromorphological changes of the gastrocnemius muscle are recognized as a vital index to evaluate nerve functional recovery. At 30 days after thermal injury, the gross, microscopic, and IF staining changes of the gastrocnemius muscles were recorded in each group (Figure 5). Gross observation revealed that the gastrocnemius muscles of injured limbs were atrophic in the moderate and severe groups. Additionally, the weight of gastrocnemius muscles were 2.35 ± 0.09 g, 1.69 ± 0.08 g, and 1.26 ± 0.05 g in the slight, moderate, and severe thermal injury groups, respectively, with significant differences found. Consistently, the H&E staining results indicated that the degree of atrophy in skeletal muscles in each group was ranked as follows: slight group < moderate group < severe group. Under the light microscope, skeletal muscle cells in the severe group presented with loss of the cytoplasm, and the myofibers were sparse and separated by large distances, with increased fibrosis and fatty infiltration.

The number of intact NMJ is used as a vital index to evaluate functional nerve recovery. As an essential constituent of NMJ, neurofilaments in the gastrocnemius muscle were evaluated via IF staining to estimate the number of

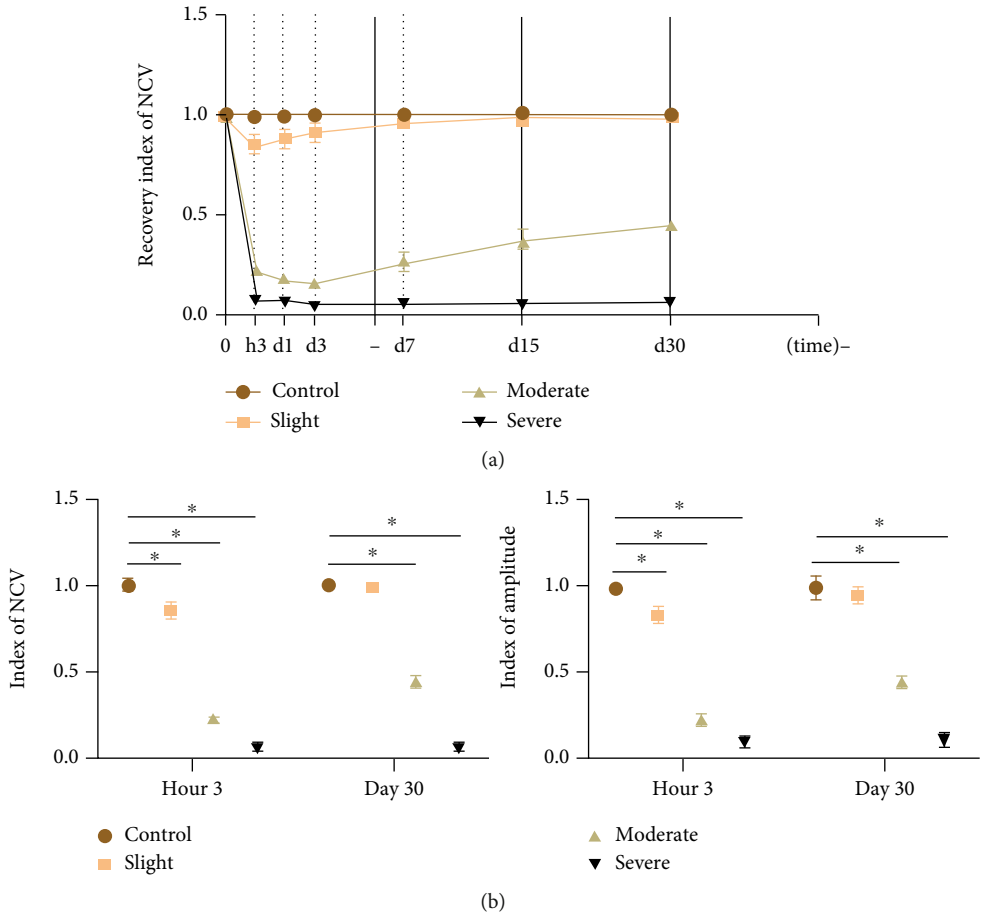

Figure 3: Nerve electrophysiological changes according to EMG analysis after slight, moderate, and severe thermal injury. (a) Recording the recovery of the NCV index in each time point (acute, subacute, and chronic) from 3 hours to 30 days after thermal injury. (b) Comparison of EMG changes in the three groups; indices of NCV and amplitude were decreased significantly after thermal injury, and the severity of injury was in the order of severe > moderate > slight ≥ control. NCV: nerve conduction velocity. ∗ represents $P < 0.05$.

NMJ. The number of neurofilaments varied and was ranked in the following order: slight group > moderate group > severe group, with significant differences. Quantitatively, there was no significant difference in the number of NMJ between the slight thermal injury group and the control. However, in the moderate thermal injury group, 58 ± 2% of NMJ was fluorescently present compared to the control group. Additionally, there was only 9 ± 8% NMJ present in the severe group compared to the control group.

3.4. Neural Fiber Changes at 30 Days after Thermal Injury. To evaluate the functional recovery of the sciatic nerve, the number of neural fibers was recorded by IF staining (anti-neurofilament) at 30 days after thermal injury (Figure 6). IF evidence revealed that the fluorescence intensity was significantly decreased afterwards in the moderate and severe thermal injury groups, while there was no significant change in the slight thermal injury group. Quantitatively, the moderate group displayed 61 ± 3% of the fluorescent intensity of the control group. And the severe group exhibited 11 ± 5% of the fluorescent intensity compared with the control group. A decrease in fluorescent intensity is assumed to correspond with the decrease in axon count, suggesting that the number of neural fibers was decreased significantly in the moderate and severe thermal injury groups (Table 2).

3.5. Peripheral Nerve Injury Environment after Thermal Injury. The peripheral nerve injury environment consists of axons, Schwann cells, macrophages, and components of the extracellular matrix (ECM), such as neurotrophic growth factors (secreted by Schwann cells) and inflammatory cytokines (secreted by macrophages) (Figure 7(a)). Neural inflammation was obtained by H&E staining after moderate and severe thermal injury, but there was no visible reaction in the slight group. The TEM results demonstrated that macrophages were activated and showed a tendency of Schwann cells to be activated, participating in inflammatory reactions in 3 days after thermal injury (Figure 7(b)). The number of Schwann cells and macrophages per area ($100\,\mu m^2$) was measured in the scope of TEM, and the results revealed that the number of macrophages was increased significantly, showing the tendency of Schwann cells to activate at 3 days after thermal injury in the moderate group. Moreover, as exhibited in Figure 7(c), the level of serum inflammatory cytokines (secreted by macrophages) varies in the three groups. Compared with the control group

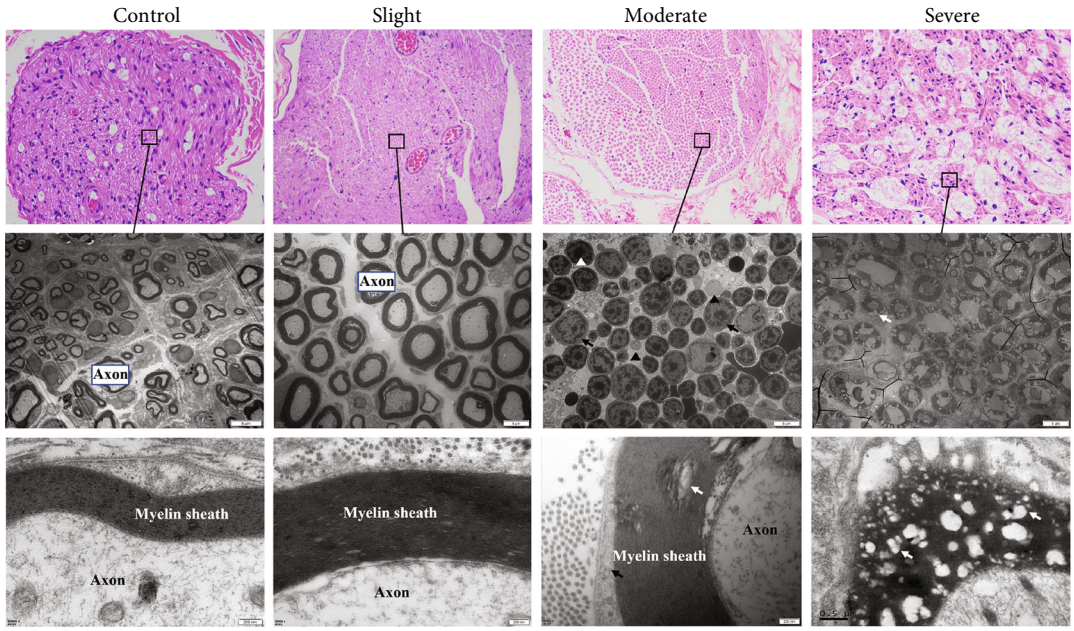

Figure 4: Nerve pathological changes assessed via light and electron microscopy after slight, moderate, and severe thermal injury. (a) Getting histologic results via light microscopy, the black box in the severe group indicates characteristics of coagulation and homogenization (H&E staining, 200x). (b, c) Comparison of the pathological changes of axons and myelin sheaths (TEM). White triangles indicate the hyperpigmentation of axonal fibers. Black arrows indicate the loose myelin sheaths with reduced anchoring particles. Black triangle indicates macrophages adjacent to the myelin sheath. White arrows indicate bubbles in myelin sheaths. TEM: transmission electron microscopy.

Table 1: Comparison of acute nerve changes after slight, moderate, and severe thermal injury (3 days).

	Slight ($n = 8$)	Moderate ($n = 8$)	Severe ($n = 8$)	P value
EMG				
NCV index	0.85 ± 0.04	0.23 ± 0.04	0.06 ± 0.07	<0.01
Amplitude decrease > 50%	0/8 (0.0%)	6/8 (75.0%)	8/8 (100%)	<0.01
Latency prolongation > 10%	0/8 (0.0%)	5/8 (62.5%)	8/8 (100%)	<0.01
Neural morphology changes				
Myelin sheath: crush	0/8 (0.0%)	6/8 (75.0%)	8/8 (100%)	<0.01
Myelin sheath: bubbles	0/8 (0.0%)	5/8 (62.5%)	8/8 (100%)	<0.01
Anchoring particles: lessen	0/8 (0.0%)	4/8 (50.0%)	8/8 (100%)	<0.01
Neural inflammation				
Myelin sheath effusion	0/8 (0.0%)	5/8 (62.5%)	8/8 (100%)	<0.01
Macrophage activation	0/8 (0.0%)	6/8 (75.0%)	8/8 (100%)	<0.01
Neural homogenization	0/8 (0.0%)	4/8 (50.0%)	8/8 (100%)	<0.01

(performed with a sham operation), levels of TNF-α and IL-1β were increased, while the levels of IL-10 were reduced in the moderate and severe groups at 3 days after thermal injury. However, there was no significant difference in the levels of TNF-α, IL-1β, and IL-10 in the four groups at 30 days after thermal injury.

4. Discussion

Spontaneous reinnervation of muscles after peripheral nerve injury has been reported in the previous studies [9, 14]. Most of these studies focused on the injury of transection, traction, and compression. However, the evidence of reinnervation after thermal injury and the underlying mechanisms are still unclear. The temperature threshold of the peripheral nerve is reportedly 58°C in rats. When the exposed temperature became higher than this threshold, the endoneurium would be destroyed, causing permanent functional damage [7]. In the present study, we found that the nerve conduction ability can be recovered spontaneously if the thermal injury degree is slight and moderate and that this process is likely regulated by inflammatory reactions, with IL-1β and TNF-α increasing and IL-10 decreasing in the peripheral nerve environment. Moreover, the severity of thermal injury

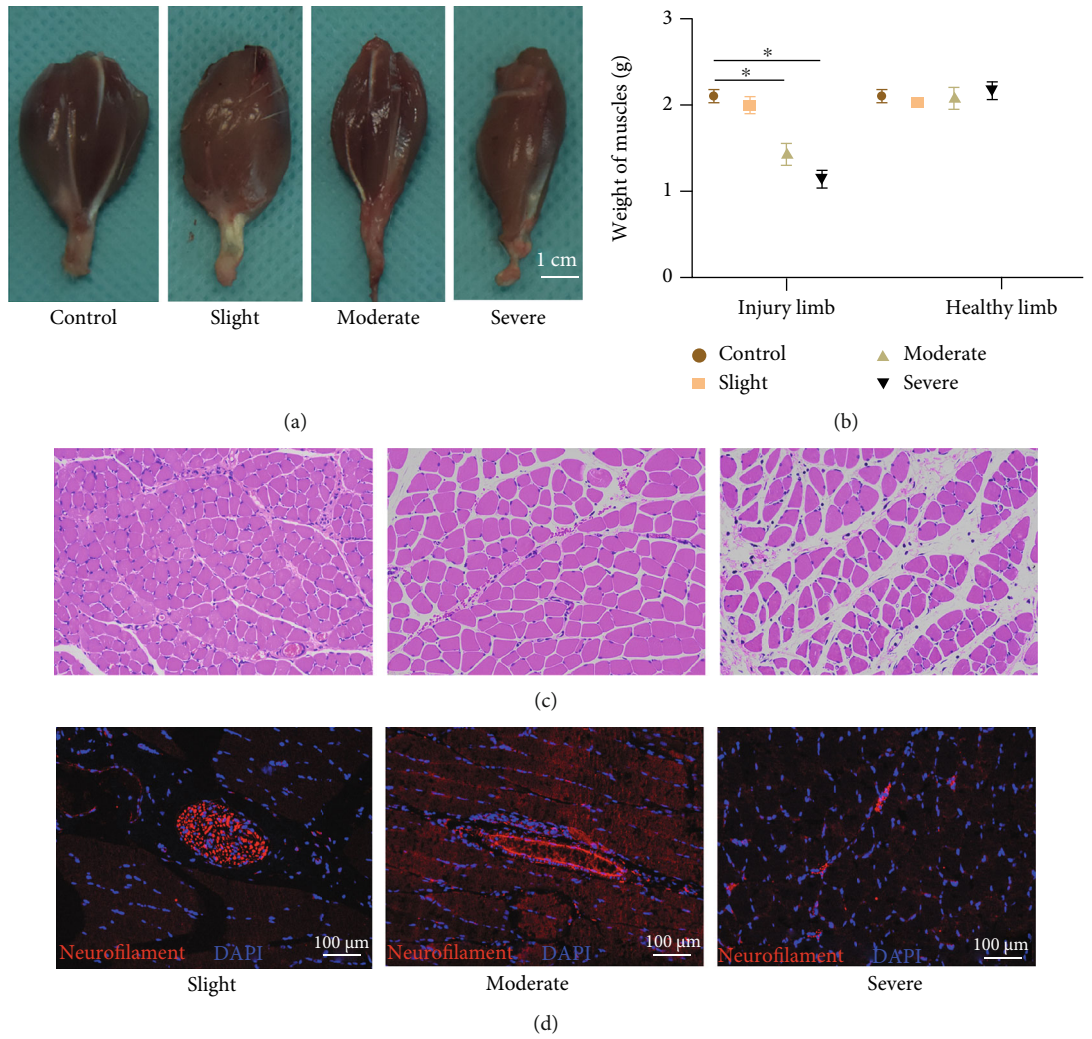

Figure 5: Macro- and micromorphological changes of gastrocnemius muscles at 30 days after thermal injury. (a) Gross observation of gastrocnemius muscles. (b) Comparison of the weight changes in the four groups; the order of weights of the injured limb are listed as follows: severe group < moderate group < slight group ≤ control group with significant difference. (c) Recording the morphology of muscle cells by microscopic observation (H&E staining, 100x). (d) Getting the number of NMJ in gastrocnemius muscles by IF staining (indexes: neurofilament and DAPI). Nuclei were stained blue using DAPI, and neural fibers stained red using antineurofilament. ∗ represents $P < 0.05$. NMJ: neuromuscular junctions; IF: immunofluorescent.

influenced the degree of recovery and determined whether the nerve reinnervated spontaneously. This finding is consistent with the previous study and may be relevant to the phenomenon of nerve thermal tolerance [16].

Acquiring the acute, subacute, and chronic evidence of functional and morphological changes after thermal injury is fundamental to elucidate the process of spontaneous reinnervation. During the acute stage of thermal injury, the conductive ability of the nerve is significantly impaired, but the degree of damage varies depending on the severity of thermal injury. During the subacute stage, the conductive ability is recovered in the slight group, but not in the moderate or severe group. Pathologic results also exhibit different consequences. In the slight group, the myelin sheaths are thick, and the neural axons are maintained as the concentric structure, whereas in the moderate group, the nerves maintained the complete structural integrity of the axons and myelin sheaths, but the damaged features were exhibited as loose myelin sheaths and reduced anchoring particles. In the severe group, the nerve exhibited features of coagulation and homogenization. Moreover, multiple bubbles were observed in the neural fibers and myelin sheaths, destroying the intact structures completely. In the chronic stage, nerve conduction experienced a gradual recovery period, and NCV returned to 45% compared to the normal at 30 days after thermal injury in the moderate group. Conversely, the conductive ability of the nerve could not be recovered in the severe group. These differences are also exhibited in morphological results. The neural fluorescent intensity in the moderate group was restored to 61% compared with the control, but only 11% had been detected in the severe group, which speculated that the number of neural fibers cannot restore if nerves are exposed to severe thermal injury.

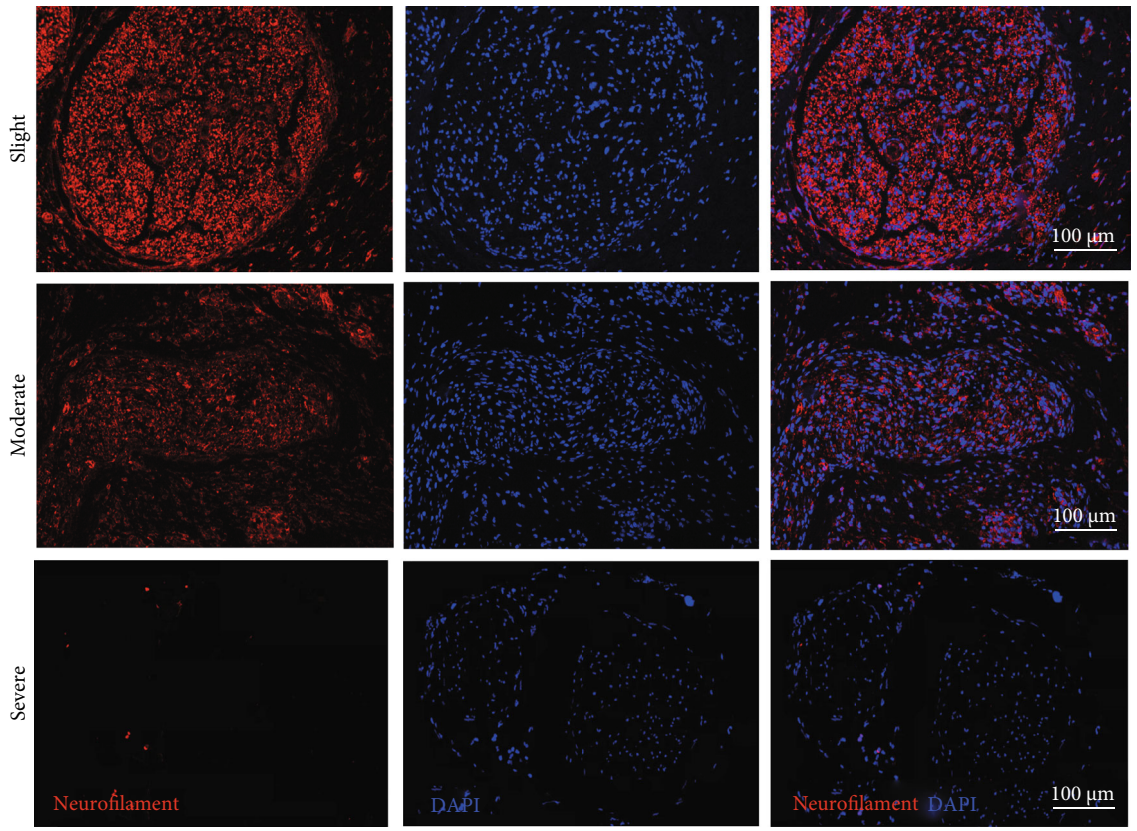

Figure 6: Number of neural fiber changes by IF staining (indexes: neurofilament and DAPI), at 30 days after slight, moderate, and severe thermal injury. Nuclei were stained blue using DAPI, and neural fibers stained red using antineurofilament. IF: immunofluorescent.

Table 2: Comparison of chronic changes after slight, moderate, and severe thermal injury (30 days).

	Slight ($n = 8$)	Moderate ($n = 8$)	Severe ($n = 8$)	P value
EMG				
NCV index	0.97 ± 0.05	0.45 ± 0.04	0.06 ± 0.08	<0.01
Amplitude decrease > 50%	0/8 (0.0%)	1/8 (12.5%)	8/8 (100%)	<0.01
Latency prolongation > 10%	0/8 (0.0%)	1/8 (12.5%)	8/8 (100%)	<0.01
Neural morphology changes				
Myelin sheath: crush	0/8 (0.0%)	1/8 (12.5%)	8/8 (100%)	<0.01
Myelin sheath: bubbles	0/8 (0.0%)	0/8 (0.0%)	0/8 (0.0%)	1.00
Anchoring particles: lessen	0/8 (0.0%)	1/8 (12.5%)	8/8 (100%)	<0.01
Inflammatory reactions	0/8 (0.0%)	0/8 (0.0%)	0/8 (0.0%)	1.00
Muscular morphology changes				
Gross weight	2.35 ± 0.09	1.69 ± 0.08	1.26 ± 0.05	<0.01
Muscular atrophy	0/8 (0.0%)	7/8 (87.5%)	8/8 (100%)	<0.01
NMJ index	0.98 ± 0.04	0.58 ± 0.02	0.09 ± 0.08	<0.01
Neural axons	0.98 ± 0.04	0.61 ± 0.03	0.11 ± 0.05	<0.01

The consequence of neural transient or permanent damage varies. Therefore, it is important to find critical indices for predicting the consequence of neural reinnervation. EMG results, including NCV and signal amplitude, reflect the conductive ability of the nerve [17]. In the present study, the EMG was detected during the entire process of reinnervation, and these results were closely associated with the structures of axons and myelin sheaths. Myelin sheaths, an essential component for signal transmission, have a structure that is also a critical index to predict reinnervation [18, 19]. Although the damaged features of loose myelin sheaths were detected in the moderate group, the nerves still kept the complete structures of axons and myelin sheaths, which predicted the capability of reinnervation. In the severe

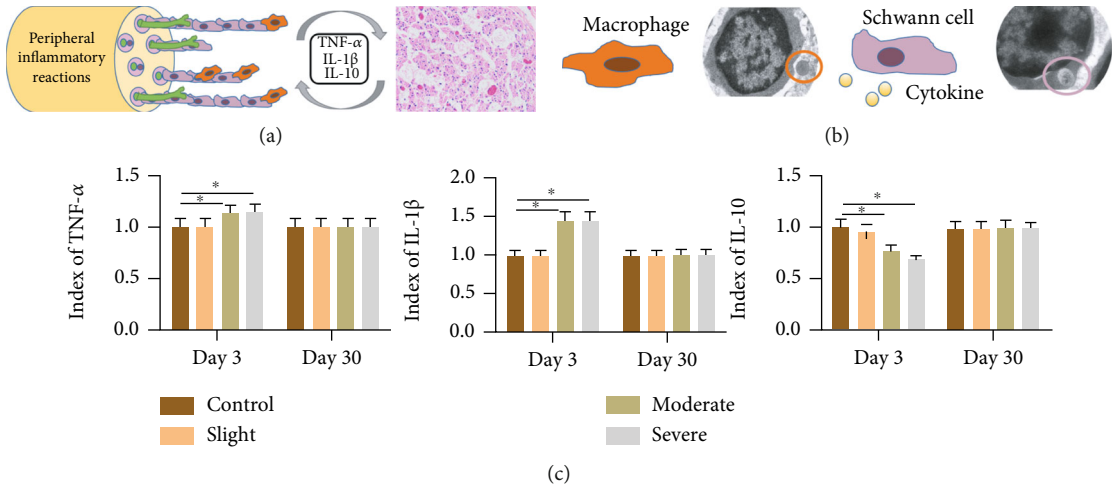

Figure 7: This consists of peripheral nerve injury environment. (a) Peripheral inflammatory reactions were observed at three days in the moderate and severe groups. (b) Macrophages were activated, showing tendency to be near Schwann cells in the moderate group. (c) Level of inflammatory cytokines varied in the control, slight, moderate, and severe groups. Red ellipse indicates the nucleus of the macrophage. Purple ellipse indicates the Schwann cell. $*$ represents $P < 0.05$.

group, the concentric structures of myelin sheaths were completely destroyed by multiple bubbles (generated by the evaporation of interstitial fluid in the cytoplasm), which predicted that the serious damage had broken the tolerant threshold and that nerves cannot spontaneously reinnervate in the following observation [16].

The morphological change of the gastrocnemius muscle is also recognized as a vital index in evaluating functional recovery of nerves. When nerves are exposed to thermal injury, the nerve conductive ability is destroyed. Additionally, the number of intact NMJ in skeleton muscles is also significantly decreased [14, 20]. Without the domination of nerves, the muscular fibers consequently become atrophic, which is accompanied by increased fibrosis and fatty infiltration [21]. Therefore, the degree of nerve recovery can be estimated by assessing morphological changes and the number of NMJ in the skeletal muscles. As presented in this study, the number of intact NMJ increased to 58% in the moderate group compared to the control at 30 days after thermal injury, while only 9% NMJ was found in the severe group. Furthermore, the weight of the gastrocnemius muscle (representing atrophy degree) was ranked in the following order: slight group > moderate group > severe group. All of these observations are consistent with the results of EMG and nerve morphological changes discussed above.

Although it has been demonstrated that the nerve itself contributes to spontaneous reinnervation in the moderate group, neural function cannot recover at an early stage. Conversely, it is observed that nerve conduction ability was continuously damaged in 3 days after thermal injury. This abnormal finding is supported by a previous study, which can be explained by the theory of local inflammation after peripheral nerve injury [7, 22, 23]. Moreover, the existence of inflammatory events after peripheral nerve injury was also confirmed [24–26]. Additionally, it was found that the anti-inflammatory effect of steroids would inhibit lipid peroxidation, which alleviated neural dysfunction after peripheral nerve injury [27]. These studies focus on the heat conduction injury. However, the neural inflammatory mechanisms resulting from exposure to thermal injury remain unclear. Our study is primarily aimed at elucidating the underlying peripheral inflammatory reactions after thermal injury. At 3 days after thermal injury, macrophages belonging to the type of M1 at the acute stage of thermal injury in the peripheral nerve environment were observed to be proliferating and exhibiting the tendency to be near myelin sheaths. These results are consistent with the recruitment of macrophages in peripheral inflammatory reactions after neural injury [24]. Furthermore, the inflammatory reaction was also confirmed by the results of serum cytokine release, such as the high expression of IL-1β and TNF-α but low expression of IL-10. All of these observations indicate the existence of peripheral inflammatory reactions after thermal injury, which may interfere in the early stage of neural recovery.

This study has some limitations. Firstly, animal models of nerve thermal injury were derived from HS, which mimic the surgical environment. Though estimated using an infrared thermodetector, the actual temperature cannot be measured to evaluate the severity of thermal injury. Secondly, the mechanisms of inflammatory reactions, especially the processes of macrophagic activation and proinflammatory cytokine release after thermal injury, warrant further investigation.

However, despite these limitations, our study first investigates the process of neural spontaneous reinnervation after thermal injury by trying to elucidate underlying peripheral inflammatory reactions. Understanding the effects and mechanisms of spontaneous peripheral nerve reinnervation after thermal injury is helpful in bridging the subjects of medicine, biology, and bioengineering to improve reinnervation. In recent decades, various promising efforts in biology and bioengineering have been explored to improve reinnervation, including nerve conduits using an extracellular matrix, gene therapy with growth factors, and even 3D

printed scaffolds [28–30]. However, these efforts are always nondirectional, without a clear path. It is critical that we determine how to promote the beneficial factors for reinnervation while preventing the harmful ones [31, 32]. Therefore, our effort to obtain a comprehensive understanding of the spontaneous reinnervation after thermal injury would be conducive to elucidating the underlying mechanism, allowing physicians to select appropriate treatments in the future.

5. Conclusion

Our results showed that the consequence of spontaneous peripheral nerve reinnervation varies, depending on the severity of thermal injury. When exposed to slight injury, neural function would recover in the acute stage. When exposed to moderate injury, nerve conductive ability is damaged significantly, requiring a gradual recovery period in the subacute and chronic stages. Lastly, when exposed to severe injury, both neural structures and functions were completely destroyed and were unable to reinnervate at all. Moreover, thermal injury generated inflammatory reactions in the peripheral nerve, which may interfere with neural recovery at the acute stage.

Abbreviations

EBDs: Energy-based devices
EMG: Electromyography
NMJ: Neuromuscular junctions
SD: Sprague-Dawley
NCV: Nerve conduction velocity
H&E: Hematoxylin and eosin
IF: Immunofluorescent
TEM: Transmission electron microscopy
ELISA: Enzyme-linked immunosorbent assay
DAPI: 4,6-Diamidino-2-phenylindole
ANOVA: One-way analysis of variance
ECM: Extracellular matrix.

Data Availability

Datasets analyzed during the current study are available from the corresponding author on reasonable request.

Ethical Approval

This study was approved by the Ethics Committee of the Second Affiliated Hospital of Zhejiang University, School of Medicine, China.

Consent

Consent is not applicable.

Conflicts of Interest

The authors declare that they have no conflict of interest.

Authors' Contributions

All authors participated in the design, execution, and interpretation of the study. YW, AWS, XY, and CL conceived and designed the study. XY, CL, CHJ, and CL performed the majority of experiments and analyzed data. XY contributed to the analyses and interpretation of the study. XY and AWS wrote the manuscript. All authors read and approved the final manuscript. Xing Yu and Chang Liu contributed equally to this study.

Acknowledgments

This study was supported by the Health Innovation Talents Project of Zhejiang Province (2021RC004), National Natural Science Foundation of China (81701144), and Zhejiang Provincial Natural Science Foundation of China (LY22H090020).

References

[1] F. Y. Chiang, K. D. Lee, K. Tae et al., "Comparison of hypocalcemia rates between ligasure and clamp-and-tie hemostatic technique in total thyroidectomies," *Head & Neck*, vol. 41, no. 10, pp. 3677–3683, 2019.

[2] X. Yang, J. Cao, Y. Yan et al., "Comparison of the safety of electrotome, harmonic scalpel, and ligasure for management of thyroid surgery," *Head & Neck*, vol. 39, no. 6, pp. 1078–1085, 2017.

[3] Z. Pogorelić, J. Katić, I. Mrklić et al., "Lateral thermal damage of mesoappendix and appendiceal base during laparoscopic appendectomy in children: comparison of the harmonic scalpel (ultracision), bipolar coagulation (ligasure), and thermal fusion technology (miseal)," *The Journal of Surgical Research*, vol. 212, pp. 101–107, 2017.

[4] A. F. Cintron-Colon, G. Almeida-Alves, J. M. VanGyseghem, and J. M. Spitsbergen, "GDNF to the rescue: GDNF delivery effects on motor neurons and nerves, and muscle reinnervation after peripheral nerve injuries," *Neural Regeneration Research*, vol. 17, no. 4, pp. 748–753, 2022.

[5] C. D. Lynch and M. Pollock, "Chapter 21 nerve thermal injury," *Progress in Brain Research*, vol. 115, pp. 453–462, 1998.

[6] K. Tamai, A. Suzuki, S. Takahashi et al., "The incidence of nerve root injury by high-speed drill can be reduced by chilled saline irrigation in a rabbit model," *Bone & Joint Journal*, vol. 99-B, no. 4, pp. 554–560, 2017.

[7] D. Xu and M. Pollock, "Experimental nerve thermal injury," *Brain*, vol. 117, no. 2, pp. 375–384, 1994.

[8] Y. C. Lin, G. Dionigi, G. W. Randolph et al., "Electrophysiologic monitoring correlates of recurrent laryngeal nerve heat thermal injury in a porcine model," *Laryngoscope*, vol. 125, no. 8, pp. E283–E290, 2015.

[9] S. Brookes, S. Voytik-Harbin, H. Zhang, L. Zhang, and S. Halum, "Motor endplate-expressing cartilage-muscle implants for reconstruction of a denervated hemilarynx," *Laryngoscope*, vol. 129, no. 6, pp. 1293–1300, 2019.

[10] K. D. Bergmeister, M. Aman, S. Muceli et al., "Peripheral nerve transfers change target muscle structure and function," *Science Advances*, vol. 5, no. 1, article u2956, 2019.

[11] L. Mu, S. Sobotka, J. Chen, and T. Nyirenda, "Nerve growth factor and basic fibroblast growth factor promote reinnervation by nerve-muscle-endplate grafting," *Muscle & Nerve*, vol. 57, no. 3, pp. 449–459, 2018.

[12] P. Dubovy, R. Jancalek, and T. Kubek, "Role of inflammation and cytokines in peripheral nerve regeneration," *International Review of Neurobiology*, vol. 108, pp. 173–206, 2013.

[13] A. Ehmedah, P. Nedeljkovic, S. Dacic et al., "Vitamin b complex treatment attenuates local inflammation after peripheral nerve injury," *Molecules*, vol. 24, no. 24, p. 4615, 2019.

[14] A. J. Rosko, R. A. Kupfer, S. S. Oh, C. T. Haring, E. L. Feldman, and N. D. Hogikyan, "Immunohistologic analysis of spontaneous recurrent laryngeal nerve reinnervation in a rat model," *Laryngoscope*, vol. 128, no. 3, pp. E117–E122, 2018.

[15] M. N. Hsu, H. T. Liao, V. A. Truong et al., "Crispr-based activation of endogenous neurotrophic genes in adipose stem cell sheets to stimulate peripheral nerve regeneration," *Theranostics*, vol. 9, no. 21, pp. 6099–6111, 2019.

[16] J. Carlander, K. Johansson, S. Lindström, A. K. Velin, C. H. Jiang, and C. Nordborg, "Comparison of experimental nerve injury caused by ultrasonically activated scalpel and electrosurgery," *The British Journal of Surgery*, vol. 92, no. 6, pp. 772–777, 2005.

[17] P. Shrager, "Ionic channels and signal conduction in single remyelinating frog nerve fibres," *The Journal of Physiology*, vol. 404, no. 1, pp. 695–712, 1988.

[18] B. B. Geren and F. O. Schmitt, "The structure of the Schwann cell and its relation to the axon in certain invertebrate nerve fibers," *Proceedings of the National Academy of Sciences of the United States of America*, vol. 40, no. 9, pp. 863–870, 1954.

[19] B. Liu, W. Xin, J. R. Tan et al., "Myelin sheath structure and regeneration in peripheral nerve injury repair," *Proceedings of the National Academy of Sciences of the United States of America*, vol. 116, no. 44, pp. 22347–22352, 2019.

[20] R. A. Kupfer, M. O. Old, S. S. Oh, E. L. Feldman, and N. D. Hogikyan, "Spontaneous laryngeal reinnervation following chronic recurrent laryngeal nerve injury," *Laryngoscope*, vol. 123, no. 9, pp. 2216–2227, 2013.

[21] D. S. Tews, "Muscle-fiber apoptosis in neuromuscular diseases," *Muscle & Nerve*, vol. 32, no. 4, pp. 443–458, 2005.

[22] R. Mohammadi, M. Azad-Tirgan, and K. Amini, "Dexamethasone topically accelerates peripheral nerve repair and target organ reinnervation: a transected sciatic nerve model in rat," *Injury*, vol. 44, no. 4, pp. 565–569, 2013.

[23] B. Siqueira Mietto, A. Kroner, E. I. Girolami, E. Santos-Nogueira, J. Zhang, and S. David, "Role of IL-10 in resolution of inflammation and functional recovery after peripheral nerve injury," *The Journal of Neuroscience*, vol. 35, no. 50, pp. 16431–16442, 2015.

[24] A. D. Gaudet, P. G. Popovich, and M. S. Ramer, "Wallerian degeneration: gaining perspective on inflammatory events after peripheral nerve injury," *Journal of Neuroinflammation*, vol. 8, no. 1, p. 110, 2011.

[25] D. Zhang, H. Sun, R. Tufano, E. Caruso, G. Dionigi, and H. Y. Kim, "Recurrent laryngeal nerve management in transoral endoscopic thyroidectomy," *Oral Oncology*, vol. 108, p. 104755, 2020.

[26] R. R. Zhang, S. L. Chen, Z. C. Cheng, Y. Y. Shen, S. Yi, and H. Xu, "Characteristics of cytokines in the sciatic nerve stumps and DRGs after rat sciatic nerve crush injury," *Military Medical Research*, vol. 7, no. 1, p. 57, 2020.

[27] E. R. Galloway, R. L. Jensen, A. T. Dailey, B. G. Thompson, and C. Shelton, "Role of topical steroids in reducing dysfunction after nerve injury," *Laryngoscope*, vol. 110, no. 11, pp. 1907–1910, 2000.

[28] C. C. Chen, J. Yu, H. Y. Ng et al., "The physicochemical properties of decellularized extracellular matrix-coated 3d printed poly(epsilon-caprolactone) nerve conduits for promoting schwann cells proliferation and differentiation," *Materials*, vol. 11, no. 9, p. 1665, 2018.

[29] A. R. Dixon, S. H. Jariwala, Z. Bilis, J. R. Loverde, P. F. Pasquina, and L. M. Alvarez, "Bridging the gap in peripheral nerve repair with 3d printed and bioprinted conduits," *Biomaterials*, vol. 186, pp. 44–63, 2018.

[30] C. F. Liao, C. C. Chen, Y. W. Lu et al., "Effects of endogenous inflammation signals elicited by nerve growth factor, interferon-γ, and interleukin-4 on peripheral nerve regeneration," *Journal of Biological Engineering*, vol. 13, no. 1, p. 86, 2019.

[31] I. Hernandez-Morato, I. Tewari, S. Sharma, and M. J. Pitman, "Blockade of glial-derived neurotrophic factor in laryngeal muscles promotes appropriate reinnervation," *Laryngoscope*, vol. 126, no. 10, pp. E337–E342, 2016.

[32] P. G. Nagappan, H. Chen, and D. Y. Wang, "Neuroregeneration and plasticity: a review of the physiological mechanisms for achieving functional recovery postinjury," *Military Medical Research*, vol. 7, no. 1, p. 30, 2020.

Hindawi
Oxidative Medicine and Cellular Longevity
Volume 2022, Article ID 5067544, 12 pages
https://doi.org/10.1155/2022/5067544

Research Article

Peroxiredoxin-5 Knockdown Accelerates Pressure Overload-Induced Cardiac Hypertrophy in Mice

Chengyun Hu,[1,2] **Feibiao Dai**,[1,2] **Jiawu Wang**,[1] **Lai Jiang**,[3] **Di Wang**,[4] **Jie Gao**,[5] **Jun Huang**,[6] **Jianfeng Luo**,[7] **Fei Tang**,[1] **Zhetao Zhang**,[8] **and Chaoliang Tang**[1]

[1]*Department of Anesthesiology, The First Affiliated Hospital of USTC, Division of Life Sciences and Medicine, University of Science and Technology of China, Hefei, Anhui 230001, China*
[2]*Department of Anesthesia, Wannan Medical College, Wuhu, Anhui 241002, China*
[3]*Department of Obstetrics and Gynecology, The First Affiliated Hospital of USTC, Division of Life Sciences and Medicine, University of Science and Technology of China, Hefei, Anhui 230001, China*
[4]*Department of Anesthesiology, The Second Affiliated Hospital of Anhui Medical University, Hefei, Anhui 230601, China*
[5]*Department of Anesthesiology, The First Affiliated Hospital of Anhui Medical University, Hefei, Anhui 230022, China*
[6]*Department of Anesthesiology, The People's Hospital of Chizhou, Chizhou, Anhui 247000, China*
[7]*Department of Cardiology, The First Affiliated Hospital of USTC, Division of Life Sciences and Medicine, University of Science and Technology of China, Hefei, Anhui 230001, China*
[8]*Department of Pharmacy, The First Affiliated Hospital of USTC, Division of Life Sciences and Medicine, University of Science and Technology of China, Hefei, Anhui 230036, China*

Correspondence should be addressed to Fei Tang; ahsynqtf@126.com, Zhetao Zhang; ahsynqzzt@126.com, and Chaoliang Tang; chaolt@ustc.edu.cn

Received 19 August 2021; Accepted 21 December 2021; Published 29 January 2022

Academic Editor: Ji Bihl

A recent study showed that peroxiredoxins (Prxs) play an important role in the development of pathological cardiac hypertrophy. However, the involvement of Prx5 in cardiac hypertrophy remains unclear. Therefore, this study is aimed at investigating the role and mechanisms of Prx5 in pathological cardiac hypertrophy and dysfunction. Transverse aortic constriction (TAC) surgery was performed to establish a pressure overload-induced cardiac hypertrophy model. In this study, we found that Prx5 expression was upregulated in hypertrophic hearts and cardiomyocytes. In addition, Prx5 knockdown accelerated pressure overload-induced cardiac hypertrophy and dysfunction in mice by activating oxidative stress and cardiomyocyte apoptosis. Importantly, heart deterioration caused by Prx5 knockdown was related to mitogen-activated protein kinase (MAPK) pathway activation. These findings suggest that Prx5 could be a novel target for treating cardiac hypertrophy and heart failure.

1. Introduction

Pathological cardiac hypertrophy is a common pathophysiological process of various cardiovascular diseases, including hypertension, myocardial infarction, and heart failure [1–3]. It presents as thickening of the ventricular wall and decreased compliance of the ventricular wall [4–6]. Multiple mechanisms have been identified in the regulation of pathological cardiac hypertrophy, including oxidative stress, inflammation, autophagy, and cardiomyocyte apoptosis [7–9]. Thus, targeting molecules or genes associated with the above processes is crucial for the treatment of pathological cardiac hypertrophy.

Peroxiredoxins (Prxs) are a superfamily of antioxidant peroxidases that scavenge hydrogen peroxide (H_2O_2) and alkyl hydroperoxides [10–13]. At present, Prxs are identified as important regulators of redox homeostasis and participate in a series of cell functions. Many studies have shown that some family members of Prxs play an important role in the development of pathological cardiac hypertrophy [14,

15]. Cardiomyocyte-specific Prx1 overexpression in mice attenuates cardiac hypertrophy and dysfunction under pressure overload [14]. Similarly, overexpression of Prx3 prevents cardiac hypertrophy and failure after myocardial infarction in mice [15]. As an important member of the Prx family, Prx5 has antioxidant protective functions and can effectively remove reactive oxygen species (ROS) [16, 17]. However, the involvement of Prx5 in cardiac hypertrophy remains unclear.

In this study, we explored the role and mechanisms of Prx5 in pathological cardiac hypertrophy and dysfunction. We confirmed that Prx5 knockdown accelerates pressure overload-induced cardiac hypertrophy and dysfunction in mice by activating oxidative stress and cardiomyocyte apoptosis. Importantly, heart deterioration caused by Prx5 knockdown was related to mitogen-activated protein kinase (MAPK) activation. These findings suggest that Prx5 could be a novel target for treating cardiac hypertrophy and heart failure.

2. Materials and Methods

2.1. Animals and Animal Model. All animal procedures in this study were approved by the Animal Care and Use Committee of Anhui Medical University. Male C57BL/6 mice (8-10 weeks, 23-26 g) were purchased from Beijing HFK Bioscience Co., Ltd. (Beijing, China) and were housed in a well-ventilated environment. Transverse aortic constriction (TAC) surgery was performed to establish pressure overload-induced cardiac hypertrophy model as previously described [18]. Two weeks before TAC surgery, mice received a heart injection of AAV9-shPrx5 (1×10^{11} viral particles/mouse) to knockdown Prx5 in the myocardium. Four weeks after TAC or the sham procedure, mice were euthanized by intraperitoneal injection of 200 mg/kg pentobarbital sodium. Then, the hearts, lungs, and tibia were harvested and measured to calculate the heart weight/body weight (HW/BW, mg/g), lung weight to body weight (LW/BW, mg/g), heart weight to tibia length (HW/TL, mg/mm), and lung weight/tibia length (LW/TL, mg/mm) ratios in the mice.

2.2. Echocardiography Analysis. Cardiac function was detected using a Vivid 7000 ultrasound equipped with a 14 MHz transducer. In short, the mice were anesthetized, and the left ventricle (LV) geometry was assessed in both parasternal long-axis and short-axis views. The heart rate (HR), LV internal diameter at end-diastole (LVIDd), LV internal diameter at end-systole (LVIDs), LV posterior wall thickness of end systolic (LVPWs), LV posterior wall thickness of end diastolic (LVPWd), interventricular septal thickness at end-diastole (IVSd), interventricular septal thickness at end-systole (IVSs), and LV fractional shortening (LVFS) were determined.

2.3. Histological and TUNEL Analysis. The mice were sacrificed immediately after echocardiography measurements, and the hearts were harvested and then placed in 4% paraformaldehyde. Then, the heart sections were prepared and stained with hematoxylin and eosin (HE) and wheat germ agglutinin (WGA) for morphological analyses and evaluation of the cross-sectional area (CSA). In addition, heart sections were stained with picrosirius red (PSR) to assess collagen deposition. To detect cardiomyocyte apoptosis, TUNEL staining was performed as described in our previous study. The sections were visualized using microscopy, and all images were analyzed using Image-Pro Plus 6.0.

2.4. Neonatal Rat Cardiomyocyte (NRCM) Culture and Treatment. Primary neonatal rat cardiomyocytes (NRCMs) were isolated from 1- to 2-day-old Sprague-Dawley rats as previously described [19]. Then, the NRCMs were cultured in plating medium consisting of DMEM/F12 containing 15% fetal bovine serum (FBS), 0.1 mM BrdU, and 100 mg/mL penicillin/streptomycin. To knockdown Prx5 in vitro, Prx5 siRNA was used according to manufacturer's instructions. Then, the NRCMs were stimulated with angiotensin II (Ang II, 1 μM) for 48 h.

2.5. Immunofluorescence Analysis. The NRCMs were fixed with 4% paraformaldehyde and permeabilized with 0.2% Triton X-100. Then, the NRCMs were stained with α-actinin and the indicated fluorescent secondary antibody and then stained with DAPI. Finally, the NRCMs were visualized under a fluorescence microscope, and all images were analyzed using Image-pro Plus 6.0.

2.6. Quantitative Real-Time PCR. Total mRNA was extracted from ventricular tissue and NRCMs and then converted to cDNA using the RNA PCR Kit). PCR amplification was performed and quantified using an ABI PRISM 7000 Sequence Detection System. The relative mRNA expression levels of target genes were analyzed and normalized to the mRNA expression level of glyceraldehyde-3-phosphate dehydrogenase (GAPDH). The sequences of the primers used are presented in Table 1.

2.7. Western Blotting. Protein lysates of ventricular tissue and NRCMs were prepared and the protein concentrations were then measured. The proteins were loaded and run on SDS-PAGE and transferred to a PVDF membrane. The PVDF membranes were subsequently blocked with 5% PVDF and incubated with primary antibodies against Prx5, GAPDH, Bax, Bcl-2, ERK, p-ERK, JNK, p-JNK, p38, and p-p38. After washing, the PVDF membranes were incubated with a secondary antibody and visualized with an infrared imaging system according to manufacturer's protocol. The specific protein expression levels were normalized to that of GAPDH.

2.8. Measurement of Oxidative Stress Level. Dihydroethidium (DHE) staining was performed according to manufacturer's protocol. In short, frozen sections of ventricular tissue were incubated with 10 μM DHE in PBS in a humidified and light-protected chamber. The images were then taken with a laser microscope and analyzed using Image-Pro Plus 6.0. In addition, superoxide dismutase (SOD), glutathione (GSH), malondialdehyde (MDA), and H_2O_2 in LV

Table 1: Primer sequences for RT-PCR assays.

Gene	Species		Sequence (5′-3′)
PRDX5	Mouse	Forward	GCTGCAAAGCCAGTTCTGTG
		Reverse	CCACTGAGGGAATGGCATCTC
PRDX5	Rat	Forward	GCAAGGTTCAGCTCCTGGCT
		Reverse	CAGGTGAGGCCTGTGCCATC
ANP	Mouse	Forward	CCTGTGTACAGTGCGGTGTC
		Reverse	AAGCTGTTGCAGCCTAGTCC
ANP	Rat	Forward	AAAGCAAACTGAGGGCTCTGCTCG
		Reverse	TTCGGTACCGGAAGCTGTTGCA
BNP	Mouse	Forward	CTCAAGCTGCTTTGGGCACAAGAT
		Reverse	AGCCAGGAGGTCTTCCTACAACAA
BNP	Rat	Forward	CAGCAGCTTCTGCATCGTGGAT
		Reverse	TTCCTTAATCTGTCGCCGCTGG
β-MHC	Mouse	Forward	TCTACCCAGCCAAGATCAAAGT
		Reverse	CCCATTCCTAATAAGCTGTGTGG
β-MHC	Rat	Forward	TCTGGACAGCTCCCCATTCT
		Reverse	CAAGGCTAACCTGGAGAAGATG
Myh7	Mouse	Forward	ACTGTCAACACTAAGAGGGTCA
		Reverse	TTGGATGATTTGATCTTCCAGGG
Myh7	Rat	Forward	TGCTGTTATTGCTGCCATTG
		Reverse	AGGAGTTATCATTCCGAACTGTC
TGF-β	Mouse	Forward	TGCTTCAGCTCCACAGAGAA
		Reverse	TGGTTGTAGAGGGCAAGGAC
TGF-β	Rat	Forward	ATTCCTGGCGTTACCTTGG
		Reverse	AGCCCTGTATTCCGTCTCCT
CTGF	Mouse	Forward	TGTGTGATGAGCCCAAGGAC
		Reverse	AGTTGGCTCGCATCATAGTTG
CTGF	Rat	Forward	ACACAAGGGTCTCTTCTGCG
		Reverse	ACAGGGTGCACCATCTTTGG
Collagen I	Mouse	Forward	TGGTACATCAGCCCGAAC
		Reverse	GTCAGCTGGATAGCGACA
Collagen I	Rat	Forward	TGGACATTAGGCGCAGGAA
		Reverse	GAGAGAGCATGACCGATGGATT
Collagen III	Mouse	Forward	ACGTAGATGAATTGGGATGCAG
		Reverse	GGGTTGGGGCAGTCTAGTC
Collagen III	Rat	Forward	CCCAACCCAGAGATCCCATT
		Reverse	GAAGCACAGGAGCAGGTGTAGA
IL-1β	Mouse	Forward	GGGCCTCAAAGGAAAGAATC
		Reverse	TACCAGTTGGGGAACTCTGC
IL-6	Mouse	Forward	AGTTGCCTTCTTGGGACTGA
		Reverse	TCCACGATTTCCCAGAGAAC
IL-17	Mouse	Forward	TCCAGAAGGCCCTCAGACTA
		Reverse	AGCATCTTCTCGACCCTGAA
TNF-α	Mouse	Forward	CCCAGGGACCTCTCTCTAATC
		Reverse	ATGGGCTACAGGCTTGTCACT
GAPDH	Mouse	Forward	AACTTTGGCATTGTGGAAGG
		Reverse	CACATTGGGGGTAGGAACAC
GAPDH	Rat	Forward	GACATGCCGCCTGGAGAAAC
		Reverse	GACATGCCGCCTGGAGAAAC

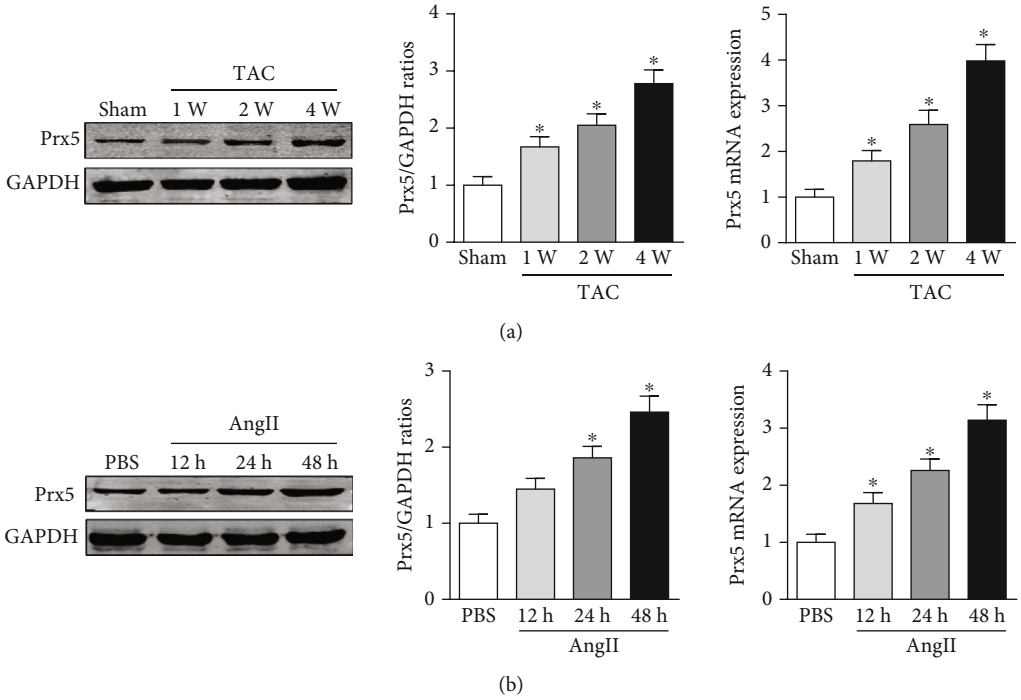

Figure 1: Prx5 expression is increased in hypertrophic hearts and isolated NRCMs. (a) The expression of Prx5 in heart tissues was measured by Western blotting and RT-PCR ($n = 4$, $^*P < 0.05$ vs. the sham group). (c) The expression of Prx5 in heart tissues was measured by Western blotting and RT-PCR ($n = 4$, $^*P < 0.05$ vs. the PBS group).

Table 2: Echocardiographic data of each group.

Groups	Sham+AAV9-shRNA	Sham+AAV9-shPrx5	TAC + AAV9-shRNA	TAC + AAV9-shPrx5
HR (bpm)	523 ± 48	519 ± 39	511 ± 40	516 ± 44
LVEDd (mm)	3.51 ± 0.23	3.63 ± 0.35	4.51 ± 0.36∗	5.32 ± 0.29$^{\#}$
LVEDs (mm)	1.93 ± 0.16	1.88 ± 0.12	3.18 ± 0.21∗	4.23 ± 0.29$^{\#}$
LVPWd (mm)	0.66 ± 0.06	0.64 ± 0.05	1.21 ± 0.11∗	1.43 ± 0.13$^{\#}$
LVPWs (mm)	1.06 ± 0.10	1.05 ± 0.09	1.83 ± 0.13∗	2.33 ± 0.15$^{\#}$
IVSd (mm)	0.64 ± 0.05	0.63 ± 0.06	1.17 ± 0.09∗	1.46 ± 0.13$^{\#}$
IVSs (mm)	1.06 ± 0.11	1.04 ± 0.10	1.82 ± 0.15∗	2.24 ± 0.16$^{\#}$
FS (%)	45.41 ± 2.68	46.53 ± 2.81	29.76 ± 3.03∗	20.34 ± 2.54$^{\#}$

$n = 8$ for each group. $^*P < 0.05$ vs. the sham group; $^{\#}P < 0.05$ vs. the TAC group.

tissue or NRCMs were detected using kits purchased from Beyotime Biotechnology Corporation (China).

2.9. Statistical Analysis. The data are expressed as the mean ± standard deviation. Comparisons between two groups were analyzed using an unpaired Student's t test. Differences among multiple groups were assessed using an analysis of variance followed by one-way analysis of variance. A value of $P < 0.05$ was considered statistically significant.

3. Results

3.1. Prx5 Expression Is Increased in Hypertrophic Hearts and Isolated NRCMs. The results showed that Prx5 expression was gradually upregulated in the hearts of mice subjected to TAC surgery (Figure 1(a)). In accordance with this, higher Prx5 levels were also detected in isolated NRCMs after Ang II stimulation (Figure 1(b)). Together, these data suggest that Prx5 may participate in the development of cardiac hypertrophy.

3.2. Prx5 Knockdown Accelerates Pressure Overload-Induced Cardiac Dysfunction. After TAC surgery, animals exhibited LV dilatation and thickening, as indicated by increased LVIDd, LVIDs, LVPWd, LVPWs, IVSd, and IVSs and decreased FS. However, Prx5 knockdown further aggravated pressure overload-induced cardiac dysfunction (Table 2). In addition, there were no significant differences in HR among the four groups.

3.3. Prx5 Knockdown Accelerates Pressure Overload-Induced Cardiac Hypertrophy. As shown in Figure 2, AAV9-shPrx5 caused decreased expression of Prx5 in hearts (Figure 2(a)). Four weeks after TAC surgery, Prx5 knockdown accelerated

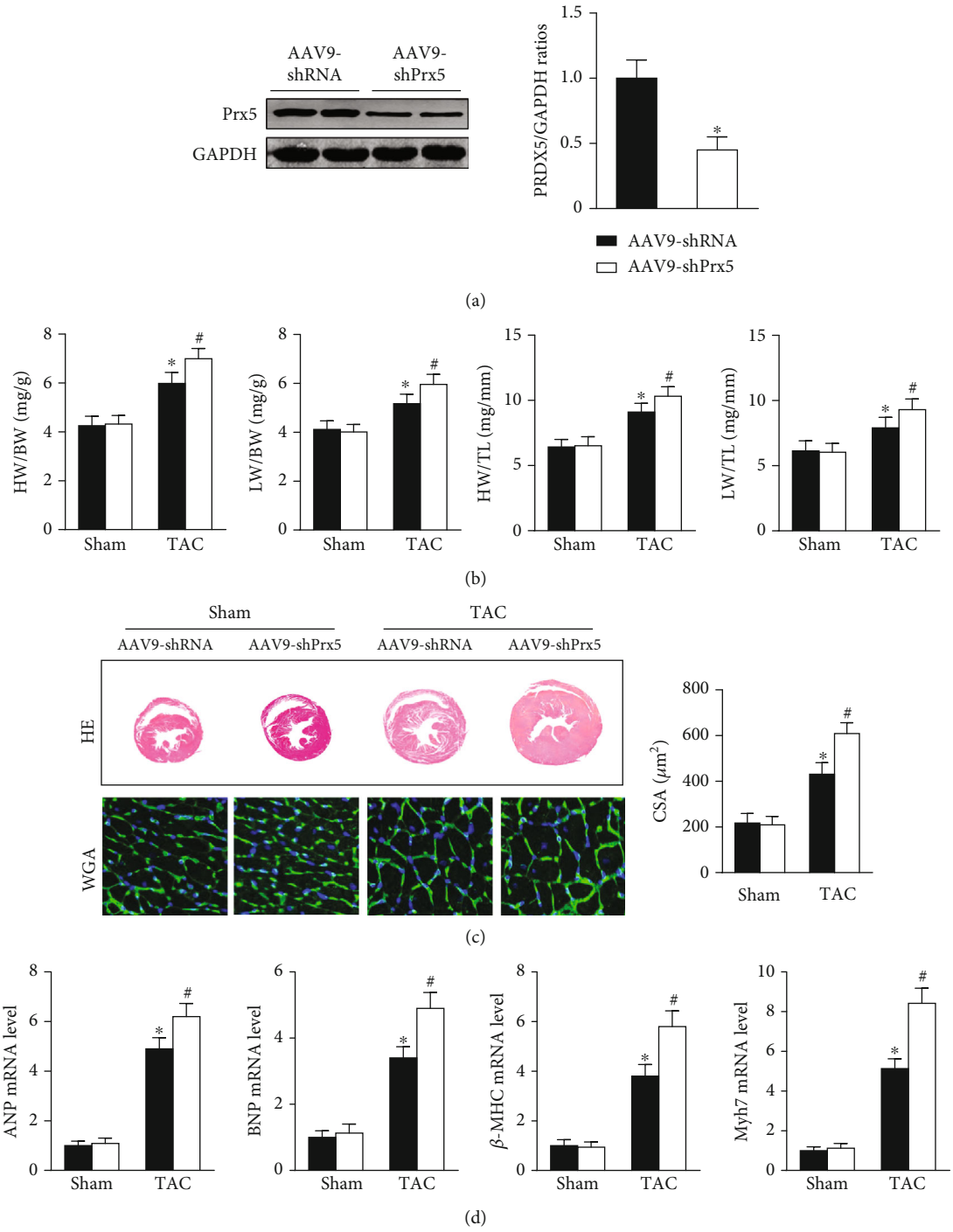

FIGURE 2: Prx5 knockdown accelerates pressure overload-induced cardiac hypertrophy. (a) The levels of Prx5 after injection with AAV9-shPrx5 ($n = 4$). (b) Results for the HW/BW ratio, HW/TL ratio, LW/BW ratio, LW/TL ratio, and CSA of each group ($n = 6$). (c) HE and WGA staining were performed in each group ($n = 6$; scale bar, 50 μm). (d) The expression of ANP, BNP, β-MHC, and Myh7 was measured by RT-PCR in each group ($n = 5$). $^{*}P < 0.05$ vs. the sham group; $^{\#}P < 0.05$ vs. the TAC group.

pressure overload-induced cardiac hypertrophy, as evidenced by increased HW/BW, HW/TL, LW/BW, and LW/TL ratios and increased CSA (Figures 2(b) and 2(c)). In addition, higher mRNA levels of atrial natriuretic peptide (ANP), brain natriuretic peptide (BNP), β-myosin heavy chain (β-MHC), and Myosin Heavy Chain 7 (Myh7) were also found in the Prx5 knockdown group after TAC surgery (Figure 2(c)).

3.4. Prx5 Knockdown Accelerates Pressure Overload-Induced Cardiac Fibrosis. As shown in Figure 3, dramatic collagen deposition was observed in the mice after TAC surgery and was further increased in the Prx5 knockdown group (Figure 3(a)). Similarly, after TAC surgery, the mRNA expression levels of several fibrosis markers, including collagen I, collagen III, transforming growth

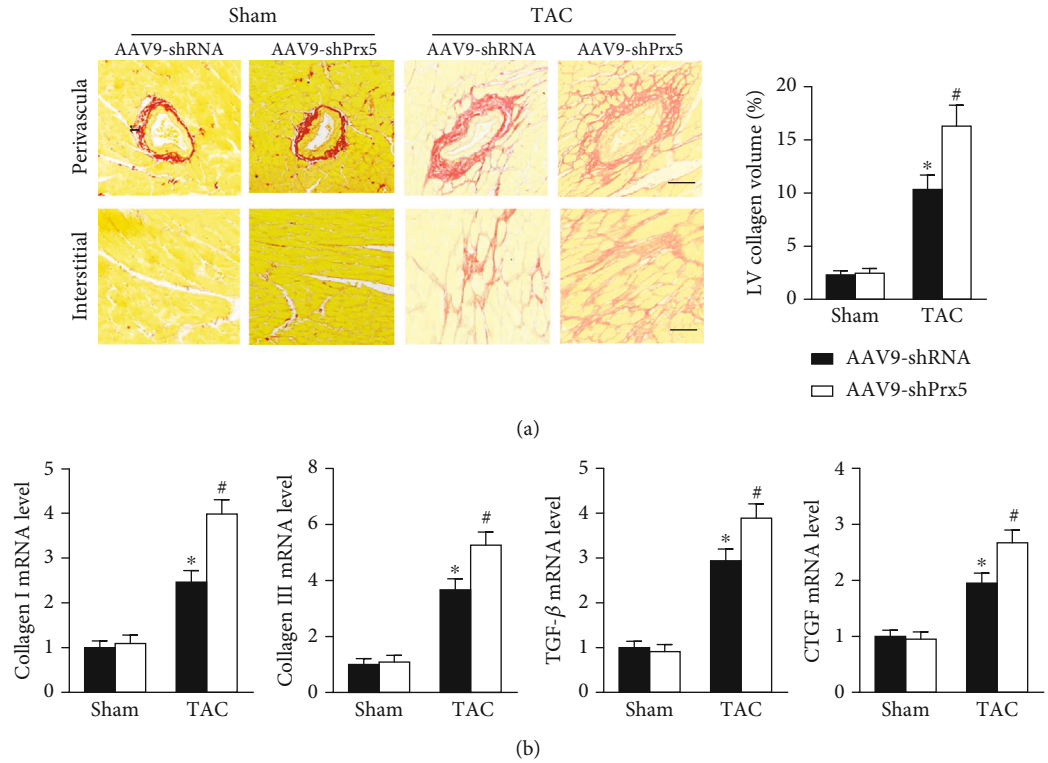

Figure 3: Prx5 knockdown accelerates pressure overload-induced cardiac fibrosis. (a) PSR staining was performed in each group ($n = 6$; scale bar, 50 μm). (b) The expression of collagen I, collagen III, TGF-β, and CTGF was measured by RT-PCR in each group ($n = 6$). $^{*}P < 0.05$ vs. the sham group; $^{\#}P < 0.05$ vs. the TAC group.

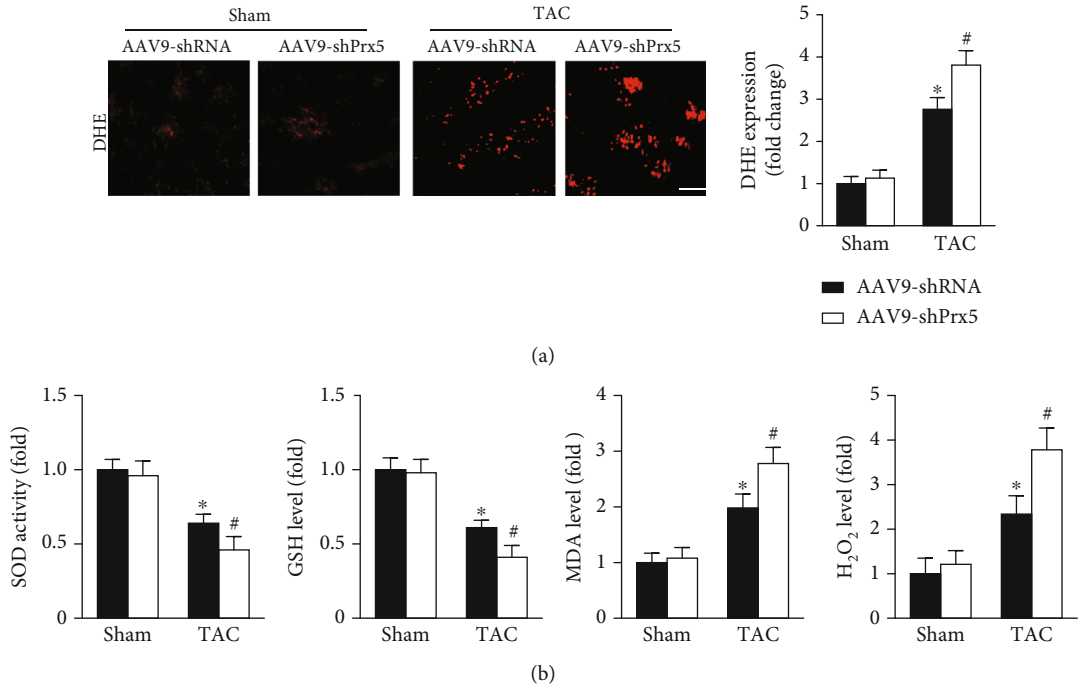

Figure 4: Prx5 knockdown accelerates pressure overload-induced oxidative stress and apoptosis. (a) DHE staining was performed in each group ($n = 5$; scale bar, 100 μm). (b) Quantitative results of SOD activity and GSH, MDA, and H_2O_2 levels in the hearts of each group ($n = 6$). $^{*}P < 0.05$ vs. the sham group; $^{\#}P < 0.05$ vs. the TAC group.

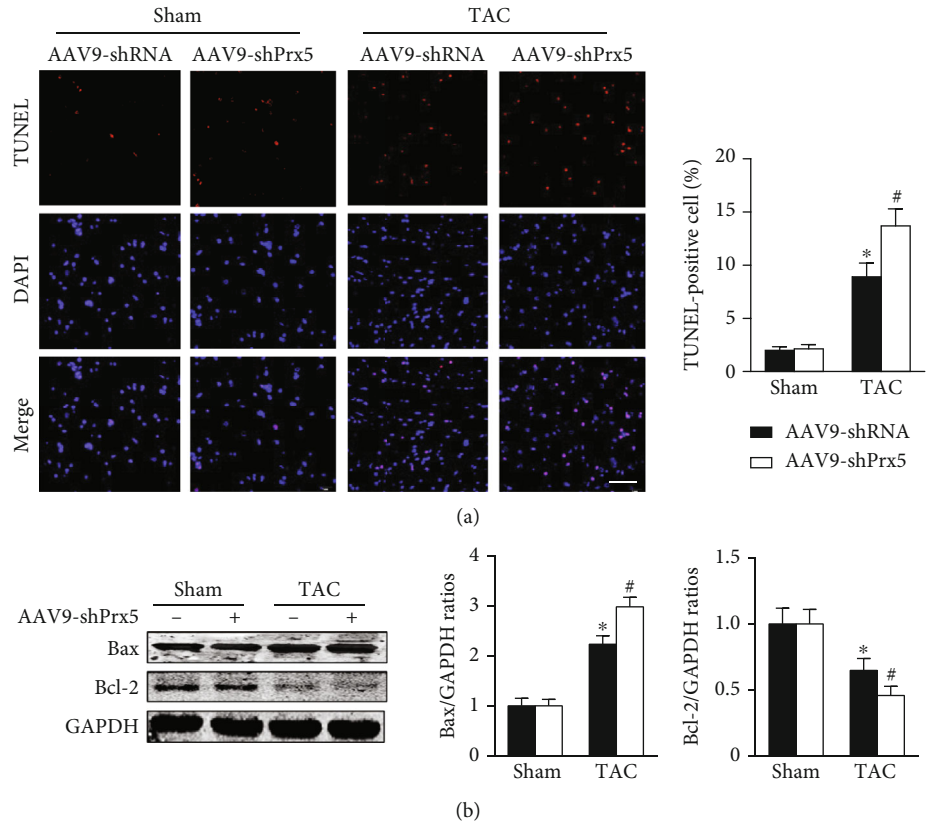

Figure 5: Prx5 knockdown accelerates pressure overload-induced apoptosis in mice. (a) TUNEL staining was performed in each group ($n = 4$; scale bar, 50 μm). (b) The expression of Bax and Bcl-2 was measured by Western blot in each group ($n = 4$). $^{*}P < 0.05$ vs. the sham group; $^{\#}P < 0.05$ vs. the TAC group.

factor (TGF)-β, and connective tissue growth factor (CTGF), were also further increased in the Prx5 knockdown group (Figure 3(b)).

3.5. Prx5 Knockdown Accelerates Pressure Overload-Induced Oxidative Stress and Apoptosis in Mice. DHE staining was used to evaluate in vivo oxidative stress levels. The results showed that the oxidative stress level was dramatically increased in the Prx5 knockdown group after TAC surgery (Figure 4(a)). Moreover, Prx5 knockdown markedly decreased SOD activity and GSH levels and increased MDA and H_2O_2 levels in TAC-treated mice (Figure 4(b)).

3.6. Prx5 Knockdown Accelerates Pressure Overload-Induced Apoptosis in Mice. TUNEL staining was used to evaluate apoptosis levels in the heart. The results showed that the number of TUNEL-positive cells was dramatically increased in the Prx5 knockdown group after TAC surgery (Figure 5(a)). Moreover, Prx5 knockdown increased Bax and decreased Bcl-2 levels in TAC-treated mice (Figure 5(b)).

3.7. Prx5 Knockdown Accelerates AngII-Induced Cardiomyocyte Hypertrophy In Vitro. Consistent with the in vivo results, si-Prx5 led to decreased expression of Prx5 in NRCMs (Figure 6(a)). After 48 h of AngII stimulation, the NRCMs exhibited clear hypertrophy by augmentation in CSA and increased mRNA levels of ANP, BNP, β-MHC, and Myh7 (Figures 6(b) and 6(c)). Interestingly, Prx5 knockdown accelerated AngII-induced cardiomyocyte hypertrophy in vitro (Figures 6(b) and 6(c)).

3.8. Prx5 Knockdown Accelerates AngII-Induced Oxidative Stress and Apoptosis In Vitro. The results showed that AngII treatment markedly decreased SOD activity and GSH levels and increased MDA and H_2O_2 levels in vitro, while these effects were further augmented by Prx5 knockdown (Figure 7(a)). TUNEL staining further showed that Prx5 knockdown further increased the number of TUNEL-positive cells in vitro (Figure 7(b)).

3.9. Effect of Prx5 on the MAPK Signaling Pathway. Previous research has widely implicated MAPK signaling in cardiac hypertrophy. Thus, we investigated whether the effects of Prx5 are associated with the MAPK signaling pathway. The results showed that the phosphorylated levels of ERK, p38, and JNK were significantly increased in TAC-treated mice. However, these effects were further augmented by Prx5 knockdown (Figure 8(a)). Consistent with the in vivo results, Prx5 knockdown also increased the phosphorylation levels of ERK, p38, and JNK in NRCMs after AngII treatment (Figure 8(b)).

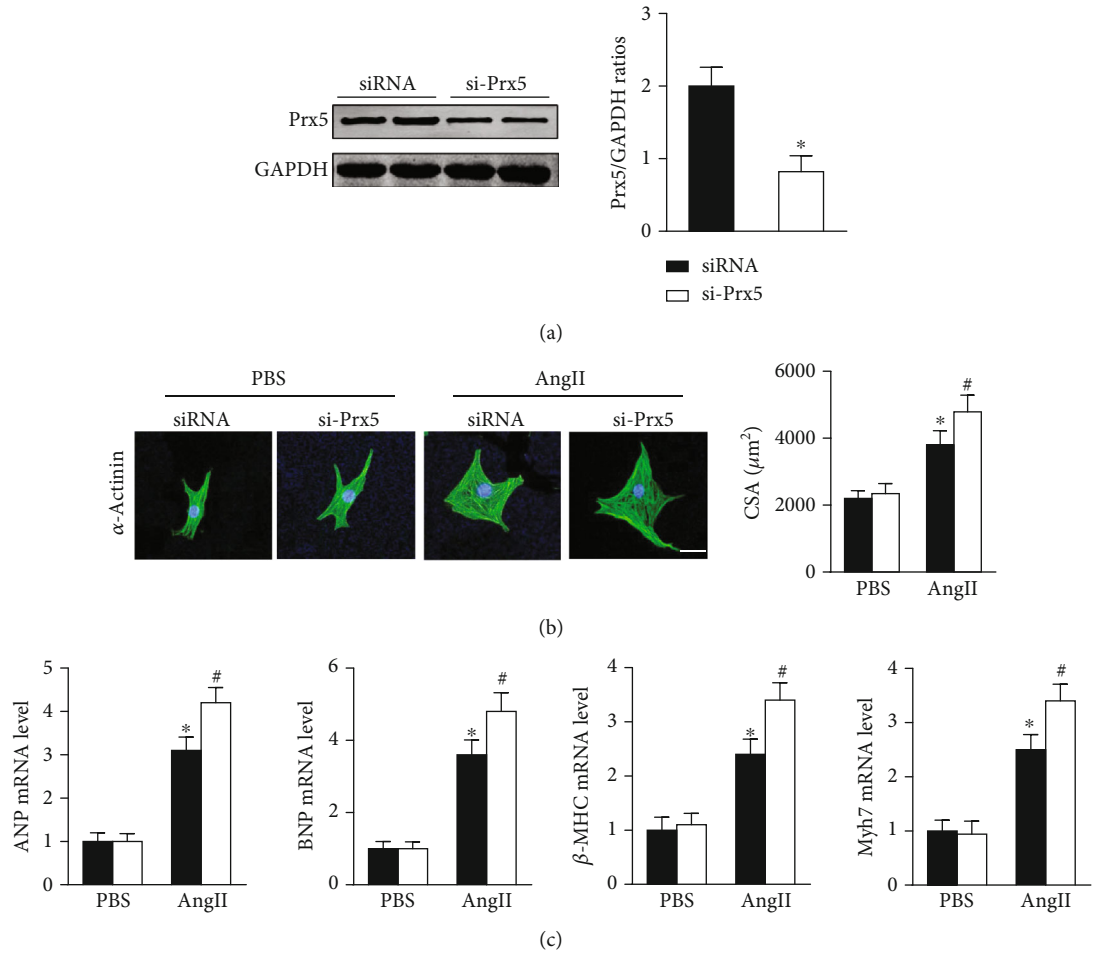

FIGURE 6: Prx5 knockdown accelerates AngII-induced cardiomyocyte hypertrophy in vitro. (a) The levels of Prx5 were measured by Western blot ($n = 4$). (b) Immunofluorescence staining for α-actinin was performed in each group ($n = 4$; scale bar, 25 μm). (c) The expression of ANP, BNP, β-MHC, and Myh7 was measured by RT-PCR in each group ($n = 6$). $^{*}P < 0.05$ vs. the PBS group; $^{\#}P < 0.05$ vs. the AngII group.

4. Discussion

In the present study, we uncovered a novel role of Prx5 in pressure overload-induced cardiac hypertrophy. The results showed that the mRNA and protein expression of Prx5 were noticeably upregulated in hypertrophic hearts and AngII-stimulated cardiomyocytes. In addition, Prx5 knockdown accelerated pressure overload-induced cardiac hypertrophy and dysfunction in mice by activating oxidative stress and cardiomyocyte apoptosis. Importantly, heart deterioration caused by Prx5 knockdown was related to MAPK activation. These findings suggest that Prx5 could be a novel target for treating cardiac hypertrophy and heart failure.

Prx5, also called PrxV/AOEB166/PMP20/PLP/ACR1, was discovered twenty years ago and is widely expressed in mammalian tissues [20]. As an important member of the Prxs family, Prx5 plays a central role in redox signal transduction and exhibits high scavenging activity toward oxidative stress [16] [21]. Previous research has shown that Prx5 exhibits a protective role in a variety of diseases, including brain lesions, aging, obesity, and cancer [22–24]. Recombinant Prx5 administration provided protection against N-methyl-D-aspartate-mediated brain lesions and neuronal death in newborn mice [22]. In an obesity model induced by a high-fat diet, deletion of Prx5 increased susceptibility to obesity and adipogenesis by increasing ROS generation and adipogenic gene expression [23]. However, little is known about the exact role and mechanisms of Prx5 in the development of cardiac hypertrophy and dysfunction. In the present study, we first confirmed that Prx5 was upregulated in hypertrophic mouse hearts and AngII-stimulated NRCMs, indicating that Prx5 might be involved in the progression and development of pathological cardiac hypertrophy. In addition, AAV9-shPrx5 was used to knock down Prx5 in the myocardium. The results showed that Prx5 knockdown accelerates pressure overload-induced cardiac dysfunction, hypertrophy, and fibrosis in mice. Consistent with the in vivo results, Prx5 knockdown also accelerated AngII-induced cardiomyocyte hypertrophy in vitro.

Oxidative stress is described as a common pathological feature of various cardiovascular diseases [25–28]. As a natural byproduct of the metabolic utilization of oxygen, ROS are oxygen-containing molecules with highly reactive properties and represent crucial drivers of oxidative stress [29–31]. Under pathological conditions of pressure overload, excessive ROS result in cardiomyocyte death or

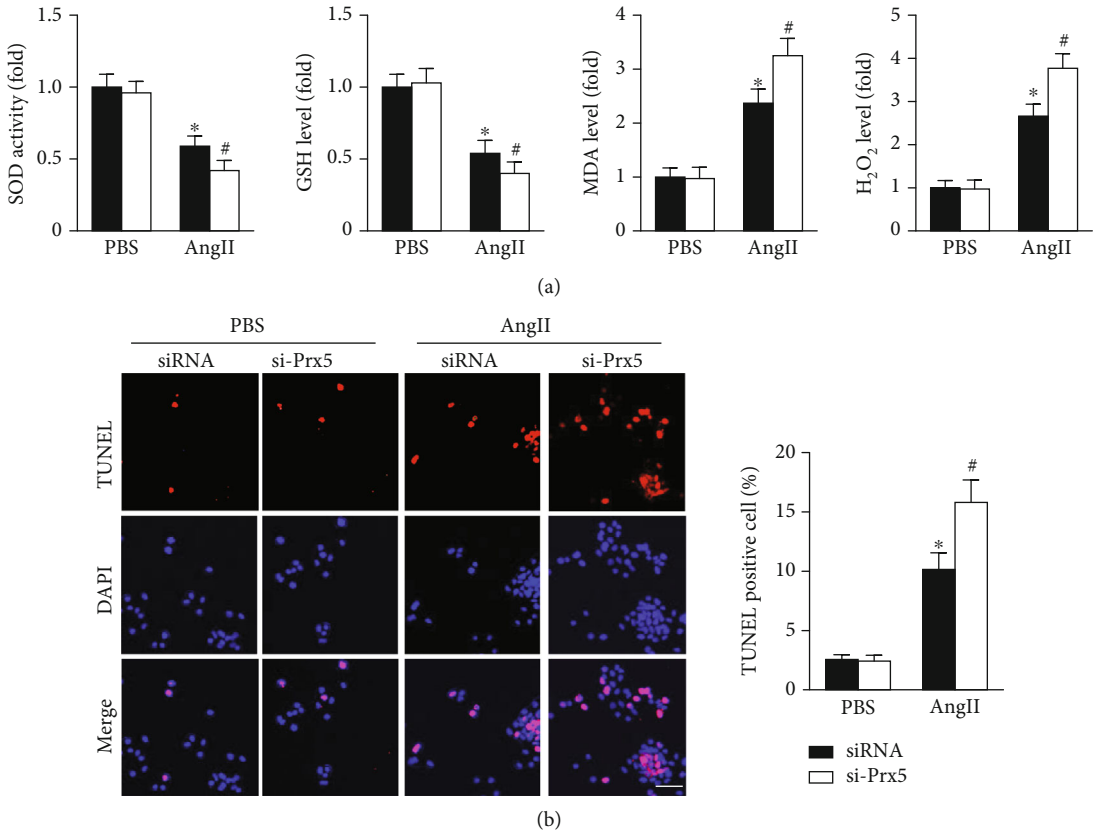

FIGURE 7: Prx5 knockdown accelerates AngII-induced oxidative stress and apoptosis in vitro. (a) Quantitative results of SOD activity and GSH, MDA, and H_2O_2 levels in the hearts of each group ($n = 6$). (c) TUNEL staining was performed in each group ($n = 4$; scale bar, 50 μm). $^*P < 0.05$ vs. the PBS group; $^\#P < 0.05$ vs. the AngII group.

functional damage and ultimately cardiac dysfunction [32–34]. There is likely benefit from the suppression of oxidative stress and countering excessive production of ROS in pathological cardiac hypertrophy therapy.

Many studies have shown that Prx5 has antioxidant protective functions and can effectively remove oxidative stress [17] [23]. Thus, we investigated whether Prx5 is involved in the occurrence of cardiac hypertrophy and dysfunction by regulating oxidative stress. The results showed that Prx5 knockdown markedly decreased SOD activity and GSH levels and increased MDA and H_2O_2 levels in TAC-treated mice. DHE staining results also showed that the oxidative stress level was dramatically increased in the Prx5 knockdown group after TAC surgery. Consistent with the in vivo results, Prx5 knockdown accelerated AngII-induced oxidative stress in vitro. These results indicate that the deterioration effect of Prx5 knockdown is related to oxidative stress.

Apoptosis is known to contribute to various cardiovascular diseases, including heart failure, myocardial infarct, and reperfusion injury [35, 36]. Previous research has also shown that cardiac hypertrophy is related to a reduced cell number due to enhanced apoptosis [37, 38]. In addition, oxidative stress has been shown to be responsible for cardiomyocyte apoptosis [39–41]. Thus, we asked whether Prx5 affects cardiomyocyte apoptosis in pathological cardiac hypertrophy. The results showed that the expression of Bax was upregulated, the expression of Bcl-2 was lower, and there were more TUNEL-positive cells in the TAC group than in the sham group. These effects were further augmented by Prx5 knockdown. In addition, the results further confirmed the in vitro cell experiments, indicating that the deterioration effect of Prx5 knockdown is associated with cardiomyocyte apoptosis.

As intracellular signaling proteins, MAPKs have been shown to regulate various cellular processes, including cell size, cell growth, and cell survival, in response to extracellular stimuli [41–43]. It is well established that the activation of MAPK signaling increases cardiac damage and exacerbates pathological cardiac hypertrophy [44–46]. In this study, Prx5 knockdown accelerated pressure overload-induced cardiac hypertrophy and dysfunction. However, the role of Prx5 in MAPK signaling activation in pathological cardiac hypertrophy was unclear. Thus, we examined the phosphorylation and total expression of ERK/JNK/p38 in hypertrophic hearts and AngII-stimulated cardiomyocytes. The results showed that Prx5 knockdown significantly induced the phosphorylation of ERK/JNK/p38 in the TAC group, but the expression of total ERK/JNK/p38 remained unchanged. These results indicate that the deterioration effect of Prx5 knockdown is associated with activation of MAPK signaling.

4.1. Clinical Significance. Pathological cardiac hypertrophy is a common pathophysiological process of various

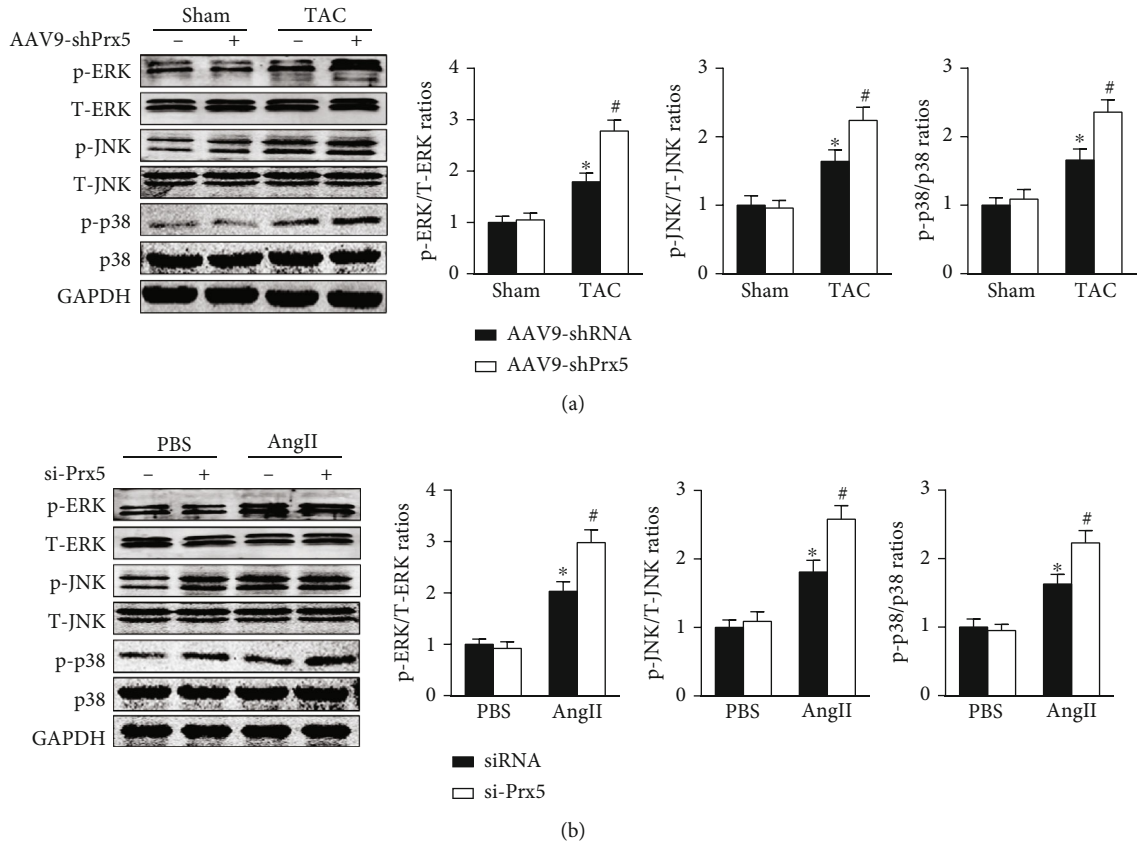

Figure 8: Effect of Prx5 on the MAPK signaling pathway. (a) The expression of p-ERK, t-ERK, p-JNK, t-JNK, p-p38, and p38 in the heart was measured by Western blotting ($n = 4$). (b) The expression of p-ERK, ERK, p-JNK, JNK, p-p38, and p38 in NVCMs was measured by Western blotting ($n = 4$). $^{*}P < 0.05$ vs. the sham or PBS group; $^{\#}P < 0.05$ vs. the TAC or AngII group.

cardiovascular diseases, including hypertension, myocardial infarction, and heart failure. Currently, there is no specific treatment to effectively reverse cardiac pathological hypertrophy and reduce the morbidity and mortality of heart failure. In this study, we demonstrated that Prx5 knockdown accelerated pressure overload-induced cardiac hypertrophy and dysfunction in mice by activating oxidative stress and cardiomyocyte apoptosis. Importantly, heart deterioration caused by Prx5 knockdown was related to MAPK activation. These findings provided a new target for the prevention and treatment of cardiac hypertrophy and heart failure.

4.2. Study Limitations. This study was subject to the following limitations. First, as pathological cardiac hypertrophy is a multifactorial syndrome, we cannot exclude the possibility that Prx5 utilizes other pathways to protect the heart under pressure overload. Thus, more research is needed to determine the mechanism underlying the cardioprotective effects of Prx5. In addition, in our study, mice received a heart injection of AAV9-shPrx5 to knock down Prx5 in the myocardium. However, animals with cardiac-specific overexpression or knockout of Prx5 may more precisely demonstrate the important function of Prx5 in pathological cardiac hypertrophy and dysfunction.

Taken together, our results have uncovered novel insights into the regulation of pathological cardiac hypertrophy and dysfunction by Prx5. The results showed that Prx5 knockdown accelerates pressure overload-induced cardiac hypertrophy and dysfunction. Our data indicate that Prx5 may be an attractive target for the prevention and treatment of pathological cardiac hypertrophy and heart failure.

Data Availability

We declare that the materials described in the manuscript, including all relevant raw data, will be freely available to any scientist wishing to use them for noncommercial purposes, without breaching participant confidentiality.

Conflicts of Interest

No conflicts of interest are declared by the authors.

Authors' Contributions

Chaoliang Tang was involved in the design and execution of experiments, data analysis, and manuscript writing. Zhetao Zhang and Fei Tang were involved in the design of the study, data analysis, and manuscript writing. Chengyun Hu, Feibiao Dai, Jiawu Wang, Lai Jiang, Di Wang, Jie Gao, Jun Huang, and Jianfeng Luo were all involved in the execution of experiments and data analysis. All authors provided final

approval of the version to be submitted. Chengyun Hu, Feibiao Dai, and Jiawu Wang contributed equally to this work.

Acknowledgments

The authors are grateful for Mr. Kai Zhang's enthusiastic support and contribution to the design of graphics. This study was supported by grants from the National Natural Science Foundation of China (grant no. 81801175 to Chaoliang Tang), the China Postdoctoral Science Foundation (grant no. 2019M662179 to Chaoliang Tang), and the Anhui Province Postdoctoral Science Foundation (grant no. 2019B324 to Chaoliang Tang).

References

[1] S. A. Mohammed, B. Paramesha, Y. Kumar, U. Tariq, S. K. Arava, and S. K. Banerjee, "Allylmethylsulfide, a sulfur compound derived from garlic, attenuates isoproterenol-induced cardiac hypertrophy in rats," *Oxidative Medicine and Cellular Longevity*, vol. 2020, Article ID 7856318, 15 pages, 2020.

[2] J. Paavola, T. Alakoski, J. Ulvila et al., "Vezf1 regulates cardiac structure and contractile function," *eBioMedicine*, vol. 51, article 102608, 2020.

[3] J. Cao, D. B. Cowan, and D. Z. Wang, "tRNA-derived small RNAs and their potential roles in cardiac hypertrophy," *Frontiers in Pharmacology*, vol. 11, article 572941, 2020.

[4] M. Nakamura and J. Sadoshima, "Mechanisms of physiological and pathological cardiac hypertrophy," *Nature Reviews. Cardiology*, vol. 15, no. 7, pp. 387–407, 2018.

[5] C. Li, F. Liu, S. Liu et al., "Elevated myocardial SORBS2 and the underlying implications in left ventricular noncompaction cardiomyopathy," *eBioMedicine*, vol. 53, article 102695, 2020.

[6] N. Kastner, K. Zlabinger, A. Spannbauer et al., "New insights and current approaches in cardiac hypertrophy cell culture, tissue engineering models, and novel pathways involving non-coding RNA," *Frontiers in Pharmacology*, vol. 11, article 1314, 2020.

[7] S. Kumari, P. B. Katare, R. Elancheran et al., "Musa balbisiana fruit rich in polyphenols attenuates isoproterenol-induced cardiac hypertrophy in rats via inhibition of inflammation and oxidative stress," *Oxidative Medicine and Cellular Longevity*, vol. 2020, Article ID 7147498, 14 pages, 2020.

[8] C. B. Zheng, W. C. Gao, M. Xie et al., "Ang II promotes cardiac autophagy and hypertrophy via Orai 1/STIM1," *Frontiers in Pharmacology*, vol. 12, article 622774, 2021.

[9] G. Q. Zhang, S. Q. Wang, Y. Chen et al., "MicroRNAs regulating mitochondrial function in cardiac diseases," *Frontiers in Pharmacology*, vol. 12, article 663322, 2021.

[10] S. G. Rhee, H. A. Woo, and D. Kang, "The role of peroxiredoxins in the transduction of H2O2Signals," *Antioxidants & Redox Signaling*, vol. 28, no. 7, pp. 537–557, 2018.

[11] S. Wang, L. Yu, G. Sun et al., "Danhong injection protects hemorrhagic brain by increasing peroxiredoxin 1 in aged rats," *Frontiers in Pharmacology*, vol. 11, p. 346, 2020.

[12] L. Jiang, Y. Gong, Y. Hu et al., "Peroxiredoxin-1 overexpression attenuates doxorubicin-induced cardiotoxicity by inhibiting oxidative stress and cardiomyocyte apoptosis," *Oxidative Medicine and Cellular Longevity*, vol. 2020, Article ID 2405135, 11 pages, 2020.

[13] S. Jaiswal, B. Joshi, J. Chen et al., "Membrane bound peroxiredoxin-1 serves as a biomarker forIn VivoDetection of sessile serrated adenomas," *Antioxidants & Redox Signaling*, 2021.

[14] C. Tang, G. Yin, C. Huang et al., "Peroxiredoxin-1 ameliorates pressure overload-induced cardiac hypertrophy and fibrosis," *Biomedicine & Pharmacotherapy*, vol. 129, article 110357, 2020.

[15] S. Matsushima, T. Ide, M. Yamato et al., "Overexpression of mitochondrial peroxiredoxin-3 prevents left ventricular remodeling and failure after myocardial infarction in mice," *Circulation*, vol. 113, no. 14, pp. 1779–1786, 2006.

[16] B. Knoops, J. Goemaere, V. Van der Eecken, and J. P. Declercq, "Peroxiredoxin 5: structure, mechanism, and function of the mammalian atypical 2-Cys peroxiredoxin," *Antioxidants & Redox Signaling*, vol. 15, no. 3, pp. 817–829, 2011.

[17] Y. Ji, S. Chae, H. K. Lee et al., "Peroxiredoxin 5 controls vertebrate ciliogenesis by modulating mitochondrial reactive oxygen species," *Antioxidants & Redox Signaling*, vol. 30, no. 14, pp. 1731–1745, 2019.

[18] Z. Wang, X. J. Zhang, Y. X. Ji et al., "The long noncoding RNA *Chaer* defines an epigenetic checkpoint in cardiac hypertrophy," *Nature Medicine*, vol. 22, no. 10, pp. 1131–1139, 2016.

[19] Y. Qiao, T. Hu, B. Yang et al., "Capsaicin Alleviates the Deteriorative Mitochondrial Function by Upregulating 14-3-3η in Anoxic or Anoxic/Reoxygenated Cardiomyocytes," *Oxidative Medicine and Cellular Longevity*, vol. 2020, Article ID 1750289, 16 pages, 2020.

[20] X. Chen, X. Cao, W. Xiao, B. Li, and Q. Xue, "PRDX5 as a novel binding partner in Nrf2-mediated NSCLC progression under oxidative stress," *Aging*, vol. 12, no. 1, pp. 122–137, 2020.

[21] M. H. Kim, H. J. Lee, S. R. Lee et al., "Peroxiredoxin 5 inhibits glutamate-induced neuronal cell death through the regulation of calcineurin-dependent mitochondrial dynamics in HT22 cells," *Molecular and Cellular Biology*, vol. 39, no. 20, 2019.

[22] F. Plaisant, A. Clippe, D. Vander Stricht, B. Knoops, and P. Gressens, "Recombinant peroxiredoxin 5 protects against excitotoxic brain lesions in newborn mice," *Free Radical Biology & Medicine*, vol. 34, no. 7, pp. 862–872, 2003.

[23] M. H. Kim, S. J. Park, J. H. Kim et al., "Peroxiredoxin 5 regulates adipogenesis-attenuating oxidative stress in obese mouse models induced by a high-fat diet," *Free Radical Biology & Medicine*, vol. 123, pp. 27–38, 2018.

[24] G. Wang, W. C. Zhong, Y. H. Bi et al., "The prognosis of peroxiredoxin family in breast cancer," *Cancer Management and Research*, vol. 11, pp. 9685–9699, 2019.

[25] R. D'Oria, R. Schipani, A. Leonardini et al., "The role of oxidative stress in cardiac disease: from physiological response to injury factor," *Oxidative Medicine and Cellular Longevity*, vol. 2020, Article ID 5732956, 29 pages, 2020.

[26] K. Hou, J. Shen, J. Yan et al., "Loss of TRIM21 alleviates cardiotoxicity by suppressing ferroptosis induced by the chemotherapeutic agent doxorubicin," *eBioMedicine*, vol. 69, article 103456, 2021.

[27] Q. Jin, Y. Jiang, L. Fu, Y. Zheng, Y. Ding, and Q. Liu, "Wenxin granule ameliorates hypoxia/reoxygenation-induced oxidative stress in mitochondria via the PKC-delta/NOX2/ROS pathway in H9c2 cells," *Oxidative Medicine and Cellular Longevity*, vol. 2020, Article ID 3245483, 16 pages, 2020.

[28] X. H. Xie, J. B. Liao, F. Fang et al., "Jian-Gan-Xiao-Zhi decoction ameliorates high-fat high-carbohydrate diet-induced

non-alcoholic fatty liver disease and insulin resistance by regulating the AMPK/JNK pathway," *Traditional Medicine Research*, vol. 6, no. 1, p. 4, 2021.

[29] A. J. P. O. de Almeida, M. S. de Almeida Rezende, S. H. Dantas et al., "Unveiling the role of inflammation and oxidative stress on age-related cardiovascular diseases," *Oxidative Medicine and Cellular Longevity*, vol. 2020, Article ID 1954398, 20 pages, 2020.

[30] A. W. Rookyard, J. Paulech, S. Thyssen et al., "A global profile of reversible and irreversible cysteine redox post-translational modifications during myocardial ischemia/reperfusion injury and antioxidant intervention," *Antioxidants & Redox Signaling*, vol. 34, no. 1, pp. 11–31, 2021.

[31] Z. Cai, Z. Wang, R. Yuan et al., "Redox-sensitive enzyme SENP3 mediates vascular remodeling via de-SUMOylation of β-catenin and regulation of its stability," *eBioMedicine*, vol. 67, article 103386, 2021.

[32] S. Peng, X. F. Lu, Y. D. Qi et al., "LCZ696 Ameliorates Oxidative Stress and Pressure Overload-Induced Pathological Cardiac Remodeling by Regulating the Sirt3/MnSOD Pathway," *Oxidative Medicine and Cellular Longevity*, vol. 2020, Article ID 9815039, 15 pages, 2020.

[33] M. Zhang, Y. Xu, J. Chen et al., "Beta3-Adrenergic receptor activation alleviates cardiac dysfunction in cardiac hypertrophy by regulating oxidative stress," *Oxidative Medicine and Cellular Longevity*, vol. 2021, Article ID 3417242, 13 pages, 2021.

[34] X. Yan, Q. Y. Zhang, Y. L. Zhang, X. Han, S. B. Guo, and H. H. Li, "Gallic acid attenuates angiotensin II-induced hypertension and vascular dysfunction by inhibiting the degradation of endothelial nitric oxide synthase," *Frontiers in Pharmacology*, vol. 11, p. 1121, 2020.

[35] L. Gao, A. Feng, C. Li, S. Schmull, and H. Sun, "Decellularized aortic scaffold alleviates H_2O_2-induced inflammation and apoptosis in CD34+ progenitor cells while driving neovasculogenesis," *BioMed Research International*, vol. 2020, Article ID 6782072, 10 pages, 2020.

[36] W. Y. Abdelzaher, S. M. Ahmed, N. N. Welson, K. F. Alsharif, G. E. Batiha, and D. A. A. Labib, "Dapsone ameliorates isoproterenol-induced myocardial infarction via Nrf2/ HO-1; TLR4/ TNF-α signaling pathways and the suppression of oxidative stress, inflammation, and apoptosis in rats," *Frontiers in Pharmacology*, vol. 12, article 669679, 2021.

[37] Y. Liang, Q. Q. Niu, and Y. H. Zhao, "Pharmacological research progress of ursolic acid for the treatment of liver diseases," *Traditional Medicine Research*, vol. 6, no. 4, p. 38, 2021.

[38] Y. Cheng, A. Shen, X. Wu et al., "Qingda granule attenuates angiotensin II-induced cardiac hypertrophy and apoptosis and modulates the PI3K/AKT pathway," *Biomedicine & Pharmacotherapy*, vol. 133, article 111022, 2021.

[39] M. Jin, H. Yu, X. Jin, L. Yan, J. Wang, and Z. Wang, "*Dracocephalum moldavica* L. extracts protect H9c2 cardiomyocytes against H_2O_2-induced apoptosis and oxidative stress," *BioMed Research International*, vol. 2020, Article ID 8379358, 12 pages, 2020.

[40] M. Yuan, M. Gong, Z. Zhang et al., "Hyperglycemia induces endoplasmic reticulum stress in atrial cardiomyocytes, and mitofusin-2 downregulation prevents mitochondrial dysfunction and subsequent cell death," *Oxidative Medicine and Cellular Longevity*, vol. 2020, Article ID 6569728, 14 pages, 2020.

[41] Y. T. Wu, L. P. Xie, Y. Hua et al., "Tanshinone I inhibits oxidative stress-induced cardiomyocyte injury by modulating Nrf2 signaling," *Frontiers in Pharmacology*, vol. 12, article 644116, 2021.

[42] G. P. Caviglia, "Edaravone and MAPK pathway: the key role of gut permeability," *Minerva Medica*, vol. 111, no. 2, p. 181, 2020.

[43] Q. Ling, F. Li, X. Zhang et al., "MAP4K1 functions as a tumor promotor and drug mediator for AML via modulation of DNA damage/repair system and MAPK pathway," *eBioMedicine*, vol. 69, article 103441, 2021.

[44] H. N. Siti, J. Jalil, A. Y. Asmadi, and Y. Kamisah, "Parkia speciosa Hassk. Empty pod extract alleviates angiotensin II-induced cardiomyocyte hypertrophy in H9c2 cells by modulating the Ang II/ROS/NO Axis and MAPK pathway," *Frontiers in Pharmacology*, vol. 12, article 741623, 2021.

[45] T. Zhao, H. J. Kee, L. Bai, M. K. Kim, S. J. Kee, and M. H. Jeong, "Selective HDAC8 inhibition attenuates isoproterenol-induced cardiac hypertrophy and fibrosis via p 38 MAPK pathway," *Frontiers in Pharmacology*, vol. 12, article 677757, 2021.

[46] S. Tamura, T. Marunouchi, and K. Tanonaka, "Heat-shock protein 90 modulates cardiac ventricular hypertrophy *via* activation of MAPK pathway," *Journal of Molecular and Cellular Cardiology*, vol. 127, pp. 134–142, 2019.

Hindawi
Oxidative Medicine and Cellular Longevity
Volume 2022, Article ID 5563759, 31 pages
https://doi.org/10.1155/2022/5563759

Review Article

A Common Feature of Pesticides: Oxidative Stress—The Role of Oxidative Stress in Pesticide-Induced Toxicity

Rasheed O. Sule,[1] **Liam Condon**,[1] **and Aldrin V. Gomes**[1,2]

[1]*Department of Neurobiology, Physiology and Behavior, University of California, Davis, Davis, CA 95616, USA*
[2]*Department of Physiology and Membrane Biology, University of California, Davis, Davis, CA 95616, USA*

Correspondence should be addressed to Aldrin V. Gomes; avgomes@ucdavis.edu

Received 28 February 2021; Accepted 17 December 2021; Published 19 January 2022

Academic Editor: Xiaoyuan Zhou

Pesticides are important chemicals or biological agents that deter or kill pests. The use of pesticides has continued to increase as it is still considered the most effective method to reduce pests and increase crop growth. However, pesticides have other consequences, including potential toxicity to humans and wildlife. Pesticides have been associated with increased risk of cardiovascular disease, cancer, and birth defects. Labels on pesticides also suggest limiting exposure to these hazardous chemicals. Based on experimental evidence, various types of pesticides all seem to have a common effect, the induction of oxidative stress in different cell types and animal models. Pesticide-induced oxidative stress is caused by both reactive oxygen species (ROS) and reactive nitrogen species (RNS), which are associated with several diseases including cancer, inflammation, and cardiovascular and neurodegenerative diseases. ROS and RNS can activate at least five independent signaling pathways including mitochondrial-induced apoptosis. Limited *in vitro* studies also suggest that exogenous antioxidants can reduce or prevent the deleterious effects of pesticides.

1. Introduction

The term pesticide is generally used to identify agrochemicals such as bactericides, fungicides, herbicides, insecticides, or rodenticides [1]. Pesticides are a group of chemicals, and sometimes microorganisms (e.g., viruses), that are used for the eradication of insects, weeds, fungi, and bacteria [1, 2]. Pesticides can be grouped into different chemical families, such as organochlorines, organophosphates, organofluorines, carbamates, pyrethroids, bipyridyl herbicides, triazine herbicides, triazoles, and chloroacetanilide herbicides [2]. Globally, about 2 million tons of pesticides are being utilized each year [3]. China is the largest pesticide-producing nation, followed by the United States and Argentina [3]. Due to the continuous rise in the worldwide population, there has been an increase in demand for agricultural products such as pesticides [4].

The World Health Organization has estimated that about 3 million workers in developing countries experience severe poisoning from pesticides each year, of which approximately 18,000 of them eventually die [5]. The broad use of pesticides for agricultural and nonagricultural purposes (e.g., industrial, commercial, and individual households) around the world indicates how important these compounds are, but the adverse risks involved for the environment, wildlife, and human health are not well investigated [6]. Individuals who apply pesticides in agricultural, occupational, or residential settings are at a high risk of direct exposure. However, the general population can also be exposed to pesticides and their degradation products indirectly at low levels through water, air, dust, and food [7]. Pesticide contamination of surface waters has been well documented worldwide and constitutes a major issue that gives rise to concerns at local, regional, national, and global levels [8]. While these indirect exposure routes involve low levels of pesticide, long-term exposure to these routes could be harmful to human health [7]. At low doses of exposure, pesticides do not seem to produce any permanent harmful effects to adult humans [9]. However, individuals who reside close to fields where pesticides are applied and agricultural workers such as

mixers, loaders, and applicators, who are in direct contact with pest control agents, exhibit pesticide poisoning [10, 11]. Other epidemiological studies have suggested that high levels of pesticide exposure are associated with increased risk of chronic diseases, including cancers, cardiotoxicity, Parkinson's disease, diabetes mellitus, neurological deficits, birth defects, and reproductive disorders [12, 13]. The increased risk of various diseases may be due to pesticides being absorbed into the body and accumulated in fat, liver, kidneys, and salivary glands [14].

Prometryn, a triazine herbicide, is relatively persistent in waters, soil, and even in air near its production or application sites and was detected at a concentration of 3–6.1 μg/L in different rivers and lakes in Europe [8]. Previous studies have shown that other triazine herbicide was found at levels as high as 21 ppb in groundwater, 42 ppb in surface waters, 102 ppb in river basins in agricultural areas, and up to 224 ppb in Midwestern U.S. streams during the summer of 1996. Triazine concentrations of up to 108 μg/L have been reported in North America rivers [15]. In addition, all triazine herbicides and their degradation products are persistent in the environment, especially in air and water, and these pesticides can damage human cardiac and immune systems and endanger the health of humans, animals, and plants [16].

A large number of hazardous organic chemicals are pesticides, and the Stockholm Convention on Persistent Organic Pollutants states that nine out of the twelve most dangerous and persistent organic chemicals in the environment belong to the organochlorine pesticide group [17]. There have been several calls and campaigns for "less pesticides, safer food" around the world especially in the European Union (EU) where over one million EU citizens from 22 member states supported an initiative to ban a broad-spectrum systemic herbicide called glyphosate due to its possibly carcinogenic effects on humans. However, pest resistance, hygiene control, and the unending demand for agriproducts have resulted in an increase in the formulation of new, more potent pesticides [18]. Long-term exposures to pesticides, due to occupational or environmental exposures, are capable of disrupting the physiology of different organs in the body, including those of the nervous, endocrine, immune, reproductive, renal, cardiovascular, and respiratory systems [19]. Pesticides' effects could be physiological or biological, causing changes at the molecular, cellular, or tissue level. Although the underlying molecular mechanisms of how pesticides induce biochemical changes are not well understood, investigation of previous research on pesticides suggest that pesticides all induce oxidative stress. Oxidative stress is an imbalance between the production of ROS and the ability of the defense system to actively detoxify and neutralize the excess ROS [20]. The present review focuses on oxidative stress induced by dominant pesticide groups (e.g., organochlorines, organophosphates, carbamates, and triazines) with emphasis on oxidative stress biomarkers and ROS generation from genetic and biochemical studies. This review also includes 3 figures and 6 supplementary tables summarizing the signaling pathways and pesticide concentration levels involved in pesticide-induced oxidative stress.

1.1. Pesticides and Organ Toxicity. Most pesticides investigated seem to damage many animal organs and tissues (supplemental table 1). Investigation of the damaged tissues suggests a multitarget mechanism, with many different pathways being affected by the pesticides. However, our understanding of the targeting of multiple sites and signaling pathways in cells is limited. While there are very few studies published discussing the toxic effects of pesticides at the systematic level, one of the most widely investigated pesticides, paraquat, is known to cause damage to the kidneys, lungs, heart, gastrointestinal tract, nervous system, and the immune system [21–23]. Some studies have also suggested links between pesticides and cancers. 1,1,1-trichloro-2,2-bis(p-chlorophenyl)ethane (DDT), and its metabolites have been associated with liver, breast, and testicular cancers [24–26]. Due to the lack of specific studies with respect to the many effects of pesticide on various tissues, it is difficult to determine if specific tissue injuries caused by pesticides are unique. The current scientific studies suggest that irrespective of the target tissue, toxicity caused by pesticides is associated with oxidative stress. Some common characteristics of oxidative stress include increased protein oxidation (carbonylation), lipid peroxidation, nucleic acid oxidation (8-OHdG), and changes in the levels of antioxidants such as glutathione and the activities of antioxidant enzymes [27].

1.2. Reactive Oxygen Species (ROS) and Pesticides. Reactive oxygen species (ROS) is a term commonly mentioned in biology and medicine. This term can be defined as oxygen-containing reactive species. ROS is a collective term that includes superoxide ($O_2^{\bullet-}$), hydrogen peroxide (H_2O_2), hydroxyl radical ($_{\bullet}OH$), singlet oxygen ($^1O_2$), peroxyl radical ($ROO^{\bullet}$), alkoxyl radical ($RO^{\bullet}$), lipid hydroperoxide (LOOH), peroxynitrite ($ONOO^-$), hypochlorous acid (HOCl), and ozone (O_3) [28]. ROS are byproducts of normal cellular metabolic processes that are required to generate energy for life processes [29]. They are produced in the reactions catalyzed by the electron transport chain, NAD(P)H oxidase, and some other specialized oxidases and are an inevitable by-product of many redox reactions. However, the amount of ROS produced in a cell under normal conditions is relatively small. As such, ROS are able to serve as signaling molecules to regulate biological and physiological processes [30]. Recent evidence also suggests that ROS function as important physiological regulators of intracellular signaling pathways [31].

During normoxia, there is a steady-state balance between ROS and cellular antioxidant systems. However, overproduction of ROS in intra- or extracellular spaces can occur due to exposure to xenobiotics and other environmental factors which can result in the onset of cellular dysfunction and apoptosis [32]. ROS are capable of causing damage to biomolecules leading to cell and tissue injury [32]. Antioxidants act by reacting with ROS and RNS to neutralize or terminate the chain reaction before key molecules in the body are affected [20]. The major enzymatic antioxidant defense mechanisms consist of different forms of superoxide dismutases (SODs), catalase (CAT), and the glutathione

peroxidases (GPXs). SODs are thought to provide a first line of defense against oxygen radicals, specifically the superoxide anion ($O_2^{\bullet-}$), which is the major ROS produced by mitochondrial respiration and various metabolic reactions. The SODs remove the potentially dangerous superoxide anions from biological systems by converting them to H_2O_2, while CAT found in peroxisomes catalyzes the conversion of two molecules of H_2O_2 to O_2 and two molecules of H_2O [33]. The most abundant intracellular antioxidant, glutathione (GSH), is involved in the protection of cells against oxidative stress [34]. However, exposure to pesticides seem to be associated with significantly increased ROS and oxidative stress induction, beyond what the intrinsic cellular antioxidant system can reduce to normal physiological levels (Figure 1, Tables 1 and 2, and Supplemental Tables 1-6).

1.3. Reactive Nitrogen Species (RNS) and Pesticides. Reactive nitrogen species (RNS) belong to a family of nitrogen moieties that are closely associated with oxygen [35]. The interaction between exogenously and endogenously produced nitric oxide (NO) with oxidants such as hydrogen peroxide (H_2O_2), superoxide anion (O_2^-), and reductants such as lithium aluminum hydride ($LiAlH_4$) typically gives rise to RNS [36]. RNS can be classified as nitric oxide-derived compounds, including nitroxyl anion (NO^-) (derived from the reduction of $\cdot NO$), nitrosonium cation (NO^+), higher oxides of nitrogen (NO_2, N_2O_4, etc.), S-nitrosothiols (RSNO), and dinitrosyl iron complexes [37]. NO is a ubiquitous intracellular messenger that regulates physiological functions including neural and cardiovascular activities. However, under pathologic conditions, NO can become deleterious because of its high reactivity with other free radicals, such as O_2^- [37]. NO^+ is created during the removal of one electron from $\cdot NO$. NO^+ can react with nucleophilic centers, producing nitroso compounds. Nitrosyl halides are liberated when •NO reacts with fluorine, chlorine, or bromine [35].

Although RNS play vital roles in numerous biological processes such as the physiological regulation of smooth muscle cells, cardiomyocytes, platelets, and nervous and juxtaglomerular cells, they are harmful to the cells if produced and present in excessive amounts [37, 38]. RNS has pleiotropic properties on cellular targets, including effects even after both posttranslational modifications and interaction of targets with ROS [37]. These effects are likely due to increased levels of RNS reacting with different biomolecules such as lipids, DNA and RNA bases, metal cofactors, and proteins. The interplay of RNS with various cellular components leads to cellular abnormalities, cell injury, and cell death via the induction of nitrosative stress. Nitrosative stress can occur when NO or related species are induced during exposure to certain xenobiotic factors such as pesticides, leading to the nitrosylation of critical protein cysteine thiols (S-nitrosylation) and metallocofactors of proteins. Nitrosylation is the addition of a nitroso (–NO) group to an active metal ion center or thiol of a protein [28].

A comprehensive study of epidemiologic and toxicologic literature implicates oxidative stress, ROS, and RNS as culprits in the damage to lipids, DNA, and proteins induced by pesticides [39, 40]. Figure 2 shows a schematic diagram summarizing some of the major effects of pesticides that lead to RNS and subsequent oxidative stress. Diquat (1,1′-ethylene-2,2′-bipyridinium ion) (DQ), a nonselective quick-acting herbicide, is used as a contact and preharvest desiccant to control terrestrial and aquatic vegetation. Fu et al. found that DQ-induced oxidative stress was caused by ROS. However, this oxidative stress was also partly caused by increased RNS generation by peroxynitrite (ONOO–) generation in hepatocytes [41]. Wang et al. found that permethrin (PER) may exhibit toxic effects on animals by NO generation [40]. A study by Jin et al. revealed that PER significantly increased the mRNA expression of induced nitric oxide synthase (iNOS) after exposure of zebrafish to PER [42]. Another study found increased NO levels in the plasma of rats treated with a low dose of PER (34.05 mg/kg b.w.) [43]. When Afolabi et al. exposed the insecticide cypermethrin (CYP) to rats, they found a significant increase in the plasma concentration of 8-nitroguanine (8-NO2Gua). CYP treatment resulted in over 200% increase in the level of 8-NO2Gua when compared with the control [44]. The elevated plasma 8-NO2Gua level in CYP-exposed rats suggests that CYP plays a role in nitrosative stress and possesses genotoxic and mutagenic potential [44]. The presence of NO and NO metabolites in blood could be a possible source for RNS that causes damage to several organs and tissues.

It has been hypothesized that the damage to cellular macromolecules (nucleic acids, proteins, and lipids) by increased ROS and RNS caused by long-term pesticide exposure leads to cell death and overall tissue damage [45]. It is worth highlighting that RNS and ROS usually work together when they are present in a cell. Under conditions such as pesticide toxicity, NO is generated via the expression of iNOS which then reacts with the superoxide radical to form highly reactive peroxynitrite (ONOO–). ONOO– then causes cellular damage by interacting with biomolecules. One such reaction is that of ONOO– with guanine which results in nitrative and oxidative DNA lesions, such as 8-NO2Gua and 8-oxodeoxyguanosine (8-OHdG), respectively [46]. Previous findings have suggested that 8-NO2Gua formation occurred to a greater extent in cancerous tissues than noncancerous tissues [47]. This supports previous studies that have linked pesticide exposure with cancer [48, 49]. Although RNS is not as well studied as ROS, the experimental data for RNS suggests that RNS can cause tissue damage and should be investigated to a greater extent, especially to determine if all pesticides can cause RNS.

1.4. Pesticides and Oxidative Stress Generation. The low molecular weight and high liposolubility of pesticides increases their absorption and toxicity level [50]. Organophosphate (OP) and carbamate pesticides produce their effects through the inhibition of carboxyl ester hydrolases, in particular acetylcholinesterase, which leads to acetylcholine accumulation [50]. Moreover, some studies have suggested that acetylcholinesterase enzyme inhibition is associated with the increase in ROS in agricultural workers exposed to OP pesticides and bipyridyl herbicides (e.g.,

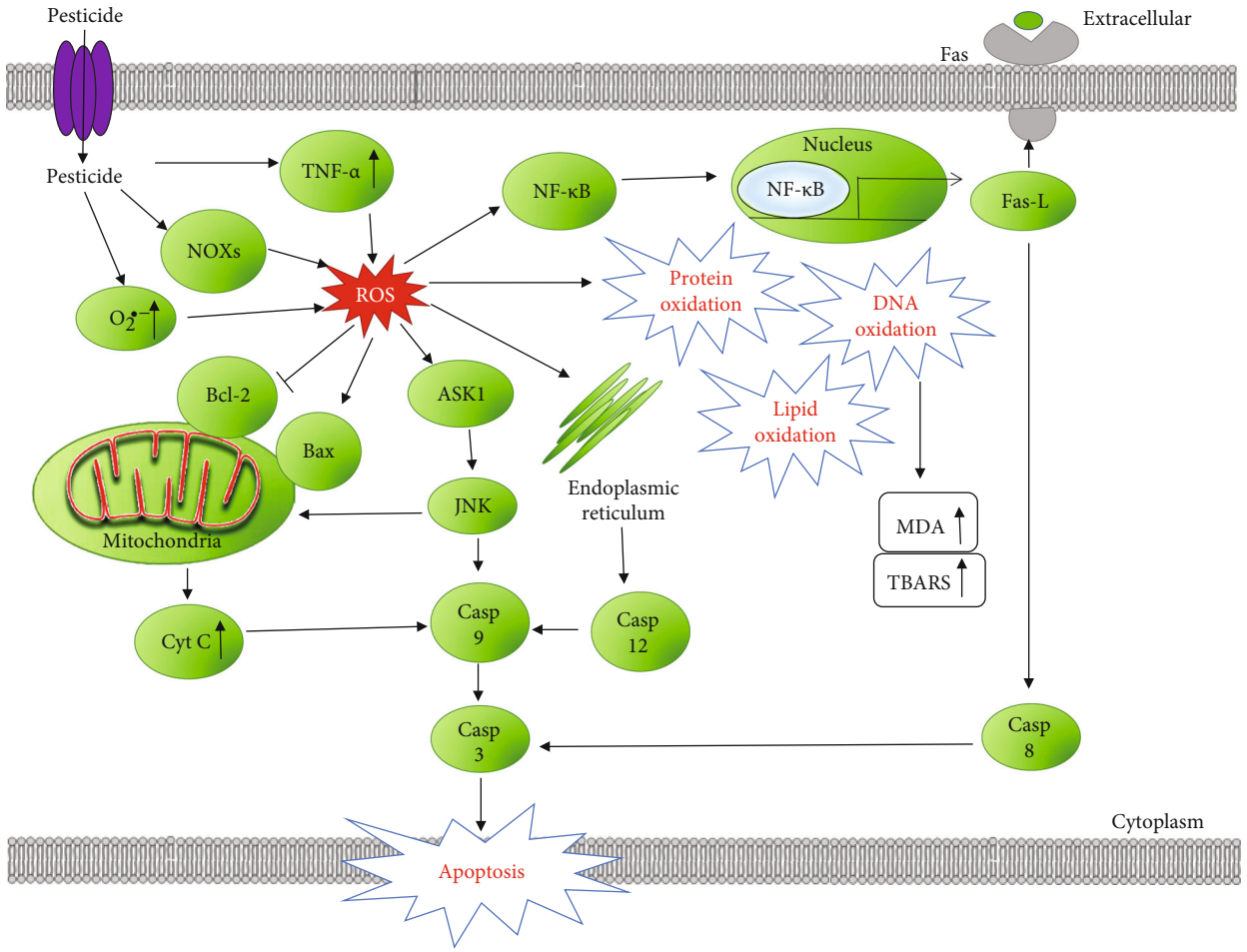

Figure 1: Schematic representation of signaling pathways involved in pesticide-induced reactive oxygen species (ROS) and oxidative stress. Pesticides increase NADPH oxidases (NOXs) and superoxide ($O_2^{\bullet-}$) levels, which leads to an increase in ROS signaling in the cell. Increased ROS may induce lipid, protein, and DNA oxidation, leading to various toxicities. These stressors lead to activation of TNFR1/TNF-α, MAPKs, NF-κB, and the mitochondrial apoptosis pathways. Continued stress leads to cell apoptosis and inflammation.

paraquat (PQ)). Oxidative stress can be induced by an increase in lipid peroxidation and a decrease in antioxidant capacity [51, 52]. Herein, some of the major classes of pesticides and the roles they play in oxidative stress generation are discussed.

1.5. Organophosphorus Pesticides. Quinalphos (QP), an organophosphorus (OP) pesticide, is used to control pests on various crops such as vegetables, fruits, cereals, rice, wheat, maize, coconut, tobacco, coffee, tea, sugarcane, jute, and cotton. Dwivedi et al. found that QP enhanced all the levels of adult rat hepatic antioxidant components, namely, SOD, CAT, GPx, and GSH-reductase, which take care of ROS generated *in vivo*. They also found a significant induction of hepatic P450 [53]. A list of OP pesticides and their effects on oxidative stress in different tissues is summarized in supplemental table 4.

Chlorpyrifos (CPF), a crystalline-kind OP insecticide, acaricide, and miticide, is mainly used to control foliage and soil-borne pests on a variety of food and feed crops [54]. Studies have implicated CPF and its derivatives in carcinogenesis [55]. Jung et al. demonstrated in their study that methyl parathion and CPF induced the production of inflammatory cytokines, such as tumor necrosis factor-α (TNF-α), interleukin-6 (IL-6), and interleukin-1β (IL-1β) in human hepatocellular carcinoma (HepG2) cells [56]. With regard to examining the deleterious effects of pesticides, Binukumar et al. found that rats chronically exposed to dichlorvos, another OP insecticide, displayed microglial activation with the induction of NADPH oxidase and proinflammatory cytokines (TNF-α, IL-1β, and IL-6) [57]. *In vitro* studies on human keratinocytes revealed the insecticide monocrotophos significantly increased NO, lactate dehydrogenase (LDH), malondialdehyde (MDA), nuclear changes, proinflammatory cytokines (TNF-α, IL-6, and IL-8), and ROS generation [58]. Several other studies conducted in rats exposed to OP pesticides have displayed similarly increased levels of proinflammatory cytokines [59–61].

Pesticides such as DQ do not bind covalently to macromolecules (i.e., lipids, proteins, and nucleic acids). However, they cause oxidative stress by generating ROS intracellularly via the reduction–oxidation (redox) cycling processes. DQ can easily cross the cell membrane and enter the cell through the dopamine transporter (DAT). While in the cell, DQ is

Table 1: The effects of the most commonly used pesticides in the agricultural market sector in 2012 on oxidative stress in different tissues.

Pesticide	Cell type/model system	ROS	SOD	GSH	CAT	GST	GPx	DD	LP	PC	AOC	MMP	Reference
Glyphosate	Human skin keratinocyte HaCaT cells	↑	↓										[178]
	Human liver carcinoma (HepG2) cells						↓	↑			↓		[179]
	Rat heart H9c2 cells											↓	[180]
	Adult albino male rats (liver)			↓					↑				[181]
	Caenorhabditis elegans					↑						↓	[182]
	Chlorella kessleri		↑	↑	↑				↑				[183]
Atrazine (ATR)	Male and female Balb/c mice	↑		↓									[184]
	Male mice (liver and kidney)		↓		↓	↓			↑		↓		[185]
	Male Wistar rats (erythrocytes)		↑	↓	↑	↑	↑						[155]
	Adult male Wistar rats (testes and epididymis)		↓		↓	↓			↑				[186]
	Male Wistar rats		↓	↓	↓				↑				[187]
	Adult male albino rats		↓	↓	↓		↓		↑				[188]
	Female Wistar rats				↓		↓		↑				[189]
	Murine microglial cells (BV-2)	↑											[190]
	Albino rats			↓	↑		↑	↑	↑				[191]
Metolachlor-S	*Scenedesmus obliquus (green algae)*	↑	↑		↑								[192]
	Parachlorella kessleri (microalga)	↑			↑				↑				[193]
	Wheat (*Triticum aestivum* L.)	↑	↑		↓				↑				[194]
2,4-Dichlorophenoxyacetic acid (2,4-D)	*Umbelopsis isabelline (Fungus)* pea (*Pisum sativum* L.)	↑	↑				↑		↑				[195, 196]
	Pea (*Pisum sativum* L.)		↑		↑		↑		↑				[196]
	Nongreen potato tuber callus		↑		↑	↑							[197]
	Male 7-week-old Kunming mice		↓		↓				↑				[198]
	Goldfish gills, *Carassius auratus*		↑		↑		↑		↑	↑			[199]
	Cnesterodon decemmaculatus			↑	↑	↑		↑					[200]
	Acanthospermum hispidum D.C., Asteraceae weed								↑				[201]
	Rat cerebellar granule cells	↑		↓	↓		↑						[202]
	Wistar rats		↓	↓	↓		↓		↑				[203]
	Wistar Albino rats		↓	↓	↓	↓	↓		↑	↑			[204]
	Male Wistar rats (liver)		↑↓		↓		↓		↑				[205]
	Male Wistar albino rats—plasma, liver, kidney, erythrocytes		↓		↓		↓		↑				[206]
	Male Wistar rats (liver)				↓								[207]
	Female B6C3F1 mice *peritoneal macrophages*			↓									[208]
Metam	*Soil bacteria*				↑↓				↑				[209]
Acetochlor	*Bufo raddei* tadpole liver							↑	↑		↓		[210]
	Female zebrafish	↑	↑		↑		↑						[211]
	Male C57BL/6 mice (testis)		↓	↓					↑				[212]
	GC-1 spermatogonia cell		↓	↓					↑				[212]
	Human liver carcinoma cells (HepG2)	↑	↓				↓					↓	[213]
	Zebrafish				↑		↑						[214]
	Primary human corneal epithelial (HCE) cells							↑	↑	↑			[215]

Table 1: Continued.

Pesticide	Cell type/model system	ROS	SOD	GSH	CAT	GST	GPx	DD	LP	PC	AOC	MMP	Reference
Chloropicrin	Human retinal pigment epithelial cells (ARPE-19)	↑											[216]
	Human lung epithelial cells (A549)	↑											[217]
	Gill tissues of Pacific oyster (Crassostrea gigas), blue mussels (Mytilus edulis)		↑	↑	↑		↑		↑				[218]
Chlorothalonil	*Polychaete Laeonereis acuta*								↑		↓		[219]
	Fish Danio rerio (gills)	↑				↑					↑		[220]
	Fish Danio rerio (liver)		↑						↑				[220]
	Isolated rat hepatocytes			↓					↑				[221]
	Botryllus schlosseri hemocytes			↓									[222]
	Male Wistar rats (liver)							↑					[223]
	Fresh water fish, *Channa punctatus*		↓	↓	↓				↑				[224]
Pendimethalin	Male Wistar rats (liver and kidney)		↓	↓	↓	↓		↑	↑	↑			[225]
	Human lymphocytes	↑						↑					[226]
	Rat bone marrow cells	↑		↓	↓			↑	↑				[226]
	Clarias batrachus (liver)		↑		↑				↑				[227]
	Fish *Channa punctatus* (brain)		↓	↓	↓	↓			↑	↑			[228]
	Fish *Channa punctatus* (gills, liver, kidney)			↓	↓	↓	↓		↑	↑			[229]
	Chinese hamster lung fibroblast (V79) cells	↑						↑					[230]
	Male mice (spleen and thymus)		↔	↓	↓		↓		↑				[145]
Ethephon	3T3 murine embryonic fibroblast (MEF) cells	↑						↑	↑				[231]
	Spinach (*Spinacia oleracea* L.)				↑								[232]
	Ipomoea cairica (Linn.) sweet	↑											[233]
	Carassius auratus goldfish blood and gills		↑		↑	↑			↑	↑			[234]
Mancozeb	Carassius auratus Goldfish—liver and kidney		↑		↑		↑		↑	↑			[235]
	Carassius auratus Goldfish—brain								↑	↑			[235]
	Cassia angustifolia		↑	↑	↑				↑				[236]
	Caenorhabditis elegans	↑				↑						↓	[237]
	Caenorhabditis elegans	↑				↑						↓	[238]
	Drosophila melanogaster	↑	↓	↓	↑	↑			↑				[239]
	Rat-1 fibroblasts, peripheral blood mononucleated cells (PBMC)	↑						↑					[240]
	Male NMRI mice		↓	↓	↓		↓		↑	↑	↓		[241]
	Rat thymocytes	↑										↓	[242]
	Human gastric adenocarcinoma (*AGS*) cells	↑										↓	[243]
	Immortalized murine mesencephalic dopaminergic (N27) cells	↑		↓				↑				↓	[80]

Table 1: Continued.

Pesticide	Cell type/model system	ROS	SOD	GSH	CAT	GST	GPx	DD	LP	PC	AOC	MMP	Reference
	Lund human mesencephalic (LUHMES) cells	↑						↑				↓	[80]
	Human neuroblastoma *SH-SY5Y* cells	↑											[244]
	Rat adrenal pheochromocytoma (PC12) cells	↑							↑				[245]
	Rat erythrocytes		↓		↓	↓			↑				[156]
Chlorpyrifos	Male Wistar rats		↓		↓		↑		↑				[63]
	Male Wistar rats (aorta, liver, plasma, and kidney)		↑						↑				[246]
	Male Swiss albino adult rats		↓	↓	↓		↓		↑				[247]
	Adult male Wistar rats	↑											[248]
	Male Wistar rats		↑		↑	↓	↓		↑				[249]
	Male Kunming mice	↑	↓	↓	↓		↓		↑				[250]
	Male Wistar rats (liver)											↓	[251]
	Soil bacteria				↓↑				↑				[209]
Metolachlor	Lettuce, bean, and pea seeds and leaves		↓		↓		↓						[252]
	8-week-old male rats		↓	↓		↓	↓		↑				[253]
	Wistar rats, liver		↓	↓	↓	↓			↑				[151]
	Albino rats, liver			↓	↓				↑				[254]
Propanil	Common carp (*Cyprinus carpio*) brain		↓	↓	↓				↑	↑			[255]
	Isolated mitochondria from potato tubers (*Solanum tuberosum)*											↓	[256]
	Nongreen potato tuber callus		↑		↑	↑							[197]
	Cnesterodon decemmaculatus			↑	↑	↑		↑					[200]
Dicamba	Isolated mitochondria Arabidopsis	↑											[257]
	Chinese hamster lung fibroblast (V79) cells	↑						↑					[230]
Trifluralin	Male Wistar albino rats—kidney, ureter, urinary bladder		↓				↓	↑	↑				[258]
	Chlamydomonas mexicana		↑		↑								[259]
	Drosophila melanogaster		↑		↑	↑		↑	↑	↑			[260]
	Male albino rats (plasma and liver)		↓	↓	↓		↑		↑				[261]
	Male rats (erythrocytes)			↓		↑			↑				[262]
	Albino rats		↓	↓	↓				↑				[263]
Acephate	*Human sperm*							↑					[264]
	Chinese hamster ovary (CHO-K1) cells			↑		↑	↑						[265]
	Porcine kidney proximal tubule *cell* line (*LLC-PK)*	↑							↑				[266]
	Human dopaminergic neuroblastoma cells (SK-N-SH)	↑							↑			↓	[267]

Table 1: Continued.

Pesticide	Cell type/model system	ROS	SOD	GSH	CAT	GST	GPx	DD	LP	PC	AOC	MMP	Reference
Paraquat (PQ)	Rat lung slices	↑											[268]
	Rat organotypic midbrain slice cultures	↑											[269]
	Rat primary mesencephalic cultures	↑											[270]
	Rat primary mesencephalic cultures	↑											[79]
	Human neural progenitor cells (hNPCs)		↓		↓				↑				[135]
	Human neural progenitor cells (hNPCs)	↑											[271]
	Human plasma								↑		↓		[51]
	Rat brain mitochondria	↑											[79]
	Nongreen potato tuber callus		↑		↑								[197]
	Amaranthus palmeri	↑	↑		↑								[272]
Glufosinate	Horseweed, palmer amaranth, kochia	↑	↑		↑				↑				[273]
	Chlorella vulgaris		↑		↑				↑				[274]

ROS: reactive oxygen species; SOD: superoxide dismutase; GSH: glutathione; CAT: catalase; GST: glutathione-S-transferase; GPx: glutathione peroxidase; DD: DNA damage; LP: lipid peroxidation; PC: protein carbonylation; AOC: antioxidant capacity; MMP: mitochondrial membrane potential; ↑: increased; ↓: decreased.

reduced by receiving a single electron from NADPH, which serves as the main source of reducing equivalents in cells. This reaction forms $NADP^+$ and a highly unstable $DQ^{+\bullet}$, which, in turn, transfers an electron to molecular oxygen (O_2) to generate $O_2^{\bullet-}$. This process goes on continuously, even in small amounts, to generate large quantities of $O_2^{\bullet-}$ and these oxygen radicals are neutralized spontaneously or enzymatically via SOD to produce H_2O_2. However, with the large increase in ROS production, the cellular protective mechanisms, either nonenzymatic components (e.g. GSH, thioredoxin, selenium, and vitamins C and E) or antioxidant enzymes (e.g., SOD, GPx, glutathione peroxidase (GR), and CAT), become overwhelmed, resulting in oxidative stress and, consequently, apoptosis [62].

Uchendu et al. indicated that CPF and deltamethrin ((S) a-cyano-3-phenoxybenzyl-(1R)-cis-3-(2.2-dibromovinyl)-2,2-dimethylcyclopropane carboxylate (DM)), which belong to the OP and pyrethroid pesticide groups, respectively, induced oxidative stress due to the generation of free radicals and alteration in antioxidant defense mechanisms. They used a mixture of OP and pyrethroid insecticides, which are common insecticides used by farmers and stored near grains in some countries such as Nigeria [63]. The Uchendu et al. study showed that rats exposed to CPF and deltamethrin, either individually or in combination, had significantly lower levels of CAT, SOD, and GPx and significantly increased levels of MDA compared to the control group [63]. It was suggested that the elevated MDA concentration was due to increased lipid peroxidation, which was induced by excessive production of ROS. The decreased activities of the antioxidant enzymes in the rats exposed to OP and pyrethroid pesticides may be due to the direct deleterious effects of ROS [63].

Another study conducted by Ojha and Gupta indicated that commonly used OP pesticides such as CPF, methyl parathion (MPT), and malathion (MLT) induced apoptosis and DNA interstrand crosslink formation [64]. Ojha and Gupta showed that all OP pesticides significantly increased caspase-3 and caspase-9 activities in rat lymphocytes [64]. Their findings support the suggestion that elevated programmed cell death or apoptosis arises in the presence of oxidative stress and activated caspase-3 and caspase-9 play a role in the breakdown of several cellular components related to DNA repair and regulation during apoptosis [64].

Multiple studies have explored the tendency of OPs to cause cytotoxicity, DNA damage, and disturb oxidative balance, which leads to oxidative stress. In one study, Lu and Yu evaluated the effects of profenofos (PFF) on rat adrenal pheochromocytoma (PC12) cells. They found that PFF and its enantiomers significantly increased intracellular ROS and MDA levels in treated PC12 cells when compared to the control [65]. Their results showed that PFF treatment resulted in a significant increase in the expression of copper/zinc superoxide dismutase (Cu-ZnSOD), glutathione-s-transferase (GST), and CAT. They also found a significant upregulation in heat shock protein (HSP 70 and HSP 90) mRNAs in PC12 cells exposed to PFF. This suggests that the increased HSPs were playing a protective role against oxidative damage [65].

A common feature of all of these publications is that organophosphorus pesticides activates ROS cellular defenses (such as increased SOD, CAT, and GST) in many cell types and tissues. However, the antioxidant protective pathways do not seem to be enough to prevent cell and tissue damage as apoptosis is a common outcome of treatment with these pesticides (supplemental table 2).

Table 2: Effects of commonly used conventional pesticide active ingredients in the home and garden market sector in 2012 on oxidative stress in different tissues.

Pesticide	Cell type/model system	Concentration/dose	Oxidative stress markers	Reference
Carbaryl	*Cantareus apertus* (digestive gland)	1 μM	Increased lipid peroxidation, increased activities of CAT, SOD, GPx, and GR, and decreased total oxyradical scavenging capacity	[275]
	Calothrix brevissima	10, 20, 30, and 40 mg/L	Increased lipid peroxidation and increased SOD, CAT, and APX activities	[276]
	Caenorhabditis elegans	0.5, 1, and 1.5 mM	Decreased SOD activity and increased CAT and GPx activities	[277]
	Mouse neuroblastoma cells (neuro 2A)	10 μM	Increased ROS level, loss of mitochondrial membrane potential, increased proapoptotic gene Bax and caspase-3 expression, and decreased antiapoptotic gene Bcl-2 expression	[278]
	Rat adrenal pheochromocytoma (PC12) cells	100 μg/mL	Increased lipid peroxidation, increased SOD activity, decreased GSH content, and decreased mitochondrial membrane potential	[279]
	Water buffalo (*Bubalus bubalis*)	1 mg/kg	Increased lipid peroxidation, increased activities of GPx, GR, GST, SOD, and CAT, and decreased GSH level	[280]
Permethrin (PER)	Rat polymorphonuclear neutrophils (PMNs)	PER (10 μM)	Increased apoptosis, protein carbonyl, and conjugated diene formation in lipids	[69]
		PER metabolites (3-PBAlc, PBAld, and 3-PBA) (10 μM)	Increased apoptosis, protein carbonyl, and conjugated diene formation in lipids	[69]
	Rat adrenal pheochromocytoma (PC12) cells	PER (10, 20, and 30 mg/L)	PER induced enantioselective oxidative stress and cytotoxicity	[281]
		1*R-trans*-PER (10, 20, and 30 mg/L)	Increased ROS generation and MDA level and decreased the activity of SOD, CAT, and GSH	[281]
		1*S-trans*-PER (10, 20, and 30 mg/L)	The toxic effect on PC12 cells induced by 1*R-trans*-PER was approximately 1.6 times higher than by 1*S-cis*-PER	[281]
	Thymic cells from C57BL/6 mice	PER (150, 300, 600, and 1000 μM	Induced $O_2^{\bullet-}$ and H_2O_2	[282]
		Lindane (37.5, 50, 75, 150, and 200 μM)	PER and lindane mixtures increased SOD activity, had no effect on CAT levels, and inhibited GPx and GSH-R-specific activities	[282]
	Wistar rats	34.05 mg/kg	Increased Nurr-1, Nrf2, and NF-κB p65 mRNA levels in the cerebellum	[91]
	Wistar rats	34.05 mg/kg	Increased plasma lipid peroxidation	[92]
	Male and female 500-day-old rats	4 mL/kg	Increased calcium and Nrf2 gene expression levels in old age	[134]
Cypermethrin	Wistar rats	25 mg/kg	Increased lipid peroxidation and protein oxidation, increased plasma IL-6 and TNF-α levels, and increased 8-NO_2Gua levels	[44]
	Wistar rats	1.5–15 mg/kg	Increased lipid peroxidation	[283]
Deltamethrin	Sprague–Dawley rats (hippocampi)	3.125 mg/kg and 12.50 mg/kg	Increased reactive free radical formation in the brain, increased nuclear Nrf2 expression, and increased HO-1 mRNA levels	[136]
	Rat adrenal pheochromocytoma (PC12) cells	10, 100 μM	Increased intracellular ROS production	[136]
	Male Wistar rats	6.25 mg/kg	Decreased CAT activity, SOD activity, and GPx activity. Increased lipid peroxidation	[63]

Table 2: Continued.

Pesticide	Cell type/model system	Concentration/dose	Oxidative stress markers	Reference
	Human colon carcinoma (HCT116) cell	1/4 IC50, 1/2 IC50, 3/4 IC50, and IC50	Increased ROS production levels, increased lipid peroxidation, increased DNA damage, decreased mitochondrial membrane potential, and increased caspase-3 activity and MAPK activation	[284]
Bifenthrin	Male ICR mice	1S-*cis*-BF (5 mg/kg)	Increased hepatic ROS level, increased serum and hepatic lipid peroxidation, decreased GSH activity, increased CAT activity, increased SOD activity, and increased Cat and Ho-1 mRNA levels	[285]
	Human umbilical vein endothelial cells *(HUVECs)*	15, 30 μM	Increased apoptosis	[286]
	Zebrafish	15, 30 μM	Increased intestinal ROS level	[286]
2-Methyl-4-chlorophenoxyacetic acid (MCPA)	Human erythrocytes	250, 500 ppm	Decreased GSH level	[287]
	Human erythrocytes	2.0 mM, 4.0 mM	Increased lipid peroxidation	[288]
	Ramalina fraxinea	20, 50, 100 mg/L	Increased lipid peroxidation	[289]
Malathion	Thymic cells from C57BL/6 mice	37.5, 75, 150, 300 μM	Induced $O_2^{\bullet-}$ and H_2O_2	[282]
	Rat erythrocytes	0.13 mg/kg	Increased lipid peroxidation, increased SOD and CAT activities, and increased total-SH content	[146]
	Male Wistar rats (cortex, striatum, cerebellum, hippocampus)	25, 50, 100, and 150 mg/kg	Increased lipid peroxidation, increased protein carbonylation, increased/decreased CAT activity, and increased/decreased SOD activity	[290]
	Prepubertal male mice	200 mg/kg	Increased lipid peroxidation, increased ROS level, decreased SH group, reduced CAT and GPx activities in the liver and kidney, decreased total SOD, Cu/Zn-SOD, and Mn-SOD activities in the liver, and decreased total SOD and Mn-SOD activities in the kidney	[291]
	Male Swiss mice	500 mg/kg	Increased lipid peroxidation, increased ROS level, increased SH group content, and increased testicular activities of SOD, Cu/Zn-SOD, Mn-SOD, Fe-SOD, and CAT	[292]
	Male Wistar rats	250 mg/kg	Increased lipid peroxidation and decreased testicular total antioxidant capacity	[293]
	Male Swiss albino mice	27 mg/kg	Increased lipid peroxidation, decreased testicular activities of SOD, CAT, and GPx, and decreased GSH level	[294]
	Wistar male rats	250 mg/kg	Increased 8-hydroxy-2′-deoxyguanosine (8-OHdG) level, increased NO level, decreased total antioxidant capacity (TAC), increased total oxidant status (TOS), decreased CAT and SOD activities, and increased DNA damage	[295]
	Sprague Dawley rats	200 mg/kg	Increased lipid peroxidation, increased NO level, and decreased GSH level	[296]
	Human liver carcinoma cell (HepG2)	6–24 mM	Increased lipid peroxidation and increased oxidative DNA damage	[297]
	Porcine cumulus-oocyte complexes	750 and 1000 μM	Increased ROS level, increased lipid peroxidation, increased protein carbonylation, increased Cu/Zn-SOD, GST, and G6PD expression levels, and decreased CAT and GPx expression levels	[298]
	Male Wistar rats	25, 50, 100, and 150 mg/kg	Increased mitochondrial superoxide production in the hippocampus, increased lipid peroxidation in the hippocampus and striatum, and decreased complex IV activity in the hippocampus	[299]

Table 2: Continued.

Pesticide	Cell type/model system	Concentration/dose	Oxidative stress markers	Reference
	Rohu (*Labeo rohita*) *liver*	5 μg/L	Increased intracellular ROS level, increased lipid peroxidation, increased activities of CAT, SOD, POD, GSH, GR, GST, and GPx, and increased DNA damage	[300]
	Human erythrocytes	25, 75, 200 μM	Increased lipid peroxidation, decreased SOD, CAT, and GPx activities	[301]
	Female Wistar rats (ovary)	50 mg/kg	Increased lipid peroxidation and decreased GSH content	[302]
	Allium cepa	0.05, 0.13, 0.26, 0.39, and 0.52 g/L	Increased lipid peroxidation, increased CAT, GST, and SOD activities, decreased APX and GR activities, and increased DNA damage	[303]
	Male Kunming mice	10^{-5} M	Increased lipid peroxidation, increased •OH level, decreased SOD, GPx, and CAT activities, decreased GSH content, and increased levels of Bax, Bcl-2, and p53 in splenic T cells	[250]

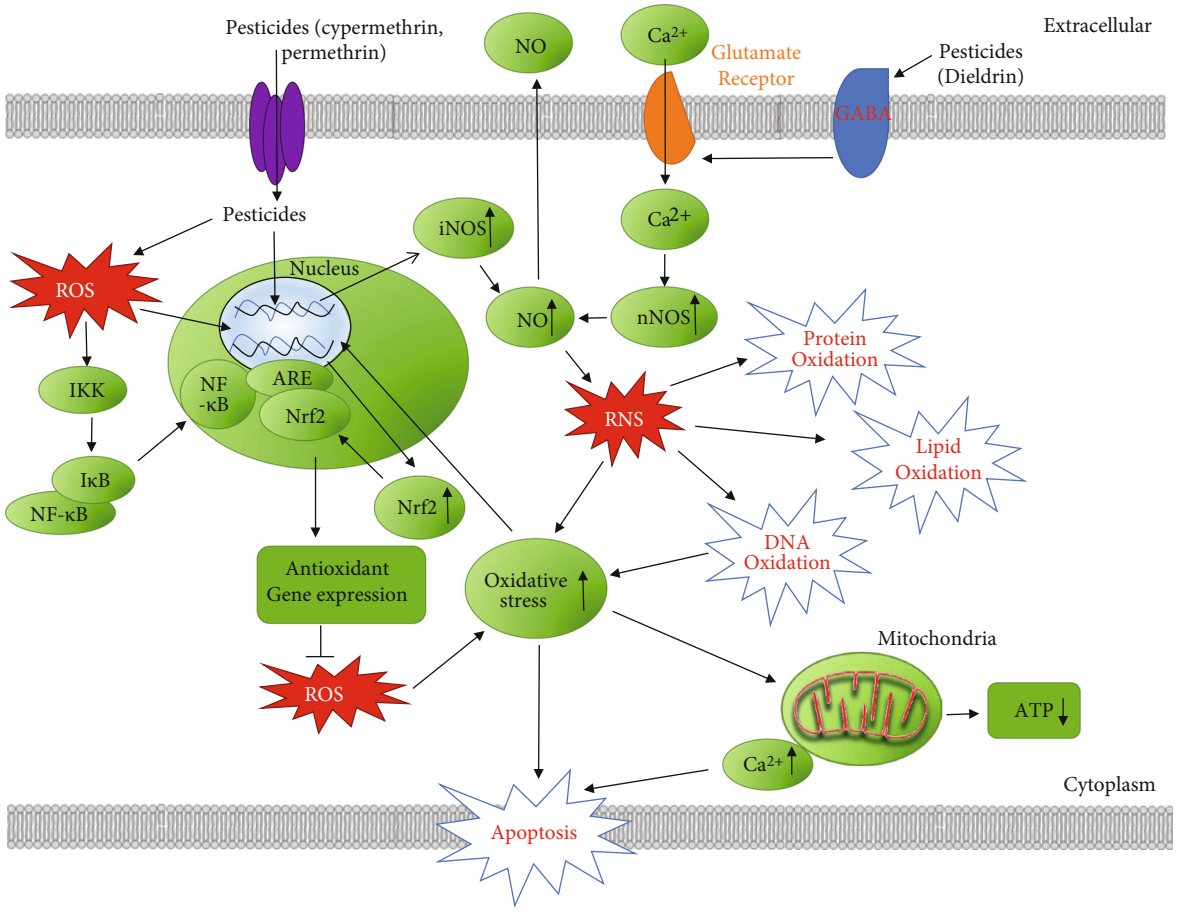

Figure 2: Schematic representation of signaling pathways involved in pesticide-induced reactive nitrogen species (RNS) signaling and oxidative stress. Pesticides including cypermethrin and permethrin increase nitric oxide (NO) and Ca^{2+} levels which increases reactive RNS signaling, thereby increasing oxidative stress in the cell. Pesticides can also lead to Keap1/Nrf2/ARE activation as well as the NF-κB pathway. Increased RNS may induce lipid, protein, and DNA oxidation, resulting in mitochondrial dysfunction and apoptosis.

1.6. Pyrethroid Insecticides. Permethrin (PER) is a type 1 pyrethroid insecticide. It is the most commonly used pyrethroid in the US and many other countries because of its high activity as an insecticide and its low mammalian toxicity [66]. PER can be used as a fungicide or insecticide for wood preservation purposes and can be found in lice shampoos or scabies treatment which increases their potential to cause harm to human health due to their widespread use

around humans [67]. Due to the worldwide use of permethrin, humans and animals may have had exposure to this compound [67]. Studies have shown that pesticides in the pyrethroid family have a role in weakening the immune system because they can induce leukocytosis, decrease natural killer (NK) cell counts, and increase the cluster of differentiation antigen 4/cluster of differentiation antigen 8 (CD4+/CD8+) ratio [68]. A study by Gabbianelli et al. showed that 10 μM of PER and its metabolites, 3-phenoxybenzyl alcohol (3-PBAlc), 3-phenoxybenzaldehyde (PBAld), and 3-phenoxybenzoic acid (3-PBA), significantly increased apoptosis in rat polymorphonuclear neutrophils (PMNs) [69]. Moreover, pyrethroids could alter the metabolism of catechol estrogens through the action of peroxidases, leading to the production of semiquinones and quinones, which are capable of forming DNA adducts [70]. In addition, quinones potentially affect DNA topoisomerase II, an enzyme that participates in DNA repair and recombination, which could lead to breaks in certain susceptible sites of the genome (breakpoint cluster regions of certain genes), modifying DNA topology through the induction of double-strand breaks (DSB) that need to be rejoined [70]. Furthermore, there are genes, such as mixed lineage leukemia (MLL), with particular susceptibility to the breakage by DNA topoisomerase II; the inhibition of this enzyme produces ruptures in this gene which participates in diverse oncogenic fusions driving the leukemogenic process [70] (Figure 3).

Like organophosphorus pesticides, pyrethroid insecticides also increase the levels of antioxidant enzymes and induces apoptosis (supplemental table 2). The lack of detailed studies with respect to the effects of many pesticides on the immune system limits what can be concluded from pyrethroid pesticide studies. However, the current data suggests that pyrethroid pesticides may have a greater effect on weakening the immune system than other pesticides.

1.7. Organochlorine (OC) Pesticides. Organochlorine (OC) pesticides are synthetic pesticides that belong to a group of chlorinated hydrocarbon derivatives, which are widely used in the chemical industry and in agriculture [1]. The chemicals identified as OC pesticides have been classified as persistent organic pollutants (POPs) because they have high persistence in the environment [1]. Despite their effective control of malaria and typhus fever, the majority of OC pesticides have been banned in most highly developed countries due to their high toxicity, slow degradation, and bioaccumulation [71]. OC insecticides such as dichloro-diphenyl-trichloroethane (DDT), hexachlorocyclohexane (HCH), aldrin, and dieldrin are among the most widely used pesticides in developing countries of Asia and Africa [1]. Dieldrin is a highly persistent OC insecticide that was widely used to control soil pests such as grasshoppers, locusts, termites, beetles, and textile pests in the agriculture field [72]. It was also effective in controlling tsetse flies, which are the vector that caused African sleeping sickness (*African trypanosomiasis*) and other tropical diseases including malaria, yellow fever, Chagas disease, Oroya fever, river blindness, and filariasis. The United States Environmental Protection Agency (USEPA) banned and restricted the use of dieldrin in 1974 due to its possible carcinogenicity to human and animal health after many years of widespread use. Since some developing countries are still using this pesticide, humans are still exposed to dieldrin mainly through contaminated foods [72]. Several postmortem studies have suggested that exposure to dieldrin has the likelihood of increasing the incidence of Parkinson's disease because significant levels of dieldrin were detected in the brains from Parkinson's patients, while no dieldrin was detected in age-matched control brains [72]. A list of other pesticides, including some not discussed in the text, and their effects on cell types or model systems are shown in supplemental table 5.

Like with organophosphorus and pyrethroid pesticides, organochlorine pesticides that are currently used can be found at low levels in the environment. The organochlorine pesticides show cellular effects that are similar to other classes of pesticides further suggesting that most pesticides may be causing some or most of their deleterious effects via excessive ROS production.

1.7.1. Paraquat. One pesticide that has been well investigated relative to others is paraquat. Exposure to paraquat is associated with the increased risk of pulmonary fibrosis, as well as lung, brain, and heat injuries [73, 74]. Paraquat can generate several types of ROS intracellularly, including $O_2^{\bullet-}$, H_2O_2, and •HO [75]. Paraquat can interact with nicotinamide adenine dinucleotide phosphate (NADPH) oxidase (NOX) and inducible nitric oxide synthase (iNOS) generating ROS and RNS in the cytosol [76]. Paraquat induced NOX type 1-(NOX1-) mediated ROS generation in dopaminergic cells [77], while it activates NOX type 2 (NOX2) in microglia [78]. High levels of NO can react with superoxide ions to form highly toxic peroxynitrite anions (ONOO–). Paraquat can also disrupt the oxidation of NAD(P)H to $NAD(P)^+$ that occurs by the mitochondrial electron transport chain (ETC) complex I, by accepting electrons to form a charged version of paraquat (PQ+). PQ+ can generate superoxide radicals ($O_2^{\bullet-}$) which can lead to other ROS products such as HO•. Brain mitochondria ETC complex III was also shown to affect the H_2O_2 levels induced by paraquat [79].

1.8. Signaling Mechanisms through Which Pesticides Induce ROS. Although the precise molecular mechanism by which acute or chronic exposure to pesticides induces oxidative stress and damage remains currently unknown, several events involving different cell signaling pathways such as changes in gene expression, activation, and/or inhibition occur. Understanding the cellular and molecular level changes is needed to elucidate the major pathways involved in pesticide-induced oxidative stress and develop potential protective agents or therapies.

1.9. Signal Transducers and Activators of Transcription (STAT). OP pesticides are amongst the most commonly used pesticides in the US. Several studies have reported that CPF increases the production of free radicals and superoxide by disrupting mitochondrial electron transport chain (ETC) complex I activity depleting the antioxidant defenses [80].

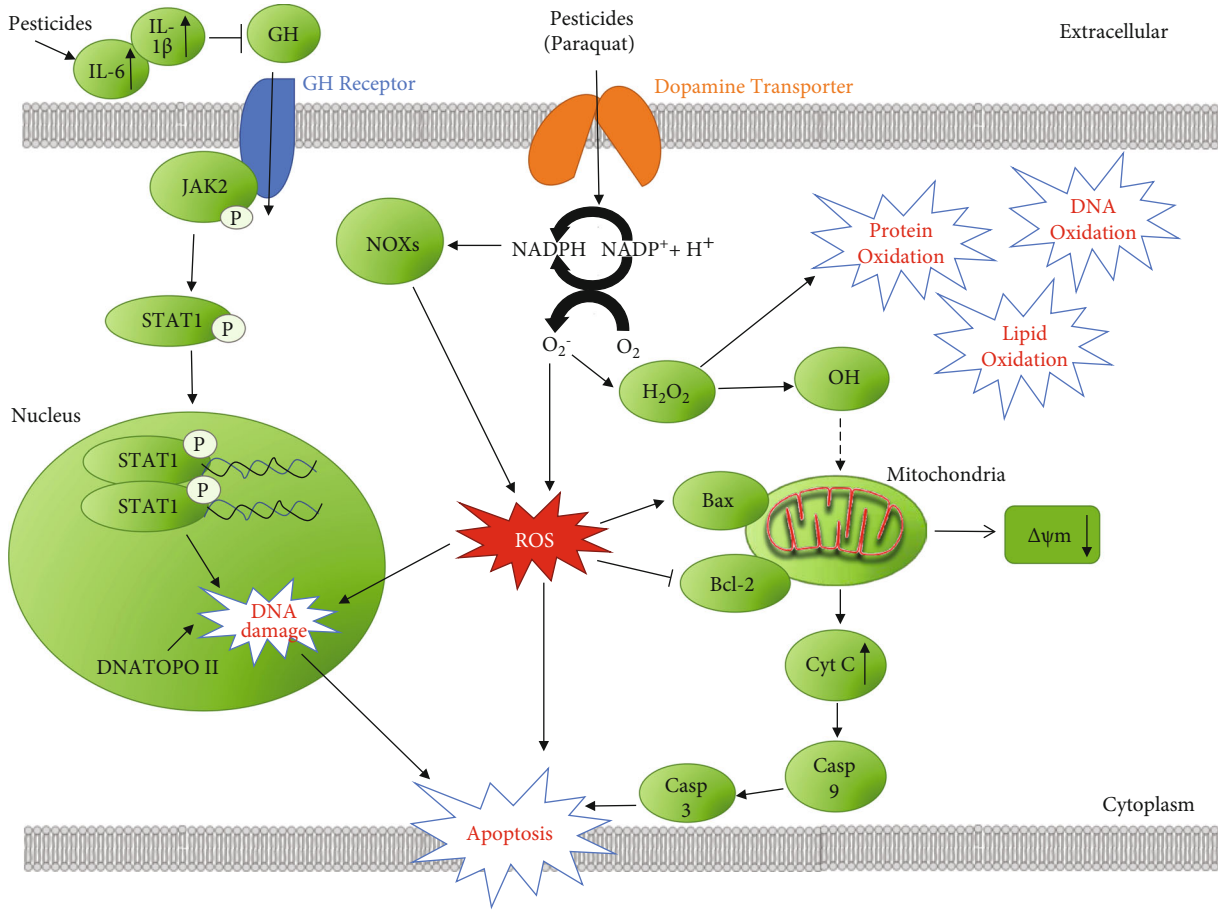

Figure 3: Schematic diagram of the mechanism by which pesticides affect DNA damage and mitochondrial function. Pesticides induce inflammatory cytokines (IL-6, IL-11, and IL-1β) and caspases that inhibit growth hormone (GH) thereby causing reproductive and birth defects in humans. Phosphorylation of the C terminal of STAT1 at residue 727 enhances the activity of other factors such as p53 that leads to DNA damage. Together with the action of DNA topoisomerase II, these molecules can cause DNA damage and eventually apoptosis. Pesticides can also induce NOXs and $O_2^{\bullet-}$ and result in an increase in ROS that leads to mitochondrial dysfunction and activates the mitochondrial apoptosis pathway. $^{\bullet}$OH may also be causing mitochondrial stress. $\Delta\psi m$: mitochondrial membrane potential.

Singh et al. reported that CPF induced a dose-dependent increase in cell death and contributed to oxidative stress by upregulating ROS generation and decreasing GSH levels in dopaminergic neuronal and human mesencephalic cells [80]. Based on the results of CPF-induced dopaminergic cell death, the group hypothesized that signal transducers and activators of transcription 1 (STAT1) regulate CPF-induced ROS production and that elevated ROS eventually leads to apoptotic cell death [80]. STAT proteins belong to a family of latent cytoplasmic transcription factors that play a major role in proliferation, growth, apoptosis, and differentiation within different cell types [81]. Janus kinase-(JAK-) STAT signaling is critical for both neuronal survival and cell death [80]. Upon the binding of ligands to their receptors, activation of JAK takes place and, in turn, phosphorylates STAT1 on tyrosine 701 and serine 727 residues. The phosphorylated STAT1 dimerizes and translocates into the nucleus, where STAT1 binds to the gamma interferon-activated site/interferon-stimulated response element (GAS/ISRE) present on the promoter region of specific target genes that regulate proinflammatory cytokines, NADPH oxidase (NOX), apoptosis, and cell cycle arrest regulators, such as caspases, Fas, and Bax [80]. STAT1 regulates cell death through both transcriptional-dependent expressions of proapoptotic genes and nontranscriptional signaling pathways [81]. In another study, OP pesticides induced a 66% decrease in intracellular ROS levels in STAT1 knockdown (KD) dopaminergic cells in comparison with scrambled small interfering RNA- (siRNA-) transfected cells exposed to the same pesticides [80]. NOX-1, a superoxide-generating NADPH-oxidase isoform, has been shown to regulate ROS generation in some cell types, including, but not limited to, monocytes, macrophages, vascular endothelial cells, and smooth muscle cells [82]. NOX-1 is the main ROS-producing enzyme during inflammation [83]. OP pesticides increased the recruitment of STAT1 to the endogenous NOX-1 promoter suggesting that NOX-1 is transcriptionally regulated by STAT1 [80]. STAT1 plays an important role in regulating ROS generation and antioxidant GSH levels in a NOX-1-dependent manner in neuronal cells treated with CPF, an OP pesticide. Mangum et al. found that OC insecticides induced NOX-dependent ROS generation in

human monocytic cells [84]. Together, these data suggest that STAT1 activation of NOX is important for ROS generation in OP pesticide-induced oxidative stress.

1.10. TNFR1/TNF-α Pathway. Some reports suggest that the death receptor pathway is one of the possible mechanisms that induce oxidative stress. The ligation of cell surface death receptors, such as the tumor necrosis factor receptor (TNFR), enables communication signals of tumor necrosis factor-alpha (TNF-α), which leads to the activation of caspase-8 that cleaves effector caspase-3, either directly or indirectly via the mitochondrial route [40]. TNF-α is a powerful and potent proinflammatory cytokine produced by macrophages/monocytes during acute inflammation and is responsible for different signaling events within cells, leading to necrosis or apoptosis [85]. The inflammatory responses induced by TNF-α are mediated by its interaction with two cell surface receptors, TNFR1 and TNFR [86]. TNF-α is also involved in the induction of cytokine production, the activation and expression of adhesion molecules, and growth stimulation [87]. Pacheco et al. showed that increased TNF-α levels by itself could induce ROS generation and oxidative stress in the L929 mouse fibrosarcoma cell line [86]. A study in rats exposed to permethrin showed that an increase in the TNF-α levels increases ROS generation and decreases the antioxidant defense system, which leads to oxidative stress [40]. Additionally, Jin et al. found that permethrin increased TNF-α mRNA expression in a concentration-dependent manner when exposed to zebrafish for 72 hours of postfertilization [42]. Zebrafish is considered a good model for investigating cytokine genes such as TNF-α [88]. A study conducted by Tyagi et al. that focused on idiopathic preterm birth documented that significantly higher levels of β-HCH (beta-hexachlorocyclohexane) and p,p′-DDE (para, para-dichlorodiphenyldichloroethylene) were observed in maternal blood of preterm birth cases ($n = 30$) as compared to term delivery ($n = 30$) from July 2012 to June 2013 in Delhi, India [89]. Tyagi et al. found that TNF-α mRNA expression was 2.31-fold higher in preterm birth cases in comparison to term delivery [89]. This suggests that pesticides might be involved in the induction of proinflammatory pathway genes such as TNF-α.

1.11. Nurr1 and the NF-κB pathway. Orphan nuclear receptor-related 1 (Nurr1) is a transcription factor that belongs to the nuclear receptor subfamily 4 group A member 2 (NR4A2) family of proteins and plays an important role in the metabolism of dopaminergic neurons [40]. Emerging evidence indicates that impaired Nurr1 function might contribute to the pathogenesis of Parkinson's disease [90]. Nurr1 exhibits anti-inflammatory actions due to its inhibitory activity towards the transcription factor NF-κB in brain tissue [40]. Carloni et al. reported in their study that permethrin induced an increase in the expression of the proinflammatory NF-κB transcription factor and a decrease in Nurr1 gene expression [91]. Another study conducted by Fedeli et al. showed that permethrin increased proinflammatory cytokine TNF-α expression and decreased IL-1β, IL-2, and IL-13 expression in the oldest treated rats [92]. These results suggest that TNF-α, Nurr1, and NF-κB pathways may be partly responsible for some of the mechanisms related to oxidative stress caused by pesticides.

1.12. Protein Kinase C Signaling Pathway. Kitazawa et al. reported that caspase-3-mediated proteolytic cleavage of protein kinase C (PKC) δ contributed to apoptosis of dopaminergic PC12 cells following exposure to dieldrin [72]. PKC can be grouped into a family of serine/threonine kinase enzymes that belong to the AGC (cAMP-dependent, cGMP-dependent, and protein kinase C) superfamily of protein kinases [93]. They are protein kinase enzymes that are able to change enzyme activity, cellular location, or association with other proteins via phosphorylation of hydroxyl groups on serine and threonine residues, resulting in a functional change of the target protein [94]. Kitazawa et al. found that exposure of PC12 cells to dieldrin triggered both a dose-dependent release and a time-dependent release of cytosolic cytochrome C which is consistent with previous literature that suggests that increased ROS production induces or triggers mitochondrial cytochrome C release into cytosol [72]. Additionally, one of the most studied caspases that plays a critical role in execution of apoptosis, caspase-3, was found to be significantly activated following dieldrin exposure. Furthermore, exposure to dieldrin resulted in the proteolytic cleavage of native PKCδ over a period of 5 hours [72]. Kitazawa et al. suggest that the proposed mechanism for dieldrin-induced apoptosis in dopaminergic cells was that ROS production triggers cytochrome C release, which activates caspase-9 and caspase-3 and in turn cleaves PKCδ, resulting in apoptotic cell death. These results implicate PKC as a signaling pathway involved in pesticide-induced oxidative stress. Further studies on PKC involvement in pesticide-induced cellular changes are needed.

1.13. NF-κB Signaling Pathway. Another OP that was extensively used before it was banned and globally phased out due to high toxicity is endosulfan. Endosulfan is primarily used to control a number of insects on food crops like tea, fruits, and vegetables and on grains and can be used as a wood preservative. Endosulfan can be released into the air, water, and soil in areas where it is applied as a pesticide [95]. A mortality study reported an increased incidence of Parkinson's mortality in rural California counties with high use of agricultural pesticides [96]. Jia et al. examined endosulfan and zineb individually and in combination for their potential to stimulate oxidative stress in human neuroblastoma cells (SH-SY5Y) *in vitro* [97]. They found that exposure to endosulfan and zineb significantly increased intracellular H_2O_2 and $O_2^{\bullet-}$ and production in neuroblastoma cells in a dose- and time-dependent manner which indicates that both pesticides induce oxidative stress [97]. Jia et al. also showed that the caspase-3 activity was significantly elevated in cells treated with endosulfan and zineb when compared with that of the control cells. The activity and expression of NF-κB, a ubiquitous transcription factor, which serves as an indicator of oxidative stress, had significantly higher levels in neuroblastoma cells treated with endosulfan and zineb individually or in combination [97]. These results suggest that the

oxidative stress induced by pesticide exposure to cells contributes, at least in part, to the activation of the NF-κB signaling pathway. It can be partly extrapolated from this study that combination or exposure to two or more pesticides causes great harm to the health of farmers, workers, and other individuals who are at a higher disposition to pesticide exposure.

1.14. Endoplasmic Reticulum (ER) Stress. The ER serves many functions including the assembly, folding, posttranslational modification, and transport of proteins. In addition, the ER stores calcium which is essential for muscle contraction. ER stress occurs when the protein folding capacity of the ER is overwhelmed, and cells with ER stress are characterized by an accumulation of misfolded proteins inside the lumen of the ER. ER stress could be induced by several conditions including hypoxia, nutrient deprivation, and pesticides. If the ER stress is severe or extended, apoptosis could be induced [18]. Several pesticides such as chlorpyrifos, 2,4-dichlorophenol, deltamethrin, and paraquat have been shown to induce ER stress. Many of these pesticides also induce apoptosis but research suggests that pesticides induce ER stress and apoptotic cell death via different pathways.

1.15. Nonmitochondrial Apoptosis Pathway. Apoptosis is a form of programmed cell death that is used to remove unwanted cells. This process is generally characterized by morphology changes including DNA fragmentation, cell shrinkage, and mRNA decay. Pesticides have been documented to induce apoptosis by triggering several different signaling pathways including intrinsic pathways involving the mitochondria and DNA damage as well as extrinsic pathways such as modulation of death receptors [98, 99]. Organophosphorus pesticides like monocrotophos, profenofos, chlorpyrifos, and acephate induce apoptosis in cultured human peripheral blood lymphocytes [100]. Chlorpyrifos and cypermethrin induce apoptosis in human SH-SY5Y neuroblastoma cells [101], while malathion induces apoptotic cell death in N2 neuroblastoma cells [102]. Chlorpyrifos action may be via FAS/TNF signaling pathways [101]. Although pesticides are typically in low concentrations in rivers, lakes, and surface water, these low concentrations have been documented to induce DNA damage and apoptosis in fish. Pyrethroid pesticides are known to be up to 1000 times more toxic in fish than in mammals and birds because of its high absorption into the gills [103].

1.16. Mitochondrial Apoptosis Pathway. A common dysfunction associated with oxidative stress is mitochondrial dysfunction [104]. In some cases, mitochondrial dysfunction causes ROS, while in some cases, ROS could cause mitochondrial dysfunction. The complexes in mitochondria are the main site for ROS production, and many pesticides have been shown to inhibit mitochondrial complexes [105, 106]. As such, it is likely that a major contributor to oxidative stress is the ROS produced by dysfunctional mitochondria. In mammals and fish, mitochondrial dysfunction is often associated with ER stress and apoptosis [103, 107].

Pentachlorophenol (PCP) and its metabolite, tetrachlorohydroquinone (TCHQ), decreased the antioxidant GSH level in the mouse liver and drastically increased lipid peroxidation via the abundant production of urinary 8-iso-prostaglandin F2α (8-iso-PGF2α) [108]. Taking into consideration existing and emerging evidence, the mitochondrial apoptosis pathway is another possible mechanism that is involved in pesticide-induced oxidative stress. B cell lymphoma 2 (Bcl-2) and BCL2-associated X (Bax) are the main mitochondrial integrity regulators in this pathway. They also influence cytochrome c release and caspase activation. Bcl-2 and Bax are two well-known proteins associated with cell death but possess opposite function. The Bcl-2 protein functions as a suppressor where it prevents apoptosis by its antioxidative activity, while the Bax protein functions as a promoter of apoptosis [40]. After mitochondrial damage, Bax is translocated from the cytosol to the mitochondria and a significant decrease in Bcl-2 expression also occurs. Due to high levels of ROS from pesticide exposure, mitochondrial cytochrome c is released into the cytoplasm, which is a critical apoptotic event [40]. Chen et al. found that TCHQ increased the expression of Hsp 70 but decreased the expression of the Bcl-2/Bax ratio and cellular apoptosis susceptibility (CAS), the genes that play a role in apoptotic and necrotic processes, in liver cells. The ratio of Bcl-2/Bax protein may account for the survival or death of intoxicated cells [108]. Their results corroborate the involvement of the mitochondrial apoptotic pathway in pesticide-induced oxidative stress.

1.17. Autophagy. Autophagy is a normal process that irreversibly degrades damaged or unwanted eukaryotic cell components. Like apoptosis, it is a form of programmed cell death but autophagy involves different pathways from apoptosis [109]. In mammals, the autophagy process involves the formation of autophagosomes (vesicles) that fuse with the lysosome. Autophagy is important in reducing the effects of oxidative stress on cells [110].

Several pesticides have been shown to increase autophagy. CPF, which was described earlier to increase apoptosis, induces autophagy in neuronal cells [111]. In one study, pretreatment of SH-SY5Y neuronal cells with rapamycin (autophagy inducer) resulted in reduced CPF toxicity (less cell death) while inhibition of autophagy resulted in increased CPF toxicity [111]. In another study in SY5Y neuronal cells, Dai et al. found that CPF induced PTEN-induced putative kinase 1 (PINK1)/parkin-regulated mitophagy (a selective form of autophagy) [112]. Experiments using the pesticide fipronil suggest that autophagy is important in reducing the effects of pesticides. In one study, autophagy was found to increase the viability of cells treated with fipronil [113]. The mechanism of action for improved cell viability may be decreased caspase 3 levels resulting in low levels of fipronil-induced apoptosis [113]. Several investigations also suggest that paraquat induces autophagy. In an interesting study, knockout of the innate proinflammatory mediator Toll-like receptor 4 (TLR4) lessened paraquat-induced cardiac dysfunction [114]. A potential mechanism for the

reduced paraquat-induced cardiac dysfunction may be via the regulation of AMPK-mediated cardiac autophagy [114]. In rat adrenal pheochromocytoma PC12 cells, rapamycin significantly decreased paraquat-induced cellular toxicity suggesting that basal autophagy has a protective role in cytotoxicity caused by paraquat [115].

1.18. Mitogen-Activated Protein Kinases (MAPKs). The mitogen-activated protein kinases (MAPKs) are serine/threonine-specific protein kinases that phosphorylate their own dual-serine and threonine residues (autophosphorylation) or those found on their substrates, to activate or deactivate their target [116]. They are involved in regulating cellular processes such as proliferation, stress response, energy metabolism, gene expression, differentiation, proinflammation, mitosis, cell survival, apoptosis, and immune defense [117]. Chen et al. showed that exposure of TCHQ activated c-Jun NH2-terminal kinase (JNK) and p38 in NIH3T3 fibroblast cells [108]. Herein, this further demonstrates that the cascades of the MAPK (JNK, p38 MAPK, and extracellular signal-regulated protein kinase (ERK)) signaling pathway is involved in TCHQ-induced oxidative stress. Pentachlorophenol (PCP) is a restricted use OC pesticide, used industrially as a wood preservative for railroad ties, utility poles, and wharf pilings and used extensively as a biocide in the leather and textile industries [118]. It is highly effective against decay from fungus and damage from wood-boring insects in timbers [119]. Its molecular structure is that of a phenol group (aromatic ring) with five chlorine atoms which makes it a persistent organic pollutant. PCP has been detected in food and several consumable products. PCP has also been found in groundwater in micromolar concentrations. Even higher levels of PCP (0.7 mM) have been reported in the vicinity of industrial point sources of chlorophenols [120]. Due to the difficulty in the degradation of PCP in the environment, its use has been banned by countries which signed the Stockholm Convention with exception to the US. The IARC (International Agency for Research on Cancer) categorized PCP as carcinogenic to humans (group 1) based on epidemiological studies that showed that exposure to PCP causes non-Hodgkin lymphoma in humans [108]. Several studies have reported that exposure to PCP increases the risk of nasal carcinoma and soft tissue sarcoma and induces hepatocellular carcinomas/adenomas, hemangiosarcomas, and pheochromocytomas in a chronic tumorigenesis mouse animal model [121, 122]. Wispriyono et al. found that 20 μM of PCP and its metabolite, TCHQ, markedly increased the number of apoptotic cells and induced DNA fragmentation in Jurkat human T cells after 10 hours of incubation. Notably, they discovered that after 1 hr of incubation, 20 μM of TCHQ phosphorylated all the MAPKs examined (i.e., extracellular signal-regulated protein kinase (ERK), p38, and c-Jun NH2-terminal kinase (JNK)). They went on to show that TCHQ-induced apoptosis disappeared almost completely when treated with both the p38 inhibitor (SB203580) and MAPK/ERK kinase inhibitor (U0126) at the same time. Wispriyono et al. came to the conclusion that p38 and ERK are likely important signal transduction pathways involved in apoptosis in the human T cell line exposed to PCP metabolite [123]. CPF (50 μM) induced redox imbalance altering the antioxidant defense system in breast cancer cells as well as increased formation of intracellular ROS and RNS. Finally, it was demonstrated by Ventura et al. that the main mechanism involved in the inhibition of CPF-induced cell proliferation is an increment of p-ERK1/2 levels mediated by H_2O_2 in breast cancer cells [124]. Apoptosis signal-regulating kinase 1 (ASK1) is a member of the mitogen-activated protein kinase (MAPK) family. ASK1 activates c-jun N-terminal kinase (JNK) and p38 in response to various stimuli including oxidative stress, endoplasmic reticulum stress, proinflammatory cytokines, infection, and calcium influx. ASK1 activates JNK and p38 by directly phosphorylating, and thereby activating, their respective MAP2Ks (also called mitogen-activated kinase kinase (MKK)), MKK4(SEK1)/MKK7, and MKK3/MKK6 [125]. Meijles et al. found that activation of cardiac ASK1 is ROS dependent in neonatal rat cardiomyocytes from perfused hearts where H_2O_2 activated ASK1 which suggests that ASK1 is selectively activated by ROS [126]. When Niso-Santano et al. exposed human neuroblastoma SH-SY5Y cells to 100 μM PQ for 24 h, they found that paraquat increased ASK1 expression and nuclear apoptosis was significantly increased in PQ-treated cells [127].

1.19. Keap1/Nrf2/ARE Pathway and Ca^{2+} Signaling. The Keap1/Nrf2/ARE pathway plays a major role in the regulation of cytoprotective responses to endogenous and exogenous stresses caused by ROS [128]. There are four components involved in the Nrf2/Keap1 pathway; they are (a) the nuclear factor erythroid2-related factor 2 (Nrf2), (b) the actin-binding Kelch-like ECH-associated protein 1 (Keap1), (c) a group of small musculoaponeurotic fibrosarcoma (Maf) proteins, (d) and antioxidant response element (ARE) which are important for the antioxidant response in this pathway [116]. Nrf2 is a transcription factor that binds to the antioxidant responsive element (ARE) in DNA that induces the expression of a group of detoxing enzymes and antioxidant proteins/enzymes. Gene expression of heme oxygenase-1 (HO-1) and NAD(P)H dehydrogenase and others are regulated by Nrf2 [74–77]. Animal models that have increased Nrf2 levels show increased protection against oxidative stress [129, 130], while Nrf2 gene knockout mice have a higher susceptibility to oxidative damage [131, 132]. Keap1, a cysteine-rich protein, acts as an adaptor protein for a Cul3-dependent E3 ubiquitin ligase complex and supports ubiquitination of Nrf2 which then gets degraded by the ubiquitin proteasome system [116]. Consequently, the gene knockout of Keap1 results in constitutively hyperactive Nrf2 signaling.

The generation of excessive ROS from exposure to pesticides leads to the progression of oxidative stress in cells resulting in an increase in the oxidation or conjugation of key cysteine residues in Keap1. These modifications typically weaken its ability to act as an E3 ligase adaptor. As a result, Keap1 loses its ability to promote ubiquitination and degradation of Nrf2. Ultimately, Nrf2 dissociates from Keap1, leading to decreased proteasomal degradation of Nrf2, accumulation of free Nrf2 in the cytosol, and translocation of

Nrf2 into the nucleus. Following Nrf2 translocation into the nucleus, it heterodimerizes with small Maf-binding proteins and binds to ARE. This binding ultimately activates ARE-dependent gene expression and initiates the transcription of antioxidant genes [116, 128]. These genes include NAD(P)H: quinine oxidoreductase 1 (Nqo1), heme oxygenase-1 (HO-1), γ-glutamylcysteine ligase (Gcl), microsomal epoxide hydrolase (Eh-1), GSTs, sulfiredoxin 1 (Srxn1), multidrug resistance-associated proteins (Mrps), bile salt efflux pump (Bsep), and carboxylesterases (Ces) [128, 133]. In a study conducted by Carloni et al., PER increased Nrf2 gene expression in the cerebellum of rats [91]. Another study found increased mRNA expression of Nrf2 (1.62-fold) and the intracellular Ca^{2+} influx in rat heart cells from 500-day-old rats exposed to PER during their early life (6th to 21st day of life) [134]. This suggests that the Keap1/Nrf2/ARE and Ca^{2+} signaling pathways might be involved in the toxic effect induced by PER. The overexpression of Nrf2 and the increased Ca^{2+} level might be due to epigenetic mechanisms that sustain the memory of pesticide contact, despite the fact that the exposure has ended [134]. Dou et al. found that the Nrf2/ARE pathway is involved in oxidative stress when induced by PQ in human neural progenitor cells (hNPCs) [135]. They detected significant upregulation in cytoplasmic and nuclear Nrf2 expression in hNPCs when exposed to 10 μM of PQ. As a result of Nrf2 increase, they examined Nrf2-ARE-dependent genes and found that HO-1 and Nqo1 mRNA expression was significantly increased at 10 and 100 μM after PQ treatment for 24 hours [135].

Deltamethrin ((S) a-cyano-3-phenoxybenzyl-(1R)-cis-3-(2.2-dibromovinyl)-2,2-dimethylcyclopropane carboxylate (DM)), one of the most potent pyrethroid insecticides with a cyano substituent [136], is used to control apple and pear suckers, plum fruit moth, caterpillars on brassicas, pea moth, aphids (apples, plums, and hops), winter moth (apples and plums), codling and tortrix moths (apples), and numerous insect pests of field crops [137]. DM plays a key role in controlling malaria vectors and is used in the manufacturing of long-lasting insecticidal mosquito nets [138]. It acts as a neurotoxin causing a prototypical type II neurological syndrome characterized by jerking leg movements and progressive writhing convulsions [136]. Treatment with DM increased free radicals in the hippocampus of rats and increased ROS in PC12 cells suggesting that DM exposure resulted in oxidative damage. The authors showed that DM caused a significant increase in cytoplasmic and nuclear Nrf2 protein expression in the cerebral cortex and hippocampus tissue. HO-1 mRNA levels were significantly elevated in tissue from both cerebral cortex and hippocampus tissues when exposed to DM [136]. Hence, they detected a marked increase in Nrf2 protein, HO-1 mRNA, and free radicals *in vivo* in response to DM. Their findings show that Nrf2 translocation from the cytoplasm to nucleus is initiated *in vivo* and is most likely a response to the DM-dependent induction of free radicals (Figure 2). Although the role of Ca^{2+} signaling in pesticide-induced cellular changes needs to be more thoroughly investigated, the Keap1/Nrf2/ARE pathway involvement in cytoprotective responses to pesticides is well supported by the current experimental data.

1.20. Possible Signaling Mechanisms through Which Pesticides Induce RNS. Kanthasamy et al. reported that dieldrin can cross the blood-brain barrier and can also be stored in adipose tissue with a half-life in humans of approximately 300 days, due to its lipophilicity [139]. Dieldrin targets neuronal ion channels in the brain through inhibition of the GABA(A) receptor, which results in hyperexcitation and a massive influx of Ca^{2+} via glutamate receptor channels. This Ca^{2+} influx can induce neuronal NOS, further increasing the production of ROS/RNS in the brain. Ca^{2+} plays an important role in numerous cellular processes including mediating cellular proliferation, apoptotic processes, the induction of oxidative stress, and physiological functions (Figure 2) [140, 141]. The detection of 3-nitrotyrosine residues on intracellular proteins exposed to different pesticides such as maneb, rotenone, and dieldrin suggests a role of RNS in diseases such as Parkinson's disease [45].

1.21. Possible Mechanisms to Reduce Oxidative Stress Induced by Pesticides. One of the major mechanisms that the body implements in fighting external toxic and harmful agents involves the immune system. The immune response consists of the antigen-non-specific response (innate) and the antigen-specific response (adaptive) [9]. Several experimental studies have reported that exposure to pesticides can exert damaging effects on the immune system [19, 42, 68, 85]. Immunocompetent cells secrete inflammatory mediators, such as cytokines, chemokines, ROS, and RNS. In particular, cytokines can regulate innate or adaptive immunity, hematopoiesis, inflammatory processes, and many other cellular activities through specific binding to their respective receptors [9].

Sometimes, the endogenous antioxidant system becomes incompetent and cannot scavenge the induced oxidative stress [142]. Several studies have reported the potential protective effect of exogenous antioxidant vitamins and minerals against pesticide-induced toxicity in animal models that exhibit alterations in their enzymatic antioxidant system [4, 143–147]. It is important to study the potentially harmful effects of pesticide exposure and various significant methods to mitigate these adverse effects. This section briefly documents the protective role of antioxidant vitamins like vitamins C and E, minerals like zinc, and other naturally occurring antioxidants like N-acetyl cysteine and epicatechin, against pesticide-induced oxidative stress in animal models.

1.22. Vitamin C. Vitamin C (ascorbic acid) is a water-soluble antioxidant. It has been shown to react directly with superoxide and hydroxyl radicals to neutralize ROS and reduce oxidative stress [4]. It has been suggested that vitamin C acts as a chain-breaking antioxidant that stops the propagation of peroxidative processes, thereby reducing lipid peroxidation caused by pesticides. Vitamin C can also do a one-electron reduction of lipid hydroperoxyl radicals via the vitamin E redox cycle [4]. A study conducted with male

albino Wistar rats by Rai et al. found that vitamin C treatment prevented oxidative stress induced by carbofuran in the erythrocytes of rats [148]. Jaiswal et al. showed that pretreatment of vitamin C with carbofuran provided significant recovery in ameliorating the altered levels of oxidative stress biomarkers. They observed that the levels of MDA, total thiols, and GSH as well as the activities of SOD, CAT, and GST were close to those of the untreated control which suggest that vitamin C is able to provide significant protection from the pesticide's intoxication in the rat heart [149].

El-Gendy et al. studied the protective effect of vitamin C (200 mg/kg b.w.) before and after administration of imidacloprid (a neonicotinoid) in male Swiss albino mice. Their study showed that oral administration of 14.976 mg/kg imidacloprid caused significant elevation of lipid peroxidation levels and the activities of antioxidant enzymes including CAT, SOD, GPx, and GST [147]. However, they reported that vitamin C might ameliorate imidacloprid-induced oxidative damage by decreasing lipid peroxidation levels (measured by thiobarbituric acid-reactive substances (TBARS)) and altering antioxidant defense systems in the liver [147].

Vitamin C treatment of CPF-intoxicated mice decreased the lipid peroxidation level and GST activity, normalized CAT, SOD, and glucose-6-phosphate dehydrogenase activities, and increased the GSH level [150]. In addition, coadministration of propanil with vitamin C ameliorated the harmful effects of propanil in most of the tested oxidative stress parameters in mice liver tissues. Their study suggested that vitamin C could be an important dietary component based on its ability to attenuate propanil-induced hepatotoxicity [151]. All of these studies suggest a clear protective role of vitamin C against pesticide-induced toxicity. Hence, it is likely that other compounds with antioxidant properties can also have significant beneficial effects against pesticide-induced toxicity.

1.23. Vitamin E. Vitamin E, present in a biologically active form as α-tocopherol, performs as an antioxidant. It is a major lipid-soluble antioxidant present in all cellular membranes and protects against lipid peroxidation [152]. It can act directly with a variety of oxygen radicals, including the peroxyl radical (ROO•), trichloromethyl radial (CCl3), and peroxide (HO•) production. Vitamin E acts by rapidly transferring its phenolic hydrogen atom to lipid peroxyl radicals resulting in the formation of two molecules that are unreactive toward polyunsaturated lipids [4].

Yousef et al. showed that when rats intoxicated with deltamethrin were exposed to vitamin E, the levels of GST and SOD were elevated and the levels of lipid peroxidation were decreased. Thus, vitamin E alleviated the harmful effects of deltamethrin that were observed, exhibiting its beneficial effects in male Sprague Dawley rats [153]. In male Wistar rats, vitamin E has shown its ameliorating effects by restoring the levels of endogenous antioxidant enzymes such as SOD, CAT, GPx, and GST, suggesting its potential antioxidant role against atrazine-induced oxidative stress [154, 155]. A study conducted by John et al. found that treatment of rats with dimethoate and malathion increased the levels of lipid peroxidation in erythrocytes; however, pretreatment of rats with vitamin E before administering dimethoate and malathion showed decreased levels of lipid peroxidation in erythrocytes. Their results display that vitamin E may ameliorate dimethoate- and malathion-induced oxidative stress by decreasing lipid peroxidation and altering antioxidant defense systems in erythrocytes [146]. Ben Amara et al. showed that exposure of rats to dimethoate for 30 days showed pronounced oxidative stress due to an increased lipid peroxidation level and decreased GSH and nonprotein thiol levels [144]. A decrease in GPx, SOD, and CAT activities was also observed, but coadministration of selenium and/or vitamin E through diet in rats improved the altered oxidative stress biomarkers [144]. These results suggest that the use of the antioxidant vitamin E may prevent or reduce many of the damaging effects of some pesticides.

1.24. Zinc. Zinc (Zn) is one of the most abundant trace elements in the body and can upregulate various transcription factors and detoxifying molecules (glutathione, SOD, glutathione S-transferase, and hemeoxygenase-1) [4]. Zn also induces the nuclear factor erythroid 2-related factor 2 (Nrf2) to act as an antioxidant and is required for enzymes involved in lipid synthesis and lipoprotein excretion [4]. Saad-Hussein et al. conducted a cross-section comparison study, comparing 80 pesticide sprayers from a small village located within an agricultural area in Upper Egypt with 80 control subjects not occupationally exposed to pesticides [142]. Their subjects had no medical history of chronic diseases, and the pesticide sprayer group had been exposed to pesticides for more than 15 years (15–30 years), without wearing any personal protective equipment. Interestingly, they found that Zn (110 mg) supplementation for 1 month significantly decreased MDA levels and increased SOD, GPx, and Zn levels in pesticide sprayers [142]. Goel et al. showed that zinc treatment to CPF-intoxicated male Sprague-Dawley rats normalized the raised levels of lipid peroxidation to within normal limits [158]. Moreover, they found that Zn treatment in these animals resulted in an elevation in GSH, CAT, and GST levels. Additionally, they found a significant decrease in the levels of SOD. However, results of studies from male and female rats revealed that Zn had greater ameliorating effects in female CPF-intoxicated rats, when compared to males, in reducing oxidative stress parameters [156, 157]. Overall, these results demonstrate the potential protective role of Zn in alleviating the hepatic toxicity, as well as emphasize a role for antioxidants in reducing pesticide toxicity [158]. Differences between females and males are now beginning to be investigated, but the current data suggests that female and male animals show unique differences with regard to pesticide and antioxidant treatments. As such, more targeted research is needed to help determine the differences between males and females.

1.25. N-Acetylcysteine. N-Acetylcysteine (NAC) is a nutritional supplement derived from L-cysteine amino acid. NAC is a well-tolerated mucolytic drug that moderates clinging mucous secretions and supports glutathione S-transferase (GST) activity. When administered orally,

deacetylation of NAC occurs while passing along the small intestine as well as the liver. Thus, its bioavailability is decreased to 4–10%. NAC stimulates glutathione biosynthesis, promotes detoxification, and acts directly as a scavenger of free radicals, especially oxygen radicals. It is a powerful antioxidant and a potential treatment option for diseases characterized by the generation of free oxygen radicals [159]. Tebuconazole (TEB), a triazole fungicide, is widely used to control fungal growth in vegetables, fruits, and seeds. It can also be used as a biocide preservative for industrial and construction material [160]. Ben Othmène et al. found that TEB increased lipid peroxidation, DNA damage, and p53 and p21 protein levels after 24 h in H9c2 cardiomyoblasts. They also suggested that TEB might induce oxidative stress in cardiac cells via the mitochondrial apoptotic pathway due to the loss of mitochondrial transmembrane potential ($\Delta\Psi m$), an increase in the Bax/Bcl-2 ratio, an activation of caspase-9 and caspase-3, a cleavage of poly (ADP-ribose) polymerase (PARP), and an increase in mitochondrial superoxide (measured by MitoSOX). However, when they treated cardiomyocytes with the ROS scavenger NAC, there was a decrease in TEB-induced DNA damage and activation of the mitochondrial pathway of apoptosis [161].

Dorval and Hontela showed that rainbow trout (*Oncorhynchus mykiss*) pretreated with NAC following exposure to endosulfan had significantly higher levels of GSH and decreased levels of lipid hydroperoxides (LOOH) [162]. Another study conducted by Cankayali et al. using male Wistar rats cotreated with dichlorvos and NAC found that NAC might prevent lipid peroxidation and decrease the risk of oxidative stress [163]. Finally, Yurumez et al. found that male NMRI mice treated with 250–500 mg/kg Mancozeb (MZB) for 40 days exhibited significantly increased lipid peroxidation, increased protein carbonyl concentration in the testes, and decreased activities of antioxidant enzymes (SOD and CAT). The total antioxidant capacity and GSH content were found to be significantly less in the testes of MZB-exposed mice [60]. However, cotreatment of MZB-exposed mice with NAC reversed the changes in oxidative stress indices found earlier with MZB. They found significantly decreased levels of lipid peroxidation, and the activities of antioxidant enzymes SOD and CAT were maintained near control levels following NAC + MZB cotreatment [60]. As with other antioxidants discussed earlier, NAC seems to also have strong antioxidative stress properties.

1.26. Epicatechin. Flavonoids are a large group of natural phenolic compounds with different subclasses that have been described as powerful antioxidants from previous *in vitro* studies [164]. The antioxidant properties of flavonoids are largely dependent on their structure, and the major contributing factor is the presence of 3′,4′-dihydroxycatechol, which has reducing capabilities and influence on the intracellular redox status [165]. Epicatechin is a flavan-3-ol, a subclass of the flavonoids found in green tea, grape, apples, and cocoa [166]. Tea extracts and/or its constituents have been reported to possess pharmacological effects such as anti-inflammatory, antibacterial, antiviral, antioxidant, antitumor, antihyperlipidemic, anticarcinogenic, and cytoprotective effects. Also, it was shown that green tea extract can scavenge nitric oxide (NO) and $O_2^{\bullet-}$ very effectively [167]. Moreover, Afolabi et al. found that cotreatment of CYP-exposed rats with epicatechin significantly reduced the formation of nitrosative nucleic acids by 51% [44]. Another study conducted to investigate the effects of catechin against PCP-induced cytotoxicity in human erythrocytes found that PCP significantly decreased GSH levels, total sulfhydryl (SH) content, and cellular antioxidant power. PCP treatment also lowered the activity of antioxidant enzymes and inhibited enzymes of glucose metabolism. However, prior treatment with catechin before incubation with PCP increased the GSH level and total SH content in erythrocytes [120]. Maheshwari and Mahmood reported that prior treatment of catechin prevented the oxidative damage of membrane lipids and lowered malondialdehyde and lipid hydroxyperoxide levels to 1.6- and 1.56-fold relative to control values. Finally, they found that catechin decreased intracellular ROS and RNS levels in PCP-treated erythrocytes [120]. In addition, Spencer et al. showed that epicatechin and its *in vivo* metabolite, 3′-O-methyl epicatechin, protected human fibroblasts from hydrogen peroxide-induced oxidative stress by inhibiting caspase-3 activation [165]. These studies suggest that epicatechin significantly mitigates pesticide-induced oxidative modifications in a concentration-dependent manner while not exhibiting any deleterious effect on its own. Catechin may be a potential chemoprotectant against pesticide toxicity, and other structurally related compounds to catechin may also be beneficial, but further experimentation is needed.

2. Conclusions

The current experimental evidence from research studies suggests that all classes of pesticides induce oxidative stress, RNS, and ROS in different cell types and animal models and that oxidative stress is one of the most important mechanisms of pesticide toxicity. Albeit not exhaustive due to the large number of pesticides available, this review covers the major classes of commonly used pesticides in the United States and the rest of the world. Pesticide exposure could come from occupational routes as well as from food, water, air, and dust. What is typically lacking in previous reviews and research publications are the molecular mechanisms involved in pesticide toxicity because of the complexity of mechanisms that may be involved with different classes of pesticides. A search of the Internet for publications that attempted to explain the mechanisms involved in pesticide toxicity revealed only two publications with one figure each.

The higher levels of oxidative stress eventually cause cell apoptosis through several pathways: the mitochondrial apoptosis pathway, Keap1/Nrf2/ARE, Ca^{2+}, TNFR1/TNF-α, Nurr1, STAT1, ASK1, MAPKs, and NF-κB pathways amongst others. Increased levels of ROS and RNS may also affect the ubiquitin proteasome system (UPS) that degrades altered and misfolded proteins [168]. Numerous reports suggest that Kelch-like ECH-associated protein-1 (Keap1), a substrate adaptor protein for a cullin-3 E3-ubiquitin ligase (Cul3)/Ring-Box- (Rbx1-) dependent complex, plays a

critical role in the ubiquitination and degradation of Nrf2, IKKβ, and Bcl-2/Bcl-xL. ROS disrupts Keap1 via modifying reactive cysteines (Cys273, Cys288, and Cys151) and then inducing a conformational change that leads to the release of Nrf2, IKKβ, and Bcl-2/Bcl-xL from Keap1 and the suspending of their ubiquitination and degradation [169–172]. UPS dysfunction could lead to various cellular malfunctions including proteotoxicity, mitochondrial dysfunction, and apoptosis.

Even though we are starting to understand the mechanisms involved in pesticide toxicity, more research is needed as it is crucial to better understand the molecular mechanisms by which pesticides induce oxidative stress. Interestingly, the T-2 toxin, which is not a pesticide, shows molecular mechanisms for toxicity similar to pesticides. The T-2 toxin induces oxidative stress in numerous cell lines causing oxidative damage to lipids, proteins, and DNA [173]. The T-2 toxin increases MDA content (lipid peroxidation representative) and CAT and SOD activities as well as decreases GSH-Px activity in rat anterior pituitary GH3 cells. Caspase-3, -8 and -9 are significantly induced by the T-2 toxin in a dose-dependent manner. While these T2 toxin-induced mechanisms are similar to pesticides, the T2 toxin also increases the mRNA levels of IL-6, IL-11, and IL-1β and inhibits the synthesis and secretion of GH. It is possible that pesticides could be working in a similar manner to T-2 toxin in regard to the induction of interleukins and growth hormone deficiency [174]. Both PCP and DDT increase IL-6 production [175]. Also, previous research found that people regularly exposed to pesticides, such as women and children raised in agricultural areas, had low levels of insulin-like growth factor-1 (IGF-1), which plays an important role in childhood growth. This makes the children at higher risk of developing growth disorders [176]. While studies suggest that antioxidants may be beneficial for reducing pesticide toxicity, further studies should focus on the possible ways to ameliorate the side effects of pesticide exposure not just via exogenous antioxidants but by influencing the signaling pathways involved in pesticide-induced oxidative stress. More studies are urgently needed to determine how sex differences may be involved in pesticide-induced toxicity, as well as if any other cellular pathways are involved in pesticide-related toxicity.

2.1. Limitations of Previous Studies. Many of the clinical studies on humans have relatively low sample sizes complicating the interpretation of the data as well as the reliability of that data to make generalized conclusions for different populations. Experimental data on gender-specific effects has not been well investigated, but experimental data suggest that xenobiotics affect males and females differently, so pesticides are likely to have gender-specific effects [156, 157]. It would be of great interest to the public to understand the variations in the response of male and female animals to pesticide exposure. It would also be important to determine if there are gender-specific differences in the possible effects of exogenous antioxidants in the mitigation of pesticide-induced oxidative stress biomarkers (lipid peroxidation, lipid oxidation, and protein oxidation), DNA fragmentation, and apoptosis.

Oxidative modification of proteins and proteolytic pathways compromise the protein quality and cell viability due to oxidative stress that arose from the increased ROS level when exposed to pesticides. These events may be among the most relevant in driving protein toxicity in several pathologies such as neurodegenerative diseases, cardiovascular diseases, cancer, reproductive diseases, and birth defects. However, the experimental data on the role of protein toxicity and the UPS in pesticide toxicity is very limited [177]. Finding novel ways to prevent pesticide toxicity may require understanding the role of the UPS pathway in this process to increase the capacity of proteolytic systems to remove intracellular oxidized proteins.

Abbreviations

CAT: Catalase
CPF: Chlorpyrifos
CYP: Cypermethrin
DDT: Dichloro-diphenyl-trichloroethane
ER: Endoplasmic reticulum
Fas-L: Fas ligand
Flt: Fms-related receptor tyrosine kinase 1
GPX: Glutathione peroxidase
GR: Glutathione reductase
GSH: Glutathione
HCH: Hexachlorocyclohexane
H_2O_2: Hydrogen peroxide
HMOX1: Heme oxygenase 1
iNOS: Inducible nitric oxide synthase
JAK: Janus kinases
JNK: c-Jun N-terminal kinases
KD: Knockdown
MAPK: Mitogen-activated *protein* kinase
MDA: Malondialdehyde
NF-κB: Nuclear factor κB
NO: Nitric oxide
NOX: NADPH oxidase
Nrf2: Nuclear factor-erythroid 2-related factor 2
PER: Permethrin
PKCδ: Protein kinase Cδ
PQ: Paraquat
RNS: Reactive nitrogen species
ROS: Reactive oxygen species
STAT: Signal transducers and activators of transcription
SOD: Superoxide dismutase
TCHQ: Tetrachlorohydroquinone
TBARS: Thiobarbituric acid-reactive substances
TLR: Toll-like receptor
TNFα: Tumor necrosis factor α
UPS: Ubiquitin proteasome system.

Data Availability

All information is from published papers and is summarized in supplemental tables.

Conflicts of Interest

All the authors have no competing conflicts of interest.

Acknowledgments

We would like to thank members of the Gomes Lab for reading and providing suggestions. Partial support was provided by the American Heart Association (AHA) award and the NIEHS/Superfund Research Program (P42 ES004699).

Supplementary Materials

Supplemental Table 1: tissue toxicity of pesticides. Supplemental Table 2: signaling pathways altered by pesticides. Supplemental Table 3: effects of commonly used conventional pesticide active ingredients in the agricultural market sector in 2012 on oxidative stress in different tissues. Supplemental Table 4: effects of most commonly used organophosphate insecticide active ingredients in the home and in 2012 on oxidative stress in different tissues. Supplemental Table 5: table showing additional pesticides that have been documented to cause oxidative stress in different tissues. Supplemental Table 6: table showing pesticide tolerable and nontoxic concentrations. *(Supplementary Materials)*

References

[1] R. Jayaraj, P. Megha, and P. Sreedev, "Review Article. Organochlorine pesticides, their toxic effects on living organisms and their fate in the environment," *Interdisciplinary Toxicology*, vol. 9, no. 3-4, pp. 90–100, 2016.

[2] N. Georgiadis, K. Tsarouhas, C. Tsitsimpikou et al., "Pesticides and cardiotoxicity. Where do we stand?," *Toxicology and Applied Pharmacology*, vol. 353, pp. 1–14, 2018.

[3] A. Sharma, V. Kumar, B. Shahzad et al., "Worldwide pesticide usage and its impacts on ecosystem," *SN Applied Sciences*, vol. 1, no. 11, p. 1446, 2019.

[4] S. Medithi, Y. D. Kasa, B. Jee, V. Kodali, and P. R. Jonnalagadda, "Organophosphate pesticide exposure among farm women and children: Status of micronutrients, acetylcholinesterase activity, and oxidative stress," *Archives of Environmental & Occupational Health*, vol. 75, pp. 1–16, 2020.

[5] J. Min, J. Han, K. Kim et al., "Human cholestatic hepatitis owing to polyoxyethylene nonylphenol ingestion," *Medicine*, vol. 96, no. 32, article e7737, 2017.

[6] C. A. Damalas and I. G. Eleftherohorinos, "Pesticide exposure, safety issues, and risk assessment indicators," *International Journal of Environmental Research and Public Health*, vol. 8, no. 5, pp. 1402–1419, 2011.

[7] A. L. Wani, A. Ara, and J. A. Usmani, "Lead toxicity: a review," *Interdisciplinary Toxicology*, vol. 8, no. 2, pp. 55–64, 2015.

[8] I. K. Konstantinou, D. G. Hela, and T. A. Albanis, "The status of pesticide pollution in surface waters (rivers and lakes) of Greece. Part I. Review on occurrence and levels," *Environmental Pollution*, vol. 141, no. 3, pp. 555–570, 2006.

[9] S. Gangemi, E. Gofita, C. Costa et al., "Occupational and environmental exposure to pesticides and cytokine pathways in chronic diseases (Review)," *International Journal of Molecular Medicine*, vol. 38, no. 4, pp. 1012–1020, 2016.

[10] Reregistration eligibility decision for prometryn, *U.S. Environmental Protection Agency, Prevention, Pesticides and Toxic Substances*, U.S. Environmental Protection Agency, Washington, D.C., 1996.

[11] G. D. Coronado, S. Holte, E. Vigoren et al., "Organophosphate pesticide exposure and residential proximity to nearby Fields," *Journal of Occupational and Environmental Medicine*, vol. 53, no. 8, pp. 884–891, 2011.

[12] R. K. Kori, M. K. Singh, A. K. Jain, and R. S. Yadav, "Neurochemical and behavioral dysfunctions in pesticide exposed farm workers: a clinical outcome," *Indian Journal of Clinical Biochemistry*, vol. 33, no. 4, pp. 372–381, 2018.

[13] A. Sabarwal, K. Kumar, and R. P. Singh, "Hazardous effects of chemical pesticides on human health-Cancer and other associated disorders," *Environmental Toxicology and Pharmacology*, vol. 63, pp. 103–114, 2018.

[14] I. A. Hundekari, A. N. Suryakar, and D. B. Rathi, "Acute organo-phosphorus pesticide poisoning in North Karnataka, India: oxidative damage, haemoglobin level and total leukocyte," *African Health Sciences*, vol. 13, no. 1, pp. 129–136, 2013.

[15] H. Xing, Z. Wang, X. Gao et al., "Atrazine and chlorpyrifos exposure induces liver autophagic response in common carp," *Ecotoxicology and Environmental Safety*, vol. 113, pp. 52–58, 2015.

[16] Q. Liu, L. Wang, H. Chen et al., "Prometryn induces apoptotic cell death through cell cycle arrest and oxidative DNA damage," *Toxicology Research*, vol. 8, no. 6, pp. 833–841, 2019.

[17] R. C. Gilden, K. Huffling, and B. Sattler, "Pesticides and health risks," *Journal of Obstetric, Gynecologic, and Neonatal Nursing*, vol. 39, no. 1, pp. 103–110, 2010.

[18] S. Mostafalou and M. Abdollahi, "Pesticides and human chronic diseases: evidences, mechanisms, and perspectives," *Toxicology and Applied Pharmacology*, vol. 268, no. 2, pp. 157–177, 2013.

[19] A. D. Souza, A. . R. Medeiros, A. C. . Souza et al., "Avaliação do impacto da exposição a agrotóxicos sobre a saúde de população rural: Vale do Taquari (RS Brasil)," *Ciência & Saúde Coletiva*, vol. 16, no. 8, pp. 3519–3528, 2011.

[20] V. Hajhashemi, G. Vaseghi, M. Pourfarzam, and A. Abdollahi, "Are antioxidants helpful for disease prevention?," *Research in Pharmaceutical Sciences*, vol. 5, no. 1, pp. 1–8, 2010.

[21] J. Chen, Y. Su, F. Lin et al., "Effect of paraquat on cytotoxicity involved in oxidative stress and inflammatory reaction: a review of mechanisms and ecological implications," *Ecotoxicology and Environmental Safety*, vol. 224, article 112711, 2021.

[22] Q. Li, X. Yang, N. Sreejayan, and J. Ren, "Insulin-like growth factor I deficiency prolongs survival and antagonizes paraquat-induced cardiomyocyte dysfunction: role of oxidative stress," *Rejuvenation Research*, vol. 10, no. 4, pp. 501–512, 2007.

[23] W. Ge, Y. Zhang, X. Han, and J. Ren, "Cardiac-specific overexpression of catalase attenuates paraquat-induced myocardial geometric and contractile alteration: role of ER stress," *Free Radical Biology & Medicine*, vol. 49, no. 12, pp. 2068–2077, 2010.

[24] B. A. Cohn, M. S. Wolff, P. M. Cirillo, and R. I. Sholtz, "DDT and breast cancer in young women: new data on the significance of age at exposure," *Environmental Health Perspectives*, vol. 115, no. 10, pp. 1406–1414, 2007.

[25] K. A. McGlynn, C. C. Abnet, M. Zhang et al., "Serum concentrations of 1,1,1-trichloro-2,2-bis(p-chlorophenyl)ethane (DDT) and 1,1-dichloro-2,2-bis(p-chlorophenyl)ethylene (DDE) and risk of primary liver cancer," *Journal of the National Cancer Institute*, vol. 98, no. 14, pp. 1005–1010, 2006.

[26] K. A. McGlynn, S. M. Quraishi, B. I. Graubard, J. P. Weber, M. V. Rubertone, and R. L. Erickson, "Persistent organochlorine pesticides and risk of testicular germ cell tumors," *Journal of the National Cancer Institute*, vol. 100, no. 9, pp. 663–671, 2008.

[27] A. R. Ravula and S. Yenugu, "Pyrethroid based pesticides - chemical and biological aspects," *Critical Reviews in Toxicology*, vol. 51, no. 2, pp. 117–140, 2021.

[28] R. Li, Z. Jia, and M. A. Trush, "Defining ROS in biology and medicine," *Reactive oxygen species*, vol. 1, no. 1, pp. 9–21, 2016.

[29] A. V. Snezhkina, A. V. Kudryavtseva, O. L. Kardymon et al., "ROS generation and antioxidant defense systems in normal and malignant cells," *Oxidative Medicine and Cellular Longevity*, vol. 2019, Article ID 6175804, 17 pages, 2019.

[30] M. Schieber and N. S. Chandel, "ROS function in redox signaling and oxidative stress," *Current Biology: CB*, vol. 24, no. 10, pp. R453–R462, 2014.

[31] T. Finkel, "Signal transduction by reactive oxygen species," *The Journal of Cell Biology*, vol. 194, no. 1, pp. 7–15, 2011.

[32] J. Mele, H. V. Remmen, J. Vijg, and A. Richardson, "Characterization of transgenic mice that overexpress both copper zinc superoxide dismutase and catalase," *Antioxidants & Redox Signaling*, vol. 8, no. 3-4, pp. 628–638, 2006.

[33] B. Halliwell and J. M. Gutteridge, "Role of free radicals and catalytic metal ions in human disease: an overview," *Methods in Enzymology*, vol. 186, pp. 1–85, 1990.

[34] J. Shi, B. Sun, W. Shi et al., "Decreasing GSH and increasing ROS in chemosensitivity gliomas with IDH1 mutation," *Tumour Biology*, vol. 36, no. 2, pp. 655–662, 2015.

[35] A. Alhasawi, F. Legendre, S. Jagadeesan, V. Appanna, and V. Appanna, "Chapter 10 - biochemical strategies to counter nitrosative stress: nanofactories for value-added products," in *Microbial Diversity in the Genomic Era*, S. Das and H. R. Dash, Eds., pp. 153–169, Academic Press, 2019.

[36] C. Auger, J. Lemire, D. Cecchini, A. Bignucolo, and V. D. Appanna, "The metabolic reprogramming evoked by nitrosative stress triggers the anaerobic utilization of citrate in Pseudomonas fluorescens," *PLoS One*, vol. 6, no. 12, article e28469, 2011.

[37] M. C. Martínez and R. Andriantsitohaina, "Reactive nitrogen species: molecular mechanisms and potential significance in health and disease," *Antioxidants & Redox Signaling*, vol. 11, no. 3, pp. 669–702, 2009.

[38] C. Vittorio, R. Sultana, G. Scapagnini et al., "Nitrosative stress, cellular stress response, and thiol homeostasis in patients with Alzheimer's disease," *Antioxidants & Redox Signaling*, vol. 8, no. 11-12, pp. 1975–1986, 2006.

[39] T. P. Brown, P. C. Rumsby, A. C. Capleton, L. Rushton, and L. S. Levy, "Pesticides and Parkinson's disease–is there a link?," *Environmental Health Perspectives*, vol. 114, no. 2, pp. 156–164, 2006.

[40] X. Wang, M. A. Martínez, M. Dai et al., "Permethrin-induced oxidative stress and toxicity and metabolism. A review," *Environmental Research*, vol. 149, pp. 86–104, 2016.

[41] Y. Fu, H. Sies, and X. G. Lei, "Opposite roles of selenium-dependent glutathione peroxidase-1 in superoxide generator diquat- and peroxynitrite-induced apoptosis and signaling," *The Journal of Biological Chemistry*, vol. 276, no. 46, pp. 43004–43009, 2001.

[42] Y. Jin, R. Chen, W. Liu, and Z. Fu, "Effect of endocrine disrupting chemicals on the transcription of genes related to the innate immune system in the early developmental stage of zebrafish (Danio rerio)," *Fish & Shellfish Immunology*, vol. 28, no. 5-6, pp. 854–861, 2010.

[43] D. Fedeli, M. Carloni, C. Nasuti, A. Gambini, V. Scocco, and R. Gabbianelli, "Early life permethrin exposure leads to hypervitaminosis D, nitric oxide and catecholamines impairment," *Pesticide Biochemistry and Physiology*, vol. 107, no. 1, pp. 93–97, 2013.

[44] O. K. Afolabi, F. A. Aderibigbe, D. T. Folarin, A. Arinola, and A. D. Wusu, "Oxidative stress and inflammation following sub-lethal oral exposure of cypermethrin in rats: mitigating potential of epicatechin," *Heliyon*, vol. 5, no. 8, article e02274, 2019.

[45] D. A. Drechsel and M. Patel, "Role of reactive oxygen species in the neurotoxicity of environmental agents implicated in Parkinson's disease," *Free Radical Biology & Medicine*, vol. 44, no. 11, pp. 1873–1886, 2008.

[46] Y. Hiraku, "Formation of 8-nitroguanine, a nitrative DNA lesion, in inflammation-related carcinogenesis and its significance," *Environmental Health and Preventive Medicine*, vol. 15, no. 2, pp. 63–72, 2010.

[47] S. Pinlaor, B. Sripa, N. Ma et al., "Nitrative and oxidative DNA damage in intrahepatic cholangiocarcinoma patients in relation to tumor invasion," *World Journal of Gastroenterology*, vol. 11, no. 30, pp. 4644–4649, 2005.

[48] M. Amizadeh, M. Safari-Kamalabadi, G. Askari-Saryazdi, M. Amizadeh, and H. Reihani-Kermani, "Pesticide exposure and head and neck cancers: a case-control study in an agricultural region," *Iranian Journal of Otorhinolaryngology*, vol. 29, no. 94, pp. 275–285, 2017.

[49] M. C. Alavanja, M. K. Ross, and M. R. Bonner, "Increased cancer burden among pesticide applicators and others due to pesticide exposure," *CA: a Cancer Journal for Clinicians*, vol. 63, no. 2, pp. 120–142, 2013.

[50] S. C. Cortés-Iza and A. I. Rodríguez, "Oxidative stress and pesticide disease: a challenge for toxicology," *Revista de la Facultad de Medicina*, vol. 66, pp. 261–267, 2018.

[51] A. Ranjbar, P. Pasalar, A. Sedighi, and M. Abdollahi, "Induction of oxidative stress in paraquat formulating workers," *Toxicology Letters*, vol. 131, no. 3, pp. 191–194, 2002.

[52] A. Prakasam, S. Sethupathy, and S. Lalitha, "Plasma and RBCs antioxidant status in occupational male pesticide sprayers," *Clinica Chimica Acta*, vol. 310, no. 2, pp. 107–112, 2001.

[53] P. D. Dwivedi, M. Das, and S. K. Khanna, "Role of cytochrome P-450 in quinalphos toxicity: effect on hepatic and brain antioxidant enzymes in ratsITRC communication no," *Food and Chemical Toxicology*, vol. 36, no. 5, pp. 437–444, 1998.

[54] *Chlorpyrifos Facts 2002*, Environmental Protection Agency, 2002, EPA 738-F-01-006.

[55] J. Noworyta-Glowacka, M. Beresinska, R. Bankowski, B. Wiadrowska, J. Siennicka, and J. K. Ludwicki, "Effect of chlorpyrifos on the profile of subpopulations immunocompetent cells B, T and NK in in vivo model," *Roczniki Panstwowego Zakladu Higieny*, vol. 65, no. 4, pp. 311–316, 2014.

[56] I. H. Jung, J. H. K. Choi, Y. Y. Chung, G. L. Lim, Y. N. Park, and S. W. Park, "Predominant Activation of JAK/STAT3 Pathway by Interleukin-6 Is Implicated in Hepatocarcinogenesis," *Neoplasia*, vol. 17, no. 7, pp. 586–597, 2015.

[57] B. K. Binukumar, A. Bal, and K. D. Gill, "Chronic dichlorvos exposure: microglial activation, proinflammatory cytokines and damage to nigrostriatal dopaminergic system," *Neuromolecular Medicine*, vol. 13, no. 4, pp. 251–265, 2011.

[58] N. Soundararajan, D. Mohan, R. Abbu, and T. Devasena, "Evaluation of cytotoxicity, oxidative stress, nuclear changes and pro-inflammatory cytokines induced by monocrotophos in human keratinocyte cells in vitro," *International Journal of Pharmacy and Pharmaceutical Sciences*, vol. 7, no. 1, 2014.

[59] S. Ayub, J. Verma, and N. Das, "Effect of endosulfan and malathion on lipid peroxidation, nitrite and TNF-alpha release by rat peritoneal macrophages," *International Immunopharmacology*, vol. 3, no. 13-14, pp. 1819–1828, 2003.

[60] Y. Yurumez, M. Cemek, Y. Yavuz, Y. O. Birdane, and M. E. Buyukokuroglu, "Beneficial effect of N-acetylcysteine against organophosphate toxicity in mice," *Biological & Pharmaceutical Bulletin*, vol. 30, no. 3, pp. 490–494, 2007.

[61] A. T. Hariri, S. A. Moallem, M. Mahmoudi, B. Memar, and H. Hosseinzadeh, "Sub-acute effects of diazinon on biochemical indices and specific biomarkers in rats: protective effects of crocin and safranal," *Food and Chemical Toxicology*, vol. 48, no. 10, pp. 2803–2808, 2010.

[62] N. Magalhães, F. Carvalho, and R. J. Dinis-Oliveira, "Human and experimental toxicology of diquat poisoning: Toxicokinetics, mechanisms of toxicity, clinical features, and treatment," *Human & Experimental Toxicology*, vol. 37, no. 11, pp. 1131–1160, 2018.

[63] C. Uchendu, S. F. Ambali, J. O. Ayo, and K. A. N. Esievo, "Chronic co-exposure to chlorpyrifos and deltamethrin pesticides induces alterations in serum lipids and oxidative stress in Wistar rats: mitigating role of alpha-lipoic acid," *Environmental Science and Pollution Research*, vol. 25, no. 20, pp. 19605–19611, 2018.

[64] A. Ojha and Y. K. Gupta, "Evaluation of genotoxic potential of commonly used organophosphate pesticides in peripheral blood lymphocytes of rats," *Human & Experimental Toxicology*, vol. 34, no. 4, pp. 390–400, 2015.

[65] X. Lu and C. Yu, "Enantiomer-specific profenofos-induced cytotoxicity and DNA damage mediated by oxidative stress in rat adrenal pheochromocytoma (PC12) cells," *Journal of Applied Toxicology*, vol. 34, no. 2, pp. 166–175, 2014.

[66] M. E. M. Nunes, L. E. Schimith, D. G. da Costa-Silva et al., "Acute exposure to permethrin modulates behavioral functions, redox, and bioenergetics parameters and induces DNA damage and cell death in larval zebrafish," *Oxidative Medicine and Cellular Longevity*, vol. 2019, Article ID 9149203, 19 pages, 2019.

[67] L. P. Naeher, D. B. Barr, N. Rithmire et al., "Pesticide exposure resulting from treatment of lice infestation in school-aged children in Georgia," *Environment International*, vol. 35, no. 2, pp. 358–362, 2009.

[68] A. Mokarizadeh, M. R. Faryabi, M. A. Rezvanfar, and M. Abdollahi, "A comprehensive review of pesticides and the immune dysregulation: mechanisms, evidence and consequences," *Toxicology Mechanisms and Methods*, vol. 25, no. 4, pp. 258–278, 2015.

[69] R. Gabbianelli, M. L. Falcioni, C. Nasuti, F. Cantalamessa, I. Imada, and M. Inoue, "Effect of permethrin insecticide on rat polymorphonuclear neutrophils," *Chemico-Biological Interactions*, vol. 182, no. 2-3, pp. 245–252, 2009.

[70] M. D. P. Navarrete-Meneses and P. Pérez-Vera, "Pyrethroid pesticide exposure and hematological cancer: epidemiological, biological and molecular evidence," *Reviews on Environmental Health*, vol. 34, no. 2, pp. 197–210, 2019.

[71] M. W. Aktar, D. Sengupta, and A. Chowdhury, "Impact of pesticides use in agriculture: their benefits and hazards," *Interdisciplinary Toxicology*, vol. 2, no. 1, pp. 1–12, 2009.

[72] M. Kitazawa, V. Anantharam, and A. G. Kanthasamy, "Dieldrin induces apoptosis by promoting caspase-3-dependent proteolytic cleavage of protein kinase Cdelta in dopaminergic cells: relevance to oxidative stress and dopaminergic degeneration," *Neuroscience*, vol. 119, no. 4, pp. 945–964, 2003.

[73] R. Subbiah and R. R. Tiwari, "The herbicide paraquat-induced molecular mechanisms in the development of acute lung injury and lung fibrosis," *Critical Reviews in Toxicology*, vol. 51, no. 1, pp. 36–64, 2021.

[74] S. Wang, R. Guo, and J. Ren, "Stress signaling in paraquat-induced target organ toxicity," *Reactive Oxygen Species*, vol. 1, no. 2, pp. 131–140, 2016.

[75] E. L. Robb, J. M. Gawel, D. Aksentijević et al., "Selective superoxide generation within mitochondria by the targeted redox cycler mitoparaquat," *Free Radical Biology & Medicine*, vol. 89, pp. 883–894, 2015.

[76] B. J. Day, M. Patel, L. Calavetta, L. Y. Chang, and J. S. Stamler, "A mechanism of paraquat toxicity involving nitric oxide synthase," *Proceedings of the National Academy of Sciences of the United States of America*, vol. 96, no. 22, pp. 12760–12765, 1999.

[77] A. C. Cristóvão, D. H. Choi, G. Baltazar, M. F. Beal, and Y. S. Kim, "The role of NADPH oxidase 1-derived reactive oxygen species in paraquat-mediated dopaminergic cell death," *Antioxidants & Redox Signaling*, vol. 11, no. 9, pp. 2105–2118, 2009.

[78] T. Taetzsch and M. L. Block, "Pesticides, microglial NOX2, and Parkinson's disease," *Journal of Biochemical and Molecular Toxicology*, vol. 27, no. 2, pp. 137–149, 2013.

[79] P. R. Castello, D. A. Drechsel, and M. Patel, "Mitochondria are a major source of paraquat-induced reactive oxygen species production in the brain," *The Journal of Biological Chemistry*, vol. 282, no. 19, pp. 14186–14193, 2007.

[80] N. Singh, V. Lawana, J. Luo et al., "Organophosphate pesticide chlorpyrifos impairs STAT1 signaling to induce dopaminergic neurotoxicity: Implications for mitochondria mediated oxidative stress signaling events," *Neurobiology of Disease*, vol. 117, pp. 82–113, 2018.

[81] H. S. Kim and M. S. Lee, "STAT1 as a key modulator of cell death," *Cellular Signalling*, vol. 19, no. 3, pp. 454–465, 2007.

[82] M. Skonieczna, T. Hejmo, A. Poterala-Hejmo, A. Cieslar-Pobuda, and R. J. Buldak, "NADPH oxidases: insights into selected functions and mechanisms of action in cancer and stem cells," *Oxidative Medicine and Cellular Longevity*, vol. 2017, Article ID 9420539, 15 pages, 2017.

[83] X.-J. Fu, Y. B. Peng, Y. P. Hu, Y. Z. Shi, M. Yao, and X. Zhang, "NADPH oxidase 1 and its derived reactive oxygen species mediated tissue injury and repair," *Oxidative Medicine and Cellular Longevity*, vol. 2014, Article ID 282854, 10 pages, 2014.

[84] L. C. Mangum, A. Borazjani, J. V. Stokes et al., "Organochlorine insecticides induce NADPH oxidase-dependent reactive oxygen species in human monocytic cells via phospholipase A2/arachidonic acid," *Chemical Research in Toxicology*, vol. 28, no. 4, pp. 570–584, 2015.

[85] J. L. Munoz-Carrillo, J. F. Contreras-Cordero, O. Gutiérrez-Coronado, P. T. Villalobos-Gutiérrez, L. G. Ramos-Gracia, and V. E. Hernández-Reyes, *Cytokine Profiling Plays a Crucial Role in Activating Immune System to Clear Infectious Pathogens*, 2019.

[86] F. J. Pacheco, F. G. Almaguel, W. Evans et al., "Docosahexanoic acid antagonizes TNF-α-induced necroptosis by attenuating oxidative stress, ceramide production, lysosomal dysfunction, and autophagic features," *Inflammation Research : Official Journal of the European Histamine Research Society*, vol. 63, no. 10, pp. 859–871, 2014.

[87] D. C. de Oliveira, A. A. Hastreiter, A. S. Mello et al., "The effects of protein malnutrition on the TNF-RI and NF-κB expression via the TNF-α signaling pathway," *Cytokine*, vol. 69, no. 2, pp. 218–225, 2014.

[88] C. Sullivan and C. H. Kim, "Zebrafish as a model for infectious disease and immune function," *Fish & Shellfish Immunology*, vol. 25, no. 4, pp. 341–350, 2008.

[89] V. Tyagi, M. D. Mustafa, T. Sharma et al., "Association of organochlorine pesticides with the mRNA expression of tumour necrosis factor-alpha (TNF-α) & cyclooxygenase-2 (COX-2) genes in idiopathic preterm birth," *The Indian Journal of Medical Research*, vol. 143, no. 6, pp. 731–738, 2016.

[90] M. Decressac, N. Volakakis, A. Björklund, and T. Perlmann, "NURR1 in Parkinson disease–from pathogenesis to therapeutic potential," *Nature Reviews. Neurology*, vol. 9, no. 11, pp. 629–636, 2013.

[91] M. Carloni, C. Nasuti, D. Fedeli et al., "Early life permethrin exposure induces long-term brain changes in Nurr1, NF-kB and Nrf-2," *Brain Research*, vol. 1515, pp. 19–28, 2013.

[92] D. Fedeli, M. Montani, M. Carloni, C. Nasuti, A. Amici, and R. Gabbianelli, "Leukocyte Nurr1 as peripheral biomarker of early-life environmental exposure to permethrin insecticide," *Biomarkers*, vol. 17, no. 7, pp. 604–609, 2012.

[93] M. E. Reyland, "Protein kinase C isoforms: Multi-functional regulators of cell life and death," *Frontiers in Bioscience (Landmark Edition)*, vol. 14, pp. 2386–2399, 2009.

[94] H. Mellor and P. J. Parker, "The extended protein kinase C superfamily," *The Biochemical Journal*, vol. 332, Part 2, pp. 281–292, 1998.

[95] P. E. Rosenfeld and L. G. H. Feng, "11 - Pesticides," in *Risks of Hazardous Wastes*, P. E. Rosenfeld and L. G. H. Feng, Eds., pp. 127–154, William Andrew Publishing, Boston, 2011.

[96] B. Ritz and F. Yu, "Parkinson's disease mortality and pesticide exposure in California 1984–1994," *International Journal of Epidemiology*, vol. 29, no. 2, pp. 323–329, 2000.

[97] Z. Jia and H. P. Misra, "Exposure to mixtures of endosulfan and zineb induces apoptotic and necrotic cell death in SH-SY5Y neuroblastoma cells, in vitro," *Journal of Applied Toxicology*, vol. 27, no. 5, pp. 434–446, 2007.

[98] D. R. Green and J. C. Reed, "Mitochondria and apoptosis," *Science*, vol. 281, no. 5381, pp. 1309–1312, 1998.

[99] A. Ashkenazi and V. M. Dixit, "Death receptors: signaling and modulation," *Science*, vol. 281, no. 5381, pp. 1305–1308, 1998.

[100] G. P. Das, A. P. Shaik, and K. Jamil, "Estimation of apoptosis and necrosis caused by pesticides in vitro on human lymphocytes using DNA diffusion assay," *Drug and Chemical Toxicology*, vol. 29, no. 2, pp. 147–156, 2006.

[101] G. Raszewski, M. K. Lemieszek, K. Łukawski, M. Juszczak, and W. Rzeski, "Chlorpyrifos and cypermethrin induce apoptosis in human neuroblastoma cell line SH-SY5Y," *Basic & Clinical Pharmacology & Toxicology*, vol. 116, no. 2, pp. 158–167, 2015.

[102] R. Venkatesan, Y. U. Park, E. Ji, E. J. Yeo, and S. Y. Kim, "Malathion increases apoptotic cell death by inducing lysosomal membrane permeabilization in N2a neuroblastoma cells: a model for neurodegeneration in Alzheimer's disease," *Cell death discover*, vol. 3, no. 1, p. 17007, 2017.

[103] C. Yang, W. Lim, and G. Song, "Mediation of oxidative stress toxicity induced by pyrethroid pesticides in fish," *Comparative Biochemistry and Physiology, Part C: Toxicology & Pharmacology*, vol. 234, article 108758, 2020.

[104] M. T. Islam, "Oxidative stress and mitochondrial dysfunction-linked neurodegenerative disorders," *Neurological Research*, vol. 39, no. 1, pp. 73–82, 2017.

[105] T. B. Sherer, J. R. Richardson, C. M. Testa et al., "Mechanism of toxicity of pesticides acting at complex I: relevance to environmental etiologies of Parkinson's disease," *Journal of Neurochemistry*, vol. 100, no. 6, 2007.

[106] A. H. Bhat, K. B. Dar, S. Anees et al., "Oxidative stress, mitochondrial dysfunction and neurodegenerative diseases; a mechanistic insight," *Biomedicine & Pharmacotherapy*, vol. 74, pp. 101–110, 2015.

[107] J. D. Malhotra and R. J. Kaufman, "ER stress and its functional link to mitochondria: role in cell survival and death," *Cold Spring Harbor Perspectives in Biology*, vol. 3, no. 9, article a004424, 2011.

[108] H.-M. Chen, Y.-H. Lee, and Y.-J. Wang, "ROS-triggered signaling pathways involved in the cytotoxicity and tumor promotion effects of pentachlorophenol and tetrachlorohydroquinone," *Chemical Research in Toxicology*, vol. 28, no. 3, pp. 339–350, 2015.

[109] C. Pellacani and L. G. Costa, "Role of autophagy in environmental neurotoxicity," *Environmental Pollution*, vol. 235, pp. 791–805, 2018.

[110] C. Rodolfo, S. Di Bartolomeo, and F. Cecconi, "Autophagy in stem and progenitor cells," *Cellular and Molecular Life Sciences*, vol. 73, no. 3, pp. 475–496, 2016.

[111] J. H. Park, J. E. Lee, I. C. Shin, and H. C. Koh, "Autophagy regulates chlorpyrifos-induced apoptosis in SH-SY5Y cells," *Toxicology and Applied Pharmacology*, vol. 268, no. 1, pp. 55–67, 2013.

[112] H. Dai, Y. Deng, J. Zhang et al., "PINK1/Parkin-mediated mitophagy alleviates chlorpyrifos-induced apoptosis in SH-SY5Y cells," *Toxicology*, vol. 334, pp. 72–80, 2015.

[113] J. H. Park, J. E. Lee, S. J. Lee et al., "Potential autophagy enhancers protect against fipronil-induced apoptosis in SH-SY5Y cells," *Toxicology Letters*, vol. 223, no. 1, pp. 25–34, 2013.

[114] S. Wang, X. Zhu, L. Xiong, Y. Zhang, and J. Ren, "Toll-like receptor 4 knockout alleviates paraquat-induced

cardiomyocyte contractile dysfunction through an autophagy-dependent mechanism," *Toxicology Letters*, vol. 257, pp. 11–22, 2016.

[115] Q. Zhou, H. Zhang, Q. Wu, J. Shi, and S. Zhou, "Pharmacological manipulations of autophagy modulate paraquat-induced cytotoxicity in PC12 cells," *International Journal of Biochemistry and Molecular Biology*, vol. 8, no. 2, pp. 13–22, 2017.

[116] Y. Jie, R. Wenkai, W. Xiaosong et al., "Oxidative stress-mediated signaling pathways: A Review," *Journal of Food, Agriculture & Environment*, vol. 11, no. 2, pp. 132–139, 2013.

[117] M. Cargnello and P. P. Roux, "Activation and function of the MAPKs and their substrates, the MAPK-activated protein kinases," *Microbiology and Molecular Biology Reviews: MMBR*, vol. 75, no. 1, pp. 50–83, 2011.

[118] U.S. Environmental Protection Agency, "Reregistration eligibility decision for pentachlorophenol," in *Prevention, Pesticides and Toxic Substances*, U.S. Environmental Protection Agency, Washington, DC, 2008.

[119] J. J. Morrell, "Chapter 17 - Protection of Wood-Based Materials," in *Handbook of Environmental Degradation of Materials (Third Edition)*, M. Kutz, Ed., pp. 343–368, William Andrew Publishing, 2018.

[120] N. Maheshwari and R. Mahmood, "Protective effect of catechin on pentachlorophenol-induced cytotoxicity and genotoxicity in isolated human blood cells," *Environmental Science and Pollution Research*, vol. 27, no. 12, pp. 13826–13843, 2020.

[121] "NTP toxicology and carcinogenesis studies of two pentachlorophenol technical-grade mixtures (CAS no. 87-86-5) in B6C3F1 mice (feed studies)," *National Toxicology Program Technical Report Series*, vol. 349, pp. 1–265, 1989.

[122] P. G. Jorens and P. J. C. Schepens, "Human pentachlorophenol poisoning," *Human & Experimental Toxicology*, vol. 12, no. 6, pp. 479–495, 1993.

[123] B. Wispriyono, M. Matsuoka, and H. Igisu, "Effects of pentachlorophenol and tetrachlorohydroquinone on mitogen-activated protein kinase pathways in Jurkat T cells," *Environmental Health Perspectives*, vol. 110, no. 2, pp. 139–143, 2002.

[124] C. Ventura, A. Venturino, N. Miret et al., "Chlorpyrifos inhibits cell proliferation through ERK1/2 phosphorylation in breast cancer cell lines," *Chemosphere*, vol. 120, pp. 343–350, 2015.

[125] S. Shiizaki, I. Naguro, and H. Ichijo, "Activation mechanisms of ASK1 in response to various stresses and its significance in intracellular signaling," *Advances in Biological Regulation*, vol. 53, no. 1, pp. 135–144, 2013.

[126] D. N. Meijles, J. J. Cull, T. Markou et al., "Redox regulation of cardiac ASK1 (apoptosis signal-regulating kinase 1) controls p38-MAPK (mitogen-activated protein kinase) and orchestrates cardiac remodeling to hypertension," *Hypertension*, vol. 76, no. 4, pp. 1208–1218, 2020.

[127] M. Niso-Santano, J. M. Bravo-San Pedro, R. Gómez-Sánchez et al., "ASK1 overexpression accelerates paraquat-induced autophagy via endoplasmic reticulum stress," *Toxicological Sciences*, vol. 119, no. 1, pp. 156–168, 2011.

[128] E. Kansanen, S. M. Kuosmanen, H. Leinonen, and A. L. Levonen, "The Keap1-Nrf2 pathway: Mechanisms of activation and dysregulation in cancer," *Redox Biology*, vol. 1, no. 1, pp. 45–49, 2013.

[129] F. Zheng, F. M. Gonçalves, Y. Abiko, H. Li, Y. Kumagai, and M. Aschner, "Redox toxicology of environmental chemicals causing oxidative stress," *Redox Biology*, vol. 34, article 101475, 2020.

[130] S. E. Purdom-Dickinson, E. V. Sheveleva, H. Sun, and Q. M. Chen, "Translational control of nrf2 protein in activation of antioxidant response by oxidants," *Molecular Pharmacology*, vol. 72, no. 4, pp. 1074–1081, 2007.

[131] K. Chan, X.-D. Han, and Y. W. Kan, "An important function of Nrf2 in combating oxidative stress: Detoxification of acetaminophen," *Proceedings of the National Academy of Sciences*, vol. 98, no. 8, pp. 4611–4616, 2001.

[132] M. Ramos-Gomez, M. K. Kwak, P. M. Dolan et al., "Sensitivity to carcinogenesis is increased and chemoprotective efficacy of enzyme inducers is lost in nrf2 transcription factor-deficient mice," *Proceedings of the National Academy of Sciences of the United States of America*, vol. 98, no. 6, pp. 3410–3415, 2001.

[133] X. Yuan, C. Xu, Z. Pan et al., "Butylated hydroxyanisole regulates ARE-mediated gene expression via Nrf2 coupled with ERK and JNK signaling pathway in HepG2 cells," *Molecular Carcinogenesis*, vol. 45, no. 11, pp. 841–850, 2006.

[134] M. S. Dhivya Vadhana, S. Siva Arumugam, M. Carloni, C. Nasuti, and R. Gabbianelli, "Early life permethrin treatment leads to long-term cardiotoxicity," *Chemosphere*, vol. 93, no. 6, pp. 1029–1034, 2013.

[135] T. Dou, M. Yan, X. Wang et al., "Nrf2/ARE pathway involved in oxidative stress induced by paraquat in human neural progenitor cells," *Oxidative Medicine and Cellular Longevity*, vol. 2016, Article ID 8923860, 8 pages, 2016.

[136] H. Y. Li, S. Y. Wu, Q. Ma, and N. Shi, "The pesticide deltamethrin increases free radical production and promotes nuclear translocation of the stress response transcription factor Nrf2 in rat brain," *Toxicology and Industrial Health*, vol. 27, no. 7, pp. 579–590, 2011.

[137] W. T. Thomson, "Agricultural Chemicals," in *Book I*, Thomson Publications, Fresno, CA, 1992.

[138] Organization, WH, *World Malaria Report 2015*, World Health Organization, 2016.

[139] A. G. Kanthasamy, M. Kitazawa, A. Kanthasamy, and V. Anantharam, "Dieldrin-Induced Neurotoxicity: Relevance to Parkinson's Disease Pathogenesis," *Neurotoxicology*, vol. 26, no. 4, pp. 701–719, 2005.

[140] B. Çiğ and M. Nazıroğlu, "Investigation of the effects of distance from sources on apoptosis, oxidative stress and cytosolic calcium accumulation via TRPV1 channels induced by mobile phones and Wi-Fi in breast cancer cells," *Biochimica et Biophysica Acta (BBA)-Biomembranes*, vol. 1848, no. 10 Part B, pp. 2756–2765, 2015.

[141] R. H. Westerink, "Modulation of cell viability, oxidative stress, calcium homeostasis, and voltage- and ligand-gated ion channels as common mechanisms of action of (mixtures of) non-dioxin-like polychlorinated biphenyls and polybrominated diphenyl ethers," *Environmental Science and Pollution Research International*, vol. 21, no. 10, pp. 6373–6383, 2014.

[142] A. Saad-Hussein, K. S. Ibrahim, M. S. Abdalla, H. A. el-Mezayen, and N. F. A. Osman, "Effects of zinc supplementation on oxidant/antioxidant and lipids status of pesticides sprayers," *Journal of Complementary and Integrative Medicine*, vol. 17, no. 1, 2019.

[143] N. S. el-Shenawy, F. el-Salmy, R. A. al-Eisa, and B. el-Ahmary, "Amelioratory effect of vitamin E on organophosphorus insecticide diazinon- induced oxidative stress in mice liver," *Pesticide Biochemistry and Physiology*, vol. 96, no. 2, pp. 101–107, 2010.

[144] I. Ben Amara, N. Soudani, A. Troudi, H. Bouaziz, T. Boudawara, and N. Zeghal, "Antioxidant effect of vitamin E and selenium on hepatotoxicity induced by dimethoate in female adult rats," *Ecotoxicology and Environmental Safety*, vol. 74, no. 4, pp. 811–819, 2011.

[145] S. M. Abou-Zeid, "Ameliorating effects of green tea on ethephon-induced immunotoxicity and oxidative stress in mice," *International Journal of Pharma Sciences and Scientific Research*, vol. 4, no. 1, pp. 1–9, 2018.

[146] S. John, M. Kale, N. Rathore, and D. Bhatnagar, "Protective effect of vitamin E in dimethoate and malathion induced oxidative stress in rat erythrocytes," *The Journal of Nutritional Biochemistry*, vol. 12, no. 9, pp. 500–504, 2001.

[147] K. S. el-Gendy, N. M. Aly, F. H. Mahmoud, A. Kenawy, and A. K. H. el-Sebae, "The role of vitamin C as antioxidant in protection of oxidative stress induced by imidacloprid," *Food and Chemical Toxicology*, vol. 48, no. 1, pp. 215–221, 2010.

[148] D. K. Rai, P. K. Rai, S. I. Rizvi, G. Watal, and B. Sharma, "Carbofuran-induced toxicity in rats: protective role of vitamin C," *Experimental and Toxicologic Pathology*, vol. 61, no. 6, pp. 531–535, 2009.

[149] S. K. Jaiswal, N. J. Siddiqi, and B. Sharma, "Carbofuran induced oxidative stress in rat heart: ameliorative effect of vitamin C," *ISRN Oxidative Medicine*, vol. 2013, Article ID 824102, 10 pages, 2013.

[150] N. Aly, K. el-Gendy, F. Mahmoud, and A. K. el-Sebae, "Protective effect of vitamin C against chlorpyrifos oxidative stress in male mice," *Pesticide Biochemistry and Physiology*, vol. 97, no. 1, pp. 7–12, 2010.

[151] C. Otuechere, S. O. Abarikwu, M. A. Rufai, A. E. Ohiozoje, E. Martins, and E. O. Farombi, "Protective effects of vitamin C against propanil-induced hepatotoxicity in Wistar rats," *Asian Pacific Journal of Tropical Disease*, vol. 2, pp. S212–S217, 2012.

[152] T. Yavuz, N. Delibas, B. Yildirim et al., "Vascular wall damage in rats induced by methidathion and ameliorating effect of vitamins E and C," *Archives of Toxicology*, vol. 78, no. 11, pp. 655–659, 2004.

[153] M. I. Yousef, T. I. Awad, and E. H. Mohamed, "Deltamethrin-induced oxidative damage and biochemical alterations in rat and its attenuation by vitamin E," *Toxicology*, vol. 227, no. 3, pp. 240–247, 2006.

[154] M. Singh, R. Sandhir, and R. Kiran, "Effects on antioxidant status of liver following atrazine exposure and its attenuation by vitamin E," *Experimental and Toxicologic Pathology*, vol. 63, no. 3, pp. 269–276, 2011.

[155] M. Singh, R. Sandhir, and R. Kiran, "Oxidative stress induced by atrazine in rat erythrocytes: Mitigating effect of vitamin E," *Toxicology Mechanisms and Methods*, vol. 20, no. 3, pp. 119–126, 2010.

[156] S. A. Mansour and A.-T. H. Mossa, "Lipid peroxidation and oxidative stress in rat erythrocytes induced by chlorpyrifos and the protective effect of zinc," *Pesticide Biochemistry and Physiology*, vol. 93, no. 1, pp. 34–39, 2009.

[157] S. A. Mansour and A.-T. H. Mossa, "Oxidative damage, biochemical and histopathological alterations in rats exposed to chlorpyrifos and the antioxidant role of zinc," *Pesticide Biochemistry and Physiology*, vol. 96, no. 1, pp. 14–23, 2010.

[158] A. Goel, V. Dani, and D. K. Dhawan, "Protective effects of zinc on lipid peroxidation, antioxidant enzymes and hepatic histoarchitecture in chlorpyrifos-induced toxicity," *Chemico-Biological Interactions*, vol. 156, no. 2, pp. 131–140, 2005.

[159] V. Mokhtari, P. Afsharian, M. Shahhoseini, S. M. Kalantar, and A. Moini, "A review on various uses of N-acetyl cysteine," *Cell Journal*, vol. 19, no. 1, pp. 11–17, 2017.

[160] J.-D. Yang, S. H. Liu, M. H. Liao, R. M. Chen, P. Y. Liu, and T. H. Ueng, "Effects of tebuconazole on cytochrome P450 enzymes, oxidative stress, and endocrine disruption in male rats," *Environmental Toxicology*, vol. 33, no. 8, pp. 899–907, 2018.

[161] Y. Ben Othmène, K. Monceaux, A. Karoui et al., "Tebuconazole induces ROS-dependent cardiac cell toxicity by activating DNA damage and mitochondrial apoptotic pathway," *Ecotoxicology and Environmental Safety*, vol. 204, article 111040, 2020.

[162] J. Dorval and A. Hontela, "Role of glutathione redox cycle and catalase in defense against oxidative stress induced by endosulfan in adrenocortical cells of rainbow trout (Oncorhynchus mykiss)," *Toxicology and Applied Pharmacology*, vol. 192, no. 2, pp. 191–200, 2003.

[163] I. Cankayali, K. Demirag, O. Eris, B. Ersoz, and A. R. Moral, "The effects ofN-acetylcysteine on oxidative stress in organophosphate poisoning model," *Advances in Therapy*, vol. 22, no. 2, pp. 107–116, 2005.

[164] M.-J. R. Howes, "Chapter 28 - Phytochemicals as Anti-inflammatory Nutraceuticals and Phytopharmaceuticals," in *Immunity and Inflammation in Health and Disease*, S. Chatterjee, W. Jungraithmayr, and D. Bagchi, Eds., pp. 363–388, Academic Press, 2018.

[165] J. P. E. Spencer, H. Schroeter, G. Kuhnle et al., "Epicatechin and its in vivo metabolite, 3′-O-methyl epicatechin, protect human fibroblasts from oxidative-stress-induced cell death involving caspase-3 activation," *The Biochemical Journal*, vol. 354, no. 3, pp. 493–500, 2001.

[166] L. A. Abdulkhaleq, M. A. Assi, M. H. M. Noor, R. Abdullah, M. Z. Saad, and Y. H. Taufiq-Yap, "Therapeutic uses of epicatechin in diabetes and cancer," *Veterinary World*, vol. 10, no. 8, pp. 869–872, 2017.

[167] A. L. Al-Malki and S. S. Moselhy, "Protective effect of vitamin E and epicatechin against nicotine-induced oxidative stress in rats," *Toxicology and Industrial Health*, vol. 29, no. 2, pp. 202–208, 2013.

[168] M. Lefaki, N. Papaevgeniou, and N. Chondrogianni, "Redox regulation of proteasome function," *Redox Biology*, vol. 13, pp. 452–458, 2017.

[169] J. Zhang, X. Wang, V. Vikash et al., "ROS and ROS-mediated cellular signaling," *Oxidative Medicine and Cellular Longevity*, vol. 2016, Article ID 4350965, 2016.

[170] H. Tian, B. F. Zhang, J. H. di et al., "Keap1: one stone kills three birds Nrf2, IKKβ and Bcl-2/Bcl-xL," *Cancer Letters*, vol. 325, no. 1, pp. 26–34, 2012.

[171] K. K. S. Nordgren and K. B. Wallace, "Keap1 redox-dependent regulation of doxorubicin-induced oxidative stress response in cardiac myoblasts," *Toxicology and Applied Pharmacology*, vol. 274, no. 1, pp. 107–116, 2014.

[172] H. Kanzaki, F. Shinohara, M. Kajiya, and T. Kodama, "The Keap1/Nrf2 protein axis plays a role in osteoclast

differentiation by regulating intracellular reactive oxygen species signaling," *Journal of Biological Chemistry*, vol. 288, no. 32, pp. 23009–23020, 2013.

[173] T. Frankič, T. Pajk, V. Rezar, A. Levart, and J. Salobir, "The role of dietary nucleotides in reduction of DNA damage induced by T-2 toxin and deoxynivalenol in chicken leukocytes," *Food and Chemical Toxicology*, vol. 44, no. 11, pp. 1838–1844, 2006.

[174] X. Liu, P. Guo, A. Liu et al., "Nitric oxide (NO)-mediated mitochondrial damage plays a critical role in T-2 toxin-induced apoptosis and growth hormone deficiency in rat anterior pituitary GH3 cells," *Food and Chemical Toxicology: An International Journal Published for the British Industrial Biological Research Association*, vol. 102, pp. 11–23, 2017.

[175] T. J. Martin, S. Gabure, J. Q. Maise, S. Snipes, M. Peete, and M. M. Whalen, "The organochlorine pesticides pentachlorophenol and dichlorodiphenyltrichloroethane increase secretion and production of interleukin 6 by human immune cells," *Environmental Toxicology and Pharmacology*, vol. 72, article 103263, 2019.

[176] A. Kartin, H. W. Subagio, S. Hadisaputro, M. I. Kartasurya, S. Suhartono, and B. Budiyono, "Pesticide exposure and stunting among children in agricultural areas," *The International Journal of Occupational and Environmental Medicine*, vol. 10, no. 1, pp. 17–29, 2019.

[177] M. Pajares, N. Jiménez-Moreno, I. H. K. Dias et al., "Redox control of protein degradation," *Redox Biology*, vol. 6, pp. 409–420, 2015.

[178] J. George and Y. Shukla, "Emptying of intracellular calcium pool and oxidative stress imbalance are associated with the glyphosate-induced proliferation in human skin keratinocytes HaCaT cells," *ISRN Dermatology*, vol. 2013, 825180 pages, 2013.

[179] V. Kašuba, M. Milić, R. Rozgaj et al., "Effects of low doses of glyphosate on DNA damage, cell proliferation and oxidative stress in the HepG2 cell line," *Environmental Science and Pollution Research*, vol. 24, no. 23, pp. 19267–19281, 2017.

[180] Y.-H. Kim, J. R. Hong, H. W. Gil, H. Y. Song, and S. Y. Hong, "Mixtures of glyphosate and surfactant TN20 accelerate cell death via mitochondrial damage-induced apoptosis and necrosis," *Toxicology In Vitro*, vol. 27, no. 1, pp. 191–197, 2013.

[181] N. S. El-Shenawy, "Oxidative stress responses of rats exposed to roundup and its active ingredient glyphosate," *Environmental Toxicology and Pharmacology*, vol. 28, no. 3, pp. 379–385, 2009.

[182] D. C. Bailey, C. E. Todt, S. L. Burchfield et al., "Chronic exposure to a glyphosate-containing pesticide leads to mitochondrial dysfunction and increased reactive oxygen species production in _Caenorhabditis elegans_," *Environmental Toxicology and Pharmacology*, vol. 57, pp. 46–52, 2018.

[183] D. M. Romero, M. C. Ríos de Molina, and Á. B. Juárez, "Oxidative stress induced by a commercial glyphosate formulation in a tolerant strain of Chlorella kessleri," *Ecotoxicology and Environmental Safety*, vol. 74, no. 4, pp. 741–747, 2011.

[184] S. Gao, Z. Wang, C. Zhang, L. Jia, and Y. Zhang, "Oral exposure to atrazine induces oxidative stress and calcium homeostasis disruption in spleen of mice," *Oxidative Medicine and Cellular Longevity*, vol. 2016, Article ID 7978219, 9 pages, 2016.

[185] N. El-Shenawy, "Mitigating effect of ginger against oxidative stress induced by atrazine herbicides in mice liver and kidney," *Journal of Biofertilizers & Biopesticides*, vol. 2, no. 1, p. 107, 2011.

[186] S. O. Abarikwu, A. C. Adesiyan, T. O. Oyeloja, M. O. Oyeyemi, and E. O. Farombi, "Changes in sperm characteristics and induction of oxidative stress in the testis and epididymis of experimental rats by a herbicide, atrazine," *Archives of Environmental Contamination and Toxicology*, vol. 58, no. 3, pp. 874–882, 2010.

[187] O. Adedosu, A. Badmus, G. Adeleke, and R. Raji, "_Telfairia occidentalis_ seed extract protects against oxidative stress, inflammation and some haematological disorders associated with atrazine- induced prostate cancer in rats," *European Journal of Cancer*, vol. 72, p. S94, 2017.

[188] M. A. Abass, S. A. Elkhateeb, S. A. Abd el-Baset, A. A. Kattaia, E. M. Mohamed, and H. H. Atteia, "Lycopene ameliorates atrazine-induced oxidative damage in adrenal cortex of male rats by activation of the Nrf2/HO-1 pathway," *Environmental Science and Pollution Research International*, vol. 23, no. 15, pp. 15262–15274, 2016.

[189] W. Liu, Y. Du, J. Liu et al., "Effects of atrazine on the oxidative damage of kidney in Wister rats," *International Journal of Clinical and Experimental Medicine*, vol. 7, no. 10, pp. 3235–3243, 2014.

[190] K. Ma, H. Y. Wu, B. Zhang, X. He, and B. X. Li, "Neurotoxicity effects of atrazine-induced SH-SY5Y human dopaminergic neuroblastoma cells via microglial activation," *Molecular BioSystems*, vol. 11, no. 11, pp. 2915–2924, 2015.

[191] W. A. Keshk, N. A. Soliman, M. M. Abo el-Noor, A. A. Wahdan, and M. M. Shareef, "Modulatory effects of curcumin on redox status, mitochondrial function, and caspace-3 expression during atrazin-induced toxicity," *Journal of Biochemical and Molecular Toxicology*, vol. 28, no. 8, pp. 378–385, 2014.

[192] H. Liu, Y. L. Xia, W. Cai, Y. Zhang, X. Zhang, and S. du, "Enantioselective oxidative stress and oxidative damage caused by _Rac-_ and _S_ -metolachlor to _Scenedesmus obliquus_," *Chemosphere*, vol. 173, pp. 22–30, 2017.

[193] D. Špoljarić Maronić, I. Štolfa Čamagajevac, J. Horvatić et al., "S-metolachlor promotes oxidative stress in green microalga _Parachlorella kessleri_ \- A potential environmental and health risk for higher organisms," *Science of the Total Environment*, vol. 637-638, pp. 41–49, 2018.

[194] Q. Qu, M. Ke, Y. Ye et al., "Enantioselective Oxidative Stress Induced by S- and Rac-metolachlor in Wheat (Triticum aestivum L.) Seedlings," *Bulletin of Environmental Contamination and Toxicology*, vol. 102, no. 3, pp. 439–445, 2019.

[195] P. Bernat, J. Nykiel-Szymańska, P. Stolarek, M. Słaba, R. Szewczyk, and S. Różalska, "2,4-Dichlorophenoxyacetic acid-induced oxidative stress: metabolome and membrane modifications in Umbelopsis isabellina, a herbicide degrader," *PLoS One*, vol. 13, no. 6, article e0199677, 2018.

[196] M. C. Romero-Puertas, I. Mccarthy, M. Gomez et al., "Reactive oxygen species-mediated enzymatic systems involved in the oxidative action of 2,4-dichlorophenoxyacetic acid," *Plant, Cell & Environment*, vol. 27, no. 9, pp. 1135–1148, 2004.

[197] F. P. Peixoto, J. Gomes-Laranjo, J. A. Vicente, and V. M. C. Madeira, "Comparative effects of the herbicides dicamba, 2,4-D and paraquat on non-green potato tuber calli," *Journal of Plant Physiology*, vol. 165, no. 11, pp. 1125–1133, 2008.

[198] D. Zhang, Y. Wu, Y. Yuan et al., "Exposure to 2,4-dichlorophenoxyacetic acid induces oxidative stress and apoptosis in

mouse testis," *Pesticide Biochemistry and Physiology*, vol. 141, pp. 18–22, 2017.

[199] T. M. Atamaniuk, O. I. Kubrak, K. B. Storey, and V. I. Lushchak, "Oxidative stress as a mechanism for toxicity of 2,4-dichlorophenoxyacetic acid (2,4-D): studies with goldfish gills," *Ecotoxicology*, vol. 22, no. 10, pp. 1498–1508, 2013.

[200] N. A. Ossana, J. M. Pérez-Iglesias, S. Soloneski, and M. L. Larramendy, "Auxinic herbicides induce oxidative stress on Cnesterodon decemmaculatus (Pisces: Poeciliidae)," *Environmental Science and Pollution Research*, vol. 26, no. 20, pp. 20485–20498, 2019.

[201] Z. Liu, P. Li, X. Sun et al., "Fluazifop-P-butyl induced ROS generation with IAA (indole-3-acetic acid) oxidation in _Acanthospermum hispidum_ D.C.," *Pesticide Biochemistry and Physiology*, vol. 143, pp. 312–318, 2017.

[202] B. Bongiovanni, P. de Lorenzi, A. Ferri et al., "Melatonin decreases the oxidative stress produced by 2,4-dichlorophenoxyacetic acid in rat cerebellar granule cells," *Neurotoxicity Research*, vol. 11, no. 2, pp. 93–99, 2007.

[203] A. Troudi, I. Ben Amara, A. M. Samet, and N. Zeghal, "Oxidative stress induced by 2,4-phenoxyacetic acid in liver of female rats and their progeny: biochemical and histopathological studies," *Environmental Toxicology*, vol. 27, no. 3, pp. 137–145, 2012.

[204] L. Tichati, F. Trea, and K. Ouali, "Potential role of selenium against hepatotoxicity induced by 2,4-dichlorophenoxyacetic acid in albino Wistar rats," *Biological Trace Element Research*, vol. 194, no. 1, pp. 228–236, 2020.

[205] W. Tayeb, A. Nakbi, I. Cheraief, A. Miled, and M. Hammami, "Alteration of lipid status and lipid metabolism, induction of oxidative stress and lipid peroxidation by 2,4-dichlorophenoxyacetic herbicide in rat liver," *Toxicology Mechanisms and Methods*, vol. 23, no. 6, pp. 449–458, 2013.

[206] W. Tayeb, A. Nakbi, M. Trabelsi, A. Miled, and M. Hammami, "Biochemical and histological evaluation of kidney damage after sub-acute exposure to 2,4-dichlorophenoxyacetic herbicide in rats: involvement of oxidative stress," *Toxicology Mechanisms and Methods*, vol. 22, no. 9, pp. 696–704, 2012.

[207] W. Tayeb, A. Nakbi, M. Trabelsi, N. Attia, A. Miled, and M. Hammami, "Hepatotoxicity induced by sub-acute exposure of rats to 2,4-Dichlorophenoxyacetic acid based herbicide "Desormone lourd"," *Journal of Hazardous Materials*, vol. 180, no. 1-3, pp. 225–233, 2010.

[208] S. B. Pruett, B. Cheng, R. Fan, W. Tan, and T. Sebastian, "Oxidative stress and sodium methyldithiocarbamate-induced modulation of the macrophage response to lipopolysaccharide in vivo," *Toxicological Sciences : An Official Journal of the Society of Toxicology*, vol. 109, no. 2, pp. 237–246, 2009.

[209] P. F. Martins, G. Carvalho, P. L. Gratão et al., "Effects of the herbicides acetochlor and metolachlor on antioxidant enzymes in soil bacteria," *Process Biochemistry*, vol. 46, no. 5, pp. 1186–1195, 2011.

[210] Y. Liu, Y. Zhang, J. Liu, and D. Huang, "The role of reactive oxygen species in the herbicide acetochlor-induced DNA damage on _Bufo raddei_ tadpole liver," *Aquatic Toxicology*, vol. 78, no. 1, pp. 21–26, 2006.

[211] Y. Zhang, W. Xue, R. Long, H. Yang, and W. Wei, "Acetochlor affects zebrafish ovarian development by producing estrogen effects and inducing oxidative stress," *Environmental Science and Pollution Research*, vol. 27, no. 22, pp. 27688–27696, 2020.

[212] X. Song, F. Zhang, D. Chen et al., "Study on systemic and reproductive toxicity of acetochlor in male mice," *Toxicology Research*, vol. 8, no. 1, pp. 77–89, 2019.

[213] T. Huang, Y. Huang, Y. Huang, Y. Yang, Y. Zhao, and C. J. Martyniuk, "Toxicity assessment of the herbicide acetochlor in the human liver carcinoma (HepG2) cell line," *Chemosphere*, vol. 243, article 125345, 2020.

[214] J. Jiang, S. Wu, X. Liu et al., "Effect of acetochlor on transcription of genes associated with oxidative stress, apoptosis, immunotoxicity and endocrine disruption in the early life stage of zebrafish," *Environmental Toxicology and Pharmacology*, vol. 40, no. 2, pp. 516–523, 2015.

[215] D. G. Goswami, R. Kant, D. A. Ammar et al., "Toxic consequences and oxidative protein carbonylation from chloropicrin exposure in human corneal epithelial cells," *Toxicology Letters*, vol. 322, pp. 1–11, 2020.

[216] M. Pesonen, M. Pasanen, J. Loikkanen et al., "Chloropicrin induces endoplasmic reticulum stress in human retinal pigment epithelial cells," *Toxicology Letters*, vol. 211, no. 3, pp. 239–245, 2012.

[217] M. Pesonen, M. Häkkinen, K. Rilla et al., "Chloropicrin-induced toxic responses in human lung epithelial cells," *Toxicology Letters*, vol. 226, no. 2, pp. 236–244, 2014.

[218] M. N. Haque, H. J. Eom, S. E. Nam, Y. K. Shin, and J. S. Rhee, "Chlorothalonil induces oxidative stress and reduces enzymatic activities of Na+/K+-ATPase and acetylcholinesterase in gill tissues of marine bivalves," *PLoS One*, vol. 14, no. 4, article e0214236, 2019.

[219] J. da Silva Barreto, F. de Melo Tarouco, F. G. A. de Godoi et al., "Induction of oxidative stress by chlorothalonil in the estuarine polychaete _Laeonereis acuta_," *Aquatic Toxicology*, vol. 196, pp. 1–8, 2018.

[220] J. da Silva Barreto, F. de Melo Tarouco, and C. E. da Rosa, "Chlorothalonil causes redox state change leading to oxidative stress generation in Danio rerio," *Aquatic Toxicology*, vol. 225, article 105527, 2020.

[221] T. Suzuki, H. Nojiri, H. Isono, and T. Ochi, "Oxidative damages in isolated rat hepatocytes treated with the organochlorine fungicides captan, dichlofluanid and chlorothalonil," *Toxicology*, vol. 204, no. 2-3, pp. 97–107, 2004.

[222] F. Cima, M. Bragadin, and L. Ballarin, "Toxic effects of new antifouling compounds on tunicate haemocytes: I. Sea-Nine 211™ and chlorothalonil," *Aquatic Toxicology*, vol. 86, no. 2, pp. 299–312, 2008.

[223] M. Lodovici, C. Casalini, C. Briani, and P. Dolara, "Oxidative liver DNA damage in rats treated with pesticide mixtures," *Toxicology*, vol. 117, no. 1, pp. 55–60, 1997.

[224] I. Ahmad and M. Ahmad, "Fresh water fish, Channa punctatus, as a model for pendimethalin genotoxicity testing: a new approach toward aquatic environmental contaminants," *Environmental Toxicology*, vol. 31, no. 11, pp. 1520–1529, 2016.

[225] M. I. Ahmad, M. F. Zafeer, M. Javed, and M. Ahmad, "Pendimethalin-induced oxidative stress, DNA damage and activation of anti- inflammatory and apoptotic markers in male rats," *Scientific Reports*, vol. 8, no. 1, p. 17139, 2018.

[226] S. M. Ansari, Q. Saquib, S. M. Attia et al., "Pendimethalin induces oxidative stress, DNA damage, and mitochondrial dysfunction to trigger apoptosis in human lymphocytes and

rat bone-marrow cells," *Histochemistry and Cell Biology*, vol. 149, no. 2, pp. 127–141, 2018.

[227] P. Gupta and S. K. Verma, "Evaluation of genotoxicity induced by herbicide pendimethalin in fresh water fish Clarias batrachus (linn.) and possible role of oxidative stress in induced DNA damage," *Drug and Chemical Toxicology*, vol. 43, pp. 1–10, 2020.

[228] H. Tabassum, M. A. Afjal, J. Khan, S. Raisuddin, and S. Parvez, "Neurotoxicological assessment of pendimethalin in freshwater fish _Channa punctata_ Bloch," *Ecological Indicators*, vol. 58, pp. 411–417, 2015.

[229] H. Tabassum, M. Ashafaq, J. Khan, M. Z. Shah, S. Raisuddin, and S. Parvez, "Short term exposure of pendimethalin induces biochemical and histological perturbations in liver, kidney and gill of freshwater fish," *Ecological Indicators*, vol. 63, pp. 29–36, 2016.

[230] Z. Sarıgöl Kılıç, S. Aydın, Ü. Ündeğer Bucurgat, and N. Başaran, "In vitro genotoxicity assessment of dinitroaniline herbicides pendimethalin and trifluralin," *Food and Chemical Toxicology*, vol. 113, pp. 90–98, 2018.

[231] M. Hodjat, M. Baeeri, M. A. Rezvanfar, M. Rahimifard, M. Gholami, and M. Abdollahi, "On the mechanism of genotoxicity of ethephon on embryonic fibroblast cells," *Toxicology Mechanisms and Methods*, vol. 27, no. 3, pp. 173–180, 2017.

[232] L. Öztürk and Y. Demir, "Effects of putrescine and ethephon on some oxidative stress enzyme activities and proline content in salt stressed spinach leaves," *Plant Growth Regulation*, vol. 40, no. 1, pp. 89–95, 2003.

[233] Z.-Y. Sun, T. J. Zhang, J. Q. Su et al., "A novel role of ethephon in controlling the noxious weed _Ipomoea cairica_ (Linn.) Sweet," *Scientific Reports*, vol. 5, no. 1, p. 11372, 2015.

[234] O. I. Kubrak, T. M. Atamaniuk, V. V. Husak et al., "Oxidative stress responses in blood and gills of _Carassius auratus_ exposed to the mancozeb-containing carbamate fungicide Tattoo," *Ecotoxicology and Environmental Safety*, vol. 85, pp. 37–43, 2012.

[235] T. M. Atamaniuk, O. I. Kubrak, V. V. Husak, K. B. Storey, and V. I. Lushchak, "The mancozeb-containing carbamate fungicide tattoo induces mild oxidative stress in goldfish brain, liver, and kidney," *Environmental Toxicology*, vol. 29, no. 11, pp. 1227–1235, 2014.

[236] U. Majid, Mahmooduzzafar, T. O. Siddiqi, and M. Iqbal, "Antioxidant response of Cassia angustifolia Vahl. to oxidative stress caused by Mancozeb, a pyrethroid fungicide," *Acta Physiologiae Plantarum*, vol. 36, no. 2, pp. 307–314, 2014.

[237] D. C. Bailey, C. E. Todt, S. E. Orfield et al., "_Caenorhabditis elegans_ chronically exposed to a Mn/Zn ethylene-bis-dithiocarbamate fungicide show mitochondrial Complex I inhibition and increased reactive oxygen species," *Neurotoxicology*, vol. 56, pp. 170–179, 2016.

[238] C. E. Todt, D. C. Bailey, A. S. Pressley et al., "Acute exposure to a Mn/Zn ethylene-bis-dithiocarbamate fungicide leads to mitochondrial dysfunction and increased reactive oxygen species production in _Caenorhabditis elegans_," *Neurotoxicology*, vol. 57, pp. 112–120, 2016.

[239] M. A. Saraiva, E. da Rosa Ávila, G. F. da Silva et al., "Exposure of Drosophila melanogaster to Mancozeb Induces Oxidative Damage and Modulates Nrf2 and HSP70/83," *Oxidative Medicine and Cellular Longevity*, vol. 2018, Article ID 5456928, 11 pages, 2018.

[240] G. Calviello, E. Piccioni, A. Boninsegna et al., "DNA damage and apoptosis induction by the pesticide Mancozeb in rat cells: Involvement of the oxidative mechanism," *Toxicology and Applied Pharmacology*, vol. 211, no. 2, pp. 87–96, 2006.

[241] M. Mohammadi-Sardoo, A. Mandegary, M. Nabiuni, S. N. Nematollahi-Mahani, and B. Amirheidari, "Mancozeb induces testicular dysfunction through oxidative stress and apoptosis: protective role ofN-acetylcysteine antioxidant," *Toxicology and Industrial Health*, vol. 34, no. 11, pp. 798–811, 2018.

[242] V. Pavlovic, S. Cekic, B. Kamenov, M. Ciric, and D. Krtinic, "The effect of ascorbic acid on Mancozeb-induced toxicity in rat thymocytes," *Folia biologica*, vol. 61, no. 3, pp. 116–123, 2015.

[243] K. Kumar, A. Sabarwal, and R. P. Singh, "Mancozeb selectively induces mitochondrial-mediated apoptosis in human gastric carcinoma cells through ROS generation," *Mitochondrion*, vol. 48, pp. 1–10, 2019.

[244] J. E. Lee, J. H. Park, S. J. Jang, and H. C. Koh, "Rosiglitazone inhibits chlorpyrifos-induced apoptosis via modulation of the oxidative stress and inflammatory response in SH-SY5Y cells," *Toxicology and Applied Pharmacology*, vol. 278, no. 2, pp. 159–171, 2014.

[245] J. E. Lee, J. H. Park, I. C. Shin, and H. C. Koh, "Reactive oxygen species regulated mitochondria-mediated apoptosis in PC12 cells exposed to chlorpyrifos," *Toxicology and Applied Pharmacology*, vol. 263, no. 2, pp. 148–162, 2012.

[246] A. A. Alvarez, E. Ramírez-San Juan, and A. Canizales-Román, "Chlorpyrifos induces oxidative stress in rats," *Toxicological & Environmental Chemistry*, vol. 90, no. 5, pp. 1019–1025, 2008.

[247] T. K. Mandal and N. S. Das, "Correlation of testicular toxicity and oxidative stress induced by chlorpyrifos in rats," *Human & Experimental Toxicology*, vol. 30, no. 10, pp. 1529–1539, 2011.

[248] A. Imam, N. A. Sulaiman, A. L. Oyewole et al., "Chlorpyrifos- and dichlorvos-induced oxidative and neurogenic damage elicits neuro-cognitive deficits and increases anxiety-like behavior in wild-type rats," *Toxics*, vol. 6, no. 4, p. 71, 2018.

[249] H. BaŞ and Y. Kalender, "Chlorpyrifos induced cardiotoxicity in rats and the protective role of quercetin and catechin," *Gazi University Journal of Science*, vol. 24, pp. 385–395, 2011.

[250] Y. Zhao, C. Fan, A. Zhang et al., "Walnut polyphenol extract protects against malathion- and chlorpyrifos-induced immunotoxicity by modulating TLRx-NOX-ROS," *Nutrients*, vol. 12, no. 3, p. 616, 2020.

[251] S. P. Pereira, M. A. S. Fernandes, J. D. Martins et al., "Toxicity assessment of the herbicide metolachlor comparative effects on bacterial and mitochondrial model systems," *Toxicology In Vitro*, vol. 23, no. 8, pp. 1585–1590, 2009.

[252] D. Štajner, M. Popović, and M. Štajner, "Herbicide induced oxidative stress in lettuce, beans pea seeds and leaves," *Biologia Plantarum*, vol. 46, no. 4, pp. 575–579, 2003.

[253] C. Otuechere, O. J. Avwioroko, S. Tinuala, S. Fayemi, and B. A. Salau, "Oral supplementation of coconut oil attenuates propanil-induced oxidative stress in the testes of rats," *Asian Journal of Biological Sciences*, vol. 13, no. 1, pp. 70–76, 2019.

[254] C. A. Otuechere, S. O. Abarikwu, V. I. Olateju, A. L. Animashaun, and O. E. Kale, "Protective effect of curcumin against the liver toxicity caused by propanil in rats,"

International Scholarly Research Notices, vol. 2014, Article ID 853697, 8 pages, 2014.

[255] M. Rehman, B. Ahmad, M. . R. Mir et al., "Propanil-induced neurotoxicity in freshwater common carp (Cyprinus carpio)," *Applied Biological Research*, vol. 18, no. 3, p. 312, 2016.

[256] F. Peixoto, J. A. Vicente, and V. M. Madeira, "The herbicide dicamba (2-methoxy-3,6-dichlorobenzoic acid) interacts with mitochondrial bioenergetic functions," *Archives of Toxicology*, vol. 77, no. 7, pp. 403–409, 2003.

[257] C. Gleason, R. C. Foley, and K. B. Singh, "Mutant analysis in Arabidopsis provides insight into the molecular mode of action of the auxinic herbicide Dicamba," *PLoS One*, vol. 6, no. 3, article e17245, 2011.

[258] Z. Denek, G. Erbil, S. Ozbal, S. C. Micili, and C. Ozogul, "The effects of resveratrol against trifluralin toxicity in the urinary tract of rats," *Toxicology and Industrial Health*, vol. 32, no. 1, pp. 106–117, 2016.

[259] M. S. Kumar, A. N. Kabra, B. Min et al., "Insecticides induced biochemical changes in freshwater microalga Chlamydomonas mexicana," *Environmental Science and Pollution Research International*, vol. 23, no. 2, pp. 1091–1099, 2016.

[260] P. Rajak, S. Khatun, M. Dutta, M. Mandi, and S. Roy, "Chronic exposure to acephate triggers ROS-mediated injuries at organismal and sub-organismal levels ofDrosophila melanogaster," *Toxicology research*, vol. 7, no. 5, pp. 874–887, 2018.

[261] S. Datta, P. Dhar, A. Mukherjee, and S. Ghosh, "Influence of polyphenolic extracts from _Enydra fluctuans_ on oxidative stress induced by acephate in rats," *Food and Chemical Toxicology*, vol. 48, no. 10, pp. 2766–2771, 2010.

[262] A. Thapar, R. Sandhir, and R. Kiran, "Acephate induced oxidative damage in erythrocytes," *Indian Journal of Experimental Biology*, vol. 40, no. 8, pp. 963–966, 2002.

[263] P. Sharma, A. Sharma, N. D. Jasuja, and S. C. Joshi, "Organophosphorous compounds and oxidative stress: a review," *Toxicological & Environmental Chemistry*, vol. 96, no. 5, pp. 681–698, 2014.

[264] M. A. T. Dhanushka and L. D. C. Peiris, "Cytotoxic and genotoxic effects of acephate on human sperm," *Journal of Toxicology*, vol. 2017, 2017.

[265] A. S. al-Sarar, A. E. Bayoumi, H. I. Hussein, and Y. Abobakr, "Cytotoxic effects of acephate, ethoprophos, and monocrotophos in CHO-K1 cells," *CyTA Journal of Food*, vol. 13, no. 3, pp. 427–433, 2015.

[266] V. S. Poovala, V. K. Kanji, H. Tachikawa, and A. K. Salahudeen, "Role of oxidant stress and antioxidant protection in acephate-induced renal tubular cytotoxicity," *Toxicological Sciences*, vol. 46, no. 2, pp. 403–409, 1998.

[267] H. Rodriguez-Rocha, A. Garcia-Garcia, C. Pickett et al., "Compartmentalized oxidative stress in dopaminergic cell death induced by pesticides and complex I inhibitors: distinct roles of superoxide anion and superoxide dismutases," *Free Radical Biology and Medicine*, vol. 61, pp. 370–383, 2013.

[268] H. M. Cochemé and M. P. Murphy, "Complex I is the major site of mitochondrial superoxide production by paraquat," *The Journal of Biological Chemistry*, vol. 283, no. 4, pp. 1786–1798, 2008.

[269] K. Shimizu, K. Matsubara, K. Ohtaki, S. Fujimaru, O. Saito, and H. Shiono, "Paraquat induces long-lasting dopamine overflow through the excitotoxic pathway in the striatum of freely moving rats," *Brain Research*, vol. 976, no. 2, pp. 243–252, 2003.

[270] D.-C. Wu, P. Teismann, K. Tieu et al., "NADPH oxidase mediates oxidative stress in the 1-methyl-4-phenyl-1,2,3,6-tetrahydropyridine model of Parkinson's disease," *Proceedings of the National Academy of Sciences of the United States of America*, vol. 100, no. 10, pp. 6145–6150, 2003.

[271] X. Chang, W. Lu, T. Dou et al., "Paraquat inhibits cell viability via enhanced oxidative stress and apoptosis in human neural progenitor cells," *Chemico-Biological Interactions*, vol. 206, no. 2, pp. 248–255, 2013.

[272] H. K. Takano, R. Beffa, C. Preston, P. Westra, and F. E. Dayan, "A novel insight into the mode of action of glufosinate: how reactive oxygen species are formed," *Photosynthesis Research*, vol. 144, no. 3, pp. 361–372, 2020.

[273] H. K. Takano, R. Beffa, C. Preston, P. Westra, and F. E. Dayan, "Reactive oxygen species trigger the fast action of glufosinate," *Planta*, vol. 249, no. 6, pp. 1837–1849, 2019.

[274] H. Qian, W. Chen, G. D. Sheng, X. Xu, W. Liu, and Z. Fu, "Effects of glufosinate on antioxidant enzymes, subcellular structure, and gene expression in the unicellular green alga _Chlorella vulgaris_," *Aquatic Toxicology*, vol. 88, no. 4, pp. 301–307, 2008.

[275] A. Leomanni, T. Schettino, A. Calisi et al., "Antioxidant and oxidative stress related responses in the Mediterranean land snail _Cantareus apertus_ exposed to the carbamate pesticide Carbaryl," *Comparative Biochemistry and Physiology Part C: Toxicology & Pharmacology*, vol. 168, pp. 20–27, 2015.

[276] K. Habib, S. Kumar, N. Manikar, S. Zutshi, and T. Fatma, "Biochemical effect of carbaryl on oxidative stress, antioxidant enzymes and osmolytes of cyanobacterium Calothrix brevissima," *Bulletin of Environmental Contamination and Toxicology*, vol. 87, no. 6, pp. 615–620, 2011.

[277] Y. Han, S. Song, H. Wu, J. Zhang, and E. Ma, "Antioxidant enzymes and their role in phoxim and carbaryl stress in _Caenorhabditis elegans_," *Pesticide Biochemistry and Physiology*, vol. 138, pp. 43–50, 2017.

[278] S. Venkatachalam, V. P. K. Muthaiah, L. Venkitasamy, F. M. Michael, and K. Chandrasekar, "Neuroprotective role of naringenin on carbaryl induced neurotoxicity in mouse neuroblastoma cells," *Journal of Pharmacology and Pharmacotherapeutics*, vol. 4, no. 3, pp. 192–197, 2013.

[279] M.-L. Xu, Y. Gao, X. Wang et al., "Effect of carbaryl on some biochemical changes in PC12 cells: the protective effect of soy isoflavone genistein, and daidzein, and their mixed solution," *CyTA Journal of Food*, vol. 14, no. 4, pp. 587–593, 2016.

[280] N. Jawad, R. Kaur, S. S. Gouri, V. K. Dumka, and S. P. Saini, "Carbamate pesticide carbaryl induces alterations in antioxidant and oxidative stress related responses of Indian buffalo (Bubalus bubalis) after sub-chronic exposure," *Toxicology International (Formerly Indian Journal of Toxicology)*, vol. 24, p. 198, 2017.

[281] F. Hu, L. Li, C. Wang, Q. Zhang, X. Zhang, and M. Zhao, "Enantioselective induction of oxidative stress by permethrin in rat adrenal pheochromocytoma (PC12) cells," *Environmental Toxicology and Chemistry*, vol. 29, no. 3, pp. 683–690, 2010.

[282] S. Olgun and H. P. Misra, "Pesticides induced oxidative stress in thymocytes," *Molecular and Cellular Biochemistry*, vol. 290, no. 1, p. 137, 2006.

[283] M. N. Tiwari, A. K. Singh, I. Ahmad et al., "Effects of cypermethrin on monoamine transporters, xenobiotic metabolizing enzymes and lipid peroxidation in the rat nigrostriatal system," *Free Radical Research*, vol. 44, no. 12, pp. 1416–1424, 2010.

[284] C. Bouaziz, I. Graiet, A. Salah, I. Ben Salem, and S. Abid, "Influence of bifentrin, a pyrethriod pesticide, on human colorectal HCT-116 cells attributed to alterations in oxidative stress involving mitochondrial apoptotic processes," *Journal of Toxicology and Environmental Health, Part A*, vol. 83, no. 9, pp. 331–340, 2020.

[285] Y. Jin, J. Wang, X. Pan, L. Wang, and Z. Fu, "_cis_ -Bifenthrin enantioselectively induces hepatic oxidative stress in mice," *Pesticide Biochemistry and Physiology*, vol. 107, no. 1, pp. 61–67, 2013.

[286] S. Park, J. Y. Lee, H. Park, G. Song, and W. Lim, "Bifenthrin induces developmental immunotoxicity and vascular malformation during zebrafish embryogenesis," *Comparative Biochemistry and Physiology, Part C: Toxicology & Pharmacology*, vol. 228, article 108671, 2020.

[287] B. Bukowska, K. Goszczyńska, and W. Duda, "Effect of 4-chloro-2-methylphenoxyacetic acid and 2,4-dimethylphenol on human erythrocytes," *Pesticide Biochemistry and Physiology*, vol. 77, no. 3, pp. 92–98, 2003.

[288] P. Duchnowicz, M. Koter, and W. Duda, "Damage of erythrocyte by phenoxyacetic herbicides and their metabolites," *Pesticide Biochemistry and Physiology*, vol. 74, no. 1, pp. 1–7, 2002.

[289] G. Sujetovienė, K. Gasauskaitė, and J. Žaltauskaitė, "Toxicity of a phenoxy herbicide on the lichen Ramalina fraxinea," *Toxicological & Environmental Chemistry*, vol. 101, no. 9-10, pp. 497–507, 2019.

[290] J. J. Fortunato, G. Feier, A. M. Vitali, F. C. Petronilho, F. Dal-Pizzol, and J. Quevedo, "Malathion-induced oxidative stress in rat brain regions," *Neurochemical Research*, vol. 31, no. 5, pp. 671–678, 2006.

[291] S. Selmi, K. Rtibi, D. Grami, H. Sebai, and L. Marzouki, "Malathion, an organophosphate insecticide, provokes metabolic, histopathologic and molecular disorders in liver and kidney in prepubertal male mice," *Toxicology Reports*, vol. 5, pp. 189–195, 2018.

[292] S. Slimen and G. N. El Fazaa Saloua, "Oxidative stress and cytotoxic potential of anticholinesterase insecticide, malathion in reproductive toxicology of male adolescent mice after acute exposure," *Iranian Journal of Basic Medical Sciences*, vol. 17, no. 7, pp. 522–530, 2014.

[293] C. Jalili, S. Roshankhah, M. R. Salahshoor, and M. M. Mohammadi, "Resveratrol attenuates malathion induced damage in some reproductive parameters by decreasing oxidative stress and lipid peroxidation in male rats," *Journal of Family & Reproductive Health*, vol. 13, no. 2, pp. 70–79, 2019.

[294] R. I. Ali and M. A. Ibrahim, "Malathion induced testicular toxicity and oxidative damage in male mice: the protective effect of curcumin," *Egyptian Journal of Forensic Sciences*, vol. 8, no. 1, p. 70, 2018.

[295] F. Karabag-Coban, I. Bulduk, R. Liman, S. Ince, I. Cigerci, and O. Hazman, "Oleuropein alleviates malathion-induced oxidative stress and DNA damage in rats," *Toxicological & Environmental Chemistry*, vol. 98, no. 1, pp. 101–108, 2016.

[296] H. Alp, I. Aytekin, N. K. Hatipoglu, A. Alp, and M. Ogun, "Effects of sulforophane and curcumin on oxidative stress created by acute malathion toxicity in rats," *European Review for Medical and Pharmacological Sciences*, vol. 16, Suppl 3, pp. 144–148, 2012.

[297] P. D. Moore, C. G. Yedjou, and P. B. Tchounwou, "Malathion-induced oxidative stress, cytotoxicity, and genotoxicity in human liver carcinoma (HepG2) cells," *Environmental Toxicology*, vol. 25, no. 3, pp. 221–226, 2010.

[298] D. Flores, V. Souza, M. Betancourt et al., "Oxidative stress as a damage mechanism in porcine cumulus-oocyte complexes exposed to malathion during in vitro maturation," *Environmental Toxicology*, vol. 32, no. 6, pp. 1669–1678, 2017.

[299] E. H. B. Delgado, E. L. Streck, J. L. Quevedo, and F. Dal-Pizzol, "Mitochondrial respiratory dysfunction and oxidative stress after chronic malathion exposure," *Neurochemical Research*, vol. 31, no. 8, pp. 1021–1025, 2006.

[300] S. Ullah, Z. Li, Z. Hasan, S. U. Khan, and S. Fahad, "Malathion induced oxidative stress leads to histopathological and biochemical toxicity in the liver of rohu (_Labeo rohita_, Hamilton) at acute concentration," *Ecotoxicology and Environmental Safety*, vol. 161, pp. 270–280, 2018.

[301] D. Durak, F. G. Uzun, S. Kalender, A. Ogutcu, M. Uzunhisarcikli, and Y. Kalender, "Malathion-induced oxidative stress in human erythrocytes and the protective effect of vitamins C and Ein vitro," *Environmental Toxicology*, vol. 24, no. 3, pp. 235–242, 2009.

[302] S. Abbasabad Arab, M. R. Nikravesh, M. Jalali, and A. R. Fazel, "Evaluation of oxidative stress indices after exposure to malathion and protective effects of ascorbic acid in ovarian tissue of adult female rats," *Electronic Physician*, vol. 10, no. 5, pp. 6789–6795, 2018.

[303] A. K. Srivastava and D. Singh, "Assessment of malathion toxicity on cytophysiological activity, DNA damage and antioxidant enzymes in root of Allium cepa model," *Scientific Reports*, vol. 10, no. 1, p. 886, 2020.

Hindawi
Oxidative Medicine and Cellular Longevity
Volume 2022, Article ID 2235335, 13 pages
https://doi.org/10.1155/2022/2235335

Research Article

Nanoscale Modification of Titanium Implants Improves Behaviors of Bone Mesenchymal Stem Cells and Osteogenesis *In Vivo*

Huangdi Li,[1] **Jinghui Huang**,[1] **Yanpeng Wang**,[2] **Ziyuan Chen**,[1] **Xing Li**,[1] **Qiuping Wei**,[3] **Xifeng Liu**,[2] **Zi Wang**,[2] **Bin Wen**,[4] **Yuetao Zhao**,[2] **Jing Liu**,[2] **and Jun Zuo**[1]

[1]*Hunan Key Laboratory of Oral Health Research, Hunan 3D Printing Engineering Research Center of Oral Care, Hunan Clinical Research Center of Oral Major Diseases and Oral Health, Xiangya Stomatological Hospital, Xiangya School of Stomatology, Central South University, Changsha 410008, China*
[2]*Molecular Biology Research Center, Center for Medical Genetics, School of Life Sciences; Hunan Province Key Laboratory of Basic and Applied Hematology, Central South University, Changsha 410078, China*
[3]*State Key Laboratory of Powder Metallurgy, School of Materials Science and Engineering, Central South University, Changsha 410083, China*
[4]*College of Landscape Architecture and Art Design, Hunan Agricultural University, Changsha 410128, China*

Correspondence should be addressed to Yuetao Zhao; ytzhao@csu.edu.cn, Jing Liu; jingliucsu@hotmail.com, and Jun Zuo; zuolaoshimentu@csu.edu.cn

Received 14 August 2021; Accepted 27 November 2021; Published 4 January 2022

Academic Editor: Xin Luo

The surficial micro/nanotopography and physiochemical properties of titanium implants are essential for osteogenesis. However, these surface characters' influence on stem cell behaviors and osteogenesis is still not fully understood. In this study, titanium implants with different surface roughness, nanostructure, and wettability were fabricated by further nanoscale modification of sandblasted and acid-etched titanium (SLA: sandblasted and acid-etched) by H_2O_2 treatment (hSLAs: H_2O_2 treated SLA). The rat bone mesenchymal stem cells (rBMSCs: rat bone mesenchymal stem cells) are cultured on SLA and hSLA surfaces, and the cell behaviors of attachment, spreading, proliferation, and osteogenic differentiation are further analyzed. Measurements of surface characteristics show hSLA surface is equipped with nanoscale pores on microcavities and appeared to be hydrophilic. *In vitro* cell studies demonstrated that the hSLA titanium significantly enhances cell response to attachment, spreading, and proliferation. The hSLAs with proper degree of H_2O_2 etching (h1SLA: treating SLA with H_2O_2 for 1 hour) harvest the best improvement of differentiation of rBMSCs. Finally, the osteogenesis in beagle dogs was tested, and the h1SLA implants perform much better bone formation than SLA implants. These results indicate that the nanoscale modification of SLA titanium surface endowing nanostructures, roughness, and wettability could significantly improve the behaviors of bone mesenchymal stem cells and osteogenesis on the scaffold surface. These nanoscale modified SLA titanium scaffolds, fabricated in our study with enhanced cell affinity and osteogenesis, had great potential for implant dentistry.

1. Introduction

Current tooth restoration has evolved success since the interfacial bone formation at machined endosseous implants [1]. Titanium implants, in particular, have been identified as ideal biomaterials in clinic due to their favorable physiochemical characteristics, biocompatibility, and osseointegration ability [2, 3]. Osseointegration, the direct contact between the vital bone and the implant at the microscopic level, plays an essential role in improving implants' efficiency and reducing risk, especially in selected patient populations (e.g., smokers and diabetics) [4–7]. Complex mechanisms (e.g., local anatomic, local biologic, systemic, or functional factors) have evolved to achieve osseointegration at high

rate. A major interest is increasing bone forming at the implant surface by controlling the implant surface characters [8–11].

The surface micro/nanotopography and physiochemical properties of titanium implants are crucial characters for osseointegration and have recently been highlighted [12–15]. The topographical micrometric features can increase osseointegration by direct bone-to-implant contact and resistance to applied loads on titanium surfaces [16]. Further nanoscale modification of the surface affecting both topography and surface chemistry has been shown to influence adhesion, motility, and proliferation of specific cells (e.g., osteoblast) by direct (cell-surface interactions) and indirect (protein-surface interactions) mechanisms [17]. The surface energy or wettability is also reported to increase the expression of key osteogenesis genes in osteoblast and displays superior degree of early osseointegration [18–21]. Evoked by those theories, multiple surface treatment techniques, e.g., sandblasted and acid-etched (SLA), alkali and heat treatment, anodic oxidation, double-etching, and magnetron sputtering, have been developed to generate micro/nanosurface structure and better bone formation *in vitro* and *in vivo* [22–25].

On the other hand, bone mesenchymal stem cells (BMSCs), the first cells to colonize the surface of the implant after its insertion, have the ability to improve bone regeneration by differentiation into parenchymal cells and the production of growth factors [26]. Controlling mesenchymal stem cells (MSCs) differentiation towards the osteogenic lineage may assist more rapid osseointegration with beneficial effects [27]. By providing topographical cues and mechanical stimuli, the micro- and nanoenvironments of stem cell differentiation can be engineered *in vitro* [28, 29]. Nevertheless, the effect of the titanium surface micro/nanofeatures on stem cell behaviors and osteogenesis *in vivo* still needs to be systematically studied.

Herein, we illustrate that titanium's topography and physiochemical property influence MSCs responses and promote osseointegration effect of the implants. Specifically, traditional titanium surface is nanoscale modified by etching the SLA titanium in hydrogen peroxide for different times to generate various micro/nanostructured topography and wettability. Subsequently, changes in surface characteristics are systematically explored, and the initial cell attachment, spreading, proliferation, and differentiation behaviors of rat bone mesenchymal stem cells (rBMSCs) are measured to evaluate the osseointegration difference *in vitro*. Finally, the osteogenesis effect is tested *in vivo*, confirming that the titanium microsurface with suitable nanostructure and wettability has the best ability to promote bone formation.

2. Materials and Methods

2.1. Sample Preparation. The samples were prepared as previously described [30]. Commercial pure TA4 titanium plate (Hunan Xiangtou Jintian Titanium Metal Co. Ltd.) was cut into disks (Φ20 mm or Φ32 mm, 2 mm thick). Then, disks were polished to Ra < 0.5 μm and sandblasted by Al_2O_3 (Φ0.25~0.5 mm) at a pressure of 0.5 mPa. After ultrasonic cleaning in acetone, absolute ethanol, and ultrapure water for 10 minutes, the etching was carried out in the boiling mixture of H_2SO_4 (Zhuzhou, Hunan) and HCl (Zhuzhou, Hunan) for several minutes. Finally, the SLA (sandblasted and acid-etched) group was obtained by washing with ultrapure water and drying with hot air. The SLA titanium plates were immersed in concentrated H_2O_2 for 1 hour and 2 hours, respectively, to form hSLA (H_2O_2 treated SLA) groups, named h1SLA (treating SLA with H_2O_2 for 1 hour) and h2SLA (treating SLA with H_2O_2 for 2 hours), respectively. Then, the materials were cleaned and dried by ultrasound. The preparation process is shown in supplementary material (Figure S1).

2.2. Surface Characterization

2.2.1. Surface Morphology. Surface morphologies were observed by scanning electron microscopy (SEM, Nova NanoSEM 230, USA). At least three points of each sample were detected. The observation and photos were taken at five magnification ratios of 1000x, 2000x, 5000x, 50000x, and 100000x, respectively.

2.2.2. Surface Roughness. Surface roughness was measured by surface profiler (wyko NT9100, USA) with each testing line of 1 mm. Five test points were randomly selected for each sample. Then, the average values of Ra (arithmetic mean deviation of contour: arithmetic mean of absolute value of contour offset within sampling length) and Rz (maximum height of profile: the sum of the average of the five largest contour peak heights and the average of the five largest contour valley depths within the sampling length) on each titanium plate were calculated by software.

2.2.3. Wettability. The water contact angles (WCA) were measured by contact angle measuring instrument (SDC-100, China) to evaluate the hydrophilicity of the sample. Three sites were randomly selected on each fresh sample surface to calculate the mean and standard deviation of water contact angle on each sample surface.

2.2.4. Surface Chemistry. Surface chemistry was analyzed by X-ray photoelectron spectroscopy (XPS, ESCALAB 250Xi, USA) with Al Kα irradiation and X-ray energy dispersive spectroscopy (EDS, Nova NanoSEM 230, USA). In XPS detection, three sites were randomly selected for each sample, and the obtained detection data were further used for spectral peak calibration, peak separation fitting, and element calibration. The spectral peak corresponding to the C1s spectral peak was 285.0 eV for calibration. The valence states of O element and Ti element were analyzed.

2.3. Isolation and Culturing of Rat BMSCs. Three-week-old male Sprague-Dawley rats were used for the isolation and culture of bone mesenchymal stem cells (BMSCs) as formerly described [31]. Briefly, the femur of rats was taken, and the bone marrow cavity was continuously rinsed with a mixture of high-glucose DMEM complete medium (Hyclone, USA) supplemented with 10% fetal bovine serum (FBS, Gibco, USA) and 100 IU/mL penicillin-streptomycin solution (Gibco, USA) until it turned white. The

morphology of cells was observed by inverted microscope (Figure S3) [32], and the cells were used for subsequent experiments when the state and quantity of cells were appropriate. Cells of passage 2-5 were seeded on titanium samples in either growth medium or osteogenic medium, which was growth medium with the addition of 50 μM ascorbic acid (Sigma, USA), 10 mM β-glycerophosphate (Sigma, USA), and 100 nM dexamethasone (Sigma, USA).

2.4. Cell Behaviors on the Surface

2.4.1. Cell Attachment. Three Φ 20 mm titanium plates were taken from each group and placed into a 12-well plate. Rat bone mesenchymal stem cells (rBMSCs) were inoculated on the titanium plates with a density of 4×10^4/well. After incubating for 4 hours, cells were fixed in 4% paraformaldehyde (Sigma, USA) followed by staining with acridine orange (A.O., Sigma, USA). After observing under fluorescence microscope (Nikon Eclipse TE300, Japan) and capturing the images, the number of cells was counted from 5 random fields for each plate and three plates for each group.

2.4.2. Cell Spreading. Three Φ 20 mm titanium plates were taken from each group and placed into a 12-well plate. rBMSCs were inoculated on the titanium plates with a density of 2×10^4/well. Cells were fixed in 4% paraformaldehyde (Sigma, USA) to explore cell spreading after incubating for 12 hours. Staining with 4′,6-diamidino-2-phenylindole (DAPI, Beyotime, China) and rhodamine-phalloidin (Cytoskeleton, USA), cells were observed under fluorescence microscope ((Nikon eclipse TE300, Japan). At a magnificence of 20x, images of 5 random fields for each plate were captured to calculate their spreading areas by Image J.

2.4.3. Cell Proliferation. Three Φ 20 mm titanium plates were taken from each group and placed into a 12-well plate. rBMSCs were inoculated on the titanium plates with a density of 2×10^4/well. After incubating for 24 h, 48 h, and 72 h, respectively, cell proliferation was measured by cell staining and CCK-8 kit (Dojindo Molecular Technologies, Japan) according to the method previously described [33]. All these experiments were conducted in triplicates.

In addition, the expression of the marker of proliferation Ki-67 (Mki67) marker at each time point was observed by immunofluorescence assay. Cells on titanium discs were fixed in 4% paraformaldehyde (Sigma, USA) for 15 min and blocked with 10% goat serum (Solarbio, China) for 30 min. Subsequently, they were incubated with the primary antibody of Mki67 (Abclonal, China) overnight at 4°C. After rinsing, the cells were further incubated with DyLight 488-conjugated anti-rabbit IgG antibodies (Abcam, U.K.) for 1 h at ambient temperature. Finally, cell nuclei were stained with 4′,6-diamidino-2-phenylindole (DAPI, Beyotime, China) for 15 min. Figures were then acquired using a fluorescence microscope (Nikon Eclipse TE300, Japan).

2.5. In Vitro Osteogenesis Ability

2.5.1. Cell Attachment and Spreading. Put three pieces for each group Φ 20 mm titanium plate and four pieces Φ32 mm titanium plate into a large dish together. The rBMSCs were inoculated on the titanium plates, and the inoculation density was about 6×10^5 per plate. After incubating for 4 d, cells were fixed in 4% paraformaldehyde (Sigma, USA). Staining with 4′,6-diamidino-2-phenylindole (DAPI, Beyotime, China) and rhodamine-phalloidin (Cytoskeleton, USA), cells were observed under fluorescence microscope ((Nikon eclipse TE300, Japan).

2.5.2. Bone-Related Gene Expression of rBMSCs. Put three pieces for each group Φ 20 mm titanium plate and four pieces Φ32 mm titanium plate into a large dish together. The rBMSCs were inoculated on the titanium plates, and the inoculation density was about 6×10^5 per plate. After incubating for 4 d and 7 d in an osteogenic medium, RNA was extracted and reverse transcribed according to manufacturer's instructions. The mRNA levels of bone-related genes alkaline phosphatase (*ALP*, Sangon Biotech, China), RUNX family transcription factor 2 (*RUNX2*, Sangon Biotech, China), collagen type I alpha 1 chain (*COL1A1*, Sangon Biotech, China), bone morphogenetic protein 2 (*BMP2*, Sangon Biotech, China), and integrin-binding sialoprotein (*BSP*, Sangon Biotech, China) in rBMSCs were evaluated by RT-PCR (Eppendorf AG 22331 Hamburg, Germany). The mRNA levels were normalized for glyceraldehyde-3-phosphate dehydrogenase mRNA (*Gapdh*, Sangon Biotech, China). The primers used are shown in supplemental instrument (Table S1).

2.5.3. Alkaline Phosphatase (ALP) Activity Assay. Three Φ 32 mm titanium plates were taken from each group and placed into a 6-well plate. rBMSCs were inoculated on the titanium plates with a density of 6×10^4/well. After incubating for 7 d and 14 d in osteogenic medium, the *ALP* activity of the adherent cells was detected using an Alkaline Phosphatase assay kit (Beyotime, China). The absorbance was measured at 405 nm by Microplate Reader (BioTek, USA), and values of ALP activity were read off according to a standard curve based on standard samples provided by the kit itself. In addition, three pieces of material were taken from each group for ALP staining experiment at 14 d. After cleaning with DPBS for 3 times, cells on titanium discs were fixed in 4% paraformaldehyde (Sigma, USA) for 15 min, incubated with BCIP/NBT ALP Color Development Kit (Beyotime, China) for 10~30 minutes, and photographed.

2.5.4. Immunofluorescence Staining. Three Φ 32 mm titanium plates were taken from each group and placed into a 6-well plate. rBMSCs were inoculated on the titanium plates with a density of 6×10^4/well. After incubating for 14 d in osteogenic medium, immunofluorescence staining was carried out to detect the expressions of osteocalcin (OCN). Cells on titanium discs were fixed in 4% paraformaldehyde (Sigma, USA) for 15 min and blocked with 10% goat serum (Solarbio, China) for 1 h. Subsequently, they were incubated with the primary antibody of OCN (Santa, USA) overnight at 4°C. After rinsing, the cells were further incubated with DyLight 488-conjugated anti-rabbit IgG antibodies (Abcam, U.K.) for 1 h at ambient temperature. Finally, they were

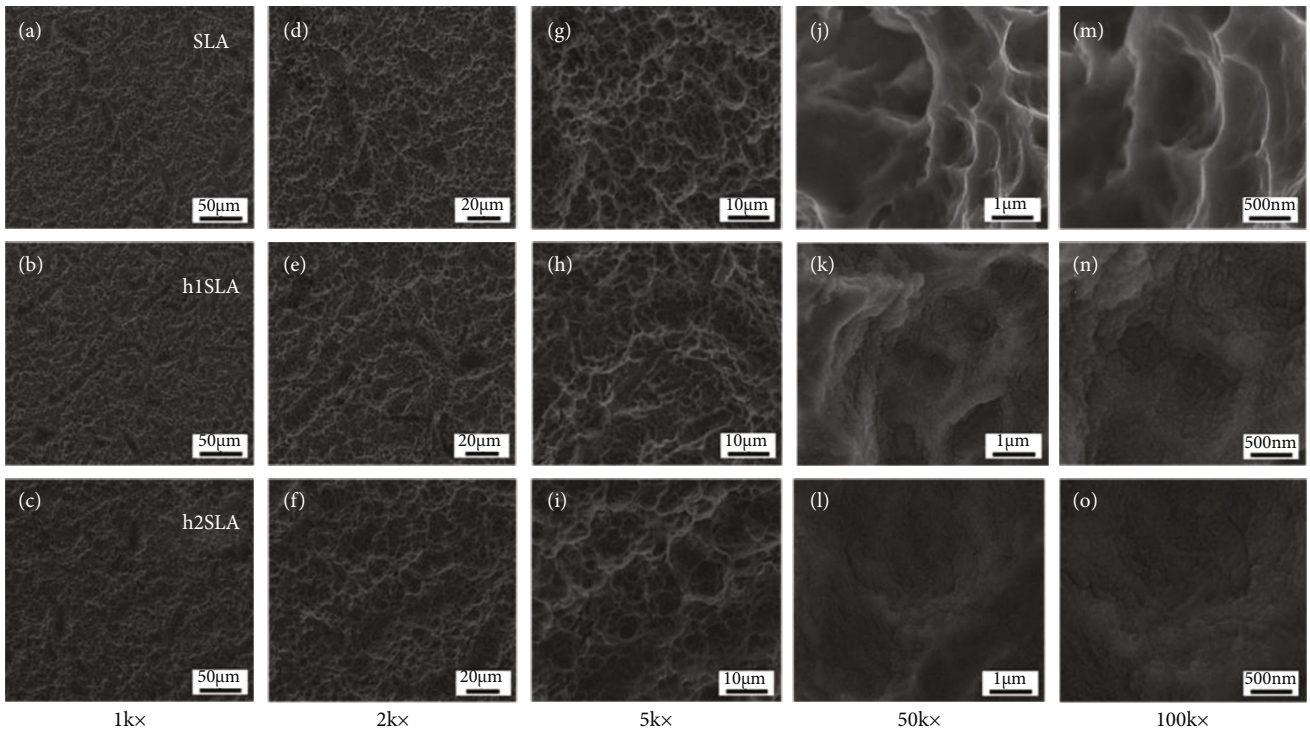

Figure 1: Scanning electron microscopy images of SLA, h1SLA, and h2SLA surface at different magnifications. (a–c) SLA, h1SLA, and h2SLA surfaces at 1k× magnification. (d–f) SLA, h1SLA, and h2SLA surfaces at 2k× magnification. (g–i) SLA, h1SLA, and h2SLA surfaces at 5k× magnification. (j–l) SLA, h1SLA, and h2SLA surfaces at 50k× magnification. (m–o) SLA, h1SLA, and h2SLA surfaces at 100k× magnification.

stained with rhodamine-phalloidin (Cytoskeleton, USA) for 1 h, and cell nuclei were stained with DAPI (Beyotime, China) for 10 min. Figures were then acquired using a fluorescence microscope (Nikon Eclipse TE300, Japan).

2.5.5. Alizarin Red Staining for Mineralization. Three Φ 32 mm titanium plates were taken from each group and placed into a 6-well plate. rBMSCs were inoculated on the titanium plates with a density of 6×10^4/well. After incubating for 14 d in osteogenic medium, cells on samples were fixed and stained with the Alizarin red S (ARS) reagent (Cyagen, China) for 15 min at room temperature. After the samples were washed with DPBS three times, images were taken. Then, the mineralized nodules were eluted with 10% hexadecylpyridinium chloride monohydrate (Sigma, USA), and the O.D. value at 570 nm was measured for quantitative detection.

2.6. In Vivo Osteogenesis Study. One-year-old male Beagles were purchased from Fuzhou Zhenhe Experimental Animal Technology Development Co., Ltd., weighing 10-13 kg, and all the *in vivo* experiments followed the protocols approved by the Animal Care and Use Committee of the Xiangya School of Stomatology, Central South University. To establish the osteogenesis model, SLA implants and h1SLA implants were separately implanted on the normal alveolar bone between the two adjacent teeth after removing the crowns from bilateral mandibular premolars of beagles (Figure S8). Six weeks later, the beagles were killed, and the rotation torque value of each implant was measured.

To determine the new bone formation on the implants, fixed sample was measured by the Cone Beam Computer Tomography (CBCT, ProMax 3D, Helsinki), and the images were generated from Planmeca Romexis. After performing the CBCT, hard tissue sections were made and stained with methylene blue magenta to observe the osteogenesis.

2.7. Statistical Analysis. Data from cellular experiments on the substrates are presented as the mean error and standard deviation of the mean error of all the measurements. Data were evaluated by analysis of significant differences among different groups, which were determined using one-way ANOVA and *t*-test by "GraphPad Prism 8.0." Asterisk (∗) represents significant differences between different substrates. * indicates $0.01 \le p < 0.05$, ** indicates $0.001 \le p < 0.01$, *** indicates $0.0001 \le p < 0.001$, and **** indicates $0.00001 \le p < 0.0001$.

3. Results and Discussion

3.1. Surface Characteristics. It is reported that hierarchical micro/nanotopography contributed to cell adhesion and bone integration *in vivo* [34]. Observed from the scanning electron microscopy (SEM) images in Figure 1, it can be seen both of the SLA (sandblasted and acid etched) and hSLA (H_2O_2 treated SLA) groups have uniform honeycomb-like

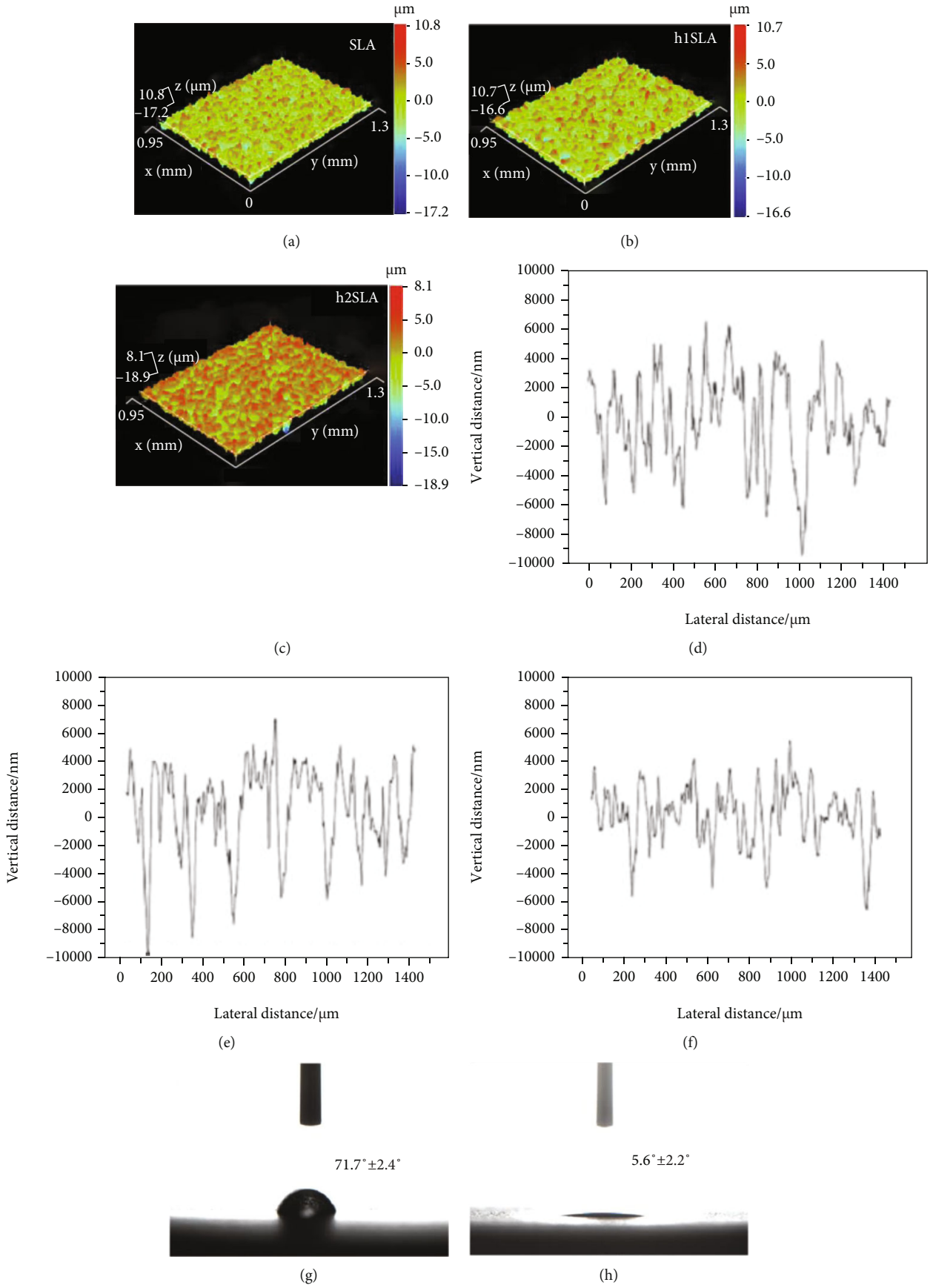

Figure 2: Continued.

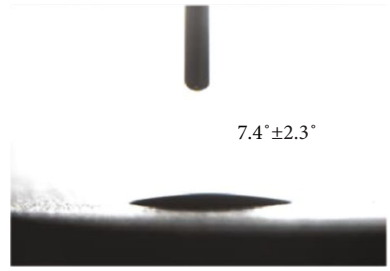

(i)

Figure 2: Roughness and wettability results of SLA, h1SLA, and h2SLA surface. (a–c) 3D surface profile of SLA, h1SLA, and h2SLA surface. (d–f) 2D analysis of SLA, h1SLA, and h2SLA surface. (g–i) Water contact angles of SLA, h1SLA, and h2SLA surface.

holes ranging from 1 μm to 3 μm at 5k× magnification (Figures 1(g)–1(i)). At the magnification of 50k× (Figures 1(j)–1(l)) and 100k×(Figures 1(m)–1(o)), for the SLA group, the wall is smooth, and the edge of the holes is sharp, with no nanostructure found. In contrast, the cavity walls of the h1SLA (treating SLA with H_2O_2 for 1 hour) and h2SLA (treating SLA with H_2O_2 for 2 hour) groups are rough, and the edges of the cavity are round and blunt. Moreover, many nanoparticles were evenly distributed between and on the cavity wall.

We find no significant difference in nanomorphology between h1SLA and h2SLA groups, indicating the longer etching time of H_2O_2 does not influence the nanostructure of surface. However, the microstructure and the surface roughness might be affected by the treatment time. Titanium surface with increased roughness that resulted from micro-scale topography is more beneficial for cells and bone tissue attachment [35]. There is no obvious difference between SLA and h1SLA samples in the 3D vision (Figures 2(a) and 2(b)) because of the short etching time, and similar profile peaks and valleys are further confirmed in the 2D analysis (Figures 2(d) and 2(e)). However, more protrusions with lower height are observed on h2SLA samples (Figure 2(c)), with lower profile peaks (Figure 2(f)), indicating longer H_2O_2 treating time may eliminate the microcavities. From the analysis of Ra (arithmetic mean deviation of contour) and Rz (maximum height of profile) (Table 1), we find no significant difference between SLA and h1SLA groups, while each parameter of h2SLA is, respectively, lower. The results indicate that the longer treatment of H_2O_2 leads to flatter microstructures without obvious changes on nanostructures.

The water contact angles (WCA) of both h1SLA and h2SLA samples are less than 10° (Figures 2(h) and 2(i)), significantly lower than that of SLA, which is about 70° (Figure 2(g)). This may be attributed to the O_2^{2-} group formed during the etching process of H_2O_2 [30]. Surface hydrophilicity is crucial in recovering the effect of micro/nanotopography on promoting osteoblastic differentiation of MSCs (mesenchymal stem cells) [36]. The combination of nanostructures and hydrophilicity could improve protein adsorption levels, leading to early and most significant blood coagulation [37] and the strongest bone response [38].

Surface chemistry is also related to the bioactivity of materials [39]. From the XPS (X-ray photoelectron spectroscopy) analysis (Figure 3) and EDS (X-ray energy dispersive spectroscopy) detection (Figure S2), we find that the content of titanium and oxygen of h1SLA and h2SLA is changed. The Ti2P spectra (Figures 3(d)–3(f)) show the vanishment of Ti^0 peak at 453.5 eV and increase of titanium oxide peak, which may be due to the oxidation of titanium with treatment of H_2O_2. The presence of metal Ti^0 on SLA samples (Figure 3(d)) suggests the oxide layer is either thin or heterogeneous [40]. In contrast, the oxide layers on the surface of the h1SLA and h2SLA groups are either thicker or more homogeneous for the absence of metal Ti^0 (Figures 3(e) and 3(f)). More details in the O1S spectra show an additional peak at 533.5 eV (Figures 3(g)–3(i)), which can be postulated to be O_2^{2-} group because of the formation of $Ti(H_2O_2)_2^{4+}$ during etching [41].

Table 1: Roughness parameters (Ra and Rz) of SLA, h1SLA, and h2SLA surfaces. Ra: arithmetic mean deviation of contour. Rz: maximum height of profile.

	SLA (μm)	h1SLA (μm)	h2SLA (μm)
Ra	2.193 ± 0.045	2.198 ± 0.050	2.003 ± 0.037
Rz	23.323 ± 0.859	23.763 ± 0.692	21.573 ± 1.178

3.2. Cell Behaviors of rBMSCs on Different Titanium Surface. We first checked the cell behaviors (e.g., attachment, spreading, and proliferation) of rBMSCs (rat bone mesenchymal stem cells) on different titanium surface. In the initial cell-implant interactions, cell adhesion is one of the most critical processes [42]. We find that both h1SLA and h2SLA surfaces display more cell attachment in comparison with SLA surfaces in Figures 4(a)–4(c). The number of adherent rBMSCs (Figure 4(d)) on h1SLA and h2SLA surfaces are both higher than that on SLA surface, with statistically significant differences.

The cytoskeletons of cells are more extended, and polygonal osteoblastic-like shapes with more obvious filopodia are observed on h1SLA and h2SLA surfaces in Figures 4(e)–4(g), which have been proved to be closely related to MSC osteogenic activity [43, 44]. As presented in Figure 4(h), the cell spreading areas on h1SLA and h2SLA surfaces are significantly larger than SLA.

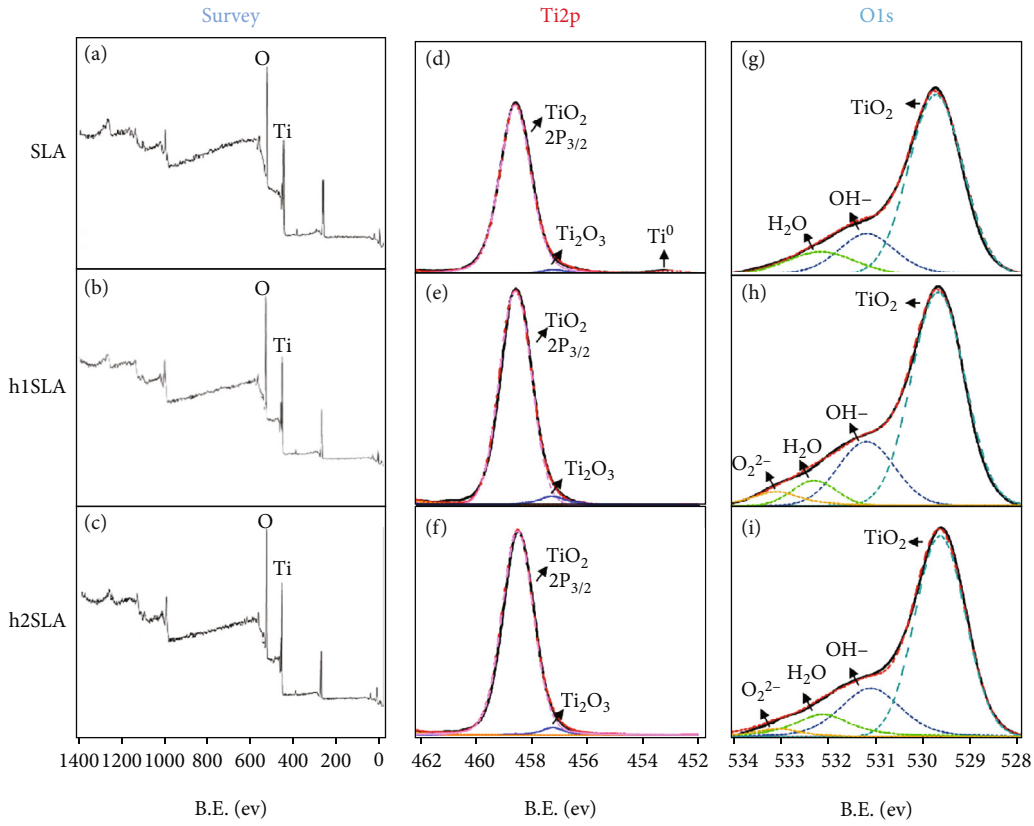

Figure 3: X-ray photoelectron spectroscopy results of SLA, h1SLA, and h2SLA surfaces. (a–c) X-ray photoelectron spectroscopy survey spectrums. (d–f) Ti2p valence analysis. (g–i) O1s valence analysis.

Cell proliferation is observed by Mki67 immunofluorescence assay (Figures 4(i)–4(l)), cell staining (Figure S4), and CCK-8 experiment (Figure S5). By immunofluorescence detection (Figures 4(i)–4(k)) and fluorescence intensity quantitative detection (Figure 4(l)), we observed that the expression of Mki67 was more robust in the treatment group, especially in h1SLA group. The cell staining further confirmed the increase of cell numbers on the h1SLA surface. From the CCK-8 test results, the cell numbers on the three surfaces have no obvious difference at 1 d. However, with the increase of time, the h1SLA surface shows significant increase in cell numbers. This may be explained by the relatively higher hydrophilicity [45] of group h1SLA. Overall, these data demonstrate that h1SLA surface is most biocompatible among them. The excellent biocompatibility of h1SLA surface for rBMSCs may be benefit for osteogenesis.

3.3. In Vitro Study of rBMSC Osteogenic Differentiation. We first observed the cell morphology on the titanium surfaces at 4 d after osteogenesis induction. As shown in Figures 5(d)–5(f), there are more cell accounts of rBMSCs on the h1SLA surfaces than the h2SLA and SLA groups, and the cells are more extended on h1SLA. This cell spreading trend is consistent with which in Figure 4 without osteogenesis induction, preliminarily indicating that h1SLA group is more conducive to osteogenic differentiation.

Real-time PCR detects the mRNA expression level of osteogenic indexes at 4 d (Figure S6) and 7 d (Figure 5(a)). *ALP* and *RUNX2* play an important role in early osteogenesis. The expression of these two genes in h1SLA group is significantly higher than that in the other two groups, followed by h2SLA group. The significant increase of other osteogenesis-related genes such as *COL1A1*, *BMP2*, and *BSP* also shows that the osteogenic properties of the materials are significantly improved after hydrogen peroxide treatment. The ALP activity at the protein level is measured at 7 d and 14 d, respectively (Figure 5(b)). Compared with SLA, the ALP protein expression in both h1SLA and h2SLA are significantly increased, whereas the h1SLA shows the highest level at 14 d. By carefully observing the ALP staining on the materials surface directly (Figures 5(g)–5(i)), it can also be observed that the ALP staining in h1SLA group is deeper than the other two groups.

We also explore the expression of osteocalcin, which is a late osteogenic marker, by immunofluorescence assay at 14 d. The green-stained protein is observed to be stronger on h1SLA and h2SLA surfaces, revealing better osteogenic effect of h1SLA and h2SLA surfaces than SLA, whereas the h1SLA shows the highest level (Figures 5(j)–5(l)). By quantitative analysis of fluorescence intensity (Figure S7), the expression of OCN in h1SLA group increased significantly. Alizarin Red staining was carried out at 14 d (Figures 5(m)–5(o)). The results show that the h1SLA has

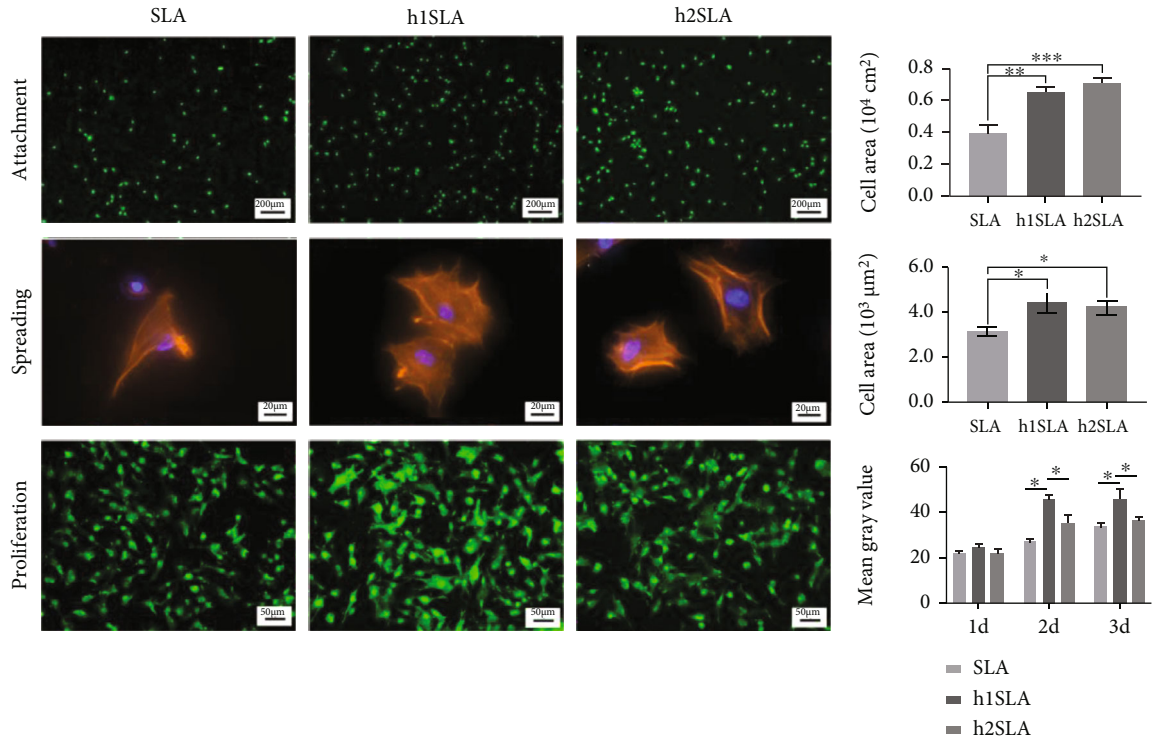

Figure 4: (a–c) Fluorescence microscopy images of rBMSCs attached to SLA (a), h1SLA (b), and h2SLA (c) surfaces stained by AO. (d) Quantitative analysis of cell attachment. (e–g) Fluorescence microscopy images of rBMSCs spreading on SLA (e), h1SLA (f), and h2SLA (g) surfaces. Orange red: rhodamine-phalloidin. Blue: DAPI. (h) Quantitative analysis of spreading areas. (i–k) Fluorescence microscopy images of Mki67 expression on SLA (i), h1SLA (j), and h2SLA (k) surfaces at 3 d. Green: Mki67. (l) Quantitative analysis of fluorescence intensity ($n = 40$).

the most obvious mineralization nodules, followed by the h2SLA group, and the SLA group has the least mineralized nodules. This difference is reflected in the quantitative test results (Figure 5(c)). These results further confirm that the h1SLA and h2SLA surface can promote bone formation than SLA, and the effect on the h1SLA surface is most significant.

3.4. In Vivo Osteogenesis Study. Inspired by rBMSCs differentiation result, we further performed the osteogenesis experiments of h1SLA *in vivo* using SLA as control. The CBCT (Cone Beam Computer Tomography) image (Figures 6(a)–6(d)) 6 weeks after implantation shows more obvious white projection around the h1SLA implants, indicating more bone formation around h1SLA than in the SLA group, and more abundant deep red staining areas around h1SLA could be observed (Figures 6(e) and 6(f)) through methylene blue acid magenta staining of hard tissue sections, which is consistent with the trend indicated by CBCT results. Meanwhile, the torque value of implant rotation from h1SLA group is greater than that of SLA group (Table 2), in line with CBCT and staining trend. Hard tissue section staining data show that BIC%, which represents the ratio of bone to implant contact, in h1SLA group is nearly 2 times higher than that in SLA group (Table 2). Animal experiments further confirm that nanostructured and hydrophilicity are more suitable for osteogenic differentiation of rBMSCs, which is very important for further clinical promotion. From those results, it could be inferred that biopotential mimicking surface, which is modified in structures, wettability, and indirectly in surface chemistry, plays a key role in the improvement of osteogenesis performance.

The surface properties of titanium implants such as topography, roughness, wettability, and chemistry have a significant impact on biological activity [46–50]. In our study, experimental results *in vitro* and *in vivo* confirm that the nanoscale modification, which brings nanostructure morphology, hydrophilicity, and chemistry change together to the titanium implants, is positive to rat bone mesenchymal stem cell responses. However, the use of rBMSCs and the rat model may still face some limitations, whether this material is suitable for human-related cell needs to be further studied. Therefore, in future research, in addition to continuing to study the decisive factors affecting material properties, human cells such as human gingival mesenchymal stem cells or human periodontal ligament stem cells will be used for osteogenesis verification [32, 51]. Besides, it has been reported that the presence of O_2^{2-} group and nanoscale modification can significantly improve the antibacterial and immunity properties to promote wound healing [52, 53], so we will also conduct relevant experiments for further studies.

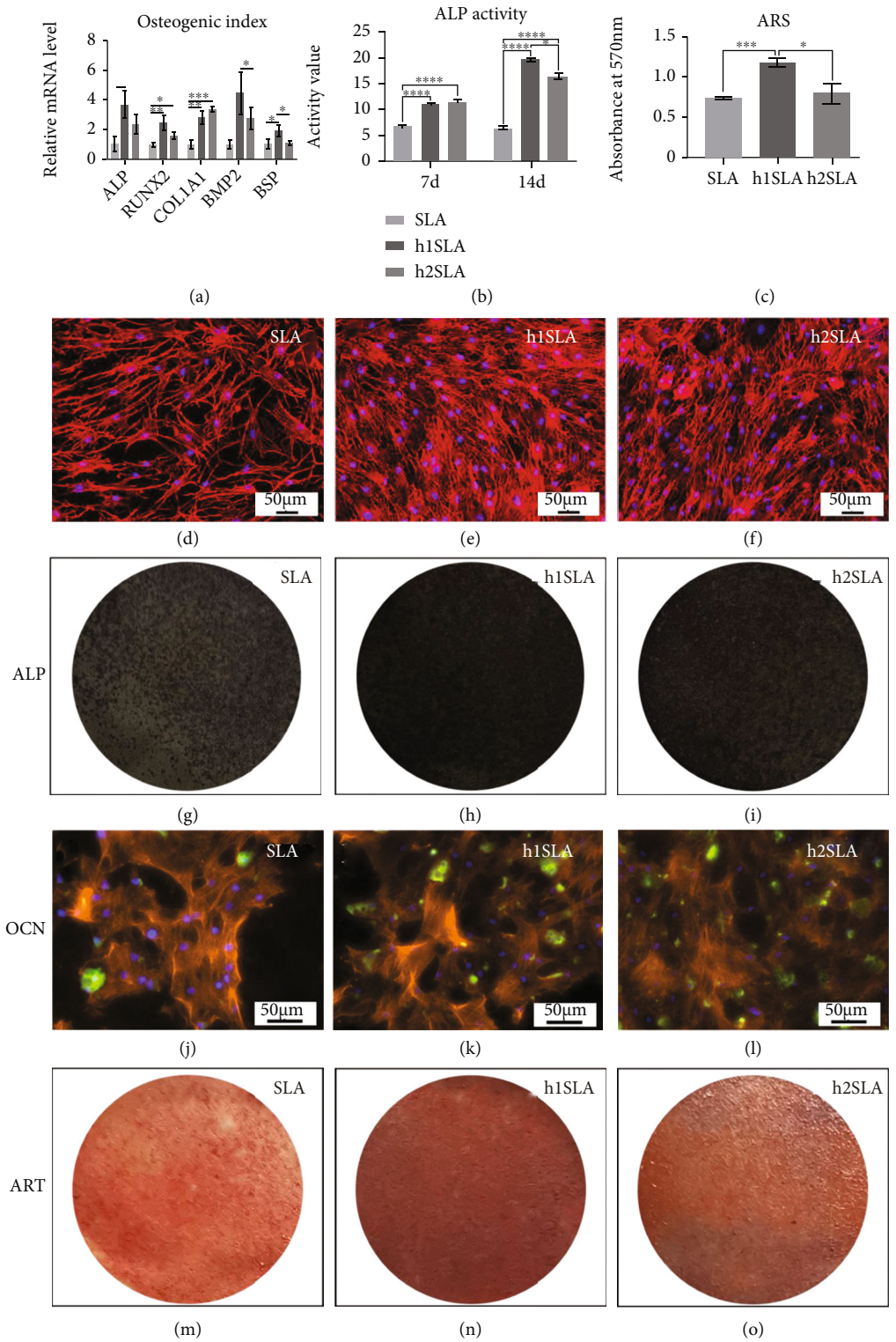

FIGURE 5: *In vitro* rBMSC osteogenic differentiation on different surfaces. (a) Expression of osteogenic index of rBMSCs on SLA, h1SLA, and h2SLA at 7 d. (b) Relative ALP activity of rBMSCs on different samples at 7 d and 14 d. (c) Quantitative detection by Alizarin red staining at 14 d. (d–f) Adhesion and spreading of cells on each surface after osteogenesis induction for 4 d. Red: rhodamine-phalloidin. Blue: DAPI. (g–i) Staining of ALP in SLA, h1SLA, and h2SLA groups at 14 d. (j–l) The expression of OCN (green) explored by immunofluorescence assay at 14 d. (m–o) Pictures of mineralization nodules deposited on different surfaces at 14 d.

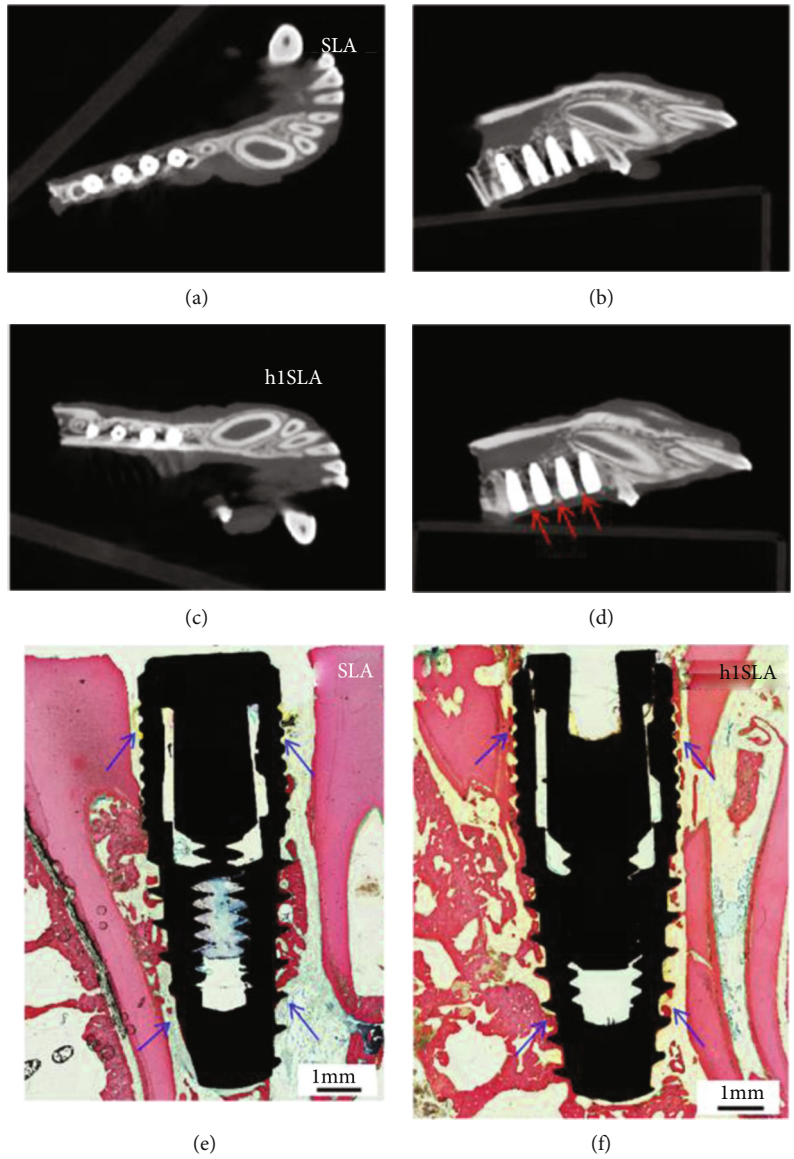

Figure 6: *In vivo* osteogenesis: (a–d) Cone Beam Computer Tomography images of SLA group and h1SLA group 6 weeks after implant surgery. (e–f) Methylene blue acid fuchsin dyeing results of hard tissue sections 6 weeks after implantation in SLA group and h1 group. Red: bone tissues. Blue arrow: new bone formation region.

Table 2: The analysis of implant rotation torque values (the second column) and hard tissue section data (between three and six columns) 6 weeks after implantation in SLA group and h1SLA group. Im.Pm: perimeter of implants. Tb.In.Pm: length of contact between trabecula and implant. Ct.In.Pm: length of contact between cortical bone and implant. BIC%: ratio of bone to implant contact.

	M ± SD (N/cm)	Im.Pm	Tb.In.Pm	Ct.In.Pm	BIC%
SLA	71.8 ± 25.6	131.400	46.262	1.361	0.362
h1SLA	84.2 ± 18.4	134.993	71.179	11.119	0.610

4. Conclusions

In this study, titanium implants with different surficial features are fabricated by simple and eco-friendly H_2O_2 treatment of SLA (sandblasted and acid-etched) titanium to improve the behaviors of stem cells and osteogenesis *in vitro* and *in vivo*. The nanoscale modification of SLA endows nanostructure, enhanced roughness, and wettability on titanium surface, which significantly promotes the attachment, spreading, proliferation, and osteogenic differentiation of rat bone mesenchymal stem cells *in vitro*. The *in vivo* experiments further confirmed the osseointegration

improvement. These results indicate that the nanoscale-modified SLA titanium may have great potential in better osteogenesis and higher implant success rate.

Data Availability

The data used to support the findings of this study are available from the corresponding author upon request.

Conflicts of Interest

The authors declare no known competing financial interests or personal relationships that could have appeared to influence the work reported in this paper.

Authors' Contributions

Huangdi Li, Jinghui Huang, and Yanpeng Wang contributed equally to this work.

Acknowledgments

This work was supported by the Natural Science Foundation of Hunan Province (nos. 2018JJ2546 and 2021JJ20083), the National Natural Science Foundation of China (NSFC) (no. 32000931), and the Fundamental Research Funds for Central Universities of the Central South University (no. 2020zzts069).

Supplementary Materials

Figure S1: Diagram of titanium sheet processing process. Figure S2: X-ray energy dispersive spectroscopy maps of SLA, h1SLA, and h2SLA surfaces. (a–c) Dark field. (d–f) Ti K spectrums. (g–i) O K spectrums. (j–l) Merged of Ti K and O K spectrums. (m–o) Quantitative analysis. Figure S3: Morphological images of rat bone mesenchymal stem cells. Figure S4: Staining of rBMSCs on SLA (a), h1SLA (b), and h2SLA (c) surface. Red: rhodamine-phalloidin. Blue: DAPI. Figure S5: Cell proliferation detected by CCK8-kit. Figure S6: Expression of osteogenic index of rBMSCs on SLA, h1SLA, and h2SLA at 4 d. Figure S7: Quantitative analysis of OCN fluorescence intensity at 14 d. Figure S8: Verify the osteogenic effect in vivo. After removing the crowns from bilateral mandibular premolars of beagles (b), hole preparation step by step (c, d), SLA implants and h1SLA implants were separately implanted on the normal alveolar bone between the two adjacent teeth (e–h). Table S1: Gene primer list. *(Supplementary Materials)*

References

[1] P. I. Brånemark, R. Adell, U. Breine, B. O. Hansson, J. Lindström, and A. Ohlsson, "Intra-osseous anchorage of dental prostheses. I. Experimental studies," *Hand Surgery*, vol. 3, no. 2, pp. 81–100, 1969.

[2] D. M. Dohan Ehrenfest, P. G. Coelho, B. S. Kang, Y. T. Sul, and T. Albrektsson, "Classification of osseointegrated implant surfaces: materials, chemistry and topography," *Trends in Biotechnology*, vol. 28, no. 4, pp. 198–206, 2010.

[3] J. C. M. Souza, M. B. Sordi, M. Kanazawa et al., "Nano-scale modification of titanium implant surfaces to enhance osseointegration," *Acta Biomaterialia*, vol. 94, pp. 112–131, 2019.

[4] G. N. Cyprus, J. W. Overlin, K. M. Hotchkiss, S. Kandalam, and R. Olivares-Navarrete, "Cigarette smoke increases pro-inflammatory markers and inhibits osteogenic differentiation in experimental exposure model," *Acta Biomaterialia*, vol. 76, pp. 308–318, 2018.

[5] H. De Bruyn, V. Christiaens, R. Doornewaard et al., "Implant surface roughness and patient factors on long-term peri-implant bone loss," *Periodontology 2000*, vol. 73, no. 1, pp. 218–227, 2017.

[6] P. G. F. P. de Oliveira, E. A. Bonfante, E. T. P. Bergamo et al., "Obesity/metabolic syndrome and diabetes mellitus on peri-implantitis," *Trends in Endocrinology and Metabolism*, vol. 31, no. 8, pp. 596–610, 2020.

[7] X. Dai, B. C. Heng, Y. Bai et al., "Restoration of electrical microenvironment enhances bone regeneration under diabetic conditions by modulating macrophage polarization," *Bioactive materials*, vol. 6, no. 7, pp. 2029–2038, 2021.

[8] H. Aita, N. Hori, M. Takeuchi et al., "The effect of ultraviolet functionalization of titanium on integration with bone," *Biomaterials*, vol. 30, no. 6, pp. 1015–1025, 2009.

[9] A. R. Ribeiro, F. Oliveira, L. C. Boldrini et al., "Micro-arc oxidation as a tool to develop multifunctional calcium-rich surfaces for dental implant applications," *Materials Science and Engineering: C*, vol. 54, pp. 196–206, 2015.

[10] Y. Xu, W. Liu, G. Zhang et al., "Friction stability and cellular behaviors on laser textured Ti-6Al-4V alloy implants with bioinspired micro-overlapping structures," *Journal of the Mechanical Behavior of Biomedical Materials*, vol. 109, article 103823, 2020.

[11] K. Liu, H. Zhang, M. Lu et al., "Enhanced bioactive and osteogenic activities of titanium by modification with phytic acid and calcium hydroxide," *Applied Surface Science*, vol. 478, pp. 162–175, 2019.

[12] Y. Zhu, H. Liang, X. Liu et al., "Regulation of macrophage polarization through surface topography design to facilitate implant-to-bone osteointegration," *Science Advances*, vol. 7, no. 14, pp. 1–14, 2021.

[13] N. Khosravi, R. S. DaCosta, and J. E. Davies, "New insights into spatio-temporal dynamics of mesenchymal progenitor cell ingress during peri-implant wound healing: provided by intravital imaging," *Biomaterials*, vol. 273, article 120837, 2021.

[14] Q. L. Ma, L. Fang, N. Jiang et al., "Bone mesenchymal stem cell secretion of sRANKL/OPG/M-CSF in response to macrophage-mediated inflammatory response influences osteogenesis on nanostructured Ti surfaces," *Biomaterials*, vol. 154, pp. 234–247, 2018.

[15] E. M. Lotz, M. B. Berger, Z. Schwartz, and B. D. Boyan, "Regulation of osteoclasts by osteoblast lineage cells depends on titanium implant surface properties," *Acta Biomaterialia*, vol. 68, pp. 296–307, 2018.

[16] K. Fischer and T. Stenberg, "Prospective 10-year cohort study based on a randomized controlled trial (RCT) on implant-supported full-arch maxillary prostheses: part 1: sandblasted and acid-etched implants and mucosal tissue," *Clinical Implant Dentistry and Related Research*, vol. 14, no. 6, pp. 808–815, 2012.

[17] T. J. Webster and J. U. Ejiofor, "Increased osteoblast adhesion on nanophase metals: Ti, Ti6Al4V, and CoCrMo," *Biomaterials*, vol. 25, no. 19, pp. 4731–4739, 2004.

[18] S. M. Hamlet, R. S. B. Lee, H. J. Moon, M. A. Alfarsi, and S. Ivanovski, "Hydrophilic titanium surface-induced macrophage modulation promotes pro-osteogenic signalling," *Clinical Oral Implants Research*, vol. 30, no. 11, pp. 1085–1096, 2019.

[19] S. Bodhak, S. Bose, and A. Bandyopadhyay, "Role of surface charge and wettability on early stage mineralization and bone cell-materials interactions of polarized hydroxyapatite," *Acta Biomaterialia*, vol. 5, no. 6, pp. 2178–2188, 2009.

[20] R. A. Gittens, L. Scheideler, F. Rupp et al., "A review on the wettability of dental implant surfaces II: biological and clinical aspects," *Acta Biomaterialia*, vol. 10, no. 7, pp. 2907–2918, 2014.

[21] N. Donos, S. Hamlet, N. P. Lang et al., "Gene expression profile of osseointegration of a hydrophilic compared with a hydrophobic microrough implant surface," *Clinical Oral Implants Research*, vol. 22, no. 4, pp. 365–372, 2011.

[22] M. Roccuzzo and T. G. Wilson, "A prospective study evaluating a protocol for 6 weeks' loading of SLA implants in the posterior maxilla," *Clinical Oral Implants Research*, vol. 13, no. 5, pp. 502–507, 2002.

[23] F. Bezerra, M. R. Ferreira, G. N. Fontes et al., "Nano hydroxyapatite-blasted titanium surface affects pre-osteoblast morphology by modulating critical intracellular pathways," *Biotechnology and Bioengineering*, vol. 114, no. 8, pp. 1888–1898, 2017.

[24] P. P. Ming, S. Y. Shao, J. Qiu et al., "Superiority of calcium-containing nanowires modified titanium surface compared with SLA titanium surface in biological behavior of osteoblasts: a pilot study," *Applied Surface Science*, vol. 416, pp. 790–797, 2017.

[25] J. Shi, X. Zhang, S. Qiao et al., "Enhanced osteointegration of tantalum-modified titanium implants with micro/nano-topography," *RSC Advances*, vol. 7, no. 73, pp. 46472–46479, 2017.

[26] A. Uccelli, L. Moretta, and V. Pistoia, "Mesenchymal stem cells in health and disease," *Nature Reviews Immunology*, vol. 8, no. 9, pp. 726–736, 2008.

[27] M. F. Pittenger, A. M. Mackay, S. C. Beck et al., "Multilineage potential of adult human mesenchymal stem cells," *Science*, vol. 284, no. 5411, pp. 143–147, 1999.

[28] Z. Chen, A. Bachhuka, S. Han et al., "Tuning chemistry and topography of nanoengineered surfaces to manipulate immune response for bone regeneration applications," *ACS Nano*, vol. 11, no. 5, pp. 4494–4506, 2017.

[29] J. Carthew, H. H. Abdelmaksoud, M. Hodgson-Garms et al., "Precision surface microtopography regulates cell fate via changes to actomyosin contractility and nuclear architecture," *Advancement of Science*, vol. 8, no. 6, pp. 1–15, 2021.

[30] Y. Xie, J. Li, Z. M. Yu, and Q. Wei, "Nano modified SLA process for titanium implants," *Materials Letters*, vol. 186, pp. 38–41, 2017.

[31] J. Zhang, W. Zhou, H. Wang, K. Lin, and F. Chen, "3D-printed surface promoting osteogenic differentiation and angiogenetic factor expression of BMSCs on Ti6Al4V implants and early osseointegration *in vivo*," *Journal of Materials Science and Technology*, vol. 35, no. 2, pp. 336–343, 2019.

[32] J. Pizzicannella, F. Diomede, A. Gugliandolo et al., "3D printing PLA/gingival stem cells/EVs upregulate miR-2861 and -210 during osteoangiogenesis commitment," *International Journal of Molecular Sciences*, vol. 20, no. 13, p. 3256, 2019.

[33] H. S. Kim, Y. J. Kim, J. H. Jang, and J. W. Park, "Surface engineering of nanostructured titanium implants with bioactive ions," *Journal of Dental Research*, vol. 95, no. 5, pp. 558–565, 2016.

[34] W. Zhang, G. Wang, Y. Liu et al., "The synergistic effect of hierarchical micro/nano-topography and bioactive ions for enhanced osseointegration," *Biomaterials*, vol. 34, no. 13, pp. 3184–3195, 2013.

[35] P. Xiu, Z. Jia, J. Lv et al., "Tailored surface treatment of 3D printed porous Ti6Al4V by microarc oxidation for enhanced osseointegration via optimized bone in-growth patterns and interlocked bone/implant Interface," *ACS Applied Materials & Interfaces*, vol. 8, no. 28, pp. 17964–17975, 2016.

[36] E. M. Lotz, R. Olivares-Navarrete, S. Berner, B. D. Boyan, and Z. Schwartz, "Osteogenic response of human MSCs and osteoblasts to hydrophilic and hydrophobic nanostructured titanium implant surfaces," *Journal of Biomedical Materials Research Part A*, vol. 104, no. 12, pp. 3137–3148, 2016.

[37] B. S. Kopf, S. Ruch, S. Berner, N. D. Spencer, and K. Maniura-Weber, "The role of nanostructures and hydrophilicity in osseointegration: in-vitro protein-adsorption and blood-interaction studies," *Journal of Biomedical Materials Research Part A*, vol. 103, no. 8, pp. 2661–2672, 2015.

[38] A. Wennerberg, R. Jimbo, S. Stübinger, M. Obrecht, M. Dard, and S. Berner, "Nanostructures and hydrophilicity influence osseointegration: a biomechanical study in the rabbit tibia," *Clinical Oral Implants Research*, vol. 25, no. 9, pp. 1041–1050, 2014.

[39] Y. T. Sul, B. S. Kang, C. Johansson, H. S. Um, C. J. Park, and T. Albrektsson, "The roles of surface chemistry and topography in the strength and rate of osseointegration of titanium implants in bone," *Journal of Biomedical Materials Research Part A*, vol. 89A, no. 4, pp. 942–950, 2009.

[40] P. Silva-Bermudez, A. Almaguer-Flores, V. I. Garcia, R. Olivares-Navarrete, and S. E. Rodil, "Enhancing the osteoblastic differentiation through nanoscale surface modifications," *Journal of Biomedical Materials Research Part A*, vol. 105, no. 2, pp. 498–509, 2017.

[41] X. Yuan, Y. Kang, J. Zuo et al., "Micro/nano hierarchical structured titanium treated by NH4OH/H2O2 for enhancing cell response," *PLoS One*, vol. 13, no. 5, article e0196366, 2018.

[42] X. Jiang, Zhang, L. Yan et al., "Biofunctionalization of a titanium surface with a nano-sawtooth structure regulates the behavior of rat bone marrow mesenchymal stem cells," *International Journal of Nanomedicine*, vol. 7, pp. 4459–4472, 2012.

[43] J. Yang, L. E. McNamara, N. Gadegaard et al., "Nanotopographical induction of osteogenesis through adhesion, bone morphogenic protein cosignaling, and regulation of microRNAs," *ACS Nano*, vol. 8, no. 10, pp. 9941–9953, 2014.

[44] R. Peng, X. Yao, and J. Ding, "Effect of cell anisotropy on differentiation of stem cells on micropatterned surfaces through the controlled single cell adhesion," *Biomaterials*, vol. 32, no. 32, pp. 8048–8057, 2011.

[45] A. Henningsen, R. Smeets, P. Hartjen et al., "Photofunctionalization and non-thermal plasma activation of titanium surfaces," *Clinical Oral Investigations*, vol. 22, no. 2, pp. 1045–1054, 2018.

[46] M. Jayaraman, U. Meyer, M. Bühner, U. Joos, and H. P. Wiesmann, "Influence of titanium surfaces on attachment of osteoblast-like cells in vitro," *Biomaterials*, vol. 25, no. 4, pp. 625–631, 2004.

[47] B. L. Banik, T. R. Riley, C. J. Platt, and J. L. Brown, "Human mesenchymal stem cell morphology and migration on micro-textured titanium," *Frontiers in Bioengineering and Biotechnology*, vol. 4, pp. 1–9, 2016.

[48] A. Zareidoost, M. Yousefpour, B. Ghaseme, and A. Amanzadeh, "The relationship of surface roughness and cell response of chemical surface modification of titanium," *Journal of Materials Science. Materials in Medicine*, vol. 23, no. 6, pp. 1479–1488, 2012.

[49] X. Li, Q. Huang, T. A. Elkhooly et al., "Effects of titanium surface roughness on the mediation of osteogenesis via modulating the immune response of macrophages," *Biomedical Materials*, vol. 13, no. 4, p. 045013, 2018.

[50] S. C. Sartoretto, A. T. N. N. Alves, R. F. B. Resende, J. Calasans-Maia, J. M. Granjeiro, and M. D. Calasans-Maia, "Early osseointegration driven by the surface chemistry and wettability of dental implants," *Journal of Applied Oral Science*, vol. 23, no. 3, pp. 279–287, 2015.

[51] F. Diomede, M. D'Aurora, A. Gugliandolo et al., "Biofunctionalized scaffold in bone tissue repair," *International Journal of Molecular Sciences*, vol. 19, no. 4, pp. 1–17, 2018.

[52] M. B. Ariganello, D. Guadarrama Bello, A. Rodriguez-Contreras et al., "Surface nanocavitation of titanium modulates macrophage activity," *International Journal of Nanomedicine*, vol. Volume 13, pp. 8297–8308, 2018.

[53] K. Gulati, S. M. Hamlet, and S. Ivanovski, "Tailoring the immuno-responsiveness of anodized nano-engineered titanium implants," *Journal of Materials Chemistry B*, vol. 6, no. 18, pp. 2677–2689, 2018.

Hindawi
Oxidative Medicine and Cellular Longevity
Volume 2021, Article ID 3119953, 13 pages
https://doi.org/10.1155/2021/3119953

Research Article

Mangiferin Inhibits PDGF-BB-Induced Proliferation and Migration of Rat Vascular Smooth Muscle Cells and Alleviates Neointimal Formation in Mice through the AMPK/Drp1 Axis

Qi Wu,[1,2,3] Yuanyang Chen,[1,2,3] Zhiwei Wang,[1,3] Xin Cai,[1,3] Yanjia Che,[1,2,3] Sihao Zheng,[1,2,3] Shun Yuan,[1,2,3] and Xiaohan Zhong[1,2,3]

[1]*Department of Cardiovascular Surgery, Renmin Hospital of Wuhan University, Wuhan, China*
[2]*Cardiovascular Surgery Laboratory, Renmin Hospital of Wuhan University, Wuhan, China*
[3]*Central Laboratory, Renmin Hospital of Wuhan University, Wuhan, China*

Correspondence should be addressed to Zhiwei Wang; wangzhiwei@whu.edu.cn

Received 15 May 2021; Accepted 19 October 2021; Published 3 December 2021

Academic Editor: Andreas Daiber

Mangiferin is a naturally occurring xanthone C-glycoside that is widely found in various plants. Previous studies have reported that mangiferin inhibits tumor cell proliferation and migration. Excessive proliferation and migration of vascular smooth muscle cells (SMCs) is associated with neointimal hyperplasia in coronary arteries. However, the role and mechanism of mangiferin action in neointimal hyperplasia is still unknown. In this study, a mouse carotid artery ligation model was established, and primary rat smooth muscle cells were isolated and used for mechanistic assays. We found that mangiferin alleviated neointimal hyperplasia, inhibited proliferation and migration of SMCs, and promoted platelets derive growth factors-BB- (PDGF-BB-) induced contractile phenotype in SMCs. Moreover, mangiferin attenuated neointimal formation by inhibiting mitochondrial fission through the AMPK/Drp1 signaling pathway. These findings suggest that mangiferin has the potential to maintain vascular homeostasis and inhibit neointimal hyperplasia.

1. Introduction

Coronary artery disease (CAD) is a growing health burden worldwide [1]. Neointimal hyperplasia of the coronary arteries is the major pathophysiological change associated with CAD [2]. Several therapeutic procedures such as balloon angioplasty, rotational atherectomy, percutaneous coronary intervention, and coronary artery bypass grafting (CABG) are used in the treatment of CAD. However, the development of restenosis caused by mechanical injuries to the coronary arteries is the most common complication, which is associated with poor prognosis and decreased long-term survival of patients with CAD [3]. The transformation of the phenotype of SMCs plays an important role in neointimal formation [4]. Current therapeutic strategies against neointimal hyperplasia are not effective for patients with CAD. Therefore, there is urgent need to identify and develop novel therapeutic agents for the treatment of coronary artery restenosis.

Mitochondria are known to produce the majority of ATP necessary for normal cellular function [5]. Relevant studies have revealed that the mitochondria are highly dynamic organelles that continually undergo fission and fusion events in order to maintain their size, distribution, and shape [5]. This process is referred to as mitochondrial dynamics. Moreover, alternations in mitochondrial function greatly influence cell fate [6]. Recent evidence supports the correlation between mitochondrial dynamics and vascular disease [7]. Mfn1 and Mfn2 are proteins located in the outer membrane of the mitochondria that are mainly involved in mitochondrial fusion [8]. Inhibition of mitochondria fission by suppressing translation of Mfn1 induces senescence of SMCs in vessels [9]. Moreover, miR-93 promotes proliferation, migration, and neointimal information of SMCs by inhibiting Mfn2 expression [10]. Drp1 plays a central role in mitochondria fission. A decrease in phosphorylation of Drp1 at Ser 616 significantly inhibits the proliferation,

migration, and neointimal formation of SMCs [11]. Therefore, mitochondrial dynamics is critical for progression of neointimal hyperplasia.

AMP-activated protein kinase (AMPK) is extremely important in the regulation of energy metabolism in cells. It is a heterotrimeric complex consisting of a catalytic α-subunit and two regulatory subunits, β and γ [12]. Usually, AMPK is mainly activated by a decrease in ATP levels, with mitochondria being the main source of ATP [13]. Recent research findings revealed that AMPK is closely associated with mitochondrial dynamics and that AMPK facilitates mitochondrial fusion by regulating proteins involved in mitochondrial dynamics [14]. This indicates that AMPK is a promising regulator of mitochondrial function.

Mangiferin was first extracted from a mango tree and is mainly composed of polyphenolic C-glucosyl-xanthone. Mangiferin has previously been shown to have antioxidant, anti-inflammatory, and antitumor activities [15–18]. It has also been associated with the progression of various diseases by modulating mitochondrial function [19–21]. Intriguingly, mangiferin was also identified as a potent AMPK activator [22]. Treatment with magniferin resulted in enhanced mitochondrial bioenergetics, increased mitochondrial membrane potential, inhibition of caspase-3 activation, and downregulation of cytochrome C leakage [22]. Accordingly, the involvement of mangiferin in the regulation of mitochondrial function via the activated AMPK signal pathway was shown. However, there are very few reports on the role of magniferin in the regulation of mitochondrial dynamics in SMCs and the maintenance of the normal structure and function of mitochondria in vessels. Since there are a high number of patients with CAD, there is a need to determine the specific mechanism by which mangiferin attenuates neointimal formation.

In this study, we demonstrated that mangiferin protects the arteries against neointima hyperplasia. Mangiferin exerted this effect by decreasing the phosphorylation of Drp1 at Ser-616 and promoting mitochondrial fusion through AMPK activation. In line with this finding, we found that the inhibition of AMPK by compound C (CC) reversed the mangiferin-induced inhibition of neointima hyperplasia. Thus, the positive effect of mangiferin is AMPK/Drp1 dependent. These findings indicate for the first time that mangiferin attenuates neointimal hyperplasia through the AMPK/Drp1 axis and that mangiferin is a potential natural compound for the treatment of restenosis artery disease.

2. Materials and Methods

2.1. Compounds and Reagents. Mangiferin was purchased from Yuanye Bio-Technology Co., Ltd. (Shanghai, China) and dissolved in DMSO. TRIzol was obtained from Yeasen Biotech Co., Ltd. (Shanghai, China). The First-Strand cDNA Synthesis Kit and SYBR Green qPCR Master Mix were purchased from Servicebio Biotech Co., Ltd. (Wuhan, China). MitoTracker Red CM-H2XRos was purchased from Yeasen Biotech Co., Ltd. (Shanghai, China), while compound C (CC) was purchased from MedChemExpress (New Jersey, USA). The Anti-AMPK, Anti-Phospho-AMPKα (Thr172), Anti-Drp1, and Anti-Phospho-DRP1 (Ser616) antibodies were obtained from Affinity Biosciences LTD (New Jersey, USA), while Anti-MMP2, Anti-SM22α, Anti-α-SMA, Anti-PCNA, Anti-CNN1, and Anti-β-Actin were purchased from Servicebio Biotech Co., Ltd. (Wuhan, China). Anti-Mfn1, Anti-Mfn2, Anti-Fis1, and Anti-OPA1 antibodies were purchased from Beyotime Biotechnology Co., Ltd. (Shanghai, China).

2.2. Isolation and Identification of Primary Rat Aortic Smooth Muscle Cells. The animal protocols used in this study were approved by the Animal Research Ethics Committee of Wuhan University. The rats were obtained from Hubei province center for disease control and prevention and weighed between 130 g and approximately 150 g. Pentobarbitone was used to anesthetize the rats, followed by isolation of the aortic arteries under sterile conditions. Fresh isolated aortas were irrigated thrice with PBS, stripping adventitia and intima in PBS with microinstruments. The aorta tissues were then cut into pieces of 2 mm^2, attached to 60 mm cell culture dishes, and incubated for 30 minutes. Thereafter, fresh DMEM/F12 medium supplemented with 20% FBS and 1% penicillin streptomycin solution was added, and floating aorta tissues were removed. The medium was replaced three days later. The tissues were incubated until SMCs crawled out of the aorta tissue to form a monolayer (the cell confluency was 50%) on the dish. The aorta tissues were then removed, the cells washed thrice with PBS and digested with 0.5% pancreatin. Digestion was terminated by adding the growth medium. The SMCs were collected and planted in 60 mm dish. Primary rat aortic smooth muscle cells in the third passage were used in this study.

2.3. RT-PCR. 100 ng total RNA was reverse transcribed to cDNA and used for RT-PCR. RT-PCR was carried out as previously described [23] to detect the mRNA expression levels of PCNA and MMP2. The PCR primer sequences used in this study are shown in Table 1.

2.4. Western Blot. For western blot, 20 μg total protein was loaded into each lane of SDS-PAGE gels. The specific protocol has been previously described [23]. The anti-mouse IgG (H+L) (DyLight™ 800 4x PEG Conjugate) and anti-rabbit IgG (H+L) (DyLight™ 800 4x PEG Conjugate) secondary antibodies were obtained from Cell Signaling Technology (Boston, US). All the bands were visualized using Odessy fluorescence imaging system (Li-Cor). The primary antibodies and their dilutions as used in this study are shown in Table 2.

2.5. Cell Migration Assay. Transwell chambers (8 mm pore size; Corning) were used to analyze the migration ability of the SMCs. Briefly, SMCs were serum starved for 24 h, and then, 1×10^4 SMCs were seeded in the upper chambers with or without mangiferin. DMEM/F12 medium supplemented with 10% FBS with or without PDGF-BB was added to the lower chamber. The cells were incubated at 37°C for 9 hours in a CO_2 incubator. Thereafter, the medium was removed and the cells washed thrice with PBS. The upper chambers were then fixed with 4% paraformaldehyde for 15 minutes at room temperature. SMCs in the upper layer were gently wiped off using a cotton swab. The fixed cells were stained

Table 1: qRT-PCR primer sequences.

Gene	Primer sequence
PCNA	Forward primer, 5′-TCCGAAGGCTTCGACACATAC-3′
	Reverse, 5′-GGACATGCTGGTGAGGTTCA-3′
MMP2	Forward, 5′-ACCTTGACCAGAACACCATCGAG-3′
	Reverse, 5′-CAGGGTCCAGGTCAGGTGTGTA-3′

Table 2: Primary antibody information and dilution in this research.

Antibody	Company	Catalog	Dilution		
			WB	IHC	IF
MMP2	Servicebio	GB11130	1 : 1000	1 : 200	—
PCNA	Servicebio	GB11010	1 : 2000	1 : 300	—
ACTB	Servicebio	GB11001	1 : 3000	—	—
α-SMA	Servicebio	GB111364	1 : 1000	1 : 500	1 : 200
SM22α	Servicebio	GB11366	1 : 1000	—	1 : 100
CNN1	Servicebio	GB11954	1 : 1000	—	1 : 500
MFN1	Beyotime	AF7461	1 : 1000	—	—
MFN2	Beyotime	AF7473	1 : 1000	—	—
OPA1	Beyotime	AF7653	1 : 1000	—	—
Fis1	Beyotime	AF8268	1 : 1000	—	—
Drp1	Beyotime	AF6735	1 : 1000	—	—
Drp1 ser616	Affinity	AF8470	1 : 1000	1 : 100	—
AMPK	CST	#2532	1 : 1000	—	—
P-AMPK	CST	#2535	1 : 1000	—	—

using 0.2% crystal violet stain for 20 minutes at room temperature, and the excess crystal violet washed with water. Cells were photographed under a microscope, and ImageJ was used to quantify the number of cells in different fields of view.

2.6. Flow Cytometry. RSMCs were seeded in 60 mm cell culture dishes and starved for 24 hours for synchronization. The cells were then pretreated with mangiferin for 6 hours and then treated with 20 ng/ml PDGF-BB for 24 hours. Thereafter, RSMCs were collected using trypsin digestion. Dihydroethidium (DHE) at final concentration of 10 μM was used to label the ROS in RSMCs for 60 min at 37°C, followed by detection using flow cytometry (excitation wavelength 488 nm, emission wavelength 575 nm).

2.7. Animal. Animal experiments were designed strictly in accordance with the Care and Use of Laboratory Animals published by the National Institutes of Health and approved by the ethical committee of the Renmin Hospital of Wuhan University (approval no.: WDRM20201107). Animals were obtained from Hubei provincial Center for Disease Control and Prevention, fed a standard diet and had free access to water. Mice were maintained in 12 hour light/dark cycles at 22°C.

Carotid ligations were performed in 12-week-old male C57BL/6J mice. Briefly, mice were first anesthetized using sodium pentobarbital. A middle neck incision was made, followed by the exposure and separation of the left common carotid artery, which was then ligated with 6-0 silk. Twelve C57BL/6J mice were divided randomly into two groups. Before ligation, one group was administered with intraperitoneal injections of mangiferin, while the other group was administered with intraperitoneal injections of corn oil for one week. After surgery, mangiferin was administered once daily for four weeks. Thereafter, the mice were anesthetized using pentobarbital sodium, followed by harvesting of the left common carotid arteries. The right common carotid arteries were also harvested and served as the controls. Finally, mice were sacrificed using high doses of pentobarbital sodium.

2.8. Histopathology Analysis. The right and left carotid arteries were collected and washed with precooled saline to remove excess blood. All collected tissues were fixed using 4% paraformaldehyde solution for 24 hours. The samples were then dehydrated in gradient concentration of alcohol and transparency with xylene, embedded in paraffin, and sectioned. Afterwards, the sections were dewaxed using xylene and hydrated in gradient alcohol. The size of intima and media was determined by staining the sections using Elastica Van Gieson (EVG) staining solution.

2.9. Immunofluorescence. Cells were cultured at a density of 1×10^5 cells per well in six-well plates containing a cover slip. After 24 hours, RSMCs were serum starved for 24 hours for synchronization. The RSMCs were then pretreated with mangiferin or equal volumes of dimethyl sulfoxide (DMSO), followed by treatment with or without 20 ng/ml PDGF-BB for 24 hours. Thereafter, the RSMCs were washed with PBS to remove excess culture medium and fixed with 4% paraformaldehyde for 15 minutes. The RSMCs were permeabilized using 0.2% Triton solution and blocked with goat serum for 60 minutes. The cells were then incubated in primary antibody at 4°C overnight, followed by incubation in Cy3 labeled secondary antibody for 1 hour at room temperature, and finally observed under a fluorescence microscope.

2.10. Mitochondrial Staining. Cells were seeded in six-well plates at a density of 1×10^5 cells per well. The cells were then treated, and thereafter, the media was removed, and the cells were stained with MitoTracker Red CM-H2XRos at a final concentration of 125 nM for 30 minutes at 37°C (excitation wavelength 579 nm, emission wavelength 599 nm). Afterwards, the staining solution was discarded, and the RSMCs washed with PBS thrice. Finally, the cells were observed under

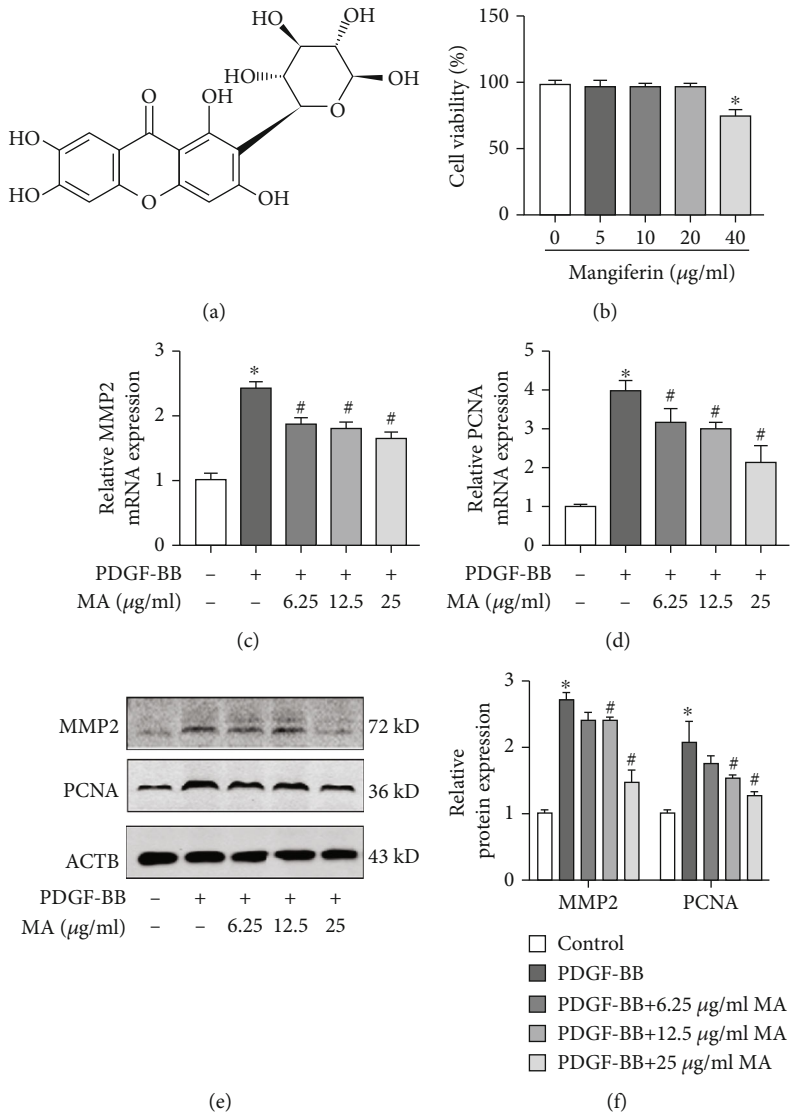

Figure 1: Mangiferin inhibited PDGF-induced proliferation and migration of RSMCs. (a) Chemical structure of mangiferin. (b) The viability of RSMCs was determined using CCK-8 assay after treatment with different concentrations of mangiferin for 24 hours. (c, d) The mRNA expression levels of PCNA and MMP2 as measured using RT-PCR. (e, f) The protein expression levels of PCNA and MMP2 as determined using western blot. All assays were conducted in triplicates and data presented as mean ± S.D. $^{*}P < 0.05$, compared with the control group. $^{\#}P < 0.05$, compared with the PDGF-BB group.

a fluorescence microscope and ImageJ software was used to analyze mitochondrial morphology.

2.11. Statistical Analysis. All the assays in this study were carried out in triplicates, and the data were expressed as mean ± SD. Unpaired *t*-test or Mann–Whitney *U* tests were used to compare the means between two groups, while one-way ANOVA was used to compare the means among three or more groups. A $P < 0.05$ was considered to be statistically significance. GraphPad Prism 7.0 was used for statistical analysis.

3. Result

3.1. Mangiferin Inhibited PDGF-BB-Induced Proliferation and Migration of RSMCs. The chemical structure of mangiferin is shown in Figure 1(a). The effect of mangiferin on cell viability was determined using the CCK-8 assay, with the results showing that 50 μg/ml mangiferin significantly inhibited the survival of RSMCs. However, mangiferin at concentrations between 6.25 and approximately 25 μg/ml did not affect cell survival (Figure 1(b)). Consequently, concentrations of mangiferin below 25 μg/ml were not used in subsequent assays. Cell proliferation and migration have been implicated in the pathophysiology of artery restenosis [24]. Mangiferin decreased the PDGF-BB-induced expression of MMP2, which is associated with cell migration (Figure 1(c)). In addition, magniferin decreased the mRNA levels of PCNA, which is associated with cell proliferation capacity (Figure 1(d)). The results of western blot were consistent with the results of qPCR (Figures 1(e) and 1(f)). The results of Transwell migration

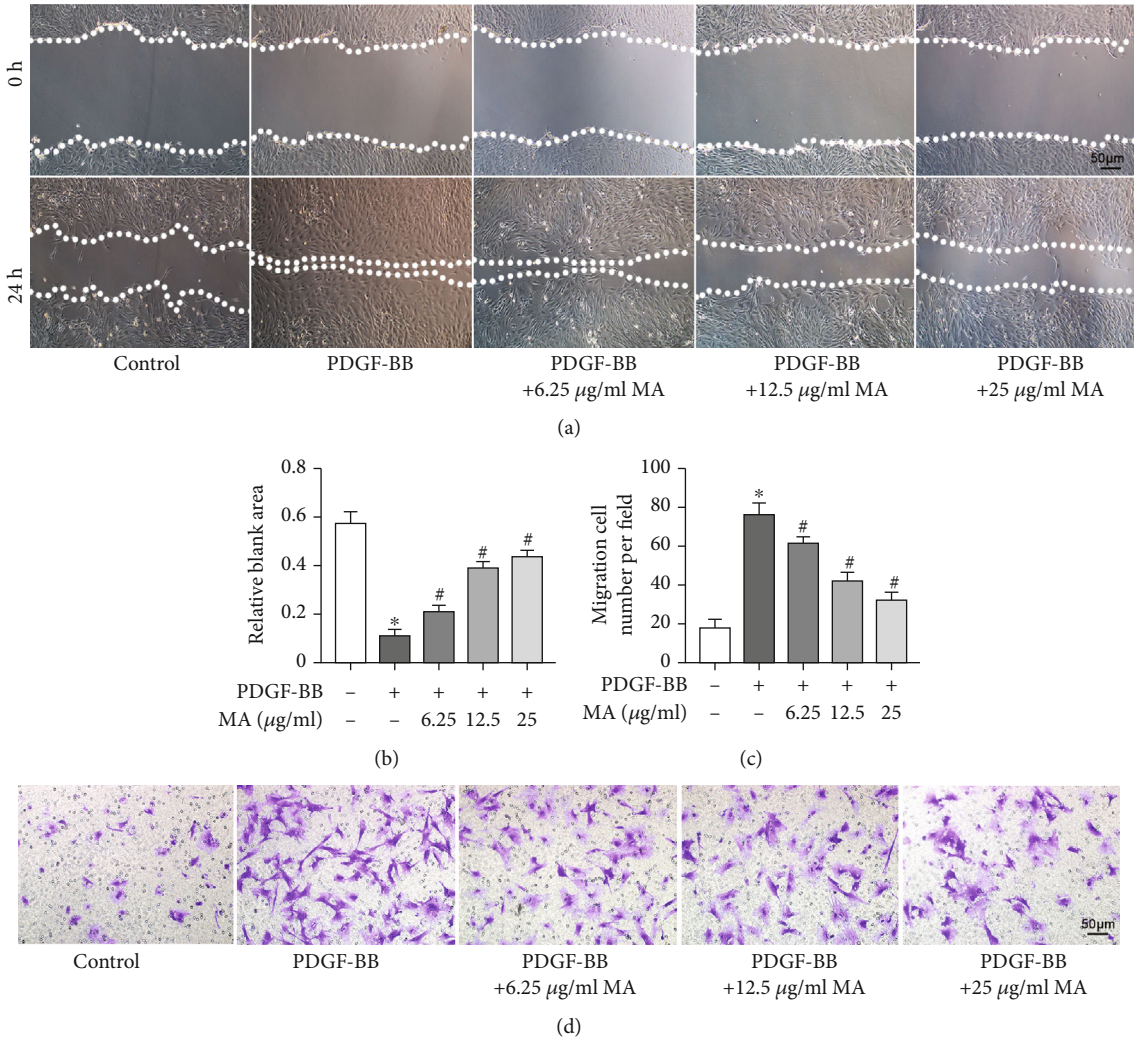

Figure 2: Mangiferin inhibited the PDGF-BB-induced proliferation and migration of RSMCs. (a, b) The migration ability of RSMCs was evaluated using the scratch assay after treatment with various concentrations of mangiferin with or without 20 ng/ml PDGF-BB for 24 hours. (c, d) The migration ability of RSMCs was assessed using Transwell assay after treatment with different concentrations of mangiferin with or without 20 ng/ml PDGF-BB for 24 hours. All assays were conducted in triplicates and data presented as mean ± S.D. $^{*}P < 0.05$, compared with the control group. $^{\#}P < 0.05$, compared with the PDGF-BB group.

assay and scratch assay indicated that mangiferin significantly inhibited PDGF-BB-induced migration of RSMCs (Figures 2(a)–2(d)).

3.2. Mangiferin Inhibits PDGF-BB-Induced Dedifferentiation of RSMCs. Phenotypic transformation is a common event in the pathophysiology of vascular disease [25].α-SMA, SM22α, and CNN1 are the markers of the contractile SMCs. To investigate the effect of mangiferin on changes in RSMCs phenotype, we detected the protein expression levels of α-SMA, SM22α, and CNN1 using western blot. PDGF-BB induced a significant decrease in the expression levels of α-SMA, SM22α, and CNN1, but mangiferin was able to reverse this effect in a dose-dependent manner (Figures 3(a)–3(d)). The results of immunofluorescence were consistent with those of western blot (Figure 3(e)).

3.3. Mangiferin Alleviated PDGF-BB-Induced Mitochondrial Fission and Increase in ROS Levels. Mitochondrial fission and fusion are closely associated with neointimal formation and the functional status of RSMCs [26]. Findings from a previous study indicated that PDGF-BB stimulated the proliferation of RSMCs partly by promoting mitochondrial fission. Staining of mitochondrial RSMCs with mitotracker staining solution demonstrated that PDGF-BB promoted mitochondrial fission and mangiferin partly reversed this effect (Figure 4(a)). Reactive oxygen species (ROS) are mainly produced during oxidative phosphorylation in the mitochondria and are closely associated with mitochondrial function. Results of flow cytometry showed that mangiferin significantly decreased PDGF-BB-induced production of ROS, further indicating its role in modulating mitochondrial function (Figure 4(b)). Mitochondrial dynamics are highly associated with the expression of mitochondrial fusion-

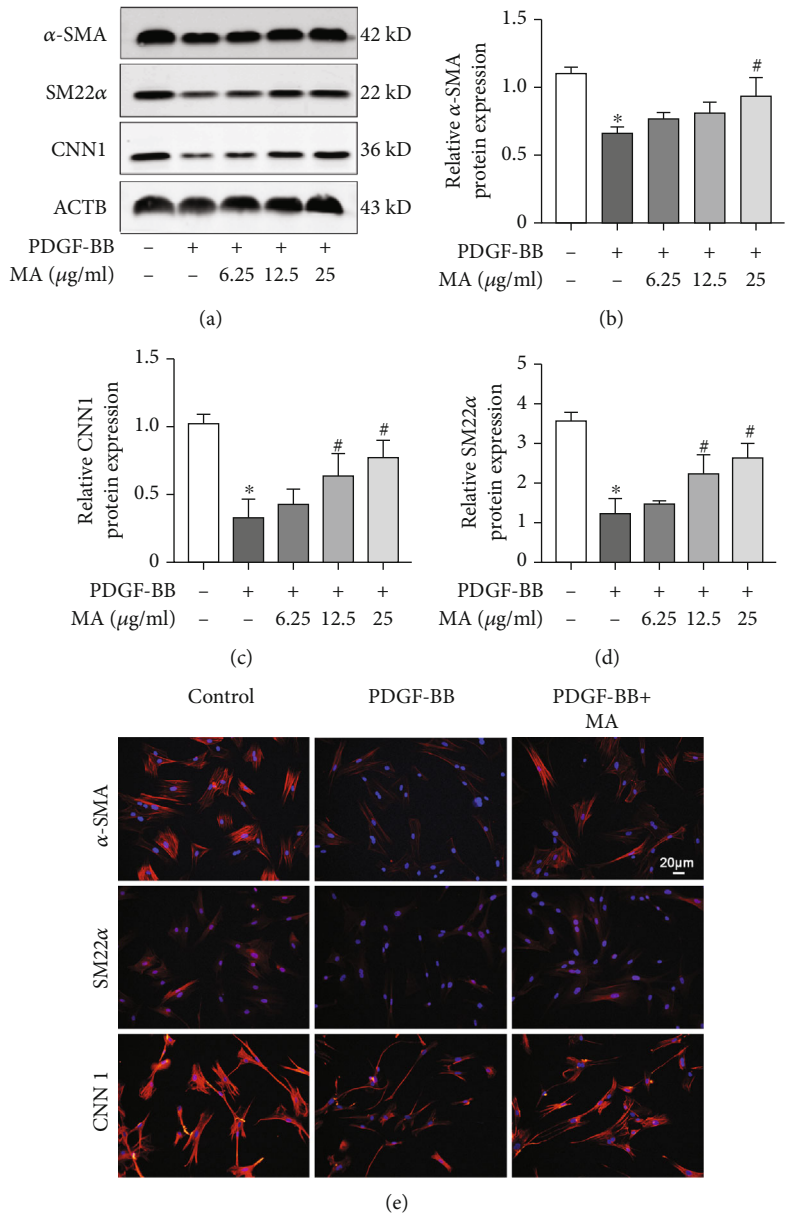

Figure 3: Mangiferin inhibited PDGF-BB-induced dedifferentiation of RSMCs. (a–d) The protein expression levels of α-SMA, SM22α, and CNN1 were detected using western blot after RSMCs were treated with different concentrations of mangiferin with or without 20 ng/ml PDGF-BB for 24 hours. (e) The expression levels of α-SMA, SM22α, and CNN1 were determined using immunofluorescence after RSMCs were treated with mangiferin with or without 20 ng/ml PDGF-BB for 24 hours. All assays were conducted in triplicates and all data presented as mean ± S.D. $^{*}P < 0.05$, compared with the control group. $^{\#}P < 0.05$, compared with the PDGF-BB group.

fission-related proteins and AMPK phosphorylation. We therefore evaluated the expression of mitochondrial fusion-fission-related proteins after treatment with or without PDGF-BB and mangiferin using western blot. PDGF-BB dramatically promoted the phosphorylation of Drp1 at Ser-616 (Figures 4(c) and 4(d)), while mangiferin partly reversed this effect in a dose-dependent manner. In addition, mangiferin also increased the expression of AMPK at Thr172 (Figures 4(c) and 4(e)). Moreover, treatment with PDGF-BB significantly decreased the expression of Mfn2 but did not significantly alter the protein levels of Mfn1, OPA1, and Fis1. However, mangiferin failed to reverse this effect.

3.4. Mangiferin Significantly Suppressed PDGF-BB-Induced RSMC Phenotype Transformation through the AMPK/Drp1 Axis. Mitochondria are the main organelles involved in energy metabolism, while AMPK plays a vital role in monitoring the energy metabolism status of cells and mitochondria [14, 27]. A previous study reported that mangiferin activates the AMPK signaling pathway [28]. This was consistent with findings from our study which showed that mangiferin increased AMPK phosphorylation in RSMCs treated with PDGF-BB. To investigate the underlying mechanism, activation of AMPK was inhibited using compound C (CC), which is a specific inhibitor of AMPK [29]. This eliminated the mangiferin-induced

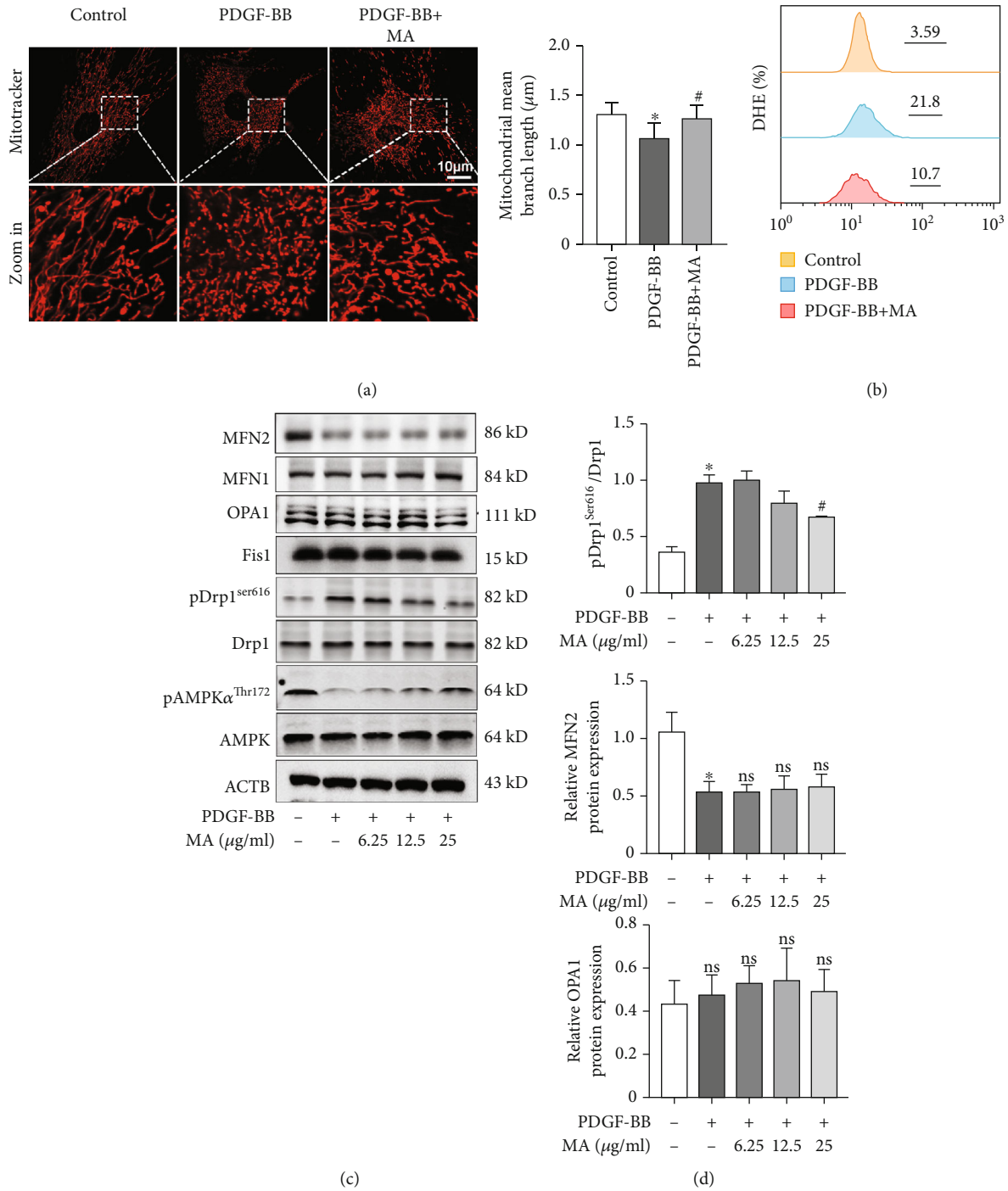

Figure 4: Continued.

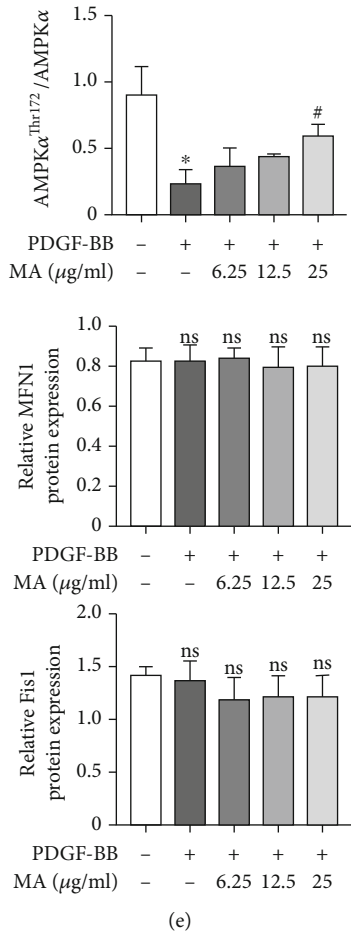

(e)

Figure 4: Mangiferin alleviated PDGF-BB-induced mitochondrial fission and increase in ROS levels. (a) RSMCs were stained with mitotracker probe after treatment with different concentrations of mangiferin with or without 20 ng/ml PDGF-BB for 24 hours. The average length of mitochondria was quantified using ImageJ software. (b) Intracellular ROS levels were detected using flow cytometry after RSMCs were treated with mangiferin with or without 20 ng/ml PDGF-BB for 24 hours. (c–e) Western blot was used to measure the protein expression levels of AMPK, pAMPKThr172, Drp1, and pDrp1Ser616 after RSMCs were treated with various concentrations of mangiferin with or without 20 ng/ml PDGF-BB for 24 hours. All assays were conducted in triplicate and all data presented as mean ± S. D. $^{*}P < 0.05$, compared with the control group. $^{\#}P < 0.05$, compared with the PDGF-BB group.

inhibition of mitochondrial fission (Figures 5(a) and 5(b)). In addition, CC significantly downregulated the phosphorylation of Drp1 at Ser-616 after treatment with mangiferin (Figures 5(c) and 5(d)). Therefore, the inhibition of PDGF-BB-induced RSMC proliferation, migration, and phenotype change by mangiferin may be mediated through the AMPK/Drp1 signaling pathway.

3.5. Mangiferin Attenuated Neointimal Formation In Vivo. To further verify the effect of mangiferin on neointimal hyperplasia, the mouse carotid artery ligation model was established. EVG staining was used to measure the size of the intima and media of carotid artery (Figure 6(a)). In this mouse model, our results showed that mangiferin dramatically decreased the ratio of intima/media compared with the ligation group (Figure 6(b)). Moreover, mangiferin decreased p-Drp1ser-616 expression and inhibited neointimal formation. In addition, there was downregulation of PCNA and MMP2, as well as upregulation of α-SMA in mice treated with mangiferin compared to the ligation group (Figures 6(c) and 6(d)). These results indicated that mangiferin inhibited neointimal hyperplasia by modulating the AMPK/Drp1 signaling pathway.

4. Discussion

Mangiferin is a natural compound with multiple positive effects on various diseases [30]. Our results indicate that mangiferin reverses the PDGF-BB-induced proliferation, migration, and phenotype change of RSMCs. In addition, mangiferin inhibited PDGF-BB-induced upregulation of Drp1 expression in RSMCs and induced phosphorylation of AMPK. Since AMPK has been shown to modulate mitochondrial dynamics, we postulated that mangiferin prevents neointimal hyperplaisa by modulating the AMPK/Drp1 signaling pathway. As expected, treatment with PDGF-BB and mangiferin inhibited the activation of AMPK in RSMCs and induced pDrp1Ser616 upregulation. Moreover, mangiferin significantly inhibited neointimal hyperplasia in the mouse carotid artery ligation model. Overall, our data strongly suggested that mangiferin inhibited neointimal

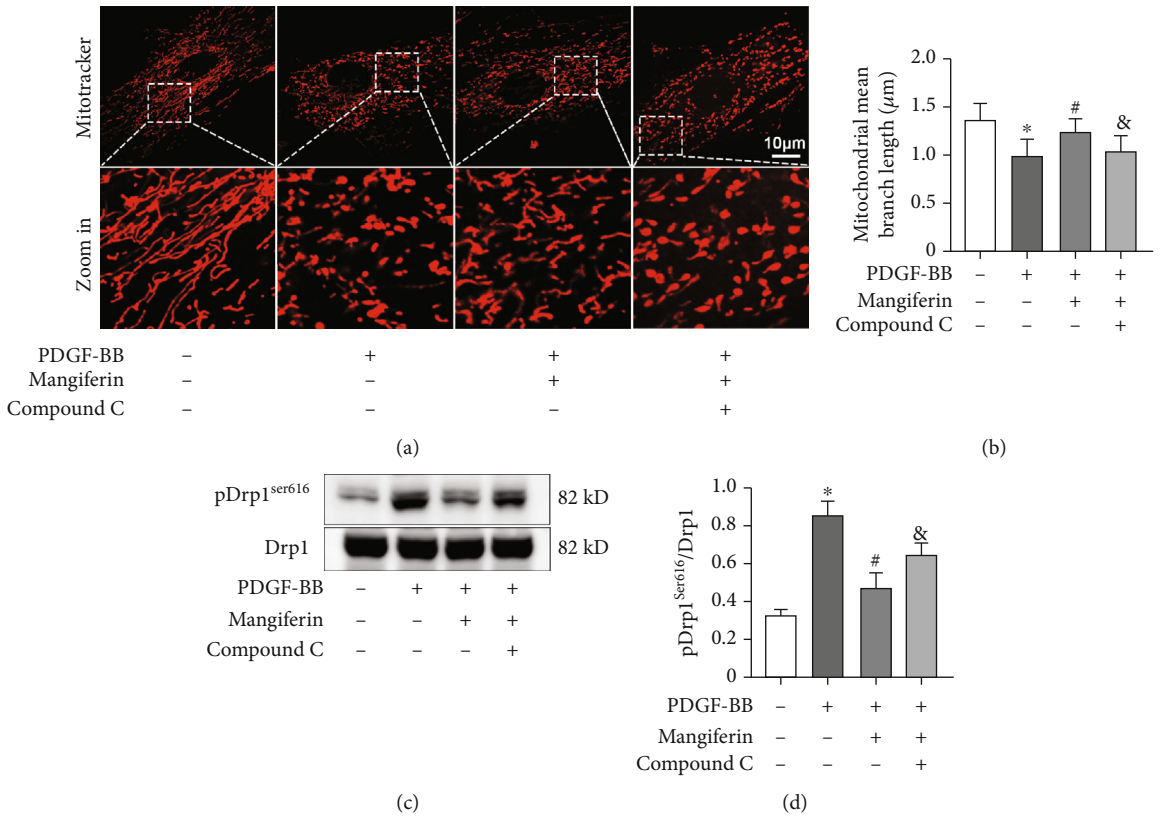

Figure 5: Mangiferin significantly suppressed PDGF-BB-induced RSMC phenotype transformation through the AMPK/Drp1 axis. (a, b) AMPK inhibitor, compound C, reverses the inhibitory effects of mangiferin on PDGF-BB-induced mitchondrial fission. (c, d) The protein expression levels of Drp1, and pDrp1^{Ser616} was determined using western blot after RSMCs were treated with or without PDGF-BB, mangiferin, and compound C.

formation in vitro and in vivo through the AMPK/Drp1 signaling pathway.

AMPK plays a vital role in modulating cellular energy balance and is activated when the ratio of AMP/ATP or ADP/ATP increases. It is well established that AMPK has potent anti-inflammatory, antioxidant, and antitumor effects [31, 32]. Several studies have demonstrated that AMPK plays a protective role in various vascular diseases [33, 34]. Mangiferin has been reported to regulate hepatic lipid metabolism via AMPK activation [35]. Therefore, we postulated that mangiferin reversed PDGF-BB-induced effects on RSMCs by activating AMPK. Metformin modulates SMC phenotype transformation by activating AMPK, thus inhibiting intracranial aneurysm progression [36]. In our study, we found that mangiferin indeed induced AMPK phosphorylation in RSMCs treated with PDGF-BB possibly through multiple mechanisms and that AMPK plays a central role in the modulation of RSMC function by mangiferin. On the one hand, mangiferin has been shown to promote glycolysis and increase the production of alpha-ketoglutarate, thus promoting AMPK phosphorylation [19]. On the other hand, ROS, which is mainly produced during mitochondrial oxidative phosphorylation, also plays a vital role in normal physiological processes [37]. However, excessive ROS accumulation also leads to mitochondrial dysfunction [38]. In this study, we found that PDGF-BB promoted generation and accumulation of ROS in RSMCs. The accumulation of ROS inhibited oxidative phosphorylation leading to decreased production of ATP, increased ADP/ATP or AMP/ATP ratio, which in turn activated the AMPK signaling pathway.

Mitochondrial dynamics plays a significant role in modulating neointimal formation, and Fis1, Drp1, OPA1, Mfn1, and Mfn2 have been closely associated with mitochondrial fission and fusion [39]. Preventing mitochondrial fission can inhibit neointimal hyperplasia as well as the proliferation and migration of SMCs [11]. PDGF-BB stimulated mitochondrial fission by increasing expression of pDrp1 (Ser616) in SMCs [40]. In our study, we found that mangiferin decreased the protein levels of pDrp1 (Ser616) in RSMCs. Drp1 is mainly located in cytoplasm, but phosphorylation at serine 616 promotes it recruitment to the outer-membrane of mitochondria and accelerates mitochondrial fission. In contrast, phosphorylation of Drp1 at serine 637 has opposite effects. In this study, mangiferin downregulated the phosphorylation of Drp1 at serine 616. ROS plays a dual role in the modulation of physiological functions of the cell. Moderate levels of ROS promote proliferation, migration, and dedifferentiation of SMCs, while high levels of ROS impair mitochondrial function, leading to a decrease in ATP synthesis, and inducing cell apoptosis [41].

Drp1 activity is strictly regulated by AMPK in SMCs, and different roles of AMPK in modulating Drp1 have been illustrated [42–44]. The activation of AMPK alleviated lead-induced phosphorylation of Drp1 (Ser616) [45]. However,

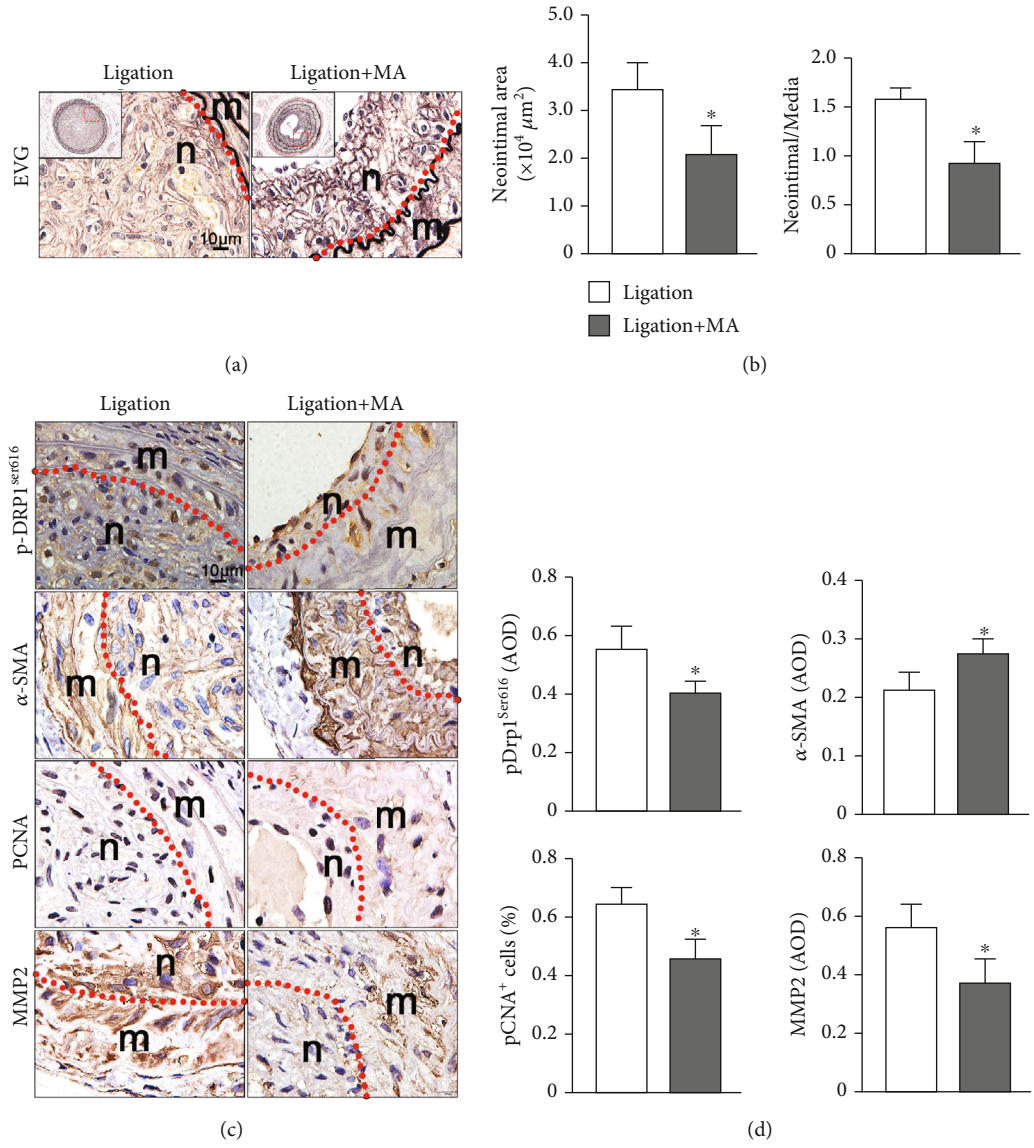

Figure 6: Mangiferin attenuated neointimal formation in vivo. (a) Intimal area and the ratio of neointima/media were measured after carotid ligation treated with or without mangiferin ($n = 6$). (b) pDrp1Ser616, α-SMA, PCNA, and MMP2 expression levels were detected using immunohistochemistry in ligated carotid arteries treated with or without mangiferin. All data were presented as mean ± S.D. $^{*}P < 0.05$, compared with the control group. $^{\#}P < 0.05$, compared with the PDGF-BB group.

another study reported that the activation of AMPK induced mitochondrial biogenesis by increasing phoshorylation of Drp1 (Ser616) to attenuate carbon tetrachloride-induced liver fibrosis in rats [46]. Several factors may account for these inconsistencies. Mitochondrial fission accelerates the rates of oxidative phosphorylation to some extent, thus increasing the levels of ATP in vitro or in vivo [44]. Since AMPK acts as an energy sensor in cells, it may promote mitochondrial fission by inducing Drp1 phosphorylation at serine 616 when ATP levels decline in vivo or in vitro. However, excessive mitochondrial fission leads to mitochondrial fragmentation, which triggers mitochondrial autophagy caused by mitochondrial dysfunction. Ultimately, the production of ATP is reduced, the AMPK signaling pathway is activated; AMPK downregulated Drp1 and contributed to mitochondrial fusion, restored mitochondrial function, and accelerated ATP production [47]. In our study, inhibition of AMPK activation by CC significantly decreased the phosphorylation of Drp1 at serine 616 and enhanced mitochondrial division in RSMCs. Taken together, mangiferin inhibited the proliferation, migration, and dedifferentiation of RSMCs mainly through the AMPK/Drp1 signaling pathway, ultimately attenuating neointimal formation.

There are limitations to our study. All assays were only repeated three times, yet repeating them five times would have increased the reliability of the results. Since several proteins are involved in modulating mitochondrial fusion and fission, there may be multiple mechanisms involved in the inhibition of neointimal formation by mangiferin other than our proposed mechanism. Therefore, there is need to explore

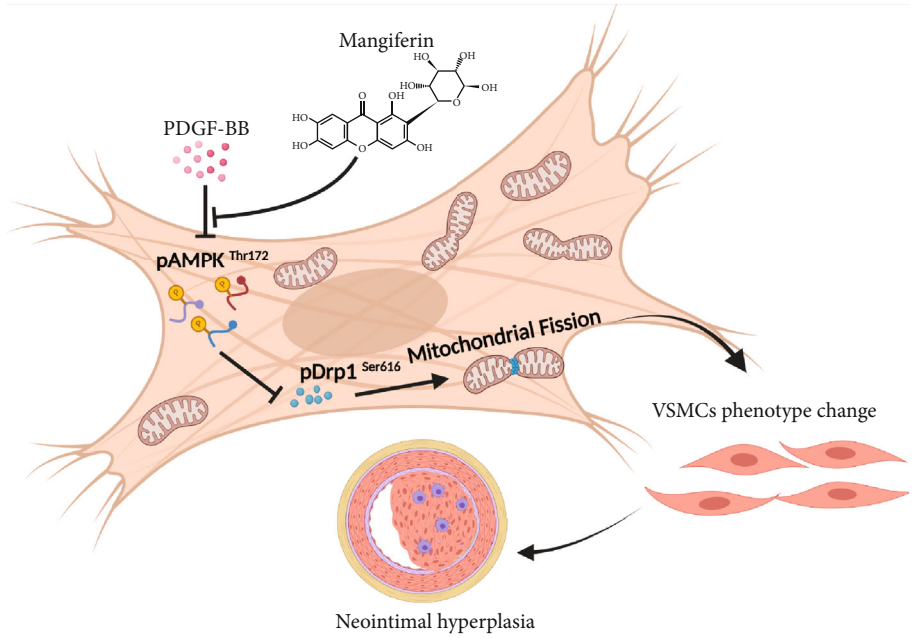

FIGURE 7: Diagram of mangiferin restraining neointimal hyperplasia. In the normal condition, VSMCs maintain contraction type, which are crucial for maintaining the physiology function of the coronary artery. PDGF-BB potent induces cell proliferation, migration, and phenotype change of VSMCs during neointimal hyperplasia. In this study, PDGF-BB inhibited AMPK phosphorylation activation at Thr 172, Drp1 was phosphorylation activated at Ser616, and then, Drp1 recruits to mitochondria accelerating mitochondrial fission, subsequently, VSMCs in coronary artery transform from contraction type to synthesis type, ultimately, contributing to the neointimal formation. However, we found that mangiferin effectively reversed the effect of PDGF-BB-induced neointimal formation.

possible alternative mechanisms. Moreover, in this study, 10 μM DHE were used to detect the ROS levels in RSMCs, the high concentrations of DHE could cause cellular membrane depolarization, this might have leaded to slightly bias in the current data, and improvement will be made in our next work.

In summary, mangiferin significantly inhibited neointimal hyperplasia induced by mouse carotid ligation by inhibiting proliferation, migration, and dedifferentiation of RSMCs. Mangiferin also inhibited PDGF-BB-induced mitochondrial fission, increased the phosphoration levels of AMPK, and significantly downregulated Drp1. Meanwhile, Drp1 is tightly modulated by AMPK. Mechanistically, AMPK inhibition reversed the mangiferin-induced positive effects on RSMCs and blocked the mangiferin-induced downregulation of Drp1 phosphorylation at serine 616; the specific mechanism is presented in Figure 7. Our results indicate that AMPK acts upstream of Drp1, inhibits Drp1 recruitment to the mitochondrial, and inhibits mitochondrial division. Taken together, mangiferin significantly ameliorated neointimal hyperplasia by modulating the AMPK/Drp1 signaling pathway.

Data Availability

The data used to support the findings of this study are available from the corresponding author upon request.

Conflicts of Interest

The authors declare that they have no conflicts of interest.

Authors' Contributions

Qi Wu, Yuanyang Chen, and Xin Cai contributed equally to this work.

Acknowledgments

This work was supported by the National Natural Science Foundation of China (Grant No. 82070481) and Nature Science Foundation of Hubei Province (Grant No. 2019CFB469).

References

[1] J. A. Jolliffe, K. Rees, R. S. Taylor, D. Thompson, N. Oldridge, and S. Ebrahim, "Exercise-based rehabilitation for coronary heart disease," *Cochrane Database of Systematic Reviews*, vol. 4, article D1800, 2001.

[2] M. A. Zain, R. T. Jamil, and W. J. Siddiqui, *Neointimal Hyperplasia*, StatPearls Publishing, 2021.

[3] W. S. Weintraub, "The pathophysiology and burden of restenosis," *American Journal of Cardiology*, vol. 100, no. 5, pp. S3–S9, 2007.

[4] W. Wu, W. Zhang, M. Choi et al., "Vascular smooth muscle-MAPK14 is required for neointimal hyperplasia by suppressing VSMC differentiation and inducing proliferation and inflammation," *Redox Biology*, vol. 22, article 101137, 2019.

[5] A. J. Roger, S. A. Munoz-Gomez, and R. Kamikawa, "The origin and diversification of mitochondria," *Current Biology*, vol. 27, no. 21, pp. R1177–R1192, 2017.

[6] K. Ma, G. Chen, W. Li, O. Kepp, Y. Zhu, and Q. Chen, "Mitophagy, mitochondrial homeostasis, and cell fate," *Frontiers in Cell and Development Biology*, vol. 8, p. 467, 2020.

[7] P. Dromparis and E. D. Michelakis, "Mitochondria in vascular health and disease," *Annual Review of Physiology*, vol. 75, no. 1, pp. 95–126, 2013.

[8] H. Chen, S. A. Detmer, A. J. Ewald, E. E. Griffin, S. E. Fraser, and D. C. Chan, "Mitofusins Mfn1 and Mfn2 coordinately regulate mitochondrial fusion and are essential for embryonic development," *Journal of Cell Biology*, vol. 160, no. 2, pp. 189–200, 2003.

[9] D. Ma, B. Zheng, H. L. Liu et al., "Klf5 down-regulation induces vascular senescence through eIF5a depletion and mitochondrial fission," *PLoS Biology*, vol. 18, no. 8, article e3000808, 2020.

[10] S. Feng, L. Gao, D. Zhang et al., "miR-93 regulates vascular smooth muscle cell proliferation, and neointimal formation through targeting Mfn2," *International Journal of Biological Sciences*, vol. 15, no. 12, pp. 2615–2626, 2019.

[11] S. Lim, S. Y. Lee, H. H. Seo et al., "Regulation of mitochondrial morphology by positive feedback interaction between PKCδ and Drp1 in vascular smooth muscle cell," *Journal of Cellular Biochemistry*, vol. 116, no. 4, pp. 648–660, 2015.

[12] S. Herzig and R. J. Shaw, "AMPK: guardian of metabolism and mitochondrial homeostasis," *Nature Reviews. Molecular Cell Biology*, vol. 19, no. 2, pp. 121–135, 2018.

[13] R. Ke, Q. Xu, C. Li, L. Luo, and D. Huang, "Mechanisms of AMPK in the maintenance of ATP balance during energy metabolism," *Cell Biology International*, vol. 42, no. 4, pp. 384–392, 2018.

[14] E. Q. Toyama, S. Herzig, J. Courchet et al., "Metabolism. AMP-activated protein kinase mediates mitochondrial fission in response to energy stress," *Science*, vol. 351, no. 6270, pp. 275–281, 2016.

[15] P. K. Jyotshna, P. Khare, and K. Shanker, "Mangiferin: a review of sources and interventions for biological activities," *Biofactors*, vol. 42, no. 5, pp. 504–514, 2016.

[16] F. Gold-Smith, A. Fernandez, and K. Bishop, "Mangiferin and cancer: mechanisms of action," *Nutrients*, vol. 8, no. 7, p. 396, 2016.

[17] S. Saha, P. Sadhukhan, and P. C. Sil, "Mangiferin: a xanthonoid with multipotent anti-inflammatory potential," *Biofactors*, vol. 42, no. 5, pp. 459–474, 2016.

[18] A. Matkowski, P. Kus, E. Goralska, and D. Wozniak, "Mangiferin - a bioactive xanthonoid, not only from mango and not just antioxidant," *Mini Reviews in Medicinal Chemistry*, vol. 13, no. 3, pp. 439–455, 2013.

[19] Z. Liu, P. Apontes, E. V. Fomenko et al., "Mangiferin accelerates glycolysis and enhances mitochondrial bioenergetics," *International Journal of Molecular Sciences*, vol. 19, no. 1, p. 201, 2018.

[20] E. Alberdi, M. V. Sánchez-Gómez, A. Ruiz et al., "Mangiferin and morin attenuate oxidative stress, mitochondrial dysfunction, and neurocytotoxicity, induced by amyloid beta oligomers," *Oxidative Medicine and Cellular Longevity*, vol. 2018, Article ID 2856063, 13 pages, 2018.

[21] L. Yu, M. Chen, R. Zhang, and Z. Jin, "Inhibition of cancer cell growth in gemcitabine-resistant pancreatic carcinoma by mangiferin phytochemical involves induction of autophagy, endogenous ROS production, cell cycle disruption, mitochondrial mediated apoptosis and suppression of cancer cell migration and invasion," *Journal of BUON*, vol. 24, no. 4, pp. 1581–1586, 2019.

[22] J. Li, M. Liu, H. Yu et al., "Mangiferin improves hepatic lipid metabolism mainly through its metabolite-norathyriol by modulating SIRT-1/AMPK/SREBP-1c signaling," *Frontiers in Pharmacology*, vol. 9, p. 201, 2018.

[23] Q. Wu, J. Hong, Z. Wang et al., "Abnormal ribosome biogenesis partly induced p53-dependent aortic medial smooth muscle cell apoptosis and oxidative stress," *Oxidative Medicine and Cellular Longevity*, vol. 2019, Article ID 7064319, 19 pages, 2019.

[24] M. A. Zain, R. T. Jamil, and W. J. Siddiqui, *Neointimal Hyperplasia*, 2021.

[25] G. K. Owens, M. S. Kumar, and B. R. Wamhoff, "Molecular regulation of vascular smooth muscle cell differentiation in development and disease," *Physiological Reviews*, vol. 84, no. 3, pp. 767–801, 2004.

[26] C. Vásquez-Trincado, I. García-Carvajal, C. Pennanen et al., "Mitochondrial dynamics, mitophagy and cardiovascular disease," *The Journal of Physiology*, vol. 594, no. 3, pp. 509–525, 2016.

[27] D. G. Hardie, F. A. Ross, and S. A. Hawley, "AMPK: a nutrient and energy sensor that maintains energy homeostasis," *Nature Reviews Molecular Cell Biology*, vol. 13, no. 4, pp. 251–262, 2012.

[28] Y. Li, Y. Wu, K. Jiang et al., "Mangiferin prevents TBHP-induced apoptosis and ECM degradation in mouse osteoarthritic chondrocytes via restoring autophagy and ameliorates murine osteoarthritis," *Oxidative Medicine and Cellular Longevity*, vol. 2019, Article ID 8783197, 17 pages, 2019.

[29] X. Liu, R. R. Chhipa, I. Nakano, and B. Dasgupta, "The AMPK inhibitor compound C is a potent AMPK-independent antiglioma agent," *Molecular Cancer Therapeutics*, vol. 13, no. 3, pp. 596–605, 2014.

[30] M. Imran, M. S. Arshad, M. S. Butt, J. H. Kwon, M. U. Arshad, and M. T. Sultan, "Mangiferin: a natural miracle bioactive compound against lifestyle related disorders," *Lipids in Health and Disease*, vol. 16, no. 1, p. 84, 2017.

[31] D. Carling, "AMPK signalling in health and disease," *Current Opinion in Cell Biology*, vol. 45, pp. 31–37, 2017.

[32] N. A. Shirwany and M. H. Zou, "AMPK in cardiovascular health and disease," *Acta Pharmacologica Sinica*, vol. 31, no. 9, pp. 1075–1084, 2010.

[33] C. Rodriguez, M. Munoz, C. Contreras, and D. Prieto, "AMPK, metabolism, and vascular function," *FEBS Journal*, vol. 288, no. 12, pp. 3746–3771, 2021.

[34] C. Rodríguez, C. Contreras, J. Sáenz-Medina et al., "Activation of the AMP-related kinase (AMPK) induces renal vasodilatation and downregulates Nox-derived reactive oxygen species (ROS) generation," *Redox Biology*, vol. 34, article 101575, 2020.

[35] M. Li, C. Wu, H. Guo, C. Chu, M. Hu, and C. Zhou, "Mangiferin improves hepatic damage-associated molecular patterns, lipid metabolic disorder and mitochondrial dysfunction in alcohol hepatitis rats," *Food & Function*, vol. 10, no. 6, pp. 3514–3534, 2019.

[36] S. Li, Y. Shi, P. Liu et al., "Metformin inhibits intracranial aneurysm formation and progression by regulating vascular smooth muscle cell phenotype switching via the AMPK/ACC pathway," *Journal of Neuroinflammation*, vol. 17, no. 1, p. 191, 2020.

[37] C. M. Palmeira, J. S. Teodoro, J. A. Amorim, C. Steegborn, D. A. Sinclair, and A. P. Rolo, "Mitohormesis and metabolic health: the interplay between ROS, cAMP and sirtuins," *Free Radical Biology & Medicine*, vol. 141, pp. 483–491, 2019.

[38] T. Ismail, Y. Kim, H. Lee, D. S. Lee, and H. S. Lee, "Interplay between mitochondrial peroxiredoxins and ROS in cancer development and progression," *International Journal of Molecular Sciences*, vol. 20, no. 18, p. 4407, 2019.

[39] L. Tilokani, S. Nagashima, V. Paupe, and J. Prudent, "Mitochondrial dynamics: overview of molecular mechanisms," *Essays in Biochemistry*, vol. 62, no. 3, pp. 341–360, 2018.

[40] L. Wang, T. Yu, H. Lee, D. K. O'Brien, H. Sesaki, and Y. Yoon, "Decreasing mitochondrial fission diminishes vascular smooth muscle cell migration and ameliorates intimal hyperplasia," *Cardiovascular Research*, vol. 106, no. 2, pp. 272–283, 2015.

[41] B. G. Durgin and A. C. Straub, "Redox control of vascular smooth muscle cell function and plasticity," *Laboratory Investigation*, vol. 98, no. 10, pp. 1254–1262, 2018.

[42] A. Li, S. Zhang, J. Li, K. Liu, F. Huang, and B. Liu, "Metformin and resveratrol inhibit Drp1-mediated mitochondrial fission and prevent ER stress-associated NLRP3 inflammasome activation in the adipose tissue of diabetic mice," *Molecular and Cellular Endocrinology*, vol. 434, pp. 36–47, 2016.

[43] J. Liu, W. Yan, X. Zhao et al., "Sirt3 attenuates post-infarction cardiac injury via inhibiting mitochondrial fission and normalization of AMPK-Drp1 pathways," *Cellular Signalling*, vol. 53, pp. 1–13, 2019.

[44] K. Schmitt, A. Grimm, R. Dallmann et al., "Circadian control of DRP1 activity regulates mitochondrial dynamics and bioenergetics," *Cell Metabolism*, vol. 27, no. 3, pp. 657–666.e5, 2018.

[45] L. Yang, X. Li, A. Jiang et al., "Metformin alleviates lead-induced mitochondrial fragmentation via AMPK/Nrf2 activation in SH-SY5Y cells," *Redox Biology*, vol. 36, p. 101626, 2020.

[46] J. W. Kang, J. M. Hong, and S. M. Lee, "Melatonin enhances mitophagy and mitochondrial biogenesis in rats with carbon tetrachloride-induced liver fibrosis," *Journal of Pineal Research*, vol. 60, no. 4, pp. 383–393, 2016.

[47] B. Zhao, L. Qiang, J. Joseph, B. Kalyanaraman, B. Viollet, and Y. Y. He, "Mitochondrial dysfunction activates the AMPK signaling and autophagy to promote cell survival," *Genes & Diseases*, vol. 3, no. 1, pp. 82–87, 2016.

Hindawi
Oxidative Medicine and Cellular Longevity
Volume 2021, Article ID 4187398, 17 pages
https://doi.org/10.1155/2021/4187398

Research Article

CaMK II Inhibition Attenuates ROS Dependent Necroptosis in Acinar Cells and Protects against Acute Pancreatitis in Mice

Qingtian Zhu,[1,2,3] **Lu Hao**,[4] **Qinhao Shen**,[1,3] **Jiajia Pan**,[3,5] **Weili Liu**,[3,5] **Weijuan Gong**,[1,3] **Lianghao Hu**,[2] **Weiming Xiao**,[1,3] **Mei Wang**,[1,3] **Xinnong Liu**,[3] **Yanbing Ding**,[1,3] **and Guotao Lu**[1,3]

[1]*Pancreatic Center, Department of Gastroenterology, The Affiliated Hospital of Yangzhou University, Yangzhou University, Yangzhou, China*
[2]*Department of Gastroenterology, Changhai Hospital, The Second Military Medical University, Shanghai, China*
[3]*Institute of Gastroenterology, Affiliated Hospital of Yangzhou University, Yangzhou University, Jiangsu, China*
[4]*Department of Gastroenterology, The First Affiliated Hospital, Zhejiang University, China*
[5]*Department of Intensive Care Unit, The Affiliated Hospital of Yangzhou University, Yangzhou University, Yangzhou, China*

Correspondence should be addressed to Xinnong Liu; xnliu@yzu.edu.cn, Yanbing Ding; ybding@yzu.edu.cn, and Guotao Lu; gtlu@yzu.edu.cn

Received 13 July 2021; Accepted 8 October 2021; Published 17 November 2021

Academic Editor: Xiuyun Liu

As a calcium-regulated protein, CaMK II is closely related to cell death, and it participates in the development of pathological processes such as reperfusion injury, myocardial infarction, and oligodendrocyte death. The function of CaMK II activation in acute pancreatitis (AP) remains unclear. In our study, we confirmed that the expression of p-CaMK II was increased significantly and consistently in injured pancreatic tissues after caerulein-induced AP. Then, we found that KN93, an inhibitor of CaMK II, could mitigate the histopathological manifestations in pancreatic tissues, reduce serum levels of enzymology, and decrease oxidative stress products. Accordingly, we elucidated the effect of KN93 in vitro and found that KN93 had a protective effect on the pancreatic acinar cell necroptosis pathway by inhibiting the production of ROS and decreasing the expression of RIP3 and p-MLKL. In addition, we identified the protective effect of KN93 on AP through another mouse model induced by pancreatic duct ligation (PDL). Together, these data demonstrated that CaMK II participates in the development of AP and that inhibiting CaMK II activation could protect against AP by reducing acinar cell necroptosis, which may provide a new idea target for the prevention and treatment of AP in the clinic.

1. Introduction

Acute pancreatitis (AP) is one of the most common and potentially devastating complications of digestive diseases, with a high mortality, great variability in severity, and high health-care costs [1–3]. Most clinical patients have mild and reversible disease, which is called mild acute pancreatitis (MAP). However, some of them may progress to severe acute pancreatitis (SAP), accompanied by extensive necrosis of pancreatic acinar cells, the activation and release of enzymes, and infiltration by a large number of inflammatory mediators [4, 5], which could induce a systemic inflammatory response and multiple organ failure, with a high mortality [6]. Animal experiments showed that inhibition of acinar cell necrosis could reduce the inflammatory response during AP [7, 8]. In the early stage of AP, effective reduction of acinar cell necrosis is the key to reducing the degree of inflammation and improving the prognosis of AP.

Increasing numbers of researchers have shown that necroptosis, a new concept of necrosis, is regulated by the RIP kinase family, including receptor interacting protein 3 (RIP3) and downstream molecule lineage kinase domain-like protein (MLKL), which are involved in the regulation of several inflammatory processes, including myocardial

infarction [9], ischemia-reperfusion injury [10], inflammatory bowel disease [11], and chronic obstructive pulmonary disease [12]. Acinar cell necroptosis plays an important role in AP [13–15] and is related to the development of AP [16]. Notably, RIP3 deficiency or p-MLKL deletion could significantly reduce the acinar cell necroptosis induced by caerulein in AP mice [17, 18].

Ca^{2+}/calmodulin-dependent protein kinase II (CaMK II), as a fundamental molecule in calcium signaling, is a heteromeric serine/threonine-specific protein kinase [19, 20]. The activated CaMK II works as a sensor of reactive oxygen (ROS) increments and correlated with a sustained kinase activity, then differentially localizing to regulate specific events [21, 22]. It has been shown that CaMK II is widely distributed in mammals, and it is highly expressed in the myocardium, brain, and kidney, where it regulates calcium homeostasis, enhances learning and memory, and maintains membrane stability, among other physiological functions [23]. However, continuous activation of CaMK II could aggravate myocardial necroptosis, subsequent malignant cardiac remodeling, and ultimately, sudden myocardial infarction via the necroptosis pathway. Inhibiting the expression and activation of CaMK II could improve the above pathological processes and reduce cell necroptosis [9, 24].

The function of CaMK II activation in AP is unclear. KN93 is a CaMK-binding specific antagonist that can reversibly and competitively inhibit CaMK II activity. KN93 has roles in Parkinson's disease, cerebral ischemia, hypoxia, and cancer pain [25, 26]. In the current article, we first confirmed that CaMK II was significantly increased in pancreatic acinar cells during AP, which is consistent with the expression of RIP3. We further verified that KN93 had dramatic effectiveness in two AP mouse models and that it decreases the expression of necrotic complexes (RIP3 and p-MLKL) in two cell lines, providing a new target for the prevention and treatment of AP in the clinic.

2. Materials and Methods

2.1. Chemicals and Reagents. KN93 was obtained from Selleck (Selleckchem, Texas, USA); caerulein, cholecystokinin (CCK), and DHE were purchased from Sigma (Sigma-Aldrich, St. Louis, MO, USA); anti-CaMK II antibody, anti-p-CaMK II antibody, anti-RIP3 antibody, anti-pMLKL antibody, anti-CD68 antibody, and anti-myeloperoxidase (MPO) were purchased from Abcam (Cambridge, UK); anti-GAPDH antibody was purchased from Sigma; and anti-RIP3 antibody was obtained from Santa Cruz Biotechnology (Santa Cruz, CA, USA). The anti-rabbit and anti-mouse secondary antibodies were purchased from Cell Signaling Technologies (Beverly, MA, USA). The LDH Cytotoxicity Assay Kit was purchased from Beyotime Biotechnology (Beijing, China); amylase kits were purchased from BioSino (BioSino BioTechnology & Science Inc., Beijing, China), and lipase kits were purchased from Nanjing Jiancheng (Nanjing Jiancheng Corp, Nanjing, China). Hoechst 33342 and propidium iodide (PI) were purchased from KeyGEN BioTECH, Nanjing, China. All flow cytometry-related antibodies were purchased from BioLegend.

2.2. Cell Culture and Stimulation. For the in vitro experiments, the mouse pancreatic acinar 266-6 cell line was obtained from ATCC (Manassas, VA, USA) and incubated in DMEM containing 10% fetal bovine serum (Gibco, Thermo Fisher Scientific), 100 U/ml penicillin, and 100 mg/ml streptomycin at 37°C with 5% CO_2 in regular air. The 266-6 cells were incubated with different doses of KN93 (0.5, 1, and 2 μM) for 30 min and then treated with 5 μM CCK for 12 h as a cell injury model of AP. Finally, the cells were collected for subsequent experiments. In the control group, the 266-6 cells were only incubated with 0.1% DMSO.

Primary pancreatic acinar cells were freshly and quickly isolated from C57BL/6 mice using collagenase IV digestion [27]. The cells were suspended in HEPES buffer and pretreated with KN93 (2 μM) for 30 min, followed by coincubation with CCK (1 μM) for 2 h. Then, the cells were stained with Hoechst 33342 (50 μg/ml) and propidium iodide (PI; 1 μM). Necrotic cells were calculated as PI-positive cells divided by Hoechst 33342-stained cells and multiplied by 100%.

2.3. Animals. All studies were approved by the Science and Technology Commission of the Affiliated Hospital of Yangzhou University municipality, and all methods were carried out in accordance with the Principles of Laboratory Animal Care (NIH publication No. 85Y50, revised 1996). C57BL/6 male mice weighing 20-25 g were purchased from GemPharmatech Co., Ltd., Nanjing, China, and housed in a temperature-controlled, appropriate humidity animal facility with 12 h light-dark cycles. All mice had unlimited access to water and commercial food.

2.4. Construction of the AP Model and KN93 Administration In Vivo. To establish the AP model, male mice were induced by intraperitoneal (i.p.) injection of caerulein (100 μg/kg, at intervals of 1 h, 7 times in total). Another AP model was induced by pancreatic duct ligation (PDL). After intraperitoneal injection of sodium pentobarbital (50 mg/kg), 1-2 cm longitudinal incisions were made in the abdomen of the mice to expose the abdominal cavity, and the duodenum was turned over to expose its distal side. At 1 cm above the duodenal papilla, blunt dissection of the tissue around the pancreatic duct was performed, and the tissue was ligated with a silk thread. Complete obstruction of the pancreatic duct was used to simulate biliary pancreatitis caused by cholelithiasis. After ligation, the abdominal cavity of the mice was layered and closed. All of the mice were placed on a 37°C constant temperature heating table for 90 min to recover from the surgery [28].

2.5. KN93 Administration In Vivo and Sample Collection. KN93 was dissolved in 100% DMSO to prepare a stock solution and then diluted in 5% DMSO solution/95% PBS before use. To verify the protective effect of KN93 against AP, KN93 (5, 10, and 20 mg/kg) was administered intraperitoneally 0 h before the administration of caerulein. All animals were anesthetized by intraperitoneal administration of sodium pentobarbital (50 mg/kg) before sacrifice. Blood

samples were collected for ELISA measurement and amylase and lipase detection. The analysis was performed according to the kit instructions. Pancreatic and pulmonary tissues were harvested, and some were fixed immediately for histological analysis, and the rest were stored at -80°C for further investigation.

2.6. Histological Analysis. Pancreatic tissue samples were fixed in 4% phosphate buffered formaldehyde, embedded in paraffin blocks, stained with hematoxylin and eosin, and then examined with a light microscope. The histopathological scoring analysis of the pancreatic and pulmonary tissues was performed blindly according to our previously described methods [29].

2.7. Immunohistochemical Analysis. Mice were anesthetized and perfused transcranially with saline and 4% paraformaldehyde. The pancreas of the mice was obtained, fixed, embedded, and cut into 5 μm thick sections. For IHC of RIP3 and p-MLKL, the slides were incubated overnight at 4°C in a humid chamber with antibodies against RIP3 (1 : 200 dilution) and p-MLKL (1 : 200 dilution) and then incubated with a biotinylated secondary antibody (1 : 500 dilution) for 60 min. Images were acquired through a light microscope.

2.8. Western Blot Analysis. For immunoblot analysis, the proteins from the pancreatic tissues were determined using a BCA protein kit (Thermo Fisher Scientific, MA, USA). Protein samples were subjected to 10% SDS-PAGE and then transferred to PVDF membranes. The membranes were blocked with 5% skim milk at room temperature for 2 h and then incubated overnight at 4°C with the following primary antibodies: anti-CaMK II (1 : 1000 dilution), anti-p-CaMK II (1 : 1000 dilution), RIP3 (1 : 1000 dilution), p-MLKL (1 : 1000 dilution), and GAPDH (1 : 2500 dilution) in blocking buffer. The membranes were washed with TBST (3×10 min) the next day and then incubated with the appropriate horseradish peroxidase-conjugated secondary antibodies for 1 h at room temperature. After washing, the protein bands were detected using the ECL Plus chemiluminescent system. Image intensity was analyzed with the ImageJ software.

2.9. Evaluation of Serum Enzymology and Enzyme-Linked Immunosorbent Assay (ELISA) Determination. The in vitro proliferation and quantitative detection of toxicity were determined by an LDH release kit. Briefly, exponentially growing 266-6 cells were seeded into 96-well microplates at a density of 5×10^3 cells/well, followed by 12 h incubation and then assayed according to the instructions of the LDH Kit. Blood samples were collected at different time points for serum enzymology (amylase and lipase) and proinflammatory cytokine detection. The analysis was performed according to the kit instructions.

2.10. Measurement of ROS Generation in Pancreatic Tissues. The assays were performed as in our previously described methods [28]. Fresh tissues from the pancreas were embedded in optimal cutting temperature (OCT) compound, and then, the samples were cut into 7 mm sections. The tissues were incubated in the dark with DHE solution for 30 min at 37°C. Slides were placed in PBS (pH = 7.4) and washed 3 times, each time for 5 min. Then, the tissues were incubated with 4′,6-diamidino-2-phenylindole, dihydrochloride (DAPI, Wuhan Servicebio Technology Co., Ltd., Wuhan, China) solution at room temperature for 10 min and washed again. Finally, the slides were observed under a fluorescence microscope.

2.11. Oxidative Stress Product Detection. Briefly, pancreatic tissues were homogenized in PBS and then centrifuged (12,000 rpm, 4°C, 30 min) to obtain supernatant. CAT, MDA, and GSH levels were determined according to the manufacturer's instructions [30].

2.12. Pancreatic Leukocyte Isolation and Preparation. Pancreatic leukocytes were isolated using a collagenase digestion method for flow cytometry analysis [31]. In brief, the pancreas was cut into pieces and digested in FACS buffer containing 2 mg/ml collagenase type IV (Sigma-Aldrich). The tissues were incubated in a shaker at 37°C for 17-20 min and then vortexed at low speed for 20 s before passage through a 70 μM filter. The above cells isolated from different tissues were subjected to RBC lysis if necessary prior to further staining or treatment.

2.13. Flow Cytometry. For surface staining, the murine cells were stained with Abs against the following: CD45.2 (clone 104), CD11b (clone M1/70), F4/80 (clone BM8), and Gr-1 (clone RB6-8C5). Cells were washed, stained with surface markers, acquired on a Beckman DxFlex and analyzed with CytExpert for DxFLEX.

2.14. Statistical Analysis. Statistical analysis was performed by the GraphPad Prism 6 software (GraphPad, San Diego, CA, USA). The *t*-test was used to analyze differences between two groups, and one-way ANOVA was used to evaluate the statistical significance among groups. The results are presented as the mean ± SEM (standard error of the mean), and $P < 0.05$ was considered statistically significant (two-tailed). At least three independent experiments were carried out for the statistical comparisons.

3. Results

3.1. CaMK II Was Persistently Highly Expressed in the Pancreatic Tissues of AP Mice. As shown in Figure 1(a) and SFigure 1, after caerulein administration, we observed that pancreatic injury began at 6 h and reached a peak at 12 h, which mainly represented edema, inflammatory cell infiltration, and acinar cell necrosis. Serum amylase and lipase, which are common biochemical markers of AP, increased gradually until 12 h and then declined at 24 h. In addition, as shown in Figure 1(b), there was an increase in the MDA and CAT levels and a decrease in the GAH level in pancreatic tissues of AP.

Immunohistochemistry (IHC) staining was used to detect that the expression of p-CaMK II in pancreatic tissues, and it was significantly elevated after AP onset, as shown in Figures 1(a) and 1(c). In addition, the expression

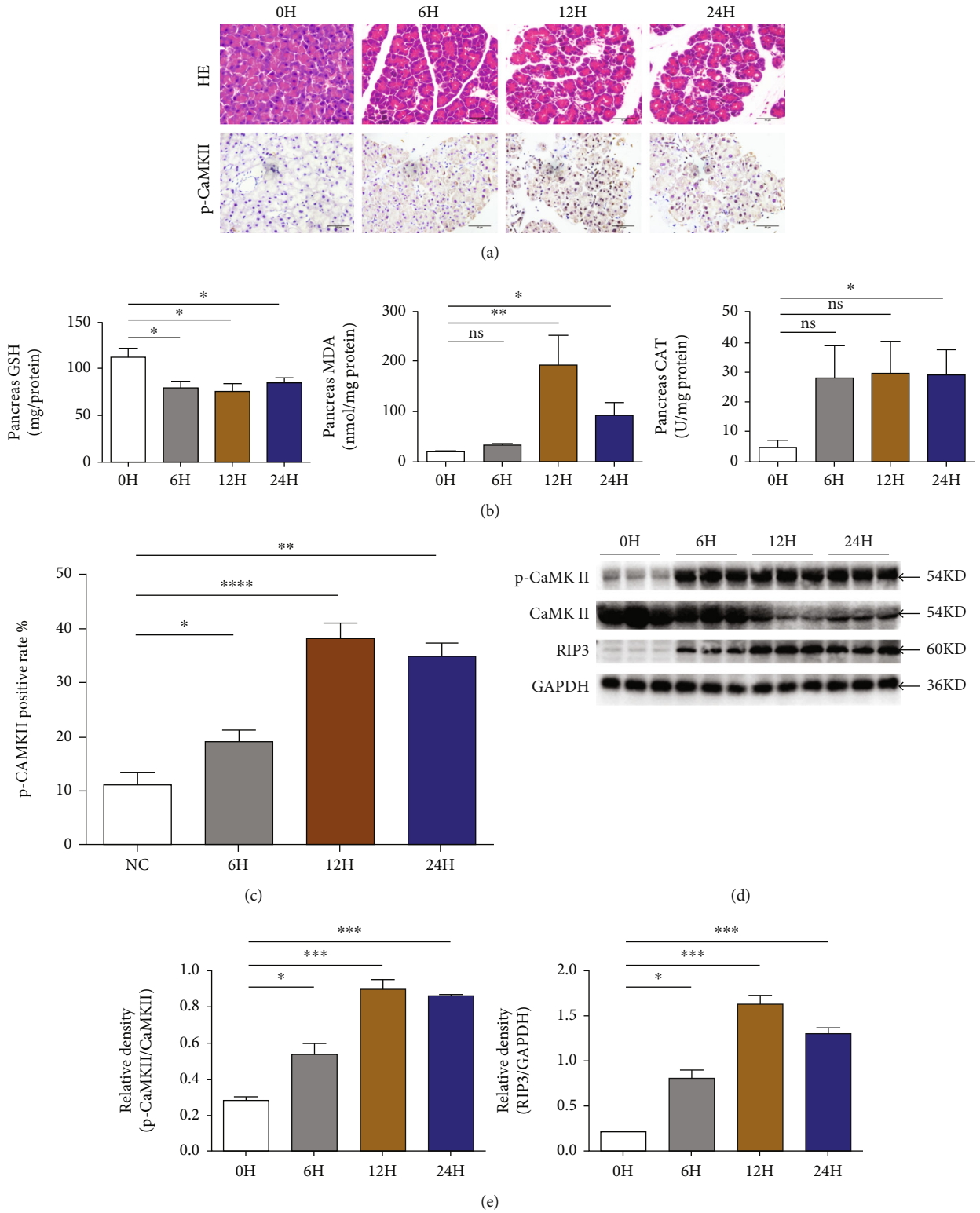

Figure 1: CaMK II was persistently highly expressed in the pancreatic tissues of AP mice. (a) Representative HE staining and immunohistochemistry images for p-CaMKII expression of pancreatic tissues in magnifications 400x. Scar bar = 50 μM. $N = 6$ each time point. (b) Levels of oxidative stress products (CAT, MDA, and GSH) of pancreas. $N = 6$ each group. (c) p-CaMK II positive rate of immunohistochemistry images in the pancreas. (d) Protein levels of p-CaMK II and RIP3 in pancreatic tissues were analyzed by Western blotting. (e) CaMK II and GAPDH were used as a control for protein loading, respectively. (b–e) $N = 3$ each time point. $^{*}P < 0.05$, $^{**}P < 0.01$, $^{***}P < 0.001$, and $^{****}P < 0.0001$.

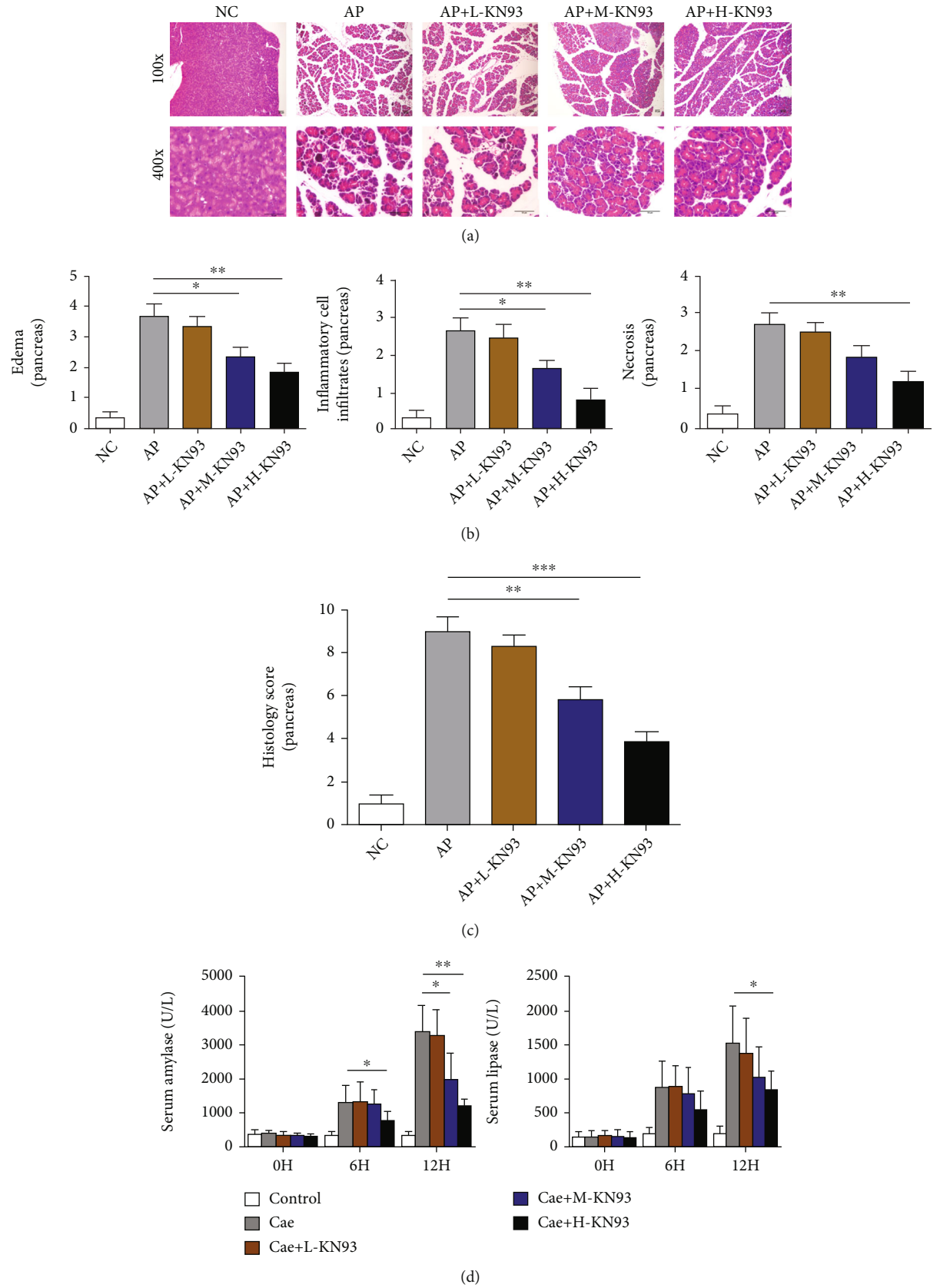

Figure 2: Continued.

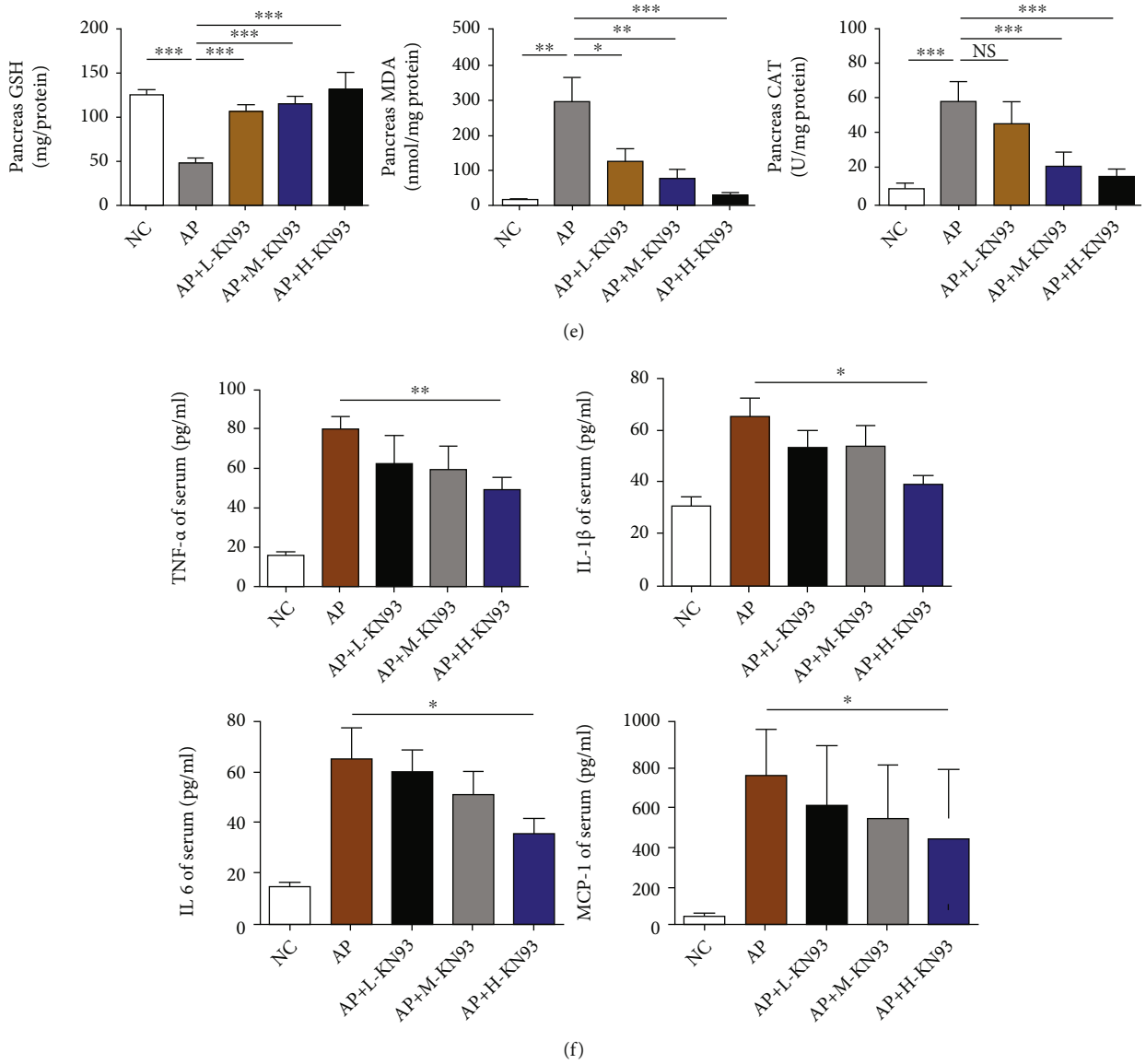

Figure 2: KN93 mitigated the severity of caerulein-induced AP in mice. (a) Representative HE staining of pancreatic tissues in magnifications 100x and 400x. Scar bar = 50 μM. (b, c) The pathological scores of pancreatic tissues. (d) Serum levels of amylase and lipase. (e) The levels of GSH, MDA, and CAT in the pancreatic tissues. (f) The serum levels of TNF-α, IL-1β, IL-6, and MCP-1 was detected by ELISA. $N = 7$ each group. $^{*}P < 0.05$ and $^{**}P < 0.01$. L, M, and H represent low-dose (5 mg/kg), medium-dose (10 mg/kg), and high-dose KN93 (20 mg/kg).

of p-CaMK II protein by Western blot detection presented the same trend as IHC staining. Accordingly, the expression of CaMK II was decreased in pancreatic acinar cells after caerulein stimulation, as shown in Figures 1(d) and 1(e).

3.2. KN93 Mitigated the Severity of Caerulein-Induced AP in Mice. Whether KN93 has a protective effect against AP has not previously been reported. Based on the high expression of p-CaMK II in caerulein-induced AP, the mice were sacrificed 12 h after the administration of caerulein. As shown in Figures 2(a)–2(d), the severity of AP was significantly reduced after KN-93 administration, accompanied by decreased inflammatory cell infiltration, decreased serum levels of amylase and lipase, and decreased acinar cell necrosis. All of the results indicated that the protective effect of KN93 on AP is dose-dependent, and the highest dose of KN-93 had the best effect without toxic side effects on the mice, as shown in SFigure 2. In addition, the levels of oxidative products (MDA, CAT, and GSH), as shown in Figure 2(e), were detected in the pancreatic tissues, and we found that MDA and CAT were decreased and GSH was significantly increased after KN93 treatment compared with AP groups. The dynamic changes of oxidative stress products may be accompanied by the levels of proinflammatory cytokines, such as IL-1β, IL-6, TNF-α, and MCP-1 on AP. Accordingly, the results showed that these serum inflammatory mediators were increased approximately 2-3-fold compared with those in the NC group, and they could be attenuated by high-dose

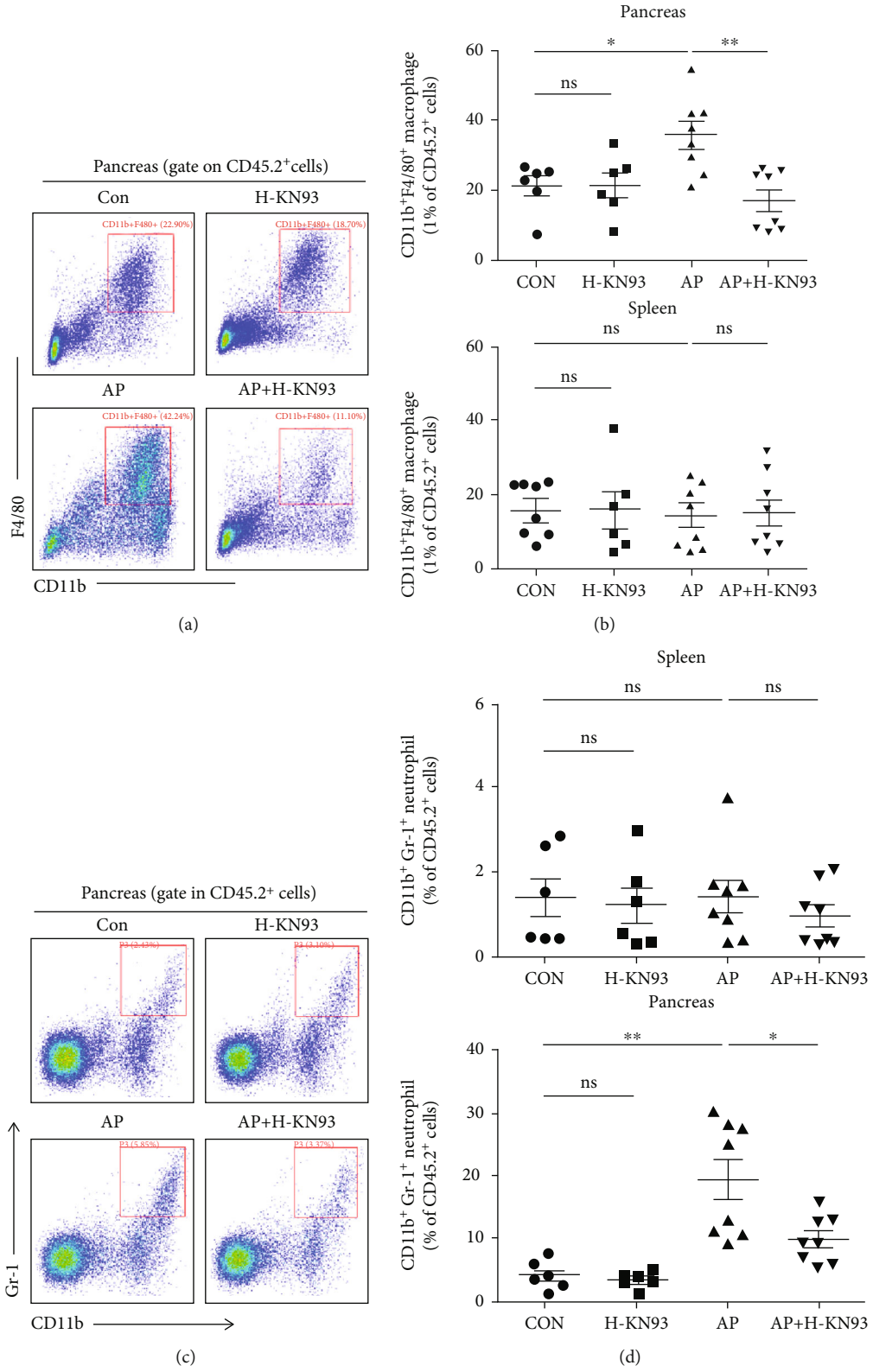

Figure 3: Continued.

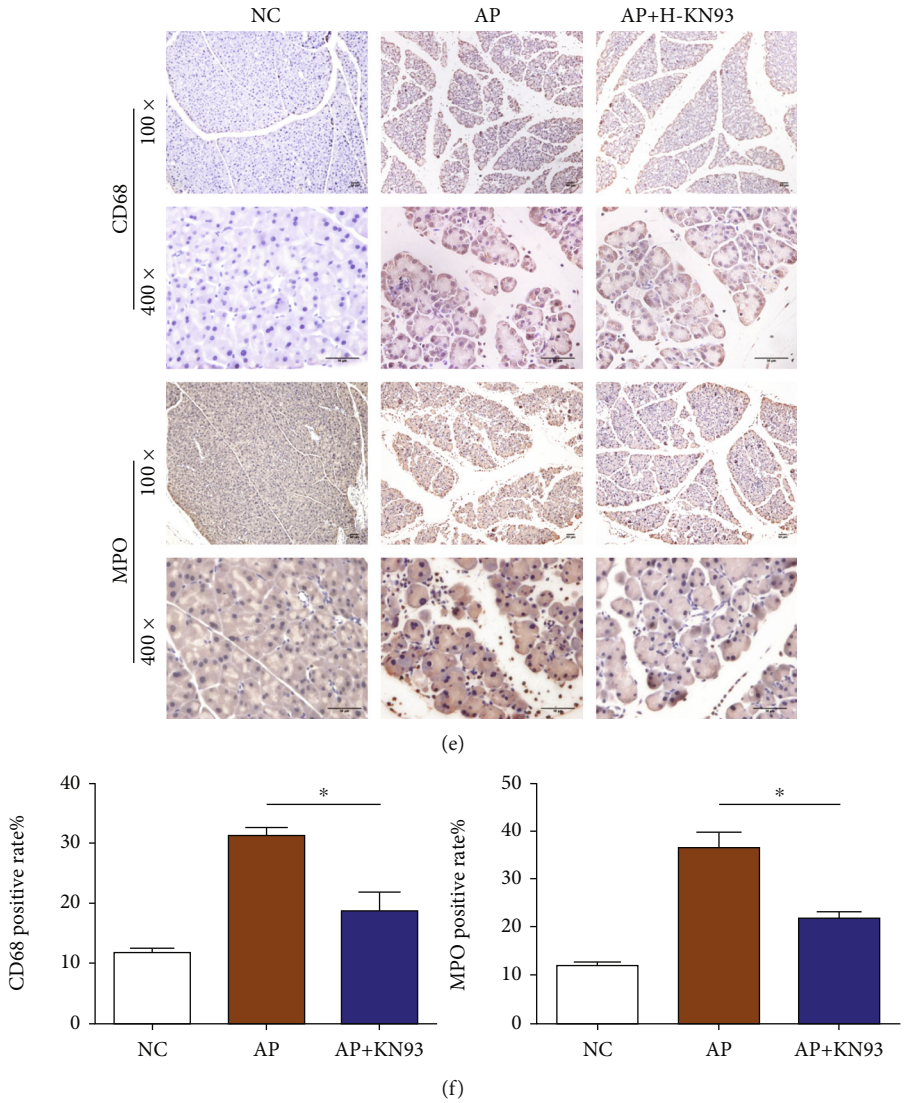

Figure 3: KN93 decreased macrophages and neutrophils in pancreatic tissues of the AP mouse model. (a–d) Leukocytes from pancreas and spleen were isolated for staining and flow cytometry analysis. Representative flow cytometry gating of pancreatic macrophages (a) and neutrophils (c) is shown. (b, d) The percentages of CD11b $^{+}$F4/80^{+} macrophages and CD11b^{+}Gr-1^{+} neutrophils from pancreas and spleen are shown (mean ± SEM) as scatter plots. $N \geqq 6$ each group. (e) Representative immunohistochemistry images for myeloperoxidase (MPO) and CD68 in the pancreas. Scar bar = 50 μM. (f) The frequencies of MPO positive rate and CD68 positive rate in pancreas. $N = 3$ each group. $^{*}P < 0.05$ and $^{**}P < 0.01$. H represents high-dose KN93 (20 mg/kg).

KN93 (H-KN93) administration, as shown in Figure 2(f), which was in accordance with the degree of pancreatic injury. In view of this, H-KN93 (20 mg/kg) was adopted to carry out functional and mechanistic research in the following experiments.

3.3. KN93 Decreased Macrophages and Neutrophils in Pancreatic Tissues of the AP Mouse Model. Increasing amounts of evidence support the importance of infiltrating leukocytes, especially macrophages and neutrophils, in the development of AP pathogenesis [31]. We established an AP model induced by caerulein and isolated leukocytes from the pancreas and spleen. As shown in Figures 3(a)–3(d), we observed that the number of activated macrophages (CD11b^{+}F4/80^{+}) and neutrophils (CD11b + GR-1^{+}) in the pancreas was significantly increased in AP mice compared with the control group, while the number of leukocytes in the spleen was not different among the four groups. Unsurprisingly, the number of infiltrating leukocytes could be reduced by KN93 administration to AP mice, while KN93 injection had no effect on the numbers or differentiation of the leukocytes in the mice.

MPO and CD68 are widely used as biomarkers of activated neutrophils and macrophages. IHC examination of MPO and CD68 in pancreatic tissues was used to further assess pancreatic tissue inflammatory cell infiltration. These results indicated that KN93 significantly decreased the infiltration of neutrophils and macrophages compared with that in the AP group (Figures 3(e) and 3 (f)), which was consistent with the flow cytometry results.

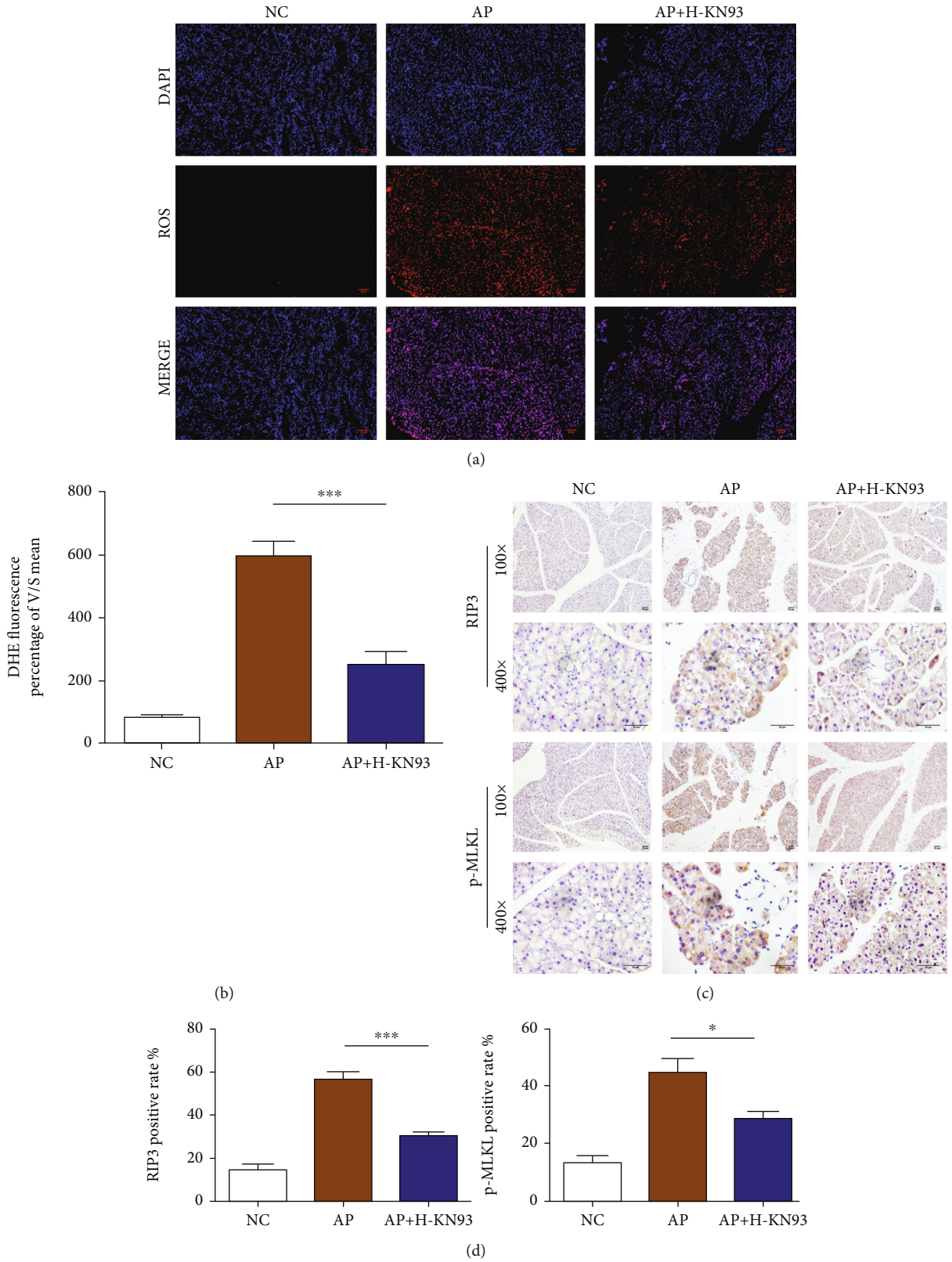

Figure 4: KN93 reduced acinar cell necroptosis and decreased the production of ROS in acinar cells in the AP mice. (a) Representative immunohistochemistry images for RIP3 and p-MLKL expression in the pancreas. Scar bar = 50 μM. (b) Representative immunofluorescence image of DHE in magnification 200x. Scar bar = 50 μM. (c) Densitometric analysis of DHE fluorescence. (d) RIP3 and p-MLKL positive rate of pancreatic acinar cells. $N = 3$ each group. $^{*}P < 0.05$, $^{**}P < 0.01$, and $^{***}P < 0.001$. H represents high-dose KN93 (20 mg/kg).

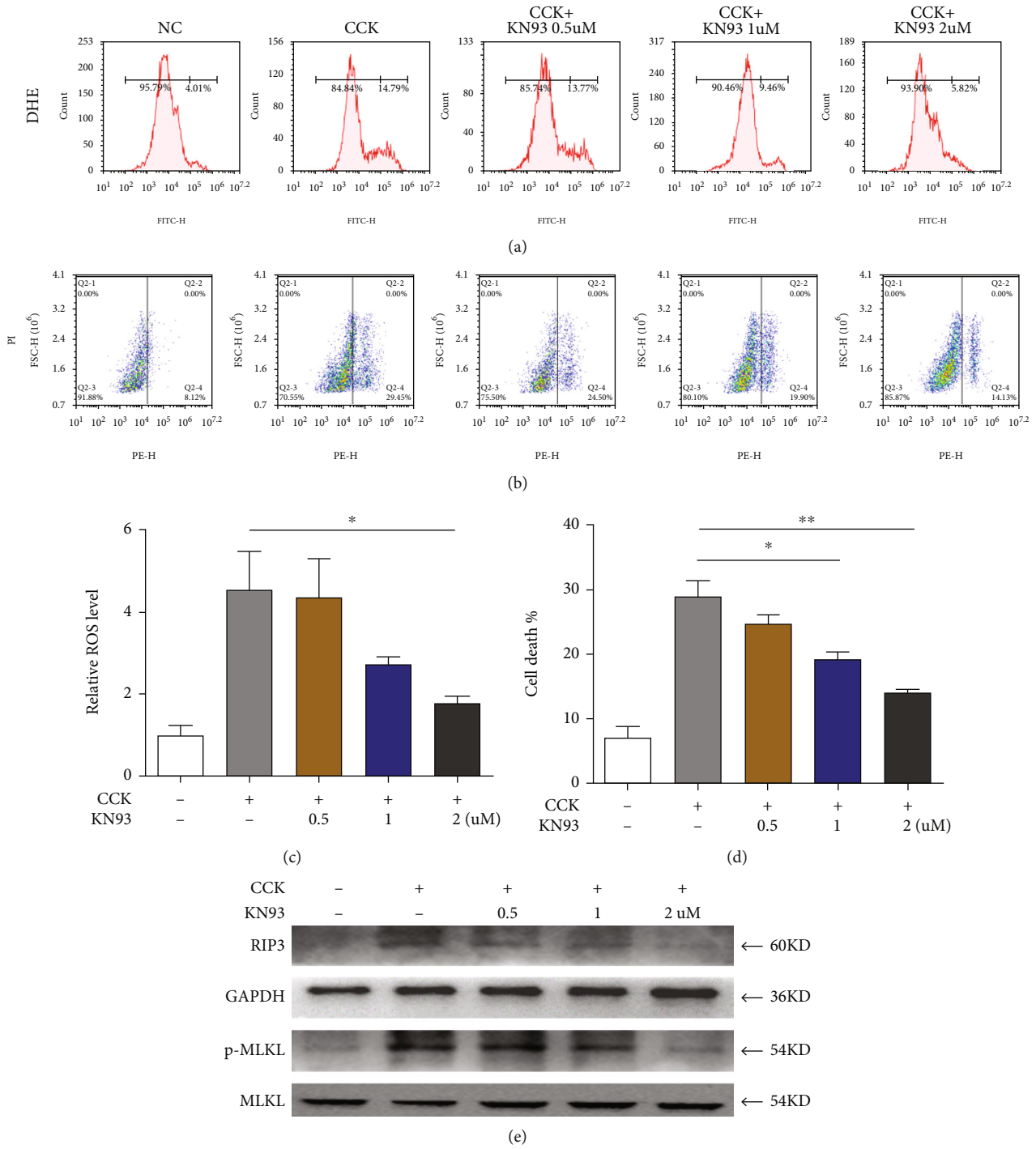

Figure 5: Continued.

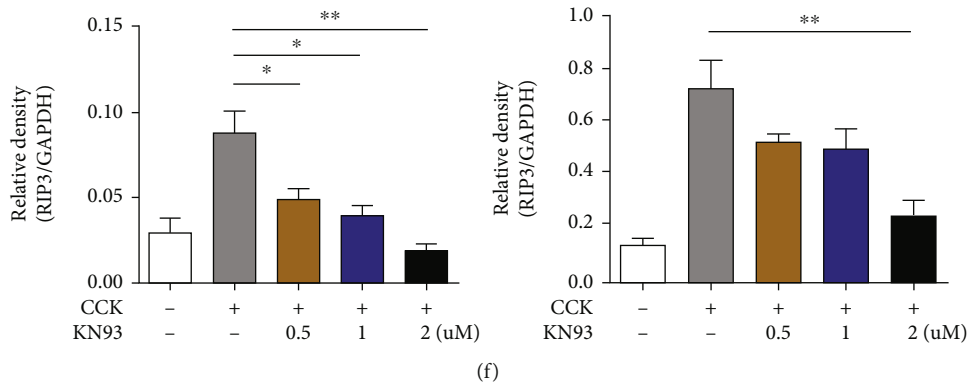

(f)

Figure 5: Effect of KN93 on 266-6 cells in vitro. (a) PI was detected by flow cytometry. (b) The reactive oxygen species (ROS) in pancreatic tissues were detected by DHE fluorescent probe. (c) The relative cell death level of 266-6 cells. (d) The relative ROS level of 266-6 cells. (e) Protein levels of RIP3 and p-MLKL in 266-6 cells were analyzed by Western blotting. (f) Relative protein expression of RIP3 and p-MLKL; GAPDH and MLKL were used as control for protein loading, respectively. $^{*}P < 0.05$ and $^{**}P < 0.01$. CCK: cholecystokinin octapeptide.

3.4. KN93 Reduced Acinar Cell Necroptosis and Decreased the Production of ROS in Acinar Cells in AP Mice. The production of ROS and the expression of RIP3 and p-MLKL have been considered to be associated with necroptosis. To further investigate the potential functions of KN93 in AP, we detected the production of ROS and the expression of RIP3 and p-MLKL in pancreatic tissues. DHE staining showed that the production of ROS was remarkably increased during AP, while H-KN93 reversed this increase (Figures 4(a) and 4(b)). As shown in Figures 4(c) and 4(d), IHC staining illustrated a significant increase in the expression of RIP3 and p-MLKL in pancreatic acinar cells, which was reduced after H-KN93 treatment. All of these data indicated that KN93 could inhibit the necroptosis pathway in acinar cells.

3.4.1. The Protective Effect of KN93 on Pancreatic Acinar Cells In Vitro. To further clarify the protective effect of KN93, the 266-6 cell line was used to establish a cellular injury model by CCK. As shown in Figures 5(a)–5(c), KN93 significantly reduced ROS production and protected against cell necrosis. In addition, CCK caused acinar cell injury, with the main manifestations following a pronounced increase in RIP3 and p-MLKL protein expression, which was decreased by KN93 (Figures 5(e)–5(f)).

Furthermore, we validated the effectiveness of KN93 on isolated pancreatic acinar cells of mice and found that KN93 had a protective effect against acinar cell necrosis in different validation methods, as shown in Figures 6(a)–6(e).

3.4.2. KN93 Mitigated the Severity of PDL-Induced AP and Prolonged Survival of Mice. We generated an additional AP mouse model (induced by pancreatic duct ligation as an SAP model) to observe the expression of RIP3 and p-MLKL (Figures 7(d) and 7(e)) and further confirm the protective effect of KN93 on AP. Unsurprisingly, all of the results were consistent, including the serum enzyme changes, the pancreatic injury, and the related acute lung injury (commonly used to assess SAP), and suggested that KN93 had a good protective effect against AP (Figures 7(a), 7(b), and 7(d), SFig 3). Most notably, KN93 treatment was applied to PDL mice at 1 day to 4 days (total 20 mg/kg) after modeling. As shown in Figure 7(f), Kaplan-Meier curves revealed a significant difference in the survival rate ($P = 0.0382$) between PDL + KN93 and PDL mice, which suggested that KN93 could reduce the long-term mortality of mice in the PDL-induced SAP model.

4. Discussion

In summary, our study confirmed that CaMK II was involved in the progression of AP and validated that its inhibitor KN93 has a protective influence both in vivo and in vitro. It is possible that KN93 may be a promising drug for the treatment and prevention of AP in clinical practice in the future.

Acute pancreatitis (AP) is an acute noninfectious inflammatory disease involving abnormal inflammation of the pancreas. The pathogenesis of AP remains unclear. Current lines of evidence indicate that the pathogenesis and prognosis of AP might be associated with the oxidative stress-related acinar cell necrosis, and antioxidation could reduce pancreatic necrosis. Our previous studies found that oxidative stress products showed dynamic changes in pancreatic tissues of mice with AP. Additionally, the caerulein-induced AP model and PDL-induced SAP are essentially caused by hypersecretion of digestive enzymes of necrosis acinar cells [32, 33]. Inhibition of this could effectively reduce the inflammatory response and relieve the progression of AP [15]. Hence, it is vitally important to search for effective and therapeutic target drugs to reduce acinar cell necrosis both in basic research and in the clinic.

CaMK II is a family of serine/threonine kinases that are regulated by the $Ca2^{+}$/calmodulin complex. CAM is a highly conserved calcium target protein, and it has no enzymatic activity under normal conditions. Once the cells are damaged by various stresses, the increased intracellular calcium content combined with CAM and subsequent activation of the downstream target protein CaMK II [19, 20]. Existing studies have confirmed that an increase of ROS production leading to CaMK II hyperactivity and perturbation in Ca2+ handing, and it has been reported to regulate and control inflammation-related diseases, such as reperfusion injury,

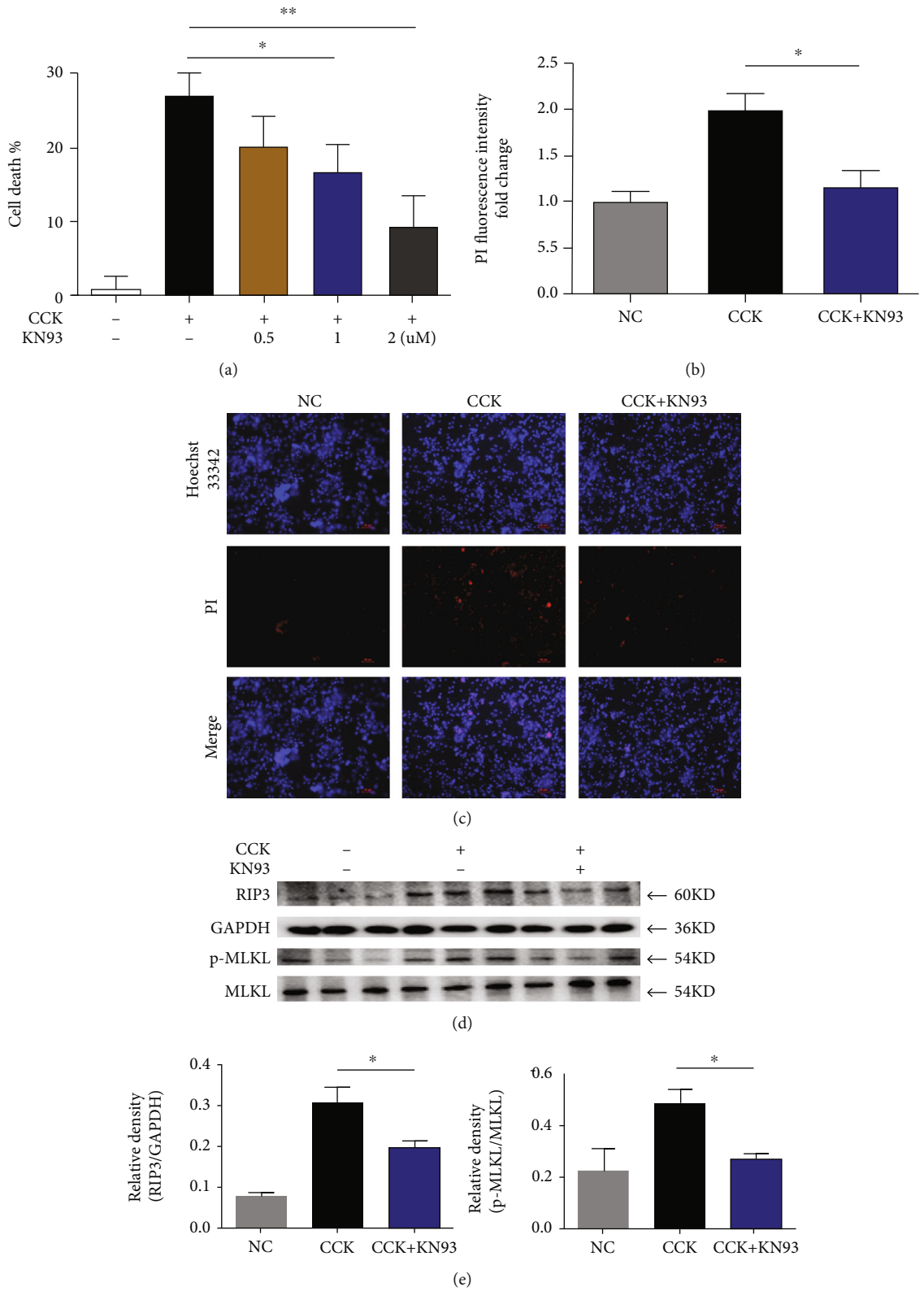

FIGURE 6: The protective effect of KN93 on pancreatic acinar cells in vitro. Freshly isolated mouse pancreatic acinar cells received prior incubation with KN93 only for 30 min. Then, cells were incubated with cholecystokinin (CCK; 1 μM) for 1 h. (a) The relative cell death level of pancreatic acinar cells. (b) Cells were further stained with Hoechst 33342 and propidium iodide (PI) for determination of cell death by epifluorescence microscopy (100x). Scar bar = 50 μM. (c) Densitometric analysis of PI fluorescence. (d) Protein levels of RIP3 and p-MLKL in pancreatic acinar cells were analyzed by Western blotting. (e) Relative protein expression GAPDH and MLKL were used as control for protein loading, respectively. $^{*}P < 0.05$ and $^{**}P < 0.01$. CCK: cholecystokinin octapeptide.

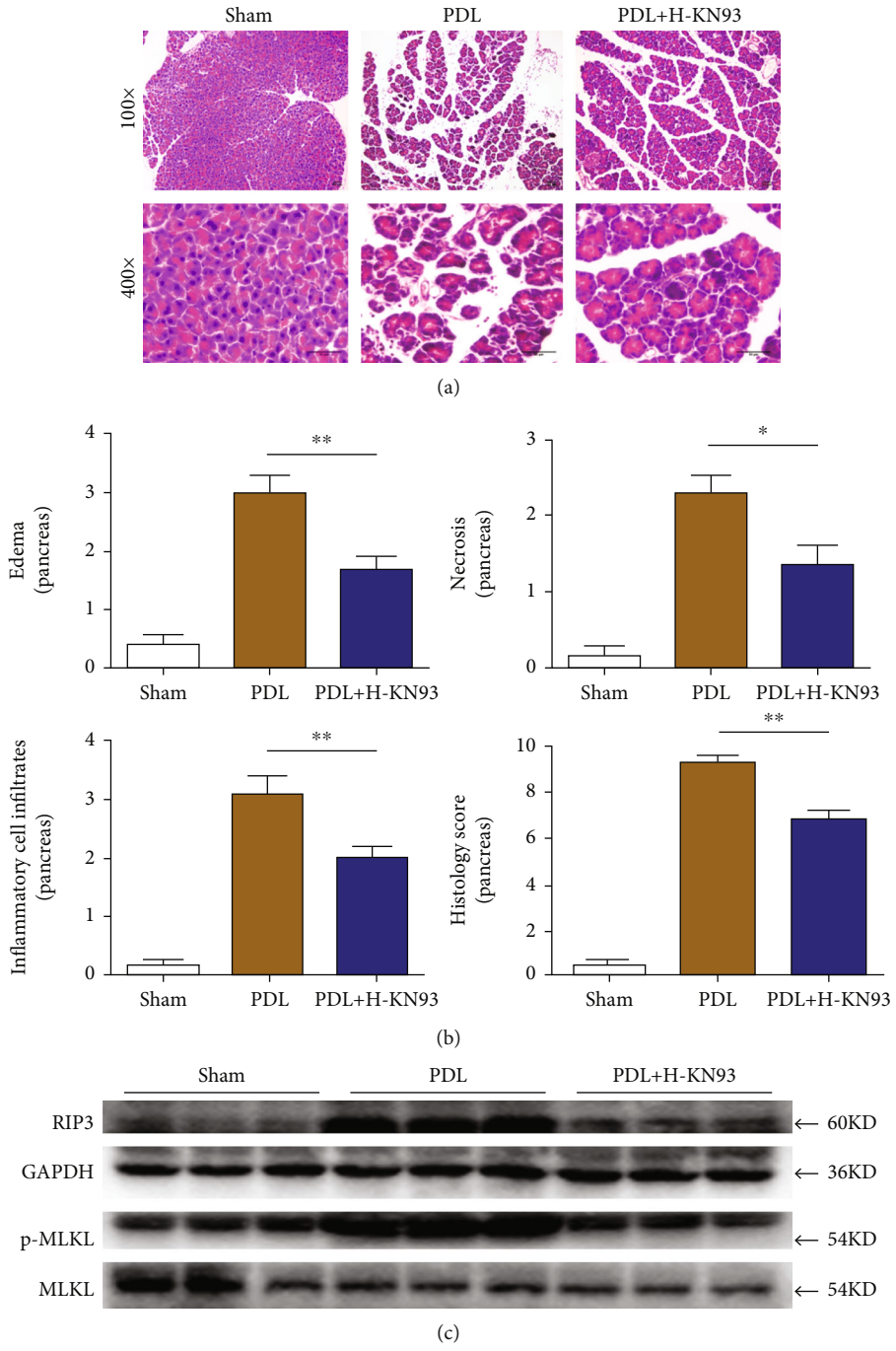

Figure 7: Continued.

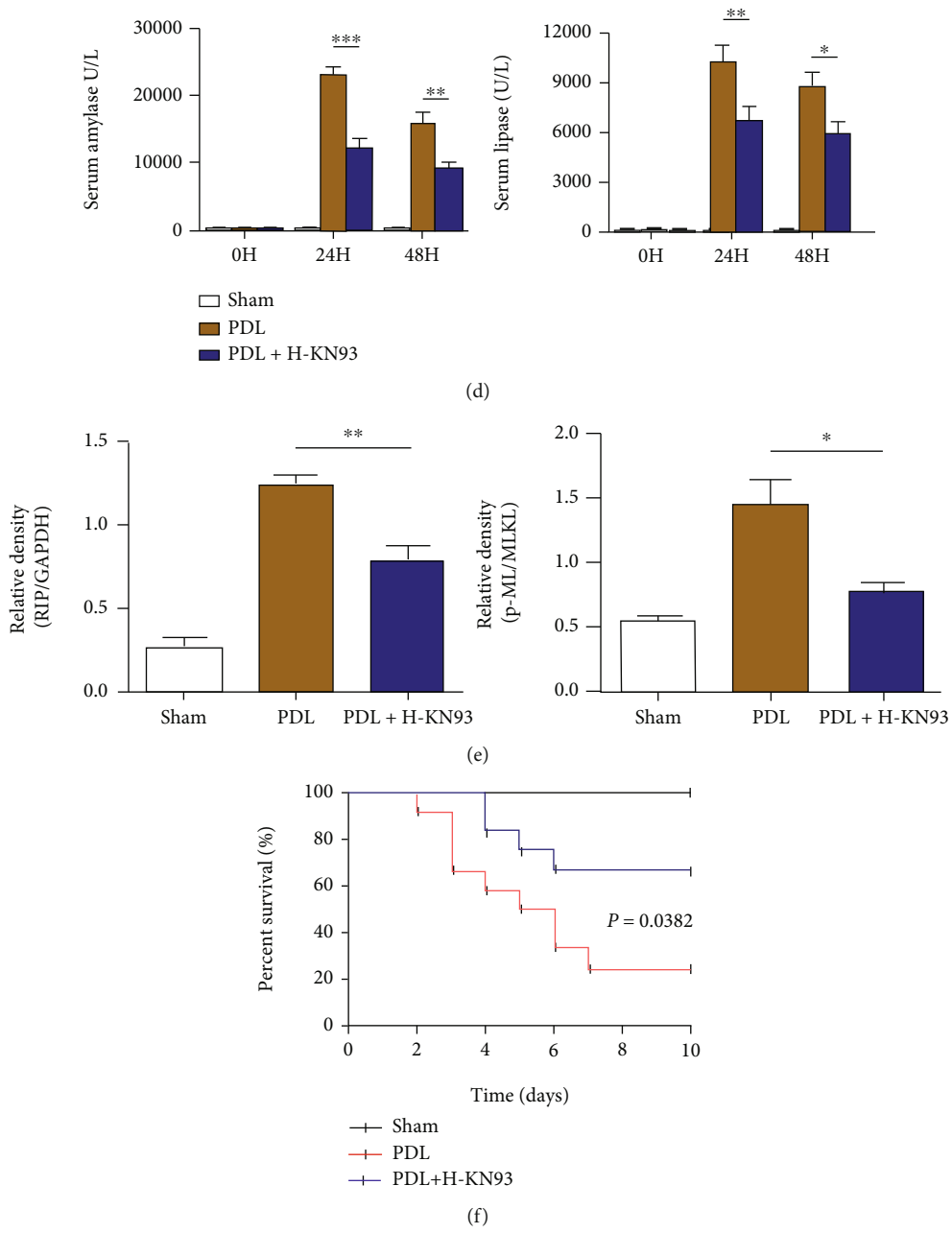

Figure 7: KN93 mitigated the severity of PDL-induced AP and prolonged survival of mice. (a) Representative HE staining of pancreas in SAP model induced by PDL in magnifications 100x and 400x. Scar bar = 50 μM. (b) Histological scores of pancreas in SAP model induced by PDL. (c) Protein levels of RIP3 and p-MLKL in pancreas were analyzed by Western blotting. (d) Serum levels of amylase and lipase in SAP model induced by PDL. (e) Relative protein expression GAPDH and MLKL were used as control for protein loading, respectively. (f) For survival studies, KN93 was applied to PDL mice 1 day to 4 days after surgery and survivorship curve of mice in SAP model induced by PDL. $N = 12$ each group. $^{*}P < 0.05$, $^{**}P < 0.01$, and $^{***}P < 0.001$. PDL: pancreatic duct ligation. H represents high-dose KN93 (20 mg/kg).

myocardial infarction, and oligodendrocyte death [34–36]. Moreover, it is clear that KN93, as a reversible and competitive inhibitor of CaMK II, has been involved in reducing cell necroptosis in several contexts, such as osteoclast genesis and cerebral arteries [37, 38]. In the present study, the role of CaMK II in AP was confirmed. We demonstrated that the expression of CaMK II was significantly upregulated in the pancreas of AP mice and in injured acinar cells (both in the 266-6 cell line and in primary pancreatic acinar cells). Thereafter, the protective effect of KN93 on AP acinar cell necrosis was verified both in vivo and in vitro. All of these results indicated that CaMK II participated in pancreatic acinar cell necroptosis and that inhibition of the activation of CaMK II may be a new clinical target for the prevention and treatment of AP.

Recent studies have shown that the pathways regulating necroptosis are important in injured cells affected by inflammatory diseases, and the RIP3-MLKL-containing necrosis

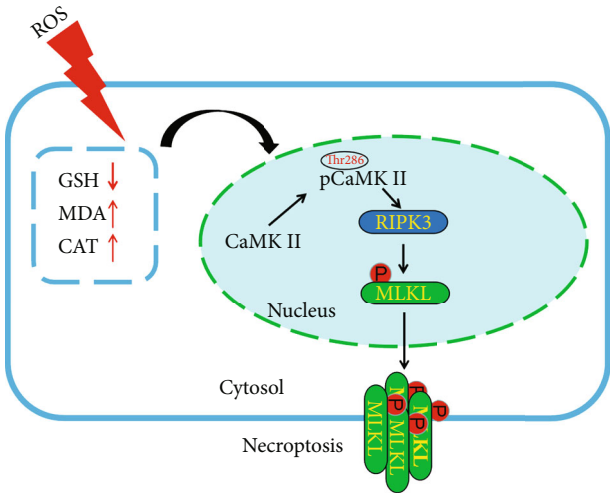

Figure 8: The mechanisms of CaMK II in damaged pancreatic tissues on AP mice.

death complex (necrosome) is considered a key marker of the necrosis pathway [39, 40]. RIP3 or MLKL knockout mice have been shown to have reduced necroptosis of pancreatic tissue in a caerulein-induced AP model compared to wild-type mice [17, 18]. CaMK II is a RIP3/MLKL substrate and delineates the myocardial and intracerebral hemorrhage necroptosis pathways [9, 41]. However, the role of CaMK II activation and its involvement in cell death-related pathway in AP was still unclear. In this study, we found that the production of ROS and the expression of RIP3 and p-MLKL were significantly upregulated in the pancreas of mice with caerulein-induced AP, and these phenomena were blocked by KN93 intervention. We observed the same protective effect in vitro (two cell lines), which was consistent with the results of the above animal experiments. All data show that CaMKII plays a crucial role in the occurrence and progression of AP by mediating necroptosis in acinar cells.

It is well known that pancreatic necrosis is a risk factor for a poor prognosis of AP patients. The mortality of patients without pancreatic necrosis is only 2%, while that of patients with pancreatic necrosis is as high as 5-30% [9]. Accordingly, a decrease in mortality is a key indicator to explore the protective effects of drugs in basic AP studies. In the present study, a mouse model of SAP was established by PDL, accompanied by massive pancreatic necrosis and significant mortality. A clear phenomenon was observed in which the mortality of SAP mice decreased significantly after KN93 treatment, which is consistent with the result that KN93 protected against acute phase injury in AP. The mortality data further verified the protective effect of KN93 against AP.

5. Conclusion

In summary, our findings demonstrated that CaMK II plays an important role in AP and that inhibiting CaMK II may protect against AP by reducing the generation of ROS and modulating the necroptosis pathway (Figure 8).

Data Availability

Our manuscript did not have publicly available data.

Conflicts of Interest

All authors of this paper have no conflicts of interest to disclose.

Authors' Contributions

Qingtian Zhu, Lu Hao, and Qinhao Shen contributed equally to this work.

Acknowledgments

This study was supported by the National Natural Science Foundation of China (No. 82000608; No. 82070668; No. 81801970), the Social development projects of Yangzhou (No. YZ2018091), the Major public health projects in Yangzhou: Screening projects of early gastrointestinal diseases (2018), and the National Natural Science Foundation of Yangzhou (No. 2018YXZX20184, Gastroenterology).

Supplementary Materials

Supplementary Figure 1: dynamic changes of pathobiology and serum enzymology on AP mice induced by caerulein. (A) Histological scores of pancreas in AP model induced by caerulein. (B) Serum levels of amylase and lipase in AP model. Supplementary Figure 2: KN93 had no toxic side effects on mice. (A) Representative HE staining of pancreas, heart, lung liver, and kindey in magnifications 100x and 400x. Scar bar=50 μM. (B) Serum levels of amylase and lipase. N=6 each group. H represent high-dose KN93 (20 mg/kg). Supplementary Figure 3: KN93 attenuated pancreatic-associated lung injury of mice with PDL-induced AP. (A) Representative HE staining of pancreas in SAP model induced by PDL in magnifications 100x and 400x. Scar bar=50 μM. (B) Histological scores of lungs in SAP model induced by PDL. N=12 each group. $^{*}P < 0.05$ and $^{**}P < 0.01$. PDL: pancreatic duct ligation. H: high-dose KN93 (20 mg/kg). *(Supplementary Materials)*

References

[1] P. G. Lankisch, M. Apte, and P. A. Banks, "Acute pancreatitis," *Lancet*, vol. 386, no. 9988, pp. 85–96, 2015.

[2] Y. C. Chan and P. S. Leung, "Acute pancreatitis: animal models and recent advances in basic research," *Pancreas*, vol. 34, no. 1, pp. 1–14, 2007.

[3] J. A. Greenberg, J. Hsu, M. Bawazeer et al., "Clinical practice guideline: management of acute pancreatitis," *Canadian Journal of Surgery*, vol. 59, no. 2, pp. 128–140, 2016.

[4] P. K. Garg and V. P. Singh, "Organ failure due to systemic injury in acute pancreatitis," *Gastroenterology*, vol. 156, no. 7, pp. 2008–2023, 2019.

[5] M. Portelli and C. D. Jones, "Severe acute pancreatitis: pathogenesis, diagnosis and surgical management," *Hepatobiliary*

& Pancreatic Diseases International, vol. 16, no. 2, pp. 155–159, 2017.

[6] T. Y. Chua, R. M. Walsh, M. E. Baker, and T. Stevens, "Necrotizing pancreatitis: diagnose, treat, consult," *Cleveland Clinic Journal of Medicine*, vol. 84, no. 8, pp. 639–648, 2017.

[7] B. Li, N. Yang, C. Li et al., "INT-777, a bile acid receptor agonist, extenuates pancreatic acinar cells necrosis in a mouse model of acute pancreatitis," *Biochemical and Biophysical Research Communications*, vol. 503, no. 1, pp. 38–44, 2018.

[8] G. Lu, Z. Tong, Y. Ding et al., "Aspirin protects against acinar cells necrosis in severe acute pancreatitis in mice," *BioMed Research International*, vol. 2016, Article ID 6089430, 10 pages, 2016.

[9] T. Zhang, Y. Zhang, M. Cui et al., "CaMKII is a RIP3 substrate mediating ischemia- and oxidative stress-induced myocardial necroptosis.[J]," *Nature Medicine*, vol. 22, no. 2, pp. 175–182, 2016.

[10] X. Li, S. Cheng, H. Hu et al., "Progranulin protects against cerebral ischemia-reperfusion (I/R) injury by inhibiting necroptosis and oxidative stress," *Biochemical and Biophysical Research Communications*, vol. 521, no. 3, pp. 569–576, 2020.

[11] S. Li, L. G. Ning, X. H. Lou, and G. Q. Xu, "Necroptosis in inflammatory bowel disease and other intestinal diseases," *World Journal of Clinical Cases*, vol. 6, no. 14, pp. 745–752, 2018.

[12] Y. Wang, J. Liu, J. S. Zhou et al., "MTOR suppresses cigarette smoke–induced epithelial cell death and airway inflammation in chronic obstructive pulmonary disease," *Journal of Immunology*, vol. 200, no. 8, pp. 2571–2580, 2018.

[13] J. Louhimo, M. L. Steer, and G. Perides, "Necroptosis is an important severity determinant and potential therapeutic target in experimental severe pancreatitis," *Cellular and Molecular Gastroenterology and Hepatology*, vol. 2, no. 4, pp. 519–535, 2016.

[14] R. Kang, M. T. Lotze, H. J. Zeh, T. R. Billiar, and D. Tang, "Cell death and DAMPs in acute pancreatitis," *Molecular Medicine*, vol. 20, no. 1, pp. 466–477, 2014.

[15] Y. R. Su, Y. P. Hong, F. C. Mei et al., "High-fat diet aggravates the intestinal barrier injury via TLR4-RIP3 pathway in a rat model of severe acute pancreatitis," *Mediators of Inflammation*, vol. 2019, 13 pages, 2019.

[16] X. Zhou, L. Xie, L. Xia et al., "RIP3 attenuates the pancreatic damage induced by deletion of ATG7," *Cell Death & Disease*, vol. 8, no. 7, article e2918, 2017.

[17] J. Wu, Z. Huang, J. Ren et al., "Mlkl knockout mice demonstrate the indispensable role of Mlkl in necroptosis," *Cell Research*, vol. 23, no. 8, pp. 994–1006, 2013.

[18] K. Newton, D. L. Dugger, A. Maltzman et al., "RIPK3 deficiency or catalytically inactive RIPK1 provides greater benefit than MLKL deficiency in mouse models of inflammation and tissue injury," *Cell Death and Differentiation*, vol. 23, no. 9, pp. 1565–1576, 2016.

[19] H. Satsu, M. Manabe, and M. Shimizu, "Activation of Ca2+/calmodulin-dependent protein kinase II is involved in hyperosmotic induction of the human taurine transporter," *FEBS Letters*, vol. 569, no. 1-3, pp. 123–128, 2004.

[20] A. Ikeda, S. Okuno, and H. Fujisawa, "Studies on the generation of Ca2+/calmodulin-independent activity of calmodulin-dependent protein kinase II by autophosphorylation. Autothiophosphorylation of the enzyme," *Journal of Biological Chemistry*, vol. 266, no. 18, pp. 11582–11588, 1991.

[21] M. R. Rusciano, E. Sommariva, V. Douin-Echinard, M. Ciccarelliv, P. Poggio, and A. S. Maione, "CaMKII activity in the inflammatory response of cardiac diseases," *International Journal of Molecular Sciences*, vol. 20, no. 18, p. 4374, 2019.

[22] S. Lu, Z. Liao, X. Lu et al., "Hyperglycemia acutely increases cytosolic reactive oxygen species viaO-linked GlcNAcylation and CaMKII activation in mouse ventricular myocytes," *Circulation Research*, vol. 126, no. 10, pp. e80–e96, 2020.

[23] G. Zalcman, N. Federman, and A. Romano, "CaMKII isoforms in learning and memory: localization and function," *Frontiers in Molecular Neuroscience*, vol. 11, p. 445, 2018.

[24] Z. Yang, C. Li, Y. Wang et al., "Melatonin attenuates chronic pain related myocardial ischemic susceptibility through inhibiting RIP3-MLKL/CaMKII dependent necroptosis," *Journal of Molecular and Cellular Cardiology*, vol. 125, pp. 185–194, 2018.

[25] X. Yang, N. Wu, L. Song, and Z. Liu, "Intrastriatal injections of KN-93 ameliorates levodopa-induced dyskinesia in a rat model of Parkinson's disease," *Neuropsychiatric Disease and Treatment*, vol. 9, pp. 1213–1220, 2013.

[26] Y. Liu, Y. Liang, B. Hou et al., "The inhibitor of calcium/calmodulin-dependent protein kinase II KN93 attenuates bone cancer pain via inhibition of KIF17/NR2B trafficking in mice," *Pharmacology, Biochemistry, and Behavior*, vol. 124, pp. 19–26, 2014.

[27] Y. Wen, C. Han, T. Liu et al., "Chaiqin chengqi decoction alleviates severity of acute pancreatitis via inhibition of TLR4 and NLRP3 inflammasome: identification of bioactive ingredients via pharmacological sub-network analysis and experimental validation," *Phytomedicine*, vol. 79, p. 153328, 2020.

[28] Y. Yamaguchi, K. Matsuno, M. Goto, and M. Ogawa, "In situ kinetics of acinar, duct, and inflammatory cells in duct ligation-induced pancreatitis in rats," *Gastroenterology*, vol. 104, article 1498e1506, 1993.

[29] Q. Zhu, X. Lin, X. Liu et al., "Dynamic changes of proteasome and protective effect of bortezomib, a proteasome inhibitor, in mice with acute pancreatitis," *Biochemical and Biophysical Research Communications*, vol. 505, no. 1, pp. 126–133, 2018.

[30] A. Djordjevic, S. Spasic, A. Jovanovic-Galovic, R. Djordjevic, and G. Grubor-Lajsic, "Oxidative stress in diabetic pregnancy: SOD, CAT and GSH-Px activity and lipid peroxidation products," *The Journal of Maternal-Fetal Medicine*, vol. 16, no. 6, pp. 367–372, 2004.

[31] J. Wu, R. Zhang, G. Hu, H. H. Zhu, W. Q. Gao, and J. Xue, "Carbon monoxide impairs CD11b(+)Ly-6C(hi) monocyte migration from the blood to inflamed pancreas via inhibition of the CCL2/CCR2 axis [J]," *Journal of Immunology Official Journal of the American Association of Immunologists*, vol. 200, no. 6, pp. 2104–2114, 2018.

[32] X. Zhan, J. Wan, G. Zhang et al., "Elevated intracellular trypsin exacerbates acute pancreatitis and chronic pancreatitis in mice," *American Journal of Physiology. Gastrointestinal and Liver Physiology*, vol. 316, no. 6, pp. G816–G825, 2019.

[33] X. Liu, Q. Zhu, Z. Min et al., "Isoliquiritigenin Ameliorates Acute Pancreatitis in Mice via Inhibition of Oxidative Stress and Modulation of the Nrf2/HO-1 Pathway," *Oxidative Medicine and Cellular Longevity*, vol. 2018, 12 pages, 2018.

[34] T. Suetomi, S. Miyamoto, and J. H. Brown, "Inflammation in nonischemic heart disease: initiation by cardiomyocyte CaMKII and NLRP3 inflammasome signaling," *AJP Heart and Circulatory Physiology*, vol. 317, no. 5, pp. H877–H890, 2019.

[35] B. Cai, C. Kasikara, A. C. Doran, R. Ramakrishnan, R. B. Birge, and I. Tabas, "MerTK signaling in macrophages promotes the synthesis of inflammation resolution mediators by suppressing CaMKII activity," *Science Signaling*, vol. 11, no. 549, article eaar3721, 2018.

[36] L. Edvinsson, G. Povlsen, H. Ahnstedt, and R. Waldsee, "CaMKII inhibition with KN93 attenuates endothelin and serotonin receptor-mediated vasoconstriction and prevents subarachnoid hemorrhage-induced deficits in sensorimotor function," *Journal of Neuroinflammation*, vol. 11, no. 1, p. 207, 2014.

[37] Y. Fu, D. Niu, W. Su et al., "Effects of Ca2+/calmodulin-dependent protein kinase pathway inhibitor KN93 on osteoclastogenesis," *International Journal of Molecular Medicine*, vol. 42, no. 4, pp. 2294–2302, 2018.

[38] J. M. Murphy, P. E. Czabotar, J. M. Hildebrand et al., "The Pseudokinase MLKL Mediates Necroptosis via a Molecular Switch Mechanism," *Immunity*, vol. 39, no. 3, pp. 443–453, 2013.

[39] J. Zhang, Y. Yang, W. He, and L. Sun, "Necrosome core machinery: MLKL," *Cellular and Molecular Life ences CMLS*, vol. 73, no. 11-12, pp. 2153–2163, 2016.

[40] Y. Xu, X. Wu, W. Hu et al., "RIP3 facilitates necroptosis through CaMKII and AIF after intracerebral hemorrhage in mice," *Neuroscience Letters*, vol. 749, p. 135699, 2021.

[41] C. E. Forsmark, S. Swaroop Vege, and C. M. Wilcox, "Acute pancreatitis," *New England Journal of Medicine*, vol. 375, no. 20, pp. 1972–1981, 2016.

Hindawi
Oxidative Medicine and Cellular Longevity
Volume 2021, Article ID 1118981, 18 pages
https://doi.org/10.1155/2021/1118981

Research Article

Irisin Rescues Blood-Brain Barrier Permeability following Traumatic Brain Injury and Contributes to the Neuroprotection of Exercise in Traumatic Brain Injury

Peipei Guo,[1,2] Zhao Jin,[2] Jin Wang,[2] Aming Sang,[2] and Huisheng Wu[1,2]

[1]*Department of Anesthesiology, The First Affiliated Hospital of Anhui Medical University, Hefei City, Anhui Province 230022, China*
[2]*Department of Anesthesiology, Zhongnan Hospital of Wuhan University, Wuhan City, Hubei Province 430071, China*

Correspondence should be addressed to Huisheng Wu; zn000482@whu.edu.cn

Peipei Guo and Zhao Jin contributed equally to this work.

Received 13 May 2021; Revised 21 August 2021; Accepted 28 September 2021; Published 16 October 2021

Academic Editor: Xiaoyuan Zhou

Traumatic brain injury (TBI) has a high incidence, mortality, and morbidity all over the world. One important reason for its poor clinical prognosis is brain edema caused by blood-brain barrier (BBB) dysfunction after TBI. The mechanism may be related to the disorder of mitochondrial morphology and function of neurons in damaged brain tissue, the decrease of uncoupling protein 2 (UCP2) activity, and the increase of inflammatory reaction and oxidative stress. In this study, we aimed to investigate the effects of exogenous irisin on BBB dysfunction after TBI and its role in the neuroprotective effects of endurance exercise (EE) in mice. The concentrations of irisin in cerebrospinal fluid (CSF) and plasma of patients with mild to severe TBI were measured by ELISA. Then, male C57BL/6J mice and UCP2 knockout mice with C57BL/6J background were used to establish the TBI model. The BBB structure and permeability were examined by transmission electron microscopy and Evans blue extravasation, respectively. The protein expressions of irisin, occludin, claudin-5, zonula occludens-1 (ZO-1), nuclear factor E2-related factor 2(Nrf2), quinine oxidoreductase (NQO-1), hemeoxygenase-1 (HO-1), cytochrome C (Cyt-C), cytochrome C oxidase (COX IV), BCL2-associated X protein (Bax), cleaved caspase-3, and UCP2 were detected by western blot. The production of reactive oxygen species (ROS) was evaluated by the dihydroethidium (DHE) staining. The levels of inflammatory factors were detected by ELISA. In this study, we found that the CSF irisin levels were positively correlated with the severity of disease in patients with TBI and both EE and exogenous irisin could reduce BBB damage in a mouse model of TBI. In addition, we used $UCP2^{-/-}$ mice and further found that irisin could improve the dysfunction of BBB after TBI by promoting the expression of UCP2 on the mitochondrial membrane of neurons, reducing the damage of mitochondrial structure and function, thus alleviating the inflammatory response and oxidative stress. In conclusion, the results of this study suggested that irisin might alleviate brain edema after TBI by promoting the expression of UCP2 on the mitochondrial membrane of neurons and contribute to the neuroprotection of EE against TBI.

1. Introduction

The huge advances in society, economy, transportation, and infrastructure have produced an increasingly convenient life, while resulted in people's higher probability of developing trauma [1, 2]. Accordingly, the incidence of traumatic brain injury (TBI) has been annually rising worldwide and remains at a continuingly high level. TBI, a common emergent and critical illness in clinic, bears an extremely high risk for disability and mortality and has an inadequately satisfying clinical prognosis. One of the main causes for a series of adverse outcomes is brain edema which is not only a consequence of TBI but also a major factor for further aggravating TBI damage [3].

TBI can destroy tight junction (TJ) proteins, the main structure of the blood-brain barrier (BBB), and cause the apoptosis of cerebrovascular endothelial cells. This allows substances that could not have access to the brain tissue to

quickly permeate into it in large quantities, so that fluids accumulate in the extracellular space, resulting in vasogenic brain edema [4, 5]. The mechanism may be that reactive oxygen species (ROS) increase after TBI, which leads to neuroinflammatory response and oxidative stress response [6]. Meanwhile, the mitochondrial membrane potential (MMP) is a significant factor accounting for the increase of ROS levels, so MMP, to some extent, is positively correlated with ROS [7]. Recently, there is increasing evidence that uncoupling protein 2 (UCP2) can dramatically reduce the production of ROS by reducing MMP [8]. The "uncoupling survival" hypothesis related to UCP2 has been further confirmed in the traumatic brain injury model [9].

It is well-established that endurance exercise (EE) can effectively exert neuroprotective effects [10–13] but the underlying mechanism has remained to be elucidated. Exercised skeletal muscle can secrete PGC-1α, and downstream factors regulated by this protein can be sheared and modified to form a hormone called irisin. Irisin has been a focus of recent studies in the fields of metabolism and the nervous system [12, 14]. Our previous research has demonstrated that irisin worked effectively on alleviating cerebral ischemia-reperfusion injury [15]. Thus in this study, we tested whether irisin could reduce brain edema after TBI and explored its specific mechanisms. In addition, we also observed whether the neuroprotective effects of EE were related to irisin.

2. Materials and Methods

2.1. Clinical Study on Patients with TBI. A total of 16 adult patients with mild to severe TBI (GCS 9-15 points) were recruited from the Department of Neurosurgery at Zhongnan Hospital of Wuhan University. They were all qualified for the strict criteria for inclusion and exclusion. Samples of cerebrospinal fluid (CSF) and plasma from TBI patients were collected. The concentrations of irisin in CSF and plasma were measured by ELISA. The severity of TBI in patients at different stages was evaluated by the Glasgow coma scale (GCS), which mainly evaluated the degree of coma and trauma in terms of eye-opening response, verbal response, and limb movement. The total score is the sum of those three scores, and the highest is 15, indicating clear consciousness. A lower score is an indicator for more severe brain injury, closely related to the degree of cerebral edema [16].

All clinical procedures were performed following the protocol approved by the Ethics Committee of Zhongnan Hospital of Wuhan University, and the informed consent of all participants and legal guardians was obtained (registration number: ChiCTR1900025962, ethics batch number: 2018008).

2.2. Animals. Three-month-old adult male C57BL/6J mice and UCP2 knockout mice with C57BL/6J background, weighing 19-23 g, were all purchased from Saiye Biotechnology Company. The UCP2 knockout mice were the global knockout model. Before the experiment, mice were placed in the same environment for more than 3 days where the temperature was 20-25°C and the light/dark cycle was 12 h. They were allowed to take in food and water freely. All experimental operations were approved by the Animal Care and Use Committee of Wuhan University, in line with the guidelines of the National Institutes of Health Laboratory Animal Care and Use Guidelines.

2.3. Endurance Exercise. Motor treadmill (electric treadmill) exercise was adopted in this study to better simulate human exercise patterns. The mice exercised 5 days a week (Monday, Tuesday, Thursday, Friday, and Saturday). The protocol of exercise for the first week was as follows: 6 m/min × 30 min × 2 d, 8 m/min × 30 min × 2 d, 10 m/min × 30 min × 1 d. The protocol of daily exercise for the following 6 weeks was as follows: 6 m/min × 10 min + 8 m/min × 15 min + 10 m/min × 15 min + 8 m/min × 10 min + 6 m/min × 10 min. Daily exercise time of mice was restricted to 15 : 00-17 : 00 to prevent the interference of the circadian rhythm and the rhythm of the time point.

2.4. TBI Model. The controlled cortical impact (CCI) method was employed and slightly adjusted in our study to set up the TBI model, which is following the existing literature [17, 18]. Briefly, after 8 h preoperative fasting but free access to water drinking, mice were anesthetized with an intraperitoneal injection of 1.5% pentobarbital sodium 50 mg/kg. Then, the mice's skull skin was disinfected, and the tops of the right skulls were cut to reveal the junction of the sagittal suture and the coronal suture. Next, the periosteum was scraped, and a bone window with a diameter of about 4 mm was drilled at a distance of 2 mm from the sagittal suture and the coronal suture. The mice were then fixed on the base of the eCCI electronic craniocerebral injury instrument (RWD Life Science Co., Ltd.), receiving 120 ms' mild to moderate TBI impact with parameters set at 4 m/s speed and 2 mm depth. Meanwhile, in the Sham operation group, only the bone window was established and no operation was performed. Then, the bone fragments and the skin were sutured. Finally, the mice were reared in separate cages under ventilation and natural light.

2.5. Experimental Groups. Mice were randomly divided into six groups: (1) Sham group, a control group that subjected to sham operation; (2) TBI group, a TBI group that underwent mild to moderate TBI impact with parameters set at 4 m/s speed and 2 mm depth; (3) irisin-treated group (Ir), and Ir group that was injected with 10 μg/kg irisin intravenously immediately after TBI impact; (4) EE group, an EE group that underwent 5 weeks of physical exercise before TBI impact; (5) EE/IgG-treated group (EE+IgG), an EE+IgG group that underwent 5 weeks of physical exercise before TBI impact and then injected with nonimmune control IgG intravenously; and (6) EE/NA-treated group (EE+NA), an EE+NA (neutralizing antibody) group that underwent 5 weeks of physical exercise before TBI impact and then injected with neutralizing antibody against irisin intravenously (20 μg per mouse, Phoenix Pharmaceuticals).

2.6. Analysis of Mice's Weight and Survival Rate. When the TBI models of mice in the four groups (Sham group, TBI

group, EE group, and Ir group) were successfully constructed, all mice were normally raised in an open and ventilated environment. The deaths of them were all spontaneous, and no euthanasia was performed. Death was defined as the following: the mouse had cardiac arrest, the collapse of the left atrium, and simple convulsions. A researcher who was unclear about the specific grouping observed the survival of the mice once a day. He timely kept records of deaths when observing the weight, the modified neurological severity score (mNSS), brain water content, and other indicators of mice at the corresponding time points.

2.7. Modified Neurological Severity Score. The modified neurological severity score (mNSS), commonly used in neurobehavioral evaluation after TBI, mainly detects mice's exercise ability, balance ability, alertness, and the like. Its score range is 0-18 points, and the score is in positive proportion to the severity of neurological damage. The test, carried out by a researcher who was unclear about the specific grouping, was on the day before TBI and 1, 3, 7, and 14 days after TBI. All mice in each group were tested for their neurological function, and they had been properly trained before modeling to adapt to this test.

2.8. Determination of Brain Water Content and Evans Blue (EB) Content. The brain water content was determined by the dry and wet weight method. The mice were decapitated, and the brains were collected 24 h after TBI. The brain was immediately weighed as wet weight and then was placed in a 110°C oven for 24 h and weighed for the dry weight. Brain water content (%) equals (wet weight − dry weight)/ wet weight × 100%.

To determine the EB content, EB physiological saline solution was injected through the femoral vein 1 h before the mice were sacrificed. The injection was indicated successful when the eyeball conjunctiva and limbs all showed blue, and then, cardiac perfusion was performed after 1 h of circulation. After deep anesthesia, the left ventricles of the mice were perfused with normal saline to the right atrial appendage till clear liquids flowed out. The mice were decapitated, and the brain was collected, made into frozen sections, and immediately placed under an inverted fluorescence microscope with blue excitation light to observe the leakage of EB. A fluorescence spectrophotometer was used to measure the content of EB in brain tissue.

2.9. Immunohistochemistry. The paraffin sections (5 μm thick) of mouse brain tissue were roasted overnight at 37°C and deparaffinized and incubated with 3% hydrogen peroxide for 15 min. After the thermal repair of the tissue antigens by microwave, the slices were cooled for 30 min at room temperature and incubated with rabbit anti-irisin antibodies (1 : 500; Phoenix Pharmaceuticals). Then, the protein expression of irisin was observed after biotin-labeled secondary antibodies, goat anti-rabbit IgG (1 : 100; KPL) incubation. Ten fields of each slice were observed under a light microscope (×400) by a blind pathologist. The integrated optical density (IOD) was measured by an Image-Pro Plus analysis system. The protein expression intensity was positively correlated with IOD.

2.10. DHE Staining. A frozen section of the brain tissue isolated from mice in different groups was incubated with dihydroethidium (DHE) which was diluted with PBS (10^{-5} M) at 37°C for 40 min and fixed with paraformaldehyde for 10 min. Then, DAPI staining solution was used to stain the nucleus for 10 min. Finally, the images were observed using a fluorescence microscope at an excitation wavelength of 490 nm and an emission wavelength of 590 nm, under which the blue-stained part was the nucleus, and the green fluorescence reflected the ROS content. The exposure time used for image acquisition of all sections was 30 ms. The DHE fluorescence intensity was quantified by ImageJ.

2.11. Western Blot. Briefly, the total proteins from the damaged brain tissue or blood were extracted by centrifugation at 4°C for 10 minutes. Then, the proteins were separated by SDS-polyacrylamide gel electrophoresis onto the nitrocellulose membrane and buffered and blocked with skimmed milk powder at room temperature for 1 h. The membranes were incubated with the rabbit anti-irisin antibody (1 : 1000; Abcam), the rabbit anti-occludin antibody (1 : 1000; CST), the rabbit anti-claudin-5 antibody (1 : 1000; Abcam), the rabbit anti-zonula occludens-1 (ZO-1) antibody (1 : 1000; CST), the rabbit anti-nuclear factor E2-related factor 2 (Nrf2) antibody (1 : 1000; CST), the mouse anti-quinine oxidoreductase (NQO-1) antibody (1 : 1000; CST), the rabbit anti-hemeoxygenase-1 (HO-1) antibody (1 : 1000; CST), the rabbit anti-cytochrome C (Cyt-C) antibody (1 : 1000; CST), the rabbit anti-cytochrome C oxidase (COX IV) antibody (1 : 1000; CST), the rabbit anti-BCL2-associated X protein (Bax) antibody (1 : 1000; CST), the rabbit anti-cleaved caspase-3 antibody (1 : 1000; Abcam), and the rabbit anti-uncoupling protein 2 (UCP2) antibody (1 : 1000; CST) at 4°C overnight. After being washed with TBST, the membranes were incubated with the secondary anti-rabbit or anti-mouse IgGs (1 : 50000; KPL) at room temperature for 30 min. Optical density analysis for quantification was performed on the ImageJ software (NIH).

2.12. ELISA. The levels of irisin in the plasma and CSF of patients with TBI were measured at 2 and 7 days after injury following the manufacturer's instructions of the ELISA kit (Boster Co., Ltd, Wuhan). At different time points, the levels of irisin, malondialdehyde (MDA), superoxide dismutase (SOD), and glutathione peroxidase (GSH-PX) in the brain tissue of mice and the levels of inflammatory factors (TNF-α, IL-1β, IL-4, and IL-10) in plasma and brain tissue of mice were detected by ELISA (Boster Co., Ltd., Wuhan).

2.13. Transmission Electron Microscope. 24 h after TBI, the mice were sacrificed under deep anesthesia. The brain tissue was quickly removed from the ice dish, and the damaged brain tissue was selected. The tissue was then fixed with 2% paraformaldehyde and 2.5% glutaraldehyde at 4°C for 2 h, rinsed 3 times with sodium arsenate buffer (pH 7.2) for about 10 min, fixed with 1% osmium acid (OsO4) at 4°C for 2 h, and rinsed again with double distilled water 3 times

for about 10 min. After that, gradient alcohol dehydration was followed by isoamyl acetate replacement. Finally, the structure of endothelial cells, tight junctions, and neuronal mitochondria reflecting the BBB was observed under the transmission electron microscope (JEM-1011, JEOL).

2.14. Brain Microvascular Extraction, Mitochondrial Extraction, and MMP Determination. The mice were decapitated under deep anesthesia, and the injured part was removed and placed in a petri dish filled with cold phosphate buffer saline (PBS). The cortex was then extracted, cut into 1 mm size, homogenized, filtered through a 41 μm pore size nylon filter, and washed 3 times with PBS. Then, the capillaries on the filter were collected and centrifuged before 15% dextran was added. The ingredients were combined thoroughly and suspended to 20% dextran, and another centrifuge was done to save cerebral capillary sediment at the bottom.

Capillaries were suspended and mixed with 2 ml 0.1% collagenase/dispase (containing 20 U/mL DNase I) and digested in a 37°C water bath for 1 h, centrifuged to remove the supernatant, and added 2 ml of culture medium to form a suspension. Then, they were spread on a 12 mL 50% Percoll solution that formed a continuous gradient after centrifugation. The purified microvascular segment was the white-and-yellow-colored layer above the red blood cell layer near the bottom. The segment was then extracted, rinsed twice with culture medium, and centrifuged. The supernatant was discarded, and the remainder was stored in liquid nitrogen for western blot.

The brain tissue around the lesion was extracted, and the mitochondria in it were separated using a mitochondrial extraction kit (NBP2-29448, NOVUSBIO). The protein concentration of each sample was adjusted to 1 g/L by using mitochondrial preservation solution, and the relative fluorescence unit (RFU) was obtained after detecting the mitochondrial membrane potential (MMP) $\Delta\Psi$m with the help of a fluorescence microplate reader, according to the instructions of the kit (GENMED, USA).

2.15. Statistical Analysis. All data were presented as mean ± SEM. Statistical analysis was carried out using SPSS 20.0 (SPSS Inc., San Rafael, CA, USA) and GraphPad Prism 5.0 (San Diego, CA, USA). Repeated measures analysis of variance (ANOVA) was used for multiple comparisons and analysis among groups, which was followed by Dunnett's post hoc test. The significance of correlations was evaluated by determining Spearman's rank correlation coefficients, and the difference of estimate of cumulative survival (Kaplan–Meier) among groups was evaluated with the log-rank test. Statistical significance was based on unpaired two-tailed Student's t-tests, with $P < 0.05$ indicating statistical significance.

3. Results

3.1. CSF Irisin Levels Were Increased and Positively Correlated with the Recovery of Disease in Patients with TBI. As shown in Figure 1, the plasma irisin levels of TBI patients in the recovery period (7 d after trauma) were slightly lower than that in the early posttraumatic period (2 d after trauma), while the CSF irisin concentrations were significantly increased ($P < 0.05$, Figures 1(a) and 1(b)). In the early posttraumatic period and recovery period, the plasma irisin levels of TBI patients were positively correlated with the CSF irisin concentrations ($P < 0.05$, Figures 1(c) and 1(d)). All these results indicated that the CSF irisin concentrations of patients with TBI were related to their recovery.

Glasgow coma scale (GCS) is one of the most commonly used clinical indicators to assess the degree of trauma in TBI patients. In this study, it was found that the CSF irisin concentrations in TBI patients were positively correlated with GCS score ($P < 0.05$, Figures 1(e) and 1(f)) in the early posttraumatic and recovery period, suggesting that the change of CSF irisin levels may be one of the significant cause for affecting the prognosis of TBI patients.

3.2. Endurance Exercise Can Increase the Level of Irisin in the Brain Tissue of Mice. Western blot was used in our study to observe the level of irisin in the brain tissue of mice with or without TBI after they exercised for a different duration. As shown in Figures 2(a) and 2(b), the brain irisin levels increased continuously during 1-5 w of exercise ($P < 0.05$) and attained the peak at 5 w, with its value being almost 3 times that of nonexercise mice (control group). However, no significant change was found after another 2 w continuing exercise, basically maintaining the peak level and slightly decreasing. This indicated that the irisin level produced by mice in physiological state after 5 w exercise reached the peak, and any more exercise brought no significant increase, so 5 w was the duration of exercise common to all the experiments concerning exercise in our study. In addition, brain irisin levels in mice suffering from TBI were significantly lower than those in the Sham operation group, but after 5 w exercise, such levels were significantly higher than those of mice in the TBI group alone ($P < 0.05$, Figures 2(c)–2(f)). The above results suggested that exercise could increase the secretion of irisin in brain tissue.

3.3. Neuroprotection of Endurance Exercise Can Be Replicated by Application of Exogenous Irisin. It has been reported that endurance exercise exerts a protective effect on TBI, cerebral ischemia-reperfusion injury, and Alzheimer's disease [10–13], and irisin, as an important peptide in the body, can be secreted by skeletal muscle and brain tissue after endurance exercise [19]. This leads our study to observe whether endurance exercise and exogenous irisin have the same neuroprotective effect on TBI.

To test this hypothesis, we first observed the expression of irisin in the brain tissue of mice after exogenous irisin treatment by western blot and immunohistochemistry. As shown in Figures 2(c)–2(f), the brain levels of irisin significantly increased in the Ir groups compared with the TBI group ($P < 0.05$), which indicated that exogenous administration of irisin could promote it to enter the brain tissue.

The TBI model used in this study results in severe damage to mice and thus high mortality, so it is of great

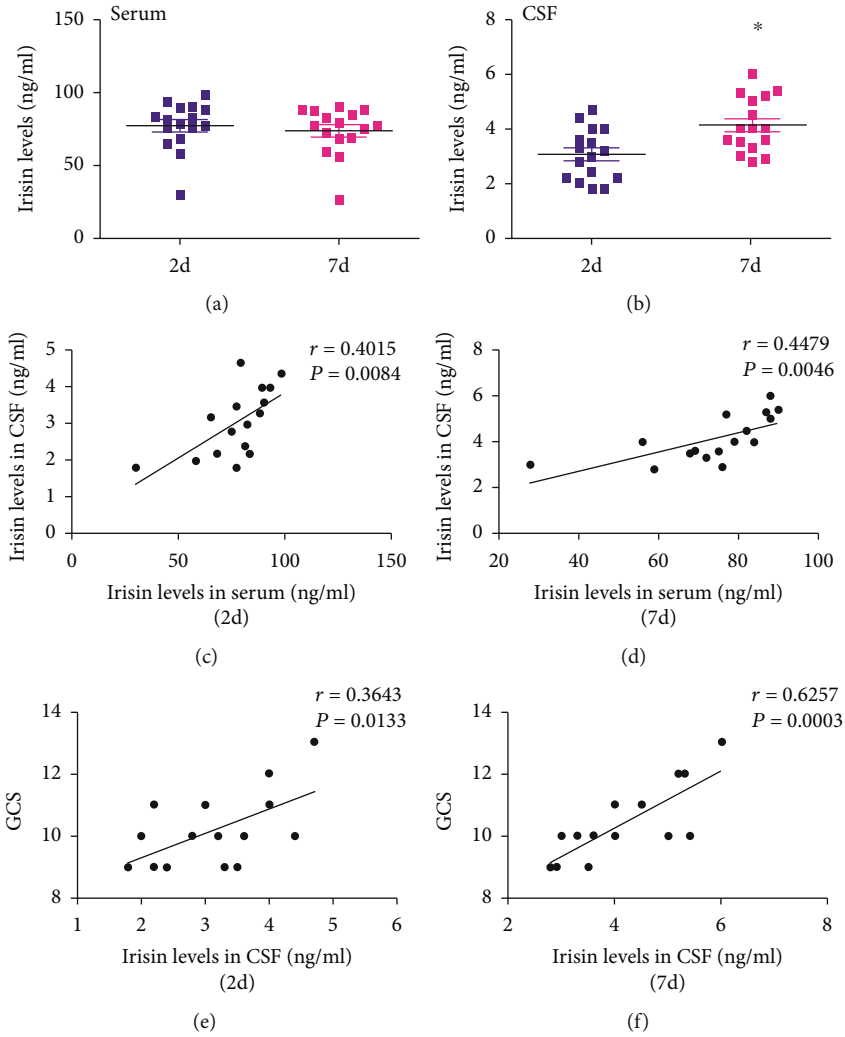

Figure 1: CSF irisin levels were increased and positively correlated with the recovery in patients with TBI. (a) The serum level of irisin was derived from patients who suffered from TBI for 2 days or 7 days. (b) The CSF level of irisin was derived from patients who suffered from TBI for 2 days or 7 days. (c) Correlations between CSF irisin levels and serum irisin levels in patients who suffered from TBI for 2 days. (d) Correlations between CSF irisin levels and serum irisin levels in patients who suffered from TBI for 7 days. (e) Correlations between GCS and CSF irisin levels in patients who suffered from TBI for 2 days. (f) Correlations between GCS and CSF irisin levels in patients who suffered from TBI for 7 days. $n = 16$. The significance of correlations was evaluated by determining Spearman's rank correlation coefficients. $^*P < 0.05$ vs. TBI for 2 days.

significance to observe the survival rate of mice in different groups. As demonstrated in Figure 3(a), the survival rate of mice in the TBI group, EE group, and Ir group was significantly lower than that of the Sham group ($P < 0.05$), while the survival rate of mice in the EE group and Ir group was significantly higher than that of the TBI group ($P < 0.05$). There was no difference between the EE group and the Ir group ($P > 0.05$).

Animal weight is also an objective indicator reflecting the survival of mice in different groups. As illustrated in Figure 3(b), the weight of animals in the TBI group was significantly lower than that in the Sham group at 7 d and 14 d after TBI ($P < 0.05$), while at other time points, there was no difference in weight among different groups ($P > 0.05$).

The modified neurological severity score (mNSS) is often used to assess changes in behaviors after TBI. The higher score represents the more severe behavioral impairment. As illustrated in Figure 3(c), on the day before TBI, there was no significant difference in mNSS results among different groups ($P > 0.05$); at day 1, day 3, day 7, and day 14 after TBI, the mNSSs of the other 3 groups were higher than those of the Sham group ($P < 0.05$), while the mNSSs of the EE and Ir groups were lower than those of the TBI group at 3, 7, and 14 days after TBI ($P < 0.05$). Compared to the EE group, the mNSSs of the EE+NA group were higher at 3, 7, and 14 days after TBI ($P < 0.05$), while there was no difference between the mNSSs of the EE group and the EE+IgG group.

The peak period of brain edema after TBI is generally 24 h after trauma, and brain water content (BWC) and EB content are effective indicators to reflect the degree of brain edema. The results of Figures 3(d)–3(f) showed that the

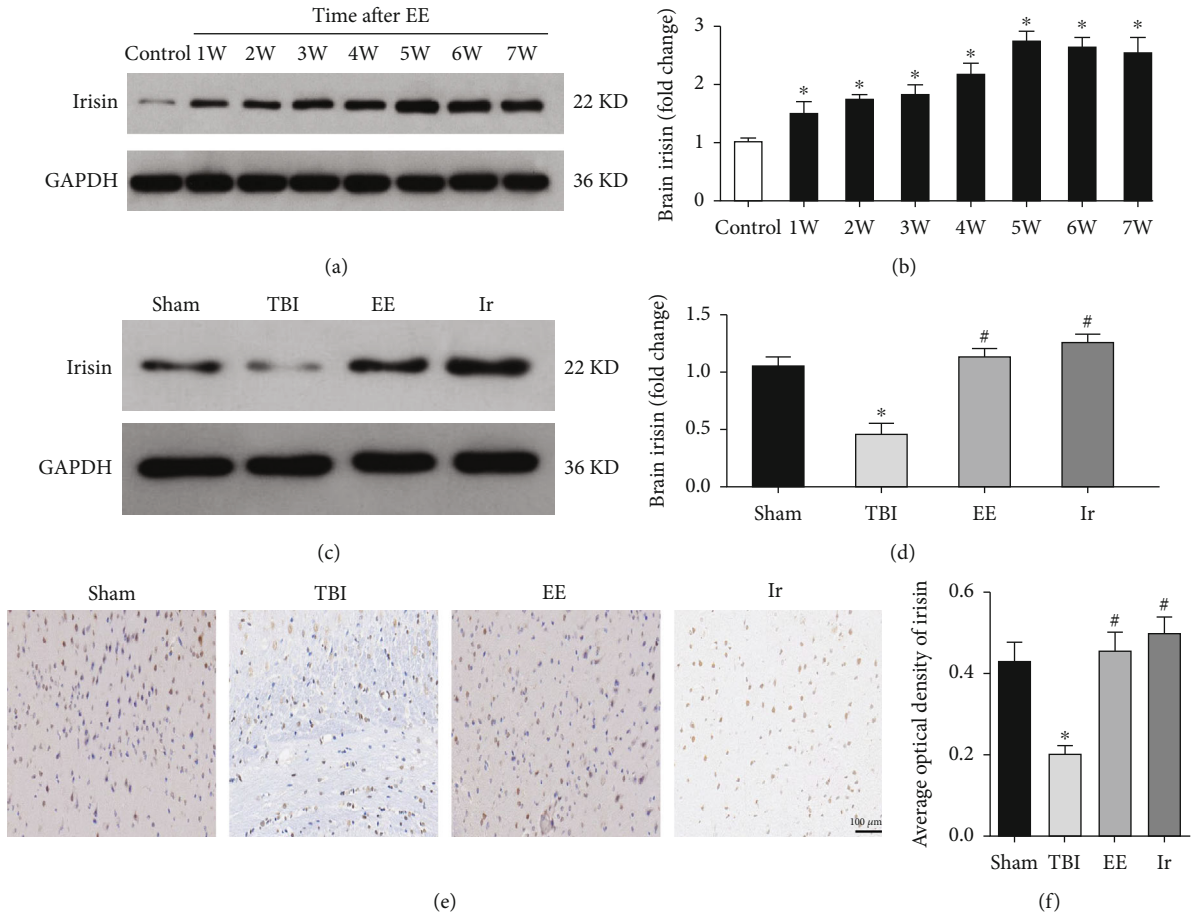

Figure 2: Endurance exercise could increase the level of irisin in the brain tissue of TBI mice. (a, b) The expression of brain irisin derived from mice underwent EE at a different time without TBI. (c, d) The expression of brain irisin derived from mice in different groups. (e, f) Immunostaining showed that irisin was detected in the brain tissue of mice in different groups. Data are expressed as the mean ± SEM. Scale bars: 100 μm. $n = 6$. Significance was determined by one-way ANOVA and Dunnett's post hoc analysis. $^{*}P < 0.05$ versus Sham group or control; $^{\#}P < 0.05$ versus TBI group.

BWC and EB content in the brain tissue increased significantly after TBI ($P < 0.05$), while the BWC and EB content in the brain tissue of the EE group and Ir group decreased slightly, compared with those in the TBI group ($P < 0.05$). All these results suggested that both endurance exercise and exogenous Irisin could, to a certain extent, reduce neurological damage after TBI, and they exerted similar effects.

3.4. Exogenous Irisin Reduced the Damage of Ultrastructure and Upregulated the TJs after TBI. TJs form as an essential barrier when multiprotein complexes extend to the endothelial cell space to form a side-to-cell diffusion. The destruction of its integrity is greatly responsible for increased BBB permeability and brain edema. Hence, in this study, we observed the changes after TBI in the ultrastructure of microvasculature and some key proteins occludin, claudin-5, and ZO-1 that constitute TJ.

As shown in Figures 4(a)–4(d), the expressions of occludin, claudin-5, and ZO-1 were significantly reduced after 24 h of TBI, compared with the Sham group ($P < 0.05$). With the treatment of exogenous irisin, the expressions of occludin, claudin-5, and ZO-1 were significantly upregulated than those in the TBI group ($P < 0.05$). These results suggested that exogenous irisin could promote the expressions of TJ-related proteins.

As shown in Figures 4(e)–4(g), the endothelial cells of the microvasculature had normal morphology without deformation and swelling, and the TJs of the plasma membrane of adjacent endothelial cells were intact, and no gaps were seen in the Sham group. In comparison, in the TBI group, capillary endothelial cells swelled and thickened significantly, and there were evident gaps in TJs between endothelial cells. Meanwhile, endothelial cells in the Ir group were slightly flat and had a slighter swelling than in the TBI group, and there was a certain gap in TJs between endothelial cells.

3.5. Exogenous Irisin Inhibited Inflammation and Oxidative Stress after TBI. TBI could cause a series of neuroinflammatory reactions, mitochondrial dysfunction, and oxidative stress, which was further followed by secondary destruction of the BBB, and a vicious circle of further aggravated inflammation. Therefore, we, respectively, observed the changes in

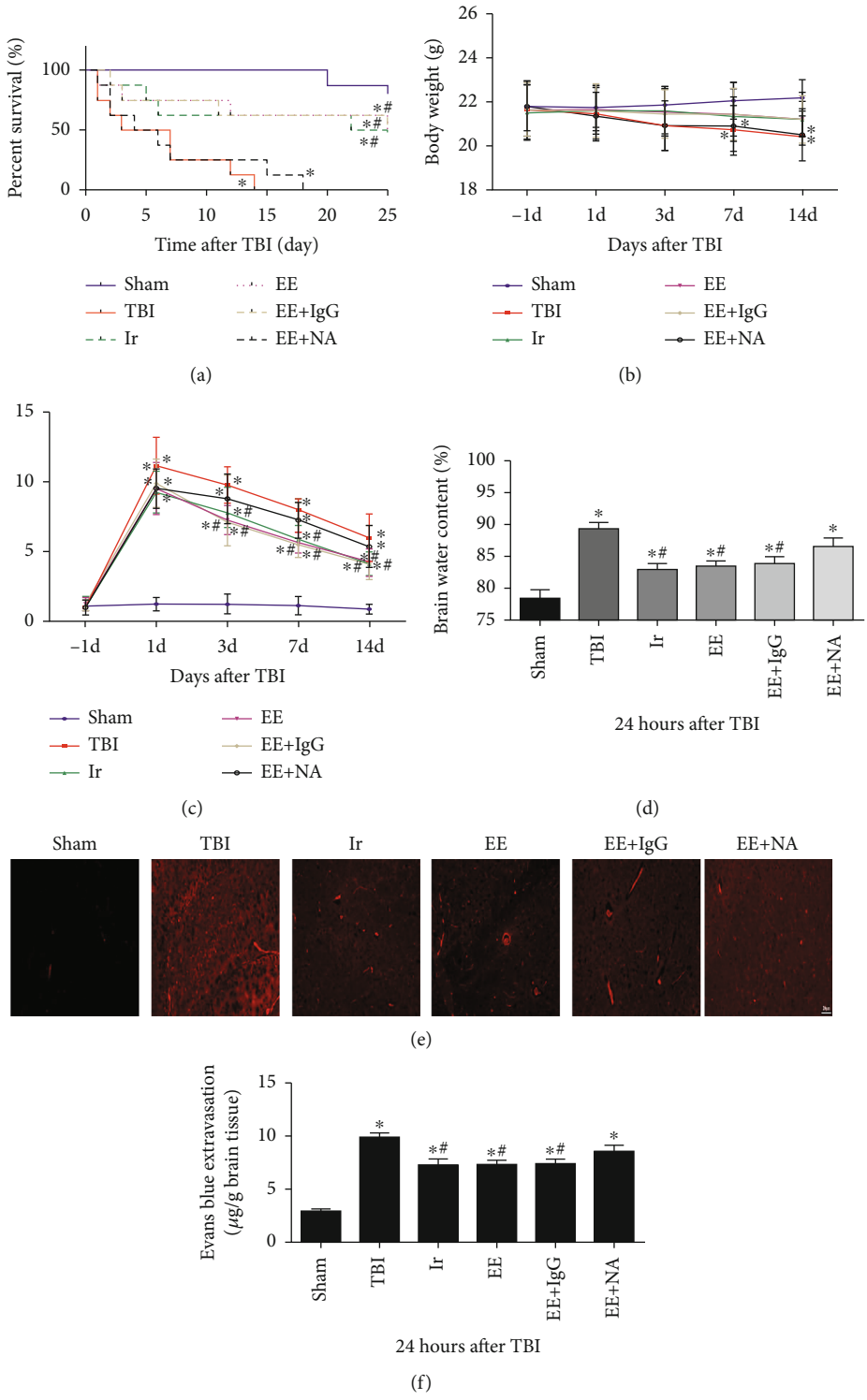

FIGURE 3: Endurance exercise and exogenous irisin have similar protective effects on mice with TBI. (a) The survival rate of mice in different groups. (b) The body weight of mice in different groups. (c) mNSS of mice in different groups. (d) The brain water content of mice in different groups. (e, f) The leakage of EB in brain tissue was observed by a fluorescence microscope in different groups. Data are expressed as the mean ± SEM. Scale bars: 20 μm. $n = 5$. Significance was determined by one-way ANOVA and Dunnett's post hoc analysis. $^{*}P < 0.05$ versus Sham group; $^{\#}P < 0.05$ versus TBI group.

the levels of proinflammatory and anti-inflammatory cytokines and the indicators of oxidative stress in the brain tissue and plasma after TBI.

As shown in Figure 5, compared with the Sham group, the levels of TNF-α and IL-1β in the brain tissue and plasma increased after TBI, while the content of IL-4 and IL-10

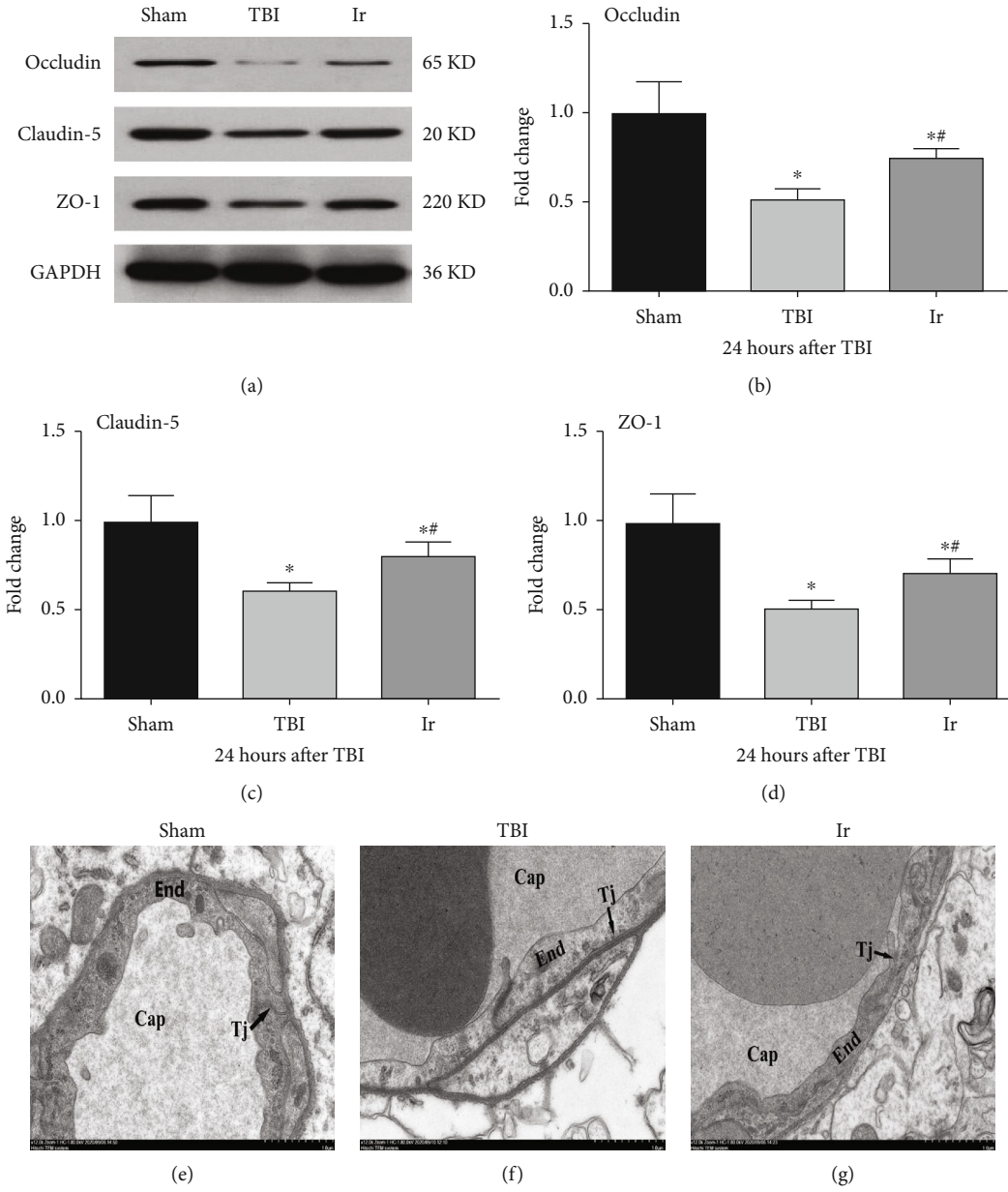

Figure 4: Effects of exogenous irisin on BBB integrity at 24 h after TBI in mice. (a–d) The expressions of occludin, ZO-1, and claudin-5 in brain tissue at 24 h after TBI using western blotting analysis. (e–g) Electron microscopic examination of microvasculature in the brain tissue at 24 h after TBI. Cap: capillary; TJ: tight junction; End: endothelial cell. Data are expressed as the mean ± SEM. Scale bars: 1.0 μm. $n = 6$. Significance was determined by one-way ANOVA and Dunnett's post hoc analysis. $^{*}P < 0.05$ versus Sham group; $^{\#}P < 0.05$ versus TBI group.

significantly reduced ($P < 0.05$, Figures 5(a)–5(h)). After treatment of exogenous irisin, the levels of TNF-α and IL-1β were significantly lower than those in the TBI group, and the levels of IL-4 and IL-10 significantly increased ($P < 0.05$, Figures 5(a)–5(h)). These results all suggested that exogenous irisin could inhibit the inflammatory response at 24 h after TBI.

As shown in Figure 6, compared with the Sham group, the production of ROS in the brain tissue and the MDA content increased significantly after TBI ($P < 0.05$), while with the treatment of exogenous irisin, the ROS production and MDA content were remarkably reduced, compared with the TBI group ($P < 0.05$). These results suggested that exogenous irisin could inhibit oxidative stress after TBI.

As shown in Figure 7, compared with the Sham group, the expressions of Nrf2 and its downstream proteins NQO-1, HO-1, SOD, and GSH-PX significantly enhanced after TBI ($P < 0.05$, Figures 7(a)–7(f)), suggesting that the oxidative stress was activated. After the treatment of exogenous irisin, the expressions of Nrf2 and its downstream proteins NQO-1, HO-1, SOD, and GSH-PX were significantly higher than those in the TBI group ($P < 0.05$, Figures 7(a)–7(f)), which suggested that exogenous irisin enhanced the intensity of antioxidative stress after TBI.

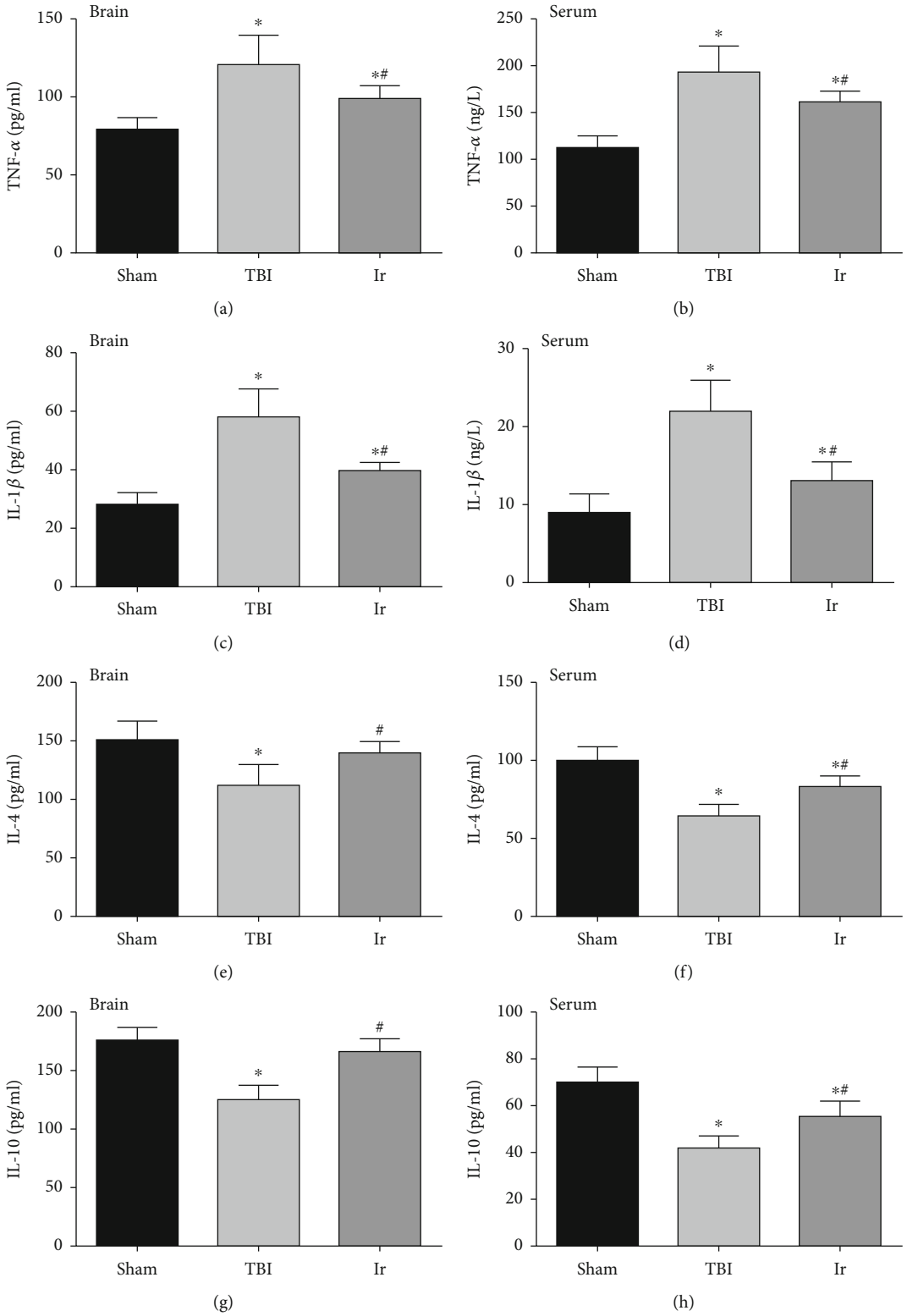

Figure 5: Effects of exogenous irisin on the inflammatory response at 24 h after TBI in mice. (a, c, e, g) Content of TNF-α, IL-1β, IL-4, and IL-10 in brain tissue at 24 h after TBI. (b, d, f, h) Content of TNF-α, IL-1β, IL-4, and IL-10 in serum at 24 h after TBI. Data are expressed as the mean ± SEM. $n = 6$. Significance was determined by one-way ANOVA and Dunnett's post hoc analysis. $^{*}P < 0.05$ versus Sham group; $^{\#}P < 0.05$ versus TBI group.

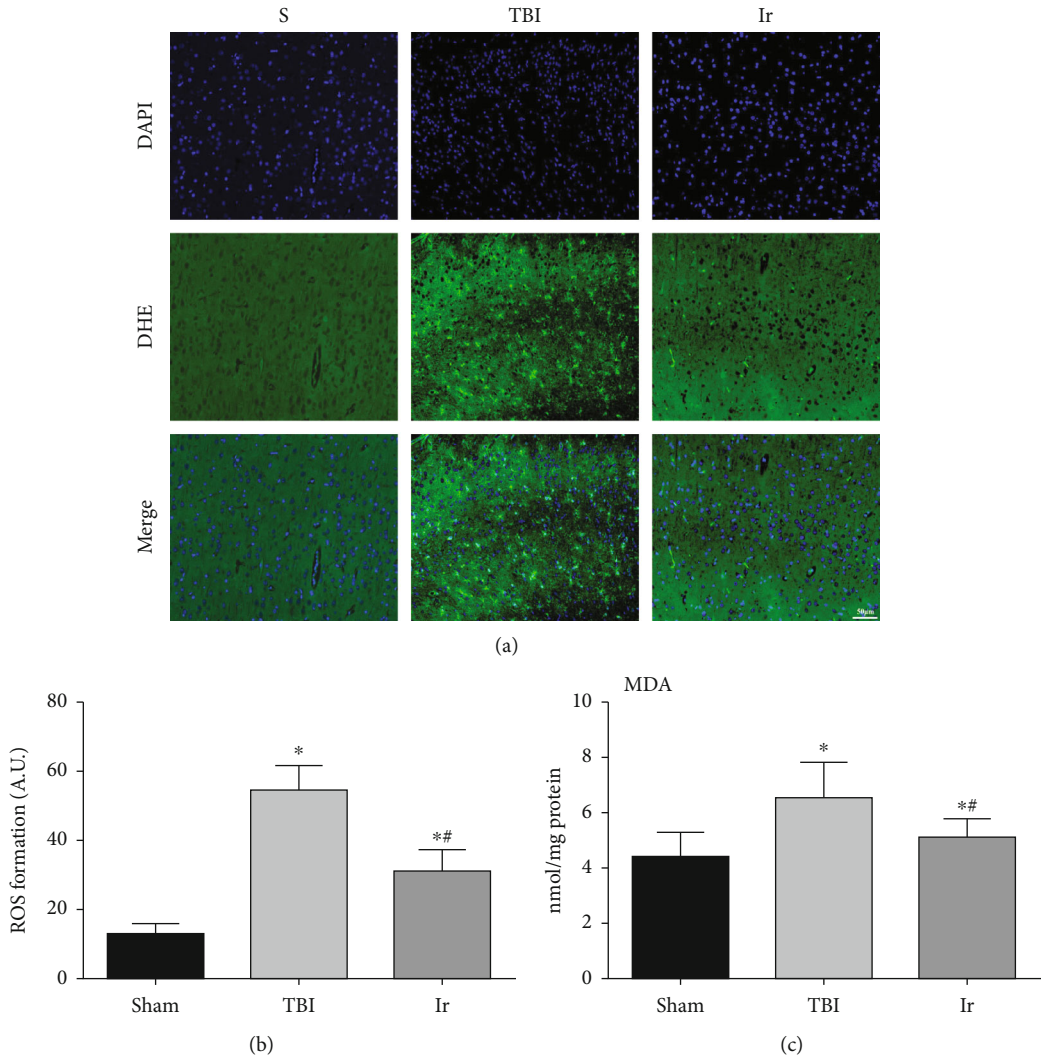

Figure 6: Effects of exogenous irisin on oxidative stress in the brain tissue at 24 hours after TBI in mice. (a, b) The extent of reactive oxygen species (ROS) production in mouse brain tissue was determined by dihydroethidium staining. (c) Measurement of MDA content in mouse brain tissue. Data are expressed as the mean ± SEM. Scale bars: 50 μm. $n = 6$. Significance was determined by one-way ANOVA and Dunnett's post hoc analysis. $^{*}P < 0.05$ versus Sham group; $^{\#}P < 0.05$ versus TBI group.

3.6. Exogenous Irisin Reduced Mitochondrial Apoptosis of Vascular Endothelial Cells in the Brain Tissue after TBI. If the typical indicators of endothelial cell mitochondrial apoptosis are detected, it could be further clarified that the effect of exogenous irisin on endothelial cells after TBI and the related mechanism of further influence on BBB permeability could be explored. As shown in Figure 8, compared with the Sham group, Cyt-C of the endothelial cells in the damaged brain region after TBI demonstrated a significantly higher proportion in the cytoplasm and mitochondria ($P < 0.05$, Figures 8(a) and 8(b)). Meanwhile, the ratio of Bax in the cytoplasm and mitochondria significantly reduced while the protein expression of cleaved caspase-3 significantly increased ($P < 0.05$, Figures 8(c)–8(f)). In contrast, compared with the TBI group, the ratio of Cyt-C in the cytoplasm and mitochondria of the Ir group was significantly lower and the ratio of Bax in the cytoplasm and mitochondria was significantly higher, while the protein expression of cleaved caspase-3 significantly dropped ($P < 0.05$, Figures 8(a)–8(f)). The above results suggested that exogenous irisin could slow down the degree to which Bax and Cyt-C transferred after TBI, and lysis of the apoptotic protein caspase-3 was pyrolyzed, thereby reducing the apoptosis of endothelial cells.

3.7. Exogenous Irisin Affected Mitochondrial Function by Regulating the Expression of UCP2. Uncoupling proteins (UCPs), members of the mitochondrial carrier protein superfamily, are a class of anionic carrier proteins located on the inner mitochondrial membrane. UCP2 located on neurons can regulate the number of mitochondria and mitochondrial membrane potential (MMP) and the absolute value of ATP as well as the generation of oxygen free radicals. Such regulation thereby affects neurotransmission or neurological function and then BBB permeability. As shown in Figures 9(a)–9(c), the mitochondria of neurons in the

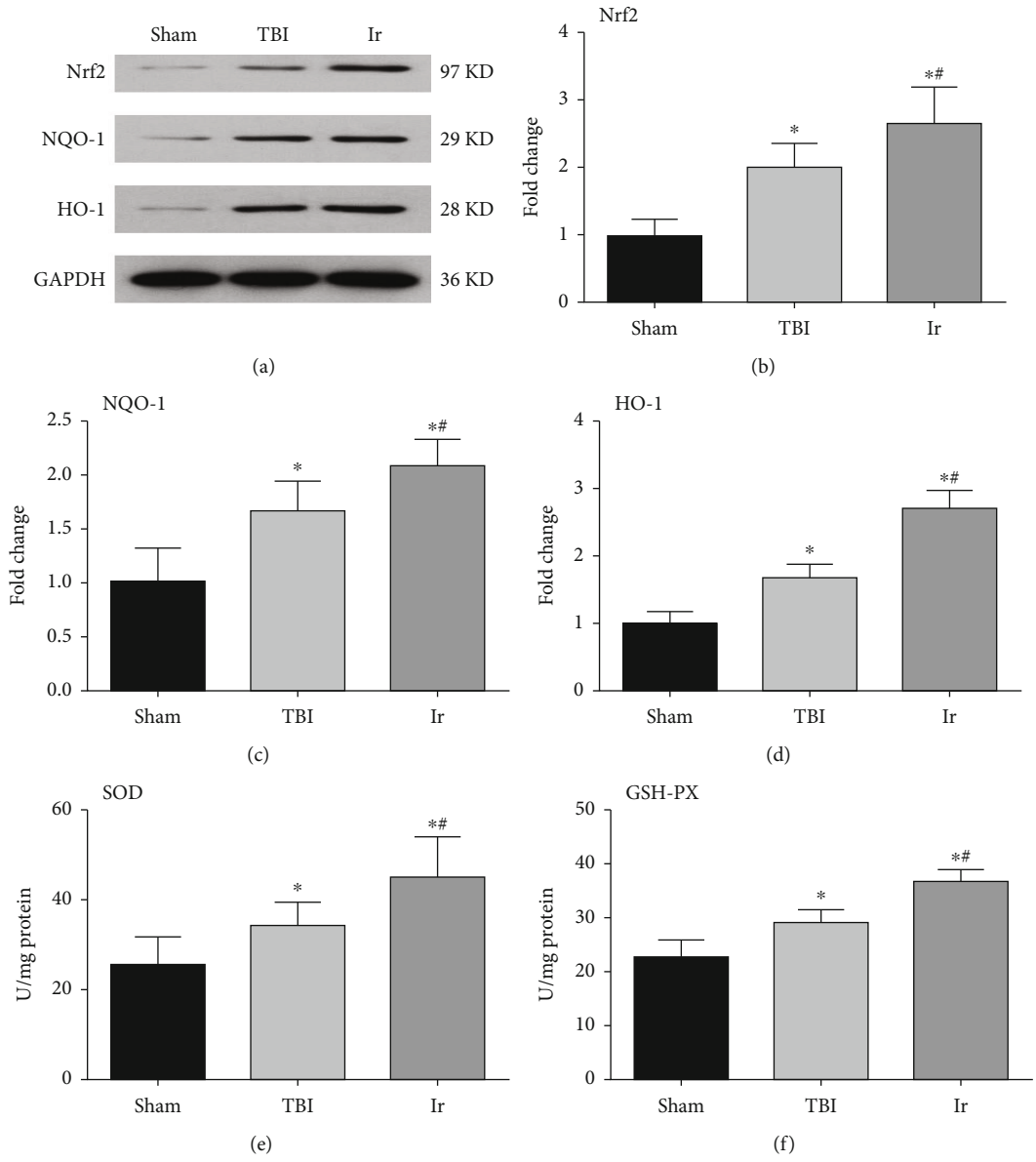

Figure 7: Effects of exogenous irisin on antioxidative response system at 24 hours after TBI in mice. (a–d) The expressions of Nrf2, NQO-1, and HO-1 in brain tissue at 24 h after TBI using western blotting analysis. (e, f) Content of SOD and GSH-PX in brain tissue at 24 h after TBI using ELISA. Data are expressed as the mean ± SEM. $n = 6$. Significance was determined by one-way ANOVA and Dunnett's post hoc analysis. $^{*}P < 0.05$ versus Sham group; $^{\#}P < 0.05$ versus TBI group.

Sham group had no obvious swelling, uniform size, and normal crista structure. A typical double-layer membrane structure was seen, with a moderate matrix electron density. By contrast, in the TBI group, neuronal mitochondria showed obvious swelling, and their bilayer membrane structures disappeared, inner chamber expanded. Furthermore, the matrix was sparse, and the matrix electron density decreased significantly, showing a vacuole shape, short, and few cristae. Inclusions of different sizes and shapes could be seen in the cristae or matrix. When it came to the Ir group, the degree of neuronal mitochondrial swelling and vacuoles was slightly less than that in the TBI group, and the matrix electron density here tended to be normal. That is, the cristae were visible, and some of the mitochondrial cristae dissolved into small bubbles, with a small number of inclusions seen in the mitochondrial matrix. Compared with the Sham group, the protein expression of UCP2 in the damaged brain area after TBI significantly weakened and MMP significantly increased, while the protein expression of UCP2 upregulated and MMP decreased in the Ir group compared with the TBI group ($P < 0.05$, Figures 9(d)–9(f)).

To further testify the correlation between the protective effects of irisin on UCP2, we used UCP2 knockout mice for further experiments. Under normal physiological conditions, there was no difference in BWC, the EB content, ROS level, and neuronal MMP between wild-type mice and $UCP2^{-/-}$ mice ($P > 0.05$, Figures 10 and 11). The increase in BWC, the EB content, and ROS level, which were all

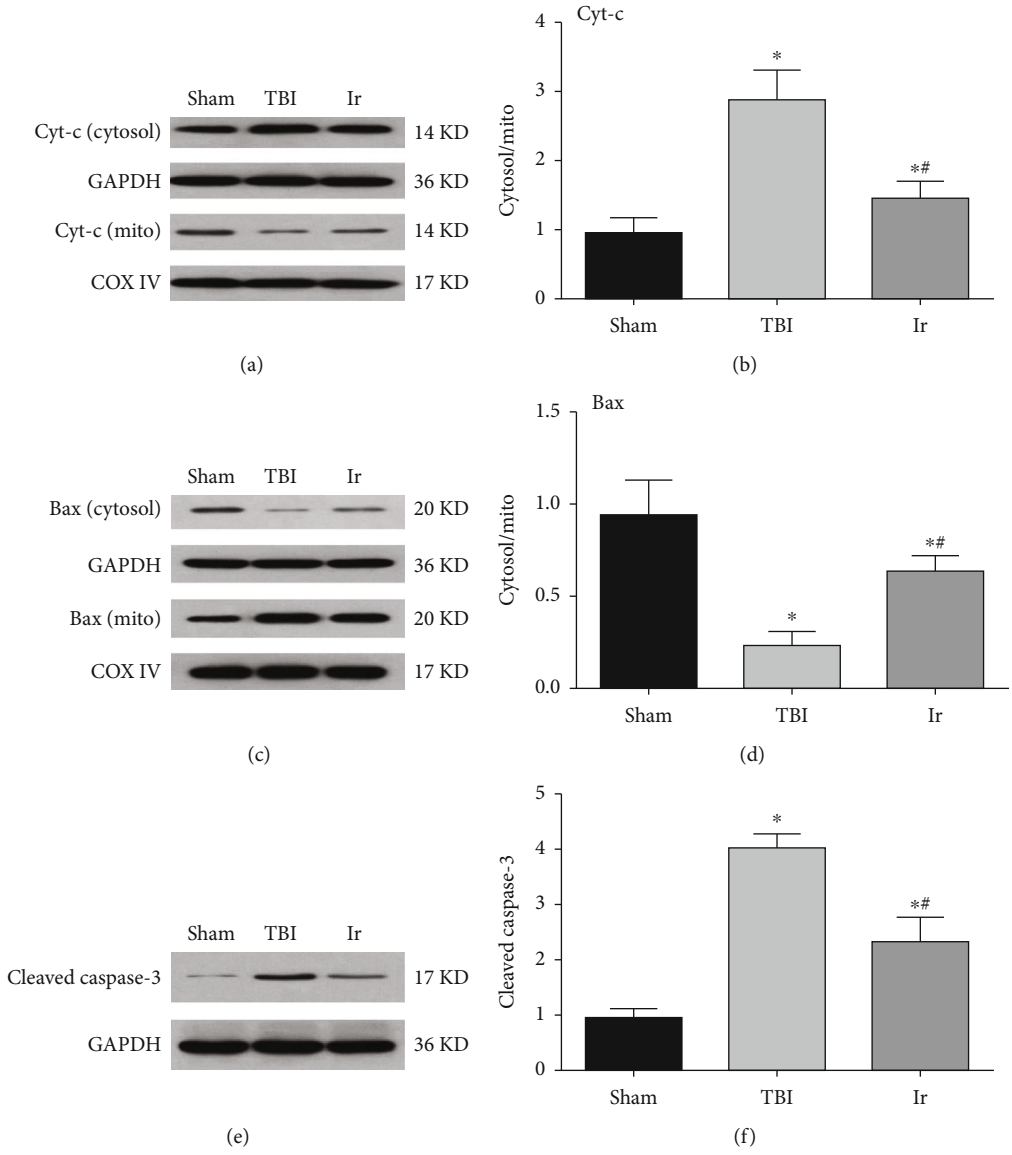

Figure 8: Effects of exogenous irisin on mitochondrial apoptosis at 24 hours after TBI in mice. (a, b) Assessment of Cyt-C in mitochondria and cytosol derived from endothelial cells of mice at 24 hours after TBI. (c, d) Assessment of Bax in mitochondria and cytosol derived from endothelial cells of mice at 24 hours after TBI. (e, f) The expression of cleaved caspase-3 in brain tissue at 24 hours after TBI using western blotting analysis. Data are expressed as the mean ± SEM. $n = 6$. Significance was determined by one-way ANOVA and Dunnett's post hoc analysis. $^{*}P < 0.05$ versus Sham group; $^{\#}P < 0.05$ versus TBI group.

caused by TBI, was more obvious in UCP2$^{-/-}$ mice than in wild-type mice ($P < 0.05$, Figures 10 and 11). After treatment with exogenous irisin, the BWC, EB content, ROS level, and neuronal MMP of the UCP2$^{-/-}$ mice were higher than those of the WT mice ($P < 0.05$, Figures 10 and 11).

4. Discussion

As the economy and society make advances, recent years have witnessed an increasing incidence of traumatic brain injury (TBI) worldwide, caused by two dominant factors: traffic accidents and falls from heights. There are more than 60 million new cases of TBI patients every year [1, 2]. This is worsened by the fact that the mechanism of the occurrence and development of TBI is complicated, and that, its prognosis is poor, which brings a heavy burden to patients' families and global medical care. Even worse, the specific mechanism of brain edema, cognitive dysfunction, and even Alzheimer's disease caused by TBI is still baffling the global health system [2]. Various animal models have been used to study the pathophysiological changes of TBI to better clinical treatment. This study selected the controlled cortical impact model (controlled cortical impact CCI), which has strong controllability and stability, accurate injury, and controllable impact time to achieve a good simulation of brain edema caused by clinical brain injury [17–21].

Recent studies have proved the remarkable protective effect of physical exercise, particularly aerobic exercise called

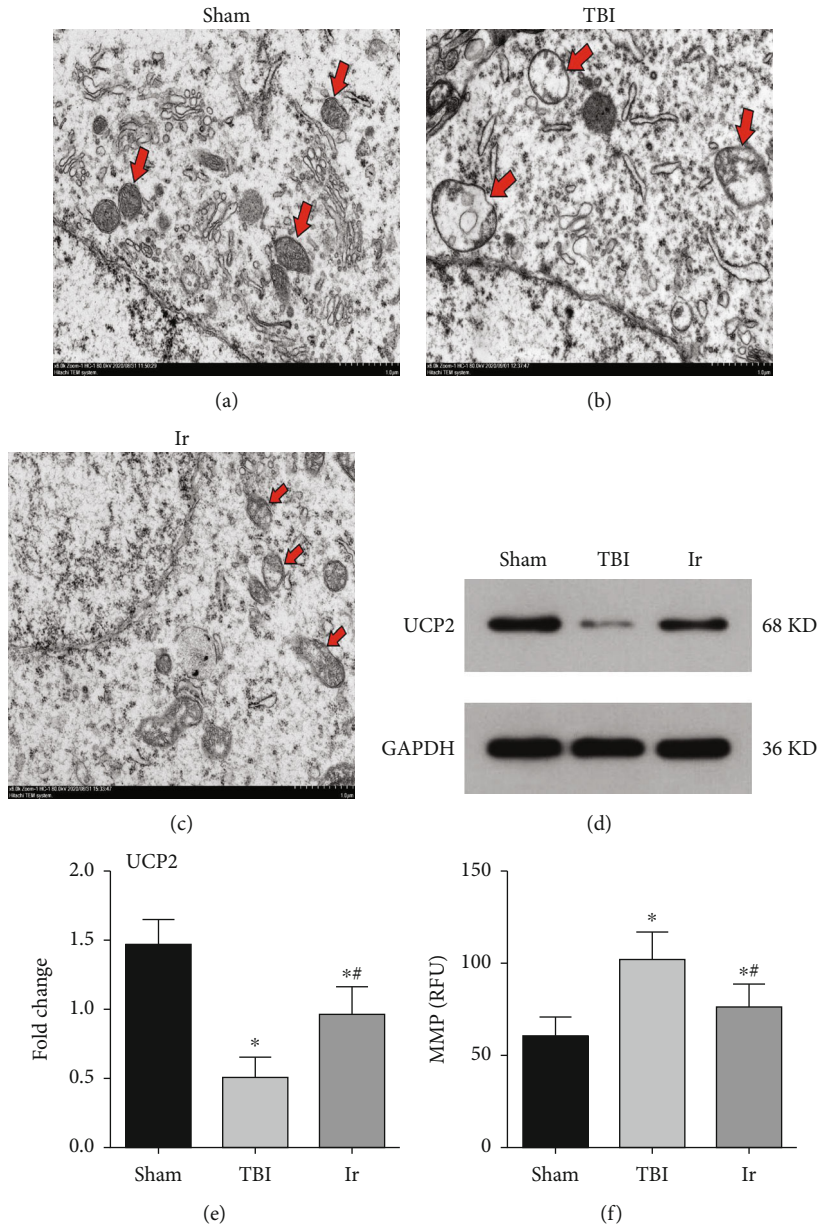

FIGURE 9: The expressions of UCP2 and ultrastructure of mice at 24 hours after TBI. (a–c) Electron microscopic examination of neuronal mitochondria in mice at 24 hours after TBI. Arrows in red indicate mitochondrial structures of neurons. (d, e) Western blotting analysis of UCP2 in brain tissue at 24 hours after TBI. (f) Assessment of neuronal MMP in mice at 24 hours after TBI. Data are expressed as the mean ± SEM. Scale bars: 1.0 μm. $n = 6$. Significance was determined by one-way ANOVA and Dunnett's post hoc analysis. $^{*}P < 0.05$ versus Sham group; $^{\#}P < 0.05$ versus TBI group.

endurance exercise (EE) on brain injury. EE can effectively alleviate a variety of brain injury including Parkinson's disease, Alzheimer's disease, and neurovascular diseases. This may be attributed to the fact that EE can increase hippocampal blood perfusion, enhance neuronal synaptic plasticity, relieve neuroinflammatory response, and even stimulate neuronal regeneration [10–13]. Although EE's protection on brain injury has been increasingly acknowledged, its specific mechanism remains to be discovered. Studies have found that exercised skeletal muscle secreted irisin, a downstream product of PGC-1α protein, and it could make fat browning by promoting the expression of UCP1 [19]. In recent years, it has been reported that irisin exerts a similar protective effect to EE on cerebral ischemia [12, 14]. Consistent with these findings, results in this study showed that the content of irisin in CSF of TBI patients was positively correlated with their prognosis. In addition, mice after exercise or treated with exogenous irisin had better results in their survival rate, cognition, and especially the outcome of cerebral edema after TBI than the TBI group. In our study, we also found that EE could increase the content of irisin in the brain tissue of mice with or without TBI. Thus, all these results indicated that the neuroprotection of EE on TBI may contribute to its promotion of irisin. Meanwhile, it is

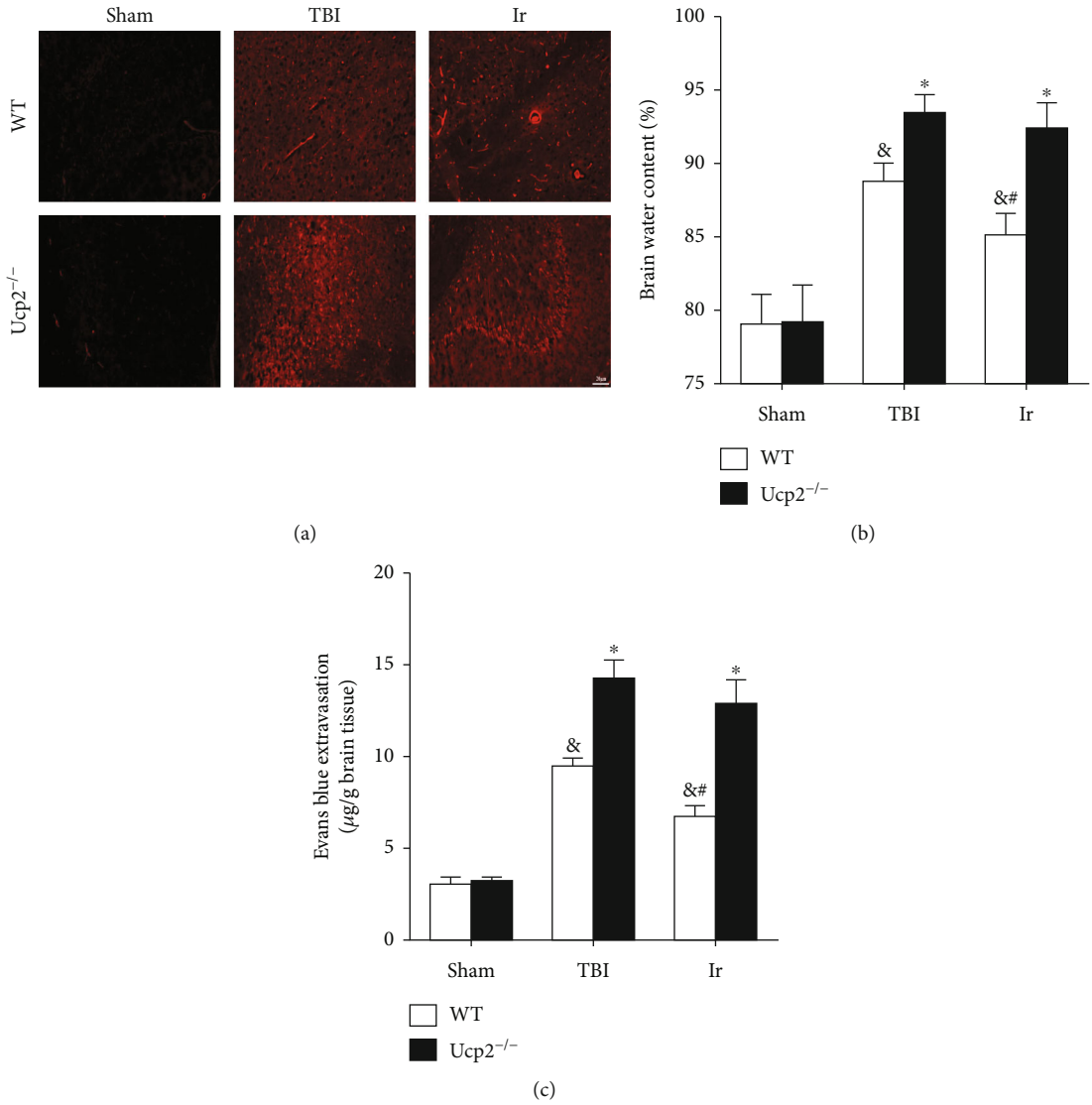

FIGURE 10: Genetic ablation of UCP2 compromised the protective effect of exogenous irisin on BBB integrity at 24 hours after TBI in mice. (a, c) Evans blue extravasation in WT and UCP2$^{-/-}$ mice at 24 hours after TBI. (b) Evaluation of brain water content in WT and UCP2$^{-/-}$ mice at 24 hours after TBI. Data are expressed as the mean ± SEM. Scale bars: 20 μm. $n = 6$. Significance was determined by one-way ANOVA and Dunnett's post hoc analysis. $^{*}P < 0.05$ versus WT mice under the same conditions; $^{\#}P < 0.05$ versus TBI group in WT mice; $^{\&}P < 0.05$ versus Sham group in WT mice.

delightfully noted that the "exercise drugs (irisin)" could effectively replace the beneficial effects of exercise. What is more, we also found that the expression of irisin in the hippocampus was upregulated in the Ir group compared to the TBI group, which indicated that exogenous administration of irisin could promote it to enter the brain tissue. Therefore, the following study was proceeded with exogenous irisin instead of EE to explore the underlying mechanisms.

An important reason for the poor prognosis of TBI is that changes in the permeability of the BBB after TBI lead to cerebral edema [17, 22]. The blood-brain barrier (BBB) refers to a barrier to prevent substances in the blood from entering the brain, formed by brain capillary walls and glial cells. It is located between brain cells and plasma and forms neurovascular units with neurons [21]. BBB is mainly composed of vascular endothelial cells, astrocytes, microglia, pericytes, continuous basement membrane and extracellular matrix, and neurons, among which cerebral microvascular endothelial cells are the main component. Cerebral microvascular endothelial cells are tightly connected with endothelial cells through a unique tight junction (TJ), and they lack openings while having weak endocytosis, so they strictly restrict the paracellular transport, effectively preventing the passage of macromolecules and toxic substances [23].

TJ is mainly composed of two major components: cytoplasmic adhesion protein and transmembrane protein. The former is the basis of TJ's supportive structure, mainly including the ZO series, of which ZO-1 functions most effectively. The main components of transmembrane proteins are occludin and claudin-5, so ZO-1, occludin, and claudin-5 proteins are essential for maintaining the physiological functions of BBB [24, 25]. Recent studies have confirmed that

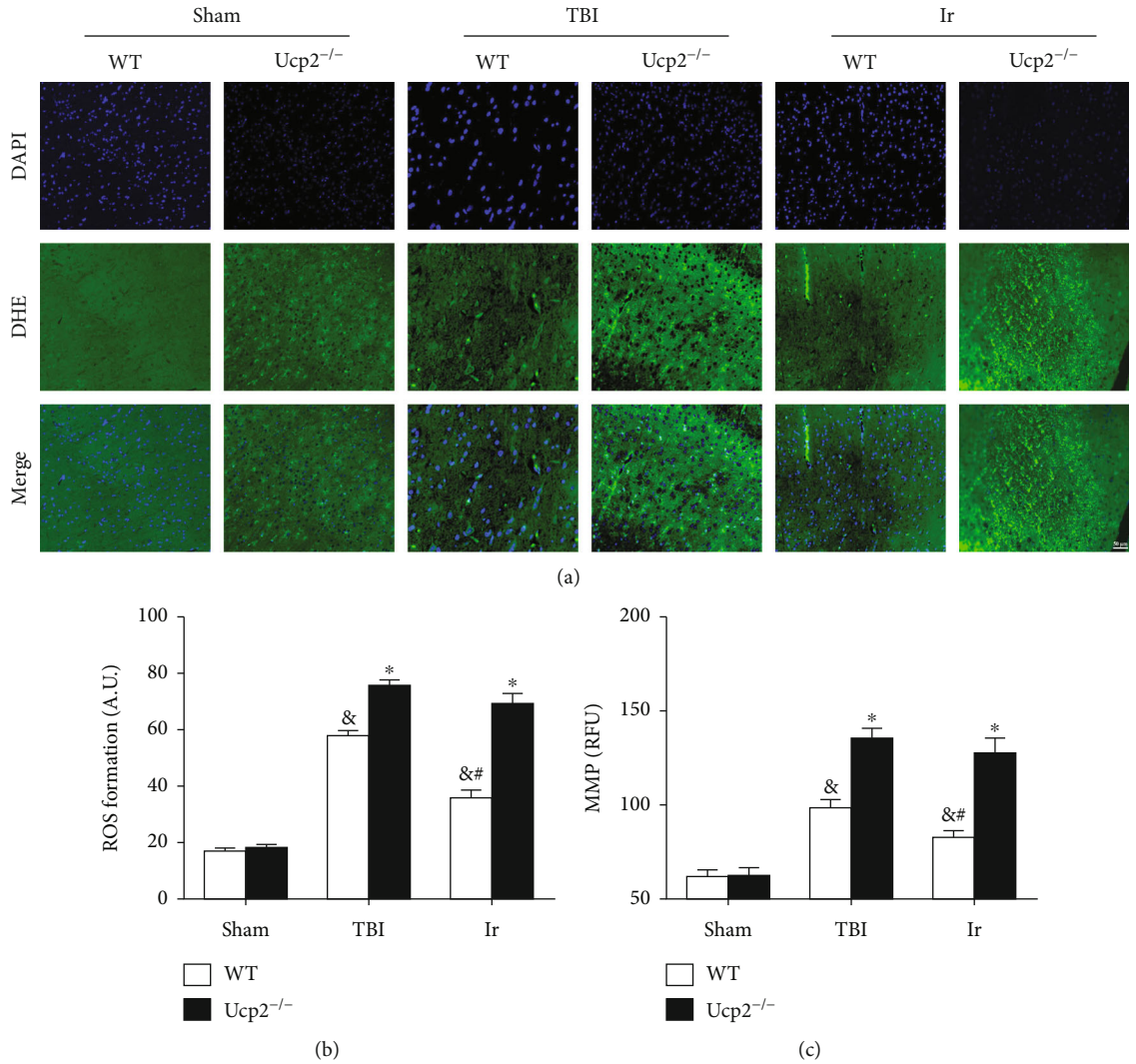

Figure 11: Genetic ablation of UCP2 compromised the protective effect of exogenous irisin on oxidative stress at 24 hours after TBI in mice. (a, b) The extent of reactive oxygen species (ROS) production in WT and UCP2$^{-/-}$ mice was determined by dihydroethidium staining. (c) Assessment of neuronal MMP in WT and UCP2$^{-/-}$ mice at 24 hours after TBI. Data are expressed as the mean ± SEM. Scale bars: 50 μm. $n = 6$. Significance was determined by one-way ANOVA and Dunnett's post hoc analysis. $^{*}P < 0.05$ versus WT mice under the same conditions; $^{\#}P < 0.05$ versus TBI group in WT mice; $^{\&}P < 0.05$ versus Sham group in WT mice.

many factors are involved in the mechanism of BBB disruption following TBI. Matrix metalloproteinase (MMP) has a critical role in the pathophysiology of BBB breakdown in TBI, and several investigators have reported the involvement of MMPs in degrading TJ proteins of the BBB [26, 27]. In addition, cytokines, chemokines, and growth factors also play an important role in the pathophysiology of TBI. The inflammatory mediators act through pinocytosis or directly act on the corresponding TJ protein. This causes the structure and function of BBB to be further dysregulated, forming vasogenic brain edema [18, 28]. The results of this study showed that the TJ ultrastructure was destroyed after TBI, the expressions of ZO-1, occludin, and claudin-5 proteins were downregulated, and the inflammatory response was enhanced. With the treatment of irisin, the expressions of ZO-1, occludin, and claudin-5 proteins were upregulated, the degree of TJ ultrastructure damage reduced, and the inflammatory response was inhibited. All these suggested that irisin may alleviate neuroinflammation and enhance the expressions of TJs.

The overwhelming majority of ATP fundamental to life activities are generated in mitochondria by oxidative phosphorylation associated with the coupling of electron transport. However, the oxidative phosphorylation of mitochondria is not completely coupled, and the uncoupling of oxidation and phosphorylation does not produce ATP, which currently attributes to uncoupling proteins on the mitochondria. Uncoupling protein (UCP), a member of the mitochondrial carrier protein superfamily, is a special carrier located on the inner mitochondrial membrane. The UCP superfamily shares a certain similarity in structure and function, and UCP2, UCP4, and UCP5 mainly exist in the nervous system, among which the mechanism of UCP2 in the nervous system has been most fully studied [9, 29]. UCP2

pumps out neuron protons under physiological conditions and lowers the concentration and gradient of protons when back in the mitochondrial matrix, reducing the number of protons flowing through ATP synthase to weaken the synthesis of ATP [30]. Meanwhile, ATP is generated when mitochondrial membrane potential (MMP) sustains oxidative phosphorylation by a potential difference caused by the numerical difference in protons on both sides of the inner membrane [31, 32]. As a result, the activation of UCP2 can reduce MMP. Neuron UCP2 can promote the change of redox state in the cell and reduce the production of mitochondrial ROS and transfer it out of mitochondria by sending redox signals through the interaction with the electron transport chain (ETC). Therefore, neuron UCP2 counts remarkably in reducing the production of ROS and reducing oxidative stress [9], and MMP, to some extent, is positively correlated with the production of mitochondrial ROS [7, 8]. Studies have confirmed that irisin may alleviate mitochondrial damage and reduce the production of ROS to inhibit oxidative stress by regulating the expression of UCP2, thereby reducing lung ischemia-reperfusion injury [33] and severe acute pancreatitis injury [34]. In the present study with the treatment of irisin, the expression of UCP2 was upregulated, the MMP was reduced, and the neuronal mitochondrial damage and oxidative stress alleviated, but these neuroprotective effects were not seen in UCP2$^{-/-}$ mice. Taken together, it was speculated that irisin may alleviate the damage of BBB after TBI and inhibit oxidative stress by promoting mitochondrial UCP2 expression.

Then, how does oxidative stress cause BBB dysfunction after TBI? Under physiological conditions, the production and elimination of active oxygen in the body maintain a constant balance. Excessive ROS production or weakened ability to clean up will lead to the consequence that oxidation in the body is stronger than antioxidation. This results in inflammatory infiltration of neutrophils and increased protease secretion, which generates a large number of active oxygen mediators. Then, oxidative stress damage follows, leading to the death of cells through apoptosis, necrosis, or autophagy [35, 36]. After TBI, impairment is observed in the function of mitochondria in the neurons in the directly damaged region, and neurons release excessive ROS making oxidative stress enhanced [23, 37–39]. These occurrences further lead to opened mitochondrial permeability transition pore (MPTP) of the mitochondrial membrane in endothelial cells of the indirect damaged area, reduced mitochondrial membrane potential (MMP), weakened respiratory chain, swollen mitochondria, and increased membrane permeability. As a result, cytochrome C (Cyt-C) in the mitochondrial membrane is released into the cytoplasm, and the proapoptotic factor Bax transfers from the cytoplasm to the mitochondrial membrane. This causes a cascade reaction of the caspase family, particularly the activation of caspase-3, leading to endothelium apoptosis [40–43]. Capillary endothelial cells in brain tissue constitute the skeleton of BBB, and their apoptosis can lead to the destruction of BBB integrity. In this study, we found that TBI promoted the transfer of Bax in the cytoplasm to the mitochondrial membrane and the release of Cyt-C from the mitochondrial membrane to the cytoplasm, which further led to the lysis of caspase-3 to cause endothelial cell apoptosis, thereby causing BBB dysfunction. In the meantime, irisin slowed down the degree of Bax and Cyt-C metastasis after TBI reduced the expression of caspase-3 and reduced the degree of endothelial cell apoptosis. Taking these into consideration, we speculated that irisin could reduce mitochondrial-mediated ROS production and inhibit oxidative stress by promoting UCP2 expression.

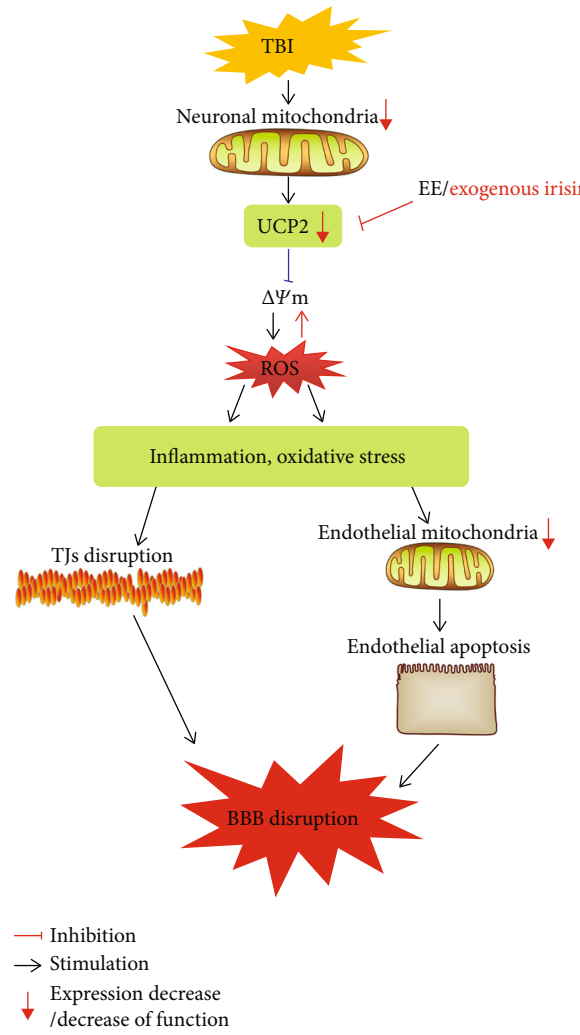

Figure 12: EE/exogenous irisin alleviates BBB disruption after TBI via the suppression of oxidative stress and neuroinflammation.

Admittedly, this study still needs further perfection in the following aspects. First of all, the number of research participants (TBI patients) in our clinical research is limited, and the period for observing their prognosis after TBI is not long enough, restricted by objective condition. This may be a stimulus for future studies to establish a multicenter study for a larger sample size. Furthermore, this study fails to testify whether there is any significant difference in irisin content and prognosis between the EE group and the nonexercise group after TBI. This appeals to further studies since exercises can stimulate the release of irisin in the body. Moreover, more attention is needed to address the issue that we focused on the damage in function and structure of

mitochondria in neurons and vascular endothelial cells after TBI, but actually, the mitochondria of other cells in the brain tissue were also damaged to varying degrees. This will also be covered in our further studies. Finally, it remains to be elucidated in future research whether UCP4 or UCP5 was also associated with the destruction of structure and function of BBB after TBI.

In summary, this study has concluded that EE may reduce the BBB damage caused by TBI through promoting the secretion of irisin in brain tissue, and its effect was similar to the treatment of exogenous irisin. In addition, we also found that irisin could exert its neuroprotection by promoting the expression of UCP2 on the mitochondrial membrane to improve the dysfunction of BBB after TBI by ultimately alleviating inflammation and oxidative stress (Figure 12).

Data Availability

All data presented in the present study are available from the corresponding author on reasonable request.

Conflicts of Interest

The authors declare no conflicts of interest.

Authors' Contributions

HSW and ZJ contributed to the design, execution, analysis, and writing. PPG conducted the experiments. JW and AMS helped with the data analysis. All authors read and approved the final manuscript. Peipei Guo and Zhao Jin contributed equally to this work.

Acknowledgments

This work was supported by the Hubei Provincial Natural Science Foundation of China (grant No. 2020CFB614) and the Zhongnan Hospital of Wuhan University Science, Technology and Innovation Seed Fund (grant Nos. znpy2019009 and znpy2019020).

References

[1] CRASH-3 trial collaborators, "Effects of tranexamic acid on death, disability, vascular occlusive events and other morbidities in patients with acute traumatic brain injury (CRASH-3): a randomised, placebo-controlled trial," *The Lancet*, vol. 394, no. 10210, pp. 1713–1723, 2019.

[2] R. Campos-Pires, T. Hirnet, F. Valeo et al., "Xenon improves long-term cognitive function, reduces neuronal loss and chronic neuroinflammation, and improves survival after traumatic brain injury in mice," *British Journal of Anaesthesia*, vol. 123, no. 1, pp. 60–73, 2019.

[3] O. L. Alves, A. J. Doyle, T. Clausen, C. Gilman, and R. Bullock, "Evaluation of topiramate neuroprotective effect in severe TBI using microdialysis," *Annals of the New York Academy of Sciences*, vol. 993, no. 1, pp. 25–34, 2003.

[4] E. Vázquez-Rosa, M. K. Shin, M. Dhar et al., "P7C3-A20 treatment one year after TBI in mice repairs the blood-brain barrier, arrests chronic neurodegeneration and restores cognition," *Proceedings of the National Academy of Sciences of the United States of America*, vol. 117, no. 44, pp. 27667–27675, 2020.

[5] Z. Sun, M. Nyanzu, S. Yang et al., "VX765 Attenuates Pyroptosis and HMGB1/TLR4/NF-κB Pathways to Improve Functional Outcomes in TBI Mice," *Oxidative Medicine and Cellular Longevity*, vol. 2020, Article ID 7879629, 21 pages, 2020.

[6] P. M. Abdul-Muneer, N. Chandra, and J. Haorah, "Interactions of oxidative stress and neurovascular inflammation in the pathogenesis of traumatic brain injury," *Molecular Neurobiology*, vol. 51, no. 3, pp. 966–979, 2015.

[7] S. H. Dai, T. Chen, X. Li et al., "Sirt3 confers protection against neuronal ischemia by inducing autophagy: involvement of the AMPK-mTOR pathway," *Free Radical Biology & Medicine*, vol. 108, pp. 345–353, 2017.

[8] P. Ježek, B. Holendová, K. D. Garlid, and M. Jabůrek, "Mitochondrial uncoupling proteins: subtle regulators of cellular redox signaling," *Antioxidants & Redox Signaling*, vol. 29, no. 7, pp. 667–714, 2018.

[9] K. P. Normoyle, M. Kim, A. Farahvar, D. Llano, K. Jackson, and H. Wang, "The emerging neuroprotective role of mitochondrial uncoupling protein-2 in traumatic brain injury," *Translational Neuroscience*, vol. 6, no. 1, pp. 179–186, 2015.

[10] M. V. Lourenco, R. L. Frozza, G. B. de Freitas et al., "Exercise-linked FNDC5/irisin rescues synaptic plasticity and memory defects in Alzheimer's models," *Nature Medicine*, vol. 25, no. 1, pp. 165–175, 2019.

[11] C. C. Chio, H. J. Lin, Y. F. Tian et al., "Exercise attenuates neurological deficits by stimulating a critical HSP70/NF-κB/IL-6/synapsin I axis in traumatic brain injury rats," *Journal of Neuroinflammation*, vol. 14, no. 1, p. 90, 2017.

[12] D. J. Li, Y. H. Li, H. B. Yuan, L. F. Qu, and P. Wang, "The novel exercise-induced hormone irisin protects against neuronal injury via activation of the Akt and ERK1/2 signaling pathways and contributes to the neuroprotection of physical exercise in cerebral ischemia," *Metabolism*, vol. 68, pp. 31–42, 2017.

[13] C. D. Wrann, J. P. White, J. Salogiannnis et al., "Exercise induces hippocampal BDNF through a PGC-1α/FNDC5 pathway," *Cell Metabolism*, vol. 18, no. 5, pp. 649–659, 2013.

[14] Z. Jin, P. Guo, X. Li, J. Ke, Y. Wang, and H. Wu, "Neuroprotective effects of irisin against cerebral ischemia/ reperfusion injury via Notch signaling pathway," *Biomedicine & Pharmacotherapy*, vol. 120, article 109452, 2019.

[15] P. Guo, Z. Jin, H. Wu et al., "Effects of irisin on the dysfunction of blood-brain barrier in rats after focal cerebral ischemia/reperfusion," *Brain and Behavior: A Cognitive Neuroscience Perspective*, vol. 9, no. 10, article e01425, 2019.

[16] G. Gao, X. Wu, J. Feng et al., "Clinical characteristics and outcomes in patients with traumatic brain injury in China: a prospective, multicentre, longitudinal, observational study," *The Lancet Neurology*, vol. 19, no. 8, pp. 670–677, 2020.

[17] B. S. Main, S. Villapol, S. S. Sloley et al., "Apolipoprotein E4 impairs spontaneous blood brain barrier repair following traumatic brain injury," *Molecular Neurodegeneration*, vol. 13, no. 1, p. 17, 2018.

[18] X. Xu, D. Yin, H. Ren et al., "Selective NLRP3 inflammasome inhibitor reduces neuroinflammation and improves long-term neurological outcomes in a murine model of traumatic brain injury," *Neurobiology of Disease*, vol. 117, pp. 15–27, 2018.

[19] P. Boström, J. Wu, M. P. Jedrychowski et al., "A PGC1-α-dependent myokine that drives brown-fat-like development

of white fat and thermogenesis," *Nature*, vol. 481, no. 7382, pp. 463–468, 2012.

[20] T. J. Krämer, N. Hack, T. J. Brühl et al., "Depletion of regulatory T cells increases T cell brain infiltration, reactive astrogliosis, and interferon-γ gene expression in acute experimental traumatic brain injury," *Journal of Neuroinflammation*, vol. 16, no. 1, p. 163, 2019.

[21] P. Assis-Nascimento, Y. Tsenkina, and D. J. Liebl, "EphB3 signaling induces cortical endothelial cell death and disrupts the blood-brain barrier after traumatic brain injury," *Cell Death & Disease*, vol. 9, no. 1, p. 7, 2018.

[22] E. A. van Vliet, X. E. Ndode-Ekane, L. J. Lehto et al., "Long-lasting blood-brain barrier dysfunction and neuroinflammation after traumatic brain injury," *Neurobiology of Disease*, vol. 145, no. undefined, article 105080, 2020.

[23] S. Farzane, A. Faleh, S. Ali, and C. Luca, "The cerebrovascular and neurological impact of chronic smoking on post-traumatic brain injury outcome and recovery: an in vivo study," *Journal of Neuroinflammation*, vol. 17, no. 1, p. 133, 2020.

[24] J. Tang, Y. Kang, L. Huang, L. Wu, and Y. Peng, "TIMP1 preserves the blood-brain barrier through interacting with CD63/integrin β1 complex and regulating downstream FAK/RhoA signaling," *Acta Pharmaceutica Sinica B*, vol. 10, no. 6, pp. 987–1003, 2020.

[25] L. Winkler, R. Blasig, O. Breitkreuz-Korff et al., "Tight junctions in the blood-brain barrier promote edema formation and infarct size in stroke-ambivalent effects of sealing proteins," *Journal of Cerebral Blood Flow & Metabolism*, vol. 41, no. 1, pp. 132–145, 2021.

[26] M. Grossetete, J. Phelps, L. Arko, H. Yonas, and G. A. Rosenberg, "Elevation of matrix metalloproteinases 3 and 9 in cerebrospinal fluid and blood in patients with severe traumatic brain injury," *Neurosurgery*, vol. 65, no. 4, pp. 702–708, 2009.

[27] F. Jia, Y. H. Pan, Q. Mao, Y. M. Liang, and J. Y. Jiang, "Matrix metalloproteinase-9 expression and protein levels after fluid percussion injury in rats: the effect of injury severity and brain temperature," *Journal of Neuroinflammation*, vol. 27, no. 6, pp. 1059–1068, 2010.

[28] F. Corrigan, K. A. Mander, A. V. Leonard, and R. Vink, "Neurogenic inflammation after traumatic brain injury and its potentiation of classical inflammation," *Journal of Neuroinflammation*, vol. 13, no. 1, p. 264, 2016.

[29] J. Mo, B. Enkhjargal, Z. D. Travis et al., "AVE 0991 attenuates oxidative stress and neuronal apoptosis via Mas/PKA/CREB/UCP-2 pathway after subarachnoid hemorrhage in rats," *Redox Biology*, vol. 20, pp. 75–86, 2019.

[30] S. Lores-Arnaiz, P. Lombardi, A. G. Karadayian, F. Orgambide, D. Cicerchia, and J. Bustamante, "Brain cortex mitochondrial bioenergetics in synaptosomes and non-synaptic mitochondria during aging," *Neurochemical Research*, vol. 41, no. 1-2, pp. 353–363, 2016.

[31] Y. Li, J. Wang, S. Chen et al., "miR-137 boosts the neuroprotective effect of endothelial progenitor cell-derived exosomes in oxyhemoglobin-treated SH-SY5Y cells partially via COX2/PGE2 pathway," *Stem Cell Research & Therapy*, vol. 11, no. 1, p. 330, 2020.

[32] E. Jangholi, Z. N. Sharifi, M. Hoseinian et al., "Verapamil inhibits mitochondria-induced reactive oxygen species and dependent apoptosis pathways in cerebral transient global ischemia/reperfusion," *Oxidative Medicine and Cellular Longevity*, vol. 2020, Article ID 5872645, 12 pages, 2020.

[33] K. Chen, Z. Xu, Y. Liu et al., "Irisin protects mitochondria function during pulmonary ischemia/reperfusion injury," *Science Translational Medicine*, vol. 9, no. 418, p. eaao6298, 2017.

[34] Y. Ren, M. Qiu, J. Zhang et al., "Low serum irisin concentration is associated with poor outcomes in patients with acute pancreatitis, and irisin administration protects against experimental acute pancreatitis," *Antioxidants & Redox Signaling*, vol. 31, no. 11, pp. 771–785, 2019.

[35] R. He, Y. Jiang, Y. Shi, J. Liang, and L. Zhao, "Curcumin-laden exosomes target ischemic brain tissue and alleviate cerebral ischemia-reperfusion injury by inhibiting ROS-mediated mitochondrial apoptosis," *Materials Science and Engineering: C*, vol. 117, article 111314, 2020.

[36] T. Nyunt, M. Britton, K. Wanichthanarak et al., "Mitochondrial oxidative stress-induced transcript variants of ATF3 mediate lipotoxic brain microvascular injury," *Free Radical Biology and Medicine*, vol. 143, pp. 25–46, 2019.

[37] J. Fang, H. Wang, J. Zhou et al., "Baicalin provides neuroprotection in traumatic brain injury mice model through Akt/Nrf2 pathway," *Drug Design, Development and Therapy*, vol. 12, pp. 2497–2508, 2018.

[38] L. Zhang, H. Wang, Y. Zhou, Y. Zhu, and M. Fei, "Fisetin alleviates oxidative stress after traumatic brain injury via the Nrf2-ARE pathway," *Neurochemistry International*, vol. 118, pp. 304–313, 2018.

[39] Y. Zhu, H. Wang, J. Fang et al., "SS-31 provides neuroprotection by reversing mitochondrial dysfunction after traumatic brain injury," *Oxidative Medicine and Cellular Longevity*, vol. 2018, Article ID 4783602, 12 pages, 2018.

[40] Y. Chen, K. Gong, Q. Xu et al., "Phosphoglycerate mutase 5 knockdown alleviates neuronal injury after traumatic brain injury through Drp1-mediated mitochondrial dysfunction," *Antioxidants & Redox Signaling*, vol. 34, no. 2, pp. 154–170, 2021.

[41] L.-f. Fan, P.-y. He, Y.-c. Peng et al., "Mdivi-1 ameliorates early brain injury after subarachnoid hemorrhage via the suppression of inflammation-related blood-brain barrier disruption and endoplasmic reticulum stress-based apoptosis," *Free Radical Biology and Medicine*, vol. 112, pp. 336–349, 2017.

[42] Z. Wang, F. Zhou, Y. Dou et al., "Melatonin alleviates intracerebral hemorrhage-induced secondary brain injury in rats via suppressing apoptosis, inflammation, oxidative stress, DNA damage, and mitochondria injury," *Translational Stroke Research*, vol. 9, no. 1, pp. 74–91, 2018.

[43] T. G. Aubrecht, A. I. Faden, B. Sabirzhanov et al., "Comparing effects of CDK inhibition and E2F1/2 ablation on neuronal cell death pathways in vitro and after traumatic brain injury," *Cell Death & Disease*, vol. 9, no. 11, p. 1121, 2018.

Hindawi
Oxidative Medicine and Cellular Longevity
Volume 2021, Article ID 5527137, 19 pages
https://doi.org/10.1155/2021/5527137

Research Article

Rosiglitazone Suppresses Renal Crystal Deposition by Ameliorating Tubular Injury Resulted from Oxidative Stress and Inflammatory Response via Promoting the Nrf2/HO-1 Pathway and Shifting Macrophage Polarization

Hongyan Lu,[1] **Xifeng Sun**,[2] **Min Jia**,[1] **Fa Sun**,[3] **Jianguo Zhu**,[3] **Xiaolong Chen**,[3] **Kun Chen**,[4] **and Kehua Jiang**[3,5]

[1]*Department of Urology, The Third Affiliated Hospital of Chongqing Medical University, Chongqing 401120, China*
[2]*Department of Urology, Medical University of Graz, Graz 8036, Austria*
[3]*Department of Urology, Guizhou Provincial People's Hospital, Guiyang 550002, China*
[4]*Prenatal Diagnosis Center, Guizhou Provincial People's Hospital, Guiyang 550002, China*
[5]*Medical College of Guizhou University, Guiyang, China*

Correspondence should be addressed to Kehua Jiang; tjjkh@sina.com

Received 25 February 2021; Revised 19 August 2021; Accepted 8 September 2021; Published 14 October 2021

Academic Editor: Xin Luo

Oxidative stress and inflammatory response are closely related to nephrolithiasis. This study is aimed at exploring whether rosiglitazone (ROSI), a regulator of macrophage (Mp) polarization, could reduce renal calcium oxalate (CaOx) deposition by ameliorating oxidative stress and inflammatory response. Male C57 mice were equally and randomly divided into 7 groups. Kidney sections were collected on day 5 or day 8 after treatment. Pizzolato staining and polarized light optical microscopy were used to detect crystal deposition. PAS staining and TUNEL assay were performed to assess the tubular injury and cell apoptosis, respectively. Gene expression was assessed by immunohistochemistry, immunofluorescence, ELISA, qRT-PCR, and Western blot. The reactive oxygen species (ROS) level was assessed using a fluorescence microplate and fluorescence microscope. Hydrogen peroxide (H_2O_2), malonaldehyde (MDA), and glutathione (GSH) were evaluated to determine oxidative stress. Lactic dehydrogenase (LDH) activity was examined to detect cell injury. Adhesion of CaOx monohydrate (COM) crystals to HK-2 cells was detected by crystal adhesion assay. HK-2 cell death or renal macrophage polarization was assessed by flow cytometry. *In vivo*, renal crystal deposition, tubular injury, crystal adhesion, cell apoptosis, oxidative stress, and inflammatory response were significantly increased in the 7-day glyoxylic acid- (Gly-) treated group but were decreased in the ROSI-treated groups, especially in the groups pretreated with ROSI. Moreover, ROSI significantly reduced renal Mp aggregation and M1Mp polarization but significantly enhanced renal M2Mp polarization. In vitro, ROSI significantly suppressed renal injury, apoptosis, and crystal adhesion of HK-2 cells and markedly shifted COM-stimulated M1Mps to M2Mps, presenting an anti-inflammatory effect. Furthermore, ROSI significantly suppressed oxidative stress by promoting the Nrf2/HO-1 pathway in HK-2 cells. These findings indicate that ROSI could ameliorate renal tubular injury that resulted from oxidative stress and inflammatory response by suppressing M1Mp polarization and promoting M2Mp polarization. Therefore, ROSI is a potential therapeutic and preventive drug for CaOx nephrolithiasis.

1. Introduction

Urolithiasis has a reported prevalence of 10% and 50% recurrence rates [1], potentially resulting in chronic kidney disease or even renal failure [2]. In addition, it has been estimated that, by 2030, the annual cost for managing urolithiasis in the United States is estimated to be about 4.6 billion dollars [3].

Table 1: Primers.

Primer (human)	Forward (5′-3′)	Reverse (5′-3′)
Ccl2	AGAATCACCAGCAGCAAGTGTCC	TCCTGAACCCACTTCTGCTTGG
CD11c	GATGCTCAGAGATACTTCACGGC	CCACACCATCACTTCTGCGTTC
iNOS	GCTCTACACCTCCAATGTGACC	CTGCCGAGATTTGAGCCTCATG
IL-6	GCACTGGCAGAAAACAACCT	TCAAACTCCAAAAGACCAGTGA
NF-κB	TGAACCGAAACTCTGGCAGCTG	CATCAGCTTGCGAAAAGGAGCC
TNF-α	CCCAGGGACCTCTCTCTAATC	ATGGGCTACAGGCTTGTCACT
CD206	CCGTATGCCGGTCACTGTTA	CAATTCCTCGATGGTGTGGA
Arg1	GTGGAAACTTGCATGGACAAC	AATCCTGGCACATCGGGAATC
IL-4	ATGGGTCTCACCTCCCAACT	GATGTCTGTTACGGTCAACTCG
IL-10	GACTTTAAGGGTTACCTGGGTTG	TCACATGCGCCTTGATGTCTG
IL-1β	ACGCTCCGGGACTCACAGCA	TGAGGCCCAAGGCCACAGGT
Nrf2	CACATCCAGTCAGAAACCAGTGG	GGAATGTCTGCGCCAAAAGCTG
HO-1	CCAGGCAGAGAATGCTGAGTTC	AAGACTGGGCTCTCCTTGTTGC
SOD1	CTCACTCTCAGGAGACCATTGC	CCACAAGCCAAACGACTTCCAG
PPARγ	CATGGCAATTGAATGTCGTGTC	CCGGAAGAAACCCTTGCAT
GAPDH	GACCTGACCTGCCGTCTA	AGGAGTGGGTGTCGCTGT

In the process of calcium oxalate (CaOx) crystal deposition, injury to the tubular epitheliums [4], which is frequently mediated by oxidative stress, plays a critical role during CaOx crystal deposition [5]. CaOx crystals upregulate NADPH oxidase p47phox and lead to overproduction of reactive oxygen species (ROS) in the tubular epitheliums. This is further enhanced by the proinflammatory effect of macrophages [6]. ROS are the leading mediators of oxidative stress injury, damaging the mitochondrial membrane and reducing the transmembrane potential [7, 8]. In addition, damaged tubular cells can act as the adhesive site for crystals, increasing their adhesion [9]. Therefore, CaOx crystal-induced oxidative stress is a critical process for nephrolithiasis formation.

Inflammation is another crucial process in nephrolithiasis formation. Following exposure to crystals, renal epitheliums express increased levels of monocyte chemotactic protein-1 (MCP1), inducing substantial Mp recruitment [10]. Mps play pivotal roles in inflammation and display different functional roles when responding to diverse microenvironmental signals [11, 12]. Two main phenotypes of Mps have been found: classically activated M1Mps, which are proinflammatory, and alternatively activated M2Mps, known to demonstrate an anti-inflammatory effect. CaOx crystals promoted M1Mp polarization which worsens the renal condition, resulting in fibrosis and chronic kidney disease [13, 14]. M1Mps reportedly promote renal crystal deposition in the mouse model [5]. On the contrary, stimulating M2Mp polarization could reduce renal injury [15–17]. Moreover, Mps have plasticity, by which polarized M1Mps can shift to M2Mps by employing specific signals [18]. Consequently, the M1/M2 Mp phenotype shift plays a pivotal role in regulating inflammation.

Nuclear factor erythroid-2-related factor 2 (Nrf2) is an antioxidative mediator which acts by regulating downstream genes [19, 20], including heme oxygenase 1 (HO-1). The Nrf2/HO-1 pathway is one of the most classical antioxidative approaches [21].

Peroxisome proliferator-activated receptor γ (PPARγ) is a nuclear receptor and inflammatory regulator [22]. PPARγ activation plays an anti-inflammatory effect by repressing intranuclear signaling pathways, containing nuclear factor-κB (NF-κB) in Mps [23], and has an antioxidant effect [24]. Moreover, PPARγ activation is critical for the polarization and maintenance of M2Mps [25, 26]. These characteristics indicate that PPARγ agonists might be a promising therapeutic option for nephrolithiasis.

However, data regarding the antioxidant and anti-inflammatory activities of PPARγ agonist ROSI are greatly limited. This study revealed that ROSI could suppress crystal deposition in the kidney of hyperoxaluric mice by inhibiting oxidative stress and inflammatory response.

2. Materials and Methods

2.1. Reagents. Glyoxylic acid (Gly) was acquired from Sigma-Aldrich (St. Louis, MO). COM crystals were prepared by the chemical method as described previously [27] and used in in vitro experiments at a concentration of 300 μg/mL. PPARγ agonist ROSI and antagonist GW9662 were both procured from MedChemExpress (MCE, China).

2.2. Animal Experiments. All animal experiments fulfilled the criteria of NIH and Guizhou Provincial People's Hospital for the humane treatment of laboratory animals and were approved by the Animal Care and Use Committee of Guizhou Provincial People's Hospital. Male C57BL/6 mice aged 6–8 weeks were acquired from the Experimental Animal Center and reared in SPF animal facilities at Guizhou Provincial People's Hospital.

In order to assess the effects of ROSI, 42 mice were equally assigned to 7 groups: the control group, 4 days

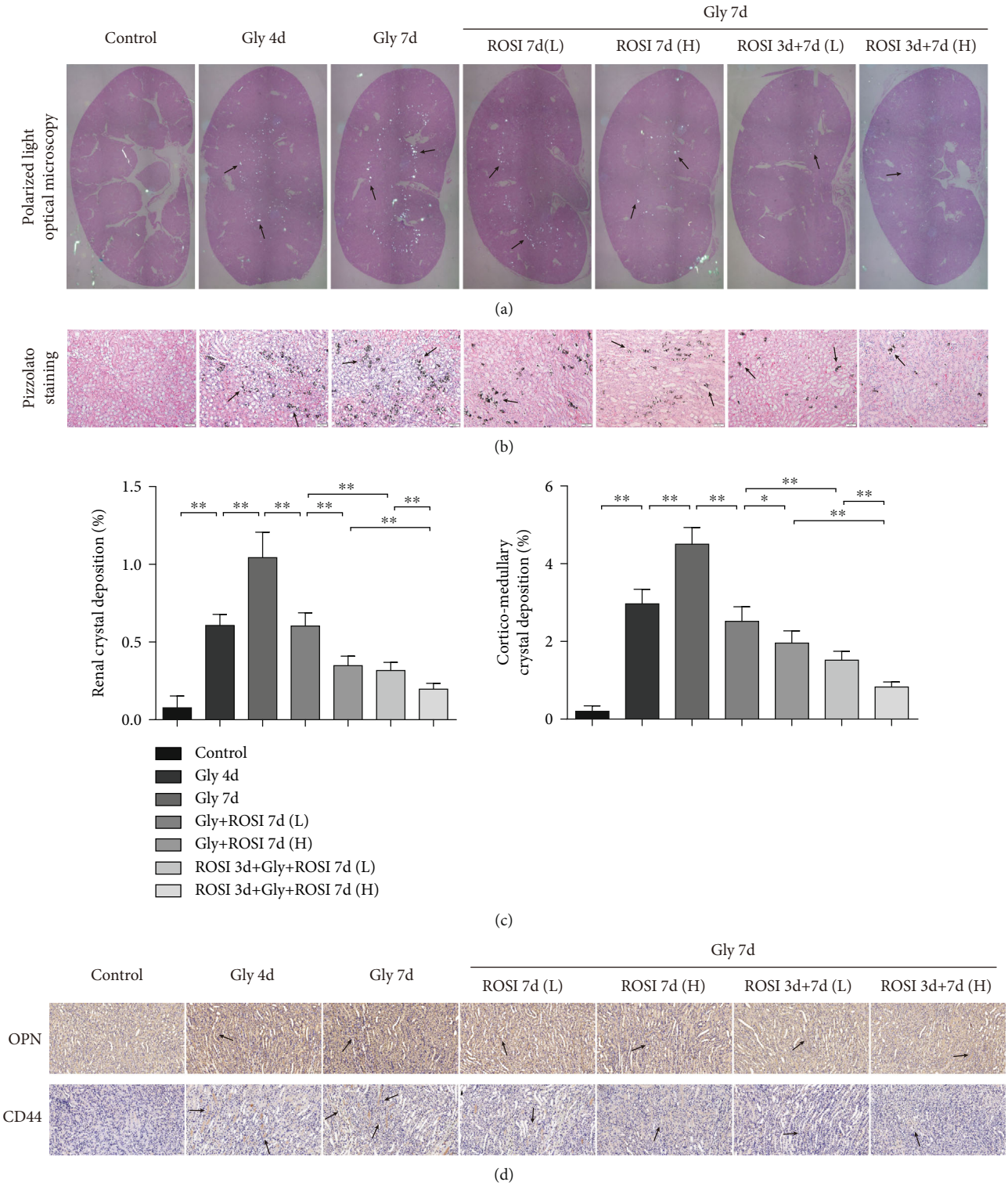

Figure 1: Continued.

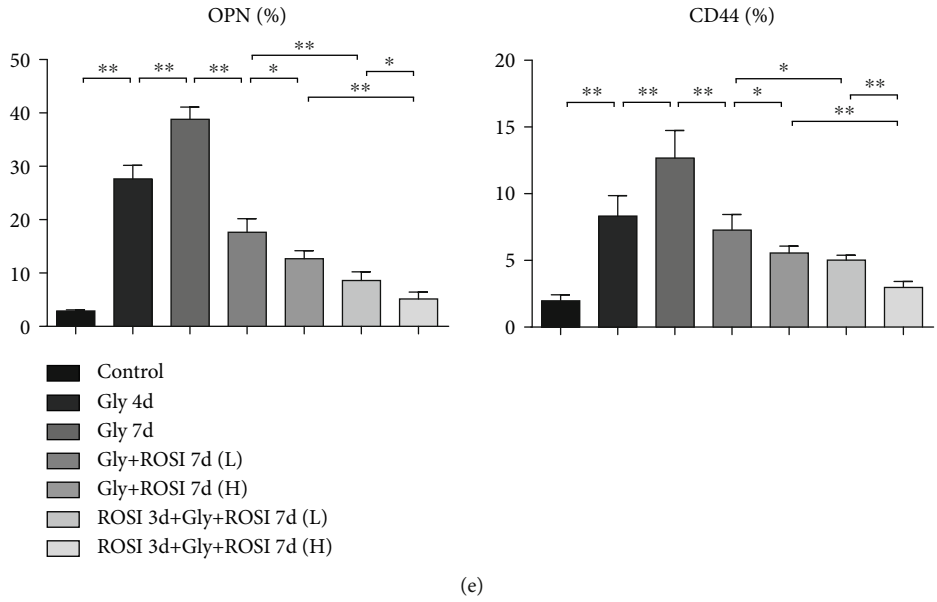

(e)

Figure 1: ROSI decreased the deposition of renal CaOx crystal in the mouse model. (a) Polarized light optical microscopy (arrows). ×20 magnification. (b) Pizzolato staining. Pizzolato staining indicates CaOx crystals (arrows). Scale bar = 50 μm. (c) The proportion of the crystal deposition area in the kidney and the proportion of crystal deposition areas in the corticomedullary border. (d) Immunohistochemical distribution of crystal-related gene OPN and crystal adhesion-related gene CD44. Scale bar = 50 μm. (e) The proportion of the IHC-positive area. Gly: glyoxylic acid; ROSI: rosiglitazone; CaOx: calcium oxalate. $^{*}p < 0.05$; $^{**}p < 0.01$.

80 mg/kg Gly (Gly 4d) group, 7 days 80 mg/kg Gly (Gly 7d) group, 7 days 80 mg/kg Gly plus 2.5 mg/kg or 5 mg/kg ROSI without pretreatment of ROSI (Gly+ROSI 7d(L)) group, Gly +ROSI 7d(H)) group, and 7 days 80 mg/kg Gly plus 2.5 mg/kg or 5 mg/kg ROSI with pretreatment of 3 days 2.5 mg/kg or 5 mg/kg ROSI (ROSI 3d+Gly+ROSI 7d(L), and ROSI 3d+Gly+ROSI 7d(H)) group. Mice were given a daily intraabdominal injection with Gly or vehicle (phosphate-buffered saline (PBS), Gibco) for 4 or 7 days. ROSI or vehicle (PBS) was administered via the gastric tube once daily. The kidneys were acquired on day 5 or day 8 after treatment to detect crystal deposition and for other related experiments.

2.3. Cell Culture and Treatment. THP-1 and HK-2 cells were purchased from the Cell Bank of the Chinese Academy of Science (Shanghai, China). THP-1 cells were cultured in RPMI-1640 (Gibco, USA) conditioned medium, and HK-2 cells were cultured in DMEM/F12 (Gibco, USA) conditioned medium containing 10% FBS and 1% penicillin-streptomycin in an incubator at 37°C and 5% CO_2.

For differentiating into M0Mps, THP-1 cells were diluted into a density of 2×10^5/mL and treated with 10 ng/mL phorbol-12-myristate-13-acetate (Sigma-Aldrich, USA) for 24 h. After removing the supernatant, the cells were washed thrice with PBS and cultured in RPMI-1640 conditioned medium for subsequent experiments.

For activating or suppressing PPARγ, THP-1 and HK-2 cells were treated with 1 μM ROSI or 10 μM GW9662, respectively, for 48 h. COM crystals (300 μg/mL) were utilized to treat cells for 48 h. HK-2 cells were transfected with Nrf2-siRNA for silencing Nrf2 expression.

2.4. Observation of the Deposition of Renal CaOx Crystal. Crystal deposition in sections was examined through Pizzolato staining, as presented previously [28]. Crystal containing calcium was determined through polarized light optical microscopy (CX31P; Olympus, Japan) in unstained sections. Crystal deposition was assessed quantitatively by ImageJ (National Institute of Health, USA) to calculate the percentage of the crystal deposition area in the entire kidney section or corticomedullary border.

2.5. Immunohistochemistry (IHC) and Immunofluorescence (IF). Briefly, kidney samples were fixed for 24 h with 4% buffered formalin before embedding into paraffin. Subsequently, sections at 4 μm thick were acquired. For IHC, the slides were incubated within antibodies for PPARγ (1 : 150, 2435, CST), iNOS (1 : 400, AF0199, Affinity), Arg1 (1 : 150, DF6657, Affinity), F4/80 (1 : 150, DF7762, Affinity), MCP1 (1 : 150, DF7577, Affinity), OPN (1 : 100, AF0227, Affinity), CD44 (1 : 100, DF6392, Affinity), IL-1β (1 : 150, AF5103, Affinity), HO-1 (1 : 200, AF5393, Affinity), Nrf2 (1 : 100, AF0639, Affinity), and SOD1 (1 : 150, AF5198, Affinity). Kidney sections were quantified through evaluating the proportion of the positive areas to the entire kidney section by ImageJ.

Immunoreactivity was examined by Histofine Simple Stain Kit for rabbit IgG following the protocol from the manufacturer. The Mp phenotypes were determined by IF staining for iNOS (1 : 100, 13120, CST) and Arg1 (1 : 100, 93668, CST). The slides of THP-1 cells were fixed for 15 minutes in 4% buffered formalin. After being rinsed with PBS and blocked with goat serum, the slides were incubated in primary antibodies at 4°C for over 12 h. Rinsed with PBS,

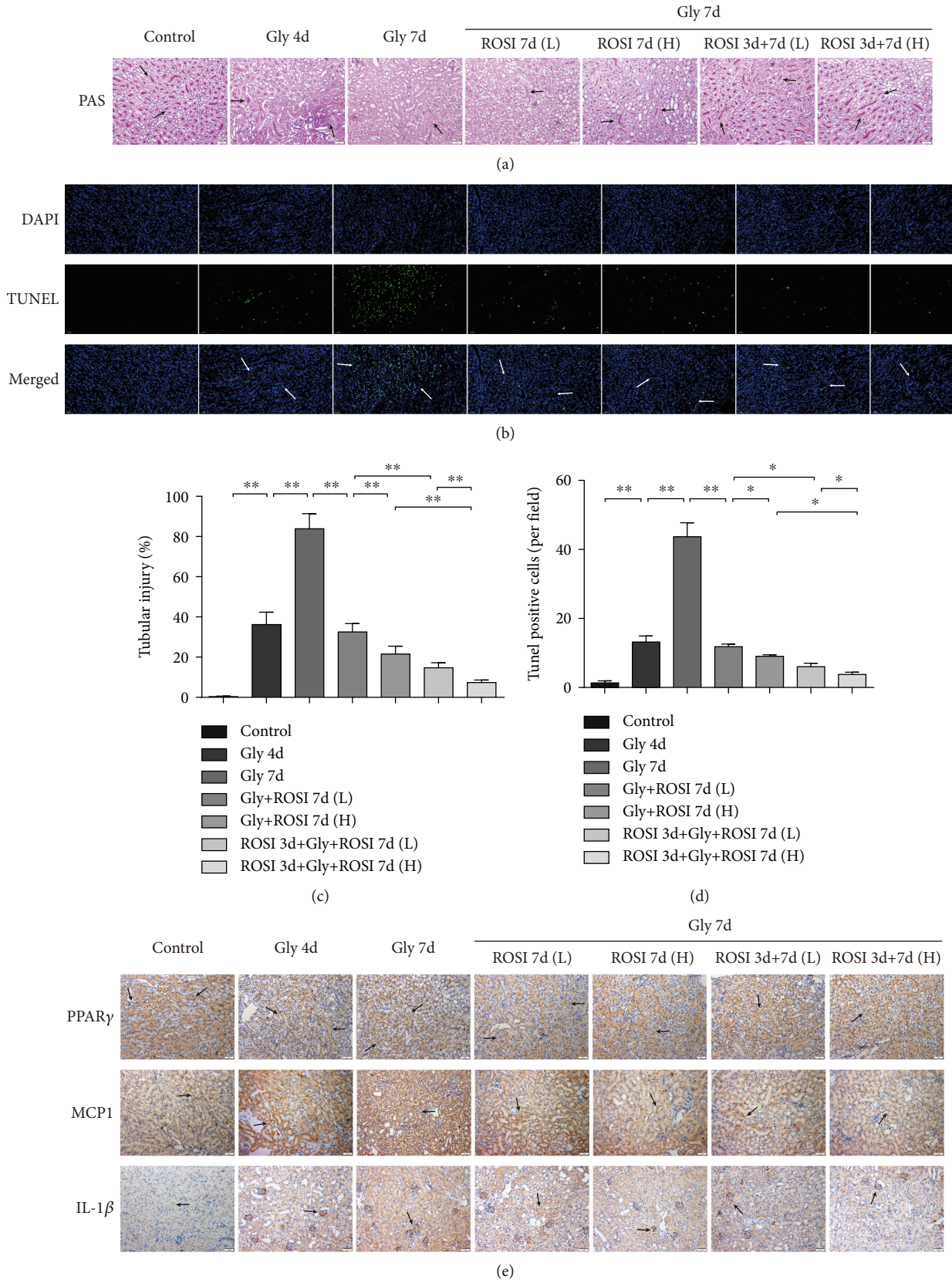

Figure 2: Continued.

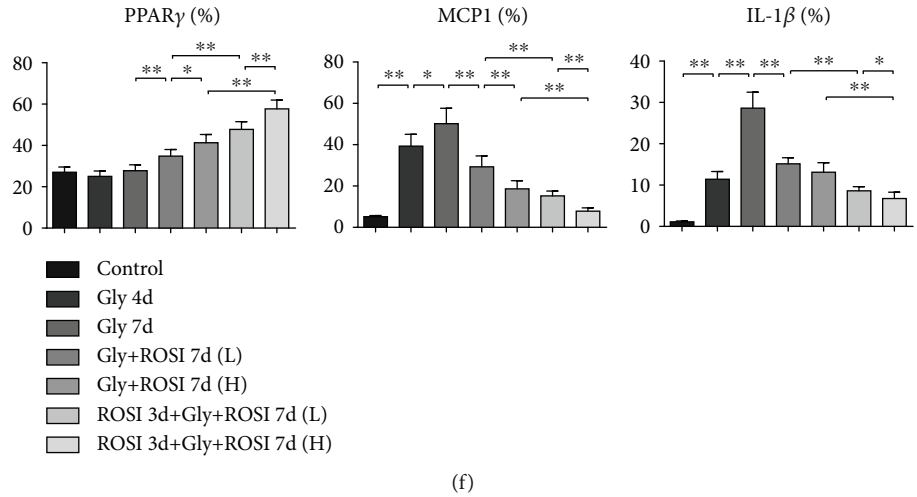

Figure 2: ROSI decreased renal tubular injury, cell apoptosis, and proinflammatory response in the mouse model. (a) PAS staining. PAS staining denotes tubular injury (arrows). Scale bar = 50 μm. (b) Cell apoptosis in the kidneys (arrows). Scale bar = 50 μm. (c) The percentage of damaged tubules displayed in PAS staining. (d) The mean number of apoptotic cells per high-power field (×400; $n = 10$ fields per section) in the TUNEL assay. (e) Immunohistochemical distribution of genetic expression of PPARγ, Mps-related molecule MCP1, and proinflammatory cytokine IL-1β. Scale bar = 50 μm. (f) The proportion of the IHC-positive area. Gly: glyoxylic acid; ROSI: rosiglitazone; PAS: periodic acid–Schiff; IL-1β: interleukin-1β; MCP1: monocyte chemotactic protein-1; PPARγ: peroxisome proliferator-activated receptor γ; IHC: immunohistochemistry. $^{*}p < 0.05$; $^{**}p < 0.01$.

the slides were incubated in Alexa Fluor-conjugated CY3- or 488-secondary antibodies (1 : 5000, G-21234, Thermo Fisher) for 1 h at room temperature. Finally, after being rinsed with PBS, the slides were counterstained with the nuclear marker DAPI and wet mounted. All images were obtained through a fluorescence microscope (Nikon TE2000-U, Japan), and the fluorescence intensity was quantified using ImageJ.

2.6. Tubular Injury and Cell Apoptosis. PAS staining was used to detect the cellular injury of renal tubules. The percentage of injured tubules was determined in 10 random fields at ×400 magnification in each section. Additionally, TUNEL assay was conducted to examine apoptotic cells in the renal tissue using the In Situ Cell Death Detection Kit (Roche, Switzerland). Positive cells in the TUNEL assay were determined in 10 random fields at ×400 magnification for every section.

2.7. qRT-PCR. Total RNA was acquired from THP-1 and HK-2 cells by TRIzol (Invitrogen, USA). Then, cDNAs were synthesized from 2 μg of total RNA by the PrimeScript RT Reagent Kit (TaKaRa). qPCR was conducted by SYBR green qPCR master mix (QIAGEN, Germany) via an ABI Prism 7300 system. All the reactions were triplicated. Target gene expression levels were quantified using the double-delta method ($2^{-\Delta\Delta Ct}$) for 3 independent experiments with normalization. Primers (provided by TSINGKE) used in experiments are listed in Table 1.

2.8. Western Blot. Whole-protein extracts were obtained with sonication and separated on 10% SDS-PAGE and then were transferred onto PVDF membrane (Millipore, USA). Blocked with TBST (pH 7.5) containing 5% BSA, the membranes were incubated within primary antibodies against MCP1 (1 : 1200, DF7577, Affinity), iNOS (1 : 800, AF0199, Affinity), Arg1 (1 : 800, DF6657, Affinity), IL-1β (1 : 800, AF5103, Affinity), phosphorylated NF-κBp65 (1 : 1000, 3039, CST), NF-κBp65 (1 : 1000, 8242, CST), PPARγ (1 : 600, 2435, CST), HO-1 (1 : 1000, AF5393, Affinity), Nrf2 (1 : 1000, AF0639, Affinity), SOD1 (1 : 1000, AF5198, Affinity), the endogenous control β-actin (1 : 1000, 4970, CST), and GAPDH (1 : 1000, 3683, CST) at 4°C overnight. The membranes were then incubated in HRP-conjugated secondary antibodies (1 : 3000, 7074, CST) for 1 h at room temperature. We used the ECL Western Blot Kit (Thermo Scientific Pierce) to examine the bands and scanned them using a LAS4000 analyzer (GE Healthcare). The immunoblot density was examined by ImageJ and normalized by β-actin or GAPDH.

2.9. Enzyme-Linked Immunosorbent Assay (ELISA). Cell supernatants were obtained after centrifugation and were stored at −80°C until further use. Secretion levels of TNF-α, IL-4, IL-6, and IL-10 were detected via specific ELISA kits, according to the instructions from the manufacturer (Dakewe, Shenzhen, China).

2.10. Measurement of Renal and Intracellular ROS Levels. ROS levels were assessed by the ROS Assay Kit containing 2,7-dichlorodi-hydrofluorescein-diacetate (DCFH-DA) (Nanjing Jiancheng Bioengineering Institute, China). Fluorescence intensities of DCFH-DA were measured by the fluorescence microplate for kidney tissues and by a fluorescence microscope for cells.

2.11. Measurement of Hydrogen Peroxide (H_2O_2), Malondialdehyde (MDA), and Glutathione (GSH). H_2O_2,

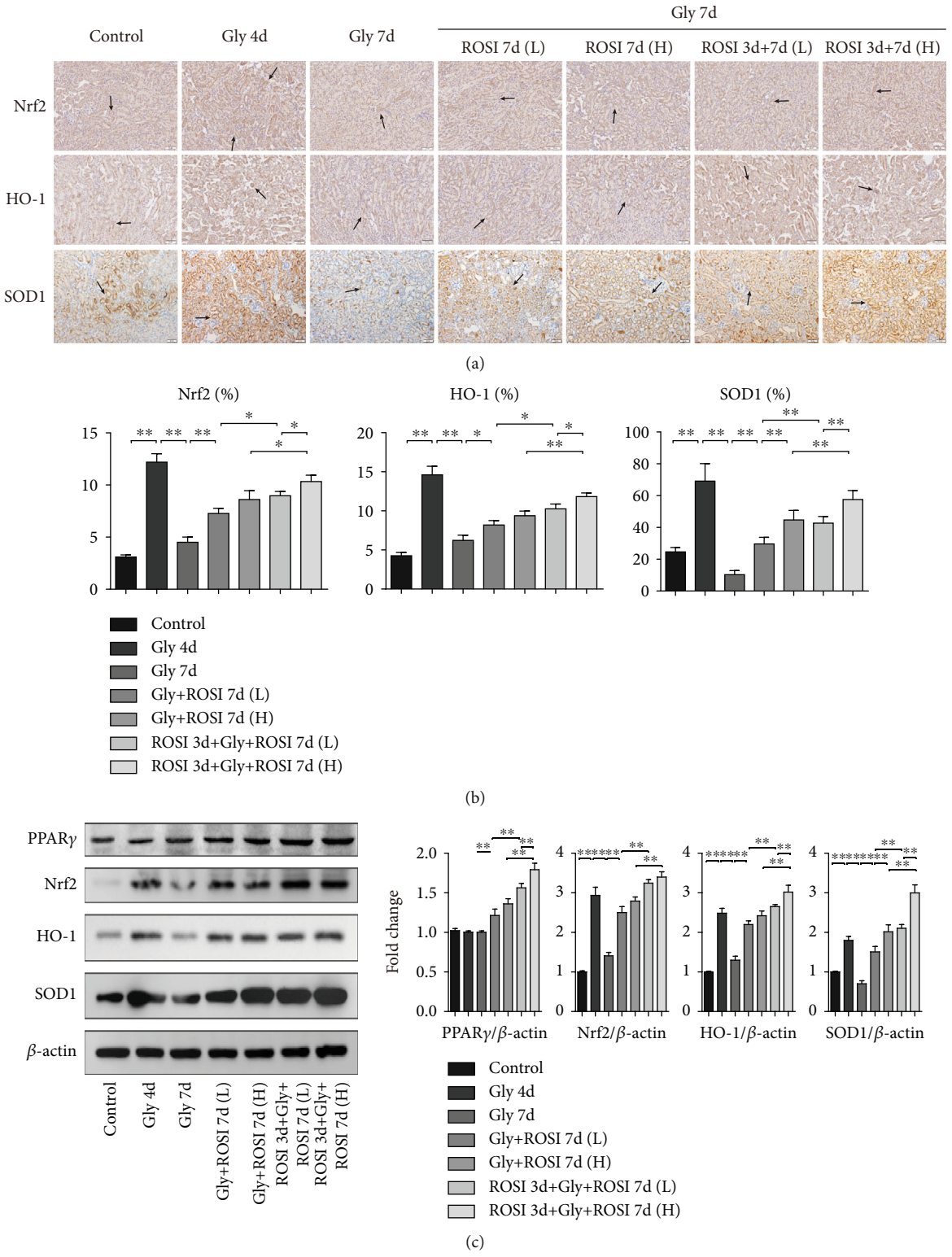

Figure 3: Continued.

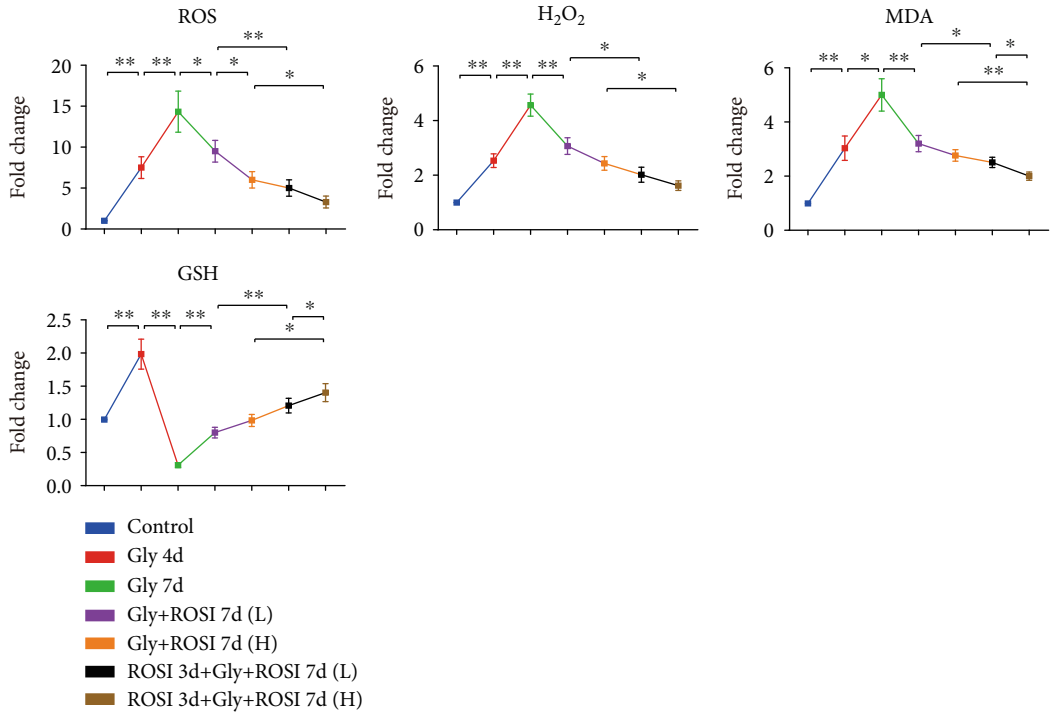

(d)

Figure 3: ROSI inhibited renal oxidative stress in the mouse model. (a) Immunohistochemical distribution of gene expression of Nrf2, HO-1, and SOD1 in the kidneys (arrows). Scale bar = 50 μm. (b) The proportion of the IHC-positive area. (c) The expression of PPARγ, Nrf2, HO-1, and SOD1 in kidney tissues by Western blotting. (d) ROS, H_2O_2, MDA, and GSH levels in mouse renal tissues. Gly: glyoxylic acid; ROSI: rosiglitazone. $^*p < 0.05$; $^{**}p < 0.01$.

MDA, and GSH activities in the renal tissues or cell supernatants were measured by the Hydrogen Peroxide Assay Kit, Lipid Peroxidation MDA Assay Kit, and GSH Assay Kit (Beyotime, China), respectively, according to instructions from manufacturers. All results were normalized according to corresponding control samples.

2.12. Lactate Dehydrogenase (LDH) Assay. Cellular LDH activities were detected using the LDH Assay Kit (Beyotime, China), according to the direction from the manufacturer. The absorbance (490 nm) was measured by a microplate reader (Thermo Multiskan MK3, USA).

2.13. Flow Cytometry. Cell death was measured through the Annexin V-FITC/PI (fluorescein isothiocyanate/propidium iodide) Apoptosis Detection Kit (R&D Systems, USA), according to the direction from the manufacturer. The fluorescence intensity of Annexin V-FITC/PI was detected through flow cytometry (BD Bioscience).

For quantifying the renal macrophage polarization in mouse kidneys, kidney tissues were minced into 1 mm^3 fragments and then digested in RPMI 1640 buffer containing 100 U/mL DNase I and 2 mg/mL collagenase type D for 60 min at 37°C and then passed through a 70 μm mesh to get single-cell suspension. Red blood cell lysis buffer (Sigma, USA) was used for lysing the red blood cells in the suspension. Mps were centrifuged and then resuspended in FACS buffer on ice. Incubated with 2.5 μg/mL Fc-blocking solution, Mps were resuspended in FACS buffer. Then, 10^6 cells were stained with 3 fluorochrome-labeled antibodies: F4/80 (eBioscience)-PE, CD11c-FITC, and CD206-FITC. Finally, Mps were detected immediately on a FACS Canto II cytometer with DIVA software (Becton Dickinson). The data were analyzed by Cyflogic V.1.2.1 software.

2.14. Crystal Adhesion Assay. HK-2 cells were cultured to 100% confluency in a 6-well plate. Stimulated with COM crystal and ROSI or/and GW9662 treatment for 48 h, the plate was thoroughly washed 3 times using PBS to remove unbound crystals from cells. The crystal quantity was examined using a microscope. Images were randomly selected from 10 visual fields (magnification of ×400) and quantified using ImageJ Pro Plus software [29]. All experimental group data were normalized to the normal control group based on 3 independently repeated experiments.

2.15. Small Interfering RNA Knockdown. For cell transfections, Nrf2 siRNA was obtained from Santa Cruz Biotechnology (Ribo, Guangzhou, China). HK-2 cells were transfected with 50 nM siRNA with Lipofectamine 2000 siRNA transfection reagent (Thermo Fisher) for 24 h before ROSI treatment.

2.16. Statistical Analysis. Data were presented as mean ± standard deviation (SD). A two-tailed t-test was conducted to identify statistical difference using GraphPad Prism 6.0

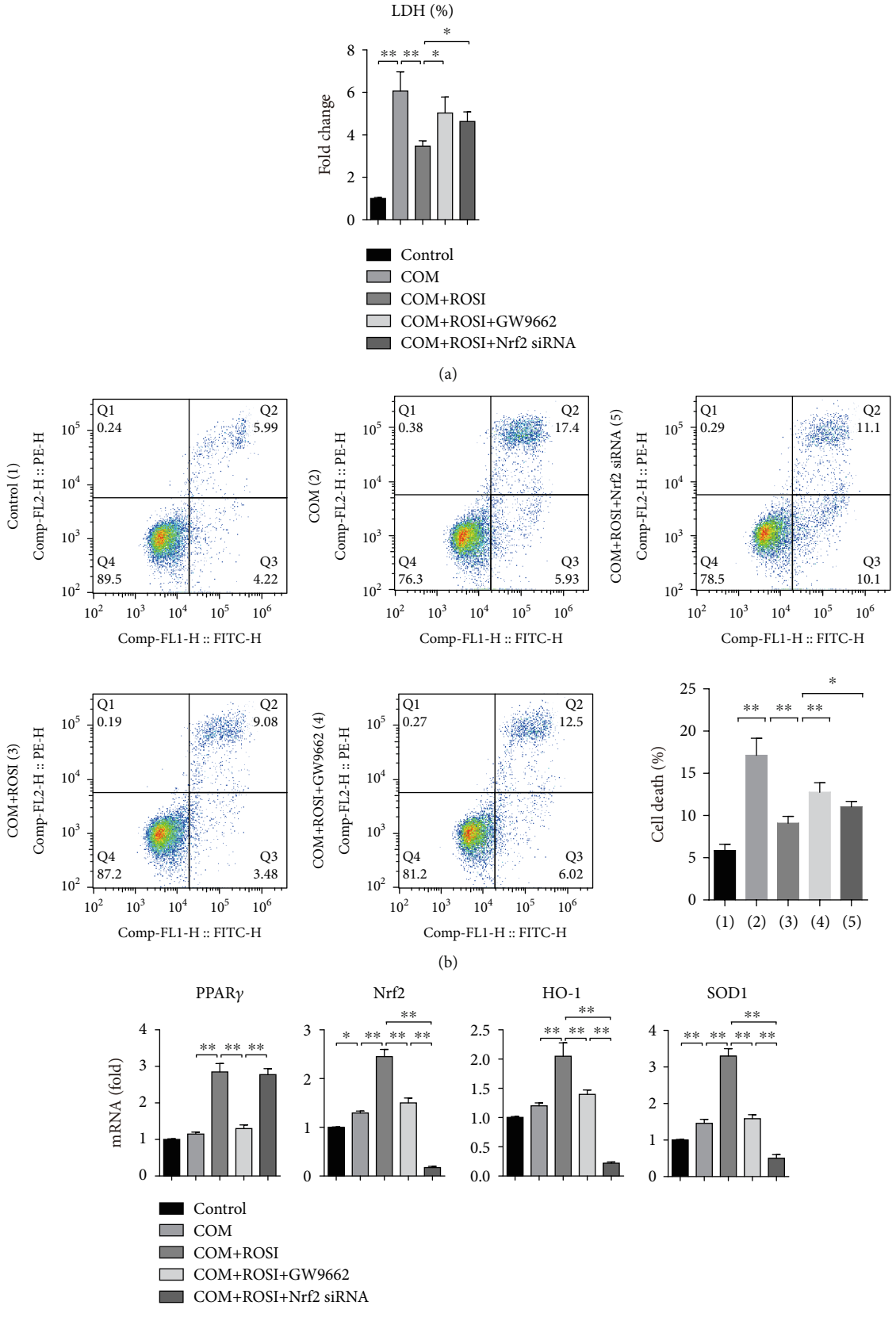

Figure 4: Continued.

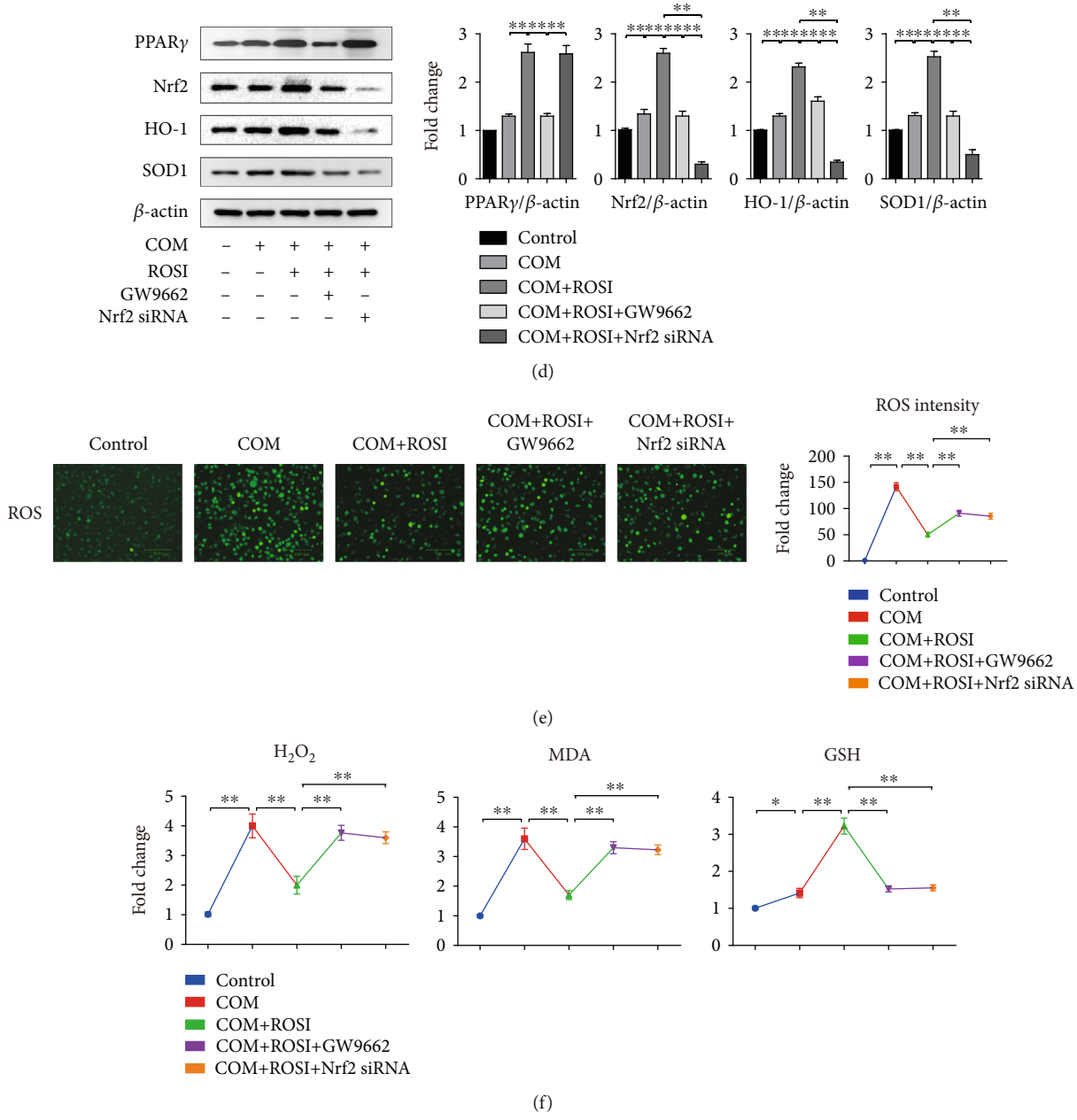

Figure 4: ROSI suppressed CaOx-induced oxidative stress injury and promoted the Nrf2/HO-1 pathway in HK-2 cell. (a) Cellular LDH levels in HK-2 cells. (b) HK-2 cell death by flow cytometry. (c) mRNA expression levels of Nrf2, HO-1, and SOD1 in HK-2 cells by qRT-PCR. (d) The expression of PPARγ, Nrf2, HO-1, and SOD1 in HK-2 cells by Western blot. (e) Detection of intracellular ROS levels by a fluorescence microscope. (f) H_2O_2, MDA, and GSH levels in HK-2 cells. COM: calcium oxalate monohydrate; ROSI: rosiglitazone. $^{*}p < 0.05$; $^{**}p < 0.01$.

(GraphPad Software, USA). Difference was considered statistically significant at $p < 0.05$.

3. Results

3.1. ROSI Suppressed the Deposition of Renal CaOx Crystals in the Mouse Model. Renal CaOx crystals were measured by polarized light microscopy and Pizzolato straining. The results revealed that crystals were mainly deposited in renal tubules at the corticomedullary borders and the number of crystals gradually increased over time in the Gly groups (Figures 1(a) and 1(b)). Crystals in the entire kidney or renal corticomedullary borders were significantly larger and more in the Gly 7d group than in the Gly 4d group. Notably, crystals were significantly decreased in ROSI treatment groups than in the Gly 7d group in a dose-dependent way. Furthermore, there were significantly fewer and smaller crystals in the ROSI pretreatment groups than in the nonpretreatment groups (Figure 1(c)).

IHC results suggested that the expression levels of the crystal-related gene osteopontin (OPN) and crystal adhesion-related gene CD44 were markedly increased in

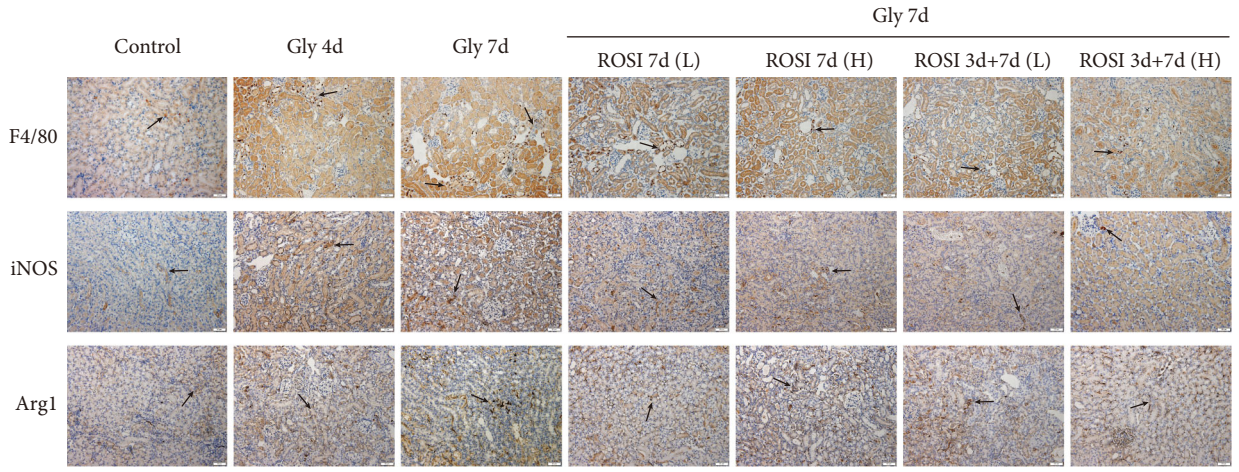

(a)

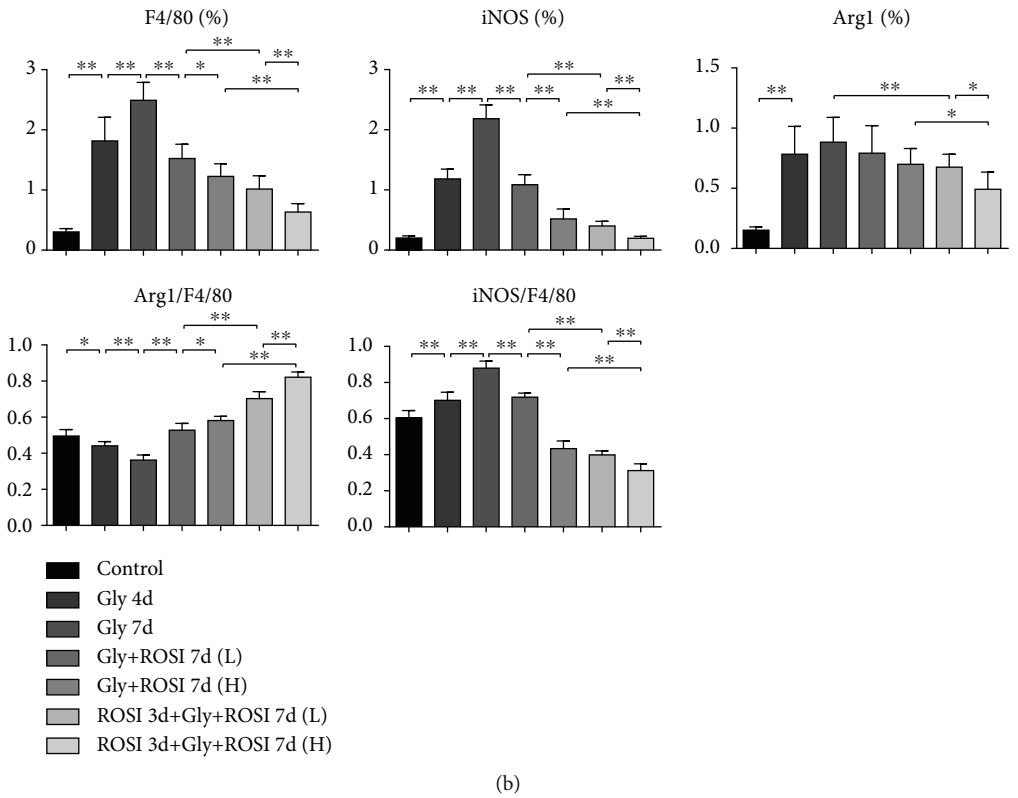

(b)

Figure 5: Continued.

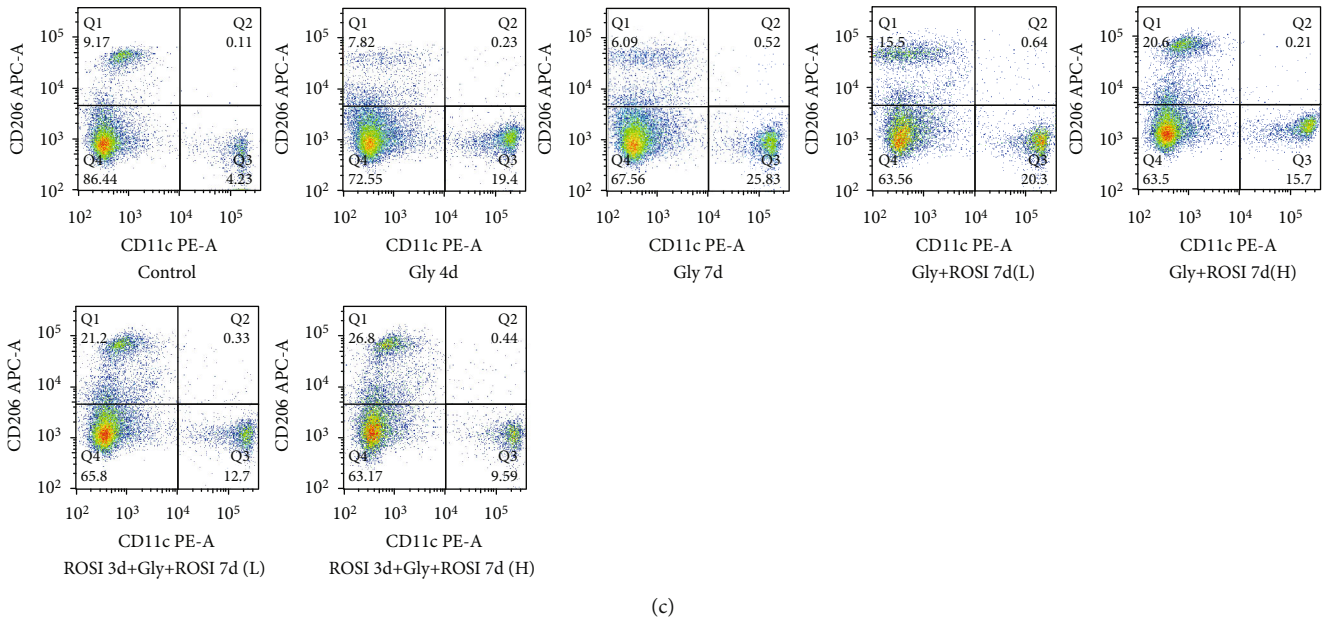

(c)

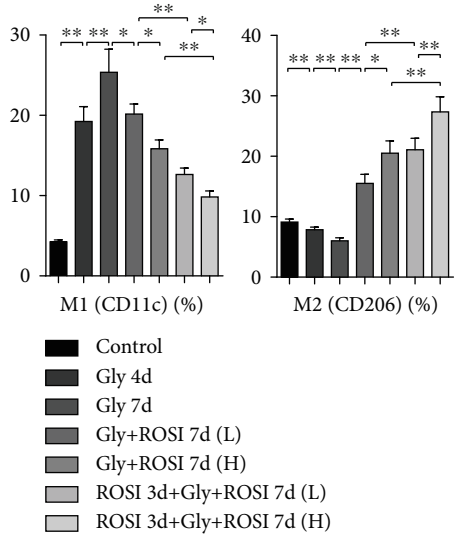

(d)

Figure 5: ROSI decreased renal macrophage recruitment and M1Mp polarization and promoted renal M2Mp polarization in the mouse model. (a) Immunohistochemical distribution of genetic expression of PPARγ, macrophage-related molecules, and proinflammatory cytokines (arrows). Scale bar = 50 μm. (b) The proportion of the IHC-positive area and the ratio of Arg1/F4/80 and iNOS/F4/80. (c) Flow cytometric detection of Mps in kidney tissues. (d) The proportion of M1Mps and M2Mps in kidney tissues. Gly: glyoxylic acid; ROSI: rosiglitazone; PPARγ: peroxisome proliferator-activated receptor γ. $^{*}p < 0.05$; $^{**}p < 0.01$.

the Gly 4d group than in the control group, increased in the Gly 7d group than in the Gly 4d group, dose dependently decreased in the ROSI treatment groups than in the Gly 7d group, and decreased in the pretreatment groups than in the nonpretreatment groups (Figures 1(d) and 1(e)).

3.2. ROSI Decreased Renal Cell Apoptosis, Tubular Injury, and Proinflammatory Response in the Mouse Model. For all groups, PAS staining showed that positively stained cells were mainly located in the renal tubules. Positive tubules were significantly fewer in the Gly 7d group and markedly more in the ROSI-treated groups than in the Gly 7d group in a dose-dependent way. In addition, positively stained tubules were substantially more in the pretreatment groups than in the nonpretreatment groups (Figures 2(a) and 2(c)).

TUNEL assay results revealed that positive cells were significantly more in the Gly 7d group, but fewer in the ROSI treatment groups than in the Gly 7d group, presenting a dose-dependent reduction. Moreover, positive cells were significantly fewer in the ROSI pretreatment groups than in the nonpretreatment groups (Figures 2(b) and 2(d)).

The expression of renal PPARγ was markedly and dose dependently increased in the ROSI treatment groups than in the Gly 7d group, and PPARγ expression was markedly increased in the ROSI pretreatment groups than in the nonpretreatment groups. The expression levels of the Mps-

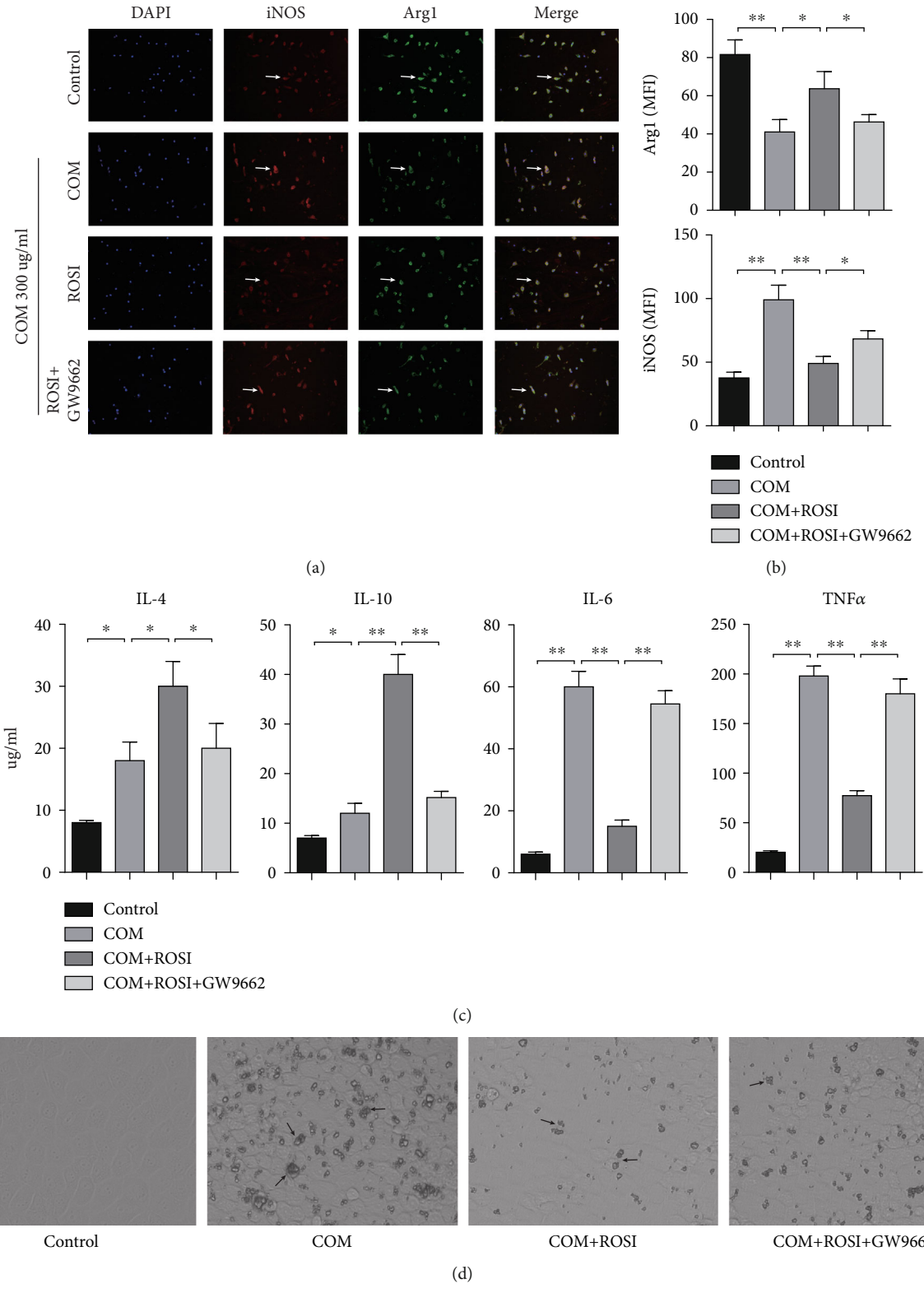

Figure 6: Continued.

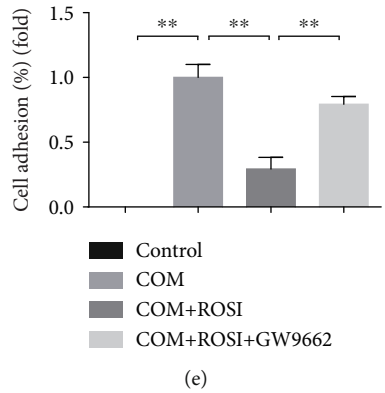

(e)

Figure 6: ROSI declined COM-stimulated M1Mp polarization and crystal adhesion and promoted M2Mp polarization in vitro. (a) Fluorescence immunohistochemical distribution of Arg1 (green) and iNOS (red) in THP-1 cells with the stimulus of COM or ROSI (1 μM) or GW9662 (10 μM) (arrows). (b) Evaluation of mean fluorescence intensity (MFI) of Arg1 and iNOS. (c) ELISA. The expression levels of IL-4, IL-10, IL-6, and TNF-α. (d) Crystal adhesion assay. COM crystal adhesion to HK-2 cells was observed (arrows). COM: calcium oxalate monohydrate; ROSI: rosiglitazone; iNOS: induced nitric oxide synthase; TNF-α: tumor necrosis factor α. $^{*}p < 0.05$; $^{**}p < 0.01$.

related molecule MCP1 and proinflammatory cytokine IL-1β were markedly increased in the Gly 4d and 7d groups; however, they were markedly decreased in the ROSI treatment groups in a dose-dependent manner. A significant decrease in expression levels of MCP1 and IL-1β was also noted in the pretreatment groups (vs. nonpretreatment groups) (Figures 2(e) and 2(f)).

3.3. ROSI Decreased Renal Oxidative Stress in the Mouse Model. Our results demonstrated that the expression of Nrf2, HO-1, SOD1, and GSH markedly increased in the Gly 4d group than in the control group, decreased in the Gly 7d group than in the Gly 4d group, dose dependently increased in the ROSI treatment groups than in the Gly 7d group, and increased in the pretreatment groups than in the nonpretreatment groups. The expression of PPARγ was markedly and dose dependently increased in the ROSI treatment groups than in the Gly 7d group and was markedly increased in the ROSI pretreatment groups than in the nonpretreatment groups (Figure 3).

The generations of ROS, H_2O_2, and MDA markedly increased in the Gly 4d group than in the control group, increased in the Gly 7d group than in the Gly 4d group, dose dependently decreased in the ROSI treatment groups than in the Gly 7d group, and decreased in the pretreatment groups than in the nonpretreatment groups (Figure 3(c)).

3.4. ROSI Suppressed Oxidative Stress Injury via Promoting the Nrf2/HO-1 Pathway in HK-2 Cell. For exploring the effect of ROSI on tubular epitheliums, we carried out cell experiments. The results revealed that LDH activity and death of HK-2 cells markedly increased in the COM group compared to the control group. Moreover, LDH activity and cell death markedly decreased after simultaneous ROSI treatment than in the COM group and increased in the GW9662 treatment group than in the ROSI group. In addition, Nrf2 silencing by siRNA also attenuated the effect of ROSI treatment (Figures 4(a) and 4(b)).

In HK-2 cells, expression of PPARγ markedly increased in the ROSI treatment group and markedly decreased in the GW9662-treated group, whereas it was not significantly affected by Nrf2-siRNA treatment. Genetic expression of Nrf2, HO-1, SOD1, and GSH markedly increased in the COM group than in the control group, increased in the ROSI group than in the COM group, and decreased in the GW9662 and Nrf2-siRNA treatment groups than in the ROSI group (Figures 4(c), 4(d), and 4(f)).

Furthermore, the productions of ROS, H_2O_2, and MDA in HK-2 cells markedly increased in the COM group than in the control group, decreased in the ROSI treatment group than in the COM group, and increased in the GW9662 and Nrf2-siRNA treatment groups than in the ROSI group (Figures 4(e) and 4(f)).

3.5. ROSI Decreased Macrophage Recruitment and Polarization of M1Mps but Increased Polarization of M2Mps in the Mouse Model. IHC showed that expression levels of Mp marker F4/80, M1Mp marker iNOS, and M2Mp marker Arg1 were markedly increased in the Gly 4d and 7d groups. However, these levels were markedly decreased in the ROSI treatment groups in a dose-dependent way, with a significant reduction observed in the ROSI pretreatment groups than in the nonpretreatment groups (Figures 5(a) and 5(b)).

Interestingly, the ratio of Arg1/F4/80 markedly decreased in the Gly 4d and 7d groups than in the control group, with a dose-dependent increase observed in the ROSI-treated groups. In addition, the ratio of Arg/F4/80 was higher in the ROSI pretreatment groups than in the nonpretreatment groups. Meanwhile, the ratio of iNOS/F4/80 demonstrated the opposite trend (Figure 5(b)).

Furthermore, the flow cytometry results of renal macrophage polarization showed that the proportion of M1Mps markedly increased in the Gly 4d and 7d groups than in the control group, with a dose-dependent decrease in the ROSI treatment groups. Meanwhile, the proportion of

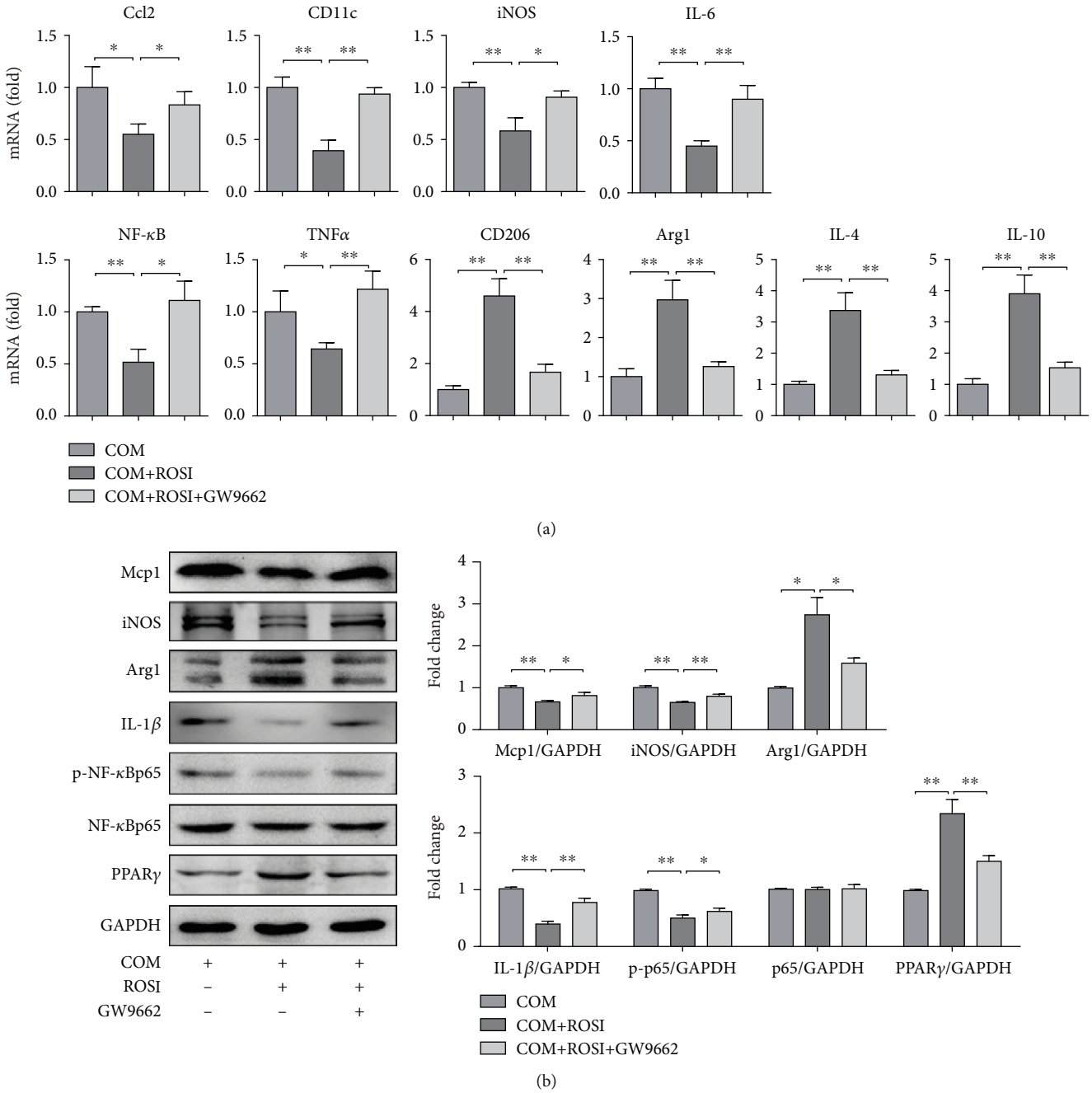

Figure 7: Genetic expression of macrophage-related molecules, proinflammatory cytokines, and anti-inflammatory cytokines. (a) mRNA levels in THP-1 cells stimulated with COM or ROSI (1 μM) or GW9662 (10 μM) by qRT-PCR. (b) Genetic expression determined by Western blot. COM: calcium oxalate monohydrate; ROSI: rosiglitazone. $^{*}p < 0.05$; $^{**}p < 0.01$.

M1Mps markedly decreased in the ROSI pretreatment groups than in the nonpretreatment groups, whereas the proportion of M2Mps demonstrated the opposite trend (Figures 5(c) and 5(d)).

3.6. ROSI Declined COM-Stimulated M1Mp Polarization and Crystal Adhesion, as well as Promoted M2Mp Polarization In Vitro. The experiments revealed that ROSI treatment upregulated renal PPARγ expression, inhibited Mp aggregation, and shifted the COM-stimulated M1Mp polarization to M2Mp polarization. Moreover, compared with the control group, THP-1 cells treated with COM primarily showed M1Mp polarization, characterized by increased expression of M1Mp marker iNOS and proinflammatory cytokines (TNF-α and IL-6), but decreased expression of M2Mp marker Arg1 and anti-inflammatory cytokines (IL-4 and IL-10) (Figures 6(a) and 6(b)).

Following COM stimulation, THP-1 cells were treated with ROSI (PPARγ agonist, 1 μM) and with or without GW9662 (PPARγ antagonist, 10 μM). The results showed

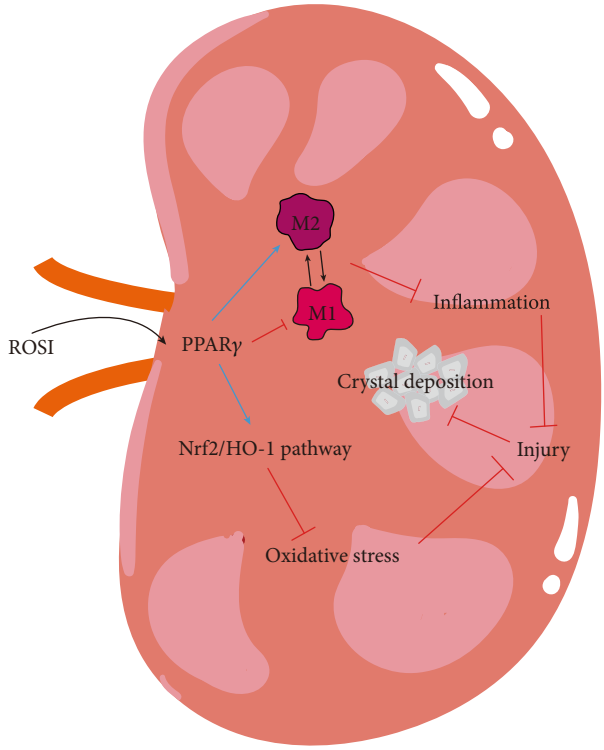

Figure 8: Mechanisms by which ROSI suppresses CaOx crystal deposition. ROSI: rosiglitazone; PPARγ: peroxisome proliferator-activated receptor γ.

that ROSI significantly decreased the expression of PPARγ, M1Mps markers (iNOS and CD11c), proinflammatory cytokines (Ccl2, IL-6, and TNF-α), phosphorylated NF-κB and IL-1β, but increased the expression of M2Mp markers (Arg1 and CD206) and anti-inflammatory cytokines (IL-4 and IL-10). However, GW9662 diminished the effects of ROSI (Figures 6 and 7). Moreover, as for the COM crystal adhesion to HK-2 cells, ROSI significantly decreased crystal adhesion, whereas GW9662 diminished the effect of ROSI (Figures 6(d) and 6(e)).

4. Discussion

Crystal deposition may result in tubular injury [30], which in turn promotes crystal deposition [31]. In the above process, oxidative stress and inflammatory response play pivotal roles [32].

Being exposed to CaOx crystals, tubular epitheliums overproduce oxidative stress products, such as ROS [6]. As a leading mediator of oxidative stress, ROS leads to tubular injury, promoting the adhesion and deposition of crystals [9]. Nrf2 is a redox-sensitive transcription factor, playing critical roles in reducing intracellular oxidative stress and tissue injury [33]. Previous reports have revealed that the Nrf2/HO-1 pathway has potent antioxidant effects [21], whereby inhibiting the formation of CaOx-induced nephrolithiasis [34, 35].

Deposition of THE CaOx crystal can pose migration and aggregation of Mps to the areas of crystal deposition [36]. Polarization of Mps is deeply involved in inflammation regulation, crystal phagocytosis, and crystal removal [37]. A previous study has revealed that CaOx crystals effectively induce M1Mp polarization, promoting renal injury and crystal deposition [38]. Furthermore, Taguchi et al. have observed that M2Mps have the ability of crystal phagocytosis and antiadherence [17]. As an agonist of PPARγ, ROSI takes a vital part in the intricate modulatory network of alternative activation of Mps [26]. Tabassum and Mahboob found that ROSI could reduce HFD-induced oxidative stress damage [39]. Deng et al. revealed that ROSI treatment inhibited renal macrophage infiltration and TGF-β and NF-κB pathway activation [40]. Liu et al. found that ROSI could regulate the TGF-β1 and HGF/c-Met pathways to play an antioxidant effect to reduce crystal deposition in the hyperoxaluria rat model [41]. In addition, previous studies have suggested that pioglitazone, another PPARγ agonist, can suppress crystal deposition, thus exhibiting prominent anti-inflammatory ability [23, 42, 43].

In this study, we observed that ROSI could suppress oxidative stress injury by upregulating the Nrf2/HO-1 pathway. Moreover, we noted that ROSI could regulate inflammation by shifting COM-stimulated M1Mp polarization toward M2Mp polarization. Namely, the above effects might suppress tubular injury synergistically, consequently reducing the deposition of crystal.

As the above speculated, our results indicated that the deposited crystals were fewer and smaller and the renal injury was also milder in the ROSI-treated groups; these effects were more pronounced in the groups with ROSI pretreatment. Furthermore, the apoptosis of HK-2 cells was significantly reduced after treating with ROSI.

Moreover, our finding revealed that the generation of oxidative stress products, i.e., ROS, MDA, and H_2O_2, was significantly reduced. Conversely, expression levels of antioxidant products, i.e., SOD1 and GSH, were significantly upregulated after treating with ROSI. In addition, the effects of ROSI for suppressing oxidative stress and inflammation were found to be dose dependent both *in vivo* and *in vitro*.

Finally, in ROSI-treated hyperoxaluria mice, the expression of renal PPARγ was markedly increased. Subsequently, the MCP1 expression and Mp recruitment reduced with the decrease in M1Mps and the increase in M2Mps. The expression of iNOS was increased, but the expression of Arg1 was decreased in the Gly 7d group, which is similar to findings of a microarray analysis of renal papillary tissues from nephrolithiasis formers [13]. Interestingly, the renal Mps mainly were polarized into M1Mps after being stimulated by CaOx crystals. In contrast, the proportion of M2Mps increased in the ROSI-treated groups, reaching up to 70%. Accordingly, ROSI may pose a shift of Mp polarization. In vitro, ROSI also exhibited an anti-inflammatory ability due to shifting polarization of Mps.

We speculate that ROSI upregulates the expression of PPARγ, whereby it exerts antioxidant and anti-inflammatory functions, which subsequently synergistically suppressed CaOx crystal deposition and renal injury. In terms of oxidative stress, ROSI potentially improves the imbalance between oxidative and antioxidant products by

upregulating the Nrf2/HO-1 pathway. Finally, in terms of inflammation, M1Mp polarization was reduced while M2Mp polarization was enhanced and, in turn, lowered the expression of MCP1 in the renal tubular epitheliums and proinflammatory cytokines from Mps; this contributed to a subsequent decrease in macrophage recruitment and renal inflammation.

It should be noted that several limitations exist in this research: (1) with pronounced high concentration of oxalate, the mouse model used in in vivo experiment fails to mimic the development of CaOx nephrolithiasis comprehensively; (2) the doses of ROSI (2.5 mg/kg, 5 mg/kg) used in mouse model were much higher than those employed in clinical settings (usually, 4 mg/d); (3) the effects of ROSI are indirect and gentle, which may be influenced by other latent factors; and (4) the preventive and therapeutic effects, as well as the safety of ROSI for clinical practice, need further confirmation by well-designed clinical researches.

5. Conclusion

Our results reveal that ROSI might decrease tubular injury-induced renal CaOx crystal deposition via suppressing oxidative stress and inflammation, mediated by promoting the Nrf2/HO-1 pathway and shifting macrophage polarization (Figure 8). Thus, ROSI could be a potential preventive and therapeutic drug for CaOx nephrolithiasis.

Abbreviations

Mps: Macrophages
ROSI: Rosiglitazone
PPARγ: Peroxisome proliferator-activated receptor γ
CaOx: Calcium oxalate
ROS: Reactive oxygen species
Gly: Glyoxylic acid
COM: Calcium oxalate monohydrate
MCP1: Monocyte chemotactic protein 1
H_2O_2: Hydrogen peroxide
MDA: Malondialdehyde
GSH: Glutathione
LDH: Lactate dehydrogenase.

Data Availability

The data on supporting information are available from the corresponding author upon reasonable request.

Additional Points

Highlights. Rosiglitazone suppresses renal crystal deposition in the hyperoxaluria mouse model. Rosiglitazone ameliorates renal epithelial oxidative and inflammatory injury in the hyperoxaluria mouse model. Rosiglitazone is a potential preventive and therapeutic drug for CaOx nephrolithiasis.

Disclosure

The funding agencies have no roles in any aspect of this study.

Conflicts of Interest

The authors declare no conflicts of interest regarding the publication of this paper.

Authors' Contributions

LHY, SXF, and JKH conceived and designed the research. LHY, SXF, and JM performed the experiments. SXF, JM, SF, ZJG, CXL, and CK analyzed the data and interpreted the results. LHY and SXF prepared the figures and wrote the manuscript. LHY, SXF, and JKH revised the manuscript. All authors reviewed and approved the final version of the manuscript. Hongyan Lu and Xifeng Sun are joint first authors.

Acknowledgments

We deeply thank Prof. Karl Pummer, Prof. Georg Hutterer, Prof. Kittinger Clemens, and Dr. Boris Hager from the Medical University of Graz for their suggestions to revise this paper. In addition, Xifeng Sun wants to thank, in particular, the unwavering companionship and support from Miss Cheng Luo in the course of preparing this paper. This study was funded by the National Natural Science Foundation of China (number: 82060136), Science and Technology Foundation of Guizhou Province (number: [2020]1Y303), Foundation of Health and Family Planning Commission of Guizhou Province (number: gzwjkj2019-1-127), Postdoctoral Natural Science Foundation of Chongqing (cstc2020jcyj-bshX0028), and Chinese Scholarship Council (CSC, no. 202107710003). We would like to thank Editage (http://www.editage.cn) for the language editing service.

References

[1] A. Neisius and G. M. Preminger, *Stones in 2012: epidemiology, prevention and redefining therapeutic standards*.

[2] A. L. Zisman, A. P. Evan, F. L. Coe, and E. M. Worcester, "Do kidney stone formers have a kidney disease?," *Kidney International*, vol. 88, no. 6, pp. 1240–1249, 2015.

[3] J. A. Antonelli, N. M. Maalouf, M. S. Pearle, and Y. Lotan, "Use of the National Health and Nutrition Examination Survey to calculate the impact of obesity and diabetes on cost and prevalence of urolithiasis in 2030," *European Urology*, vol. 66, no. 4, pp. 724–729, 2014.

[4] S. R. Khan, K. J. Byer, S. Thamilselvan et al., "Crystal-cell interaction and apoptosis in oxalate-associated injury of renal epithelial cells," *Journal of the American Society of Nephrology*, vol. 10, Supplement 14, pp. S457–S463, 1999.

[5] K. Taguchi, A. Okada, S. Hamamoto et al., "Proinflammatory and metabolic changes facilitate renal crystal deposition in an obese mouse model of metabolic syndrome," *Journal of Urology*, vol. 194, no. 6, pp. 1787–1796, 2015.

[6] T. Umekawa, H. Tsuji, H. Uemura, and S. R. Khan, "Superoxide from NADPH oxidase as second messenger for the expression of osteopontin and monocyte chemoattractant protein-1 in renal epithelial cells exposed to calcium oxalate crystals," *BJU International*, vol. 104, no. 1, pp. 115–120, 2009.

[7] J. Wu, Z. Tao, Y. Deng et al., "Calcifying nanoparticles induce cytotoxicity mediated by ROS-JNK signaling pathways," *Urolithiasis*, vol. 47, no. 2, pp. 125–135, 2019.

[8] P. R. Dominguez-Gutierrez, E. P. Kwenda, S. R. Khan, and B. K. Canales, "Immunotherapy for stone disease," *Current Opinion in Urology*, vol. 30, no. 2, pp. 183–189, 2020.

[9] J. G. Kleinman, E. A. Sorokina, and J. A. Wesson, "Induction of apoptosis with cisplatin enhances calcium oxalate crystal adherence to inner medullary collecting duct cells," *Urological Research*, vol. 38, no. 2, pp. 97–104, 2010.

[10] T. Umekawa, N. Chegini, and S. R. Khan, "Oxalate ions and calcium oxalate crystals stimulate MCP-1 expression by renal epithelial cells," *Kidney International*, vol. 61, no. 1, pp. 105–112, 2002.

[11] T. A. Wynn, A. Chawla, and J. W. Pollard, "Macrophage biology in development, homeostasis and disease," *Nature*, vol. 496, no. 7446, pp. 445–455, 2013.

[12] S. K. Biswas and A. Mantovani, "Macrophage plasticity and interaction with lymphocyte subsets: cancer as a paradigm," *Nature Immunology*, vol. 11, no. 10, pp. 889–896, 2010.

[13] K. Taguchi, A. Okada, S. Hamamoto et al., "M1/M2-macrophage phenotypes regulate renal calcium oxalate crystal development," *Scientific Reports*, vol. 6, no. 1, 2016.

[14] C. Li, X. Y. Ding, D. M. Xiang et al., "Enhanced M1 and impaired M2 macrophage polarization and reduced mitochondrial biogenesis via inhibition of AMP kinase in chronic kidney disease," *Cellular Physiology and Biochemistry*, vol. 36, no. 1, pp. 358–372, 2015.

[15] H. J. Anders, B. Suarez-Alvarez, M. Grigorescu et al., "The macrophage phenotype and inflammasome component NLRP3 contributes to nephrocalcinosis-related chronic kidney disease independent from IL-1-mediated tissue injury," *Kidney International*, vol. 93, no. 3, pp. 656–669, 2018.

[16] S. Lee, S. Huen, H. Nishio et al., "Distinct macrophage phenotypes contribute to kidney injury and repair," *Journal of the American Society of Nephrology*, vol. 22, no. 2, pp. 317–326, 2011.

[17] K. Taguchi, A. Okada, H. Kitamura et al., "Colony-stimulating factor-1 signaling suppresses renal crystal formation," *Journal of the American Society of Nephrology*, vol. 25, no. 8, pp. 1680–1697, 2014.

[18] A. Sica and A. Mantovani, "Macrophage plasticity and polarization: in vivo veritas," *Journal of Clinical Investigation*, vol. 122, no. 3, pp. 787–795, 2012.

[19] L. Gao, M. C. Zimmerman, S. Biswal, and I. H. Zucker, "SelectiveNrf2Gene deletion in the rostral ventrolateral medulla evokes hypertension and sympathoexcitation in mice," *Hypertension*, vol. 69, no. 6, pp. 1198–1206, 2017.

[20] X. Sun, H. Zuo, C. Liu, and Y. Yang, "Overexpression of miR-200a protects cardiomyocytes against hypoxia-induced apoptosis by modulating the kelch-like ECH-associated protein 1-nuclear factor erythroid 2-related factor 2 signaling axis," *International Journal of Molecular Medicine*, vol. 38, no. 4, pp. 1303–1311, 2016.

[21] A. Loboda, M. Damulewicz, E. Pyza, A. Jozkowicz, and J. Dulak, "Role of Nrf2/HO-1 system in development, oxidative stress response and diseases: an evolutionarily conserved mechanism," *Cellular and Molecular Life Sciences*, vol. 73, no. 17, pp. 3221–3247, 2016.

[22] S. Kersten, B. Desvergne, and W. Wahli, "Roles of PPARs in health and disease," *Nature*, vol. 405, no. 6785, pp. 421–424, 2000.

[23] S. Z. Duan, M. G. Usher, and R. M. Mortensen, "Peroxisome proliferator-activated receptor-gamma-mediated effects in the vasculature," *Circulation Research*, vol. 102, no. 3, pp. 283–294, 2008.

[24] K. Taguchi, A. Okada, S. Hamamoto et al., "Differential roles of peroxisome proliferator-activated receptor-α and receptor-γ on renal crystal formation in hyperoxaluric rodents," *PPAR Research*, vol. 2016, Article ID 9605890, 11 pages, 2016.

[25] C. J. Villanueva and P. Tontonoz, "Licensing PPARγ to Work in Macrophages," *Immunity*, vol. 33, no. 5, pp. 647–649, 2010.

[26] J. I. Odegaard, R. R. Ricardo-Gonzalez, M. H. Goforth et al., "Macrophage-specific PPARγ controls alternative activation and improves insulin resistance," *Nature*, vol. 447, no. 7148, pp. 1116–1120, 2007.

[27] W. Chiangjong and V. Thongboonkerd, "A novel assay to evaluate promoting effects of proteins on calcium oxalate crystal invasion through extracellular matrix based on plasminogen/plasmin activity," *Talanta*, vol. 101, pp. 240–245, 2012.

[28] P. Pizzolato, "Histochemical recognition of calcium oxalate," *Journal of Histochemistry & Cytochemistry*, vol. 12, no. 5, pp. 333–336, 1964.

[29] A. Vinaiphat, S. Aluksanasuwan, J. Manissorn, S. Sutthimethakorn, and V. Thongboonkerd, "Front Cover: Response of renal tubular cells to differential types and doses of calcium oxalate crystals: integrative proteome network analysis and functional investigations," *Proteomics*, vol. 17, no. 15-16, 2017.

[30] M. Hirose, K. Tozawa, A. Okada et al., "Glyoxylate induces renal tubular cell injury and microstructural changes in experimental mouse," *Urological Research*, vol. 36, no. 3-4, pp. 139–147, 2008.

[31] A. L. Rodgers, "Physicochemical mechanisms of stone formation," *Urolithiasis*, vol. 45, no. 1, pp. 27–32, 2017.

[32] S. R. Khan, "Reactive oxygen species as the molecular modulators of calcium oxalate kidney stone formation: evidence from clinical and experimental investigations," *Journal of Urology*, vol. 189, no. 3, pp. 803–811, 2013.

[33] Q. Ma, "Role of nrf2 in oxidative stress and toxicity," *Annual Review of Pharmacology and Toxicology*, vol. 53, no. 1, pp. 401–426, 2013.

[34] Y. Li, J. Zhang, H. Liu et al., "Curcumin ameliorates glyoxylate-induced calcium oxalate deposition and renal injuries in mice," *Phytomedicine*, vol. 61, p. 152861, 2019.

[35] J. Xi, J. Jing, Y. Zhang et al., "SIRT3 inhibited the formation of calcium oxalate-induced kidney stones through regulating NRF2/HO-1 signaling pathway," *Journal of Cellular Biochemistry*, vol. 120, no. 5, pp. 8259–8271, 2018.

[36] L. Zuo, K. Tozawa, A. Okada et al., "A paracrine mechanism involving renal tubular cells, adipocytes and macrophages promotes kidney stone formation in a simulated metabolic syndrome environment," *Journal of Urology*, vol. 191, no. 6, pp. 1906–1912, 2014.

[37] A. Okada, T. Yasui, Y. Fujii et al., "Renal macrophage migration and crystal phagocytosis via inflammatory-related gene expression during kidney stone formation and elimination in mice: detection by association analysis of stone-related gene expression and microstructural observation," *Journal of Bone and Mineral Research*, vol. 25, no. 12, pp. 2701–2711, 2010.

[38] T. Ito, "Significance of macrophage and cytokines in expression of stone matrix," *The Japanese Journal of Urology*, vol. 87, no. 5, pp. 865–874, 1996.

[39] A. Tabassum and T. Mahboob, "Role of peroxisome proliferator-activated receptor-gamma activation on visfatin advanced glycation end products and renal oxidative stress in obesity-induced type 2 diabetes mellitus," *Human & Experimental Toxicology*, vol. 37, no. 11, pp. 1187–1198, 2018.

[40] J. Deng, Y. Xia, Q. Zhou et al., "Protective effect of rosiglitazone on chronic renal allograft dysfunction in rats," *Transplant Immunology*, vol. 54, pp. 20–28, 2019.

[41] Y. D. Liu, S. L. Yu, R. Wang et al., "Rosiglitazone suppresses calcium oxalate crystal binding and oxalate-induced oxidative stress in renal epithelial cells by promoting PPAR-γ activation and subsequent regulation of TGF-β1 and HGF expression," *Oxidative Medicine and Cellular Longevity*, vol. 2019, Article ID 4826525, 14 pages, 2019.

[42] K. Taguchi, A. Okada, T. Yasui et al., "Pioglitazone, a peroxisome proliferator activated receptor γ agonist, decreases renal crystal deposition, oxidative stress and inflammation in hyperoxaluric rats," *Journal of Urology*, vol. 188, no. 3, pp. 1002–1011, 2012.

[43] Z. Chen, P. Yuan, X. Sun et al., "Pioglitazone decreased renal calcium oxalate crystal formation by suppressing M1 macrophage polarization via the PPAR-γ-miR-23 axis," *American Journal of Physiology. Renal Physiology*, vol. 317, no. 1, pp. -F137–f151, 2019.

Hindawi
Oxidative Medicine and Cellular Longevity
Volume 2021, Article ID 9925647, 15 pages
https://doi.org/10.1155/2021/9925647

Research Article

The DNA Repair Enzyme XPD Is Partially Regulated by PI3K/AKT Signaling in the Context of Bupivacaine-Mediated Neuronal DNA Damage

Wei Zhao,[1] Lei Zeng,[2] Jiaming Luo,[1] Ji Li,[1] Luying Lai,[1] Shiyuan Xu,[1] and Zhongjie Liu[1]

[1]*Department of Anesthesiology, Zhujiang Hospital, Southern Medical University, 253 Industrial Road, Guangzhou City, Guangdong Province, China*
[2]*Department of Laboratory Medicine, Zhujiang Hospital, Southern Medical University, 253 Industrial Road, Guangzhou City, Guangdong Province, China*

Correspondence should be addressed to Shiyuan Xu; xsy998@smu.edu.cn and Zhongjie Liu; 13580562690@163.com

Received 4 April 2021; Revised 4 September 2021; Accepted 11 September 2021; Published 7 October 2021

Academic Editor: Xin Luo

Bupivacaine, a local anesthetic widely used for regional anesthesia and pain management, has been reported to induce neuronal injury, especially DNA damage. Neurons employ different pathways to repair DNA damage. However, the mechanism underlying bupivacaine-mediated DNA damage repair is unclear. A rat neuronal injury model was established by intrathecal injection of (3%) bupivacaine. An in vitro neuronal injury model was generated by exposing SH-SY5Y cells to bupivacaine (1.5 mmol/L). Then, a cDNA plate array was used to identify the DNA repair genes after bupivacaine exposure. The results showed that xeroderma pigmentosum complementary group D (XPD) of the nuclear excision repair (NER) pathway was closely associated with the repair of DNA damage induced by bupivacaine. Subsequently, Western blot assay and immunohistochemistry indicated that the expression of the repair enzyme XPD was upregulated after DNA damage. Downregulation of XPD expression by a lentivirus aggravated the DNA damage induced by bupivacaine. In addition, phosphatidyl-3-kinase (PI3K)/AKT signaling in neurons was inhibited after exposure to bupivacaine. After PI3K/AKT signaling was inhibited, bupivacaine-mediated DNA damage was further aggravated, and the expression of XPD was further upregulated. However, knockdown of XPD aggravated bupivacaine-mediated neuronal injury but did not affect PI3K/AKT signaling. In conclusion, the repair enzyme XPD, which was partially regulated by PI3K/AKT signaling, responded to bupivacaine-mediated neuronal DNA damage. These results can be used as a reference for the treatment of bupivacaine-induced neurotoxicity.

1. Introduction

Local anesthesia (LA) has been widely used for surgical anesthesia and short- and long-term pain management since 1884 [1]. An amide-type local anesthetic, bupivacaine, is one of the most widely used local anesthetics for during labor and postoperative pain management. Previous studies have shown that bupivacaine might be neurotoxic, even at clinically relevant concentrations [2, 3]. However, the exact mechanism underlying the neurotoxicity of bupivacaine is unclear.

DNA breakage arising from oxidative damage is a significant threat to the genome stability in mature neurons [4, 5]. Our previous studies also revealed that oxidative stress is essential for neurotoxicity induced by bupivacaine [6, 7]. Oxidative stress is a crucial factor in DNA damage. Repair of those DNA lesions caused by oxidative stress requires the activity and interaction of different DNA repair pathways [8, 9], including base excision repair (BER), nuclear excision repair (NER), strand break (single- and double-stranded) repair, and homologous recombination (HR). DNA damage repair mechanisms are known to play an essential role in bupivacaine-mediated neurotoxicity. However, it is not clear which repair pathways are primarily involved in the pathological process of bupivacaine

neurotoxicity. Therefore, studying the exact repair mechanism is necessary to prevent neuronal DNA damage mediated by bupivacaine.

Herein, a cDNA microplate array was used after SH-SY5Y cells were exposed to bupivacaine. The data revealed that the expression of XPD(/ERCC2), the gene that is essential for the NER pathway, is significantly increased. Subsequently, in vivo and in vitro experiments verified that the DNA repair enzyme XPD plays an essential role in bupivacaine-mediated neurotoxicity. The critical enzyme XPD may be closely involved in the repair of bupivacaine-mediated neuronal DNA damage. However, how XPD is regulated in the context of bupivacaine-mediated neuronal DNA damage remains unknown. The phosphatidyl-3-kinase (PI3K)/AKT signaling pathway is essential for protecting neuronal cells from oxidative stress [10]. According to our previous proteomics study, PI3K is inhibited in the context of bupivacaine-mediated neurotoxicity [7]. Although PI3K signaling has been reported to play an essential role in regulating bupivacaine-mediated neurotoxicity, the association between XPD and PI3K signaling is unknown.

Therefore, the present study had two specific aims: (1) to explore whether and verify that XPD is the key for bupivacaine-mediated neuronal DNA damage repair and (2) to determine the possible mechanism by which XPD is regulated by the PI3K signaling pathway.

2. Materials and Methods

2.1. Chemicals and Reagents. The bupivacaine hydrochloride was purchased from Sigma Chemical Co. (St. Louis, MO). Dulbecco's modified Eagle's medium (DMEM)/F12, fetal bovine serum, and penicillin and streptomycin were purchased from Thermo Fisher Scientific (Waltham, MA, USA). The pancreatic enzyme (including or excluding) EDTA was purchased from Gibco, USA. LY294002 was purchased from SelleckChem, USA.

2.2. Cell Culture and Treatment. The SH-SY5Y cell line was purchased from the Chinese Academy of Sciences (Shanghai, China). SH-SY5Y cells were held at 37°C in 5% CO_2 in DMEM/F12 medium supplemented with 10% FBS and 1% penicillin/streptomycin. The culture medium was replaced daily during cell growth. Cells were grown in a 75 mm flask and subcultured in 6-well (seeding density 5.0×10^5 cells) or 12-well (planting density of 1.0×10^5 cells) plates. Experiments were conducted when cells reached 85% confluence. SH-SY5Y cells were treated with LY294002 (10 μM) for 2 h before bupivacaine stimulation [11]. Following the termination of cell culture, the cells and medium were collected and stored at -80°C until analysis.

2.3. Animals and Treatment. Age-matched 10-week-old male Sprague-Dawley rats weighing approximately 250 g at the commencement of the experiment were supplied by the center of animals of Southern Medical University, Guangzhou. Rats were kept in a temperature-controlled environment with access to food and water. All animal procedures were approved by and performed in compliance with the ethical guidelines of the Animal Ethics Committee of Southern Medical University.

Intrathecal catheterization was performed as previously described [12]. The L4~5 intervertebral space was selected to insert the PE10 catheter (Smith Medical, UK). The rats from the model group were intrathecally administered 3% bupivacaine 20 μL. In contrast, rats in the control groups were administered 20 μL of normal saline. All injections were performed on a Wednesday or Friday between 2 and 4 pm to avoid possible time-dependent variations in pharmacokinetics. Before the test, rats were allowed at least two days to rest for recovery from the operation. Rats having any problem with tail movements or motor dysfunction in the hind limbs were not used in the ensuing experiments.

2.4. Mechanical/Thermal Thresholds. All animals were tested for mechanical thresholds and thermal thresholds as described [13] before and after injection of 3% bupivacaine. All behavioral testers were blinded to the experimental grouping information. Mechanical thresholds were assessed by measuring the paw withdrawal threshold (PWT) with a set of Von Frey filaments (0.04-0.2 g; Ugo Basile, Gemonio, Italy). The filament was applied to the plantar surface of the left hind paw at a vertical angle for up to 3 s from the bottom. Fifty percent of mechanical withdrawal threshold (MWT) values were determined using the up-down method.

Thermal thresholds were assessed by measuring the paw withdrawal latency to radiant heat stimuli. Each animal was placed in elevated chambers on a Plexiglas floor and acclimated to the testing environment for 30 minutes before the experiments. The radiant heat source (plantar test, 37370; Ugo Basile, SRL, Gemonio, Italy) was applied to the center of the plantar surface of the left hind paw with at least a 3-minute interval. The average withdrawal latency of the trials was recorded as the response latency.

2.5. TUNEL Assay. After 24 h treatment with bupivacaine, the frozen transverse sections from the lumbar enlargement of the spinal cord from every group were acquired. According to manufacturer's instructions, sections were tested with In Situ Cell Death Detection Kit, Fluorescein (Roche Diagnostics GmbH, Germany). Immunocytochemistry analysis of mouse primary neuron cells labeling NeuN with ab177487 (Abcam, Cambridge, MA, USA) is at 1/100. Goat Anti-Rabbit IgG H&L (Alexa Fluor® 594) (ab150080) at 1/1000 was used as the secondary antibody (Red). The fluorescence images were visualized under a fluorescence microscope (Carl Zeiss, Jena, Germany). The TUNEL-positive neurons were identified by colocalizing the TUNEL signal (green fluorescence) and NeuN (red fluorescence). The total number of TUNEL positive neurons in the spinal cord was counted from each slide.

2.6. Cell Viability. SH-SY5Y cells were seeded at a density of 1×10^4 cells per well in a 96-well cell culture plate, and cell viability was determined with the Cell Counting Kit-8 (CCK8, Dojindo, Japan) according to manufacturer's instructions as previously described [14]. Briefly, after

exposure to bupivacaine (0, 0.5, 1.0, 1.5, 2.0, and 2.5 mM) for 24 h, CCK-8 solution (10 μL/well) was added to the SH-SY5Y cell culture medium. Then, the 96 well-plate was incubated for an additional 4 h at 37°C, according to the manufacturer. The optical density of the homogeneous purple solutions was measured at 450 nm using a spectrophotometer. The cell half-maximal inhibitory concentration (IC50) was calculated using the GraphPad software [15].

2.7. Detection of Lactate Dehydrogenase (LDH). The levels of LDH in the cell culture medium released from injured SH-SY5Y cells were determined by the LDH Cytotoxicity Assay kit (Invitrogen, USA) following manufacturer's instruction. Briefly, the SH-SY5Y cells were plated in 6-well plates for 24 h. After being treated with bupivacaine (0, 0.5, 1.0, 1.5, 2.0, and 2.5 mM), the cell culture medium was collected from SH-SY5Y cells and assayed for LDH levels. The absorbance at a wavelength of 450 nm was measured and quantified.

2.8. cDNA Plate Array. Signosis's proprietary cDNA plate array is a plate-based hybridization profiling analysis that monitors the expression of dozens of genes through reverse transcription of mRNA into cDNA [16]. About 10^4-10^5 SH-SY5Y cells with (as an experimental group) and without (as control group) exposure to 1.5 mM bupivacaine were washed with 200 μL ice-cold 1× PBS and add 100 μL ice-cold cell lysis buffer and then subject to snap-frozen at -80°C. The 20 μL cDNA was synthesized from each sample and labeled with biotin and ready for hybridization on the plate. Targeted genes are then specifically captured onto individual wells on a scale, instead of membranes, through a precoated gene-specific oligonucleotide. Then, the captured cDNAs are tested with streptavidin-HRP. The microplate luminometer was used to report the relative light units (RLUs). The expression level of genes is directly proportional to the luminescent intensity.

2.9. Heatmap and Clustering. The heatmap, a graphical representation of data with the individual values in a matrix, was represented as grids of colors plus clustering on both rows and columns. The heatmap-2 function in R based on the cDNA Plate Assay data was used to generate heatmaps of differentially expressed genes [17]. Samples were divided into different clusters using Ward's hierarchical clustering method, and the expression of genes was shown in colors in the center of the heatmap. The heatmap was available from the package "gplot" as an enhanced version or its basic function stats in R ted. (https://CRAN.R-project.org/package=gplots).

2.10. Western Blotting. Tissue or cells were lysed in a lysis buffer by sonication. After centrifugation, the protein was collected. The protein concentration was determined by the Bradford method and proceeded for Western blotting. An equal amount of protein extracts was separated by 10% SDS-PAGE and transferred to PVDF membranes (Immobilon-P, Millipore, Bedford, MA, USA). The blots were blocked with 5% BSA at room temperature for 1 hour and incubated overnight at 4°C with primary antibodies against p-γ-H2AX (rabbit, 1 : 1000; cell signaling), Bax and Bcl-2 (rabbit, 1 : 1000; cell signaling), XPD (rabbit, 1 : 1000; cell signaling), PI3K, AKT, p-AKT (rabbit, 1 : 1000; cell signaling), p-PI3K (rabbit,1 : 1000, Abcam), and β-actin (rabbit, 1 : 2000; cell signaling). Then, these blots were incubated with HRP-conjugated secondary antibody, developed in ECL solution, and exposed onto hyperfilm (Amersham Biosciences) for 1-10 min. Specific bands were evaluated by apparent molecular size. The protein abundance was most often measured using an optical density (OD) algorithm. The intensity of the selected bands was captured and quantified by a densitometric method used by the Image J software 1.48a (http://imagej.nih.gov).

2.11. Immunohistochemistry. After treatment with bupivacaine for 24 h, the lumbar spinal enlargement of rats was obtained.

Immunohistochemistry was performed to detect the expression of XPD in the spinal cord tissue. Briefly, samples were fixed with 4% polyoxymethylene, embedded in paraffin, and sectioned at a thickness of 5 μm. Then, the sections were dewaxed in xylene and rehydrated in graded ethanol, followed by incubation in H_2O_2 (3%) for 10 min to block endogenous peroxidase. Then, sections were incubated with anti-XPD at 4°C overnight, followed by incubation with the appropriate secondary antibodies for 45 min at room temperature. The sections were stained with hematoxylin and observed under a microscope (Olympus-IX51; Olympus Corporation, San Jose, CA, USA). Integrated optical density (IOD) of the positively stained area was measured immunohistochemical of spinal cord tissue. The XPD expression level in the spinal cord was represented by integral optic density (IOD). The selected images were then converted into an 8-bit grayscale. Then, the IODs of each image were counted and measured using Image-Pro Plus v6.0 software (Media Cybernetics Inc., Bethesda, MD, USA).

2.12. Flow Cytometry. Flow cytometric analyses were carried out to detect the percentages of apoptotic cells. After exposure to bupivacaine for 24 h, a total of 5×10^5 SH-SY5Y cells were collected and assayed by the FITC Annexin V Apoptosis Detection Kit (BD Pharmingen) following manufacturer's instruction. Briefly, cells were incubated with 5 μL Annexin V-FITC for 20 min. After removing the media, cells were incubated with 5 μL propidium iodide (PI). Gently vortex the cells and incubate for 15 min at RT (25°C) in the dark. Cells samples were analyzed by the flow cytometer (BD Biosciences FACS Calibur, USA) within 1 h.

2.13. Comet Assay. The comet assay was used to detect DNA damage in individual cells as previously described [18]. Briefly, the SH-SY5Y cells were plated in 12-well plates, and the extent of DNA damage was measured by the kit (Trevigen's Comet Assay® Kit) following manufacturer's instructions. Images were acquired on a Carl Zeiss fluorescence microscopy (Jena, Germany). At least 50 randomly selected cells were analyzed by the Comet Assay Software Project.

2.14. Lentivirus-Mediated Gene Silencing of XPD. According to the cDNA sequence of XPD (Target Seq: TGGCCCTGA TCATGGCATA), shRNA was designed and synthesized, which was then annealed into the hU6-MCS-CMV-EGFP vector. After being identified by sequencing, hU6-MCS-CMV-EGFP vector and packaging vector were cotransfected into SH-SY5Y cells. Seventy-two hours later, the recombinant lentivirus-mediated gene silencing of XPD was obtained after harvesting and concentrating as previously described [18]. The fluorescence intensity was obtained 48 h after the cells were transfected with lentivirus. These images were used to determine the efficiency of lentivirus infection (shown as Supplemental Figure 1 A). Then, Q-PCR was used to detect mRNA levels of XPD after lentivirus infection in SH-SY5Y cells (shown as Supplemental Figure 1 B).

2.15. Statistical Analysis. All the data were represented as mean ± SD. The graphs and statistical data were completed by GraphPad Prism (GraphPad Software 8.0, Inc., La Jolla, CA). The statistical significance was determined by one-way analysis of variance (ANOVA) followed by the Tukey-Kramer test. The differences of $p < 0.05$ were considered statistically significant.

3. Results

3.1. Bupivacaine-Induced Apoptosis in Rat Spinal Cord Tissue and Behavioral Changes In Vivo. Accumulating evidence has shown that the local anesthetics (bupivacaine) are potentially neurotoxic and that neurologic impairment after spinal anesthesia may result from the direct neurotoxic effect of bupivacaine [19]. As shown in Figure 1, TUNEL staining revealed that after intrathecal application of bupivacaine (3%), the percentage of apoptotic neurons (Figures 1(a) and 1(b); $n = 6$; $^{****}p = 0.0001$) in spinal cord tissue slices was significantly increased. The data showed that bupivacaine induced neuronal apoptosis in rat spinal cord tissue. Furthermore, behavioral tests for mechanical and thermal thresholds were assessed before and 24 h after bupivacaine injection. The paw withdrawal mechanical threshold (PWMT) (Figure 1(c); $^{****}p = 0.0001$) and paw withdrawal threshold latency (PWTL) (Figure 1(d); $^{****}p = 0.0001$) were significantly increased in the bupivacaine group compared with the control group. These data showed that bupivacaine induced behavioral changes in rats.

3.2. Bupivacaine-Induced Neurotoxic Injury in SH-SY5Y Cells. SH-SY5Y cells are undifferentiated human neuroblastoma cells [20]. After exposure to different concentrations (0.5, 1.0, 1.5, 2.0, and 2.5 mM) of bupivacaine, the CCK-8 assay was used to assess SH-SY5Y cell viability. Then, the dose inhibition curve was plotted (Figure 1(e)). The half inhibitory concentration (IC50) of bupivacaine was approximately 1.5 mM. LDH is a marker of cytotoxicity. Compared with control treatment, bupivacaine induced SH-SY5Y cell cytotoxicity in a dose-dependent manner. Bupivacaine at 1.5 mM concentration started to demonstrate significant cytotoxicity compared to the control group (Figure 1(f); $n = 3$; $^{*}p = 0.0394$, $^{****}p < 0.0001$). Thus, 1.5 mM was selected as the concentration of bupivacaine for further in vitro studies.

3.3. Identification of DNA Repair Pathways In Vitro by a cDNA Microplate Array. Accumulating evidence suggests that DNA damage is repaired by overlapping multiple DNA repair pathways [21]. Repair of these DNA lesions induced by bupivacaine may also require the activity and interaction of different DNA repair pathways, including BER and NER [22, 23]. To investigate the critical enzymes associated with DNA damage repair pathways, a cDNA plate array was used to measure DNA repair gene expression in SH-SY5Y cells treated with bupivacaine. Cells were exposed to 1.5 mM bupivacaine, and a cDNA plate array was used to detect the mRNA expression of DNA repair genes. As shown in Figure 2(a), a ratio > 0 indicated that the expression of the indicated gene was upregulated in the bupivacaine group compared with the control group, while a ratio < 0 indicated that the expression of the gene was downregulated. A ratio greater than 1 or less than -1 indicated that there was a one order of magnitude difference. A ratio greater than 2 or less than -2 meant there were two orders of magnitude differences. The cDNA microplate array results showed that bupivacaine resulted in differential expression of the following genes (Table 1): DNA-PKcs, PTEN, NTH1, RAD9, CSB, GADD45, XPD, XPC-HR23B, and P53.

Bidirectional hierarchical clustering heatmaps were made based on the identified DNA repair genes' cDNA levels. As shown in Figure 2(b), the samples could be separated by group (control and bupivacaine) according to cDNA expression, indicating the changes in the expression of the identified genes related to treatment whit bupivacaine. Furthermore, the identified repair genes were mainly associated whit the NER pathways.

3.4. The Expression of the NER Pathway-Related Gene XPD Was Significantly Increased after Bupivacaine-Induced DNA Damage In Vivo and In Vitro. Q-PCR was used to test the mRNA expression of XPD over time after exposure to 1.5 mM bupivacaine in vitro. Additionally, Western blotting was used to measure the protein expression of XPD. Compared with control treatment, bupivacaine treatment significantly increased the mRNA expression of XPD (Figure 3(a); $^{***}p = 0.0035$, $^{****}p < 0.0001$) at different time points, especially at 12 h. The protein expression of XPD was also significantly increased at different time points, especially at 24 h (Figures 3(b) and 3(c); $^{***}p = 0.001$, $^{****}p < 0.0001$ vs. the control group).

Western blotting was used to evaluate the relative expression of XPD in vivo in rat spinal cord tissue (Figures 3(d) and 3(e); $^{****}p < 0.0001$), while immunohistochemical was used to assess the relative expression of XPD in rat spinal cord tissue (Figures 3(f) and 3(g); $^{**}p = 0.0028$). The data showed that the expression of XPD was significantly increased in the bupivacaine-treated group compared with the control group.

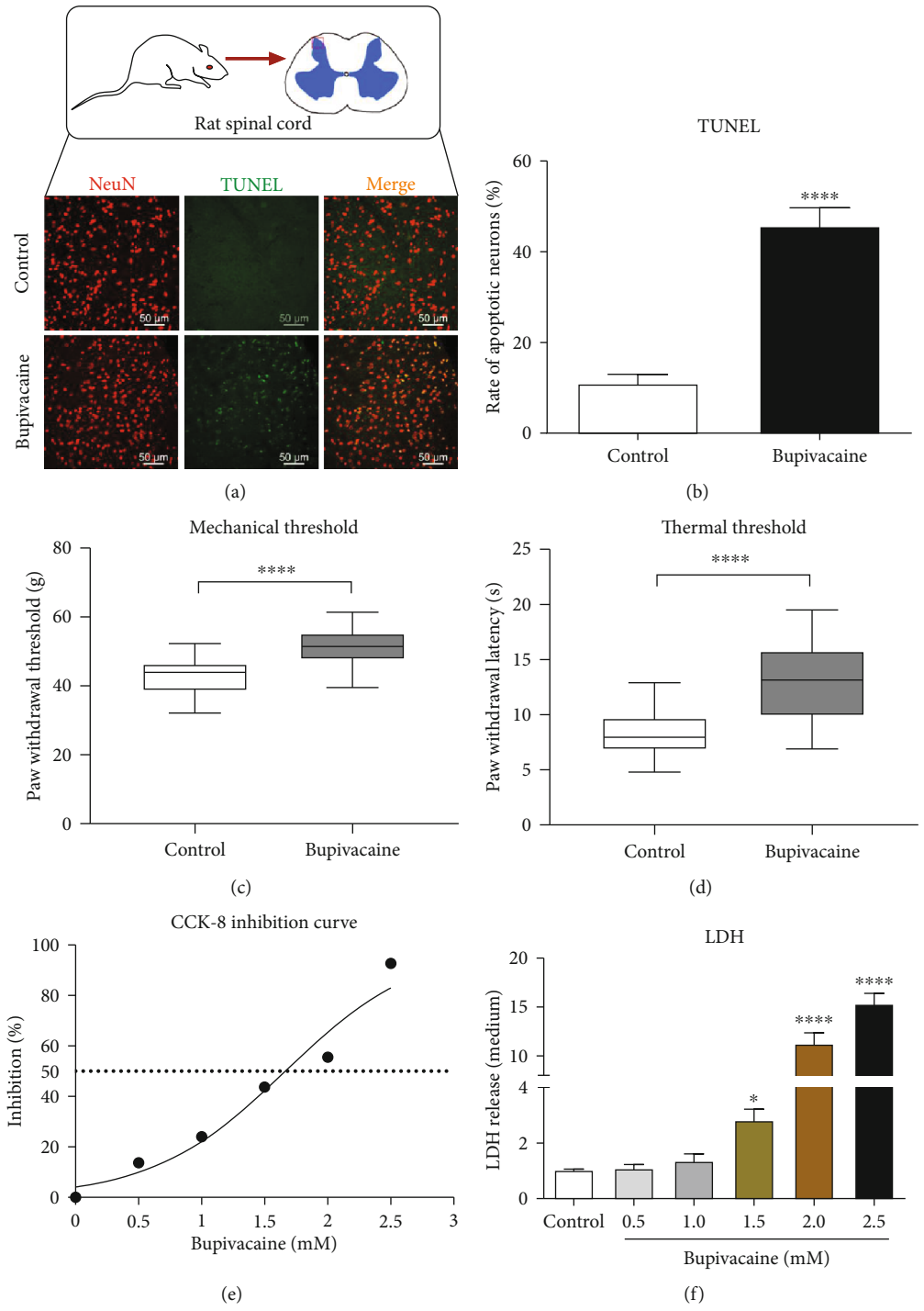

Figure 1: Bupivacaine causes neurotoxic damage. In vivo, bupivacaine-induced apoptotic damage in rat spinal cord tissue and behavioral changes. The rats in the neuronal damage model group were intrathecally administered 20 μL of 3% bupivacaine, while rats in the control group were administered normal saline. Twenty-four hours after treatment with bupivacaine, the TUNEL staining was performed to determine the cell apoptosis rate ((a, b) $n = 6$; $^{****}p = 0.0001$) in spinal cord tissue slices. NeuN was used to label mature neurons. TUNEL/NeuN positive cells (a) represent apoptotic neurons. The PWMT and PWTL were increased in the bupivacaine-treated group compared with the control group ((c, d) $n = 6$; $^{****}p = 0.0001$). The in vivo data are shown as the mean ± SD. Bupivacaine may induce SH-SY5Y cell neurotoxicity in vitro. After SH-SY5Y cells were exposed to different concentrations of bupivacaine, the dose inhibition curve was plotted ((e) $n = 3$), and the IC50 of bupivacaine was calculated as 1.5 mmol/L. The release of LDH was determined to assess cytotoxicity ((f) $n = 3$; $^{*}p = 0.0394$ and $^{****}p < 0.0001$ vs. the control group). The data are shown as the mean ± SD.

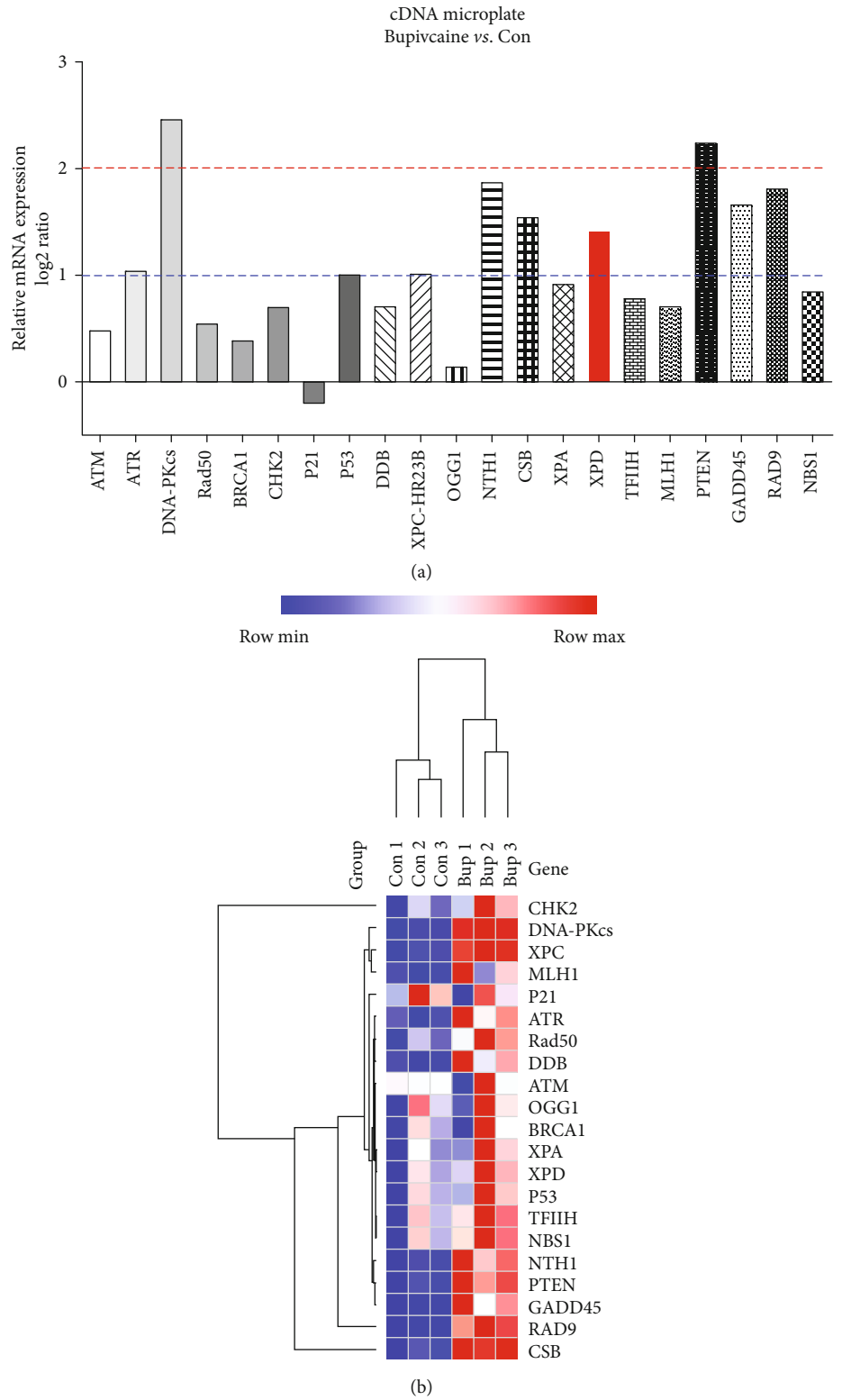

Figure 2: The expression of DNA damage repair genes was determined with a cDNA plate array after SH-SY5Y cells were exposed to bupivacaine. As shown in (a), a ratio > 0 indicates that the expression of the indicated gene was upregulated in the bupivacaine (Bup) group compared with the control (C) group, and a ratio < 0 indicates that the expression of the gene was downregulated. A ratio greater than 1 or less than -1 indicated that there was a one order of magnitude difference. A ratio greater than 2 or less than -2 indicated that there were two orders of magnitude difference. A heatmap of the 21 DNA repair proteins is shown in (b). Each column represents a sample (control group: Con1~3; bupivacaine group: Bup1~3), and each row represents one of the DNA repair proteins. The cDNA levels of the DNA repair genes are indicated by the different colors, with the color changing from green to red with increasing expression.

Table 1: DNA repair gene expression in SH-SY5Y cells after exposure to bupivacaine was assessed with a cDNA plate array. The differentially expressed repair genes were mainly associated with the NER pathway.

C-*vs*-B (significant genes)	Pathways names	KEGG no.
SB, XPC-HR23B, XPD	Nucleotide excision repair	map03420
PTEN, RAD9, GADD45, ATR, P53	DDR(cell cycle)	map04110
DNA-PKcs	Nonhomologous end-joining	map03450
NTH1	Base excision repair	map03410

3.5. Knockdown of XPD Expression Significantly Aggravated Bupivacaine-Induced Neuronal DNA Damage and Neurotoxicity. Cytotoxicity and DNA damage induced by bupivacaine were aggravated after XPD knockdown. Bupivacaine-treated SH-SY5Y cells were infected with an XPD-GV211-RNAi-expressing lentivirus. GV211-NC was used as a control lentivirus. DNA damage was aggravated in bupivacaine and GV211-RNAi-treated SH-SY5Y cells compared with bupivacaine and GV211-NC-treated SH-SY5Y cells. The data showed that in the comet assay, the olive tail moment was significantly higher (Figures 4(d) and 4(e); $^{\&}p = 0.0002$); ($^{*}p < 0.0001$, and $^{\#}p < 0.0001$ vs. the control group), while phosphorylation level of γ-H2AX, a marker of DNA damage, was significantly increased (Figures 4(a) and 4(b); $^{\&}p = 0.0243$); ($^{*}p = 0.0013$, and $^{\#}p = 0.0243$ vs. the control group). In addition, the ratio of the apoptosis-related protein Bcl-2/Bax was reduced (Figures 4(a) and 4(c); $^{\&}p = 0.0100$); ($^{*}p = 0.0008$, and $^{\#}p < 0.0001$ vs. the control group), and apoptosis was significantly increased as determined by flow cytometry (Figures 4(f) and 4(g); $^{\&}p = 0.0308$); ($^{*}p < 0.0412$, and $^{\#}p < 0.0003$ vs. the control group).

3.6. Inhibition of PI3K/AKT Signaling Aggravated Bupivacaine-Induced Neuronal DNA Damage and Upregulated the Expression of XPD. Previous studies have shown that the PI3K/AKT pathway plays a vital role in oxidative neurotoxicity [24]. Our latest data also showed that PI3K/AKT is closely involved in bupivacaine-induced neurotoxicity [7]. Furthermore, XPD can inhibit tumor cell growth and invasion by regulating the PI3K/AKT pathway [25]. The relationship between the XPD and PI3K/AKT pathways in the bupivacaine-mediated oxidative neurotoxicity is unclear.

PI3K/AKT signaling was inhibited, and bupivacaine was administered to induce neuronal DNA damage. We utilized the inhibitor LY294002 (10 μM) to suppress the PI3K/AKT pathway [26]. LY294002 treatment alone significantly increased XPD expression in SH-SY5Y cells (Figures 5(a) and 5(b); $^{*}p = 0.0005$). Moreover, the expression of XPD was further increased in the LY294002 and bupivacaine treated group compared with the control group (Figures 5(a) and 5(b); $^{\&}p = 0.0254$). LY294002 was used to suppress the activation of the PI3K/AKT signaling pathway in many previous studies [27]. Here, LY294002 (10 μM) further inhibited the protein expression of p-PI3K (Figures 5(c) and 5(d); $n = 3$; $\#p = 0.0316$) and p-AKT (Figures 5(c) and 5(e); $n = 3$; $^{\#}p = 0.0346$) after bupivacaine treatment. Furthermore, the expression of the apoptosis-related proteins Bax/Bcl-2 and the DNA damage marker p-γH2AX was further increased in the LY294002 and bupivacaine-treated group compared with the bupivacaine-treated group (Figure 5(f), $^{\#}p = 0.0115$; Figure 5(g), $^{\#}p = 0.0360$).

3.7. Knockdown of XPD Did Not Affect the PI3K/AKT Pathway. In SH-SY5Y cells, bupivacaine increased the expression of XPD (Figures 6(a) and 6(b)). The expression of XPD was downregulated by the XPD-GV211-RNAi-expressing lentivirus (GV211-NC served as a control lentivirus group; Figures 6(a) and 6(b); $^{\#}p = 0.0413$). p-PI3K (Figure 6(c); $^{*}p = 0.0060$, $^{\#}p = 0.0291$) and p-AKT (Figure 6(d); $^{*}p = 0.0345$, and $^{\#}p = 0.0242$; vs. the control group) expression was inhibited by bupivacaine. Nevertheless, the downregulation of XPD expression induced by the XPD-GV211-RNAi-expressing lentivirus did not further reduce p-PI3K and p-AKT compared with that in the bupivacaine group (Figure 6(c); $p = 0.8535$; Figure 6(d); $p = 9396$).

4. Discussion

Previous studies have shown that bupivacaine can cause neuronal oxidative DNA damage [7, 14]. Repair of oxidative DNA damage is mainly accomplished by excision repair mechanisms such as BER [8] and NER [28]. However, it remains unclear whether specific repair pathways and essential repair proteins are involved in repairing bupivacaine-induced oxidative DNA damage.

cDNA plate arrays can detect differences in mRNA expression levels among different treatment groups with high sensitivity [16]. Hundreds of repair enzymes are involved in repairing DNA damage caused by bupivacaine through a large and complex network of repair mechanisms. However, due to the limitations of the cDNA plate array, we were unable to detect all the genes involved in DNA damage repair. Only the essential DNA repair genes reported in the relevant literature could be studied. This is a limitation of the current study.

A cDNA plate array was used to identify regulatory and repair enzymes necessary for DNA damage repair in the context of bupivacaine-induced SH-SY5Y cytotoxicity. The results showed that bupivacaine caused differential expression of the following genes (Table 1): DNA-PKcs, PTEN, NTH1, RAD9, CSB, GADD45, XPD, XPC-HR23B, and P53. Furthermore, in a previous study, bupivacaine was shown to cause oxidative damage to DNA in SH-SY5Y cells. The DNA damage initiated the NER pathway. NER is a universal and versatile process that involves two subpathways: global genome NER (GG-NER) and transcription-coupled

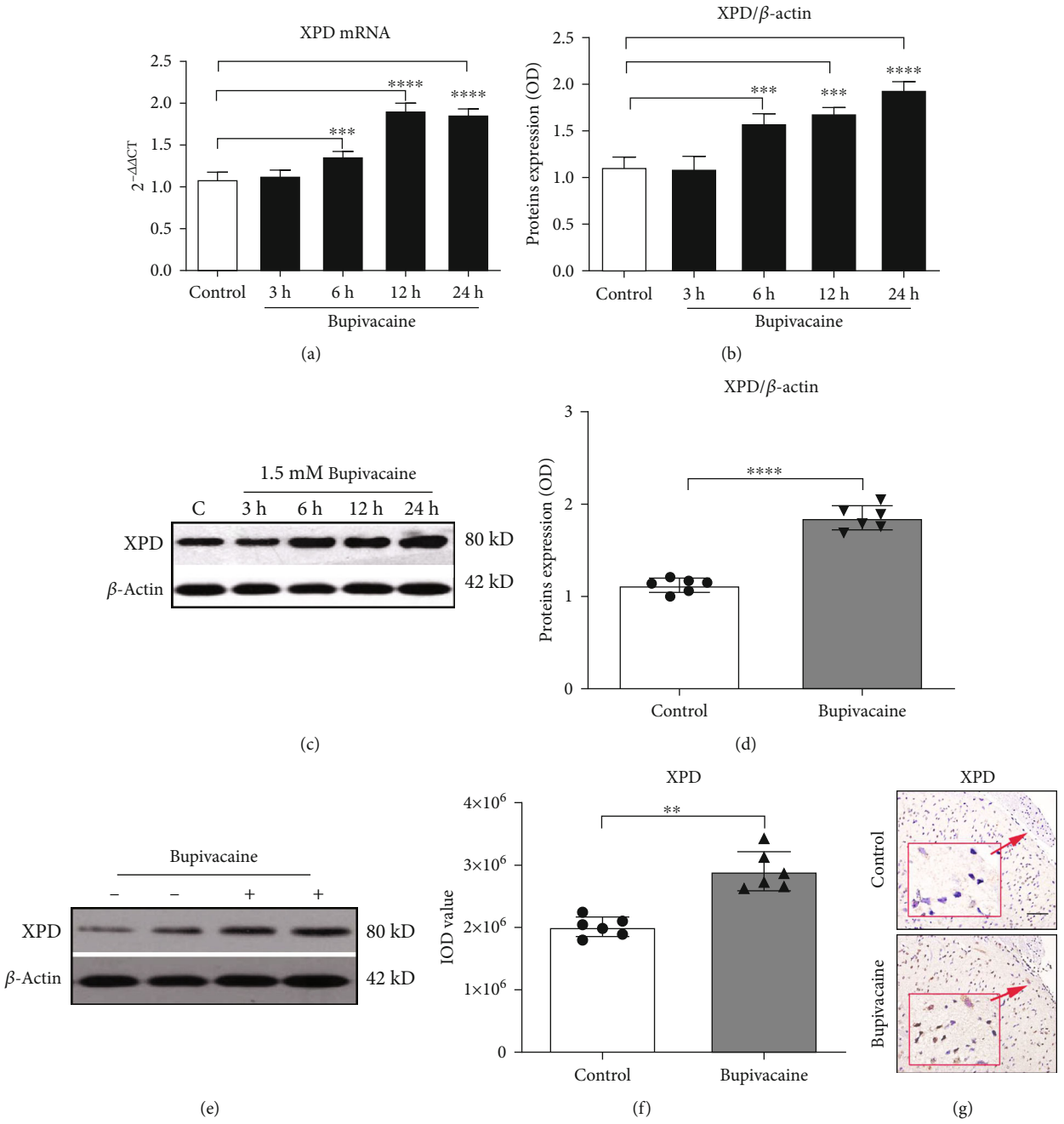

Figure 3: The expression of the crucial NER pathway-associated repair enzyme XPD was significantly increased after exposure to bupivacaine in vivo and in vitro. The mRNA expression of XPD (a) was significantly increased in bupivacaine-treated cells compared with control cells at different time points, especially at 12 h ((a) $n = 3$; $^{***}p = 0.0035$, $^{****}p < 0.0001$), and the protein expression of XPD was also significantly increased at different time points, especially at 24 h ((b, c) $n = 3$; $^{***}p = 0.001$ and $^{****}p < 0.0001$ vs. the control group). The expression of XPD in spinal cord tissue was significantly increased in the rat spinal neurotoxicity model compared with the control group (Western blotting: (d, e) $n = 6$; $^{****}p < 0.0001$; immunohistochemistry: (f, g) $n = 6$; $^{**}p = 0.0028$). The in vivo data are presented as the mean ± SD.

NER (TC-NER). XPD is the common repair enzyme of GG-NER and TC-NER pathways [29]. The expression of the vital repair enzyme XPD was increased, and this enzyme participated in repairing oxidative DNA damage (Figure 2). Our previous study [18] also suggested that XPD participates in repairing oxidative DNA damage caused by bupivacaine in neurons. Therefore, XPD may be the most critical restriction enzyme in NER, the primary DNA repair pathway in mammalian cells [29, 30]. Nevertheless, the critical regulatory mechanism of the repair enzyme XPD in bupivacaine-induced DNA damage is unknown.

The PI3K/AKT pathway is an intracellular signal transduction pathway that promotes metabolism, proliferation, cell survival, growth, and angiogenesis in response to

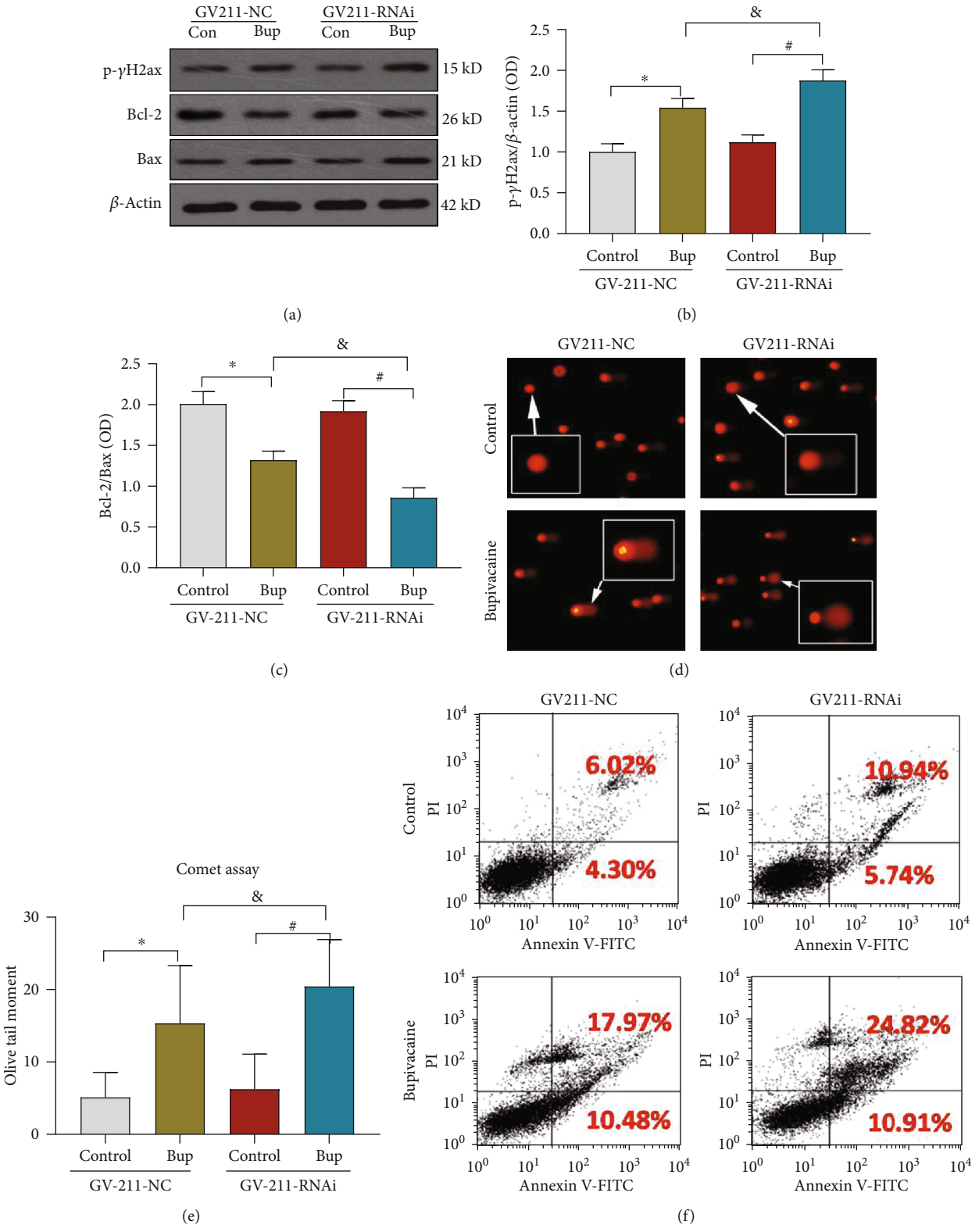

Figure 4: Continued.

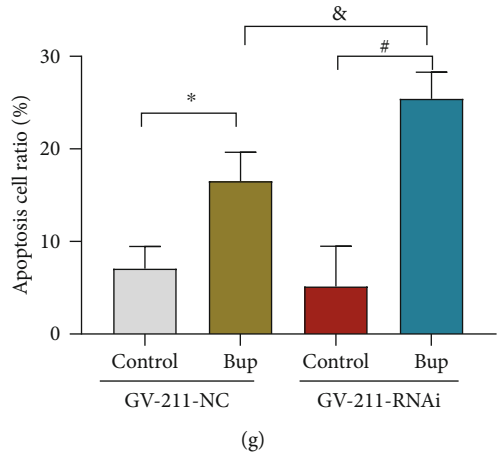

Figure 4: Downregulation of XPD expression further aggravated the neurotoxicity caused by bupivacaine. After XPD expression was downregulated with the XPD-GV211-RNAi-expressing lentivirus, the SH-SY5Y cell apoptosis and DNA damage induced by bupivacaine were exacerbated. GV211-NC served as a control lentivirus. DNA damage was aggravated in bupivacaine-treated SH-SY5Y cells in which XPD expression was inhibited (Bup-GV211-RNAi) compared to the control group (Bup-GV211-NC), as the phosphorylation of γ-H2AX, a DNA damage marker, was significantly increased ((a, b) $n = 3$; $^{\&}p = 0.0243$), ($^{*}p = 0.0013$, and $^{\#}p = 0.0243$, vs. the control group). Furthermore, the expression of the apoptosis-related proteins Bcl-2 and Bax was reduced ((a, c) $n = 3$; $^{\&}p = 0.0100$) ($^{*}p = 0.0008$, and $^{\#}p < 0.0001$ vs. the control group), and the olive tail moment was significantly higher in the comet assay ((d, e) $n = 3$; $^{\&}p = 0.0002$) ($^{*}p < 0.0001$, and $^{\#}p < 0.0001$ vs. the control group). Moreover, suppression of XPD expression significantly increased the apoptosis ratio, as determined by flow cytometry ((f, g) $n = 3$; $^{\&}p = 0.0308$) ($^{*}p < 0.0412$, and $^{\#}p < 0.0003$ vs. the control group). The data are shown as the mean ± SD of three independent experiments.

extracellular signals [31]. Several studies have suggested that activation of PI3K/AKT signaling can inhibit neural damage. Lei and Chen found that resveratrol attenuates brain damage in permanent focal cerebral ischemia via PI3K/AKT signaling pathway activation in rats [32]. Deng et al. suggested that berberine protects rotenone-treated SH-SY5Y cells by activating the PI3K/AKT signaling pathway [33]. A previous study showed that the PI3K/AKT signaling plays a crucial role in activating and regulating different pathways in the context of bupivacaine-induced neurotoxicity [7]. Our results (Figure 5) also showed that the activation of PI3K/AKT signaling was decreased in SH-SY5Y cells after exposure to bupivacaine. Whether there is a relationship between XPD and PI3K/AKT signaling is unclear. PI3K/AKT signaling is vital in maintaining genomic stability through involving DNA damage repair and cell cycle regulation [34, 35]. Emerging data suggest that the activation of PI3K/AKT signaling promotes cell survival partly by regulating the DNA damage response (DDR) [36]. LY294002 blocks the recruitment of translesion synthesis polymerases at sites of the DNA damage, thus hindering the progression of the DNA replication fork, leading to replication stress and cell death [37]. In this study, LY294002 increased the expression of the apoptosis-related proteins Bax, BCL-2, and p-γH2AX (markers of DNA damage) (Figures 5(e)–5(g)). Aggravation of DNA damage led to more of the repair enzyme XPD in the DNA repair process until neuronal apoptosis was induced. PI3K/AKT inhibition by LY294002 further increased the bupivacaine-induced expression of the repair enzyme XPD (Figures 5(a) and 5(b)). In contrast, downregulation of the XPD gene had no significant effect on PI3K/AKT signaling activation. These data indicated that the repair enzyme-XPD might be regulated by the PI3K/AKT signaling in response to DNA damage and plays a crucial role in combatting bupivacaine-induced neurotoxicity. Because XPD is expressed at low levels, the protein expression of XPD in the GV-211-RNAi-treated group was not significantly reduced. However, XPD expression was significantly upregulated after bupivacaine treatment. Thus, the effect of lentivirus was more obvious in bupivacaine-treated cells (as shown in Figure 6(b)). To verify the lentivirus knockdown efficiency, we obtained the fluorescence images of SH-SY5Y cells after infection with the GV-211-RNAi-expressing lentivirus and performed Q-PCR; the Q-PCR data are shown in Supplemental Figure 1. Therefore, a complete knockout strategy must be considered in future studies.

Bupivacaine, which is widely used clinically for regional nerve blockade and pain management [38], can induce neurotoxicity. Ruppen et al. showed large variations in the bupivacaine concentration in the cerebrospinal fluid (CSF) of patients who received spinal anesthesia [39]. Experimental studies in animal models have shown that the concentration at which bupivacaine causes neurotoxicity damage varies greatly. One criticism of the study may be the dose and concentration of local anesthetic used. Although a lower concentration of bupivacaine (0.5%-0.75%) is generally accepted as safe, previous studies have shown that bupivacaine might be neurotoxic at clinically relevant concentrations [2, 3]. Cauda equina syndrome, a severe neurological complication, has been associated with spinal anesthesia achieved with 0.5%-0.75% bupivacaine [40]. Because local anesthetic solutions rarely induce neurologic injury, larger dosages are required to observe their neurotoxic effects. A previous study showed that rats given 2.13% bupivacaine incurred only minimal morphologic damage without

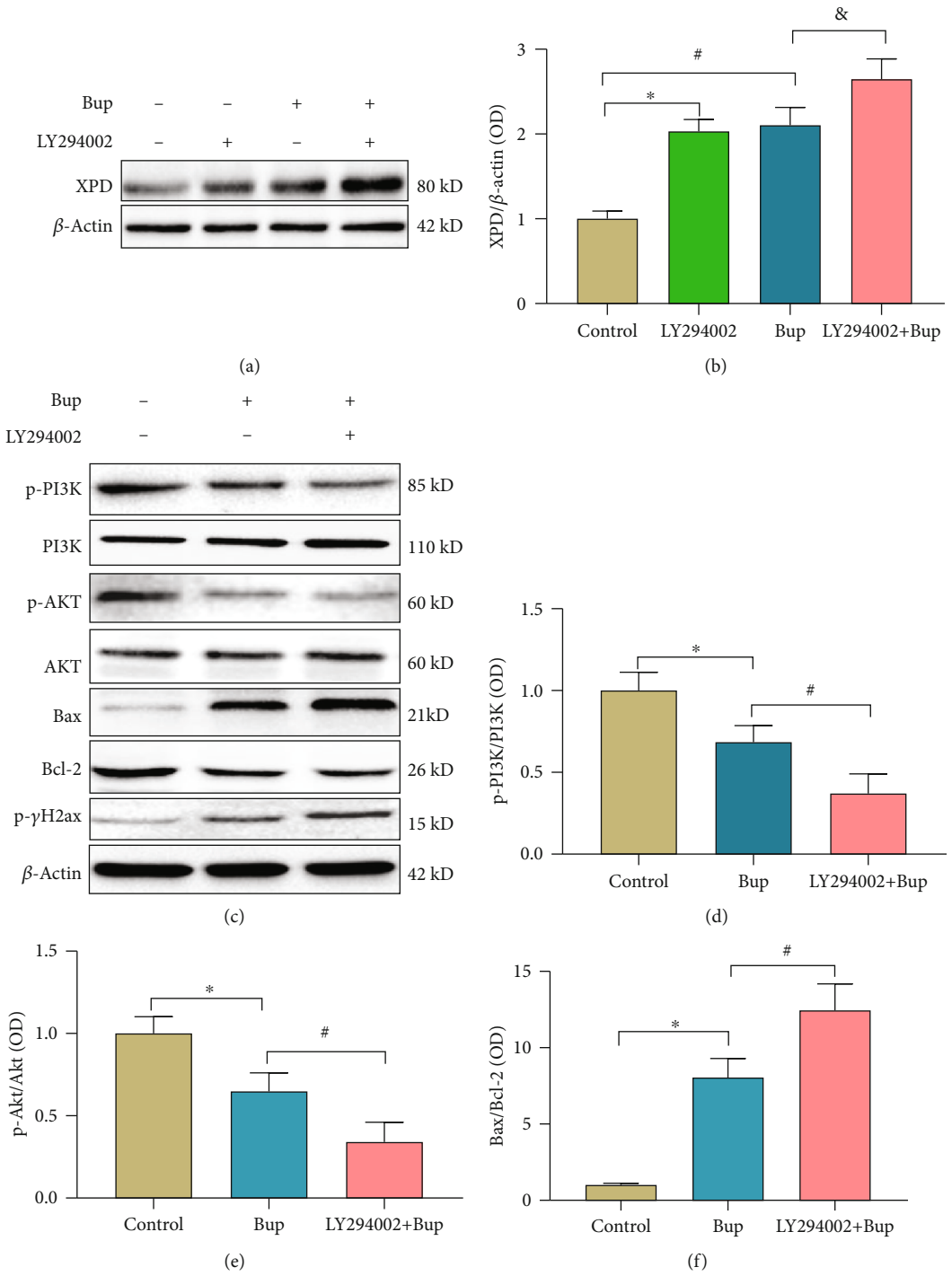

Figure 5: Continued.

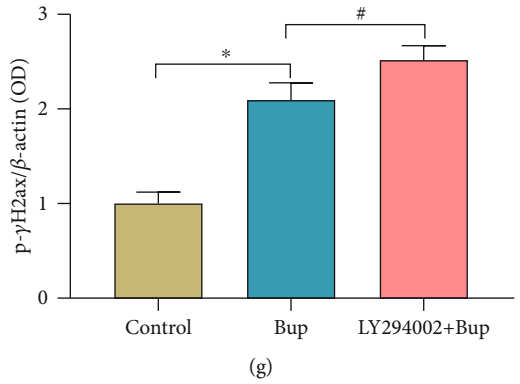

Figure 5: Inhibition of PI3K/AKT aggravated SH-SY5Y injury caused by bupivacaine and further increase the expression of XPD. Treatment with LY294002, a PI3K/AKT inhibitor, alone significantly increased XPD expression in SH-SY5Y cells ((a, b) $n = 3$; $^{*}p = 0.0005$). Moreover, the expression of XPD was further increased in the bupivacaine and LY294002-treated group compared with the bupivacaine-treated group ((a, b) $n = 3$; $^{\&}p = 0.0254$) ($^{\#}p = 0.0003$ vs. the control group). LY294002 (10 μM) further inhibited the protein expression of p-PI3K ((c, d) $n = 3$; $^{\#}p = 0.0316$) ($^{*}p = 0.0308$ vs. the control group) and p-AKT ((c, e) $n = 3$; $^{\#}p = 0.0346$) ($^{*}p = 0.0198$ vs. the control group) after bupivacaine treatment. The expression of the apoptosis-related proteins Bax and Bcl-2 and p-γH2AX (markers of DNA damage) was increased in the 10 μM LY294002 and bupivacaine-treated group compared with the bupivacaine group ((f) $^{\#}p = 0.0115$; (g) $n = 3$; $^{\#}p = 0.0360$) ((f) $^{*}p = 0.0011$ vs. the control group) ((g) $^{*}p = 0.0003$ vs. the control group). The data are shown as the mean ± SD of three independent experiments.

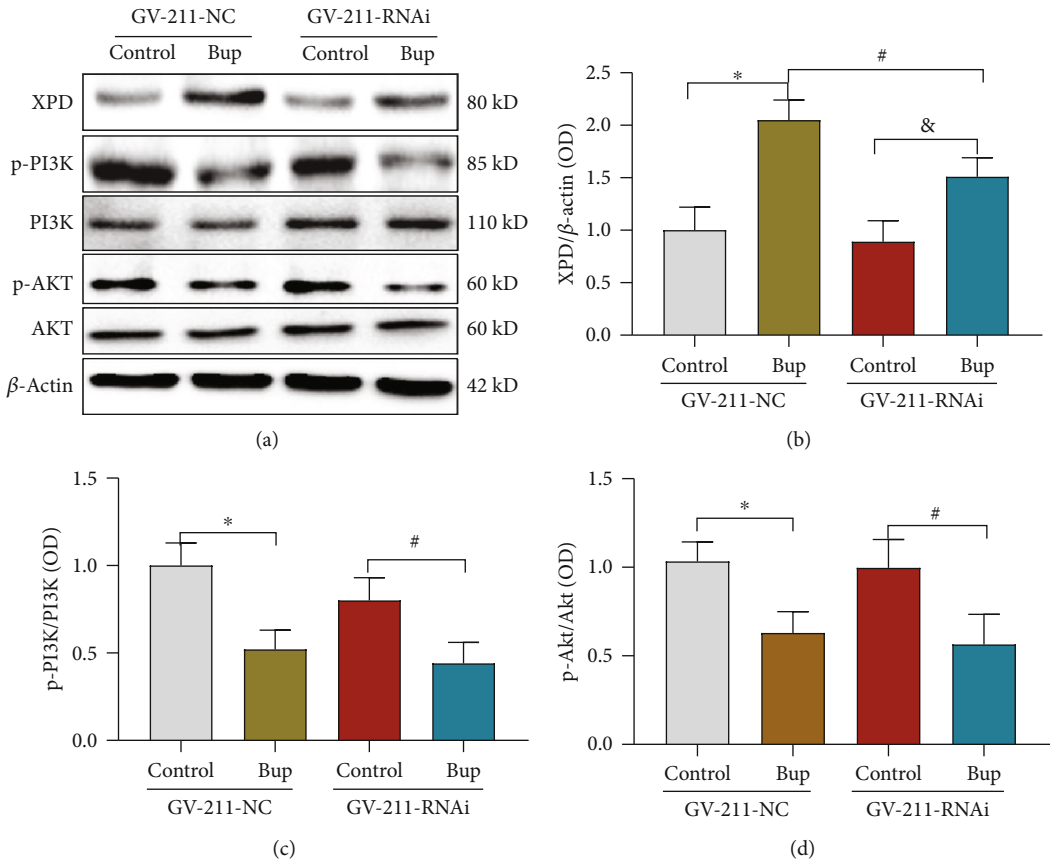

Figure 6: Downregulation of XPD expression did not affect the PI3K/AKT pathway. In SH-SY5Y cells, bupivacaine increased the expression of XPD ((a, b) $n = 3$; $^{*}p = 0.0009$ and $^{\&}p = 0.0208$ vs. the control group). The expression of XPD was downregulated by the XPD-GV211-RNAi-expressing lentivirus, and GV211-NC served as a control lentivirus ((a, b) $n = 3$; $^{\#}p = 0.0413$). p-PI3K and p-AKT expression was inhibited by bupivacaine ((a, c) $^{*}p = 0.0060$ and $^{\#}p = 0.0291$; (a, d) $^{*}p = 0.0345$ and $^{\#}p = 0.0242$ vs. the control group). Nevertheless, the expression of p-PI3K ((a, c) $n = 3$; $p = 0.8535$) and p-AKT ((a, d) $n = 3$; $p = 0.9396$) was not further reduced in the group in which XPD expression was downregulated compared with the GV-211-NC-treated group. The data are shown as the mean ± SD of three independent experiments.

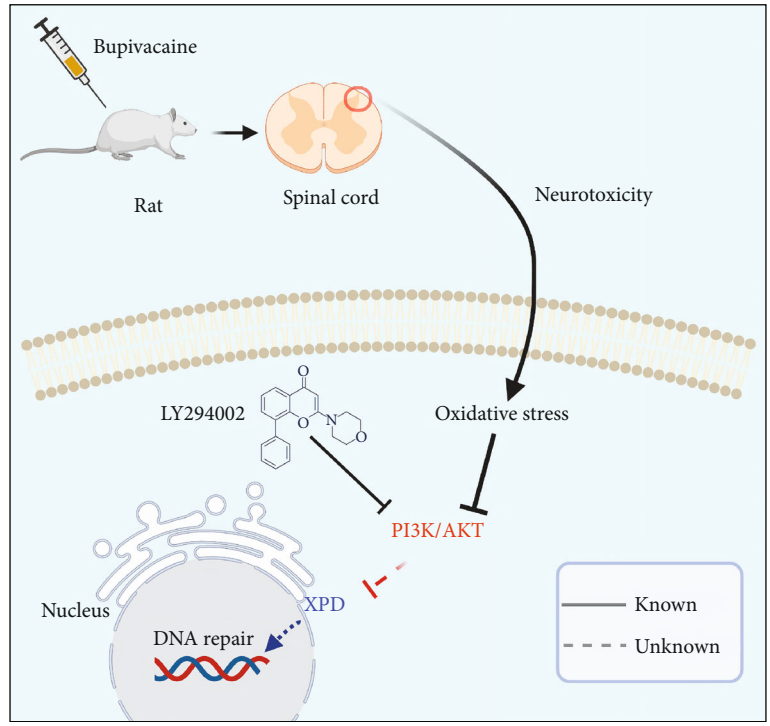

Figure 7: Graphical abstract. Bupivacaine may cause neuronal oxidative DNA damage. Damaged DNA activates a largely unknown repair mechanism. Our study showed that XPD is closely involved in repairing bupivacaine-induced oxidative DNA damage in neurons. Notably, XPD may be partially regulated by the PI3K/AKT pathway.

functional impairment. To study the neurotoxicity of bupivacaine, high concentrations that cause neuronal injury are usually used. The possible mechanism of injury was studied. In this study, 3% was selected as the bupivacaine concentration in the preliminary experiment [41, 42]. The degree of neuronal apoptosis is thought to play a role in pain behavior. Garraway et al. showed that neuronal apoptosis occurs at the same time as the onset of mechanical allodynia. In addition, the immunohistochemical analysis revealed distinct morphological signs of apoptosis in neurons at 24 h after stimulation [43]. This is consistent with the results in Figure 1(a).

SH-SY5Y neuroblastoma cells are a type of the human nervous system with a low degree of differentiation. Both differentiated and undifferentiated SH-SY5Y cells have been widely used in mechanistic studies on the pathogenesis, prevention, and treatment of central nervous system diseases [44, 45]. This paper is aimed at establishing a model simulating bupivacaine-induced neuronal injury in adult patients with differentiated and matured neurons. Thus, differentiated SH-SY5Y cells were more suitable than undifferentiated SH-SY5Y cells in this study. However, it has been found that undifferentiated SH-SY5Y cells are more sensitive to drug toxicity [46]. To study the neuronal damage caused by bupivacaine, we selected undifferentiated SH-SY5Y cells as cell models. SH-SY5Y cells, whether differentiated or undifferentiated, are nervous system tumor-derived cells. Thus, they cannot fully simulate the toxicity in normal neurons, which is a limitation of this study. The CCK-8 assay was used to measure cell viability, and the IC50 (1.5 mmol/L) of bupivacaine was calculated. When bupivacaine is administered at a concentration of 1–1.5 mmol/L [45, 47], nerve cells can be detected [45, 48]. Therefore, a bupivacaine concentration of 1.5 mmol/L was selected as the drug concentration for further study.

Ultimately, we drew a schematic of the proposed mechanism, which is shown in Figure 7: XPD, an enzyme of the NER pathway, may play an essential role in repairing bupivacaine-induced neuronal oxidative DNA damage. The repair enzyme XPD may be partially regulated by the PI3K/AKT signaling in response to DNA damage. These findings may be used as a reference for treating bupivacaine-induced neurotoxicity.

Data Availability

All the data supporting the results were shown in the paper and can be available from the corresponding authors.

Conflicts of Interest

The authors declare no competing interests.

Authors' Contributions

Wei Zhao, Lei Zeng, and Jiaming Luo contributed equally to this work. Wei Zhao performed the experiments, analyzed data, and wrote the manuscript. Lei Zeng and Jiaming Luo served the in vivo experiments, analyzed data, and revised the manuscript. Ji Li and Luying Lai performed the in vitro experiments. Shiyuan Xu and Zhongjie Liu were responsible

for study design and data analysis and revised the manuscript.

Acknowledgments

All work was supported by the National Natural Science Foundation of China (Nos. 81701464, 81771315, and 81974187) and the Hong Kong Scholars Program (XJ2019055).

Supplementary Materials

Supplemental Figure 1: validation of the lentivirus infection efficiency. *(Supplementary Materials)*

References

[1] Q. T. Meng, Z. Y. Xia, J. Liu, D. A. Bayliss, and X. Chen, "Local anesthetic inhibits hyperpolarization-activated cationic currents," *Molecular Pharmacology*, vol. 79, no. 5, pp. 866–873, 2011.

[2] J. Kato, J. Konishi, H. Yoshida et al., "Cauda equina syndrome following combined spinal and epidural anesthesia: a case report," *Canadian Journal of Anesthesia/Journal canadien d'anesthésie*, vol. 58, no. 7, pp. 638–641, 2011.

[3] Y. Xiang, W. Wang, S. Jing, Z. Zhang, and D. Wang, "Vocal fold paralysis and cauda equina syndrome following spinal-epidural anesthesia," *Medicine*, vol. 100, no. 3, article e24374, 2021.

[4] P. Poprac, K. Jomova, M. Simunkova, V. Kollar, C. J. Rhodes, and M. Valko, "Targeting free radicals in oxidative stress-related human diseases," *Trends in Pharmacological Sciences*, vol. 38, no. 7, pp. 592–607, 2017.

[5] T. A. Kunkel, "Celebrating DNA's repair crew," *Cell*, vol. 163, no. 6, pp. 1301–1303, 2015.

[6] Z. J. Liu, W. Zhao, Q. G. Zhang et al., "Ogg1 involvement in high glucose-mediated enhancement of bupivacaine-induced oxidative DNA damage in Sh-Sy5y cells," *Oxidative Medicine and Cellular Longevity*, vol. 2015, Article ID 683197, 11 pages, 2015.

[7] W. Zhao, Z. Liu, X. Yu et al., "Itraq proteomics analysis reveals that Pi3k is highly associated with bupivacaine-induced neurotoxicity pathways," *Proteomics*, vol. 16, no. 4, pp. 564–575, 2016.

[8] A. Shah, K. Gray, N. Figg, A. Finigan, L. Starks, and M. Bennett, "Defective base excision repair of oxidative DNA damage in vascular smooth muscle cells promotes atherosclerosis," *Circulation*, vol. 138, no. 14, pp. 1446–1462, 2018.

[9] S. van der Veen and C. M. Tang, "The BER necessities: the repair of DNA damage in human-adapted bacterial pathogens," *Nature Reviews Microbiology*, vol. 13, no. 2, pp. 83–94, 2015.

[10] S. Fu, X. Luo, X. Wu et al., "Activation of the melanocortin-1 receptor by Ndp-Msh attenuates oxidative stress and neuronal apoptosis through Pi3k/Akt/Nrf2 pathway after intracerebral hemorrhage in mice," *Oxidative medicine and cellular longevity*, vol. 2020, Article ID 8864100, 13 pages, 2020.

[11] L. Pruccoli, F. Morroni, G. Sita, P. Hrelia, and A. Tarozzi, "Esculetin as a bifunctional antioxidant prevents and counteracts the oxidative stress and neuronal death induced by amyloid protein in Sh-Sy5y cells," *Antioxidants*, vol. 9, no. 6, 2020.

[12] C. Mazur, B. Fitzsimmons, F. Kamme, B. Nichols, B. Powers, and E. Wancewicz, "Development of a simple, rapid, and robust intrathecal catheterization method in the rat," *Journal of Neuroscience Methods*, vol. 280, pp. 36–46, 2017.

[13] M. J. Kim, S. Y. Lee, K. Y. Yang et al., "Differential regulation of peripheral IL-1β-induced mechanical allodynia and thermal hyperalgesia in rats," *Pain*, vol. 155, no. 4, pp. 723–732, 2014.

[14] X. J. Yu, W. Zhao, Y. J. Li et al., "Neurotoxicity Comparison of Two Types of Local Anaesthetics: Amide- Bupivacaine versus Ester-Procaine," *Scientific Reports*, vol. 7, no. 1, article 45316, 2017.

[15] J. Si, Y. Ma, J. W. Bi et al., "Shisa3 brakes resistance to Egfr-Tkis in lung adenocarcinoma by suppressing cancer stem cell properties," *Journal of Experimental & Clinical Cancer Research*, vol. 38, no. 1, 2019.

[16] N. Dastagir, A. Lazaridis, K. Dastagir, K. Reimers, P. M. Vogt, and V. Bucan, "Role of lifeguard β-isoform in the development of breast cancer," *Oncology Reports*, vol. 32, no. 4, pp. 1335–1340, 2014.

[17] M. P. Dragomir, S. Tudor, K. Okubo et al., "The non-coding RNome after splenectomy," *Journal of Cellular and Molecular Medicine*, vol. 23, no. 11, pp. 7844–7858, 2019.

[18] W. Zhao, Z. Liu, J. Luo et al., "The roles of Parp-1 and Xpd and their potential interplay in repairing bupivacaine-induced neuron oxidative DNA damage," *Aging*, vol. 13, no. 3, pp. 4274–4290, 2021.

[19] K. Zhang, S. Yang, and C. Luo, "Tnf-alpha and Tnf-R1 regulate bupivacaine-induced apoptosis in spinal cord dorsal root ganglion neuron," *European Journal of Pharmacology*, vol. 833, pp. 63–68, 2018.

[20] L. J. Chen, Y. Q. Gao, X. J. Li, D. H. Shen, and F. Y. Sun, "Melatonin protects against Mptp/Mpp+ -induced mitochondrial DNA oxidative damage in vivo and in vitro," *Journal of Pineal Research*, vol. 39, no. 1, pp. 34–42, 2005.

[21] P. J. McKinnon, "Genome integrity and disease prevention in the nervous system," *Genes & Development*, vol. 31, no. 12, pp. 1180–1194, 2017.

[22] P. Li, R. A. Stetler, R. K. Leak et al., "Oxidative stress and DNA damage after cerebral ischemia: potential therapeutic targets to repair the genome and improve stroke recovery," *Neuropharmacology*, vol. 134, no. Part B, pp. 208–217, 2018.

[23] V. Shafirovich and N. E. Geacintov, "Removal of oxidatively generated DNA damage by overlapping repair pathways," *Free Radical Biology & Medicine*, vol. 107, pp. 53–61, 2017.

[24] X. Meng, C. Zhang, Y. Guo et al., "Tbhq attenuates neurotoxicity induced by methamphetamine in the Vta through the Nrf2/Ho-1 and Pi3k/Akt signaling pathways," *Oxidative medicine and cellular longevity*, vol. 2020, Article ID 8787156, 13 pages, 2020.

[25] J. Jian, S. Li, L. Z. Liu et al., "Xpd inhibits cell growth and invasion and enhances chemosensitivity in esophageal squamous cell carcinoma by regulating the Pi3k/Akt signaling pathway," *International Journal of Molecular Medicine*, vol. 46, no. 1, pp. 201–210, 2020.

[26] L. X. Tao, S. S. Ji, D. Szaloki et al., "An optically active isochroman-2 *H* -chromene conjugate potently suppresses neuronal oxidative injuries associated with the PI3K/Akt and MAPK signaling pathways," *Acta Pharmacologica Sinica*, vol. 42, no. 1, pp. 36–44, 2021.

[27] S. Kumar, J. Xu, R. S. Kumar et al., "The small Gtpase Rap1b negatively regulates neutrophil chemotaxis and transcellular

diapedesis by inhibiting Akt activation," *The Journal of Experimental Medicine*, vol. 211, no. 9, pp. 1741–1758, 2014.

[28] J. P. Melis, H. van Steeg, and M. Luijten, "Oxidative DNA damage and nucleotide excision repair," *Antioxidants & Redox Signaling*, vol. 18, no. 18, pp. 2409–2419, 2013.

[29] G. Kokic, A. Chernev, D. Tegunov, C. Dienemann, H. Urlaub, and P. Cramer, "Structural basis of Tfiih activation for nucleotide excision repair," *Nature Communications*, vol. 10, no. 1, 2019.

[30] J. Liu, H. Fang, Z. Chi et al., "Xpd localizes in mitochondria and protects the mitochondrial genome from oxidative DNA damage," *Nucleic Acids Research*, vol. 43, no. 11, pp. 5476–5488, 2015.

[31] F. Xu, L. Na, Y. Li, and L. Chen, "RETRACTED ARTICLE: Roles of the Pi3k/Akt/Mtor signalling pathways in neurodegenerative diseases and tumours," *Cell & Bioscience*, vol. 10, no. 1, 2020.

[32] J. Lei and Q. Chen, "Resveratrol attenuates brain damage in permanent focal cerebral ischemia via activation of Pi3k/Akt signaling pathway in rats," *Neurological Research*, vol. 40, no. 12, pp. 1014–1020, 2018.

[33] H. Deng, Y. Jia, D. Pan, and Z. Ma, "Berberine alleviates rotenone-induced cytotoxicity by antioxidation and activation of Pi3k/Akt signaling pathway in Sh-Sy5y cells," *Neuroreport*, vol. 31, no. 1, pp. 41–47, 2020.

[34] N. Lamm, S. Rogers, and A. J. Cesare, "The Mtor pathway: implications for DNA replication," *Progress in Biophysics and Molecular Biology*, vol. 147, pp. 17–25, 2019.

[35] T. T. Huang, E. J. Lampert, C. Coots, and J. M. Lee, "Targeting the Pi3k pathway and DNA damage response as a therapeutic strategy in ovarian cancer," *Cancer Treatment Reviews*, vol. 86, article 102021, 2020.

[36] Y. Ma, Y. Vassetzky, and S. Dokudovskaya, "mTORC1 pathway in DNA damage response," *Biochimica et Biophysica Acta (BBA) - Molecular Cell Research*, vol. 1865, no. 9, pp. 1293–1311, 2018.

[37] F. Villafanez, I. A. Garcia, S. Carbajosa et al., "Akt inhibition impairs PCNA ubiquitylation and triggers synthetic lethality in homologous recombination-deficient cells submitted to replication stress," *Oncogene*, vol. 38, no. 22, pp. 4310–4324, 2019.

[38] C. E. Firanescu, J. de Vries, P. Lodder et al., "Vertebroplasty versus sham procedure for painful acute osteoporotic vertebral compression fractures (VERTOS IV): randomised sham controlled clinical trial," *BMJ*, vol. 361, 2018.

[39] W. Ruppen, L. A. Steiner, J. Drewe, L. Hauenstein, S. Brugger, and M. D. Seeberger, "Bupivacaine concentrations in the lumbar cerebrospinal fluid of patients during spinal anaesthesia†," *British Journal of Anaesthesia*, vol. 102, no. 6, pp. 832–838, 2009.

[40] X. Chen, Z. Xu, R. Lin, and Z. Liu, "Persistent cauda equina syndrome after cesarean section under combined spinal- epidural anesthesia: a case report," *Journal of Clinical Anesthesia*, vol. 27, no. 6, pp. 520–523, 2015.

[41] S. Sakura, Y. Kirihara, T. Muguruma, T. Kishimoto, and Y. Saito, "The comparative neurotoxicity of intrathecal lidocaine and bupivacaine in rats," *Anesthesia and Analgesia*, vol. 101, no. 2, pp. 541–547, 2005.

[42] T. Muguruma, S. Sakura, Y. Kirihara, and Y. Saito, "Comparative somatic and visceral antinociception and neurotoxicity of intrathecal bupivacaine, levobupivacaine, and dextrobupivacaine in rats," *Anesthesiology*, vol. 104, no. 6, pp. 1249–1256, 2006.

[43] S. M. Garraway, S. A. Woller, J. R. Huie et al., "Peripheral noxious stimulation reduces withdrawal threshold to mechanical stimuli after spinal cord injury: role of tumor necrosis factor alpha and apoptosis," *Pain*, vol. 155, no. 11, pp. 2344–2359, 2014.

[44] M. Yusuf, K. Leung, K. J. Morris, and E. V. Volpi, "Comprehensive cytogenomic profile of the in vitro neuronal model Sh-Sy5y," *Neurogenetics*, vol. 14, no. 1, pp. 63–70, 2013.

[45] A. Malet, M. O. Faure, N. Deletage, B. Pereira, J. Haas, and G. Lambert, "The comparative cytotoxic effects of different local anesthetics on a human neuroblastoma cell line," *Anesthesia and Analgesia*, vol. 120, no. 3, pp. 589–596, 2015.

[46] X. Zhou, J. Bouitbir, M. E. Liechti, S. Krahenbuhl, and R. V. Mancuso, "Para-halogenation of amphetamine and methcathinone increases the mitochondrial toxicity in undifferentiated and differentiated Sh-Sy5y cells," *International Journal of Molecular Sciences*, vol. 21, no. 8, 2020.

[47] R. Werdehausen, S. Fazeli, S. Braun et al., "Apoptosis induction by different local anaesthetics in a neuroblastoma cell line," *British Journal of Anaesthesia*, vol. 103, no. 5, pp. 711–718, 2009.

[48] R. Perez-Castro, S. Patel, Z. V. Garavito-Aguilar et al., "Cytotoxicity of local anesthetics in human neuronal cells," *Anesthesia and Analgesia*, vol. 108, no. 3, pp. 997–1007, 2009.

Hindawi
Oxidative Medicine and Cellular Longevity
Volume 2021, Article ID 1676152, 15 pages
https://doi.org/10.1155/2021/1676152

Research Article

XIST Inhibition Attenuates Calcium Oxalate Nephrocalcinosis-Induced Renal Inflammation and Oxidative Injury via the miR-223/NLRP3 Pathway

Peng Lv,[1] Haoran Liu,[2,3] Tao Ye,[1] Xiaoqi Yang,[1] Chen Duan,[1] Xiangyang Yao,[1] Bo Li,[1] Kun Tang,[1] Zhiqiang Chen,[1] Jianhe Liu,[3] Yaoliang Deng,[4] Tao Wang,[5] Jinchun Xing,[5] Chaozhao Liang,[2] Hua Xu,[1] and Zhangqun Ye[1]

[1]*Department of Urology, Tongji Hospital, Tongji Medical College, Huazhong University of Science and Technology, Wuhan, China*
[2]*Department of Urology, The First Affiliated Hospital of Anhui Medical University, Institute of Urology, Anhui Medical University, Hefei, China*
[3]*Department of Urology, The Second Affiliated Hospital of Kunming Medical University, Kunming, China*
[4]*Department of Urology, The First Affiliated Hospital of Guangxi Medical University, Nanning, China*
[5]*Department of Urology, The First Affiliated Hospital of Xiamen University, Xiamen, China*

Correspondence should be addressed to Chaozhao Liang; liang_chaozhao@ahmu.edu.cn and Hua Xu; xuhuawhu@163.com

Peng Lv and Haoran Liu contributed equally to this work.

Received 21 April 2021; Revised 4 July 2021; Accepted 6 August 2021; Published 2 September 2021

Academic Editor: Chaoliang Tang

The roles of the lncRNA X inactive specific transcript (XIST) in many diseases, including cancers and inflammatory sickness, have been previously elucidated. However, renal calculus remained poorly understood. In this study, we revealed the potential effects of XIST on kidney stones that were exerted via inflammatory response and oxidative stress mechanisms. We established a glyoxylate-induced calcium oxalate (CaOx) stone mouse model and exposed HK-2 cells to calcium oxalate monohydrate (COM). The interactions among XIST, miR-223-3p, and NOD-like receptor protein 3 (NLRP3) and their respective effects were determined by RNAs and protein expression, luciferase activity, and immunohistochemistry (IHC) assays. Cell necrosis, reactive oxygen species (ROS) generation, and inflammatory responses were detected after silencing XIST, activating and inhibiting miR-223-3p, and both knocking down XIST and activating miR-223-3p in vitro and in vivo. The XIST, NLRP3, caspase-1, and IL-1β levels were notably increased in kidney samples from glyoxylate-induced CaOx stone model mice. XIST knockdown significantly suppressed the inflammatory damage and ROS production and further attenuated oxalate crystal deposition. miRNA-223-3p mimics also exerted the same effects. Moreover, we verified the interactions among XIST, miRNA-223-3p and NLRP3, and the subsequent effects. Our results suggest that the lncRNA XIST participates in the formation and progression of renal calculus by interacting with miR-223-3p and the NLRP3/Caspase-1/IL-1β pathway to mediate the inflammatory response and ROS production.

1. Introduction

The prevalence of kidney stones disease among adults in China has been approximately 10.63% in recent decades, and this prevalence continues to increase; the recurrence rate in the first 5 years after the first kidney stone is also continuously increasing [1, 2]. Calcium oxalate (CaOx) stones, which account for 80% of all renal calculus cases, induce a renal inflammatory response, resulting in renal tubular cell necrosis and additional CaOx crystal deposition [3, 4]. The NLRP3 protein was first identified in autoimmune diseases and recruited the adaptor molecule ASC through PYD-PYD

interactions, then recruited procaspase-1 to form the inflammasome complex [5, 6]. Activated caspase-1 participates in the processing of the cytokine prointerleukin-1β into its mature and active secreted form [7]. Increasing evidence suggests that NLRP3 plays a significant role in the pathogenesis of autoinflammatory, autoimmune, and chronic inflammatory and metabolic diseases [8–10].

Competing endogenous RNAs (ceRNAs) may play critical roles in RNA-RNA interactions and could explain the relationship among long noncoding RNAs (lncRNAs), miRNAs, and mRNAs [11]. The 3′-untranslated regions (UTRs) of lncRNAs and mRNAs have common base sites at which miRNAs can bind and thereby influence the expression of downstream proteins [12, 13]. The lncRNA XIST is indispensable for X-chromosome inactivation in mammals, which contributes to regulating the associated RNA-binding proteins (RBPs), chromatin modification, and gene silencing [14, 15]. Emerging evidence suggests that XIST participates in regulating inflammation, tissue injury, and cancer [16–18]. Moreover, Shen et al. reported that silencing XIST attenuated sepsis-induced acute liver injury and prevented inflammatory responses, ROS production, and cell apoptosis by inhibiting the BRD4 expression [19]. Nevertheless, the mechanism by which XIST regulates CaOx-induced renal inflammation and injury is largely unknown.

In this research, we studied the competing interactions among XIST/miRNA-223/NLRP3 in CaOx monohydrate-treated HK-2 cells and a glyoxylate-induced CaOx mouse model. We found that XIST sponges miR-223-3p to enhance renal tubular epithelial cell inflammatory responses and damage by activating the NLRP3/Caspase-1/IL-1β pathway.

2. Materials and Methods

2.1. Cell Culture and Transfection. HK-2 cells were purchased from American Type Culture Collection (ATCC, USA) and maintained in Roswell Park Memorial Institute 1640 medium (HyClone, UT) supplemented with 10% fetal bovine serum (Sigma, USA) at 37°C in a humid 5% CO_2 atmosphere. Cell viability was assessed with a Cell Counting Kit (Beyotime, China). To silence the expression of XIST, a validated small interfering RNA (siRNA) specifically targeting XIST (si-XIST, GCACAAACTCAATTCTCTA) was synthesized by RiboBio (Guangzhou, China). To overexpress or knock down miRNA-223, synthetic miRNA oligonucleotides (miR-223-3p mimic: 5′-3′: UGUCAGUUUGUCAAAUACCCCA, miR-223-3p inhibitor: 5′-3′: UGUCAGUUUGUCAAAUACCCCA) and the corresponding negative controls were purchased from RiboBio (Guangzhou, China). We transfected chemosynthetic siRNA or miRNA oligonucleotides by using Lipofectamine 3000 (Invitrogen, USA).

2.2. Animal Experiments. Our experiments were conducted in accordance with the criteria established by the National Institutes of Health Guide for the Care and Use of Laboratory Animals. Then, eight-week-old C57BL/6J male mice were raised under specific pathogen-free conditions at the Laboratory Animal Center of Tongji Hospital. Each mouse received saline or glyoxylate via intraperitoneal injection every day for one week. Eight-week-old mice in the treatment group were intravenously injected with 3×10^{12} viral genomes of rAAV-sh-XIST or a rAAV vector as a negative control (produced by Vigene, China) in a volume of 100 μl via the tail vein. Two weeks after the rAAV injection, immunofluorescence analysis was performed to confirm that the mouse kidneys were infected with rAAV (Supplementary Figure S1). In the miRNA-223 intervention group, a long-acting miRNA-223 antagonist was injected via the tail vein on days 1 and 4. The mice were sacrificed and dissected after one week, and bilateral kidney specimens were then fixed in 4% paraformaldehyde for further experiments. The animal study was approved by the Ethics Committee of Tongji Hospital.

2.3. CaOx Crystal Measurement. Renal paraffin sections were dewaxed and stained with hematoxylin-eosin according to the standard experimental procedure. The stained samples were then observed under a polarizing microscope (Zeiss, Germany). Moreover, stained renal paraffin sections were analyzed by the Pizzolato method to verify the amount of CaOx crystal deposition [20]. Finally, the quantity of CaOx crystals was determined with ImageJ software (National Institutes of Health, USA).

2.4. Tubular Injury and Necrosis Detection. The renal paraffin sections were dewaxed and then subjected to periodic acid-Schiff (PAS) staining. Kidney damage was scored according to the following four aspects: tubular necrosis, epithelial cell apoptosis, intraluminal cast formation, and brush border loss. We randomly selected nonoverlapping microscopic fields of view and calculated the ratio of tubular injury. Grades 0 to 5 represented 0%, ≤10%, 11–25%, 26–45%, 46–75%, and ≥76% injury, respectively. Cell necrosis in the renal section samples was assessed via TdT-mediated dUTP nick-end labeling (TUNEL). Positive cells were counted in ten randomly selected nonoverlapping microscopic fields of view.

2.5. Real-Time Quantitative PCR. Total RNA was collected by using TRIzol Reagent (Invitrogen, USA) according to the standard experimental procedure, and complementary DNA was synthesized by using an All-in-one RT SuperMix Perfect RT-PCR Kit (Vazyme, China). Real-time quantitative PCR was performed with SYBR Green Master Mix (Yeasen, 11201-11203) to assess RNA expression levels on a Bio-Rad CFX96 system, and the target RNA levels were normalized to those of GAPDH or U6. The sequences of all the primers are listed in Supplementary Table 1.

2.6. Flow Cytometry. HK-2 cells were cultured in six-well plates together with 100 μg/ml COM (Sigma-Aldrich, USA) and treated with various transfection reagents for 2 h. Next, the cells were treated with 2,7-dichlorofluorescein diacetate (DCFH-DA, BD Bioscience, USA) for 30 minutes at 37°C. Finally, internal ROS production in the cells was detected via flow cytometry at wavelengths of 485 nm and 538 nm. HK-2 cells were cultured in six-well plates together with 100 μg/ml COM for 24 h and then stained with an Annexin

V-FITC and PI Apoptosis Detection Kit (BD, USA). The necrosis of entire whole population of stained cells was monitored by flow cytometry (BD, USA).

2.7. Determination of Superoxide Dismutase (SOD), Lactate Dehydrogenase (LDH), Malondialdehyde (MDA), and Hydrogen Peroxide (H_2O_2) Levels. The levels of LDH and MDA, which are used to assess cell membrane destruction and lipid peroxidation, respectively, in the supernatants of cultured HK-2 cells were measured using commercial LDH and MDA assay kits (Beyotime Biotech, China) according to the manufacturer's instructions. To further measure the antioxidative enzyme activities in HK-2 cells, the SOD and H_2O_2 levels were assessed using commercially available assay kits (Beyotime Biotech, China) according to the respective manufacturer's instructions.

2.8. Measurement of ROS Generation. Treated HK-2 cells were cultured with DCFH-DA (S0033, Beyotime Biotech, China) for 30 minutes. Intracellular ROS generation in tubular epithelial cells (TECs) was detected by flow cytometry (BD Bioscience, USA) with excitation and emission wavelengths of at 488 and 525 nm, respectively. Intracellular ROS generation was also monitored by using a fluorescence microscope (Nikon, Japan). The levels of ROS generation were quantified with ImageJ software.

2.9. Mitochondrial Membrane Potential Assay. Tetramethyl rhodamine ethyl ester (TMRE) (ab113852, Abcam, USA) was used to determine the mitochondrial membrane potential. In brief, treated TECs were incubated with 150 nM TMRE diluted in warm culture medium for 15 minutes. The cells were then washed twice with warm PBS, and the fluorescence intensity was detected using a plate reader at excitation/emission wavelengths of 520/590 nm.

2.10. Western Blot Analysis. Whole protein was harvested from HK-2 cells with RIPA buffer containing a complete protease inhibitor cocktail (Servicebio, China), and the protein concentrations were determined by using a BCA Kit (Beyotime, China). The protein samples were separated and then incubated with antibodies against NLRP3 (Boster, China, BM4490), caspase-1 (Absin, China, abs119750), IL-1β (Absin, China), and GAPDH (Absin, China, abs132004) at 4°C overnight. Next, the cells were incubated with the appropriate corresponding horseradish peroxidase-conjugated secondary antibodies (Cell Signaling Technology, USA) at room temperature for 2 h and visualized with an ECL solution (Millipore, USA) on a ChemiDoc XRS instrument (Bio-Rad, USA). The relative expression levels of the proteins were analyzed with ImageJ software (National Institutes of Health, USA).

2.11. Dual-Luciferase Reporter Gene Assay. To construct the luciferase reporter vectors, the 3′-UTRs of XIST and NLRP3, which included a wild-type putative miR-223-3p binding site and an artificially mutated putative binding site, were inserted into the pGL4.13 plasmid. Then, HK-2 cells were cotransfected with the plasmids and artificial miR-223-3p mimics and inhibitor. After 2 days of transfection, the Dual-Luciferase Reporter Assay System (Promega, Madison, WI, USA) was used to detect the luciferase activity. The firefly luciferase activity is presented as the relative expression level and was normalized to that of the Renilla luciferase activity.

2.12. Immunohistochemistry. Renal paraffin sections were dewaxed and processed according to the standard experimental procedure, and the samples were incubated with the anti-NLRP3 (1 : 400, Servicebio, China, GB11300), anti-caspase-1 (1 : 1000, Servicebio, China, GB11383), anti-IL-1β (1 : 600, Servicebio, China, GB11113), anti-SOD2 (1 : 200, Boster, China, BM4813), and anti-NOX2 (1 : 600, Boster, China, BA2811) antibodies overnight at 4°C. The relative expression of the corresponding proteins was analyzed with ImageJ software (National Institutes of Health, USA).

2.13. RNA Fluorescence In Situ Hybridization (FISH). After the injection of mice with different doses of COM, kidney samples were harvested and fixed in paraffin wax. The sections were dewaxed and then treated with protease K at 37°C for 20 minutes. Denaturation was performed with denatured solutions containing different percentages of ethyl alcohol at -20°C. The sections were incubated with probes at 37°C for 12 h and then washed three times. Fluorescent labeling and nuclear staining were used to observe the differences in RNA expression among the groups.

3. Statistical Analysis

GraphPad Prism 8.4 and Stata SE15.1 were used to analyze the data. The experimental data are shown as the mean ± SD. We performed *t*-tests and one-way analysis of variance (ANOVA) to compare the differences among diverse groups. *P* values <0.05 were considered as statistically significant.

4. Results

4.1. XIST and NLRP3 Expression Was Significantly Increased in the CaOx Nephrocalcinosis Mouse Model. We established a glyoxylate-induced CaOx nephrocalcinosis mouse model by injecting mice with different doses of glyoxylate (0 mg/kg, 50 mg/kg, and 100 mg/kg) for seven days. Then, we performed HE staining and Pizzolato staining and then observed under a polarized optical microscope that the quantity of CaOx increased with increasing doses of glyoxylate (Figure 1(a)). Additionally, PAS staining showed that the injury caused by CaOx became more extensive after glyoxylate injection (Figure 1(b)). TUNEL staining revealed significant cell death after glyoxylate injection (Figure 1(b)). Moreover, immunohistochemistry analysis revealed high expression levels of NLRP3, caspase-1, and IL-1β in nephrocalcinosis samples (Figure 1(c)). We also found that the RNA expression levels of XIST, NLRP3, caspase-1, and IL-1β were highly elevated in the samples of glyoxylate-induced CaOx kidney stones (Figures 1(d) and 1(e)).

4.2. Inhibition of XIST Attenuated CaOx-Induced Renal Inflammation and Oxidative Injury In Vitro. HK-2 cells were cultured with different doses of COM crystals for different

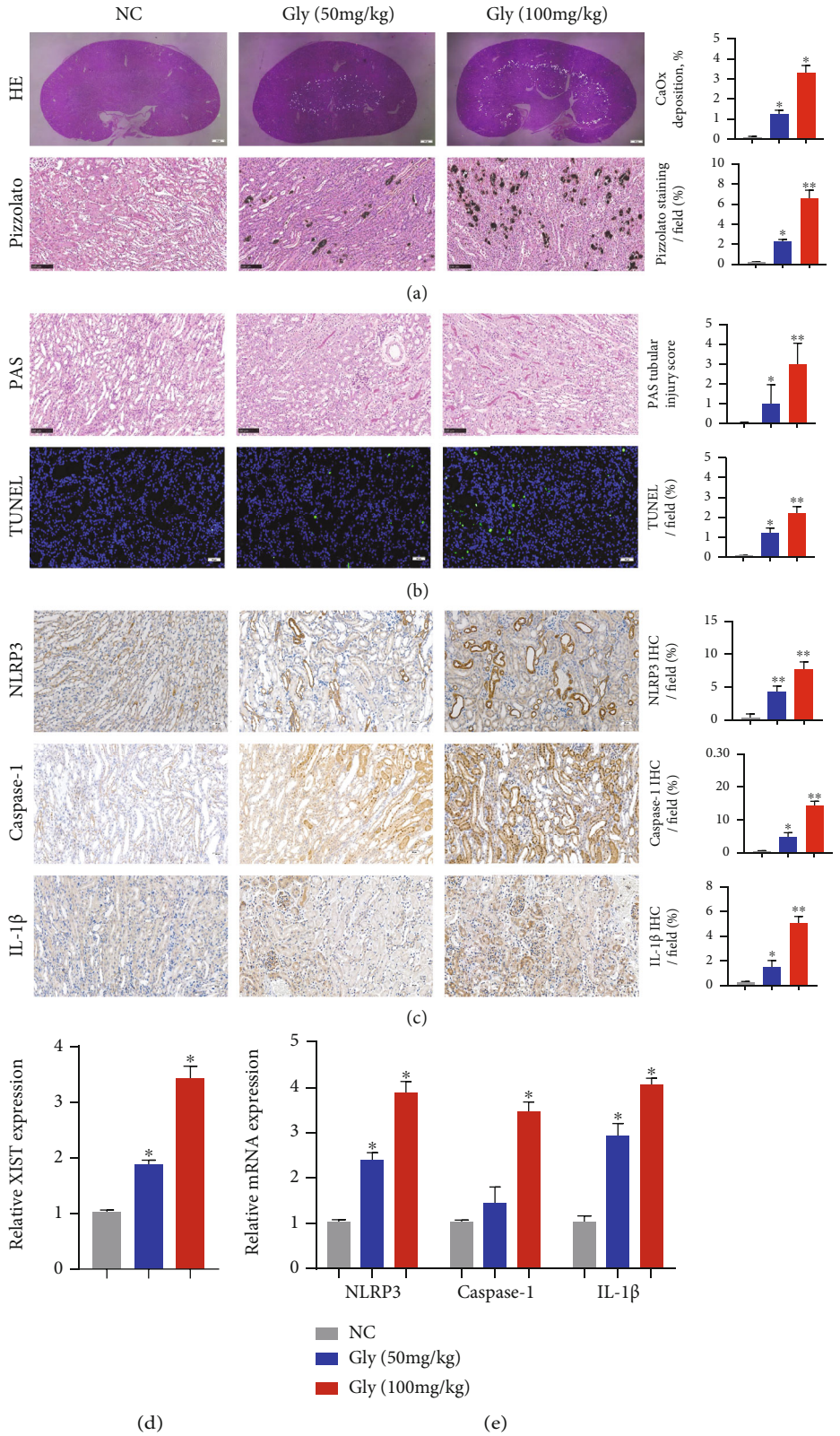

Figure 1: XIST and NLRP3 expression was significantly increased in the CaOx nephrocalcinosis mouse model. (a) Polarizing microscopy and Pizzolato staining were performed to verify the crystal deposition after the administration of glyoxylate at varying concentrations to CaOx nephrocalcinosis model mice. (b) PAS and TUNEL staining was used to observe the kidney injury. (c) The levels of NLRP3, Caspase-1, and IL-1β and the positive ratio were detected by IHC. (d, e) The expression levels of XIST, NLRP3, Caspase-1, and IL-1β in kidney samples were determined by qPCR. The data are presented as the mean ± SD of three independent experiments. $^{*}P < 0.05$; $^{**}P < 0.01$, as assessed via Student's t-test (a–c) and one-way ANOVA (d, e).

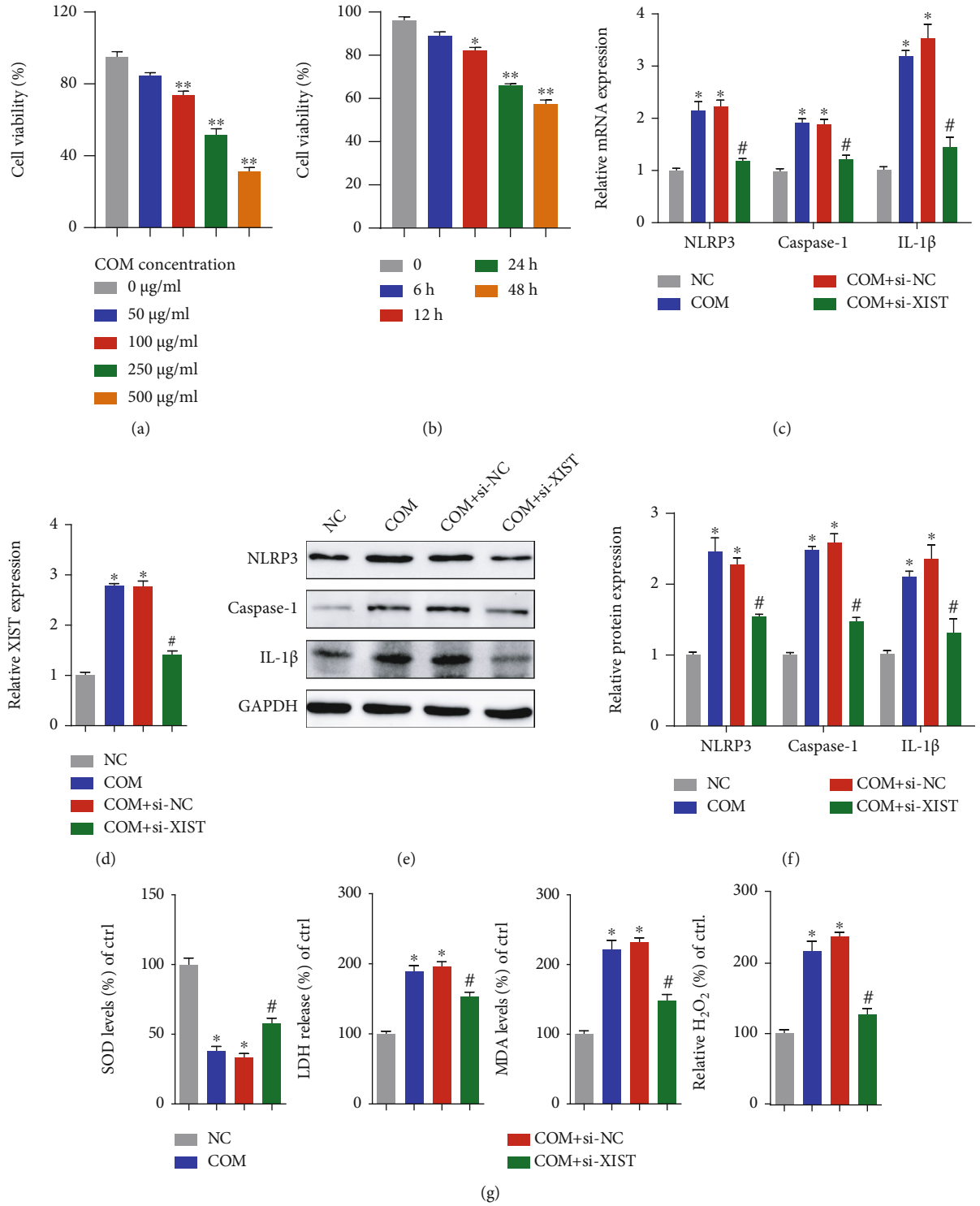

Figure 2: Continued.

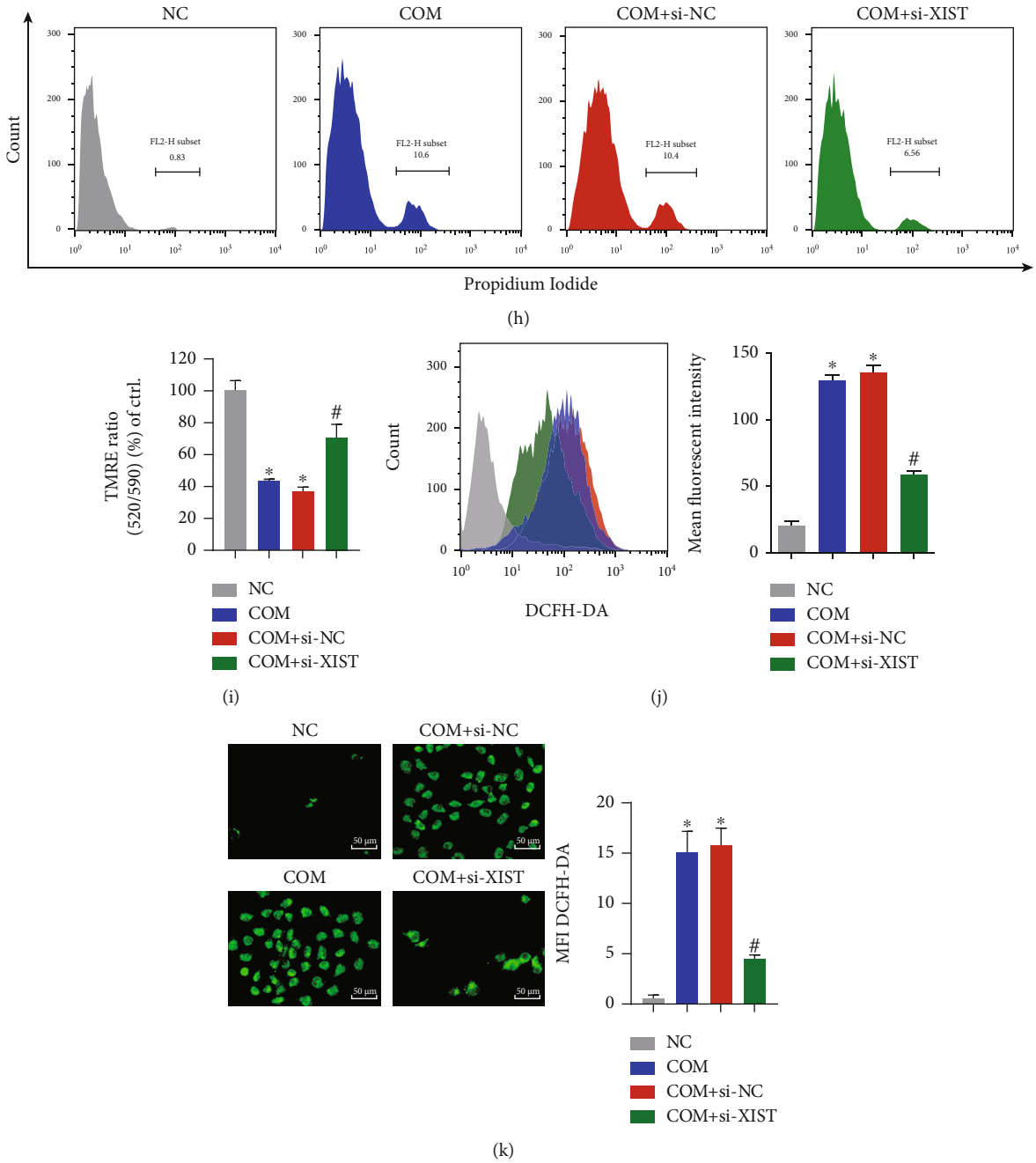

Figure 2: Inhibition of XIST attenuated CaOx-induced renal inflammation and oxidative injury in vitro. COM at various doses (0 μg/ml, 50 μg/ml, 100 μg/ml, 250 μg/ml, and 500 μg/ml) was cocultured with HK-2 cells, and the cell viability was detected. (b) Cells were cocultured with 100 μg/ml COM for different amounts of time (0 h, 6 h, 12 h, 24 h, and 48 h), and the cell viability was examined. (c, d) qRT-PCR was used to detect the expression of XIST, NLRP3, Caspase-1, and IL-1β in HK-2 cells. (e, f) Western blotting also showed changes in the protein levels of NLRP3, Caspase-1, and IL-1β in HK-2 cells. (g) The generation of SOD, LDH, MDA, and H_2O_2 after different treatments was examined. (h) Flow cytometry was performed to assess cell necrosis. (i) TMRE was used to determine the mitochondrial membrane potential. Flow cytometry (j) and DCFH-DA (k) were used to detect ROS production in fluorescently labeled HK-2 cells. The data are presented as the mean ± SD of three independent experiments. $^*P < 0.05$; $^{**}P < 0.01$, versus the NC group, $\#P < 0.05$, versus the COM+si-NC group, as determined by one-way ANOVA (a–d, f–k).

durations to determine the optimal concentration and pretreatment time. We ultimately chose 100 μg/ml as the treatment concentration and 8 h as the precondition duration (Figures 2(a) and 2(b)). To explore the effects of XIST, we transfected HK-2 cells with XIST siRNA and found that the RNA and protein levels of XIST, NLRP3, caspase-1, and IL-1β were significantly decreased (Figures 2(c)–2(f) and Supplementary Figure S2(a)). Then, XIST was knocked down, which clearly decreased the COM-induced LDH levels, H_2O_2 concentrations, and intercellular MDA

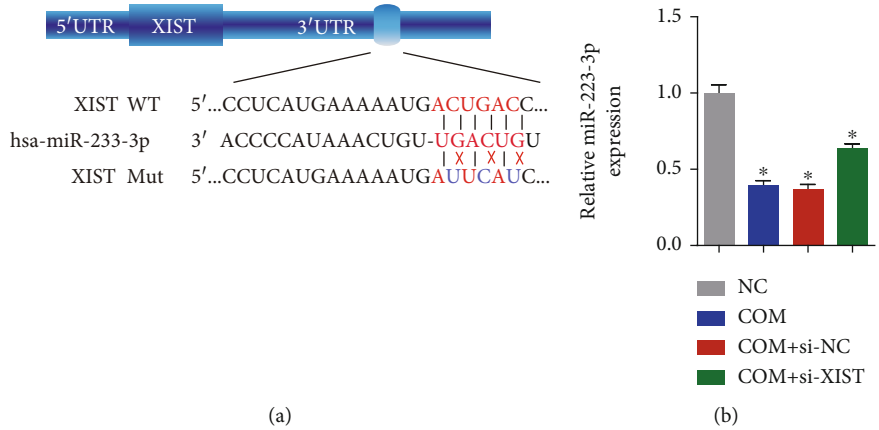

(a) (b)

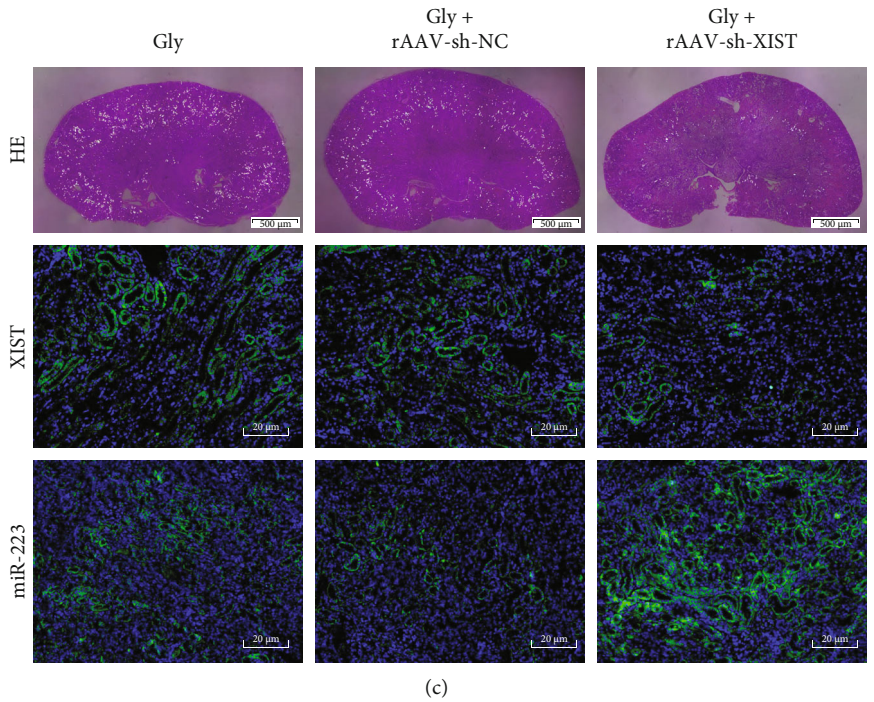

(c)

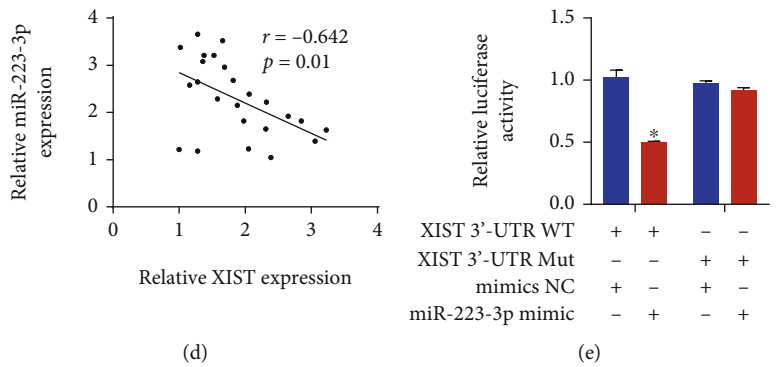

(d) (e)

Figure 3: Continued.

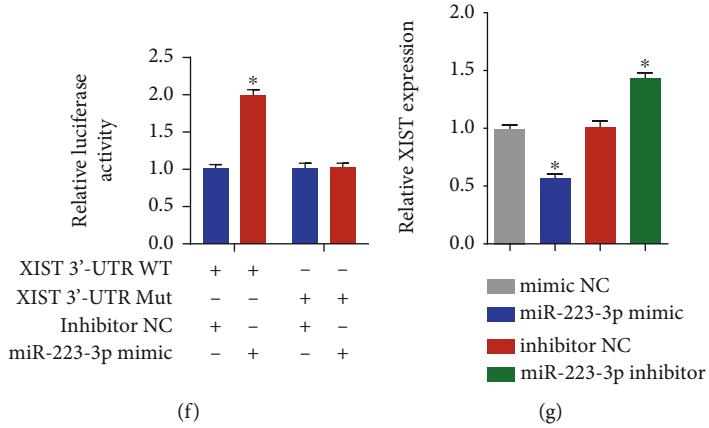

Figure 3: miR-223-3p directly bound to the 3′-UTR of XIST to suppress its expression. (a) Diagrammatic sketch of the WT and mutated XIST 3′-UTR targeting miR-223-3p. (b) qRT-PCR analysis was performed to determine the level of miR-223-3p in HK-2 cells. (c) Polarizing microscopy was performed to verify the crystal deposition in the CaOx nephrocalcinosis model. Fluorescence in situ hybridization was performed to examine the expression of XIST and miR-223-3p in the CaOx nephrocalcinosis model under different treatments. (d) The relationship between XIST and miR-223-3p was determined by Pearson analysis. The interaction of the 3′-UTR of XIST and the miR-223-3p mimics (e) or inhibitor (f) was verified via the dual-luciferase reporter gene assay. (g) The XIST levels in HK-2 cells were quantified by qRT-PCR. The data are presented as the mean ± SD of three independent experiments. $^{*}P < 0.05$; $^{**}P < 0.01$, as determined by one-way ANOVA (b, e–g) and Pearson's correlation test (d).

generations in vitro; in contrast, the SOD levels were increased after XIST knockdown (Figure 2(g)). Flow cytometry analysis of PI staining showed that the amount of necrosis was decreased after transfection with si-XIST (Figure 2(h)). TMRE was used to further explore the mitochondrial injury and revealed that si-XIST alleviated the COM-induced loss of mitochondrial membrane potential (Figure 2(i)). Moreover, the ROS production was substantially decreased in the si-XIST group compared to the COM + si-NC group (Figures 2(j) and 2(k)). In summary, we found that suppression of XIST could prohibit the COM-induced inflammatory response and oxidative stress.

4.3. MiR-223-3p Directly Bound to the 3′-UTR of XIST to Suppress Its Expression. The interaction of lncRNAs and miRNAs is a core mechanism that exerts regulatory effects. To further explore the mechanism by which XIST affects CaOx nephrocalcinosis, we focused on miR-223-3p, which was identified as a potential binding target of XIST via StarBase 3.0, TargetScan and miRWalk (Figure 3(a)). We first detected the miR-223-3p level after siRNA transfection and found that its expression was enhanced compared to that in the si-NC group (Figure 3(b)). Meanwhile, FISH was performed to detect the expression levels of XIST and miRNA-223 in the renal tissues of CaOx nephrocalcinosis mice treated with rAAV-sh-XIST (Figure 3(c)), demonstrating that the levels of XIST were negatively correlated with the levels of miRNA-223 (Figure 3(d)). We constructed wild-type (WT) and mutant (Mut) XIST 3′-UTR luciferase reporter vectors to determine whether miR-223-3p mimics interact with XIST. The luciferase activity was notably inhibited in the WT group, while the activity in the Mut group was not significantly altered (Figure 3(e)). Transfection of the miR-223-3p inhibitor increased the luciferase activity in the WT group but did not significantly change that in the Mut group (Figure 3(f)). Additionally, the expression of XIST was decreased in HK-2 cells transfected with the miR-223-3p mimics and increased in those transfected with the miR-223-3p inhibitor (Figure 3(g)). These results suggested that the 3′-UTR of XIST directly binds to miR-223-3p and participates in biological regulation.

4.4. MiR-223-3p Inhibited the Expression of NLRP3 by Directly Binding to Its 3′-UTR. We performed bioinformatics analysis to determine whether the 3′-UTR of NLRP3 contains a binding site for miR-223-3p (Figure 4(a)). We first found that the levels of NLRP3 were negatively associated with the levels of miR-223-3p (Figure 4(b)). To further verify the interaction, we constructed luciferase reporter vectors encoding the 3′-UTR of NLRP3 with the WT and Mut miR-223-3p binding sequences. After cotransfection with the miR-223-3p mimics, the luciferase activity in the WT group was substantially suppressed, while that in the Mut group was not substantially altered (Figure 4(c)). The miR-223-3p inhibitor was then transfected together with the two luciferase reporter vectors, and the luciferase activity in the WT group was notably elevated, while that in the Mut group was not substantially altered (Figure 4(d)). These experiments indicated that miR-223-3p directly binds to the 3′-UTR of NLRP3. To explore the function of miR-223-3p in CaOx-induced nephrocalcinosis and renal injury, we transfected miR-223-3p mimics and an inhibitor into COM-treated HK-2 cells. qRT-PCR and Western blot showed that miR-223-3p activation led to decreases in the expression of NLRP3, caspase-1, and IL-1β, while miR-223-3p inhibition caused the opposite phenomenon

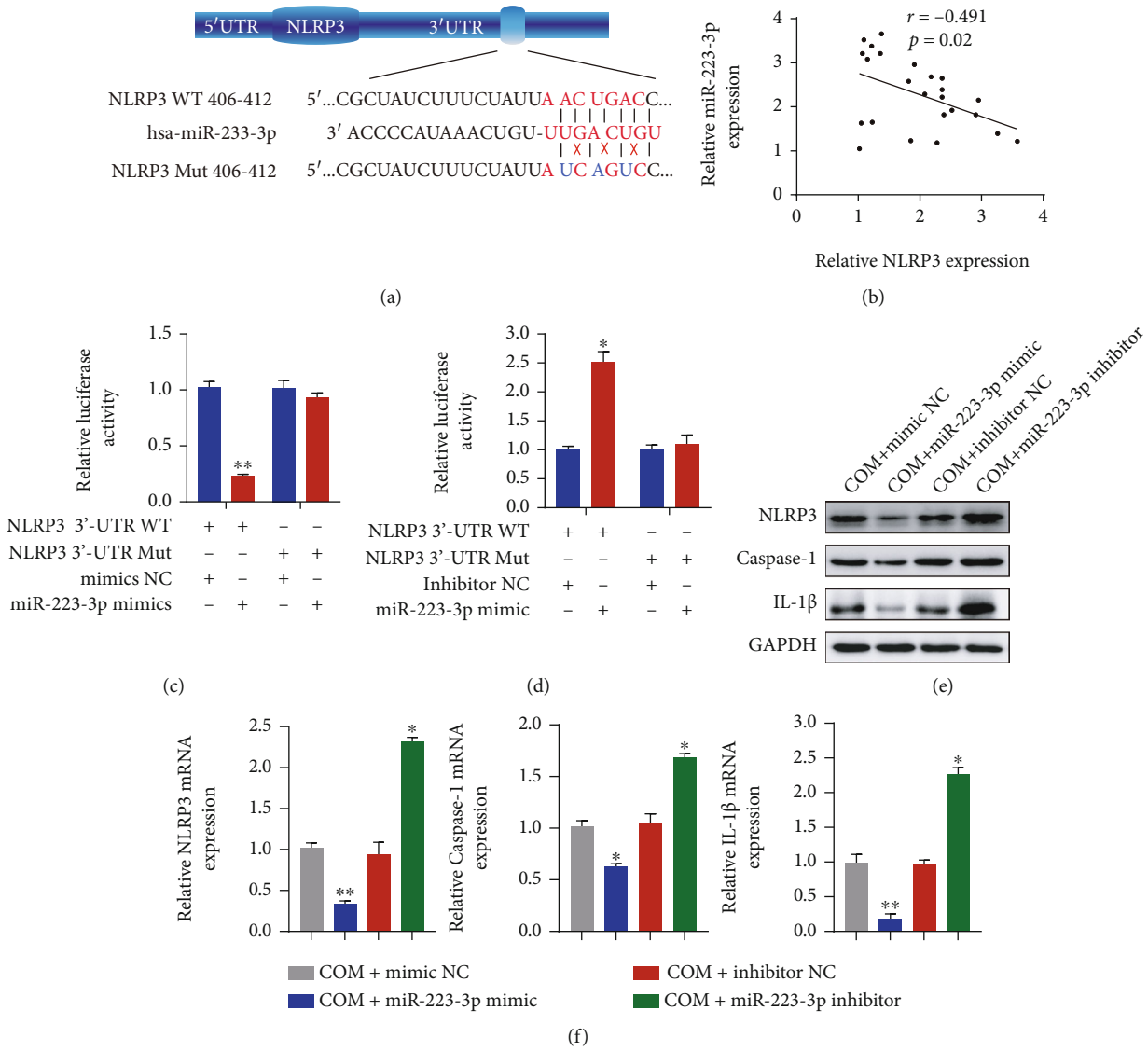

Figure 4: miR-223-3p inhibited the NLRP3 expression by directly binding to its 3′-UTR. (a) Diagrammatic sketch of the WT and mutated NLRP3 3′-UTR targeting miR-332-3p. (b) Pearson correlation analysis of NLRP3 and miR-223-3p was performed. A dual-luciferase reporter assay was performed to examine the interaction between the 3′-UTR of NLRP3 and the miR-223-3p mimics (c) or inhibitor (d). The expression levels of NLRP3, Caspase-1, and IL-1β in HK-2 cells transfected with the miR-223-3p mimics or inhibitor were detected by Western blotting (e) and qRT-PCR (f). The data are presented as the mean ± SD of three independent experiments. $^{*}P < 0.05$; $^{**}P < 0.01$, as determined by one-way ANOVA (c–f) and Pearson's correlation test (b).

(Figures 4(e) and 4(f) and Supplementary Figure S2(b)). These data suggest that miR-223-3p inhibits NLRP3 expression by directly binding to its 3′-UTR.

4.5. MiR-223-3p Reversed the Effect of XIST on COM-Induced Renal Tubular Epithelial Cell Inflammation and Oxidative Injury. To verify the internal functions of XIST and miRNA-223 in vitro, Western blot and qRT-PCR were performed, revealing that decreased levels of NLRP3, caspase-1, and IL-1β in COM-treated HK-2 cells cotransfected with si-XIST and the miRNA-223 inhibitor compared with those transfected with the miRNA-223 inhibitor alone (Figures 5(a) and 5(b) and Supplementary Figure S2(c)). Then, we detected the SOD levels after transfection with si-XIST, the miR-233 inhibitor, or both. The SOD expression was notably decreased by the miR-223-3p inhibitor, whereas si-XIST partially reversed this effect (Figure 5(c)). Additionally, the LDH levels, H_2O_2 concentrations, and intercellular MDA production showed opposite outcomes compared to the level of SOD (Figures 5(e)–5(f)). Moreover, PI staining was performed to detect COM-induced HK-2 necrosis (Figure 5(g)), demonstrating that si-XIST significantly reduced COM-induced HK-2 necrosis, while the miR-223-3p inhibitor abolished this treatment effect. In addition, si-XIST alleviated the COM-induced loss of mitochondrial membrane potential, while the combination of miR-223-3p inhibitor and si-XIST enhanced the COM-induced loss of mitochondrial

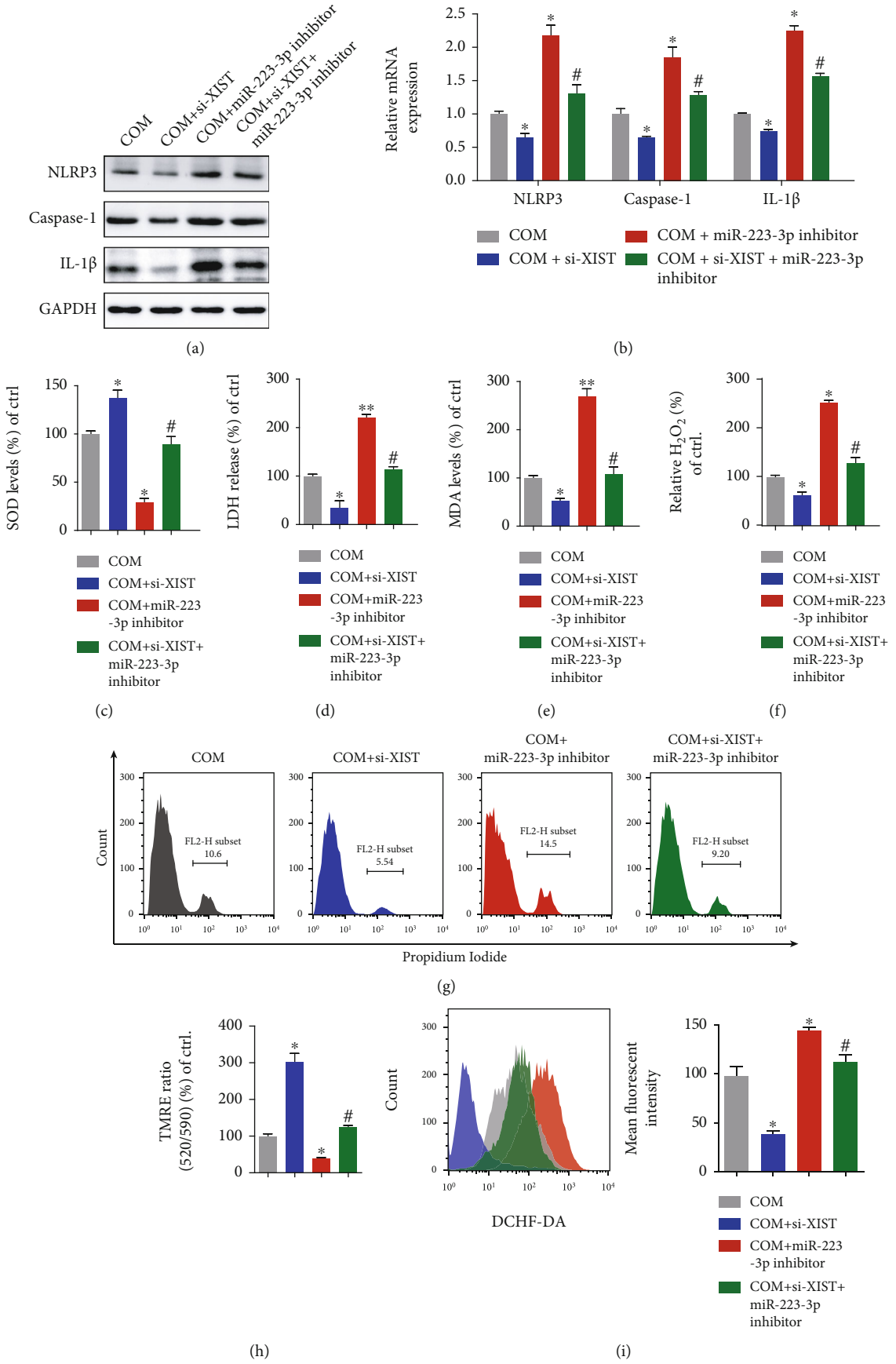

Figure 5: Continued.

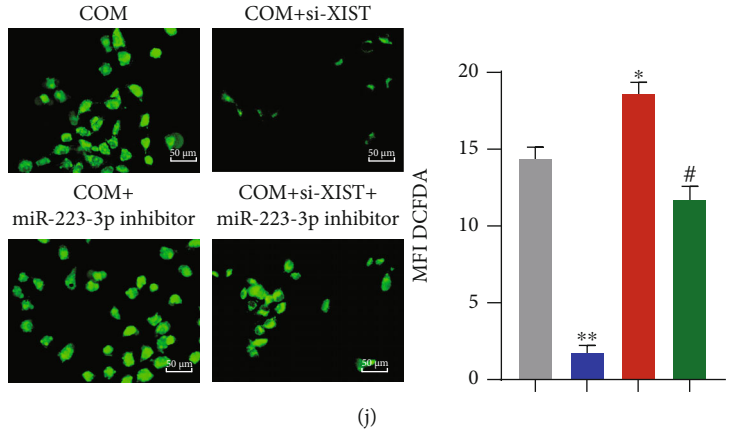

(j)

Figure 5: miR-223-3p reversed the effect of XIST on COM-induced renal tubular epithelial cell inflammation and oxidative injury. The levels of NLRP3, Caspase-1, and IL-1β in HK-2 cells cotransfected with si-XIST, the miR-223-3p inhibitor, or both were examined by Western blot (a) and qRT-PCR (b). The SOD expression (c), LDH release (d), MDA levels (e), and H_2O_2 generation (f) were detected in HK-2 cells transfected with si-XIST, the miR-223-3p inhibitor or si-XIST, and the miR-223-3p inhibitor in combination. (g) HK-2 necrosis was determined by flow cytometry. (h) The mitochondrial membrane potential was detected at Ex/Em wavelengths of 520/590 nm. Flow cytometry (i) and DCFH-DA (j) were used to assess the ROS production in HK-2 cells treated with si-XIST, the miR-223-3p inhibitor or si-XIST, and the miR-223-3p inhibitor in combination. The data are presented as the mean ± SD of three independent experiments. $^{*}P < 0.05$; $^{**}P < 0.01$, versus the COM group, $\#P < 0.05$, versus the COM+inhibitor 223 group, as determined by one-way ANOVA (a–j).

membrane potential (Figure 5(h)). Moreover, the ROS burst was enhanced by the miR-223-3p inhibitor and attenuated by the miR-223-3p inhibitor and si-XIST in combination (Figures 5(i) and 5(j)). Altogether, these results suggest that the inhibition of miR-223-3p enhances the inflammatory response and ROS production, while si-XIST attenuates these effects and decreases the kidney tubular cell damage.

4.6. XIST Inhibition Alleviated CaOx Crystal Deposition and CaOx Nephrocalcinosis-Induced Inflammatory and Oxidative Kidney Injury via the XIST-miR-223-3p-NLRP3 ceRNA Pathway. To verify the ability of the interaction between XIST and miR-223-3p in decreasing the CaOx deposition by suppressing renal inflammatory and oxidative injury in vivo, we administered the effects of rAAV-sh-XIST, antagomiR-223-3p, or both to CaOx nephrocalcinosis mice. Next, HE and Pizzolato staining was performed, and the cells were observed under the polarized optical microscope. The results showed that silencing XIST notably decreased the CaOx deposition, while inhibiting miR-223-3p significantly increased the CaOx deposition (Figure 6(a)). Moreover, PAS and TUNEL staining suggested that the kidney injury was less extensive in the rAAV-sh-XIST group and more extensive in the antagomiR-223-3p group (Figure 6(b)). On the other hand, the IHC results indicated that the expression levels of the proinflammatory markers NLRP3, Caspase-1, and IL-1β and the prooxidant NOX2 were prominently decreased after rAAV-sh-XIST injection and significantly increased after antagomiR-223-3p administration, while the SOD2 expression showed the opposite changes (Figures 6(c) and 6(d)). In addition, no significant changes were observed in CaOx nephrocalcinosis mice injected with both rAAV-sh-XIST and antagomiR-223-3p. These results indicate that miR-223-3p reversed the effect of XIST on COM crystal-induced renal tubular epithelial cell inflammation and oxidative stress injury (Figures 6(a)–6(d)). Therefore, downregulation of XIST can attenuate the ROS burst, protect renal tubular cell against injury, and further decrease crystal deposition in subjects with CaOx nephrocalcinosis.

Taken together, these results indicate that XIST inhibition decreases CaOx crystal-induced inflammatory and oxidative kidney injury by interacting with miR-223-3p and the NLRP3/Caspase-1/IL-1β pathway (Figure 7).

5. Discussion

Kidney stone formation is ascribed to multiple factors, including infection, metabolism, and other diseases [1, 3]. The progression of kidney stone formation involves CaOx crystal adhesion, growth, and advancement in renal tubules and the pelvis. Previous studies revealed that renal tubular epithelial cells exposed to CaOx generated excess ROS and an inflammatory response, thereby leading to further renal injury and increased CaOx deposition [21–23]. Therefore, the development of diagnostic markers and targeted treatments that delay or attenuate the progression of CaOx nephrocalcinosis is highly essential.

An increasing number of studies have indicated that lncRNAs play irreplaceable roles in multiple transcriptional and posttranscriptional biological processes, including chromatin modification, DNA repair, preservation of mRNA stability, and miRNA sponging [24–26]. XIST was one of the first lncRNAs to be discovered in the 1990s and participates in the regulation of many cancer-related processes and the inflammatory response [14, 27]. XIST, which also acts as a molecular sponge for miR-133a-3p, was shown to act as a ceRNA to reverse the repression of RohA and promote the

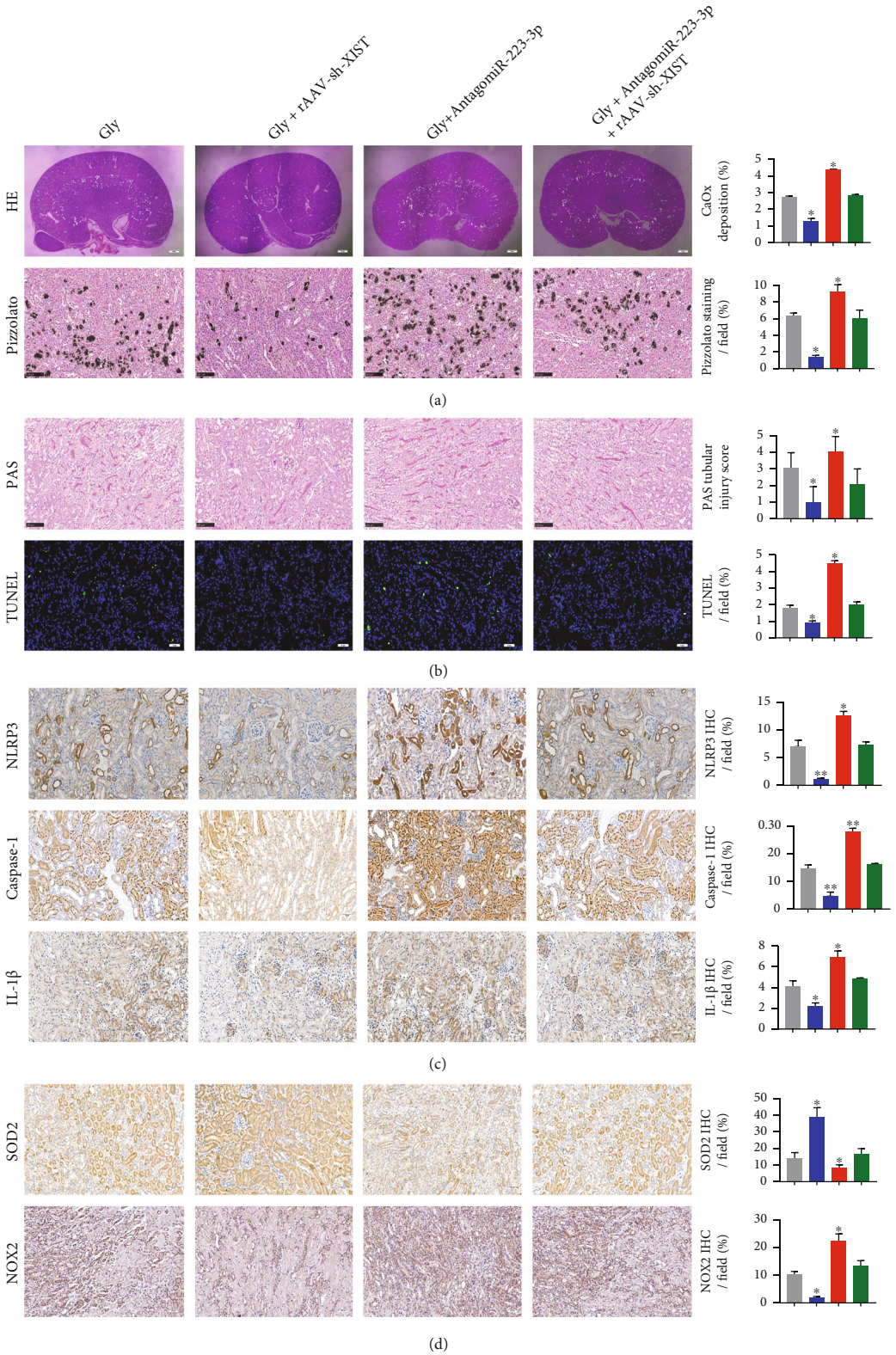

Figure 6: XIST inhibition alleviated CaOx crystal deposition and CaOx nephrocalcinosis-induced inflammatory and oxidative kidney injury via the XIST-miR-223-3p-NLRP3 ceRNA pathway. Polarization microscopy and Pizzolato staining were used to detect the crystal deposition in CaOx nephrocalcinosis model mice injected with rAAV-sh-XIST, antagomiR-223-3p, or both. (b) Kidney injuries were observed in CaOx nephrocalcinosis mice injected with rAAV-sh-XIST, antagomiR-223-3p, or both by PAS and TUNEL staining. The levels of NLRP3, Caspase-1, IL-1β (c), and SOD2 and NOX2 (d) in renal tissues were detected via IHC. The data are presented as the mean ± SD of three independent experiments. $^{*}P < 0.05$; $^{**}P < 0.01$, as determined by one-way ANOVA (a–d).

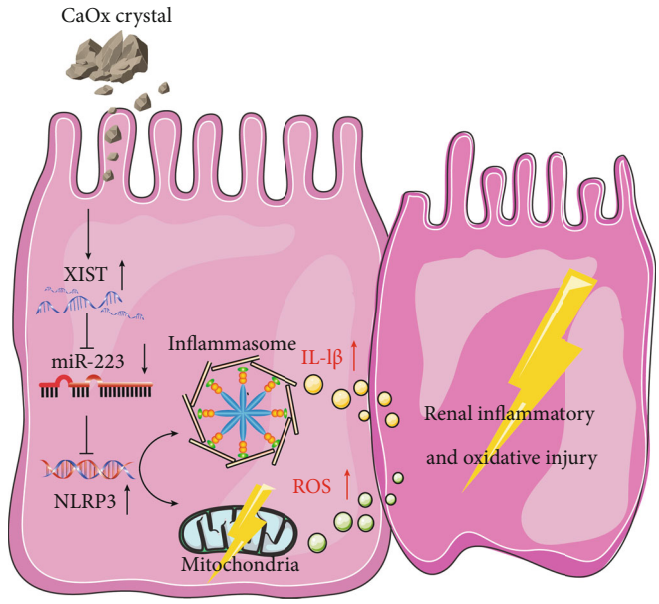

FIGURE 7: Schematic diagram XIST inhibition decreases CaOx crystal-induced inflammatory and oxidative kidney injury by interacting with miR-223-3p and the NLRP3/Caspase-1/IL-1β pathway.

progression of inflammatory colorectal cancer [28]. Additionally, XIST enhanced lipopolysaccharide- (LPS-) induced acute respiratory distress syndrome by upregulating the levels of interferon regulatory factor 2 by binding to miR-204 [29]. Hence, we hypothesized that the lncRNA XIST is a crucial factor that participates in the pathophysiological processes of inflammatory diseases. In this study, we first unveiled the ceRNA mechanism by which XIST regulates CaOx-induced inflammation and ROS disorders.

Activation of the NLRP3 inflammasome leads to the initial stages and progression of many diseases, including kidney stones [30, 31]. NLRP3 knockdown sufficiently ameliorated podocyte autophagy and protected podocytes from diabetic nephropathy-induced injury [32]. Moreover, Ying et al. demonstrated that NLRP3 interacted with miR-495, whose increased expression inhibited the activation of the NLRP3 inflammasome and downregulated inflammatory cell infiltration and responses in subjects with acute lung injury [33]. Additionally, NLRP3 activation contributed to robust ROS production and inflammatory responses via TXNIP in subjects with hyperoxaluria and in a kidney CaOx rat model [34]. In accordance with these findings, our experiments suggested that NLRP3 was activated in the CaOx-induced renal tubular epithelial cell injury in vitro and in vivo model.

NLRP3 was shown to be activated by the crystal deposition of monosodium urate into the joints, which induced inflammatory responses, and another study found that NLRP3-deficient mice were protected from crystal-related injuries [35, 36]. Moreover, NLRP3 blockade was shown to alleviate the inflammatory injury induced by cholesterol crystals in atherosclerosis [37, 38]. Anders et al. found that NLRP3-deficient mice fed an oxalate-rich diet failed to develop CaOx nephrocalcinosis and that their kidneys were protected from nephrocalcinosis-related fibrosis [39]. In addition, Mulay et al. showed that intrarenal calcium oxalate crystal deposition caused tubular damage, inflammation, and renal failure via the dendritic cell (DC) secretion of inflammatory cytokines and that IL-1β blockade decreased tubular injury [31]. Overall, NLRP3 is closely related to diseases induced by different kinds of crystals, including CaOx crystals.

To explore the internal relationship between the changes in XIST and NLRP3, we focused on the ceRNA hypothesis. We found that miR-223-3p may be a specific bridge between XIST and NLRP3, but the role of miR-223-3p in CaOx nephrocalcinosis has not been described. MiRNAs alter the gene expression by targeting mRNAs in the posttranscriptional regulation period [40]. MiR-223-3p is considered a key regulator of inflammation and immune processes, ranging from myeloid differentiation to neutrophil function, macrophage polarization, and activation [41–43]. Neudecker et al. indicated that the expression of miR-223-3p was increased in subjects with inflammatory bowel disease (IBD) and that it limited the inflammatory response by inhibiting the NLRP3 inflammasome in the intestinal nonspecific immune responses [44]. Consistent with previous studies, we discovered that miR-223-3p bound to the 3′-UTRs of both the XIST and NLRP3 and was associated with their cooperation with each other. In addition, the elevated expression of miR-223-3p significantly inhibited the mRNA translated products of NLRP3.

Taken together, these results showed that XIST enhanced the translation of NLRP3 by competitively binding to miR-223-3p to thereby release NLRP3 mRNA; these phenomena exacerbated the inflammatory response and ROS production, leading to renal tubular epithelial cell injury. This new mechanistic insight into the molecular regulatory

function of lncRNAs provided by our research will be crucial for the further exploration of novel diagnostic and therapeutic strategies for nephroliths.

Data Availability

The data used to support the findings of this study are included within the article.

Ethical Approval

All animal experiments were approved by Tongji Hospital (TJ201800631), performed in accordance with the European Directive for the Protection of Animals Used for Scientific Purposes, and reported in accordance with the ARRIVE guidelines.

Disclosure

The funders had no role in the study design, data collection, data analysis, interpretation, or writing of the report.

Conflicts of Interest

The authors declare that the research was conducted in the absence of any commercial or financial relationships that could be construed as a potential conflict of interest.

Authors' Contributions

This study was performed in collaboration with all authors. Hua Xu, Haoran Liu, and Chaozhao Liang conceived the outline and designed the study. Peng Lv drafted the article. Peng Lv, Tao Ye, Xiaoqi Yang, Chen Duan, Xiangyang Yao, Bo Li, and Kun Tang performed the experiments. Peng lv and Haoran Liu contributed to the figures and tables. Hua Xu, Zhiqiang Chen, Tao Wang, Yaoliang Deng, Jianhe Liu, Jinchun Xing, and Zhangqun Ye revised the final manuscript together with all authors. Peng Lv and Haoran Liu contributed equally to this work and share first authorship.

Acknowledgments

We give our sincere gratitude to all other researchers who helped us with this study. This study was supported by the National Natural Science Foundation of China (8167031233) and the Department of Science and Technology of Anhui Province (KJ2020A0167).

Supplementary Materials

Supplementary Table 1: list of primer sequences used for the real-time qPCR analysis. Supplementary Figure S1: immunofluorescence analysis of GFP and XIST expression in mouse kidneys. (A) Mice were injected with rAAV vector or rAAV-sh-XIST (rAAV-2/9-eGFP) via the tail vein. At eight-week postinjection, their kidneys were snap frozen and whole mounted for imaging (magnification, ×40). (B) qPCR analysis of XIST in mouse kidneys. GAPDH was used as the internal control. The data are shown as the mean ± SD. One representative plot of $n = 6$ samples is shown. $^{*}P < 0.05$; $^{**}P < 0.01$, as determined by Student's t-test. Supplementary Figure S2: relative quantification of the protein expression of NLRP3, Caspase-1, and IL-1β by in Western blot. GAPDH was used as the internal control. The data are shown as the mean ± SD. $^{*}P < 0.05$; $^{**}P < 0.01$, as determined by one-way ANOVA (A–D). *(Supplementary Materials)*

References

[1] F. L. Coe, A. Evan, and E. Worcester, "Kidney stone disease," *The Journal of Clinical Investigation*, vol. 115, no. 10, pp. 2598–2608, 2005.

[2] W. Wang, J. Fan, G. Huang et al., "Prevalence of kidney stones in mainland China: a systematic review," *Scientific Reports*, vol. 7, p. 41630, 2017.

[3] S. R. Mulay, A. Evan, and H. J. Anders, "Molecular mechanisms of crystal-related kidney inflammation and injury. Implications for cholesterol embolism, crystalline nephropathies and kidney stone disease," *Nephrology, Dialysis, Transplantation*, vol. 29, no. 3, pp. 507–514, 2014.

[4] A. P. Evan, "Physiopathology and etiology of stone formation in the kidney and the urinary tract," *Pediatric Nephrology*, vol. 25, no. 5, pp. 831–841, 2010.

[5] H. M. Hoffman, J. L. Mueller, D. H. Broide, A. A. Wanderer, and R. D. Kolodner, "Mutation of a new gene encoding a putative pyrin-like protein causes familial cold autoinflammatory syndrome and Muckle-Wells syndrome," *Nature Genetics*, vol. 29, no. 3, pp. 301–305, 2001.

[6] T. Fernandes-Alnemri, J. Wu, J. W. Yu et al., "The pyroptosome: a supramolecular assembly of ASC dimers mediating inflammatory cell death via caspase-1 activation," *Cell Death and Differentiation*, vol. 14, no. 9, pp. 1590–1604, 2007.

[7] N. A. Thornberry, H. G. Bull, J. R. Calaycay et al., "A novel heterodimeric cysteine protease is required for interleukin-1β processing in monocytes," *Nature*, vol. 356, no. 6372, pp. 768–774, 1992.

[8] L. Ferrucci and E. Fabbri, "Inflammageing: chronic inflammation in ageing, cardiovascular disease, and frailty," *Nature Reviews. Cardiology*, vol. 15, no. 9, pp. 505–522, 2018.

[9] Z. Zhong, E. Sanchez-Lopez, and M. Karin, "Autophagy, NLRP3 inflammasome and auto-inflammatory/immune diseases," *Clinical and Experimental Rheumatology*, vol. 34, 4 Suppl 98, pp. 12–16, 2016.

[10] N. Esser, S. Legrand-Poels, J. Piette, A. J. Scheen, and N. Paquot, "Inflammation as a link between obesity, metabolic syndrome and type 2 diabetes," *Diabetes Research and Clinical Practice*, vol. 105, no. 2, pp. 141–150, 2014.

[11] Y. Tay, J. Rinn, and P. P. Pandolfi, "The multilayered complexity of ceRNA crosstalk and competition," *Nature*, vol. 505, no. 7483, pp. 344–352, 2014.

[12] Y. X. Song, J. X. Sun, J. H. Zhao et al., "Non-coding RNAs participate in the regulatory network of CLDN4 via ceRNA mediated miRNA evasion," *Nat Commun*, vol. 8, no. 1, p. 289, 2017.

[13] H. J. Park, P. Ji, S. Kim et al., "3′ UTR shortening represses tumor-suppressor genes in trans by disrupting ceRNA crosstalk," *Nature Genetics*, vol. 50, no. 6, pp. 783–789, 2018.

[14] A. Loda and E. Heard, "Xist RNA in action: past, present, and future," *PLoS Genetics*, vol. 15, no. 9, article e1008333, 2019.

[15] N. Brockdorff, J. S. Bowness, and G. Wei, "Progress toward understanding chromosome silencing by Xist RNA," *Genes & Development*, vol. 34, no. 11-12, pp. 733–744, 2020.

[16] B. B. Shenoda, S. Ramanathan, R. Gupta et al., "Xist attenuates acute inflammatory response by female cells," *Cellular and Molecular Life Sciences*, vol. 788, p. 299, 2020.

[17] Z. Li, Y. Zhang, N. Ding et al., "Inhibition of lncRNA XIST improves myocardial I/R injury by targeting miR-133a through inhibition of autophagy and regulation of SOCS2," *Molecular Therapy - Nucleic Acids*, vol. 18, pp. 764–773, 2019.

[18] W. Wei, Y. Liu, Y. Lu, B. Yang, and L. Tang, "LncRNA XIST promotes pancreatic cancer proliferation through miR-133a/EGFR," *Journal of Cellular Biochemistry*, vol. 118, no. 10, pp. 3349–3358, 2017.

[19] C. Shen and J. Li, "LncRNA XIST silencing protects against sepsis-induced acute liver injury via inhibition of BRD4 expression," *Inflammation*, vol. 44, no. 1, pp. 194–205, 2020.

[20] P. Pizzolato, "Histochemical recognition of calcium oxalate," *The Journal of Histochemistry and Cytochemistry*, vol. 12, pp. 333–336, 1964.

[21] S. R. Khan, "Reactive oxygen species, inflammation and calcium oxalate nephrolithiasis," *Translational Andrology and Urology*, vol. 3, no. 3, pp. 256–276, 2014.

[22] A. Okada, S. Nomura, Y. Higashibata et al., "Successful formation of calcium oxalate crystal deposition in mouse kidney by intraabdominal glyoxylate injection," *Urological Research*, vol. 35, no. 2, pp. 89–99, 2007.

[23] H. Liu, T. Ye, X. Yang et al., "H19 promote calcium oxalate nephrocalcinosis-induced renal tubular epithelial cell injury via a ceRNA pathway," *eBioMedicine*, vol. 50, pp. 366–378, 2019.

[24] T. R. Mercer, M. E. Dinger, and J. S. Mattick, "Long noncoding RNAs: insights into functions," *Nature Reviews. Genetics*, vol. 10, no. 3, pp. 155–159, 2009.

[25] Y. Kondo, K. Shinjo, and K. Katsushima, "Long non-coding RNAs as an epigenetic regulator in human cancers," *Cancer Science*, vol. 108, no. 10, pp. 1927–1933, 2017.

[26] J. M. Engreitz, N. Ollikainen, and M. Guttman, "Long noncoding RNAs: spatial amplifiers that control nuclear structure and gene expression," *Nature Reviews. Molecular Cell Biology*, vol. 17, no. 12, pp. 756–770, 2016.

[27] L. Li, G. Lv, B. Wang, and L. Kuang, "XIST/miR-376c-5p/OPN axis modulates the influence of proinflammatory M1 macrophages on osteoarthritis chondrocyte apoptosis," *Journal of Cellular Physiology*, vol. 235, no. 1, pp. 281–293, 2020.

[28] X. Yu, D. Wang, X. Wang et al., "CXCL12/CXCR4 promotes inflammation-driven colorectal cancer progression through activation of RhoA signaling by sponging miR-133a-3p," *Journal of Experimental & Clinical Cancer Research*, vol. 38, no. 1, p. 32, 2019.

[29] S. Wang, F. Cao, X. Gu et al., "LncRNA XIST, as a ceRNA of miR-204, aggravates lipopolysaccharide-induced acute respiratory distress syndrome in mice by upregulating IRF2," *International Journal of Clinical and Experimental Pathology*, vol. 12, no. 7, pp. 2425–2434, 2019.

[30] B. Z. Shao, Z. Q. Xu, B. Z. Han, D. F. Su, and C. Liu, "NLRP3 inflammasome and its inhibitors: a review," *Frontiers in Pharmacology*, vol. 6, p. 262, 2015.

[31] S. R. Mulay, O. P. Kulkarni, K. V. Rupanagudi et al., "Calcium oxalate crystals induce renal inflammation by NLRP3-mediated IL-1β secretion," *The Journal of Clinical Investigation*, vol. 123, no. 1, pp. 236–246, 2013.

[32] Y. Hou, S. Lin, J. Qiu et al., "NLRP3 inflammasome negatively regulates podocyte autophagy in diabetic nephropathy," *Biochemical and Biophysical Research Communications*, vol. 521, no. 3, pp. 791–798, 2020.

[33] Y. Ying, Y. Mao, and M. Yao, "NLRP3 inflammasome activation by microRNA-495 promoter methylation may contribute to the progression of acute lung injury," *Molecular Therapy Nucleic Acids*, vol. 18, pp. 801–814, 2019.

[34] S. Joshi, W. Wang, A. B. Peck, and S. R. Khan, "Activation of the NLRP3 inflammasome in association with calcium oxalate crystal induced reactive oxygen species in kidneys," *The Journal of Urology*, vol. 193, no. 5, pp. 1684–1691, 2015.

[35] F. Martinon, V. Pétrilli, A. Mayor, A. Tardivel, and J. Tschopp, "Gout-associated uric acid crystals activate the NALP3 inflammasome," *Nature*, vol. 440, no. 7081, pp. 237–241, 2006.

[36] B. Pazár, H. K. Ea, S. Narayan et al., "Basic calcium phosphate crystals induce monocyte/macrophage IL-1β secretion through the NLRP3 inflammasome in vitro," *Journal of Immunology*, vol. 186, no. 4, pp. 2495–2502, 2011.

[37] Z. Hoseini, F. Sepahvand, B. Rashidi, A. Sahebkar, A. Masoudifar, and H. Mirzaei, "NLRP3 inflammasome: its regulation and involvement in atherosclerosis," *Journal of Cellular Physiology*, vol. 233, no. 3, pp. 2116–2132, 2018.

[38] P. Duewell, H. Kono, K. J. Rayner et al., "NLRP3 inflammasomes are required for atherogenesis and activated by cholesterol crystals," *Nature*, vol. 464, no. 7293, pp. 1357–1361, 2010.

[39] H. J. Anders, B. Suarez-Alvarez, M. Grigorescu et al., "The macrophage phenotype and inflammasome component NLRP3 contributes to nephrocalcinosis-related chronic kidney disease independent from IL-1-mediated tissue injury," *Kidney International*, vol. 93, no. 3, pp. 656–669, 2018.

[40] X. Yuan, N. Berg, J. W. Lee et al., "MicroRNA miR-223 as regulator of innate immunity," *Journal of Leukocyte Biology*, vol. 104, no. 3, pp. 515–524, 2018.

[41] J. B. Johnnidis, M. H. Harris, R. T. Wheeler et al., "Regulation of progenitor cell proliferation and granulocyte function by microRNA-223," *Nature*, vol. 451, no. 7182, pp. 1125–1129, 2008.

[42] C. H. T. Hall, E. L. Campbell, and S. P. Colgan, "Neutrophils as components of mucosal homeostasis," *Cellular and Molecular Gastroenterology and Hepatology*, vol. 4, no. 3, pp. 329–337, 2017.

[43] G. Zhuang, C. Meng, X. Guo et al., "A novel regulator of macrophage activation: miR-223 in obesity-associated adipose tissue inflammation," *Circulation*, vol. 125, no. 23, pp. 2892–2903, 2012.

[44] V. Neudecker, M. Haneklaus, O. Jensen et al., "Myeloid-derived miR-223 regulates intestinal inflammation via repression of the NLRP3 inflammasome," *The Journal of Experimental Medicine*, vol. 214, no. 6, pp. 1737–1752, 2017.

Hindawi
Oxidative Medicine and Cellular Longevity
Volume 2021, Article ID 4899688, 10 pages
https://doi.org/10.1155/2021/4899688

Review Article

Cognitive Dysfunction after Heart Disease: A Manifestation of the Heart-Brain Axis

Chengyang Xu,[1,2] **Xueshu Tao**,[3] **Xiaonan Ma**,[1,2] **Rui Zhao**,[1,2] **and Zhipeng Cao**[1,2]

[1]*Department of Forensic Pathology, School of Forensic Medicine, China Medical University, No. 77, Puhe Road, Shenyang North New Area, Shenyang 110122, China*
[2]*Department of Forensic Pathophysiology, School of Forensic Medicine, China Medical University, No. 77, Puhe Road, Shenyang North New Area, Shenyang 110122, China*
[3]*Department of Pain Medicine, The First Hospital of China Medical University, Shenyang, China. No. 155 Nanjing North Street, Heping District, Shenyang, 110001, China*

Correspondence should be addressed to Rui Zhao; rzhao@cmu.edu.cn and Zhipeng Cao; zpcao@cmu.edu.cn

Received 29 April 2021; Accepted 31 July 2021; Published 18 August 2021

Academic Editor: Ryuichi Morishita

The functions of the brain and heart, which are the two main supporting organs of human life, are closely linked. Numerous studies have expounded the mechanisms of the brain-heart axis and its related clinical applications. However, the effect of heart disease on brain function, defined as the heart-brain axis, is less studied even though cognitive dysfunction after heart disease is one of its most frequently reported manifestations. Hypoperfusion caused by heart failure appears to be an important risk factor for cognitive decline. Blood perfusion, the immune response, and oxidative stress are the possible main mechanisms of cognitive dysfunction, indicating that the blood-brain barrier, glial cells, and amyloid-β may play active roles in these mechanisms. Clinicians should pay more attention to the cognitive function of patients with heart disease, especially those with heart failure. In addition, further research elucidating the associated mechanisms would help discover new therapeutic targets to intervene in the process of cognitive dysfunction after heart disease. This review discusses cognitive dysfunction in relation to heart disease and its potential mechanisms.

1. Introduction

The structure and the function of the heart and brain have been studied for several decades due to their important roles in life. With further understanding of the independent mechanisms of the two organs, scientists began to seek a connection between the heart and the brain, which was announced by Barrow in the middle of the 19th century ([1]).

The occurrence of brain disease, including cerebrovascular diseases, degenerative diseases of the nervous system, and infectious diseases of the central nervous system, can lead to myocardial injury and even cardiac dysfunction, which is described as the brain-heart axis [2–4]. On the other hand, the physiological activities and processes of the brain, such as cognitive ability and language capabilities, are directly affected by cardiac function, which is described as the heart-brain axis [5–8]. Cardiac dysfunction due to various causes, not only existing brain disease, can lead to new brain injury [8]. In this context, an increasing number of studies have focused on the connection between the heart and the brain.

Surprisingly, few studies have explored the effects of heart disease on brain function, one of the manifestations of the heart-brain axis [9]. Herein, cognitive dysfunction and its potential mechanisms are discussed.

2. Cognitive Dysfunction after Heart Disease

In 1982, the term "cardiogenic dementia" was quoted in an editorial of *The Lancet*, and it is characterized as patients suffering from cognitive decline after heart disease [10]. Up to 50% of patients with heart failure (HF) reportedly develop a certain degree of cognitive impairment, with 10% of patients suffering from more severe symptoms [11–13]. In contrast, only 26% of patients with treated chronic heart

failure (CHF) develop vascular cognitive impairment [14]. The number of people grappling with heart disease has increased along with the aging population. Indeed, the incidence of HF increases with advancing age and is the most common cause of hospitalization in the United States, especially among people over 64 years old [15, 16]. Due to the lower cognitive reserve of the elderly, this population is more likely to develop cognitive dysfunction after heart disease [17].

As the main cause of HF, the high morbidity of coronary artery disease has led to the widespread implementation of coronary artery bypass grafting (CABG). In the United States alone, approximately 300,000 people undergo CABG each year [18]. In general, CABG surgery is safe in most cases; the complications mainly include postcardiac surgery syndrome, hypotensive brain injury, embolic stroke, visual defects, epilepsy, residual movement disorders, and rare peripheral nerve damage [19]. Most patients (80-90%) undergoing CABG surgery reportedly experience cognitive dysfunction at discharge [20]. Routine clinical examination found that the degree of cognitive impairment, measured by the Canadian Stroke Scale, Syndrom Kurztest, and psychiatric assessment, was often not obvious because it mainly manifested in the subcortex, involving executive dysfunction, depression, and anxiety. Over time, 42% of patients reportedly developed long-term (5 years) cognitive deficits [19]. Biomarkers of myocardial injury and cardiac dysfunction, such as cardiac troponin T (cTnT) and pro-N-terminal B-type natriuretic peptide (NT-proBNP), have been associated with lower cognitive ability among the elderly (over 60 years old), even in the absence of clinical disease [21–26]. This further illustrates that cardiac and cognitive functions are closely related.

The most obvious clinical manifestation of Alzheimer's disease (AD), a severe degenerative disease of the nervous system, is impaired cognitive function [27, 28]. Compared with a decreased total brain parenchymal volume of 0.32% per year in healthy aging individuals and brain parenchymal loss of 2% per year in AD patients, the annual loss of brain parenchymal volume was approximately 1% in patients with both high NT-proBNP levels and high carotid intima media thickness caused by reduced blood supply to the brain [29, 30]. In fact, biomarkers of myocardial injury and cardiac dysfunction have been repeatedly associated with changes in the brain structures of the elderly and the young, but only the elderly exhibit poor cognitive abilities [31]. This may be due to the higher cognitive reserve of young individuals, which can prevent the harmful effects of clinical heart disease on cognitive ability [17]. In view of these findings, it is hypothesized that the heart-brain axis runs through the processes of life [31].

3. Potential Mechanisms of Cognitive Dysfunction after Heart Disease

Many research groups have explored the potential mechanisms of cognitive impairment based on the important functions of the heart and brain and their interconnectivity. Among them, blood perfusion and inflammation are the two main mechanisms that have been explored (Figure 1).

3.1. Blood Perfusion. The brain is a highly energy-consuming organ, accounting for approximately 20% and 25% of the body's oxygen and glucose, respectively [32]. Its function depends on a sufficient supply of oxygen and energy via the bloodstream [33]. With fluctuations in blood flow and blood pressure throughout the body, multiple systems, including the cerebrovascular self-regulation mechanism, work together to maintain the cerebral blood flow within a stable range [34]. The heart is where cerebral perfusion pressure is generated, and intra- and extracranial blood vessels change cerebral perfusion, as they deliver blood to the brain [35]. The brain receives approximately 15% of the cardiac output [36].

Hypoperfusion due to low cardiac output is a key factor in cardiovascular disease, which accelerates changes in the brain structure [37, 38]. In the case of long-term systemic hypoperfusion, the blood flow regulation mechanism may not be able to compensate to protect the brain, resulting in insufficient cerebral perfusion, which is associated with impaired brain function [32]. Decreased cerebral blood flow in patients with HF has been associated with increased prevalence of cognitive dysfunction, and even a subclinical decrease in cardiac output has been associated with impaired cognitive function [39–41]. Patients with CHF are more prone to brain parenchymal loss, especially gray matter, due to low cerebral blood flow [42–44]. This is because the higher metabolic demand of gray matter requires more than two-thirds of the cerebral blood flow [32, 36]. Reduced gray matter volume was reportedly associated with impairment of various cortical areas involved in executive cognitive function [45]. Furthermore, surgery to improve cardiac function, such as heart transplantation or resynchronization, has been shown to help develop cognitive function [46, 47]. Therefore, cardiac dysfunction can lead to hypoperfusion and ultimately cause cognitive impairment.

Vascular damage in the brain itself, such as small vessel disease, may also increase the vulnerability of the brain to changes in perfusion pressure [27]. In contrast, changes in cerebral blood flow homeostasis can promote clinical or subclinical brain injury by aggravating microvascular damage. For example, fluctuations in cerebral perfusion can lead to changes in microvascular structure, expression of vascular cell receptors, microvascular permeability, and vascular remodeling [48, 49].

Increasing evidence supports the role of blood perfusion in the pathogenesis of AD [27, 28]. Early AD without symptoms manifests as cognitive decline caused by hypoperfusion, and increasing cerebral blood flow has been shown to improve AD symptoms [28]. This also supports the close connection between blood perfusion and cognitive decline.

In the case of cerebral hypoperfusion, the metabolic activity of the whole brain is significantly reduced [50]. Specifically, the metabolic level of the parietal area in patients with HF was reportedly reduced compared with that in healthy volunteers [51, 52]. However, in HF patients with hibernating myocardium and impaired global left ventricular

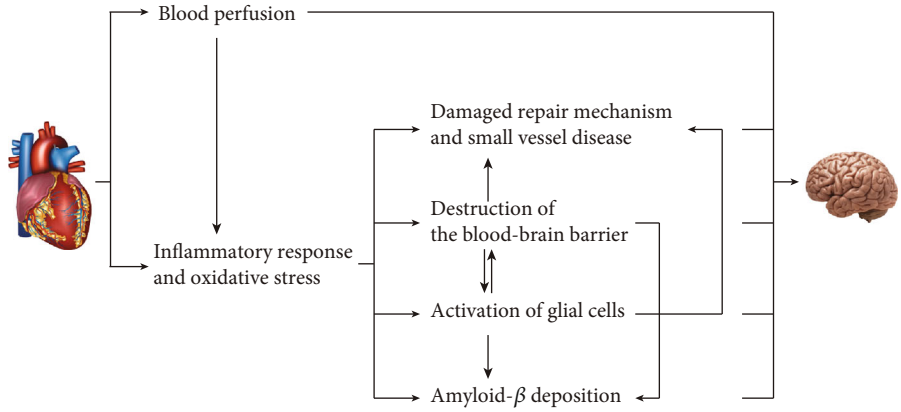

Figure 1: Potential mechanisms of cognitive dysfunction after heart diseases.

function, the metabolism of the frontal lobe area was compensatorily increased, while glucose metabolism of the hippocampus and parahippocampus, which are vulnerable to dementia, was decreased, leading to memory loss [50, 53]. These differential changes in metabolic activity were related to self-regulation efficiency in different areas [54]. As part of the neocortex, the frontal lobe may have higher self-regulation efficiency and sensitivity than the original cortex, including the hippocampus and parahippocampus [55]. Therefore, when cerebral blood flow begins to decrease, the forehead area may be compensated first to maintain a certain degree of energy metabolism.

Except for heart diseases, such as myocarditis and myocardial infarction (MI) that directly lead to inflammation, hypoperfusion can cause inflammation of brain tissues in diseases with decreased cardiac function, such as HF [56]. In response to hypoperfusion injury or interruption of perfusion, cell respiration is quickly exhausted, and adenosine triphosphate (ATP) is consumed and regenerated without compensation. Subsequently, reactive oxygen species (ROS) are produced [57, 58]. Specific inflammatory changes are discussed in the next section.

Aerobic exercise has demonstrated amelioratory effects on the blood supply to the brain. On the basis of the mechanism discussed above, aerobic exercise is beneficial for cardiac disease patients with cognitive impairment. Regular aerobic physical activity can increase the blood flow in the prefrontal cortex, promote the formation of blood vessels in the frontal cortex, and increase the concentration of the vascular endothelial growth factor [59]. Moreover, long-term continuous aerobic exercise can promote cardiovascular health by increasing vagal tone and reducing sinus node sympathetic nerve activity [60]. Tanne et al. reported that HF patients with the New York Heart Association (NYHA) functional class III status and an ejection fraction of 35% demonstrated improved selective attention and mental exercise speed after long-term aerobic exercise [15].

3.2. Inflammatory Response and Oxidative Stress. The inflammatory response and oxidative stress are usually interdependent and may be potentially associated with brain dysfunction after heart disease [61, 62]. Studies have reported that inflammation occurs in the brain after MI. However, local inflammation of the skeletal muscle has no effect on the heart and brain, indicating that the connection between the heart and the brain is closer than that of other organs when the heart is injured [63]. On the one hand, several heart diseases, such as myocarditis and MI, will directly cause inflammation; on the other hand, hypoperfusion caused by diseases with decreased heart function will also lead to brain inflammation [56]. In addition, decreased cardiac function can change inflammatory marker levels in the brain [64]. The expression of inflammatory genes, such as toll-like receptor- (TLR-) 4, tumor necrosis factor- (TNF-) α, and interleukin- (IL-) 6, was significantly upregulated in the cortex and hippocampus in a mouse model of HF [65]. As for the pathological mechanism of HF, the landmark event in its early stage is the appearance of a large number of proinflammatory factors in the heart and peripheral circulation, such as TNF-α, IL-1, IL-6, IL-8, and monocyte chemoattractant protein- (MCP-) 1, mainly derived from neutrophils, monocytes, and macrophages [66]. These proinflammatory factors reach the brain via the bloodstream, causing inflammation in the brain.

TNF-α, which is considered the main regulator of the brain's proinflammatory response, can cause cell damage and death by increasing neurotoxicity via neuronal glutamate [67, 68]. Recent studies have shown that the ASK1-p38-TNF-α pathway is involved in the destruction of tight junctions soon after chronic cerebral hypoperfusion [69]. Insufficient cerebral perfusion affects the level of IL-1β in the central nervous system, which is an important regulator of the inflammatory cascade [70]. TNF-α and IL-1β in the ischemic brain can reportedly induce the production of IL-6, and increased IL-6 levels in the serum and cerebrospinal fluid are related to cognitive impairment [71]. Furthermore, the presence of IL-1β and TNF-α can upregulate the expression and function of CD73, which plays a protective role in the occurrence of white matter lesions induced by cerebral hypoperfusion and cognitive impairment by regulating the activation of glial cells and expression of proinflammatory cytokines [72]. Specifically, upregulation of CD73 expression and activity in the corpus callosum after chronic hypoperfusion mediates the production of adenosine, which can inhibit

the release of inflammatory cytokines IL-1β, IL-6, and TNF-α. Therefore, CD73 plays a key role in the counter-regulatory feedback mechanism, helping to relieve inflammation [69].

The inflammatory response and oxidative stress mainly cause cognitive dysfunction through damage to the self-repair mechanism, destruction of the blood-brain barrier (BBB), and activation of glial cells [61, 73, 74]. Among them, the damaged BBB and activated glial cells will also affect each other, leading to deposition of amyloid-β (Aβ) and causing damage to the cognitive function of the brain [75–77].

In view of the importance of the inflammatory response and oxidative stress, anti-inflammatory or antioxidant therapies have become an innovative clinical approach [78]. Naturally, the optimal drug should simultaneously treat heart disease and cognitive dysfunction, and angiotensin-converting enzyme inhibitors (ACEIs) have received the most attention. Among them, enalapril inhibits the proinflammatory activity of angiotensin II [79, 80]. Continuous treatment with enalapril has been shown to reduce acute and chronic inflammation in the heart and brain [63]. Animal experiments suggested that the effectiveness of ACEIs on neuroinflammation after MI was based on acute application, since late application missed the acute anti-inflammation stage and was not beneficial for alleviating chronic neuroinflammation [81]. As for other noncardiac treatment drugs, translocator protein inhibitors, such as 4′-chlordiazepam, are believed to modulate neuroinflammation and exert cardioprotective effects during ischemia-reperfusion injury through antioxidant mechanisms [82]. Nonsteroidal anti-inflammatory drugs have also demonstrated a certain effectiveness against amyloid deposition [83].

3.2.1. Damaged Repair Mechanism and Development of Small Vessel Disease. The inflammatory response and oxidative stress are believed to play important roles in neurovascular dysfunction. Oxidative stress can cause endothelial dysfunction, BBB disruption, and cytokine production [61]. In turn, inflammation can enhance oxidative stress by upregulating the expression of enzymes that produce ROS and downregulating antioxidant defense capabilities [62]. Further, the inflammatory response and oxidative stress disrupt the repair mechanism of damaged white matter by interfering with the proliferation, migration, and differentiation of oligodendrocyte progenitor cells [73, 84]. The loss of growth factors, which are produced by the brain, reportedly occurs in vascular cognitive impairment, further damaging the repair mechanism and aggravating cognitive impairment [74].

Apolipoprotein E (ApoE) subsequently affects neurovascular units through pericytes, causing changes in microvascular flow and triggering neurodegenerative changes [85]. Cerebral arterioles are particularly vulnerable to these changes, promoting the development of small vessel diseases, such as cerebral amyloid angiopathy and arteriole sclerosis [9]. Small vessel diseases lead to weakened cerebral vasoconstriction, which in turn promotes cerebral blood pressure changes [86, 87]. Combined, these factors eventually lead to cognitive impairment, stroke symptoms, and changes in brain structure, such as white matter lesions, lacunar infarction, and substantial bleeding [9].

Overall, the inflammatory response and hypoperfusion can damage the brain repair mechanism, which in turn promote the occurrence of small vessel diseases.

3.2.2. Destruction of the Blood-Brain Barrier. Abnormal function of the BBB, including activated endothelial cells, destroyed pericytes, and abnormal endothelial-endothelial and endothelial-pericyte connections, occupies an important position in the pathogenesis of cognitive dysfunction after heart disease [35]. Inflammation and ROS are thought to be involved in these changes, since the generation of ROS destroys the ion gradient [88]. Endothelial cells, the main component of the BBB, have been shown to be damaged by an increase in intracellular calcium ion levels [89]. In addition, pericytes are reportedly involved in regulating BBB function and are highly likely to cause destructive inflammation [85, 90]. The breakdown of the BBB is caused by activation of the proinflammatory pathway of pericytes, involving cyclophilin A-nuclear factor-κB-matrix-metalloproteinase-9 [69, 74]. Cerebral endothelial tight junction proteins, such as claudin-5, play a key role in maintaining the BBB [91]. Thus, decreased levels of claudin-5 in the corpus callosum destroy the BBB via the ASK1-p38-TNF-α pathway. Animal experiments have demonstrated that the use of compound K811, a specific ASK1 inhibitor, can prevent cognitive impairment in a mouse model of hypoperfusion [72]. ASK1 may be a new target molecule for the treatment of cognitive dysfunction caused by cerebral hypoperfusion.

Damage to the BBB increases its permeability, causing leakage of plasma components and exchange of substances [92]. After the occurrence of hypoperfusion, immunoglobulin (Ig) G leakage from the corpus callosum indicated BBB rupture [93]. This leakage occurred when glial cells, including astrocytes and microglia, were not observed to be activated [94]. Moreover, the level of proinflammatory markers was related to the degree of BBB rupture [95]. Notably, the complete BBB plays an important role in preventing extravasation of toxic factors from circulating to the brain parenchyma. For instance, peripheral blood-derived substances, such as thrombin, can aggravate central nervous system inflammation [96, 97]. BBB dysfunction thus further exacerbates microvascular damage, promotes secondary inflammation, and damages blood vessel tension, leading to luminal stenosis and tissue ischemia [98].

Generally, destruction of the BBB by ROS and inflammation after heart disease will lead to further aggravation of inflammation and promote contact of neurotoxic proteins with neurons. The relationship between BBB destruction and immune cell activation is described later.

3.2.3. Activation of Glial Cells. After inflammation occurs, astrocytes are activated slightly earlier than microglia [63]. The activation of astrocytes after MI is directly related to the inflammation induced by infarction, and may be caused by proinflammatory cytokines [75]. ^{11}C-methionine uptake can help reflect inflammation in the brain [99]. Neutrophils and proinflammatory monocytes display higher rates of methionine uptake, which affects the activation of astrocytes

[100]. In addition, active astrocytes may be neurotoxic and produce specific inflammatory cytokines and ROS [75].

The increased permeability of the BBB also enhances the adhesion and migration of monocytes from the periphery to the central nervous system, and then differentiation into microglia to promote neuroinflammation [76]. As the main agonist of neuroinflammation, the production of microglia is the central nervous system's immune response to local injury or systemic activation [101]. Neuroinflammation is considered key to the progression of AD [102], in which microglia are activated by amyloid deposition and exert neurotoxic effects, thereby further aggravating inflammation and expanding amyloid deposition [77]. Subsequently, the activated microglia produce a large amount of proinflammatory cytokines, leading to cumulative damage to the tissue [103]. Miyanohara et al. reported that proinflammatory cytokines (such as IL6 and TNF-α) and obvious tissue damage were significantly detected in the white matter of a mouse model of chronic cerebral hypoperfusion with BCAS [104]. Proinflammatory cytokines also play an important role in oligodendrocyte toxicity [105]. This relationship is maturation-dependent, i.e., proinflammatory cytokines are more toxic to immature oligodendrocytes than mature oligodendrocytes [106].

To study the mechanism of inflammation in depth, Miyanohara et al. confirmed that transient receptor potential melastatin 2 (TRPM2), a Ca2+ permeable channel, participated in cognitive impairment related to chronic cerebral hypoperfusion by enhancing the production of cytokines, leading to subsequent white matter damage [104, 107]. Specifically, TRPM2, expressed in microglia/macrophages, mediated the upregulation of proinflammatory cytokines in white matter [104]. In the regulation of TRPM2, ROS was considered an endogenous agonist of TRPM2, and high concentrations of hydrogen peroxide induced TRPM2-mediated neuronal death [108–110].

Apart from TRPM2, IL1R, CX3CRI, leptin, and tamoxifen may also be involved in regulation of the inflammatory response. Zhou et al. reported that the loss of IL1R expression improved white matter damage and promoted the migration of oligodendrocyte precursor cells from the subventricular zone [111]. Further, CX3CR1 silencing in microglia reduced cytokine release, white matter damage, and cognitive impairment [112]. Leptin reportedly increased the expression of proinflammatory cytokines induced by hypoxia in BV2 microglia [113]. Du et al. reported that leptin receptor deletion protected mice from cognitive dysfunction induced by cerebral hypoperfusion and white matter damage by inhibiting glial cell activation and the proinflammatory response, which promoted the expression of anti-inflammatory cytokines in white matter and activation of M2 microglia [114]. Tamoxifen significantly reduced the activation and inflammatory response of microglia, facilitated the polarization of microglia to the M2 phenotype, enhanced the proliferation and differentiation of oligodendrocyte precursor cells, and reduced the expression of TNF-α and IL-1β [115].

In short, inflammation and destruction of BBB permeability after heart disease promote the activation of glial cells, leading to neuroinflammation, which is considered an important factor in the progression of AD.

3.2.4. Amyloid-β Deposition. Although HF and cognitive dysfunction in patients with AD have long been considered independent factors, an increasing number of studies have confirmed that they may be related, with similarities such as common risk factors and similar epidemiological stratification [88]. Moreover, AD-related neuropathology was reported in a rat model after acute blood perfusion ceased, including Aβ deposition in the hippocampus, endothelium, and neocerebral cortex, which led to neuronal death [116].

Under normal circumstances, Aβ is removed from the brain through the BBB, the interstitial bulk flow clearance (glymphatic) system, or meningeal lymphatic vessels [117, 118]. Under chronic hypoperfusion, these drainage systems are damaged, and Aβ accumulates in the perivascular space [119]. In the process of Aβ deposition, new evidence suggests that immune mediators also contribute to disease progression, especially in microglia [76]. Such scavenger cells play a role in both the inflammatory cascade and Aβ clearance in the brain [120]. Chronic low blood flow and glucose transport conditions result in only a few activated microglia in the area around the Aβ plaque, accompanied by impaired function [76]. Thus, the ability of microglia to eliminate Aβ is further reduced, providing an ideal environment for accumulation, aggregation, and further formation of plaques. In addition, active astrocytes also express high levels of amyloid precursor protein [121]. Therefore, astrocyte activation induced by heart disease may lead to a vicious cycle of amyloid production and further neuroinflammation [122].

Studies with mouse models of AD and AD patients reported that Aβ, in turn, caused oxidative imbalance through Aβ accumulation in the mitochondria, which aggravated mitochondrial dysfunction, ROS production, and overall oxidative imbalance [123, 124]. The cycle was further exacerbated by the inflammatory response and oxidative stress causing vasoconstriction and promoting destruction of the BBB. Aβ accumulation in the brain also reportedly has a profound effect on blood vessels, thereby promoting neurodegenerative processes [88].

In summary, under the condition of chronic hypoperfusion, damage to the drainage system and decreased ability of glial cells to clear Aβ lead to the accumulation of Aβ, eventually causing cognitive impairment. Interestingly, HF with preserved ejection fraction can promote cognitive dysfunction in AD and vice versa [88]. Overall, HF and cognitive dysfunction are interrelated, and their common pathogenesis may be systemic [125]. In view of the important roles of the heart and brain, the relationship between them must be taken seriously.

4. Future Direction

Cognitive dysfunction occurs in a large number of patients with heart disease, causing a great burden to families and the healthcare system. However, systematic research still needs to be conducted. Recently, increasing evidence has shown that extracellular vesicles are involved in molecular transport within and between organs, including interactions between the heart and brain [126]. In the brain, exosomes have important physiological functions, such as promoting

signal transmission between neurons and glial cells and participating in Aβ metabolism [127, 128]. At present, exosomes, as members of extracellular vesicles, are also known to participate in the heart-brain axis. Sun et al. described a new mechanism of brain damage originating from the heart, in which high levels of microRNA- (miR-) 1 were produced in the ischemic and marginal regions of the heart in a mouse model of MI. Transported by exosomes from the heart, miR-1 reached the hippocampus, reduced the expression of tubulin polymerization-promoting protein, and affected the stability of microtubules in neurons [129]. Furthermore, the expression of miR-133b, which is responsible for the development of midbrain dopaminergic neurons, was reportedly decreased in circulation after MI [130].

In addition to probing the mechanisms of cognitive dysfunction after heart disease, the clinical application of these mechanisms is also an important point for scientists and doctors. The impact on cognitive function of drugs used to treat heart disease needs to be carefully evaluated, especially new therapies such as sacubitril/valsartan. Theoretically, neprilysin inhibition reduces Aβ degradation in the central nervous system, thereby increasing the risk of AD [131]. ACEI drugs pose similar risks, as they are involved in the process of converting amyloid-β1-42 into Aβ1-40. ACEIs block this process and increase the deposition of Aβ1-42 in the brain [59]. However, the specific role of these drugs in the process of cognitive dysfunction remains to be further elucidated.

Conflicts of Interest

The authors declare that there are no conflicts of interest regarding the publication of this paper.

Authors' Contributions

Chengyang Xu and Xueshu Tao contributed equally to this work.

Acknowledgments

This study was financially supported by the National Natural Science Foundation of China (grant number 82002001), the Natural Science Foundation of Liaoning Province (grant number 20180530004), and the Open Project of Forensic Pathology Key Laboratory, Ministry of Public Security of China (grant number GABFYBL201804).

References

[1] C. Templin, J. Hänggi, C. Klein et al., "Altered limbic and autonomic processing supports brain-heart axis in Takotsubo syndrome," *European Heart Journal*, vol. 40, no. 15, pp. 1183–1187, 2019.

[2] C. Xu, A. Zheng, T. He, and Z. Cao, "Brain-heart axis and biomarkers of cardiac damage and dysfunction after stroke: a systematic review and meta-analysis," *International Journal of Molecular Sciences*, vol. 21, no. 7, p. 2347, 2020.

[3] Z. Chen, P. Venkat, D. Seyfried, M. Chopp, T. Yan, and J. Chen, "Brain-heart interaction: cardiac complications after stroke," *Circulation Research*, vol. 121, no. 4, pp. 451–468, 2017.

[4] I. Altun, Y. Unal, O. Basaran et al., "Increased epicardial fat thickness correlates with aortic stiffness and N-terminal pro-brain natriuretic peptide levels in acute ischemic stroke patients," *Texas Heart Institute Journal*, vol. 43, no. 3, pp. 220–226, 2016.

[5] H. Fuhrer, M. Reinhard, and W. D. Niesen, "Paradigm change? Cardiac output better associates with cerebral perfusion than blood pressure in ischemic stroke," *Frontiers in Neurology*, vol. 8, p. 706, 2017.

[6] A. M. Hooghiemstra, A. E. Leeuwis, A. S. Bertens et al., "Frequent cognitive impairment in patients with disorders along the heart-brain axis," *Stroke*, vol. 50, no. 12, pp. 3369–3375, 2019.

[7] P. A. Wolf, R. D. Abbott, and W. B. Kannel, "Atrial fibrillation as an independent risk factor for stroke: the Framingham Study," *Stroke*, vol. 22, no. 8, pp. 983–988, 1991.

[8] D. Battaglini, C. Robba, A. Lopes da Silva et al., "Brain-heart interaction after acute ischemic stroke," *Critical Care*, vol. 24, no. 1, p. 163, 2020.

[9] M. A. van Buchem, G. J. Biessels, H. P. Brunner la Rocca et al., "The heart-brain connection: a multidisciplinary approach targeting a missing link in the pathophysiology of vascular cognitive impairment," *Journal of Alzheimer's Disease*, vol. 42, Suppl 4, pp. S443–S451, 2014.

[10] S. T. Mccarthy, L. Wollner, G. A. Rosenberg, and K. Y. Haaland, "Cardiogenic dementia," *Lancet*, vol. 318, no. 8256, p. 1171, 1981.

[11] S. J. Pressler, "Cognitive functioning and chronic heart failure," *The Journal of Cardiovascular Nursing*, vol. 23, no. 3, pp. 239–249, 2008.

[12] R. L. Vogels, J. M. Oosterman, B. van Harten et al., "Profile of cognitive impairment in chronic heart failure," *Journal of the American Geriatrics Society*, vol. 55, no. 11, pp. 1764–1770, 2007.

[13] M. Huijts, R. J. van Oostenbrugge, A. Duits et al., "Cognitive impairment in heart failure: results from the Trial of Intensified versus standard Medical therapy in Elderly patients with Congestive Heart Failure (TIME-CHF) randomized trial," *European Journal of Heart Failure*, vol. 15, no. 6, pp. 699–707, 2013.

[14] G. Zuccalà, G. onder, C. Pedone et al., "Hypotension and cognitive impairment: selective association in patients with heart failure," *Neurology*, vol. 57, no. 11, pp. 1986–1992, 2001.

[15] D. Tanne, D. Freimark, A. Poreh et al., "Cognitive functions in severe congestive heart failure before and after an exercise training program," *International Journal of Cardiology*, vol. 103, no. 2, pp. 145–149, 2005.

[16] L. H. Curtis, D. J. Whellan, B. G. Hammill et al., "Incidence and prevalence of heart failure in elderly persons, 1994-2003," *Archives of Internal Medicine*, vol. 168, no. 4, pp. 418–424, 2008.

[17] Y. Stern, "Cognitive reserve in ageing and Alzheimer's disease," *Lancet Neurology*, vol. 11, no. 11, pp. 1006–1012, 2012.

[18] D. B. Mark and M. F. Newman, "Protecting the brain in coronary artery bypass graft surgery," *JAMA*, vol. 287, no. 11, pp. 1448–1450, 2002.

[19] G. C. Román, "Vascular dementia may be the most common form of dementia in the elderly," *Journal of the Neurological Sciences*, vol. 203-204, pp. 7–10, 2002.

[20] G. W. Roach, M. Kanchuger, C. M. Mangano et al., "Adverse cerebral outcomes after coronary bypass surgery," *The New England Journal of Medicine*, vol. 335, no. 25, pp. 1857–1864, 1996.

[21] S. S. Mirza, R. F. A. G. de Bruijn, P. J. Koudstaal et al., "The N-terminal pro B-type natriuretic peptide, and risk of dementia and cognitive decline: a 10-year follow-up study in the general population," *Journal of Neurology, Neurosurgery, and Psychiatry*, vol. 87, no. 4, pp. 356–362, 2016.

[22] B. Sabayan, M. A. van Buchem, A. J. M. de Craen et al., "N-terminal pro-brain natriuretic peptide and abnormal brain aging: the AGES-Reykjavik Study," *Neurology*, vol. 85, no. 9, pp. 813–820, 2015.

[23] L. B. Daniels, G. A. Laughlin, D. Kritz-Silverstein et al., "Elevated Natriuretic Peptide Levels and Cognitive Function in Community- dwelling Older Adults," *The American Journal of Medicine*, vol. 124, no. 7, pp. 670.e1–670.e8, 2011.

[24] K. van den Hurk, Y. D. Reijmer, E. van den Berg et al., "Heart failure and cognitive function in the general population: the Hoorn Study," *European Journal of Heart Failure*, vol. 13, no. 12, pp. 1362–1369, 2011.

[25] P. G. van Peet, A. J. M. de Craen, J. Gussekloo, and W. de Ruijter, "Plasma NT-proBNP as predictor of change in functional status, cardiovascular morbidity and mortality in the oldest old: the Leiden 85-plus Study," *Age (Dordrecht, Netherlands)*, vol. 36, no. 3, p. 9660, 2014.

[26] T. Kerola, T. Nieminen, S. Hartikainen, R. Sulkava, O. Vuolteenaho, and R. Kettunen, "B-type natriuretic peptide as a predictor of declining cognitive function and dementia–a cohort study of an elderly general population with a 5-year follow-up," *Annals of Medicine*, vol. 42, no. 3, pp. 207–215, 2010.

[27] P. B. Gorelick, A. Scuteri, S. E. Black et al., "Vascular contributions to cognitive impairment and dementia: a statement for healthcare professionals from the American Heart Association/American Stroke Association," *Stroke*, vol. 42, no. 9, pp. 2672–2713, 2011.

[28] J. C. de la Torre, "Chapter 3 cerebrovascular and cardiovascular pathology in Alzheimer's disease," *International Review of Neurobiology*, vol. 84, pp. 35–48, 2009.

[29] R. I. Scahill, C. Frost, R. Jenkins, J. L. Whitwell, M. N. Rossor, and N. C. Fox, "A longitudinal study of brain volume changes in normal aging using serial registered magnetic resonance imaging," *Archives of Neurology*, vol. 60, no. 7, pp. 989–994, 2003.

[30] L. C. Silbert, J. F. Quinn, M. M. Moore et al., "Changes in premorbid brain volume predict Alzheimer's disease pathology," *Neurology*, vol. 61, no. 4, pp. 487–492, 2003.

[31] M. G. J. Veugen, R. M. A. Henry, H. P. Brunner-la Rocca et al., "Cross-sectional associations between cardiac biomarkers, cognitive performance, and structural brain changes are modified by age," *Arteriosclerosis, Thrombosis, and Vascular Biology*, vol. 38, no. 8, pp. 1948–1958, 2018.

[32] B. Sabayan, M. A. van Buchem, S. Sigurdsson et al., "Cardiac and carotid markers link with accelerated brain atrophy: the AGES-Reykjavik Study (Age, Gene/Environment Susceptibility-Reykjavik)," *Arteriosclerosis, Thrombosis, and Vascular Biology*, vol. 36, no. 11, pp. 2246–2251, 2016.

[33] M. Erecińska and I. A. Silver, "Tissue oxygen tension and brain sensitivity to hypoxia," *Respiration Physiology*, vol. 128, no. 3, pp. 263–276, 2001.

[34] D. Attwell, A. M. Buchan, S. Charpak, M. Lauritzen, B. A. MacVicar, and E. A. Newman, "Glial and neuronal control of brain blood flow," *Nature*, vol. 468, no. 7321, pp. 232–243, 2010.

[35] K. Ritz, M. A. van Buchem, and M. J. Daemen, "The heart-brain connection: mechanistic insights and models," *Netherlands Heart Journal*, vol. 21, no. 2, pp. 55–57, 2013.

[36] C. K. Willie and K. J. Smith, "Fuelling the exercising brain: a regulatory quagmire for lactate metabolism," *The Journal of Physiology*, vol. 589, no. 4, pp. 779-780, 2011.

[37] B. V. Zlokovic, "Neurovascular pathways to neurodegeneration in Alzheimer's disease and other disorders," *Nature Reviews. Neuroscience*, vol. 12, no. 12, pp. 723–738, 2011.

[38] K. Kisler, A. R. Nelson, A. Montagne, and B. V. Zlokovic, "Cerebral blood flow regulation and neurovascular dysfunction in Alzheimer disease," *Nature Reviews. Neuroscience*, vol. 18, no. 7, pp. 419–434, 2017.

[39] O. B. Paulson, J. O. Jarden, J. Godtfredsen, and S. Vorstrup, "Cerebral blood flow in patients with congestive heart failure treated with captopril," *The American Journal of Medicine*, vol. 76, no. 5, pp. 91–95, 1984.

[40] B. R. Choi, J. S. Kim, Y. J. Yang et al., "Factors associated with decreased cerebral blood flow in congestive heart failure secondary to idiopathic dilated cardiomyopathy," *The American Journal of Cardiology*, vol. 97, no. 9, pp. 1365–1369, 2006.

[41] A. L. Jefferson, J. J. Himali, R. Au et al., "Relation of left ventricular ejection fraction to cognitive aging (from the Framingham Heart Study)," *The American Journal of Cardiology*, vol. 108, no. 9, pp. 1346–1351, 2011.

[42] M. Muller, Y. van der Graaf, A. Algra et al., "Carotid atherosclerosis and progression of brain atrophy: the SMART-MR study," *Annals of Neurology*, vol. 70, no. 2, pp. 237–244, 2011.

[43] S. R. Seaman and I. R. White, "Review of inverse probability weighting for dealing with missing data," *Statistical Methods in Medical Research*, vol. 22, no. 3, pp. 278–295, 2013.

[44] A. Horstmann, S. Frisch, R. T. Jentzsch, K. Muller, A. Villringer, and M. L. Schroeter, "Resuscitating the heart but losing the brain: brain atrophy in the aftermath of cardiac arrest," *Neurology*, vol. 74, no. 4, pp. 306–312, 2010.

[45] M. Amanzio, S. Palermo, M. Stanziano et al., "Investigating neuroimaging correlates of early frailty in patients with behavioral variant frontotemporal dementia: a MRI and FDG-PET study," *Frontiers in Aging Neuroscience*, vol. 13, article 637796, 2021.

[46] D. D. Roman, S. H. Kubo, S. Ormaza, G. S. Francis, A. J. Bank, and S. J. Shumway, "Memory improvement following cardiac transplantation," *Journal of Clinical and Experimental Neuropsychology*, vol. 19, no. 5, pp. 692–697, 1997.

[47] R. J. Petrucci, J. G. Rogers, L. Blue et al., "Neurocognitive function in destination therapy patients receiving continuous-flow vs pulsatile-flow left ventricular assist device support," *The Journal of Heart and Lung Transplantation*, vol. 31, no. 1, pp. 27–36, 2012.

[48] G. J. del Zoppo and T. Mabuchi, "Cerebral microvessel responses to focal ischemia," *Journal of Cerebral Blood Flow and Metabolism*, vol. 23, no. 8, pp. 879–894, 2003.

[49] T. Hayashi, K. Deguchi, S. Nagotani et al., "Cerebral ischemia and angiogenesis," *Current Neurovascular Research*, vol. 3, no. 2, pp. 119–129, 2006.

[50] M. Yun, B. Nie, W. Wen et al., "Assessment of cerebral glucose metabolism in patients with heart failure by ^{18}F-FDG PET/CT imaging," *Journal of Nuclear Cardiology*, 2020.

[51] M. S. Kim and J. J. Kim, "Heart and brain interconnection - clinical implications of changes in brain function during heart failure," *Circulation Journal*, vol. 79, no. 5, pp. 942–947, 2015.

[52] C. W. Lee, J. H. Lee, T. H. Lim et al., "Prognostic significance of cerebral metabolic abnormalities in patients with congestive heart failure," *Circulation*, vol. 103, no. 23, pp. 2784–2787, 2001.

[53] C. Domingos, J. M. Pêgo, and N. C. Santos, "Effects of physical activity on brain function and structure in older adults: a systematic review," *Behavioural Brain Research*, vol. 402, article 113061, 2020.

[54] M. A. Horsfield, J. L. Jara, N. P. Saeed, R. B. Panerai, and T. G. Robinson, "Regional differences in dynamic cerebral autoregulation in the healthy brain assessed by magnetic resonance imaging," *PLoS One*, vol. 8, no. 4, article e62588, 2013.

[55] O. M. Henriksen, M. B. Vestergaard, U. Lindberg et al., "Interindividual and regional relationship between cerebral blood flow and glucose metabolism in the resting brain," *Journal of Applied Physiology*, vol. 125, no. 4, pp. 1080–1089, 2018.

[56] I. Akiguchi, H. Tomimoto, T. Suenaga, H. Wakita, and H. Budka, "Alterations in glia and axons in the brains of Binswanger's disease patients," *Stroke*, vol. 28, no. 7, pp. 1423–1429, 1997.

[57] S. Love and J. S. Miners, "Cerebral hypoperfusion and the energy deficit in Alzheimer's disease," *Brain Pathology*, vol. 26, no. 5, pp. 607–617, 2016.

[58] X. Zhu, M. A. Smith, K. Honda et al., "Vascular oxidative stress in Alzheimer disease," *Journal of the Neurological Sciences*, vol. 257, no. 1-2, pp. 240–246, 2007.

[59] T. O. Mene-Afejuku, M. Pernia, U. N. Ibebuogu et al., "Heart failure and cognitive impairment: clinical relevance and therapeutic considerations," *Current Cardiology Reviews*, vol. 15, no. 4, pp. 291–303, 2019.

[60] M. L. M. Rêgo, D. A. R. Cabral, and E. B. Fontes, "Cognitive deficit in heart failure and the benefits of aerobic physical activity," *Arquivos Brasileiros de Cardiologia*, vol. 110, no. 1, pp. 91–94, 2018.

[61] C. Marchesi, P. Paradis, and E. L. Schiffrin, "Role of the renin-angiotensin system in vascular inflammation," *Trends in Pharmacological Sciences*, vol. 29, no. 7, pp. 367–374, 2008.

[62] R. Gill, A. Tsung, and T. Billiar, "Linking oxidative stress to inflammation: toll-like receptors," *Free Radical Biology & Medicine*, vol. 48, no. 9, pp. 1121–1132, 2010.

[63] J. T. Thackeray, H. C. Hupe, Y. Wang et al., "Myocardial inflammation predicts remodeling and neuroinflammation after myocardial infarction," *Journal of the American College of Cardiology*, vol. 71, no. 3, pp. 263–275, 2018.

[64] C. Toledo, D. C. Andrade, H. S. Díaz, N. C. Inestrosa, and R. del Rio, "Neurocognitive disorders in heart failure: novel pathophysiological mechanisms underpinning memory loss and learning impairment," *Molecular Neurobiology*, vol. 56, no. 12, pp. 8035–8051, 2019.

[65] X. Hong, L. Bu, Y. Wang et al., "Increases in the risk of cognitive impairment and alterations of cerebral β-amyloid metabolism in mouse model of heart failure," *PLoS One*, vol. 8, no. 5, article e63829, 2013.

[66] N. Glezeva and J. A. Baugh, "Role of inflammation in the pathogenesis of heart failure with preserved ejection fraction and its potential as a therapeutic target," *Heart Failure Reviews*, vol. 19, no. 5, pp. 681–694, 2014.

[67] R. T. Perry, J. S. Collins, H. Wiener, R. Acton, and R. C. Go, "The role of TNF and its receptors in Alzheimer's disease," *Neurobiology of Aging*, vol. 22, no. 6, pp. 873–883, 2001.

[68] J. Y. Zou and F. T. Crews, "TNFα potentiates glutamate neurotoxicity by inhibiting glutamate uptake in organotypic brain slice cultures: neuroprotection by NFκB inhibition," *Brain Research*, vol. 1034, no. 1-2, pp. 11–24, 2005.

[69] X. Hou, X. Liang, J. F. Chen, and J. Zheng, "Ecto-5′-nucleotidase (CD73) is involved in chronic cerebral hypoperfusion-induced white matter lesions and cognitive impairment by regulating glial cell activation and pro-inflammatory cytokines," *Neuroscience*, vol. 297, pp. 118–126, 2015.

[70] S. S. Shaftel, W. S. Griffin, and M. K. O'Banion, "The role of interleukin-1 in neuroinflammation and Alzheimer disease: an evolving perspective," *Journal of Neuroinflammation*, vol. 5, no. 1, p. 7, 2008.

[71] C. B. Wright, R. L. Sacco, T. R. Rundek, J. B. Delman, L. R. E. Rabbani, and M. S. V. Elkind, "Interleukin-6 is associated with cognitive function: the Northern Manhattan Study," *Journal of Stroke and Cerebrovascular Diseases*, vol. 15, no. 1, pp. 34–38, 2006.

[72] K. Toyama, N. Koibuchi, K. Uekawa et al., "Apoptosis signal-regulating kinase 1 is a novel target molecule for cognitive impairment induced by chronic cerebral hypoperfusion," *Arteriosclerosis, Thrombosis, and Vascular Biology*, vol. 34, no. 3, pp. 616–625, 2014.

[73] J. E. Simpson, M. S. Fernando, L. Clark et al., "White matter lesions in an unselected cohort of the elderly: astrocytic, microglial and oligodendrocyte precursor cell responses," *Neuropathology and Applied Neurobiology*, vol. 33, no. 4, pp. 410–419, 2007.

[74] G. M. Savva, S. B. Wharton, P. G. Ince, G. Forster, F. E. Matthews, and C. Brayne, "Age, neuropathology, and dementia," *The New England Journal of Medicine*, vol. 360, no. 22, pp. 2302–2309, 2009.

[75] P. Bascuñana, A. Hess, T. Borchert et al., "^{11}C-Methionine PET identifies astroglia involvement in heart-brain inflammation networking after acute myocardial infarction," *Journal of Nuclear Medicine*, vol. 61, no. 7, pp. 977–980, 2020.

[76] F. L. Heppner, R. M. Ransohoff, and B. Becher, "Immune attack: the role of inflammation in Alzheimer disease," *Nature Reviews. Neuroscience*, vol. 16, no. 6, pp. 358–372, 2015.

[77] A. H. Jacobs, B. Tavitian, and the INMiND consortium, "Noninvasive molecular imaging of neuroinflammation," *Journal of Cerebral Blood Flow and Metabolism*, vol. 32, no. 7, pp. 1393–1415, 2012.

[78] X. Fu, J. Zhang, L. Guo et al., "Protective role of luteolin against cognitive dysfunction induced by chronic cerebral hypoperfusion in rats," *Pharmacology, Biochemistry, and Behavior*, vol. 126, pp. 122–130, 2014.

[79] C. Curtiss, J. N. Cohn, T. Vrobel, and J. A. Franciosa, "Role of the renin-angiotensin system in the systemic vasoconstriction of chronic congestive heart failure," *Circulation*, vol. 58, no. 5, pp. 763–770, 1978.

[80] A. Douillette, A. Bibeau-Poirier, S. P. Gravel et al., "The pro-inflammatory actions of angiotensin II are dependent on p65

phosphorylation by the IκB kinase complex∗," *The Journal of Biological Chemistry*, vol. 281, no. 19, pp. 13275–13284, 2006.

[81] T. Borchert, A. Hess, M. Lukačević, T. L. Ross, F. M. Bengel, and J. T. Thackeray, "Angiotensin-converting enzyme inhibitor treatment early after myocardial infarction attenuates acute cardiac and neuroinflammation without effect on chronic neuroinflammation," *European Journal of Nuclear Medicine and Molecular Imaging*, vol. 47, no. 7, pp. 1757–1768, 2020.

[82] D. Morin, J. Musman, S. Pons, A. Berdeaux, and B. Ghaleb, "Mitochondrial translocator protein (TSPO): from physiology to cardioprotection," *Biochemical Pharmacology*, vol. 105, pp. 1–13, 2016.

[83] J. C. Anthony, J. C. S. Breitner, P. P. Zandi et al., "Reduced prevalence of AD in users of NSAIDs and H2 receptor antagonists," *Neurology*, vol. 54, no. 11, pp. 2066–2071, 2000.

[84] K. Arai and E. H. Lo, "Astrocytes protect oligodendrocyte precursor cells via MEK/ERK and PI3K/Akt signaling," *Journal of Neuroscience Research*, vol. 88, no. 4, pp. 758–763, 2010.

[85] A. Armulik, G. Genové, M. Mäe et al., "Pericytes regulate the blood-brain barrier," *Nature*, vol. 468, no. 7323, pp. 557–561, 2010.

[86] M. Freitas-Andrade, P. Carmeliet, C. Charlebois, D. B. Stanimirovic, and M. J. Moreno, "PlGF knockout delays brain vessel growth and maturation upon systemic hypoxic challenge," *Journal of Cerebral Blood Flow and Metabolism*, vol. 32, no. 4, pp. 663–675, 2012.

[87] G. Wallays, D. Nuyens, R. Silasi-Mansat et al., "Notch3 Arg170Cys knock-in mice display pathologic and clinical features of the neurovascular disorder cerebral autosomal dominant arteriopathy with subcortical infarcts and leukoencephalopathy," *Arteriosclerosis, Thrombosis, and Vascular Biology*, vol. 31, no. 12, pp. 2881–2888, 2011.

[88] G. Daniele, S. DiLucia, P. G. Masci, and F. del Monte, "Heart and brain: complex relationships for left ventricular dysfunction," *Current Cardiology Reports*, vol. 22, no. 8, p. 72, 2020.

[89] K. P. Doyle, R. P. Simon, and M. P. Stenzel-Poore, "Mechanisms of ischemic brain damage," *Neuropharmacology*, vol. 55, no. 3, pp. 310–318, 2008.

[90] R. D. Bell, E. A. Winkler, I. Singh et al., "Apolipoprotein E controls cerebrovascular integrity via cyclophilin A," *Nature*, vol. 485, no. 7399, pp. 512–516, 2012.

[91] A. Nanou, M. Bourbouli, S. Vetrano, U. Schaeper, S. Ley, and G. Kollias, "Endothelial Tpl2 regulates vascular barrier function via JNK-mediated degradation of claudin-5 promoting neuroinflammation or tumor metastasis," *Cell Reports*, vol. 35, no. 8, p. 109168, 2021.

[92] B. V. Zlokovic, "The blood-brain barrier in health and chronic neurodegenerative disorders," *Neuron*, vol. 57, no. 2, pp. 178–201, 2008.

[93] J. H. Seo, N. Miyamoto, K. Hayakawa et al., "Oligodendrocyte precursors induce early blood-brain barrier opening after white matter injury," *The Journal of Clinical Investigation*, vol. 123, no. 2, pp. 782–786, 2013.

[94] W. Duan, L. Gui, Z. Zhou et al., "Adenosine A_{2A} receptor deficiency exacerbates white matter lesions and cognitive deficits induced by chronic cerebral hypoperfusion in mice," *Journal of the Neurological Sciences*, vol. 285, no. 1-2, pp. 39–45, 2009.

[95] T. Uchida, M. Mori, A. Uzawa et al., "Increased cerebrospinal fluid metalloproteinase-2 and interleukin-6 are associated with albumin quotient in neuromyelitis optica: their possible role on blood-brain barrier disruption," *Multiple Sclerosis*, vol. 23, no. 8, pp. 1072–1084, 2017.

[96] Y. Yang, M. Zhang, X. Kang et al., "Thrombin-induced microglial activation impairs hippocampal neurogenesis and spatial memory ability in mice," *Behavioral and Brain Functions*, vol. 11, no. 1, p. 30, 2015.

[97] S. A. Villeda, J. Luo, K. I. Mosher et al., "The ageing systemic milieu negatively regulates neurogenesis and cognitive function," *Nature*, vol. 477, no. 7362, pp. 90–94, 2011.

[98] F. Vancheri, G. Longo, S. Vancheri, and M. Henein, "Coronary Microvascular Dysfunction," *Journal of Clinical Medicine*, vol. 9, no. 9, p. 2880, 2020.

[99] S. Hashimoto, M. Inaji, T. Nariai et al., "Usefulness of [^{11}C] methionine PET in the differentiation of tumefactive multiple sclerosis from high grade astrocytoma," *Neurologia Medico-Chirurgica (Tokyo)*, vol. 59, no. 5, pp. 176–183, 2019.

[100] J. T. Thackeray, J. P. Bankstahl, Y. Wang, K. C. Wollert, and F. M. Bengel, "Targeting amino acid metabolism for molecular imaging of inflammation early after myocardial infarction," *Theranostics*, vol. 6, no. 11, pp. 1768–1779, 2016.

[101] S. Rivest, "Regulation of innate immune responses in the brain," *Nature Reviews. Immunology*, vol. 9, no. 6, pp. 429–439, 2009.

[102] A. Cagnin, D. J. Brooks, A. M. Kennedy et al., "In-vivo measurement of activated microglia in dementia," *Lancet*, vol. 358, no. 9280, pp. 461–467, 2001.

[103] J. A. Smith, A. Das, S. K. Ray, and N. L. Banik, "Role of pro-inflammatory cytokines released from microglia in neurodegenerative diseases," *Brain Research Bulletin*, vol. 87, no. 1, pp. 10–20, 2012.

[104] J. Miyanohara, M. Kakae, K. Nagayasu et al., "TRPM2 channel aggravates CNS inflammation and cognitive impairment via activation of microglia in chronic cerebral hypoperfusion," *The Journal of Neuroscience*, vol. 38, no. 14, pp. 3520–3533, 2018.

[105] L. Peferoen, M. Kipp, P. van der Valk, J. M. van Noort, and S. Amor, "Oligodendrocyte-microglia cross-talk in the central nervous system," *Immunology*, vol. 141, no. 3, pp. 302–313, 2014.

[106] J. J. Volpe, H. C. Kinney, F. E. Jensen, and P. A. Rosenberg, "The developing oligodendrocyte: key cellular target in brain injury in the premature infant," *International Journal of Developmental Neuroscience*, vol. 29, no. 4, pp. 423–440, 2011.

[107] A. L. Perraud, A. Fleig, C. A. Dunn et al., "ADP-ribose gating of the calcium-permeable LTRPC2 channel revealed by Nudix motif homology," *Nature*, vol. 411, no. 6837, pp. 595–599, 2001.

[108] S. Kaneko, S. Kawakami, Y. Hara et al., "A critical role of TRPM2 in neuronal cell death by hydrogen peroxide," *Journal of Pharmacological Sciences*, vol. 101, no. 1, pp. 66–76, 2006.

[109] S. Yamamoto, S. Shimizu, S. Kiyonaka et al., "TRPM2-mediated Ca^{2+} influx induces chemokine production in monocytes that aggravates inflammatory neutrophil infiltration," *Nature Medicine*, vol. 14, no. 7, pp. 738–747, 2008.

[110] Y. Hara, M. Wakamori, M. Ishii et al., "LTRPC2 Ca^{2+}-permeable channel activated by changes in redox status confers

susceptibility to cell death," *Molecular Cell*, vol. 9, no. 1, pp. 163–173, 2002.

[111] Y. Zhou, J. Zhang, L. Wang et al., "Interleukin-1β impedes oligodendrocyte progenitor cell recruitment and white matter repair following chronic cerebral hypoperfusion," *Brain, Behavior, and Immunity*, vol. 60, pp. 93–105, 2017.

[112] Y. Liu, X. M. Wu, Q. Q. Luo et al., "CX3CL1/CX3CR1-mediated microglia activation plays a detrimental role in ischemic mice brain via p38MAPK/PKC pathway," *Journal of Cerebral Blood Flow and Metabolism*, vol. 35, no. 10, pp. 1623–1631, 2015.

[113] W. H. Yang, S. C. Liu, C. H. Tsai et al., "Leptin induces IL-6 expression through OBRl receptor signaling pathway in human synovial fibroblasts," *PLoS One*, vol. 8, no. 9, article e75551, 2013.

[114] Y. du, Y. Song, X. Zhang et al., "Leptin receptor deficiency protects mice against chronic cerebral hypoperfusion-induced neuroinflammation and white matter lesions," *Mediators of Inflammation*, vol. 2020, Article ID 7974537, 11 pages, 2020.

[115] Y. Chen, Y. Tian, H. Tian et al., "Tamoxifen promotes white matter recovery and cognitive functions in male mice after chronic hypoperfusion," *Neurochemistry International*, vol. 131, p. 104566, 2019.

[116] G. Aliev, M. A. Smith, J. C. de la Torre, and G. Perry, "Mitochondria as a primary target for vascular hypoperfusion and oxidative stress in Alzheimer's disease," *Mitochondrion*, vol. 4, no. 5-6, pp. 649–663, 2004.

[117] J. J. Iliff, M. Wang, Y. Liao et al., "A paravascular pathway facilitates CSF flow through the brain parenchyma and the clearance of interstitial solutes, including amyloid β," *Science Translational Medicine*, vol. 4, no. 147, article 147ra111, 2012.

[118] J. M. Tarasoff-Conway, R. O. Carare, R. S. Osorio et al., "Clearance systems in the brain–implications for Alzheimer disease," *Nature Reviews. Neurology*, vol. 11, no. 8, pp. 457–470, 2015.

[119] A. Liesz, "The vascular side of Alzheimer's disease," *Science*, vol. 365, no. 6450, pp. 223-224, 2019.

[120] M. Bordeleau, A. ElAli, and S. Rivest, "Severe chronic cerebral hypoperfusion induces microglial dysfunction leading to memory loss in APPswe/PS1 mice," *Oncotarget*, vol. 7, no. 11, pp. 11864–11880, 2016.

[121] G. R. Frost and Y. M. Li, "The role of astrocytes in amyloid production and Alzheimer's disease," *Open Biology*, vol. 7, no. 12, 2017.

[122] E. Rodriguez-Vieitez, L. Saint-Aubert, S. F. Carter et al., "Diverging longitudinal changes in astrocytosis and amyloid PET in autosomal dominant Alzheimer's disease," *Brain*, vol. 139, no. 3, pp. 922–936, 2016.

[123] Y. Matsuoka, M. Picciano, J. la Francois, and K. Duff, "Fibrillar β-amyloid evokes oxidative damage in a transgenic mouse model of Alzheimer's disease," *Neuroscience*, vol. 104, no. 3, pp. 609–613, 2001.

[124] S. M. de la Monte and J. R. Wands, "Molecular indices of oxidative stress and mitochondrial dysfunction occur early and often progress with severity of Alzheimer's disease," *Journal of Alzheimer's Disease*, vol. 9, no. 2, pp. 167–181, 2006.

[125] J. Wang, B. J. Gu, C. L. Masters, and Y. J. Wang, "A systemic view of Alzheimer disease – insights from amyloid-β metabolism beyond the brain," *Nature Reviews. Neurology*, vol. 13, no. 10, pp. 612–623, 2017.

[126] P. Venkat, J. Chen, and M. Chopp, "Exosome-mediated amplification of endogenous brain repair mechanisms and brain and systemic organ interaction in modulating neurological outcome after stroke," *Journal of Cerebral Blood Flow and Metabolism*, vol. 38, no. 12, pp. 2165–2178, 2018.

[127] C. Frühbeis, D. Fröhlich, W. P. Kuo, and E. M. Krämer-Albers, "Extracellular vesicles as mediators of neuron-glia communication," *Frontiers in Cellular Neuroscience*, vol. 7, 2013.

[128] D. Fröhlich, W. P. Kuo, C. Frühbeis et al., "Multifaceted effects of oligodendroglial exosomes on neurons: impact on neuronal firing rate, signal transduction and gene regulation," *Philosophical Transactions of the Royal Society of London. Series B, Biological Sciences*, vol. 369, no. 1652, article 20130510, 2014.

[129] L. L. Sun, M. J. Duan, J. C. Ma et al., "Myocardial infarction-induced hippocampal microtubule damage by cardiac originating microRNA-1 in mice," *Journal of Molecular and Cellular Cardiology*, vol. 120, pp. 12–27, 2018.

[130] S. Acharya, A. Salgado-Somoza, F. M. Stefanizzi et al., "Non-coding RNAs in the brain-heart axis: the case of Parkinson's disease," *International Journal of Molecular Sciences*, vol. 21, no. 18, 2020.

[131] J. A. Cannon, L. Shen, P. S. Jhund et al., "Dementia-related adverse events in PARADIGM-HF and other trials in heart failure with reduced ejection fraction," *European Journal of Heart Failure*, vol. 19, no. 1, pp. 129–137, 2017.

Hindawi
Oxidative Medicine and Cellular Longevity
Volume 2021, Article ID 9993704, 16 pages
https://doi.org/10.1155/2021/9993704

Research Article

TMIGD1 Inhibited Abdominal Adhesion Formation by Alleviating Oxidative Stress in the Mitochondria of Peritoneal Mesothelial Cells

Yunhua Wu,[1,2] **Enmeng Li**,[1] **Zijun Wang**,[1] **Tianli Shen**,[1] **Cong Shen**,[3] **Dong Liu**,[2] **Qiuying Gao**,[4] **Xuqi Li**,[1,5] **and Guangbing Wei**[1]

[1]*Department of General Surgery, The First Affiliated Hospital of Xian Jiaotong University, Xian, 710061 Shaanxi, China*
[2]*Department of General Surgery, Shaanxi Provincial People's Hospital, Xi'an, 710061 Shaanxi, China*
[3]*Department of Radiology, The First Affiliated Hospital of Xi'an Jiaotong University, Xi'an, 710061 Shaanxi, China*
[4]*Department of Haematology, Shaanxi Provincial People's Hospital, Xi'an, 710061 Shaanxi, China*
[5]*Department of Talent Highland, The First Affiliated Hospital of Xian Jiaotong University, Xian, 710061 Shaanxi, China*

Correspondence should be addressed to Xuqi Li; lixuqi@163.com and Guangbing Wei; weiguangbing1208@163.com

Received 30 March 2021; Revised 27 June 2021; Accepted 12 July 2021; Published 14 August 2021

Academic Editor: Xiaoyuan Zhou

Background. Postoperative abdominal adhesion remains one of the frequent complications after abdominal surgery and lacks effective intervention. Peritoneal mesothelial cell injury and healing play crucial roles in the process of adhesion formation, and identifying this mechanism might provide new insight into possible new therapeutic strategies for this disease. Transmembrane and immunoglobulin domain-containing 1 (TMIGD1) has been proven to protect renal epithelial cells from injury induced by oxidative stress and has also been identified as a novel adhesion molecule. Here, we investigated the role of TMIGD1 and its possible mechanism in adhesion formation. *Materials and Methods.* Immunohistochemistry (IHC), qPCR, and immunofluorescence (IHF) were used to detect the expression of TMIGD1. The grade and tenacity score of adhesion were used to evaluate the adhesion formation conditions. A TMIGD1-overexpressing HMrSV5 cell line was established. MTT assay, Western blotting, Annexin V apoptosis analysis, and CK19 staining were used to measure mesothelial cell viability, apoptosis, and completeness. ROS and MDA detection were used to measure mesothelial cell oxidative stress levels. JC-1 staining, IHF, and transmission electron microscopy were performed to assess mitochondrial function. Scratch-wound and adhesion assays were used to evaluate the adhesion ability of mesothelial cells. *Results.* First, we showed that TMIGD1 was decreased in mouse abdominal adhesion tissue and peritoneal mesothelial cells. Second, TMIGD1 overexpression inhibited adhesion formation. Third, TMIGD1 overexpression protected mesothelial cells from hydrogen peroxide- (H_2O_2-) induced oxidative stress injury. Fourth, TMIGD1 overexpression alleviated oxidative stress by protecting the mitochondrial function of mesothelial cells. In addition, TMIGD1 overexpression enhanced mesothelial cell adhesion. *Conclusion.* Our findings suggest that TMIGD1 protects mesothelial cells from oxidative stress injury by protecting their mitochondrial function, which is decreased in regular abdominal adhesion tissue. In addition, TMIGD1 enhances peritoneal mesothelial cell adhesion to promote healing.

1. Background

Postoperative abdominal adhesion remains one of the most frequent complications after abdominal surgery, which occurs in approximately 67-93% of patients undergoing abdominal operations [1]. It further leads to intestinal obstruction, chronic abdominal pain, female infertility, and many other complications [2]. However, there is no effective management strategy for postoperative abdominal adhesion other than enterolysis, which is an invasive method with a high probability of reinjury and readhesion [3]. Although it brings about a large number of serious health problems,

multifarious innovations attempted to prevent postoperative abdominal adhesion have so far failed to take effect.

Adhesion formation is a complicated pathophysiologic process that involves the inflammatory response, fibrosis, and mesothelial cell healing [4]. The mesothelium is a monolayer located on the peritoneum that forms a smooth peritoneal surface [5]. After abdominal injury or trauma, the inflammatory response is activated, followed by the formation of fibrosis, and the injured mesothelia cells heal within 7-10 days after the surgical procedure [6]. Mesothelial cell plays a critical role in the process of peritoneal tissue healing and adhesion formation. Mesothelial cell damage, loss, and epithelial-mesenchymal transition might be causes of abdominal adhesion following peritoneal damage [7]. In addition, adhesion could be effectively alleviated if some measures are used to enhance the regeneration ability of mesothelial cells and to rebuild the intact mesothelial cell layer in the early stage of abdominal adhesion [8]. Nevertheless, the underlying mechanism is elusive at present.

Oxidative stress is defined as a disrupted balance between oxidative molecules and inadequate antioxidant defense mechanisms [9]. Although the severity varies, it occurs in almost all surgery, such as endoscopic and Lichtenstein hernia repair [10]. Oxidative stress generates reactive oxygen species (ROS), which are highly destructive to cellular functions; it not only has a direct cytotoxic effect on mesothelial cells but also induces apoptosis of mesothelial cells [11]. Both mechanisms create a further injury of the mesothelial cells lining in the abdominal cavity beyond the injury created by surgical manipulation and enhance the probability of creating postoperative adhesions. The major intracellular sources of ROS are the electron transport chain in the mitochondria [12]. Some articles pointed out that hypoxia alters mitochondrial fusion and fission and oxidative phosphorylation, which causes overproduction of ROS by remodeling the electron transport chain [13].

As a family member of IGPR-1, transmembrane and immunoglobulin domain-containing 1 (TMIGD1) has been identified to be a novel cell adhesion molecule. Recent studies have demonstrated that TMIGD1 protects epithelial cells from oxidative injury. Downregulation of TMIGD1 is associated with increased peritoneal damage after oxidative stress induced by ischemia and reperfusion in mice [14]. These findings suggest a protective role of TMIGD1 against oxidative stress in the process of adhesion formation, but the underlying mechanism remains unclear. TMIGD1 also regulates the expression of p21Cip1/p27Kip1 in some renal cancers, acting as a tumor suppressor [15]. This study tested the hypothesis that TMIGD1 protects mesothelial cells from oxidative stress injury by protecting their mitochondrial function and enhances peritoneal mesothelial cell adhesion to promote healing, whose expression is suppressed in abdominal adhesion formation. Our findings support TMIGD1 as a therapeutic target to prevent postoperative abdominal adhesion, and TMIGD1 upregulating agents could be used during surgery to prevent adhesion.

2. Materials and Methods

2.1. Model of Adhesion. A C57BL/6 mouse abdominal adhesion model was established as previously described [16]. Twenty mice were randomly divided into two groups. After the mice were anesthetized (25% W/V isoflurane in propylene glycol) and sterilized, a 1 cm long incision was made in the central part of the mouse abdomen. The lower right cecum and the adjacent abdominal wall were scraped to the needle-like hemorrhagic spots to establish the postoperative abdominal adhesion model. The cecum was then placed in the abdominal cavity adjacent to the damaged abdominal wall, and the abdominal cavity was finally closed. Animals were sacrificed at 3 or 10 days following the procedure, and then two independent researchers assessed the score of adhesion. Then, tissue specimens were collected, including abdominal adhesion tissue and the surrounding normal bowel wall of the cecum and right-side abdominal wall (used as normal peritoneal tissue). The adhesion score system was as reported previously [17].

2.2. Cell Culture and Establishment of the TMIGD1-Overexpressing Cell Line. The human mesothelial cell line HMrSV5 was purchased from the Shanghai Institute of Cell Biology, Chinese Academy of Sciences, and cultured in minimum essential medium (Gibco, Thermo Fisher Scientific, Beijing, China) supplemented with 10% FBS (Gibco BRL, Carlsbad, CA, USA) at 37°C and 5% CO_2. The overexpression vectors for humans were purchased from GenePharma Co., Ltd. (Shanghai, China). The transfection was implemented in accordance with the manufacturer's guidelines.

2.3. Lentivirus Transfection. The transfection of TMIGD1-overexpression lentivirus in vivo was as follows. Twenty-four mice were randomly split into three groups: the sham group only underwent open and close operations, and the other two groups underwent abdominal adhesion model operations as described above. After establishment of the abdominal adhesion model, 50 μL 1×10^9 lentivirus was spared around the injured peritoneal tissue, and then the injured cecum was placed adjacent to the injured abdominal wall. Ten days after the operation, the mice were sacrificed, and the expression of TMIGD1 in the peritoneal tissue of TMIGD1-overexpressing mice was tested by IHC and IHF to prove that the construction was successful. Adhesion tissue was collected and divided into two parts: one part was stored at -80°C, and the other part was fixed with 10% paraformaldehyde.

2.4. Immunohistochemistry (IHC) and Immunofluorescence (IHF) Staining. First, tissues collected from the abdominal cavity of mice were immersed in 10% formol for 24 hours. Next, 4 μm thick paraffin sections were obtained, and IHF and IHC were performed according to the manufacturer's instructions. Sections were incubated with primary antibodies against TMIGD1 (1 : 100, Bioss, Beijing, China), HSP60 (1 : 500, Wuhan Servicebio Technology Co., Ltd., China), and CK19 (1 : 50, Wuhan Google Biotechnology Co., Ltd., Wuhan, China) over one night at 4°C. A series of pictures were taken using a Nikon Eclipse C1 confocal laser scanning microscope (Nikon Corporation, Tokyo, Japan). The assessment IHC was performed as reported previously [18], and at least five fields were selected for every section. The scoring

system was as follows: a score of 0 indicated tissues with no expression, a score of 1 indicated tissue with weakly positive expression, a score of 2 indicated tissues with positive expression, a score of 3 indicated tissues with strongly positive expression, and a score of 4 indicated tissues with extremely abundant expression. For the evaluation of the expression of TMIGD1 in the IHF, we randomly selected at least ten fields for each section and measured the related green marked TMIGD1 or red marked HSP60 in CK19-marked mesothelial cells.

2.5. Western Blotting. Western blotting was performed, following that reported in some studies [19]. A RIPA Protein Extraction Kit (HeTe, Xi'an, Shaanxi, China) was used to extract protein from mesothelial cells. A 12% sodium dodecyl sulfate polyacrylamide gel was used for electrophoresis. The primary antibodies, including anti-TMIGD1 (Bioss, Beijing, China, 1 : 1000 dilution), anti-Bcl2 (Proteintech, Chicago, USA, 1 : 5000 dilution), anti-Bax (Proteintech, Chicago, USA, 1 : 5000 dilution), and anti-GAPDH (Proteintech, Chicago, USA, 1 : 5000 dilution) antibodies, were used to label-related proteins in this research. A chemiluminescence detection system (Millipore, Billerica, MA, USA) was used to test protein expression. These results were normalized to GAPDH and column-plotted by GraphPad Prism 7 software.

2.6. Quantitative (Q) Real-Time- (RT-) PCR. Total RNA was extracted from mouse specimens using TRIzol (Invitrogen, Thermo Fisher Scientific, California, USA), and the PrimeScript RT Reagent Kit (TaKaRa, Osaka, Japan) was used for synthesis of complementary DNA (cDNA) in accordance with the manufacturer's guidelines. RT-PCR was performed using an IQ5 instrument (Bio-Rad, CA, USA) by SYBR Green fluorescence signal detection assays (TaKaRa, Osaka, Japan) and primers. The $-2^{\Delta\Delta Ct}$ method was used to analyze the expression of mRNA. The primers used in this study were as listed below: sense and antisense primers to mouse TMIGD1 (5′-GACCCGAATTCAGAAACAC-3′ and 5′-GCCCTTCT CAAAACGTA-3′) and sense and antisense primers to human TMIGD1 (5′-CTCCCATGCCATCCCTTGTTA-3′ and 5′-C GATCCTTTGCGAATGGAGAAAT-3′).

2.7. ROS Measurement. The changes in cellular ROS levels were tested through the following steps. First, 5×10^6 mesothelial cells were inoculated on cover slips. After 24 h of cultivation, mesothelial cells were treated with H_2O_2 at a concentration of 500 μM (Sigma Chemical Co., St. Louis, MO, USA) for 12 h. Next, after washing twice, the mesothelial cells and 10 μM 2′,7′-dichlorofluorescein diacetate (DCFH-DA) were cocultured in the dark for 30 min at 37°C. Finally, a Leica microscope was used to take photos of ROS fluorescence in mesothelial cells after washing once again. The intensity was measured using ImageJ software.

2.8. ROS and MDA Measurement in Specimens. Frozen pathological tissue specimens were made into sections, which were stored at -80°C. ROS staining was performed using dyeing solution (catG0002, Wuhan Servicebio Technology Co., Ltd., China) according to the manufacturer's instructions, and then, the cells were cultured in DAPI dyeing solution (catG1012, Wuhan Servicebio Technology Co., Ltd., China). Sections were observed by fluorescence microscopy. The ratio of ROS-positive nuclei to total nuclei was calculated as the ROS expression level. The level of MDA was measured by a kit (Jincheng, Nanjing, China) according to the manufacturer's instructions. The results were normalized by the total protein.

2.9. Transmission Electron Microscopy (TEM) Analysis of Mitochondrial Morphology. A 2 mm^2 piece of peritoneal adhesion tissue was collected and fixed in 2.5% glutaraldehyde. Then, the specimens were made into 70 nm slices and observed by TEM. We collected at least one specimen from each mouse and measured the mitochondrial length in at least three fields for one slice.

2.10. Survival Analysis of Mesothelial Cells. The MTT assay is an instrument for detecting the number of living cells. Approximately 5×10^3 mesothelial cells were inoculated on several 96-well plates for 12 h, and then, mesothelial cells were treated with distinct concentrations of H_2O_2 (1000 μM, 500 μM, 250 μM, 125 μM and 62.5 μM). Approximately 24 h later, the cells were soaked in 20 μL MTT at a concentration of 5 mg/mL for 4 h, and the MTT crystals were soluble in DMSO. Cell viability was measured by a microplate reader (Thermo Fisher Scientific, Waltham, USA).

2.11. Apoptosis Analysis. Cell apoptosis was tested by a kit (Affinity BioReagents) following the instructions.

2.12. Mitochondrial Membrane Potential. Mitochondrial membrane potential was measured by a kit (JC-1: Solebo Biotechnology Co., Ltd.) following the instruction.

2.13. Scratch-Wound Assay and Adhesion Analysis. A scratch-wound assay was conducted to test the migratory potential of TMIGD1-overexpressing mesothelial cells and normal mesothelial cells. HMrSV5 cells were inoculated on 6-well plates. Cells grew to confluence and were scratched by a 200 μL pipette tip. After culturing for 48 h at 37°C and 5% CO_2, pictures were taken using a photomicroscope (Leica DFC950 camera; Leica Microsystems, Wetzlar, Germany). The cell migration ratio was quantitated by Scion Image software (beta 4.0.2, Scion, Frederick, MD). Cell adhesion was assessed by a kit (Bestbio, Beijing, China) in accordance with the instructions.

2.14. Statistics. Data collection and analysis were performed using SPSS 18.0 (Chicago, IL, USA) in this study. The results are presented as the percentages, absolute numbers, and the mean ± standard deviation. The t tests or one-way ANOVA was used to analyze normally distributed data. The differences were tested by the least significant difference method (LSD) test among the groups. The Kruskal-Wallis test was used for nonnormally distributed data analysis. The χ-squared test or Fisher's exact test was used for quantitative data analysis. $P < 0.05$ was considered statistically significant.

Day	Log | FC |	Gene.symbol
Day 1	−1.379707	Usp18
	−1.07022	Cubn
Day 3	−1.5	Tmigd1
	1.19	Papss2
Day 7	1.34	Papss2
	1.53	Gpr65
Day 14	−1.039304	Snx25
	−1.000779	Nipsnap3a
	1.034921	Tlr4
	1.500115	Stxbp5
	1.261083	Ube2i
	1.715832	Lims2

(a)

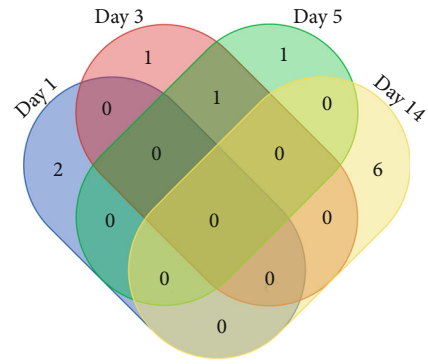

(b)

Figure 1: Analysis of the GEO dataset GSE4715. (a) GEO2R software showing the gene name of differentially expressed genes compared with normal peritoneum at different times, screening criteria: |LogFC| >1 and $P < 0.05$ (https://www.ncbi.nlm.nih.gov/geo/). (b) Venn diagram showing the coexpression of different genes in different time periods.

3. Results

3.1. TMIGD1 Expression Is Decreased in Mesothelial Cells. We discovered that TMIGD1 expression is decreased in abdominal adhesion tissue compared to normal peritoneum at postoperative day (POD) 3 through analyzing the microarray data from the GSE4715 dataset in GEO (gene 2R software; adhesion tissue vs. normal peritoneum; screening criteria: |LogFC| >1 and $P < 0.05$; https://www.ncbi.nlm.nih.gov/geo/, Figures 1(a) and 1(b)). To validate this finding further, we measured TMIGD1 expression in mouse abdominal adhesion tissues via IHC. These analyses indicated that TMIGD1 expression is decreased in adhesion tissue compared to normal peritoneum at POD 3 and POD 10 (Figures 2(a) and 2(b)). q-PCR assays revealed the same molecular alteration in adhesion tissue (Figure 2(c)).

To explore the effect of TMIGD1 in mesothelial cells, we examined TMIGD1 expression in mesothelial cells of normal and adhesion tissue in noninterventional adhesion model mice at two time points (POD 3 and POD 10) using double immunofluorescence staining. The intensity of TMIGD1 (fluorescence green) was weakened in mesothelial cells of adhesion tissue at POD 3 and POD 10 (Figures 2(d) and 2(e)), contrary to normal peritoneum, in which numerous TMIGD1-expressing mesothelial cells were observed. As such, we speculate that the downregulation of TMIGD1 is a reason for mesothelial cell injury in the process of adhesion formation.

3.2. TMIGD1 Inhibits Abdominal Adhesion Formation. TMIGD1 expression is decreased in adhesion tissue compared with a normal control peritoneum in mice undergoing abdominal adhesion model operation. We hypothesize that TMIGD1 acts as an antiadhesion factor in the process of abdominal adhesion formation.

To validate whether TMIGD1 might inhibit abdominal adhesion formation, we created adhesions in wild-type mice that were locally treated with lentivirus overexpressing TMIGD1 during adhesion formation, which resulted in significantly increased TMIGD1 expression in mesothelial cells of the injured peritoneum surface (Figures 3(a)–3(d)) compared to the control vector-infected mice. TMIGD1 expression resulted in significantly decreased adhesion formation compared with control vector-infected mice, which was tested by both the grade and tenacity score of adhesion (Figures 3(e) and 3(f)).

In summary, TMIGD1 acts as an anti-adhesion factor in the process of abdominal adhesion formation. Low TMIGD1 expression increased postoperative abdominal adhesion formation.

3.3. TMIGD1 Protects Mesothelial Cells from Oxidative Stress Injury. To determine whether TMIGD1 protects mesothelial cells from H_2O_2-induced cell injury, we constructed HMrSV5 cell lines that stably express TMIGD1 (Figures 4(a) and 4(b)) and treated both the control cell line and TMIGD1-overexpressing cell line with different concentrations of H_2O_2. Subsequently, an MTT assay was used to measure cell viability, and we found that the expression of TMIGD1 increased the survival of mesothelial cells in response to cell injury (Figure 4(c)). Then, the expression of apoptosis-associated proteins such as Bax and Bcl-2 and Annexin V apoptosis assays was used to assess mesothelial cell apoptosis. Bax expression was significantly decreased; however, Bcl-2 expression was significantly increased in the TMIGD1-overexpression group compared with the control group

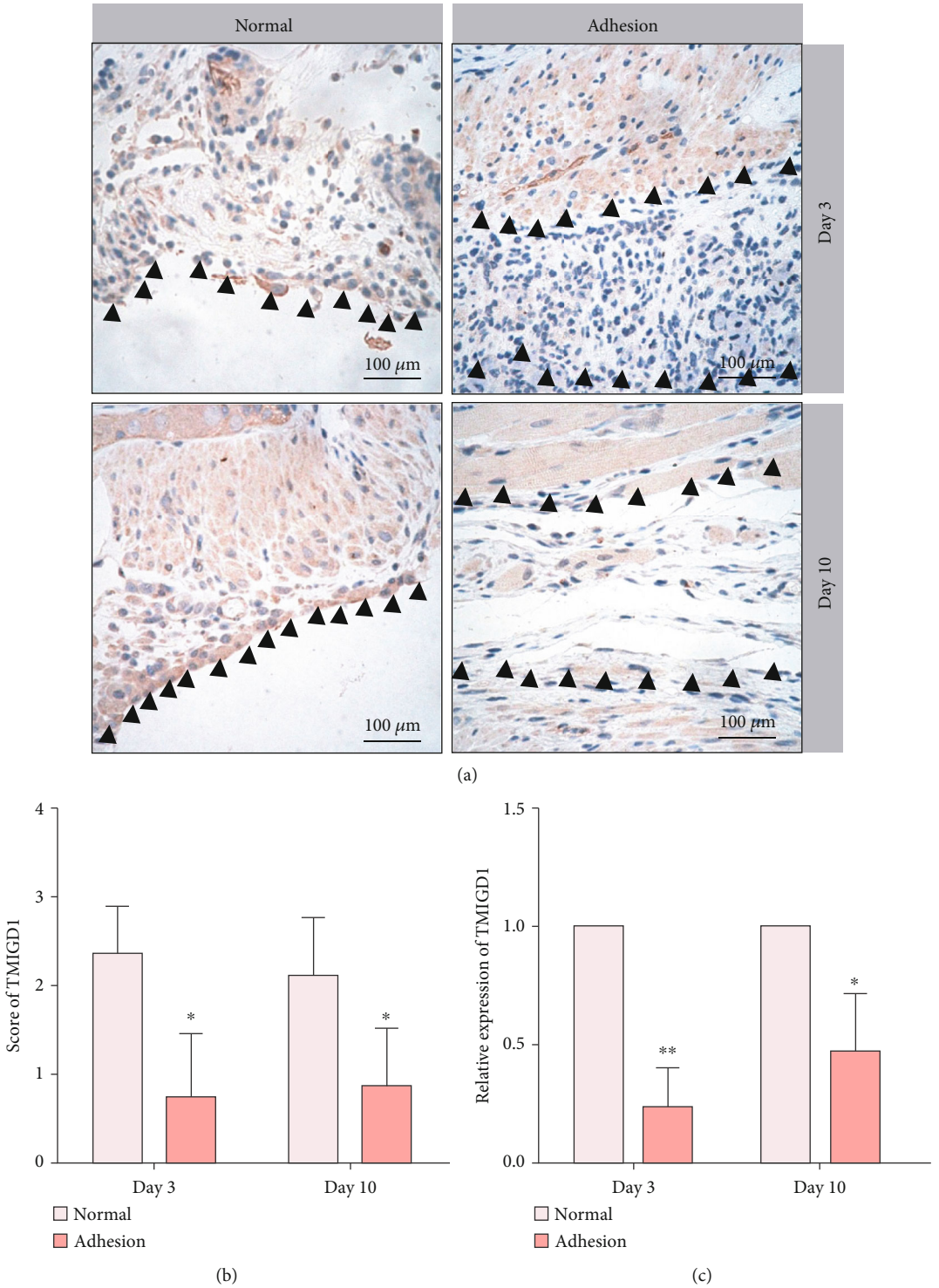

Figure 2: Continued.

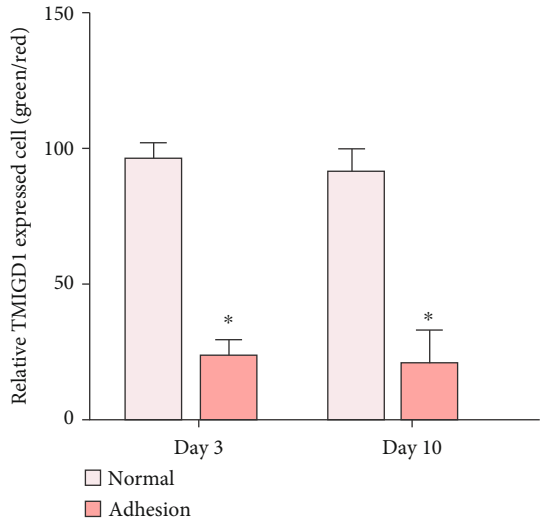

(d)

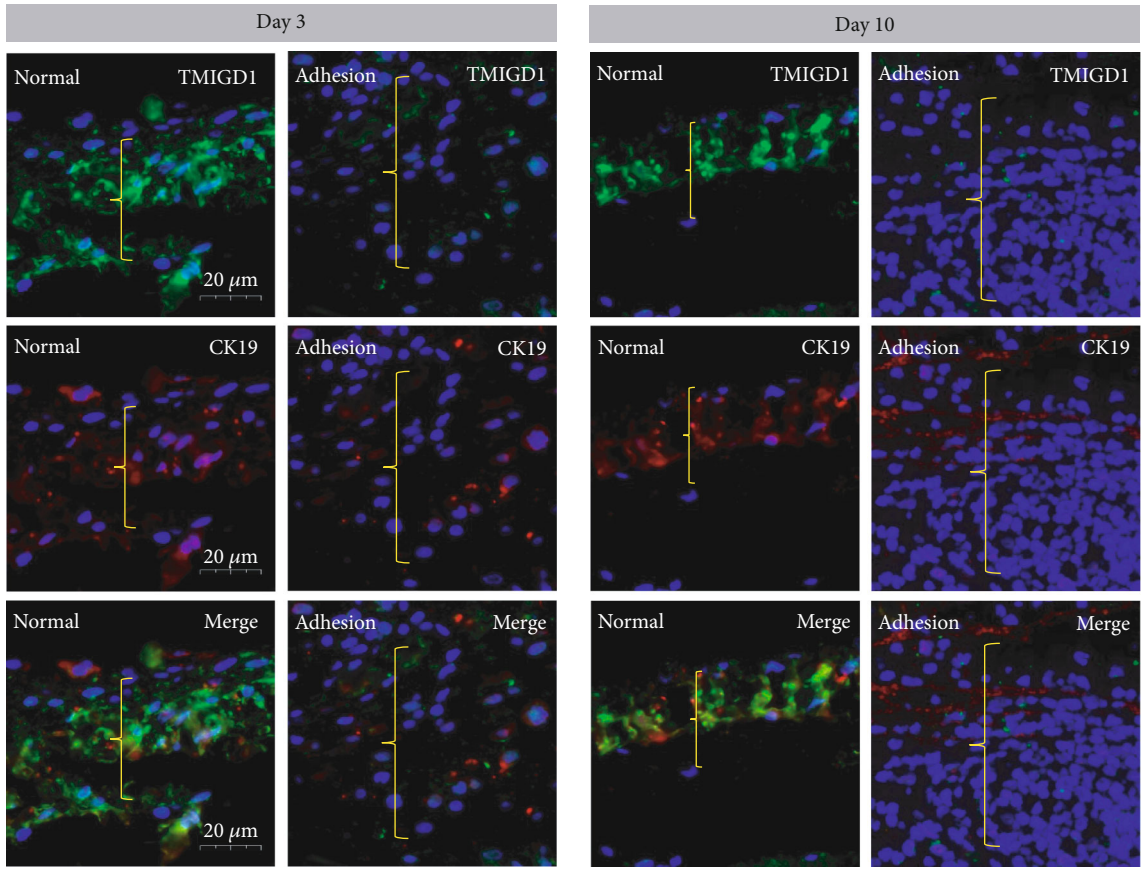

(e)

Figure 2: TMIGD1 expression is decreased in mesothelial cells. (a) IHC showing TMIGD1 expression in adhesion tissue and normal peritoneum of a mouse abdominal adhesion model at POD 3 and 10. $N = 10$; the black arrows mark the normal peritoneum or adhesion tissue; 400x magnification. (b) Score of TMIGD1 in the pictures of IHC of adhesion tissue and normal peritoneum of the mouse abdominal adhesion model at POD 3 and 10. $N = 10$; *compared to normal tissue, $P < 0.05$; t test. (c) Quantitation of qPCR for TMIGD1 shows downregulation of expression in mouse adhesion tissue (compared to the normal peritoneum of each time point) at POD 3 and 10. $N = 10$; *compared to normal tissue, $P < 0.05$; **compared to normal tissue, $P < 0.01$; t test. (d) IHF for TMIGD1 (green) and CK19 (red) in mouse adhesion tissue at POD 3 and 10. $N = 10$; the yellow brackets show normal peritoneum or adhesion tissue; 900x magnification. (e) Quantification of corresponding fluorescence intensities for TMIGD1 in mesothelial cells of IHF. $N = 10$; *compared to normal tissue, $P < 0.05$; t test.

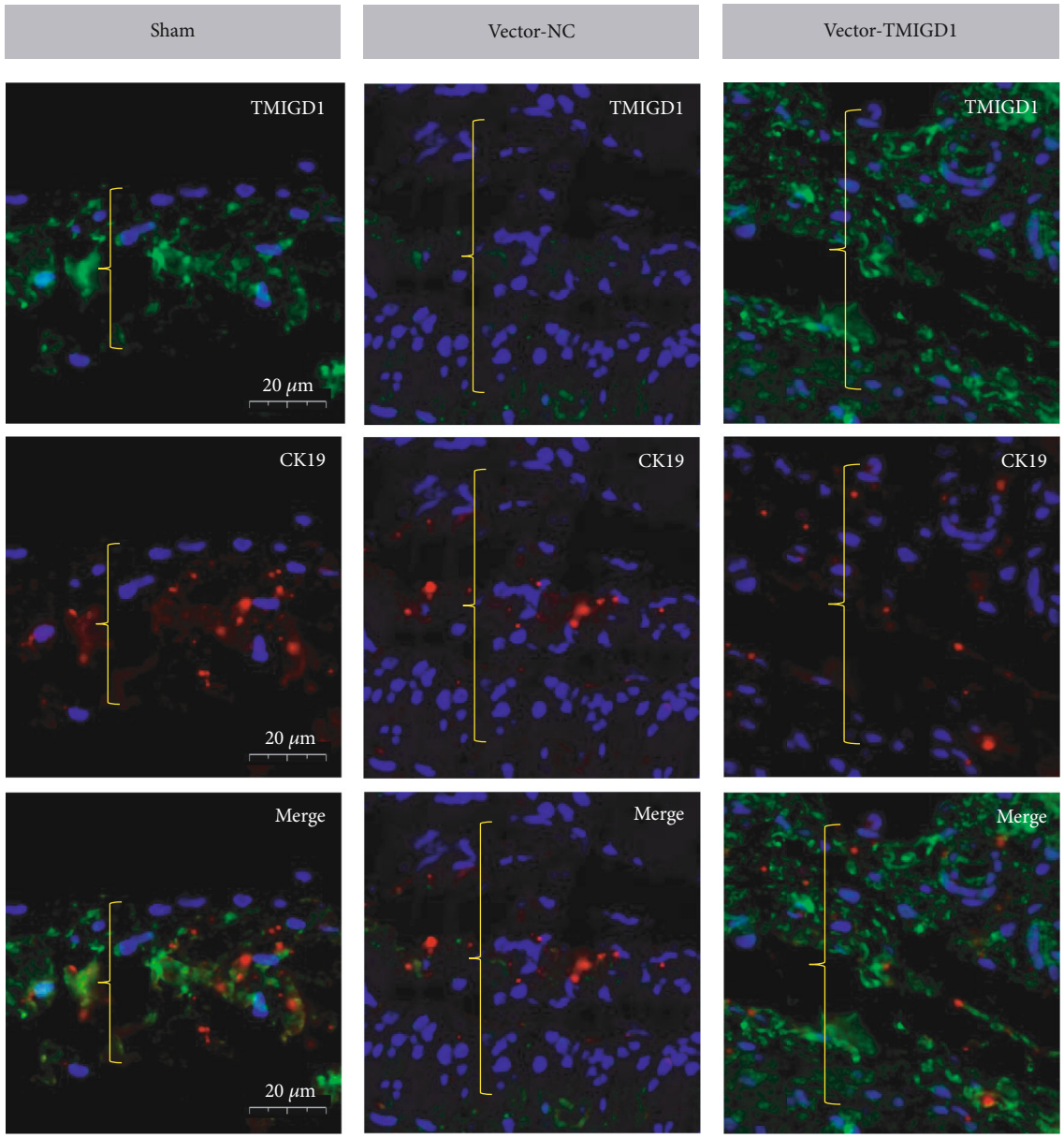

(a)

Figure 3: Continued.

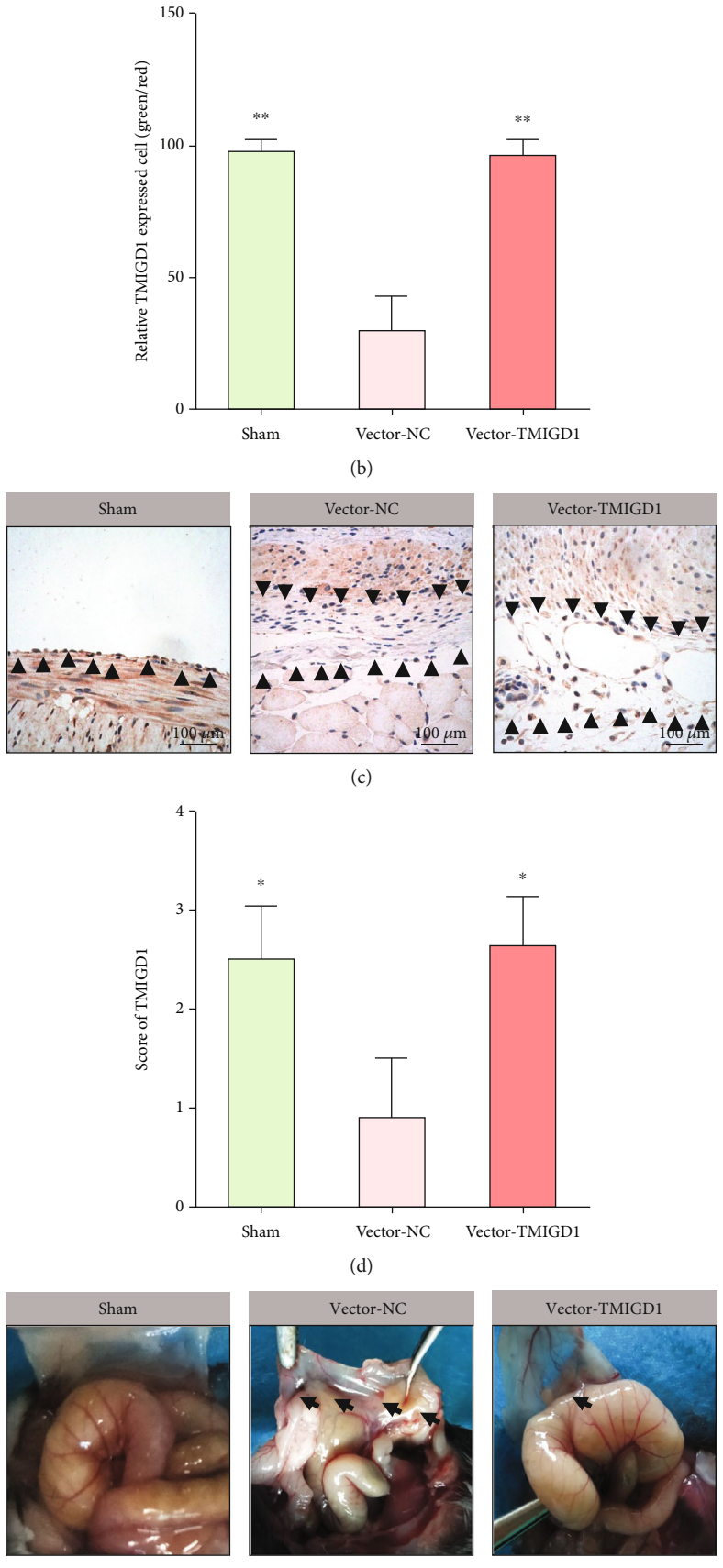

Figure 3: Continued.

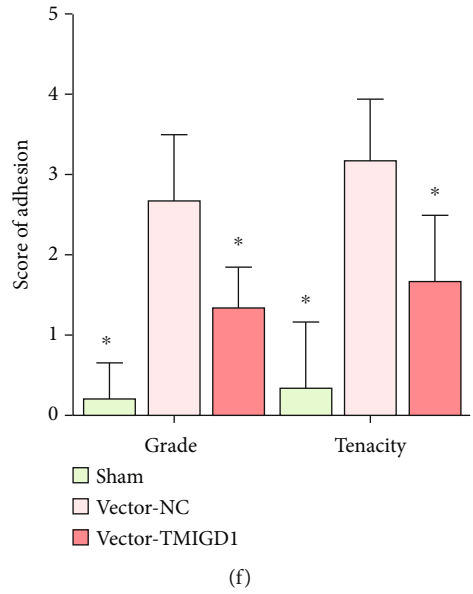

Figure 3: TMIGD1 inhibits abdominal adhesion formation. (a) IHF for TMIGD1 (green fluorescence) and CK19 (red fluorescence) in each group. $N = 10$; the yellow brackets show normal peritoneum or adhesion tissue; 900x magnification. (b) Quantification of relative positive TMIGD1 expression in the CK19-marked mesothelial cells in each group. $N = 10$; **compared to the vector-normal control (NC) group, $P < 0.01$; abnormal distribution, Kruskal-Wallis test. (c) IHC showing the expression of TMIGD1 in each group. $N = 10$; the black arrows mark the normal peritoneum or adhesion tissue; 400x magnification. (d) TMIGD1 scores in the IHC images of each group. $N = 10$; * compared to the vector-NC group, $P < 0.05$; abnormal distribution, Kruskal-Wallis test. (e) Typical gross observation of abdominal adhesion conditions in each group. $N = 10$; the black arrows mark adhesion tissue. (f) Application of an objective grade and tenacity adhesion score by two independent researchers quantifies the relative adhesion severity of each group. $N = 10$; *compared to the vector-NC group, $P < 0.05$; abnormal distribution, Kruskal-Wallis test.

(Figures 4(d) and 4(e)). Similarly, Annexin V apoptosis analysis suggested that the ratio of apoptotic cells in the TMIGD1-overexpression group was significantly decreased compared with that in the control group (Figures 4(f) and 4(g)), which was quantified by flow cytometry. This finding was further validated in vivo. CK19 staining of mouse peritoneal specimens at POD 10 showed that the TMIGD1-overexpression group had a higher mesothelial cell completeness rate than the vector control group (Figures 4(h) and 4(i)).

Taken together, these data suggested that the presence of TMIGD1 protects mesothelial cells from hydrogen peroxide-induced oxidative stress injury.

3.4. TMIGD1 Alleviates Oxidative Stress by Protecting the Mitochondrial Function of Mesothelial Cells. To verify that TMIGD1 protects mesothelial cells from injury by alleviating oxidative stress, we measured the ROS level in the different TMIGD1-expressing and H_2O_2-treated groups and found that the ROS level was significantly decreased in the TMIGD1-overexpressing group compared to the control group under the induction of hydrogen peroxide (Figures 5(a) and 5(b)). IHF demonstrated that the sham operation group and the TMIGD1-overexpression group had lower levels of ROS in the adhesion tissue of mice than the control vector group (Figures 5(c) and 5(d)). In addition, we detected the oxidative stress injury-relevant marker MDA in normal peritoneal or adhesion tissue specimens and found that MDA was significantly higher in the vector control group than in the sham group, but significantly lower in the TMIGD1 overexpression group than in the vector control group (Figure 5(e)).

Since mitochondria is a major source of ROS, the increase of ROS may indicate mitochondrial dysfunction [12]. It has been reported that TMIGD1 interacts with the mitochondrial outer membrane protein SYNJ2BP and can be recruited to mitochondria [20]. In view of the above exploration, we hypothesized that TMIGD1 alleviates oxidative stress by protecting the mitochondrial function of mesothelial cells. To zero in on the role of TMIGD1 in mesothelial cells, we measured the mitochondrial membrane potential level of mesothelial cells from the TMIGD1-overexpression group and the control group of HMrSV5 cell lines by JC-1 staining that was treated with H_2O_2; results displayed that the mitochondrial membrane potential was significantly decreased in the mesothelial cells from the control group compared to the TMIGD1-overexpression group (Figures 6(a) and 6(b)). We also used TEM to assess any mitochondrial alterations of mesothelial cells in the peritoneal tissue specimens and found that mitochondria in the sham-operation group appeared to be small elliptic/circular high electron-dense structures with clear and compact mitochondrial crista in TEM 2D sections. In the TEM section of the control vector group, there were a number of round/swollen structures present whose volume enlarged and electron density decreased, with mitochondrial crista of cytoplasm arefaction or destruction. However, in the TMIGD1-overexpression group, the swelling of mitochondria structures lighten, the volume of mitochondria structures decreased, and the electron

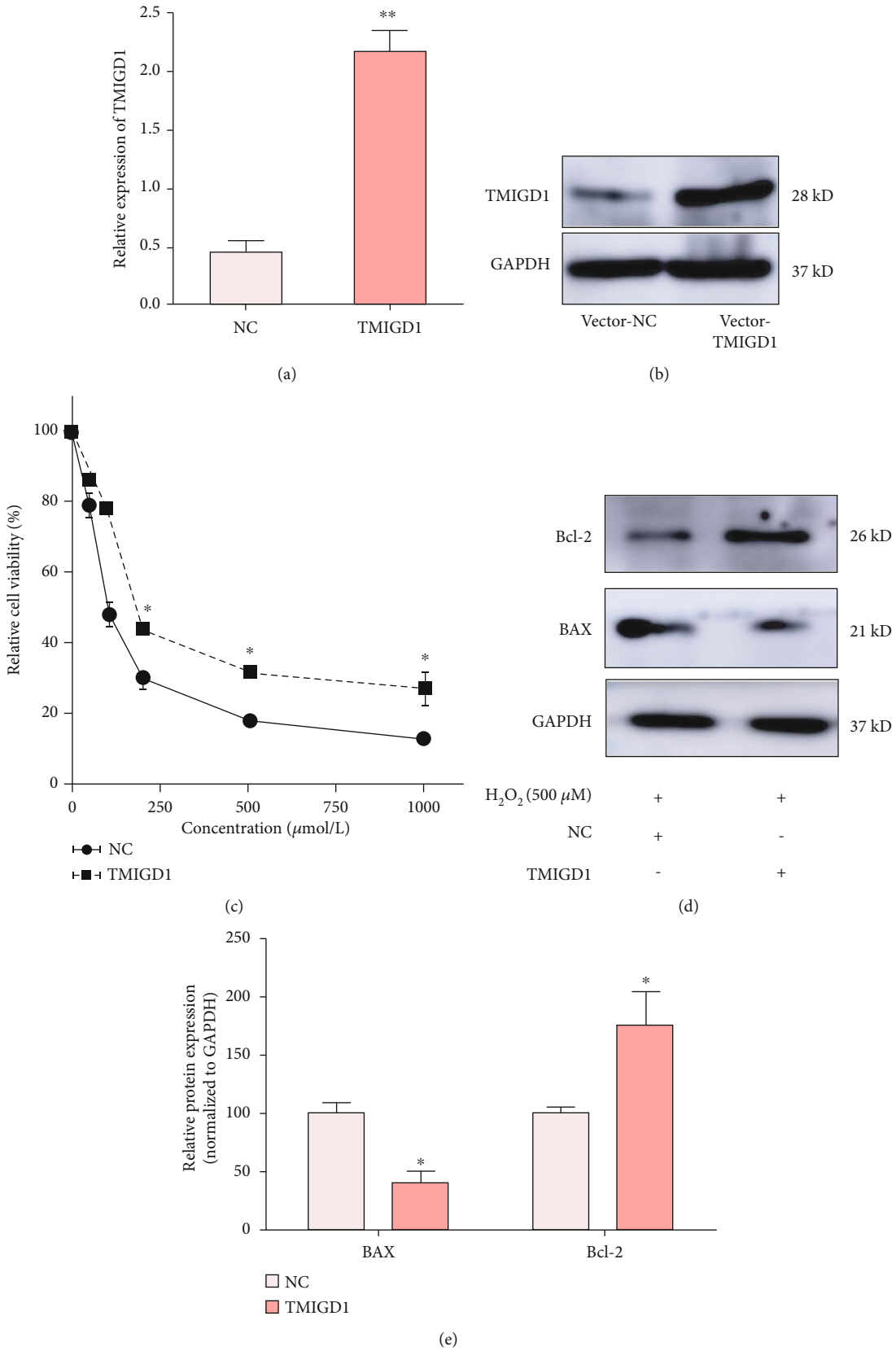

Figure 4: Continued.

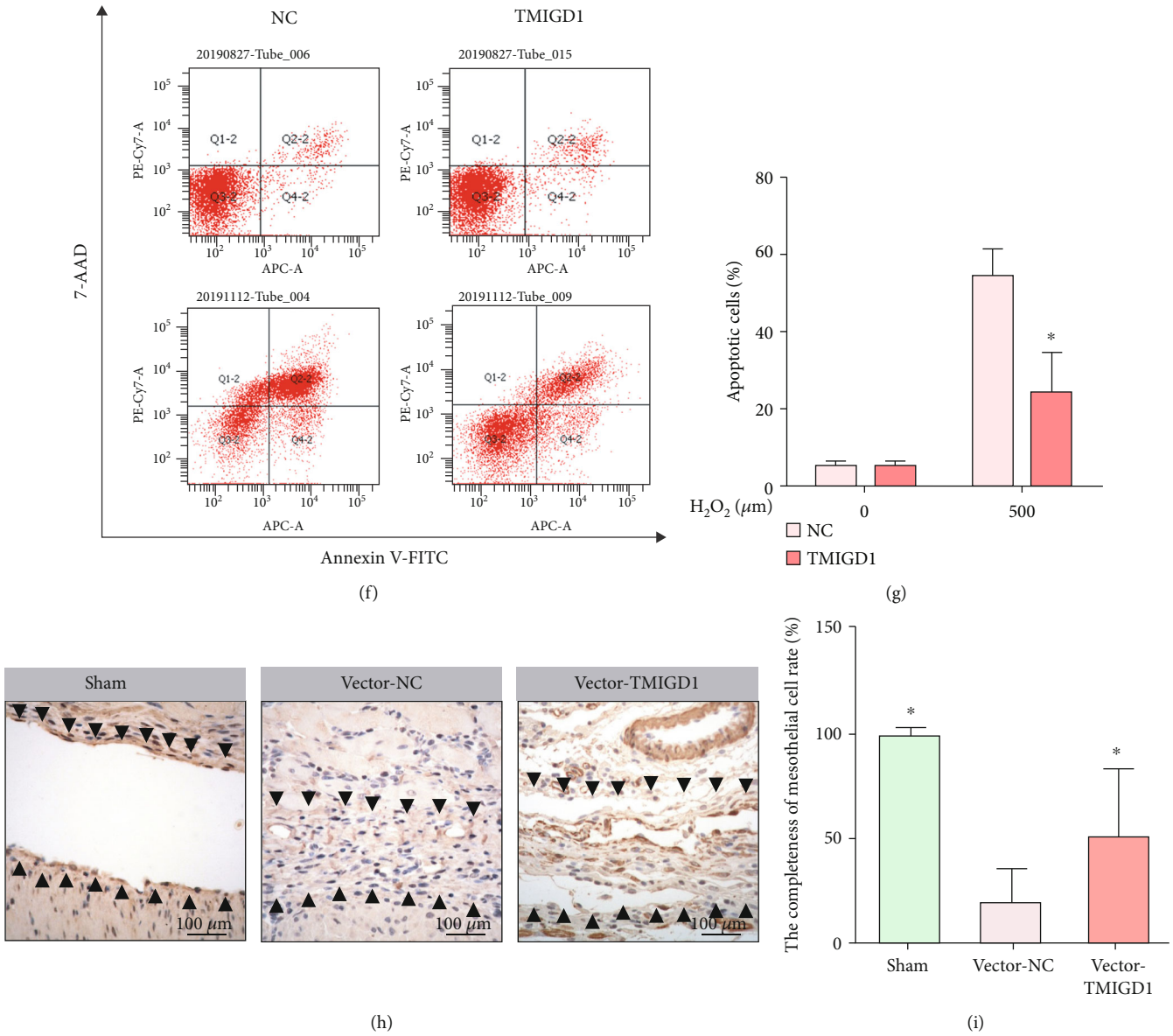

Figure 4: TMIGD1 protects mesothelial cells from oxidative stress injury. (a) qPCR identified TMIGD1 expression in the NC and TMIGD1-overexpressing cell lines. $N = 3$; **compared to the NC, $P < 0.01$, t test. (b) Western blotting identified TMIGD1 expression in the NC and TMIGD1-overexpressing cell lines; $N = 3$. (c) MTT assay showing the viability of mesothelial cells undergoing oxidative stress injury induced by different concentrations of H_2O_2 in the NC and TMIGD1-overexpressing cell lines. $N = 5$; *compared to the NC, $P < 0.05$; t test. (d) Western blotting showing the apoptosis-related protein expression of mesothelial cells undergoing oxidative stress injury induced by H_2O_2. $N = 3$. (e) Quantification of the apoptosis-related protein expression of mesothelial cells undergoing oxidative stress injury induced by H_2O_2. *Compared to the NC, $P < 0.05$; t test. (f) The apoptosis levels of mesothelial cells examined by flow cytometry transfected with a vector of NC or TMIGD1 overexpression and treated with H_2O_2 for 24 hours (mean ± SD). $N = 3$. (g) Quantification of the apoptosis levels of mesothelial cells examined by flow cytometry. *Compared to the NC treated with 500 μM of H_2O_2, $P < 0.05$; t test. (h) CK19 staining showing the severity of mesothelial cell injury in each group. $N = 10$; the black arrows mark the normal peritoneum or adhesion tissue; 400x magnification. (i) The completeness rate of peritoneal mesothelial cells in each group. $N = 10$; *compared to the vector-NC group, $P < 0.05$; abnormal distribution, Kruskal-Wallis test.

density increased compared to the control vector group. Mitochondrial morphologies similar to those of the sham-operation group constitute the majority (Figures 6(c) and 6(d)). In brief, it was shown that the TMIGD1-overexpression group had a significantly more regular mitochondrial morphology than the control vector group, which strikingly contributed to normal function.

To further verify our result, we performed IHF to detect the HSP60 (a mitochondrial chaperonin, marked mitochondria with normal structure and function) [21] in CK19-marked mesothelial cells and found that HSP60 was expressed higher in the sham and TMIGD1 overexpression group when compared to the control group (Figures 6(e) and 6(f)), suggesting that TMIGD1 overexpression reduced

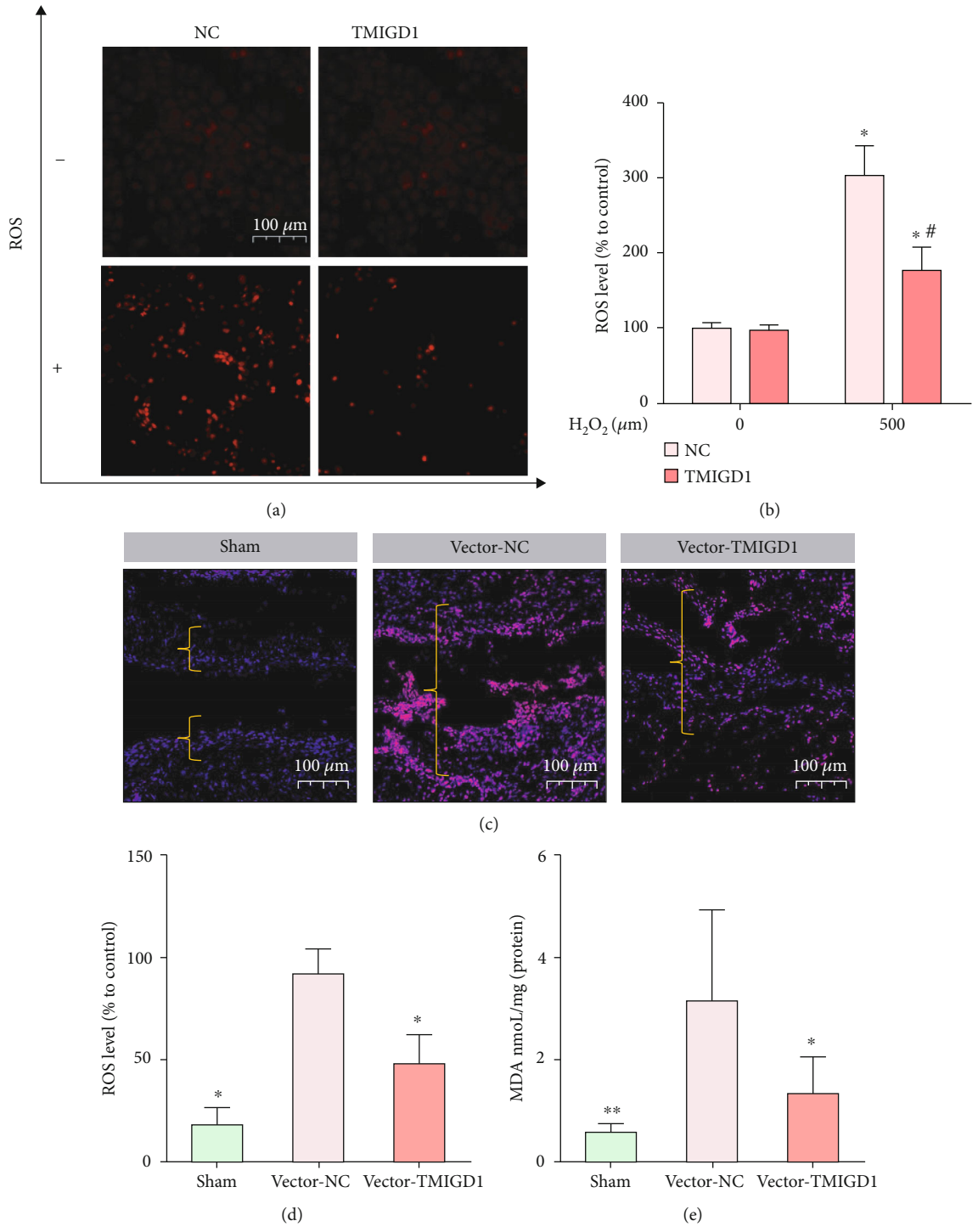

Figure 5: TMIGD1 alleviates oxidative stress in the mesothelial cells. (a) ROS levels in mesothelial cells transfected with a vector of NC or TMIGD1 overexpression and treated with H_2O_2 (mean ± SD). $N = 3$; 200x magnification. (b) Quantification of ROS levels in mesothelial cells transfected with a vector of NC or TMIGD1 overexpression and treated with H_2O_2. *Compared to mesothelial cells without the induction of H_2O_2, $P < 0.05$; #compared to the NC group with the induction of 500 μM of H_2O_2, $P < 0.05$; t test. (c) IHF showing the ROS intensity in each group; the yellow brackets show normal peritoneum or adhesion tissue. $N = 5$; 400x magnification. (d) Quantification of relative ROS intensity in each group. $N = 5$; *compared to the vector-NC group, $P < 0.05$; abnormal distribution, Kruskal-Wallis test. (e) The MDA level in each group. $N = 10$; *compared to the vector-NC group, $P < 0.05$; **compared to the vector-NC group, $P < 0.01$; abnormal distribution, Kruskal-Wallis test.

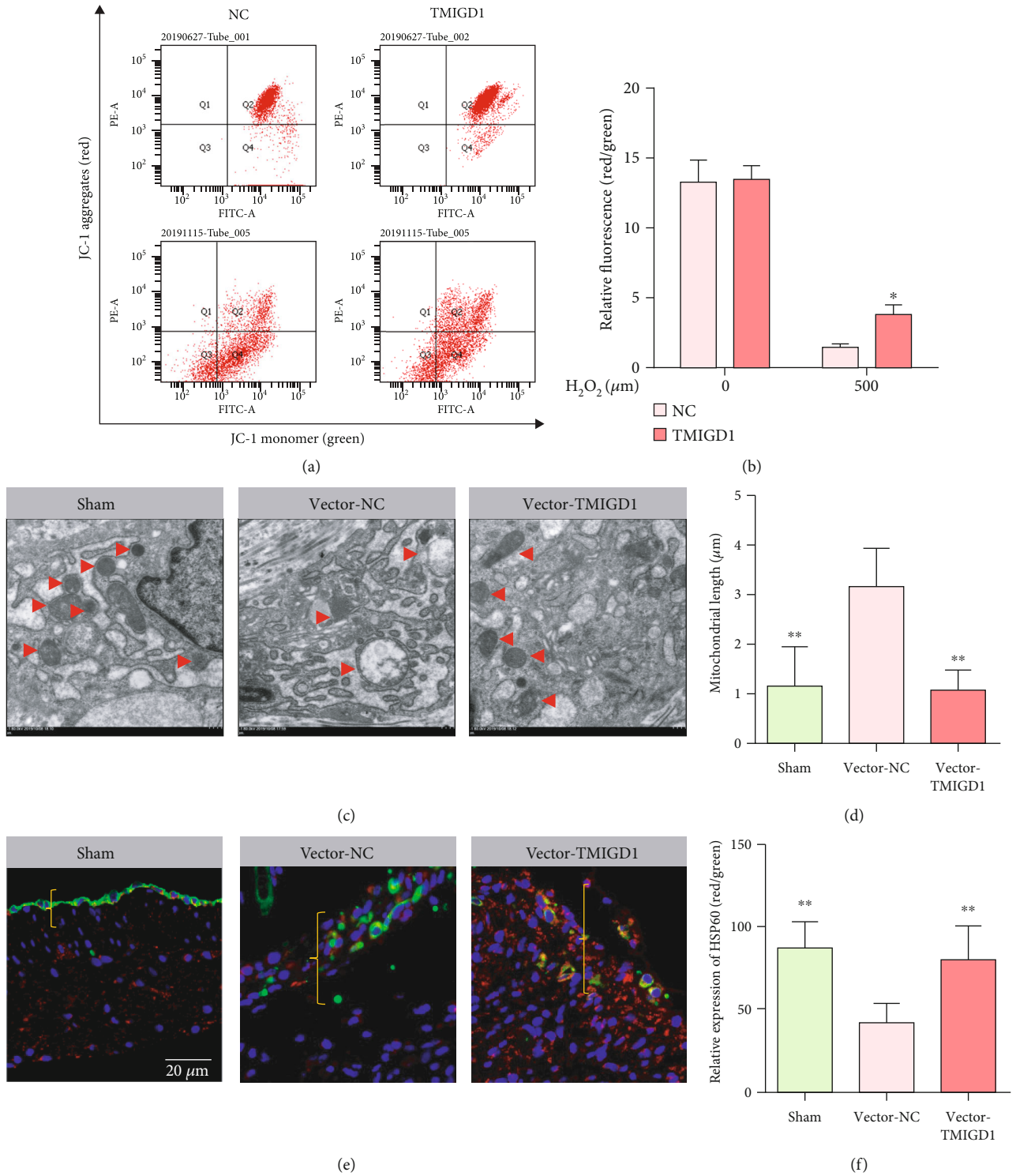

Figure 6: TMIGD1 alleviates oxidative stress by protecting the mitochondrial function of mesothelial cells. (a) JC-1 staining showing the mitochondrial membrane potential level of mesothelial cells. The flow cytometry scatter plot showing the distribution of cell populations with JC-1 aggregates (red) and JC-1 monomers (green); $N = 3$. (b) Histogram of the relative ratio of red to green fluorescence (mean ± SD). $N = 3$; *compared to the NC with the induction of H_2O_2, $P < 0.05$; t test. (c) Transmission electron microscopy scan of mitochondrial conditions in each group. $N = 3$; the red arrow marks mitochondria, 10000x magnification. (d) The mitochondrial length in each group. $N = 3$; **compared to the vector-NC, $P < 0.01$; abnormal distribution, Kruskal-Wallis test. (e) IHF staining of mitochondria in each group. $N = 10$; the red marked HSP60, the green marked the CK19, and the blue marked the DAPI; the yellow brackets show normal peritoneum or adhesion tissue; 10000x magnification. (f) Quantification of relative HSP60 expression in each group of (e). $N = 3$; **compared to the vector-NC, $P < 0.01$; abnormal distribution, Kruskal-Wallis test.

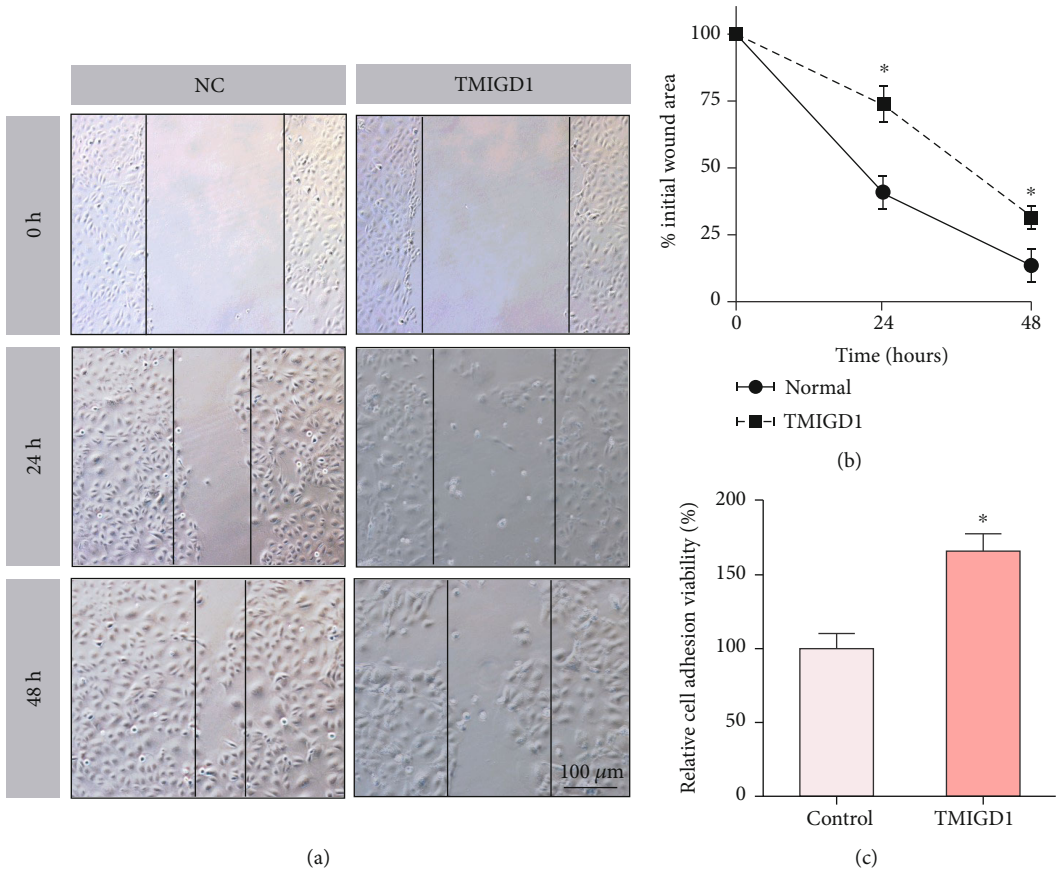

Figure 7: TMIGD1 promotes cell adhesion between mesothelial cells. (a) The cell scratch assay showing the ratio of cell migration in the NC and TMIGD1-overexpressing cell lines at different time points. $N = 5$; 100x magnification. (b) Quantitation of the wound scratch healing rate of NC- and TMIGD1-overexpressing cell lines at different time points. $N = 5$; *compared to the NC, $P < 0.05$; t test. (c) Cell adhesion viability in the NC and TMIGD1-overexpressing cell lines. $N = 5$; *compared to the NC, $P < 0.05$; t test.

the number of damaged mitochondria by ROS in adhesion formation.

Apparently, our findings provide insight into a new possible mechanism through which TMIGD1 can exert its function in preventing mesothelial cells from oxidative stress.

3.5. TMIGD1 Promotes Cell Adhesion between Mesothelial Cells. Cell adhesion plays a main role in cell injury and healing. TMIGD1 was predicted to act as a cell adhesion molecule in some previous studies.

To determine whether TMIGD1 promotes mesothelial cell adhesion, a cell scratch assay was performed. The migration rate of mesothelial cells of the TMIGD1-overexpressing cell line was significantly decreased compared with that of the control cell line (Figures 7(a) and 7(b)). To directly prove this, we assessed the adhesive capability of mesothelial cells and found that cell adhesion was enhanced between mesothelial cells of the TMIGD1-overexpressing cell line (Figure 7(c)). Taken together, TMIGD1 promotes cell adhesion between mesothelial cells.

4. Discussion

The peritoneum is a double-layered tissue that lines in the abdominal cavity and the surface of intra-abdominal organs, consisting of a continuous mesothelial monolayer and underlying connective tissue [22]. Abdominal adhesion formation is a process of damaged peritoneum healing [6], in which mesothelial cell healing plays a considerable role. Under inflammatory conditions, mesothelial cells undergo apoptosis, die, or transform into mesenchymal cells, all of which result in further damage to the peritoneum [7]. Thus, elucidating the underlying mechanism of mesothelial cell injury and healing is extremely essential to understand how postoperative abdominal adhesion forms. In this study, we showed that TMIGD1 protects mesothelial cells from H_2O_2-induced oxidative stress injury by protecting mitochondria. However, TMIGD1 expression is decreased in abdominal adhesion tissue. In addition, TMIGD1 promotes cell adhesion.

Oxidative stress is a regular process that occurs in the healing of a damaged peritoneum [23]. However, little is known about the molecular mechanism of oxidative stress injury of abdominal adhesion [11]. The peritoneal tissue microenvironment is proinflammatory after damage. Necrotic cells, clots, and recruited inflammatory cells release a large amount of ROS [24]. Although a certain concentration of ROS is beneficial for tissue healing, a large amount of ROS damages peritoneal mesothelial cells, which leads to mesothelial cell death and apoptosis and contributes to the transformation of mesothelial cells into mesenchymal cells [25, 26]. We have

demonstrated that TMIGD1 overexpression reduces ROS levels in mesothelial cells both in vitro and in vivo, which is useful to prevent ROS injury in mesothelial cells. In some previous studies, TMIGD1 was considered an ROS scavenger gene in kidney epithelial cells [14]; here, we showed that it has an identical effect in mesothelial cells. However, ROS produced by mesothelial cells count only a part of ROS produced in the inflammatory environment of adhesion. Follow-up experiments are needed to explore other specific mechanisms by which TMIGD1 reduces ROS levels in adhesive environments.

After injury or trauma, ischemia and hypoxia lead to the accumulation of large amounts of ROS. Under this ischemic condition, the source of ROS in cells mainly comes from remodeled mitochondrial electron transport chains (approximately 70% of ROS come from mitochondria); thus, protecting mitochondrial function is very important for reducing ROS [13]. It has been reported that TMIGD1 can localize to mitochondria [20]. Here, we demonstrated that TMIGD1-overexpressing mesothelial cells have significantly more normal mitochondria, suggesting that TMIGD1 inhibits mesothelial cell mitochondrial injury induced by ROS, which might be our new findings and partly illustrate the possible mechanism by which TMIGD1 reduces ROS.

The results presented here demonstrated that TMIGD1 promotes cell adhesion. Under the influence of inflammation, the injured mesothelial cells around the injured peritoneal area may be shed from the peritoneal tissue and die. Thus, promoting cell adhesion could modify the poor state and promote cells floating in the abdominal cavity to adhere to the peritoneal tissue, which may be beneficial to peritoneum healing [27]. Mesothelial cell healing of the peritoneum may originate from the migration of proliferating mesothelial cells at the edge of the incision, stem cells, transformation of macrophages, exfoliation and implantation of free-floating serosal cells in the abdominal cavity [4]. Promoting cell adhesion may be another mechanism by which TMIGD1 participates in peritoneal healing.

The limitation of this study is that we did not explore these results in human abdominal adhesion because of the extremely low expression of TMIGD1 in other human tissues except renal tissues. However, we must not exclude the possibility that local administration of TMIGD1 drugs may be effective for the prevention of adhesion formation. Our findings likely declare the possible mechanism of abdominal adhesion formation that contributes to the treatment and prevention of postoperative abdominal adhesion formation.

5. Conclusion

In conclusion, TMIGD1 protects mesothelial cells from oxidative stress injury by protecting their mitochondrial function, which is decreased in regular abdominal adhesion tissue. In addition, TMIGD1 enhances peritoneal mesothelial cell adhesion to promote healing.

Data Availability

The data used to support the findings of this study are available from the corresponding author upon request.

Disclosure

This manuscript has been previously made public only on a preprint server (https://www.researchsquare.com/article/rs-23239/v1) (doi:10.21203/rs.3.rs-23239/v1).

Conflicts of Interest

The authors declare that they have no conflicts of interest.

Authors' Contributions

Yunhua Wu and Enmeng Li contributed equally to this work.

Acknowledgments

This study was supported by the National Natural Science Foundation of China (No. 81970456 and No. 81770521), Shaanxi Key Research and Development Program (No. 2019SF-052), and the Clinical Innovation and Creativity Funds for Undergraduates of the 1st Affiliated Hospital of XJTU (Grant No. 20ZD06).

References

[1] H. Ellis, B. Moran, J. Thompson et al., "Adhesion-related hospital readmissions after abdominal and pelvic surgery: a retrospective cohort study," *The Lancet*, vol. 353, no. 9163, pp. 1476–1480, 1999.

[2] Z. Alpay, G. M. Saed, and M. P. Diamond, "Postoperative adhesions: from formation to prevention," *Seminars in Reproductive Medicine*, vol. 26, no. 4, pp. 313–321, 2008.

[3] N. Tabibian, E. Swehli, A. Boyd, A. Umbreen, and J. H. Tabibian, "Abdominal adhesions: a practical review of an often overlooked entity," *Annals of Medicine and Surgery*, vol. 15, pp. 9–13, 2017.

[4] W. Arung, M. Meurisse, and O. Detry, "Pathophysiology and prevention of postoperative peritoneal adhesions," *World Journal of Gastroenterology*, vol. 17, no. 41, pp. 4545–4553, 2011.

[5] S. E. Mutsaers, "Mesothelial cells: their structure, function and role in serosal repair," *Respirology*, vol. 7, no. 3, pp. 171–191, 2002.

[6] R. Beyene, S. Kavalukas, and A. Barbul, "Intra-abdominal adhesions: anatomy, physiology, pathophysiology, and treatment," *Current Problems in Surgery*, vol. 52, no. 7, pp. 271–319, 2015.

[7] L. Aroeira, A. Aguilera, J. Sánchez-Tomero et al., "Epithelial to mesenchymal transition and peritoneal membrane failure in peritoneal dialysis patients: pathologic significance and potential therapeutic interventions," *Journal of the American Society of Nephrology : JASN*, vol. 18, no. 7, pp. 2004–2013, 2007.

[8] K. Kawanishi and K. Nitta, "Cell sheet-based tissue engineering for mesothelial cell injury," *Contributions to Nephrology*, vol. 185, pp. 66–75, 2015.

[9] V. Liakopoulos, S. Roumeliotis, X. Gorny, T. Eleftheriadis, and P. R. Mertens, "Oxidative stress in patients undergoing peritoneal dialysis: a current review of the literature," *Oxidative Medicine and Cellular Longevity*, vol. 2017, Article ID 3494867, 14 pages, 2017.

[10] L. B. Rahul Saini, N. S. Hadke, B. C. Koner, R. Singh, and P. Lal, "Evaluation of oxidative stress response in endoscopic and lichtenstein hernia repair: a randomized control study," *International Journal of Abdominal Wall and Hernia Surgery*, vol. 3, no. 4, pp. 148–154, 2020.

[11] A. Awonuga, J. Belotte, S. Abuanzeh, N. M. Fletcher, M. P. Diamond, and G. M. Saed, "Advances in the pathogenesis of adhesion development: the role of oxidative stress," *Reproductive Sciences*, vol. 21, no. 7, pp. 823–836, 2014.

[12] A. Agarwal and S. Allamaneni, "Role of free radicals in female reproductive diseases and assisted reproduction," *Reproductive Biomedicine Online*, vol. 9, no. 3, pp. 338–347, 2004.

[13] D. Fuhrmann and B. Brüne, "Mitochondrial composition and function under the control of hypoxia," *Redox Biology*, vol. 12, pp. 208–215, 2017.

[14] E. Arafa, P. Bondzie, K. Rezazadeh et al., "Tmigd1 is a novel adhesion molecule that protects epithelial cells from oxidative cell injury," *The American Journal of Pathology*, vol. 185, no. 10, pp. 2757–2767, 2015.

[15] R. Meyer, X. Zou, M. Ali et al., "Tmigd1 acts as a tumor suppressor through regulation of p21cip1/p27kip1 in renal cancer," *Oncotarget*, vol. 9, no. 11, pp. 9672–9684, 2018.

[16] J. Bi, S. Zhang, Z. du et al., "Peripheral serotonin regulates postoperative intra-abdominal adhesion formation in mice," *Scientific Reports*, vol. 7, no. 1, article 10001, 2017.

[17] P. Sandoval, J. Jiménez-Heffernan, G. Guerra-Azcona et al., "Mesothelial-to-mesenchymal transition in the pathogenesis of post-surgical peritoneal adhesions," *The Journal of Pathology*, vol. 239, no. 1, pp. 48–59, 2016.

[18] Y. Wu, G. Wei, J. Yu et al., "Danhong injection alleviates postoperative intra-abdominal adhesion in a rat model," *Oxidative Medicine and Cellular Longevity*, vol. 2019, Article ID 4591384, 11 pages, 2019.

[19] G. Wei, Y. Wu, Q. Gao et al., "Gallic acid attenuates postoperative intra-abdominal adhesion by inhibiting inflammatory reaction in a rat model," *Medical Science Monitor*, vol. 24, pp. 827–838, 2018.

[20] C. Hartmann, Y. Schwietzer, D. Kummer et al., "The mitochondrial outer membrane protein synj2bp interacts with the cell adhesion molecule tmigd1 and can recruit it to mitochondria," *BMC Molecular and Cell Biology*, vol. 21, no. 1, p. 30, 2020.

[21] B. Bukau and A. L. Horwich, "The hsp70 and hsp60 chaperone machines," *Cell*, vol. 92, no. 3, pp. 351–366, 1998.

[22] A. Maciver, M. McCall, and A. James Shapiro, "Intra-abdominal adhesions: cellular mechanisms and strategies for prevention," *International Journal of Surgery*, vol. 9, no. 8, pp. 589–594, 2011.

[23] P. Koninckx, V. Gomel, A. Ussia, and L. Adamyan, "Role of the peritoneal cavity in the prevention of postoperative adhesions, pain, and fatigue," *Fertility and Sterility*, vol. 106, no. 5, pp. 998–1010, 2016.

[24] Z. Rabbani, J. Mi, Y. Zhang et al., "Hypoxia inducible factor 1alpha signaling in fractionated radiation-induced lung injury: role of oxidative stress and tissue hypoxia," *Radiation Research*, vol. 173, no. 2, pp. 165–174, 2010.

[25] M. Cano Sanchez, S. Lancel, E. Boulanger, and R. Neviere, "Targeting oxidative stress and mitochondrial dysfunction in the treatment of impaired wound healing: a systematic review," *Antioxidants*, vol. 7, no. 8, p. 98, 2018.

[26] S. ten Raa, M. van den Tol, W. Sluiter, L. J. Hofland, C. van Eijck, and H. Jeekel, "The role of neutrophils and oxygen free radicals in post-operative adhesions," *The Journal of Surgical Research*, vol. 136, no. 1, pp. 45–52, 2006.

[27] S. Kitamura, N. Horimoto, K. Tsuji et al., "The selection of peritoneal mesothelial cells is important for cell therapy to prevent peritoneal fibrosis," *Tissue Engineering Part A*, vol. 20, no. 3-4, pp. 529–539, 2014.

Hindawi
Oxidative Medicine and Cellular Longevity
Volume 2021, Article ID 4158495, 11 pages
https://doi.org/10.1155/2021/4158495

Research Article

OC-STAMP Overexpression Drives Lung Alveolar Epithelial Cell Type II Senescence in Silicosis

Tian Li[1], **Xin-yu Yang**[1], **Ding-jie Xu**[2], **Zi-yi Gao**[3], **Yi-bing Gao**[3], **Fu-yu Jin**[3], **Ya-qian Li**[3], **Shu-peng Liu**[1], **Shi-feng Li**[3], **Xue-min Gao**[3], **Wen-chen Cai**[3], **Na Mao**[3], **Zhong-qiu Wei**[1], **He-liang Liu**[3], **Ying Sun**[1], **Fang Yang**[3], **and Hong Xu**[1,3]

[1]*Basic Medical College, Hebei Key Laboratory for Chronic Diseases, North China University of Science and Technology, Tangshan, Hebei Province 063210, China*
[2]*Traditional Chinese Medicine College, North China University of Science and Technology, Tangshan, Hebei Province 063210, China*
[3]*School of Public Health, Hebei Key Laboratory for Organ Fibrosis Research, North China University of Science and Technology, Tangshan, Hebei Province 063210, China*

Correspondence should be addressed to Hong Xu; xuhong@ncst.edu.cn

Received 11 June 2021; Accepted 27 July 2021; Published 14 August 2021

Academic Editor: Chaoliang Tang

Cellular senescence has been considered an important driver of many chronic lung diseases. However, the specific mechanism of cellular senescence in silicosis is still unknown. In the present study, silicotic rats and osteoclast stimulatory transmembrane protein (*Ocstamp*) overexpression of MLE-12 cells were used to explore the mechanism of OC-STAMP in cellular senescence in alveolar epithelial cell type II (AEC2). We found an increasing level of OC-STAMP in AEC2 of silicotic rats. Overexpression of *Ocstamp* in MLE-12 cells promoted epithelial-mesenchymal transition (EMT), endoplasmic reticulum (ER) stress, and cellular senescence. Myosin heavy chain 9 (MYH9) was a potential interacting protein of OC-STAMP. Knockdown of *Ocstamp* or *Myh9* inhibited cellular senescence in MLE-12 cells transfected with pcmv6-*Ocstamp*. Treatment with 4-phenylbutyrate (4-PBA) to inhibit ER stress also attenuated cellular senescence *in vitro* or *in vivo*. In conclusion, OC-STAMP promotes cellular senescence in AEC2 in silicosis.

1. Introduction

Silicosis is a chronic occupational lung disease caused by long-term inhalation of free crystalline silica dust and is characterized by silicotic lesions and progressive massive fibrosis [1]. Injury, loss, and disruption of alveolar epithelial cell type II (AEC2) play a central role in pulmonary fibrosis due to its critical function in alveolar niche homeostasis through the production of pulmonary surfactant and as progenitor cells to self-renew and transdifferentiate into AEC1 [2].

Cellular senescence is now considered an important driving mechanism for chronic lung diseases, particularly chronic obstructive pulmonary disease (COPD) and idiopathic pulmonary fibrosis (IPF) [3]. Cellular senescence occurs due to replicative and stress-related senescence with activation of p53 and $p16^{INK4a}$, respectively, leading to activation of $p21^{CIP1}$ and cell cycle arrest [3, 4]. As silicosis is an age-related and chronic occupational lung disease, silicotic patients showed significantly shorter and telomerase gene variants compared with healthy controls in response to exposure to silica [5]. Our previous study showed increasing levels of p21, cleaved caspase-3, and phosphorylated histone H_2AX (γH_2AX) in rats exposed to inhaled silica over time [6]. We also found that silica, matrix stiffening, or their combination triggered DNA damage and replication stress in AEC2 [7]. Therefore, cellular senescence may be a key contributor to silicosis, but the exact mechanism is still unknown.

In our preliminary study, we found that the receptor activator of nuclear factor kappa-B ligand (RANKL) signaling pathway, a classic signaling pathway for regulating osteoclast

differentiation, is activated in the lungs of silicotic rats, and it promoted lung inflammation and proteolytic phenotype of macrophages [8]. Interestingly, we found that the expression of osteoclast stimulatory transmembrane protein (OC-STAMP) was found in AEC2, unlike the RANKL and RANK expression in lung macrophages. Several studies have documented that OC-STAMP has an important role in cell fusion in osteoclast precursor cells and foreign body giant cells to exert function in pathogenic bone resorption [9, 10]. To date, specific knowledge about the role and regulation of OC-STAMP remains limited [11].

Furthermore, endoplasmic reticulum (ER) stress and the unfolded protein response (UPR) have been linked to lung fibrosis through regulation of AEC apoptosis, epithelial-mesenchymal transition (EMT), myofibroblast differentiation, and M2 macrophage polarization [12]. ER stress can be targeted to improve the inflammatory and cellular senescence in chronic respiratory diseases [13]. Therefore, the present study examined the molecular mechanism of ER stress and cellular senescence crosstalk regulated by OC-STAMP overexpression.

2. Methods

2.1. Silicosis Model. Wistar rats (3 w old) were employed in this study. A silicosis model was induced by inhalation of $50 \pm 10\,\mu g/m^3$ of silica (s5631; Sigma-Aldrich, St. Louis, MO, USA; ground and then heated at 180°C for 6 h) for 32 w and inhalation of pure air as the control group. To inhibit ER stress, rats received 4-phenylbutyrate (4-PBA, P21005, Sigma-Aldrich) at 100 mg/Kg once daily from 24 w until 32 w [1]. All animal protocols were reviewed and approved by the Committee on the Ethics of North China University of Science and Technology (LX2019033), and they complied with the US National Institutes of Health Guide for the Care and Use of Laboratory Animals [14].

2.2. Cell Culture and Treatment. The MLE-12 cell line was obtained from the Chinese Academy of Sciences cell library (Shanghai, China). Cells were plated in $6\,cm^2$ dishes and transfected with pCMV6-Entry (PS100001, OriGene Technologies Inc., MD, USA) and pCMV6-*Ocstamp* (MR207985, OriGene), or they were transfected with small interfering RNAs (siRNAs) targeted against *Ocstamp* and *Myh9* (RiboBio, Guangzhou, China), and treated with 50 μg/mL silica or 1 mmol/L 4-PBA [1]. The target sequences of *Ocstamp*-siRNAs were CAAACGTCTTAGGCAAGT, TGGACTTCATCCTCTTCGT, and CTCAGAAGTTACCA CTGT, and the target sequences of *Myh9*-siRNAs were GCTGCCAAGAAGTTGGTAT, CCATGAATTATGGGCAT, and GCAGAACATCCAGGAACTT.

2.3. Immunohistochemistry and Immunofluorescence Staining. Immunohistochemical staining was performed using published protocols [15] with antibodies directed against OC-STAMP (1 : 100 dilution, 2051. PB1; FabGennix Inc., Frisco, TX, USA), ABCA3 (1 : 200 dilution, ab24751, Abcam, Cambridge, UK), P21 (1 : 100 dilution, ab109520, Abcam, Cambridge, UK), α-smooth muscle actin (α-SMA, 1 : 200 dilution, ab32575, Abcam, Cambridge, UK), Proliferating Cell Nuclear Antigen (PCNA, 1 : 100 dilution, GTX100539, Genetex, Irvine, CA, USA), and Phospho-PERK (p-PERK, 1 : 100 dilution, DF7576, Affinity, Cincinnati, OH, USA) at a concentration of 1 : 200. Immunofluorescence staining was performed using published protocols with antibodies directed against ABCA3/OC-STAMP, p21/α-SMA, and p-PERK at a concentration of 1 : 200.

2.4. Western Blot. Western blot was performed using published protocols [16] with antibodies directed against OC-STAMP (2051. PB1; FabGennix Inc.), collagen type I (Col I) (ab34710, Abcam), α-SMA (ab32575, Abcam), E-cadherin (ab76055, Abcam), N-cadherin (ARG23870,Arigo), p-Smad2/3 (8828 s, Cell Signaling Technology, MA, USA), Smad2/3 (5678, Cell Signaling Technology), Phospho ataxia telangiectasia and Rad3-related protein (p-ATR, DF7512, Affinity), Phospho ataxia telangiectasia mutated (p-ATM, AF8410, Affinity), p-p53-S15 (AP0083, Abclonal), p21 (ab109520, Abcam), p16 (A0262, Abclonal), p-PERK (DF7576, Affinity), p-IRE1α (ab48187, Abcam), Phospho-nuclear factor-kappaB (p-NF-κB, ARG51516, Arigo), transforming growth factor-β1 (TGF-β1, ARG56429, Arigo), TGF-β receptor I (TGFβR1, A16396, Abclonal), and TGF-β receptor II (TGFβR2, ARG59501, Arigo) at a concentration of 1 : 1000.

2.5. Coimmunoprecipitation (CoIP). The interaction of OC-STAMP with Myh9 was evaluated by Co-IP. The cells were lysed in RIPA (R0020, Solarbio Life Sciences, Beijing, China) buffer containing 1% protease inhibitors. Then, 30 μL of sepharose beads (FO115, Santa Cruz Biotechnology, Santa Cruz, CA, USA) and cell lysates (2 g/L) were mixed to a volume of 400 μL and incubated for 2 h at 4°C on a shaker for preclearing. The clear supernatant was incubated overnight with anti-Myh9, anti-IgG antibody, and Protein A sepharose at 4°C. The beads were collected and washed 3 times with PBS before being boiled in a 2× loading buffer at 95°C for 5 min. Western blotting was used to analyse the CoIP results.

2.6. Real-Time Quantitative Polymerase Chain Reaction (PCR) Analysis. Reverse transcription (K1622, Thermo Scientific, USA or ZR102, ZOMANBIO, China) was performed according to company recommendations. Amplification by real-time PCR was carried out using the 2× SYBR qPCR Mix (ZF102, ZOMANBIO, China) system [17]. The sequence details were as follows: (1) Rat *Oc-stamp*: Forward: Forward: TGCTGGGCTGTGTTACTGAG, Reverse: GTGT GAAGTCGGAAGGCTGA; (2) Rat *Gapdh*, Forward: GGTG AAGGTCGGTGTGAACG, Reverse: CTCGCTCCTGGAAG ATGGTG. The results were calculated via the $2^{-\triangle\triangle CT}$ method.

2.7. Statistical Analysis. Statistical analyses were performed using SPSS 20.0 software (IBM Corp., Armonk, NY, USA). Two-group comparisons were made using unpaired Student's *t*-test, and multiple-group comparisons were made using one-way analysis of variance followed by Tukey's post hoc test. Statistical significance was achieved when $P < 0.05$ at a 95% confidence interval.

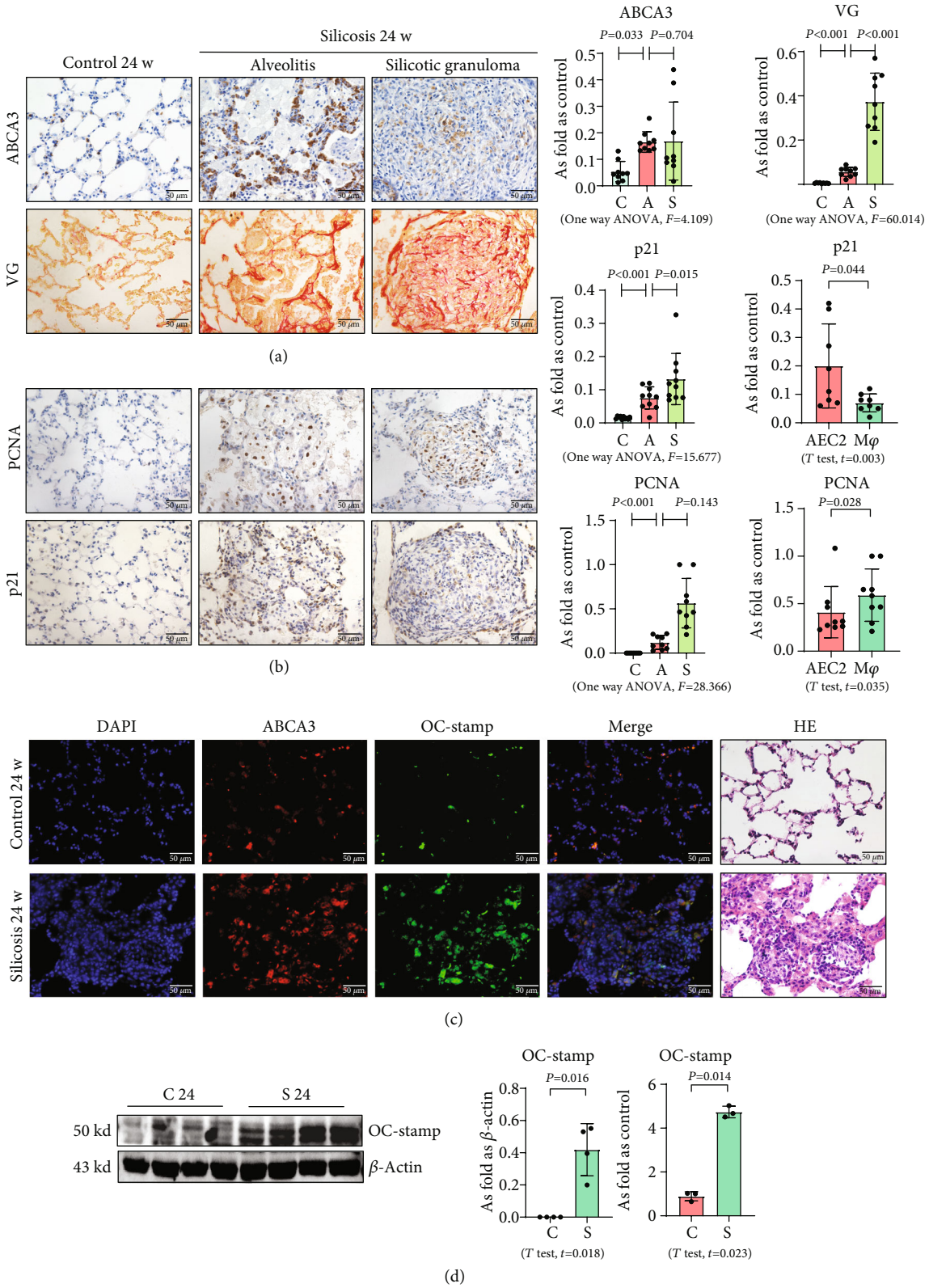

Figure 1: An increased level of OC-STAMP in silicotic rats. (a) Positivity of ABCA3 and collagen in silicotic rats; data are presented as the mean ± SD; $n = 8$ per group. (b) Positivity of p21 and PCNA in silicotic rats; data are presented as the mean ± SD; $n = 8$ per group. (c) Coexpression of ABCA3 and OC-STAMP in silicotic rats; (d) protein and mRNA levels of OC-STAMP in silicotic rats. Data are presented as the mean ± SD; $n = 3$ per group.

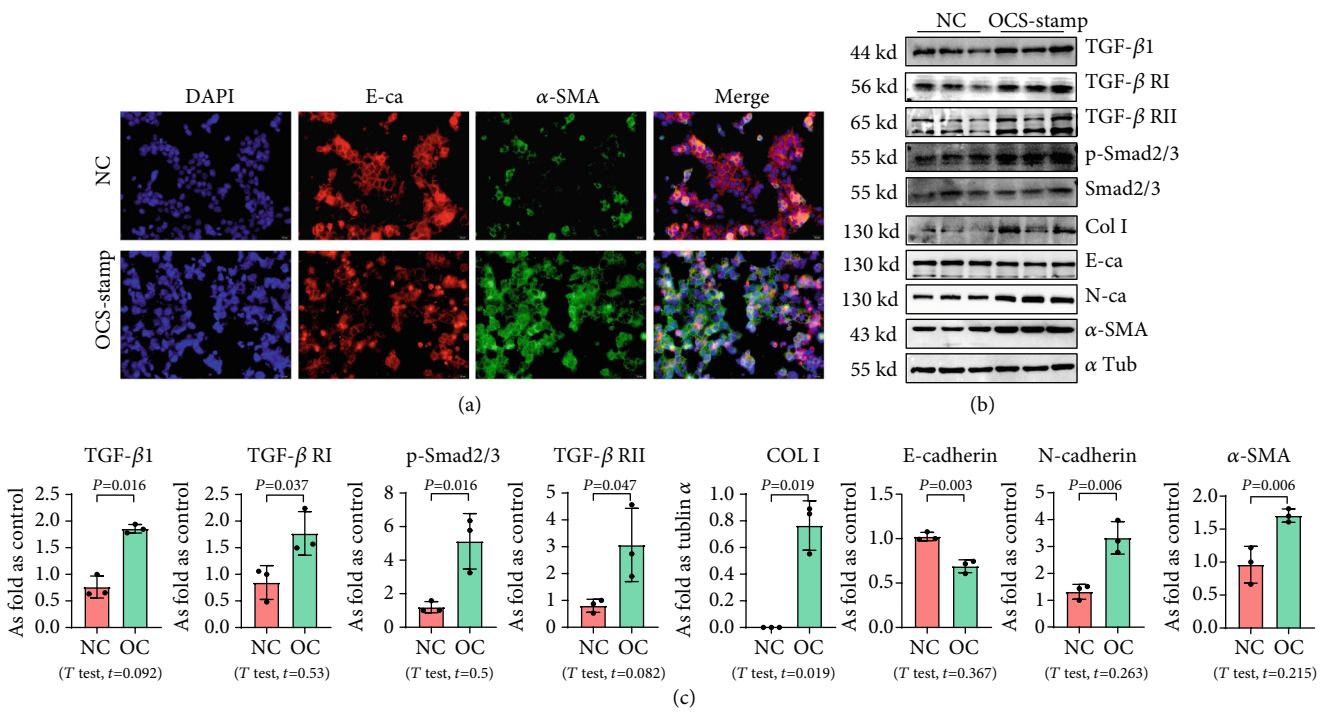

FIGURE 2: Overexpression of OC-STAMP promotes EMT in MLE-12 cells. (a) Coexpression of E-cadherin and α-SMA in MLE-12 cells. Bar = 50 μm; (b) levels of TGF-β1, TGF-β1 R1, TGF-β1 R2, p-Smad2/3, Col I, E-cadherin, N-cadherin, and α-SMA in MLE-12 cells, measured by Western blotting. Data are presented as the mean ± SD; $n = 3$ per group.

3. Results

3.1. Silica Increases the Level of OC-STAMP in a Silicotic Model. Silicotic rats were investigated in the present study, and our published reports have well documented that inhalation of silica promotes macrophage activation, myofibroblast differentiation, and collagen deposition [1, 6]. First, we used ABCA3 to identify AEC2 in silicotic rat lungs, and we found that hyperplastic AEC2 can be observed in silicotic lesions, inflammatory alveoli, and lymph nodes (Figure 1(a)). Although AEC2 in silicotic rats showed a "hyperplastic" phenotype, most of these cells showed expression of p21 but not of PCNA (Figures 1(b) and 1(c)). These results suggested that an increased level and activation of AEC2 showed a cellular senescence phenotype in rats exposed to silica. We also found coexpression of ABCA3 and OC-STAMP in silicotic rats (Figure 1(d)). The protein and mRNA levels of OC-STAMP were also increased in silicotic rats (Figure 1(d)).

3.2. Overexpression of OC-STAMP Promotes EMT in MLE-12 Cells. For exploring the effect of OC-STAMP on AEC2, MLE-12 cells were transfected with the pCMV6-*Ocstamp* plasmid. As shown in Figure 2, the major profibrotic signaling pathways were measured in OC-STAMP-overexpressing cells. IF staining showed increased expression of α-SMA, as well as decreased expression of E-cadherin in MLE-12 cells transfected with pCMV6-*Ocstamp*. Overexpression of OC-STAMP also increased the levels of TGF-β1, TGF-β1 receptors, p-Smad, col I, N-cadherin, and α-SMA. The expression of E-cadherin was reduced in MLE-12 cells transfected with pCMV6-Ocstamp.

3.3. Overexpression of OC-STAMP Promotes ER Stress and Cellular Senescence in MLE-12 Cells. Transfection with pCMV6-Ocstamp promoted ER stress in MLE-12 cells (Figure 3(a)). As shown in Figure 3(b), overexpression of OC-STAMP induced positive staining of SA-β-gal in MLE-12 cells. IF staining showed increased positive expression of p21 and reduced expression of PCNA in MLE-12 cells transfected with pCMV6-*Ocstamp* (Figure 3(c)). The levels of p-ATM, p-ATR, p-p53, p21, and p16 were also increased in MLE-12 cells transfected with pCMV6-*Ocstamp* (Figure 3(d)). Furthermore, silencing of *Ocstamp* inhibited cellular senescence and ER stress in MLE-12 cells transfected with *Ocstamp* (Figure 4).

3.4. Overexpression of OC-STAMP Induces Insensitivity in Silica-Induced MLE-12 Cells. First, the cell apoptosis in MLE-12 cells treated with or without 50 μg/mL silica was measured by flow cytometry; silica did not exhibit cytotoxicity in MLE-12 cells at a concentration of 50 μg/mL (Figure S1). As shown in Figure 5, the pCMV6-Entry and pCMV6-*Ocstamp* cells were treated with 50 μg/mL silica. Silica promoted cellular senescence in MLE-12 cells transfected with pCMV6-Entry, but it did not increase the activation of cellular senescence signaling in pCMV6-*Ocstamp* cells. Also, silica treatment did not change the EMT-related proteins in MLE-12 cells transfected with pCMV6-*Ocstamp*.

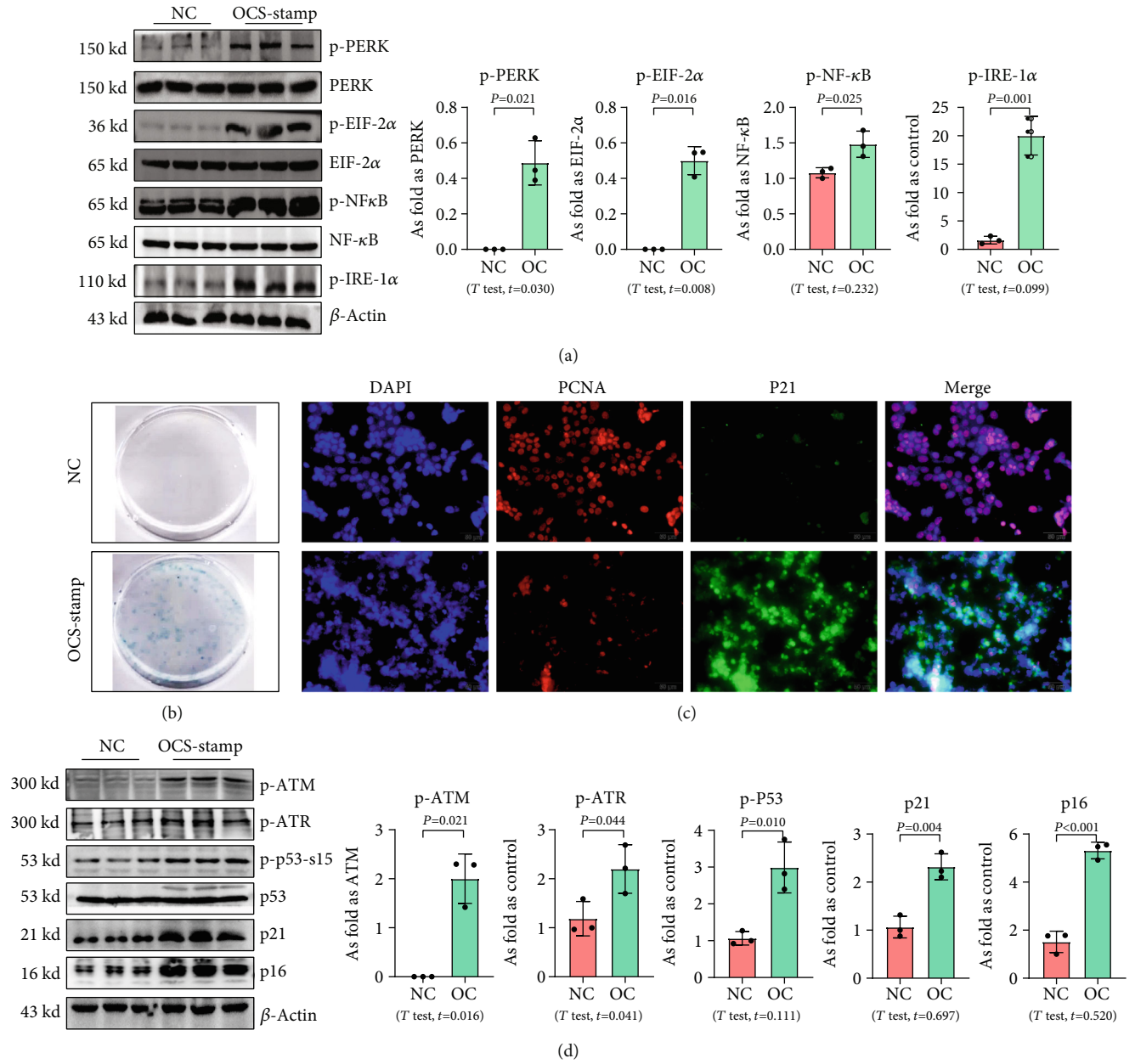

FIGURE 3: Overexpression of OC-STAMP promotes ER stress and cellular senescence in MLE-12 cells. (a) Levels of p-PERK, p-EIF 2α, p-NF-κB, and p-IRE 1α in MLE-12 cells, measured by Western blotting. Data are presented as the mean ± SD; $n = 3$ per group; (b) SA-β-gal staining; (c) coexpression of PCNA and p21 in MLE-12 cells. Bar = 50 μm; (d) levels of p-ATM, p-ATR, p-p53, p21, and p16 in MLE-12 cells measured by Western blotting. Data are presented as the mean ± SD; $n = 3$ per group.

We used 4-PBA to explore the role of ER stress in cellular senescence induced by OC-STAMP overexpression or silica, and we found that treatment with 4-PBA inhibited the activation of senescence signaling in silica-induced or OC-STAMP overexpressing MLE-12 cells (Figures 6 and 7).

3.5. OC-STAMP Interacts with MYH9 to Promote Cellular Senescence. To explore the effect of OC-STAMP in MLE-12 cells, we screened for potential OC-STAMP interacting proteins. We performed CoIP using an anti-OC-STAMP antibody followed by LC-MS/MS assay. MYH9 was identified as a potential OC-STAMP interacting protein. As shown in Figure 8, Western blot analysis of the precipitates with an OC-STAMP antibody indicated OC-STAMP CoIP with MYH9. Downregulated expression of MYH9 with siRNA also inhibited senescence signaling in *Ocstamp*-overexpressing MLE12 cells.

3.6. Inhibition of ER Stress Attenuates Cellular Senescence in Silicotic Rats. In the present study, the established model [1] was used to explain the effect of ER stress on cellular senescence in silicotic rats. Treatment with 4-PBA attenuated

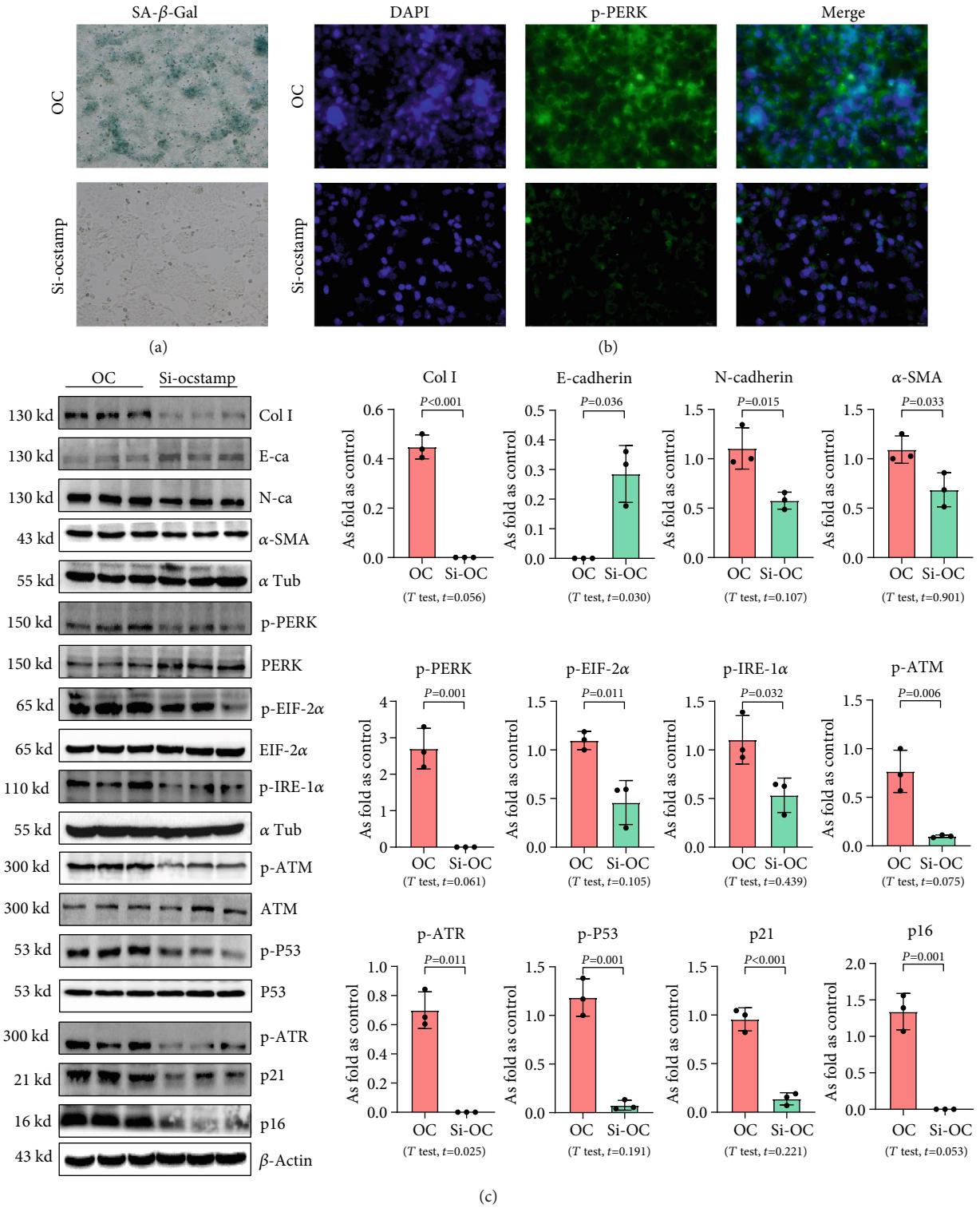

Figure 4: Knockdown of OC-STAMP inhibits EMT, ER stress, and cellular senescence in MLE-12 cells. (a) SA-β-gal staining; (b) expression of p-PERK in MLE-12 cells observed by IF staining, Bar = 50 μm; (c) levels of Col I, E-cadherin, N-cadherin, α-SMA, p-PERK, p-EIF 2α, p-IRE-1α, p-ATM, p-ATR, p-p53, p21, and p16 in MLE-12 cells, measured by Western blotting. Data are presented as the mean ± SD; n = 3 per group.

the activation of senescence signaling, collagen deposition, and high expression of OC-STAMP in silicotic rats, which suggested that blocking of ER stress inhibited cellular senescence in pulmonary fibrosis induced by silica (Figure 9).

4. Discussion

Hypertrophy and hyperplasia of AEC2 is one of the prominent features of silicosis and is consistently associated with

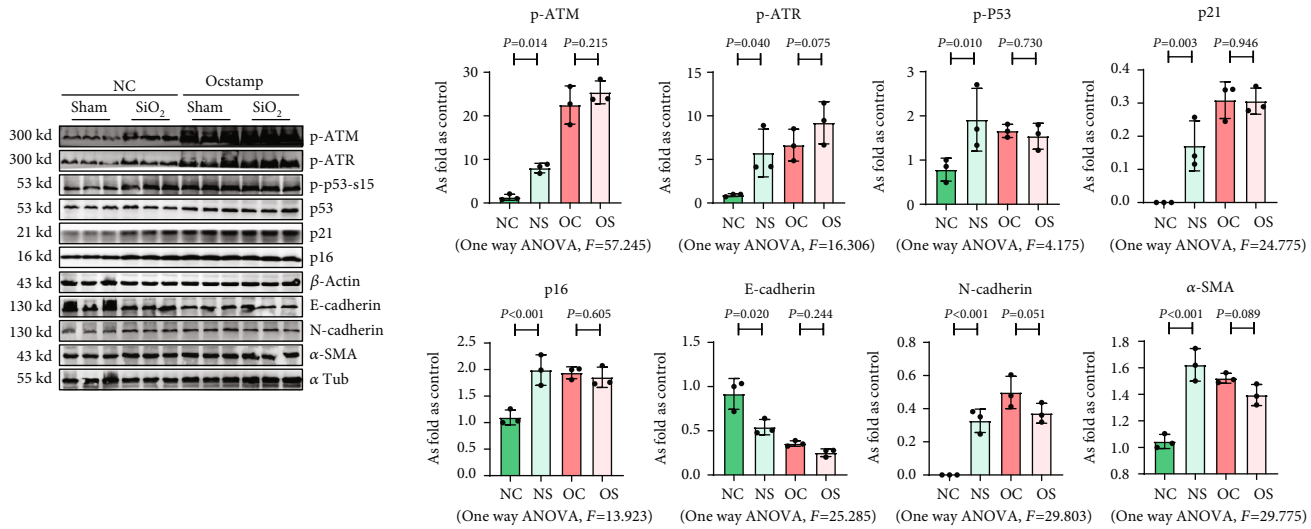

FIGURE 5: Overexpression of OC-STAMP induces insensitivity in silica-induced MLE-12 cells. Levels of p-ATM, p-ATR, p-p53, p21, p16, E-cadherin, N-cadherin, α-SMA in NC, and OC MLE-12 cells treated with or without silica, measured by Western blotting. Data are presented as the mean ± SD; $n = 3$ per group.

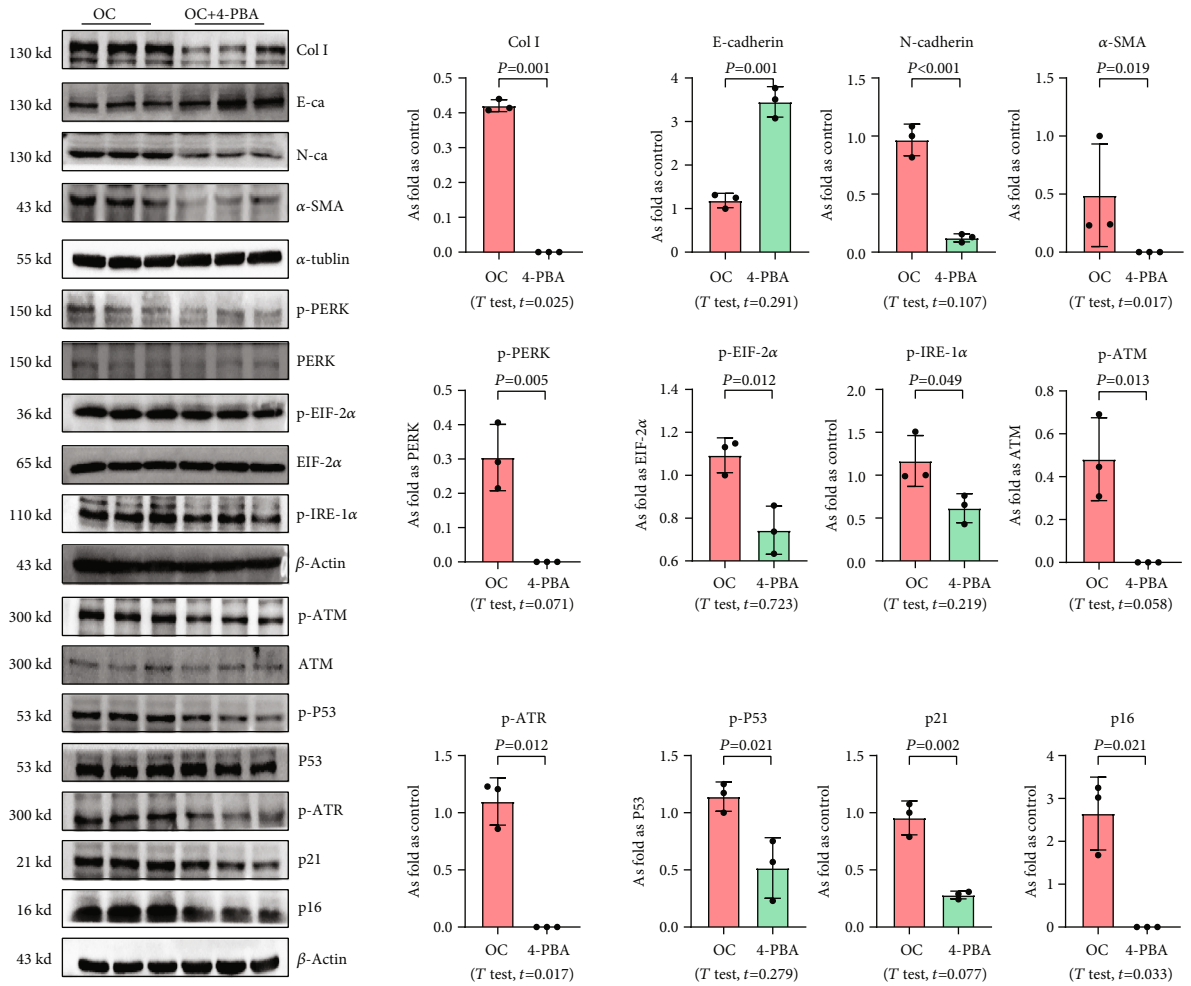

FIGURE 6: 4-PBA treatment inhibits EMT, ER stress, and cellular senescence in OC-STAMP-overexpressing MLE-12 cells. Levels of Col I, E-cadherin, N-cadherin, α-SMA, p-PERK, p-EIF 2α, p-IRE-1α, p-ATM, p-ATR, p-p53, p21, and p16 in MLE-12 cells, measured by Western blotting. Data are presented as the mean ± SD; $n = 3$ per group.

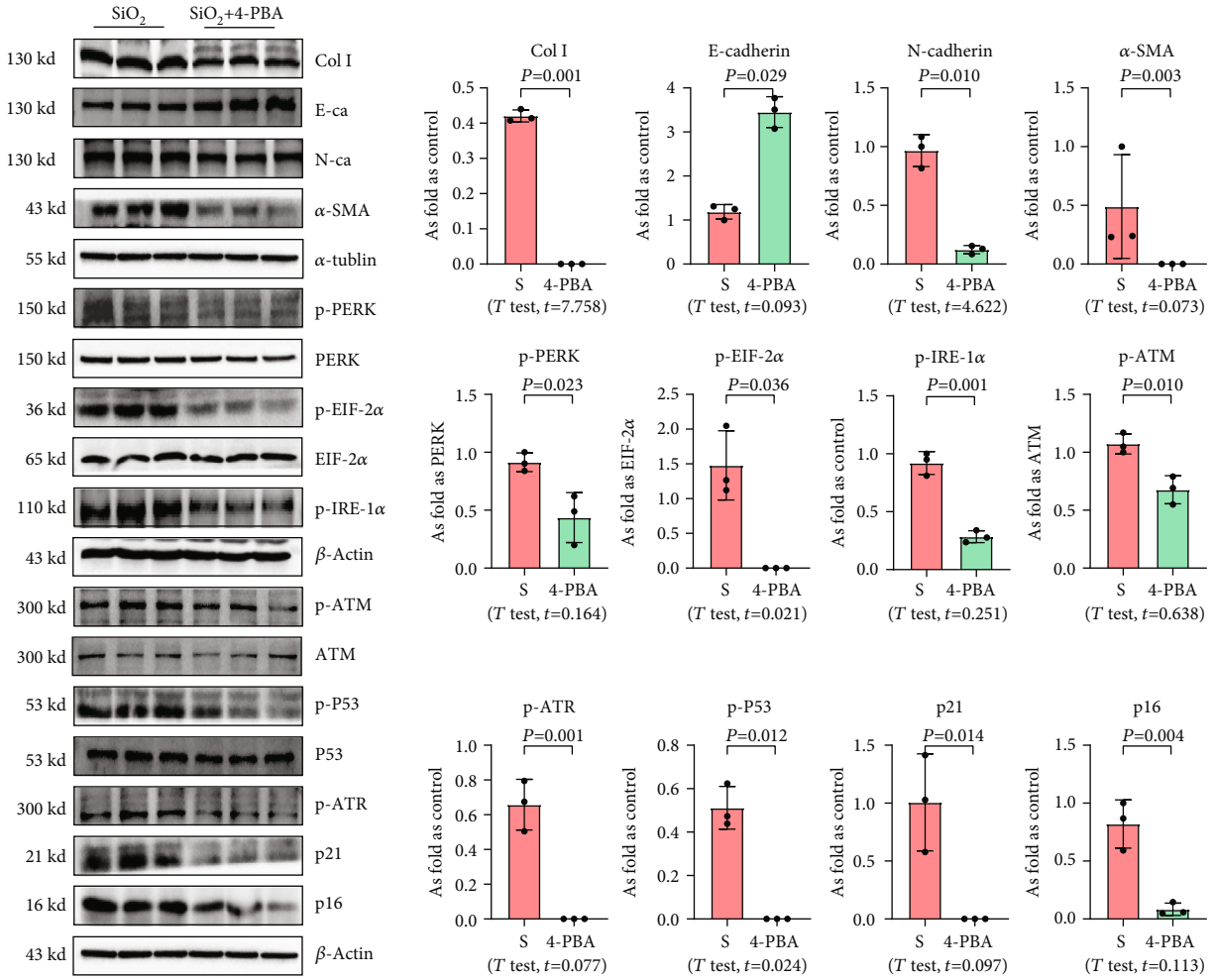

Figure 7: 4-PBA treatment inhibits EMT, ER stress, and cellular senescence in silica-treated MLE-12 cells. Levels of Col I, E-cadherin, N-cadherin, α-SMA, p-PERK, p-EIF 2α, p-IRE-1α, p-ATM, p-ATR, p-p53, p21, and p16 in MLE-12 cells treated with silica, measured by Western blotting. Data are presented as the mean ± SD; $n = 3$ per group.

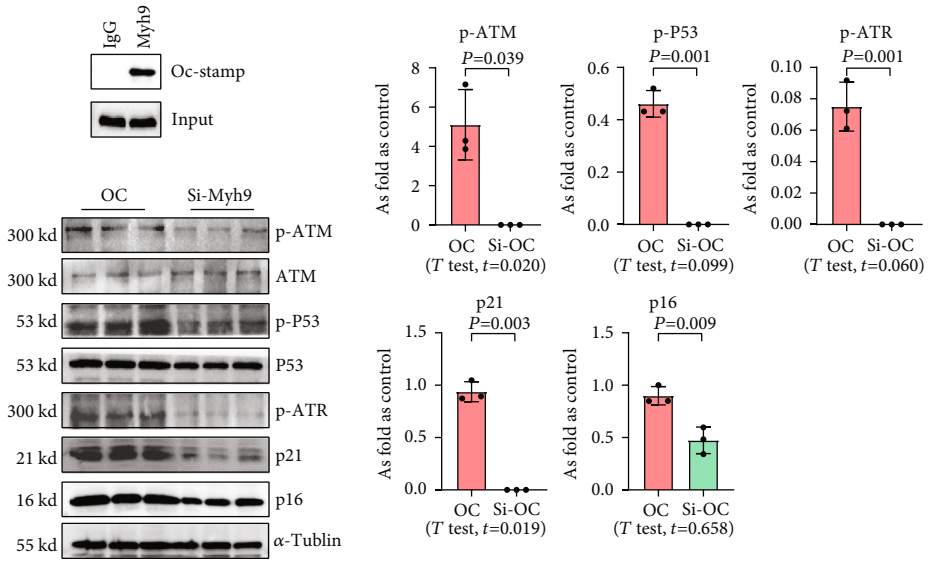

Figure 8: OC-STAMP interacts with MYH9. (a) Co-IP of OC-STAMP and MYH9; (b) levels of p-ATM, p-ATR, p-p53, p21, and p16 in siRNA-*Myh9* treated MLE-12 cells, measured by Western blotting. Data are presented as the mean ± SD; $n = 3$ per group.

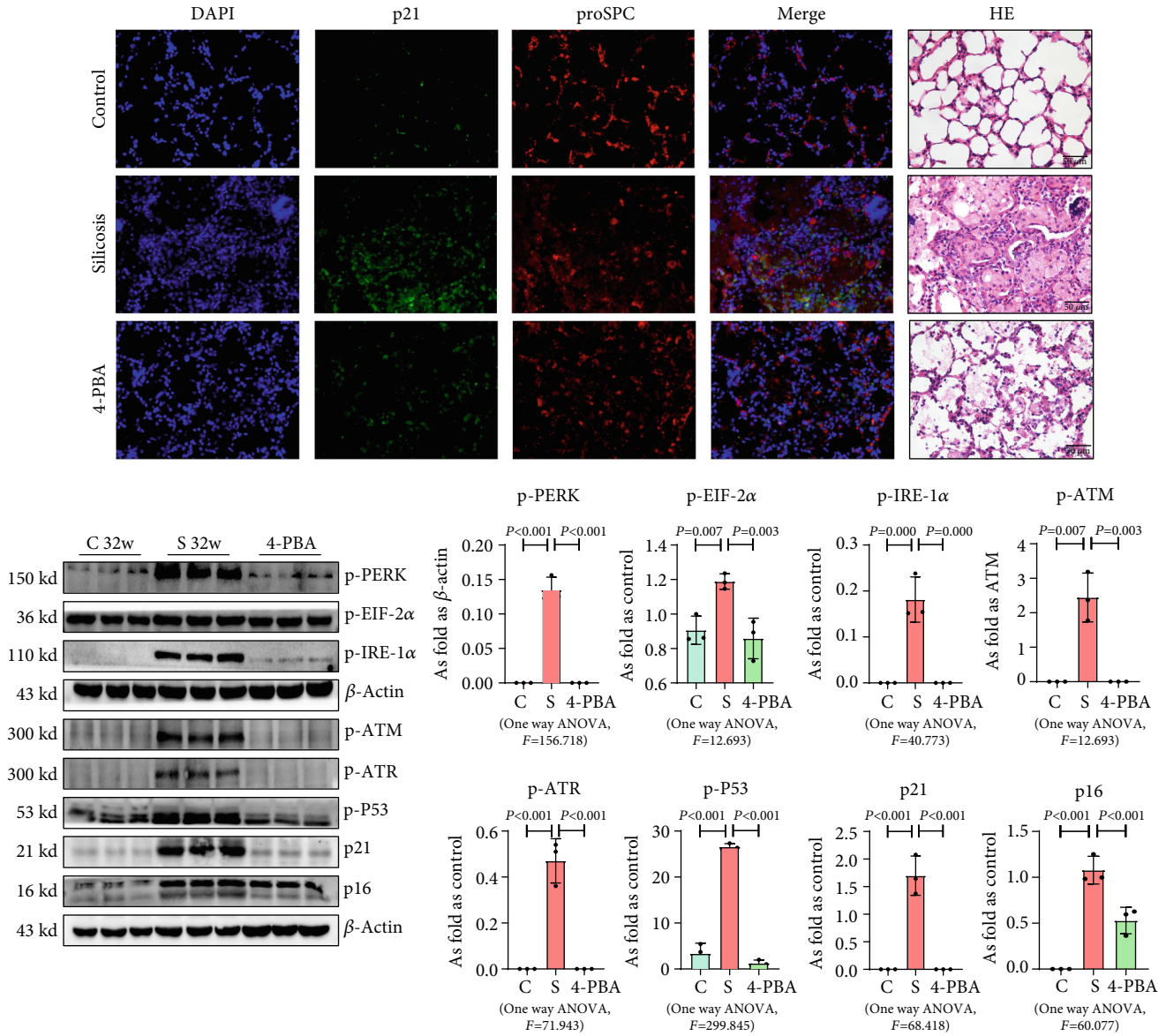

Figure 9: 4-PBA attenuates cellular senescence in silicotic rats. (a) Coexpression of p21 and proSPC in silicotic rats, Bar = 50 μm; (b) levels of p-PERK, p-EIF 2α, p-IRE-1α, p-ATM, p-ATR, p-p53, p21, and p16 in MLE-12 cells treated with silica, measured by Western blotting. Data are presented as the mean ± SD; $n = 3$ per group.

alveolitis, but the contribution of AEC2 in the pathogenesis of silicosis is largely unknown [18, 19]. Several studies have suggested that hypertrophic and hyperplastic AEC2 was proliferative AEC2, as well as enhanced production and secretion of phospholipids and surfactant proteins for lung injury and repair [20, 21]. In the present study, we analyzed the number of AEC2, collagen deposition, expression of p21 and PCNA in normal alveoli, alveolitis (consisting of macrophages and hypertrophic AEC2), and silicotic granulomas. As observed in previous studies, hypertrophic and hyperplastic AEC2 was mostly located in the alveolitis-affected area and showed a senescent phenotype with more collagen deposition. An in vitro study also showed activation of cellular senescence signaling in silica-treated MLE-12 cells. Furthermore, ER stress markers were also observed in hypertrophic and hyperplastic AEC2, which suggested that stress-related senescent AEC2 may be a potential trigger for silicosis.

Most importantly, we found overexpression of OC-STAMP, one of the major factors of RANKL signaling, derived EMT, ER stress, and cellular senescence in MLE-12 cells, which showed some similar features in rats exposed to silica. OC-STAMP knockout (KO) mice showed normal skeleton, growth, and bone metabolic markers, and OC-STAMP-deficient cells isolated from bone marrow were able to differentiate into TRAP-positive osteoclasts under RANKL stimulation but could not fuse into multinucleated cells, which suggested the specific role of OC-STAMP in osteoclast multinucleation or cell fusion rather than osteoclast differentiation [9, 10]. Thus, several studies have proposed that OC-

STAMP is involved in pathogenic bone resorption rather than normal bone metabolism [11]. Furthermore, OC-STAMP induced a phenotypic switch in macrophage polarization and suppressed the M1 proinflammatory state [22]. We have been described the potential proinflammatory effect of OC-STAMP in macrophages, as a member of the RANKL signaling pathway in silicosis [8]. In the present study, we found a different mechanism of OC-STAMP in AEC2 and promoted EMT, ER-stress, and cellular senescence in MLE-12 cells, which could be blocked by *Ocstamp*-siRNA or 4-PBA. Furthermore, ER stress has been reported to be associated with EMT and resulted in an increase in the p16 and p21 levels in lung epithelial cells in pulmonary fibrosi [23]. ER stress has been also observed in senescence induced by different stimuli and has been proposed as the consequence of senescent phenotype [24]. Combined with our previous study [1, 25], we speculated that the EMT, ER stress, and cellular senescence worked together in silicosis, at least in part, by the overexpression of OC-STAMP.

Our data showed that OC-STAMP interacted with nonmuscle myosin class II, isoform A (NM II-A, also known as MYH9), which regulated the senescent signaling pathway. MYH9 is an actin-binding molecular motor and is encoded by the *Myh9* gene, which participates in many crucial cellular processes, such as adhesion, cell migration, cytokinesis and polarization, maintenance of cell shape, and signal transduction [26]. It has been reported that MYH9 localization and filament assembly can be modulated by the interaction with S100A16 during kidney injury or TGF-β stimulation to promote cytoskeleton reorganization and EMT progression in renal tubulointerstitial fibrosis [27]. TGF-β1 increased MYH9 expression, and siRNA-mediated knockdown of *MYH9* remarkably repressed TGF-β1-induced lung fibroblast-to-myofibroblast differentiation [28]. Furthermore, inducible conditional knockout of Myh9 in the renal tubules of adult mice resulted in progressive kidney disease with expansion of ER tubules and activation of ER stress [29]. Our data showed that OC-STAMP interacted with MYH9, which regulated cellular senescence signaling in MLE-12 cells and may have an important role in silicosis. This study has some limitations. First, the results should be verified in clinical samples to strengthen the meaning of high expression of OC-STAMP in silicosis. Furthermore, the cross talk between ER stress and senescence in silicosis still needs to be explored to better understand age-related lung pathology and pathophysiology. Further studies are needed to consider and overcome these limitations.

In summary, we have shown that cellular senescence of AEC2 participates in silicosis formation. In the context of profibrotic insults, overexpression of OC-STAMP in MLE-12 cells exacerbates ER stress, EMT, and cellular senescence, and it may play an important role in silicosis. Blockage of ER stress protects against cellular senescence and pulmonary fibrosis in response to silica exposure.

Data Availability

The underlying data of the study can be obtained by contacting the authors if it is reasonable.

Conflicts of Interest

The authors declare that they have no competing interests.

Authors' Contributions

All authors contributed to data analysis and drafting or revision of the article. All authors have agreed on the journal to which the article will be submitted, gave final approval of the version to be published, and agree to be accountable for all aspects of the work.

Acknowledgments

This work was funded by the National Natural Science Foundation of China (No. 81972988), the National Natural Science Foundation of Hebei Province (H2020209052), and the Science and Technology Project of Hebei Education Department (No. ZD2019077).

Supplementary Materials

Figure S1: the cell apoptosis in MLE-12 cells treated with silica or not. There was no statistically significant difference in apoptosis rate between MLE-12 cells treated with or without 50 μg/mL silica. *(Supplementary Materials)*

References

[1] L. Zhang, D. Xu, Q. Li et al., "_N_ -acetyl-seryl-aspartyl-lysyl-proline (Ac-SDKP) attenuates silicotic fibrosis by suppressing apoptosis of alveolar type II epithelial cells via mediation of endoplasmic reticulum stress," *Toxicology and Applied Pharmacology*, vol. 350, pp. 1–10, 2018.

[2] J. Katzen and M. F. Beers, "Contributions of alveolar epithelial cell quality control to pulmonary fibrosis," *The Journal of Clinical Investigation*, vol. 130, no. 10, pp. 5088–5099, 2020.

[3] P. J. Barnes, J. Baker, and L. E. Donnelly, "Cellular senescence as a mechanism and target in chronic lung diseases," *American Journal of Respiratory and Critical Care Medicine*, vol. 200, no. 5, pp. 556–564, 2019.

[4] S. Hamsanathan, J. K. Alder, J. Sellares, M. Rojas, A. U. Gurkar, and A. L. Mora, "Cellular senescence: the trojan horse in chronic lung diseases," *American Journal of Respiratory Cell and Molecular Biology*, vol. 61, no. 1, pp. 21–30, 2019.

[5] Y. Fan, C. Zheng, N. Wu, Y. Li, X. Huang, and Q. Ye, "Telomerase gene variants and telomere shortening in patients with silicosis or asbestosis," *Occupational and Environmental Medicine*, vol. 78, no. 5, pp. 342–348, 2021.

[6] L. Shifeng, X. Hong, Y. Xue et al., "Ac-SDKP increases α-TAT 1 and promotes the apoptosis in lung fibroblasts and epithelial cells double-stimulated with TGF-β1 and silica," *Toxicology and Applied Pharmacology*, vol. 369, pp. 17–29, 2019.

[7] G. Li, S. Chen, Y. Zhang et al., "Matrix stiffness regulates α-TAT1-mediated acetylation of α-tubulin and promotes silica-induced epithelial-mesenchymal transition via DNA damage," *Journal of Cell Science*, vol. 134, 2020.

[8] F. Jin, F. Geng, D. Xu et al., "Ac-SDKP attenuates activation of lung macrophages and bone osteoclasts in rats exposed to silica by inhibition of TLR4 and RANKL signaling pathways,"

Journal of Inflammation Research, vol. 14, pp. 1647–1660, 2021.

[9] T. Ishii, M. Ruiz-Torruella, A. Ikeda et al., "OC-STAMP promotes osteoclast fusion for pathogenic bone resorption in periodontitis via up-regulation of permissive fusogen CD9," *The FASEB Journal*, vol. 32, no. 7, pp. 4016–4030, 2018.

[10] H. Witwicka, S. Y. Hwang, P. Reyes-Gutierrez et al., "Studies of OC-STAMP in osteoclast fusion: a new knockout mouse model, rescue of cell fusion, and transmembrane topology," *PLoS One*, vol. 10, no. 6, article e0128275, 2015.

[11] J. Kodama and T. Kaito, "Osteoclast multinucleation: review of current literature," *International Journal of Molecular Sciences*, vol. 21, no. 16, 2020.

[12] A. Burman, H. Tanjore, and T. S. Blackwell, "Endoplasmic reticulum stress in pulmonary fibrosis," *Matrix Biology*, vol. 68-69, pp. 355–365, 2018.

[13] M. Manevski, T. Muthumalage, D. Devadoss et al., "Cellular stress responses and dysfunctional mitochondrial-cellular senescence, and therapeutics in chronic respiratory diseases," *Redox Biology*, vol. 33, article 101443, 2020.

[14] J. M. Worlein, K. Baker, M. Bloomsmith, K. Coleman, and T. L. Koban, "The eighth edition of the guide for the care and use of laboratory animals (2011); implications for behavioral management," *American Journal of Primatology*, vol. 73, pp. 98–98, 2011.

[15] Z. Hui, X. Dingjie, Y. Yuan et al., "Silicosis decreases bone mineral density in rats," *Toxicology and Applied Pharmacology*, vol. 348, pp. 117–122, 2018.

[16] Y. Chen, D. Xu, J. Yao et al., "Inhibition of miR-155-5p Exerts Anti-Fibrotic Effects in Silicotic Mice by Regulating Meprin α," *Molecular Therapy - Nucleic Acids*, vol. 19, pp. 350–360, 2020.

[17] X. Gao, D. Xu, S. Li et al., "Pulmonary silicosis alters microRNA expression in rat lung and miR-411-3p exerts antifibrotic effects by inhibiting MRTF-A/SRF signaling," *Molecular Therapy - Nucleic Acids*, vol. 20, pp. 851–865, 2020.

[18] O. Lesur, A. M. Cantin, A. K. Tanswell, B. Melloni, J. F. Beaulieu, and R. Begin, "Silica exposure induces cytotoxicity and proliferative activity of type II pneumocytes," *Experimental Lung Research*, vol. 18, no. 2, pp. 173–190, 1992.

[19] D. W. Porter, A. F. Hubbs, R. Mercer et al., "Progression of lung inflammation and damage in rats after cessation of silica inhalation," *Toxicological Sciences*, vol. 79, no. 2, pp. 370–380, 2004.

[20] B. E. Miller, L. A. Dethloff, and G. E. Hook, "Silica-induced hypertrophy of type II cells in the lungs of rats," *Laboratory Investigation; A Journal of Technical Methods and Pathology*, vol. 55, no. 2, pp. 153–163, 1986.

[21] R. J. Panos, A. Suwabe, C. C. Leslie, and R. J. Mason, "Hypertrophic alveolar type II cells from silica-treated rats are committed to DNA synthesis in vitro," *American Journal of Respiratory Cell and Molecular Biology*, vol. 3, no. 1, pp. 51–59, 1990.

[22] H. Yuan, J. He, G. Zhang, D. Zhang, X. Kong, and F. Chen, "Osteoclast stimulatory transmembrane protein induces a phenotypic switch in macrophage polarization suppressing an M1 pro-inflammatory state," *Acta Biochimica et Biophysica Sinica*, vol. 49, no. 10, pp. 935–944, 2017.

[23] T. H. G. Phan, P. Paliogiannis, G. K. Nasrallah et al., "Emerging cellular and molecular determinants of idiopathic pulmonary fibrosis," *Cellular and Molecular Life Sciences: CMLS*, vol. 78, no. 5, pp. 2031–2057, 2021.

[24] T. Parimon, M. S. Hohmann, and C. Yao, "Cellular senescence: pathogenic mechanisms in lung fibrosis," *International Journal of Molecular Sciences*, vol. 22, no. 12, 2021.

[25] S. Li, Y. Li, H. Xu et al., "ACE2 attenuates epithelial-mesenchymal transition in MLE-12 cells induced by silica," *Drug Design, Development and Therapy*, vol. 14, pp. 1547–1559, 2020.

[26] G. Asensio-Juarez, C. Llorente-Gonzalez, and M. Vicente-Manzanares, "Linking the landscape of MYH9-related diseases to the molecular mechanisms that control non-muscle myosin II-A function in cells," *Cells*, vol. 9, no. 6, 2020.

[27] H. Sun, A. Zhao, M. Li et al., "Interaction of calcium binding protein S100A16 with myosin-9 promotes cytoskeleton reorganization in renal tubulointerstitial fibrosis," *Cell Death & Disease*, vol. 11, no. 2, p. 146, 2020.

[28] X. Sun, M. Zhu, X. Chen, and X. Jiang, "MYH9 inhibition suppresses TGF-β1-stimulated lung fibroblast-to-myofibroblast differentiation," *Frontiers in Pharmacology*, vol. 11, article 573524, 2021.

[29] K. L. Otterpohl, B. W. Busselman, I. Ratnayake et al., "Conditional Myh9 and Myh10 inactivation in adult mouse renal epithelium results in progressive kidney disease," *JCI Insight*, vol. 5, 2020.

Hindawi
Oxidative Medicine and Cellular Longevity
Volume 2021, Article ID 7356266, 12 pages
https://doi.org/10.1155/2021/7356266

Research Article

Deficiency of ROS-Activated TRPM2 Channel Protects Neurons from Cerebral Ischemia-Reperfusion Injury through Upregulating Autophagy

Xupang Hu,[1] **Lijuan Wu**,[1,2] **Xingyu Liu**,[1] **Yi Zhang**,[1] **Min Xu**,[1] **Qiuyuan Fang**,[1] **Lin Lu**,[3] **Jianguo Niu**,[4] **Tarek Mohamed Abd El-Aziz**,[5,6] **Lin-Hua Jiang**,[7] **Fangfang Li**,[1] **and Wei Yang**[1]

[1]*Department of Biophysics, and Department of Neurosurgery of the First Affiliated Hospital, Zhejiang University School of Medicine, Hangzhou 310058, China*
[2]*School of Medicine, Taizhou University, Taizhou 318000, China*
[3]*School of Medicine, Zhejiang University City College, Hangzhou 310015, China*
[4]*Ningxia Key Laboratory of Craniocerebral Diseases, Ningxia Medical University, Yinchuan 750004, China*
[5]*Department of Cellular and Integrative Physiology, University of Texas Health Science Center at San Antonio, San Antonio, TX 78229-3900, USA*
[6]*Zoology Department, Faculty of Science, Minia University, El-Minia 61519, Egypt*
[7]*School of Biomedical Sciences, Faculty of Biological Sciences, University of Leeds, Leeds, UK*

Correspondence should be addressed to Fangfang Li; 0618314@zju.edu.cn and Wei Yang; yangwei@zju.edu.cn

Xupang Hu, Lijuan Wu, and Xingyu Liu contributed equally to this work.

Received 18 May 2021; Accepted 29 June 2021; Published 28 July 2021

Academic Editor: Chaoliang Tang

Cerebral ischemia-reperfusion (I-R) transiently increased autophagy by producing excessively reactive oxygen species (ROS); on the other hand, activated autophagy would remove ROS-damaged mitochondria and proteins, which led to cell survival. However, the regulation mechanism of autophagy activity during cerebral I-R is still unclear. In this study, we found that deficiency of the TRPM2 channel which is a ROS sensor significantly decreased I-R-induced neuronal damage. I-R transiently increased autophagy activity both *in vitro* and *in vivo*. More importantly, TRPM2 deficiency decreased I-R-induced neurological deficit score and infarct volume. Interestingly, our results indicated that TRPM2 deficiency could further activate AMPK rather than Beclin1 activity, suggesting that TRPM2 inhibits autophagy by regulating the AMPK/mTOR pathway in I-R. In conclusion, our study reveals that ROS-activated TRPM2 inhibits autophagy by downregulating the AMPK/mTOR pathway, which results in neuronal death induced by cerebral I-R, further supporting that TRPM2 might be a potential drug target for cerebral ischemic injury therapy.

1. Introduction

The balance of reactive oxygen species (ROS) production and elimination maintains the cellular redox homeostasis, which is vital to cell survival in various physiological and pathological conditions [1]. Cerebral ischemia-reperfusion (I-R) is a clinical disorder characterized by severe neurological dysfunctions, which is a leading cause of long-term disability and death globally [2]. Due to the drastic interruption of blood supply, followed by reperfusion, the balance of generation of excessive ROS and the tissue's ability to detoxify ROS are disrupted. The I-R injury was found dependent on the reintroduction of oxygen, indicating that ROS would possibly be the main cause of neuronal death in reperfusion injury [3]. ROS overproduction leading to cell death was a complex mode involving necrosis, autophagy, and apoptosis in I-R injury [4].

As a ROS sensor, the TRPM2 channel is a Ca^{2+} permeable nonselective cation channel and is activated by the adenosine diphosphate-ribose (ADPR) [5] that is generated through poly(ADPR)polymerase (PARP)/poly(ADPR)glycohydrolase (PARG) pathway [6]. Recent studies have linked TRPM2 to cerebral I-R injury. For example, TRPM2 deficiency or pharmacological inhibition of TRPM2 prevented oxygen and glucose deprivation reperfusion- (OGD-R-) induced neuronal death in cultured mouse cortical neurons [7, 8]. In addition, the neuronal death of TRPM2 knockout (TRPM2 KO) mice induced by the transient middle cerebral artery occlusion (tMCAO) model was substantially attenuated compared to that of WT mice [9]. In addition, previous studies reported that TRPM2 mediated neuronal death in I-R by resulting in Zn^{2+} accumulation [10], regulating NMDAR expression level [11] and inducing inflammation [12]. Since brain I-R injury is a complex pathological process, it is still important to explore whether TRPM2 mediated I-R injury by regulating other critical pathways.

Accumulating evidence has indicated that autophagy plays a critical role during cerebral I-R injury. For example, inhibition of autophagy in the reperfusion phase reinforces I-R injury [13], indicating a protective role that autophagy plays in cerebral I-R. In contrast, a recent study reported that Beclin1 deficiency or RNAi knockdown protected the neuronal death in the tMCAO model, suggesting that Beclin1-dependent autophagy mediated the neuronal damage during I-R injury [14]. In addition to Beclin1, it has been demonstrated that hypoxia or ischemia enhances AMP-activated protein kinase (AMPK) activity [15], which further inhibited its downstream protein mammalian target of rapamycin (mTOR) to enhance autophagy [16]. Therefore, modulating autophagy and its upregulated molecular pathways may be beneficial for the treatment of ischemic stroke. Interestingly, recent studies reported that TRPM2 regulates autophagy [17, 18]. For example, a recent study found that TRPM2 deficiency inhibited H_2O_2-induced AMPK phosphorylation in neutrophils, suggesting the regulation of the AMPK signaling pathway by TRPM2 [17]. Besides, a recent study reported that TRPM2 channel activation mediated calcium influx, which activated calcium/calmodulin-dependent protein kinase II (CaMK II) and subsequently phosphorylated Beclin1 to inhibit autophagy [18]. It will be attractive to determine whether TRPM2 mediates I-R injury by regulating autophagy.

In this study, we investigated the role of TRPM2 in autophagy-dependent cerebral I-R. The underlying rationale was that I-R-induced oxidative stress activates TRPM2 channels [19], and TRPM2 activation leads to Ca^{2+} influx, which in turn affects autophagy flux [18]. Our results demonstrated that the ROS-activated TRPM2 channel impairs autophagy induction by regulating the AMPK/mTOR pathway during cerebral I-R.

2. Materials and Methods

2.1. Animals. The $TRPM2^{-/-}$ mice were generated in University of Leeds [20] and the mice used in this study were bred in Zhejiang University. All experiments were approved by and conducted following the ethical guidelines of the Zhejiang University Animal Experimentation Committee.

2.2. Antibodies and Reagents. Antibodies against Cathepsin B (1 : 1000, 21718S), cleaved caspase 3 (1 : 1000, Asp175, #9661), caspase 3 (1 : 1000, #9662), phosphorylated-AMPK, AMPK (1 : 1000, 2532S), phosphorylated-mTOR (1 : 1000, #2974), and mTOR (1 : 1000, #2983) were purchased from Cell Signaling Technology (CST, US). Secondary antibodies (1 : 2000) conjugated to horseradish peroxidase were purchased from Santa Cruz Biotechnology. All chemicals were obtained from Sigma-Aldrich or MedChemExpress unless stated otherwise. Stock solutions of compounds were prepared in dimethylsulphoxide (DMSO) or water. The stock chemicals were stored as aliquots at -20°C.

2.3. Preparation of tMCAO Mouse Model. Microsurgery of tMCAO was conducted on the 8-week-old wild-type (C57BL/6) or TRPM2 knockout male mice. Mice were anesthetized for surgery via inhalation of isoflurane. We utilized laser Doppler flowmetry (Moor Instruments, Devon, UK) to monitor the cerebral blood flow (CBF) in the territory of the middle cerebral artery (MCA). Animals with less than 80% reduction in CBF in the core of the MCA territory were excluded from the study.

Transient focal cerebral ischemia was induced by MCAO as described previously [21–23]. Briefly, a 6–0 nylon monofilament suture was inserted into the internal carotid to occlude the origin of the MCA. The nylon suture was removed after 1.5 hours to allow reperfusion. Mice were given a tail vein injection of LY294002 (MCE, HY-10108, 5 mg/kg) or intracerebroventricular injection of 7.5 μg 3-methyladenine (3-MA, Sigma, M9281) at the beginning of reperfusion. The same volume of PBS was given to control mice. After the completion of microsurgery, mice were transferred to a heated cage (37°C) for recovery and then transferred to their cages.

2.4. Evaluation of Neurological Deficit Score and Infarct Volume. Neurological deficit scores were evaluated after 24 h of reperfusion according to the following rule: 0, no deficit; 1, failure of extending of contralateral forelimb; 2, circling to the right side; 3, falling to the contralateral side; and 4, lacking spontaneous motor activity. After evaluation of the neurological deficit score, the mice were sacrificed, and brain tissue was dissected. After storing at -20°C for 30 minutes, infarct volumes were stained with 2,3,5-triphenyltetrazolium hydrochloride (TTC; 0.25%; Sigma, T8877) and fixed in 4% paraformaldehyde overnight. Finally, the infarct areas were measured with the ImageJ software (National Institutes of Health) and determined by a researcher blinded to the experiments.

2.5. Viral Injection. Five-week-old mice were prepared for stereotaxic injection. The detailed protocols have been described previously [24] with minor modifications. Briefly, animals were placed into the anesthesia induction chamber with 2.5% isoflurane and then immobilized on a stereotaxic apparatus. A volume of GFP-mRFP-LC3-AAV virus solution was injected into the bilateral cortex region (1 μl, bregma = 0.20 mm; lateral ± 3.20 mm; ventral 1.50 mm) using

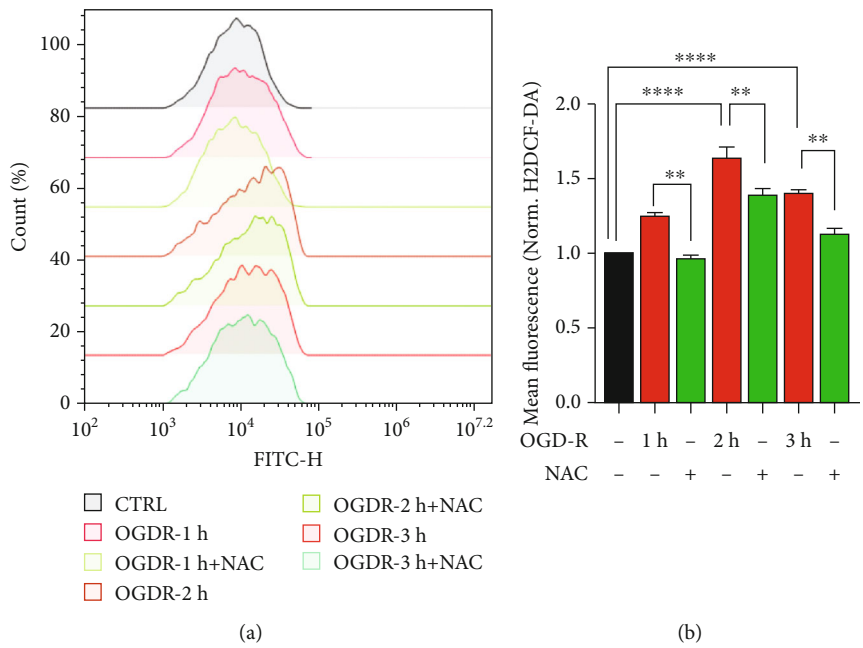

Figure 1: Time-lapse of ROS production under OGD-R treatment. (a) Primary cortical neurons treated with medium alone (CTRL) or 1 h of OGD plus different time (1 h, 2 h, or 3 h) of reperfusion (OGD-R) minus or plus NAC (5 mM) were stained with H2DCF-DA and subjected to FACS (number of cells ≥ 2000). (b) Mean ± SEM data from 2 independent experiments. Each experiment performed 2-3 biological replicates. $^{**}p < 0.01$; $^{****}p < 0.0001$; one-way ANOVA with post hoc Tukey test.

a microinjector with a glass electrode at a rate of 0.1 μl min^{-1} with an infusion pump. The syringe needle was left in place for 10 min and withdrawn, and the injection repeated in the opposite hemisphere and then suturing the skin of the head by applying iodophor for disinfection. The mice were placed in a clean cage and with access to water and food ad lib for 3 weeks until the virus expressed for tMCAO. Three weeks later, the tMCAO was performed on these mice. Animals that had undergone tMCAO microsurgery were deeply anesthetized with pentobarbital (100 mg kg^{-1}, i.p.) and perfused transcranial with saline followed by 4% PFA in 0.1 M PBS, pH 7.4. Brains were removed, postfixed overnight in 4% PFA at 4°C and transferred to 30% sucrose in 0.1 M PBS, pH 7.4. Coronal sections (50 μm) were cut on a cryostat (Leica CM3050 S, Leica Biosystems, IL, USA) and stored in 0.1 M PBS. Sections were then mounted on DAPI-Fluoromount-G overnight. The images were taken using a LSM880 inverted confocal microscope fitted with a ×63 oil objective (LSM880, Carl Zeiss, Jena, Germany) and appropriate excitation (GFP, 494 nm; mRFP, 548 nm) and emission (GFP, 519 nm; mRFP, 562 nm) wavelengths.

2.6. Primary Cortical Neuronal Cell Culture and OGD Reperfusion Procedures. The dissected cortex from embryonic day 17 fetal mice were digested with 0.25% trypsin (Invitrogen; 25200-056) for 8 minutes. Then, Dulbecco's modified Eagle's medium (DMEM) supplemented with 20% fetal bovine serum (FBS) was added to inactivate trypsin. The cell suspension was obtained with triturating 2-3 times with the above medium. Approximately 10^5 cells/cm^2 were seeded onto poly-D-lysine (Sigma; P7405)-coated glass-bottom dishes (Cellvis; D29-20-1-N) for live cell imaging. For Western blot, cells were seeded and cultured in cell culture dishes (Corning). Neurons were grown in Neurobasal medium (Gibco; 21103049) supplemented with 2% B27 Supplement (Gibco; 17504044) and 0.25% GlutaMAX Supplement (Gibco; 35050-061). Cultures were maintained for 8–11 days before treatment.

For OGD treatment, DIV8–11 primary cultured neurons were refreshed with glucose-free DMEM (Gibco; 11966025). Cells were then immediately placed in Hypoxia Incubator Chamber (Stemcell; 27310) loaded with mixed gas containing 5% CO_2 and 95% N_2 as indicated. For reperfusion, neurons were refreshed with the normal culture medium.

2.7. SH-SY5Y Cell Culture and OGD Reperfusion Procedures. The SH-SY5Y cell lines were seeded onto poly-D-lysine (Sigma; P7405)-coated glass-bottom dishes (Cellvis; D29-20-1-N) for live cell imaging. Cells were grown in DMEM/F12 (Gibco; 11320033) supplemented with 10% FBS (PAN; ST30-3302).

For OGD treatment, cultured cells were refreshed with glucose-free DMEM (Gibco; 11966025). Cells were then immediately placed in Hypoxia Incubator Chamber (Stemcell; 27310) loaded with mixed gas containing 5% CO_2 and 95% N_2 for 6 hours. Cells were refreshed with normal culture medium during the reperfusion stage for 6 hours. For live cell autophagy flux experiments, cells were simultaneously incubated with N-(p-amylcinnamoyl) anthranilic acid (ACA, MCE, HY-118628), Torin 1 (MCE, HY-13003), or N-acetyl cysteine (NAC, Sigma, A7250) at its working concentration as indicated during reperfusion stage.

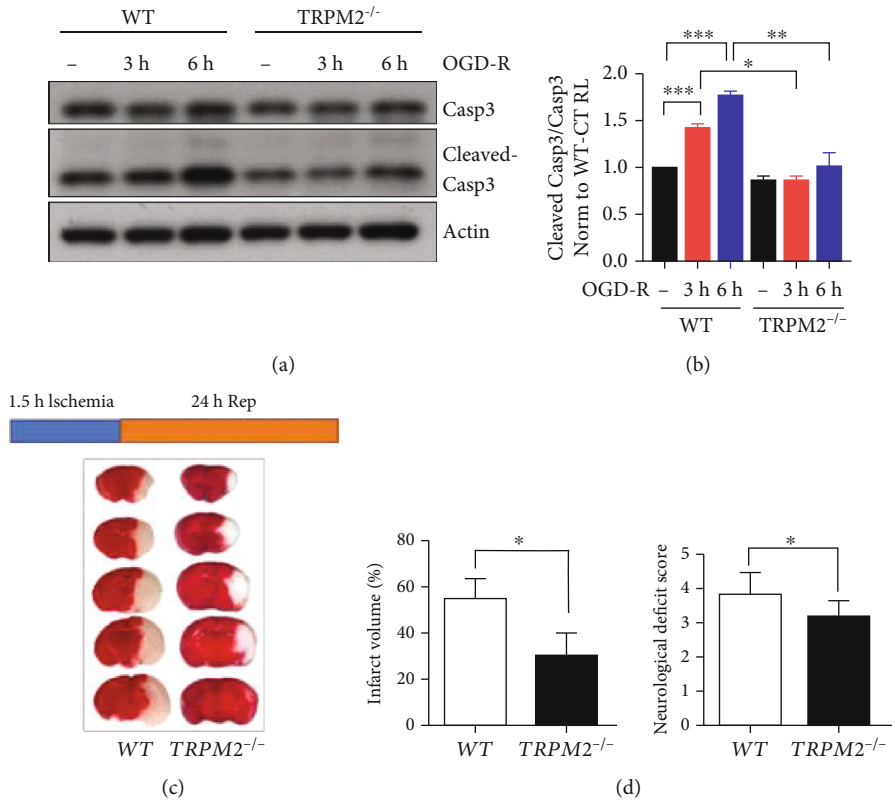

FIGURE 2: I-R induced neuronal death, which could be rescued by TRPM2 deficiency. (a) Primary cultured cortical neurons were subjected to 1 h of OGD followed by 3 or 6 h of reperfusion (OGD-R 3 h and OGD-R 6 h) at DIV9. The cleaved Casp3, Casp3, and actin levels in cultured neurons were determined by Western blot. (b) Semiquantitative analysis showed the ratio of the cleaved Casp3 and Casp3 band intensities. (c) Mice were subjected to middle cerebral artery occlusion for 1.5 h, and reperfusion was allowed by removing the monofilament suture. Animals were euthanized 24 h after tMCAO, and representative TTC-stained brain slices from each group are shown. (d) Infarct volumes were determined by TTC staining in the bar charts (mean ± SD, $n = 6$). The neurological deficit scores of each group are presented. Data was quantified from 3–4 independent experiments. $^{*}p < 0.05$; $^{**}p < 0.01$; $^{***}p < 0.001$; ne-way ANOVA with post hoc Tukey test.

2.8. Transient Transfection. Primary cortical neurons were transfected with Mouse Neuron Nucleofector Kit (VPG-1001, Lonza, Basel, Switzerland) according to the manufacturer's protocol. Briefly, 1×10^6 cells were collected during primary neuronal culture and then resuspended with 100 μL Nucleofector Solution containing 4 μg DNA. The cell suspension was transferred into the cuvette and electroporated with Nucleofector Program O-005. Approximately 50% of neurons can be transfected.

2.9. Cytosolic ROS Measurements in Primary Cortical Neurons. Cytosolic ROS production was measured by using cell-permeant 2′,7′-dichlorodihydrofluorescein diacetate (H2DCF-DA) (Biotium). Upon cleavage of the acetate groups by intracellular esterase and oxidation, the nonfluorescent H2DCF-DA is converted to the highly fluorescent DCF. Briefly, cells were treated with various agents for the desired length of time and then incubated with HBSS (GIBCO®) containing 10 μM H2DCF-DA for 30 minutes at 37°C/5% CO_2. Cells (>5000) were collected using ACCU TASE™ (STEMCELL™), washed, and resuspended in PBS prior to analysis using a ACEA NovoCyte™ flow cytometer (Agilent Technologies, No. 205, Zhaohui Road, Hangzhou, Zhejiang, China). Cytometer settings were optimized for green (FITC-H) fluorescence, and data were analyzed with the NovoExpress 1.4.1 Software (Agilent Technologies, No. 205, Zhaohui Road, Hangzhou, Zhejiang, China).

2.10. Electron Microscopy. The primary cortical neurons subjected with OGD reperfusion were fixed by 2.5% glutaraldehyde in 0.1 M cacodylate buffer. After rinsing in 0.1 M phosphate buffer (pH 7.3), the samples were postfixed in ferrocyanide-reduced osmium tetroxide. These sections were examined in a FEI Tecnai Spirit (T12) transmission electron microscope with a Gatan US4000 4k × 4k CCD at the Zhejiang University EM core facility.

2.11. Live-Cell Imaging of Autophagy Influx. Following the desired treatments, cells were imaged at 37°C using a LSM880 inverted confocal microscope fitted with a ×63 oil objective at appropriate excitation (GFP, 488 nm; mCherry, 548 nm) and emission (GFP, 519 nm; mCherry, 562 nm) wavelengths.

2.12. Cathepsin B Activity Assay. Cathepsin B activity was examined by Cathepsin B Assay Kit (Magic Red) (ab270772, Abcam) according to the manufacturer's protocol. Briefly, following the desired treatments cells were loaded with

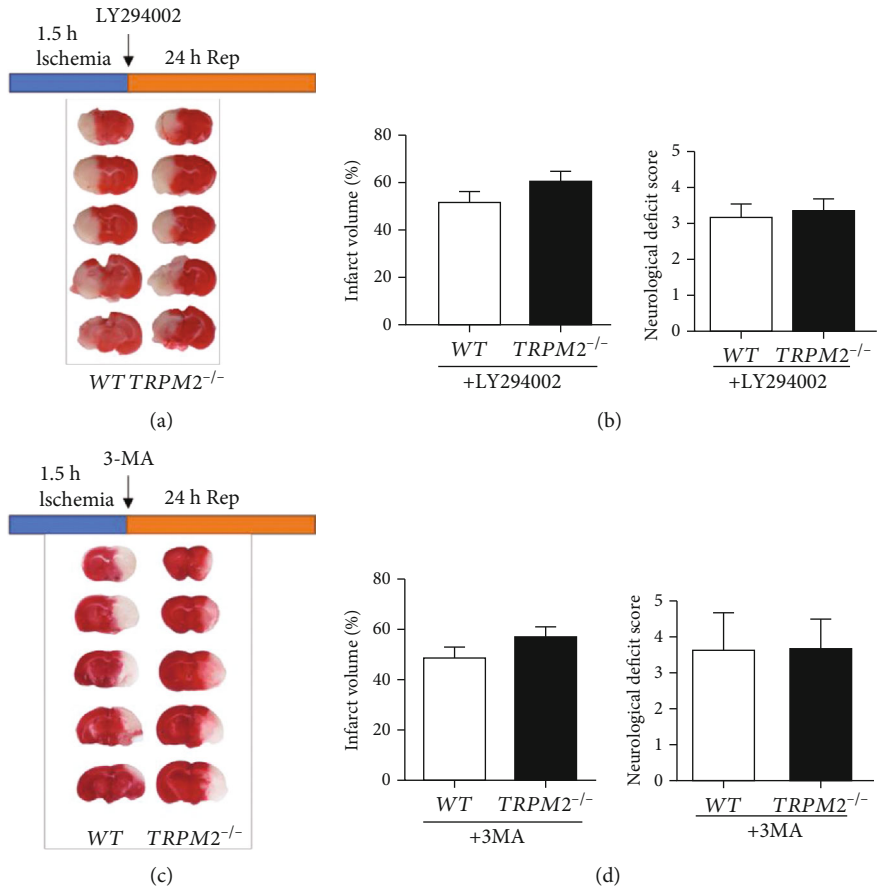

Figure 3: Inhibition of autophagy abolishes the protection of TRPM2 deficiency in I-R injury. Mice were subjected to middle cerebral artery occlusion for 1.5 h, and reperfusion was allowed for 24 h with (a) LY294002 (5 mg/kg) or (c) 3-MA (7.5 μg) by removing the monofilament suture. Animals were euthanized 24 h after tMCAO, and representative TTC-stained brain slices from each group are shown. Infarct volume and neurological deficit score were presented in the bar charts with treatment of (b) LY294002 or (d) 3MA (mean ± SD, $n = 6$). Unpaired Student's t-test.

substrate and incubated for 60 min at 37°C protected from light.

2.13. Western Blot. Proteins in the lysates of the cortex were separated on 10% SDS-PAGE and subjected to Western blotting using corresponding primary antibodies and HRP-conjugated secondary antibodies. Bands were detected by chemiluminescence and quantified using Image J.

2.14. Data Analysis. Colocalization between mRFP-LC3 and GFP-LC3 was analyzed using the Imaris software (Bitplane). All experiments were performed at least three times (n), and the values are presented as mean ± SEM or SD. Statistical significance was determined using the Student t-test or one-way ANOVA, followed by Tukey's post hoc test. Probability (p) values are indicated with *, **, ***, and ****, which correspond to values of 0.05, 0.01, 0.001, and 0.0001, respectively.

3. Results

3.1. ROS Level Has Been Accumulated in I-R Injury, while TRPM2 Deficiency Protected Neurons from I-R Injury. ROS overproduction has been proposed as the main cause of reperfusion injury, which could further lead to necrosis, autophagy, apoptosis, and necroptosis resulting in organ remodeling [3]. Therefore, firstly, we examined the ROS production during OGD-R treatment. We found that the ROS level had a modest increase since 1 h of reperfusion which was reduced by ROS scavenger N-acetyl-L-cysteine (NAC). Interestingly, the ROS production was significantly induced at 2 h of reperfusion while followed by a slight decrease at 3 h of reperfusion (Figure 1). Besides, we found that the caspase 3 activation was significantly enhanced with OGD-R time at 3 hours and 6 hours (Figures 2(a) and 2(b)). These results indicated that significant neuronal apoptosis and ROS overproduction were caused by I-R injury. Previous studies reported that TRPM2-KO mice protected neurons from I-R injury [10]. To verify this, we also performed the tMCAO experiment and confirmed that TRPM2 deficiency significantly reduced I-R-induced infarct volume and neurological deficit score (Figures 2(c) and 2(d)). Since the mechanism by which TRPM2 deficiency protects neurons from I-R injury remains unclear, we further explored the mechanism by which ROS-activated TRPM2 ion channel mediated neuronal death in I-R.

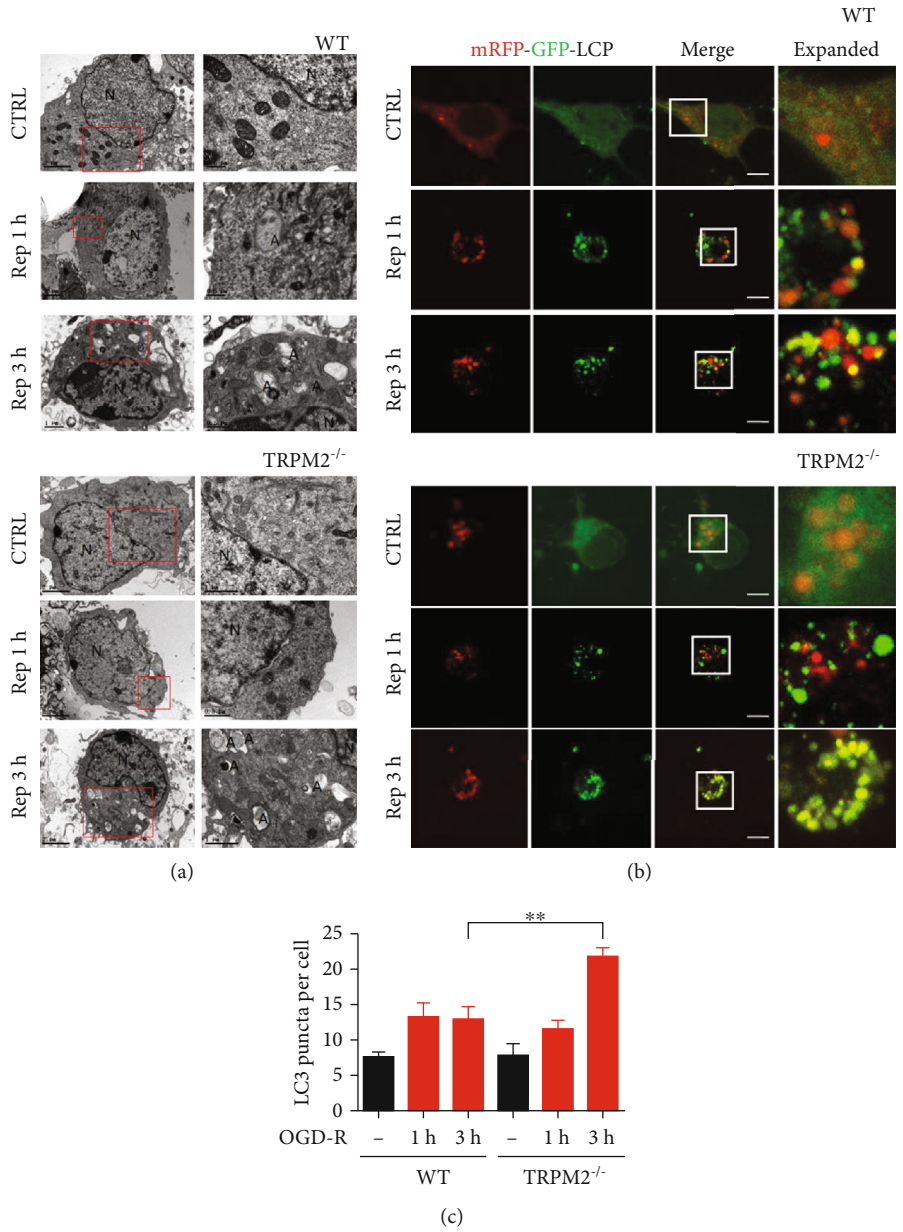

Figure 4: TRPM2 deficiency promotes autophagy induction under OGD-R in primary cortical neurons. (a) Primary cultured neurons from WT and TRPM2 KO mice were subjected to 2 h of OGD plus 1 or 3 h of reperfusion in DIV9. Autophagosome was observed by electron microscopy. Autophagosome was labelled as A and nucleus as N. (b) Primary cultured neurons transfected with mRFP-GFP-LC3 were subjected to 1.5 h of OGD plus 1 or 3 h of reperfusion (OGD-R 1 h and OGD-R 3 h) in DIV9. Representative z-stack confocal images showing the colocalization of mRFP-LC3 with GFP-LC3 induced by OGD-R. (c) Columns represent number of mRFP-GFP-LC3 puncta per cell (mean ± SEM). Scale bars: 10 μm. Data was quantified from 3–4 independent experiments. $^{**}p < 0.01$; one-way ANOVA with post hoc Tukey test.

3.2. TRPM2 Deficiency Protected Neurons from I-R Injury in a Promoting Autophagy Induction Manner In Vitro and In Vivo. Previous studies have shown that autophagy activity plays a critical role in I-R injury, but which mechanism is still debatable [13]. Since the TRPM2 channel is activated by ROS and ADPR [25], and several studies have suggested TRPM2 can regulate autophagy [26, 27], we first tested whether TRPM2 was involved in autophagy-dependent I-R injury. As expected, TRPM2 deficiency mice strongly reduced the infarct volume and improved neurological deficit score in the tMCAO model, which can be abolished by two autophagy inhibitors, LY294002 and 3-MA (Figure 3). Inhibition of autophagy in the tMCAO wild-type mice *per se* seemed not to alter the infarct volume and neurological deficit score. These data indicated that TRPM2 deficiency protected neurons from I-R injury by increased autophagy activity.

To further explore how TRPM2 deficiency rescued neuron death through upregulating autophagy, autophagosome was visualized by electronic microscopy. The autophagosome formation was slightly induced at 1 hour of reperfusion both

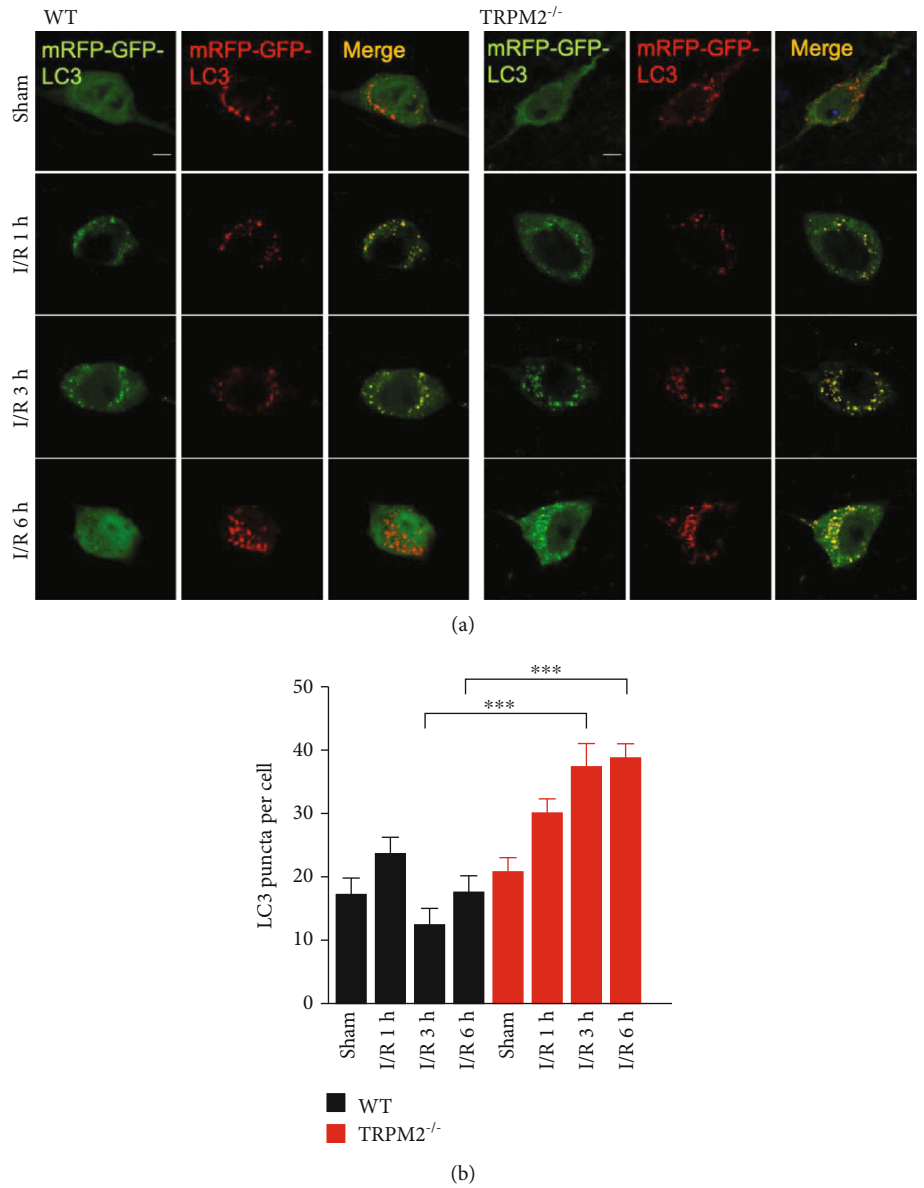

Figure 5: TRPM2 deficiency promotes autophagy induction during I-R injury *in vivo*. (a) WT and TRPM2-KO mice were subjected to sham or MCAO for 1.5 h followed by 1, 3, or 6 h of reperfusion. Then, brain slices were mounted, and confocal images were taken. Representative images of cells expressing AAV-mRFP-GFP-LC3 of brain slices from WT and TRPM2-KO mice are shown. (b) Summary graph showing the quantification of the number for overlapped puncta, as determined by colocalization of all cells from the experiments shown in (a). Columns represent number of mRFP-GFP-LC3 puncta per cell (mean ± SEM). Scale bars: 5 μm. Data was quantified from 3–4 independent experiments. $^{***}p < 0.001$; one-way ANOVA with post hoc Tukey test.

in WT and TRPM2-KO neurons (Figure 4(a)). However, after 3 hours of reperfusion, the number of autophagosome was largely increased. Besides, compared to WT neurons, there were more autophagosomes in TRPM2-KO neurons (Figure 4(a)). These data indicated that TRPM2 deficiency enhanced autophagy induction under OGD-R conditions. To further confirm our findings, we exogenously expressed the tandem mRFP-GFP-LC3 to monitor autophagic flux [28] in cultured primary neurons. GFP fluorescence is quenched upon fusion between autophagosome and lysosome due to the low lysosomal pH, whereas the mRFP signal remains stable at low pH. Therefore, the yellow signal (merged of mRFP and GFP) indicates the presence of autophagosome, while the red signal indicates autolysosome. Our results showed that OGD-R increased the autophagosome formation (GFP+/mRFP+) both in WT and TRPM2-KO neurons in a reperfusion-time-dependent manner (Figure 4(b)). At reperfusion of 1 hour, there is no significant difference between WT and TRPM2-KO neurons. However, at 3 hours of reperfusion, there is more autophagosome (GFP+/mCherry+) in TRPM2-KO neurons compared to WT neurons (Figures 4(b) and 4(c)), suggesting that TRPM2 deficiency upregulated autophagy induction during I-R.

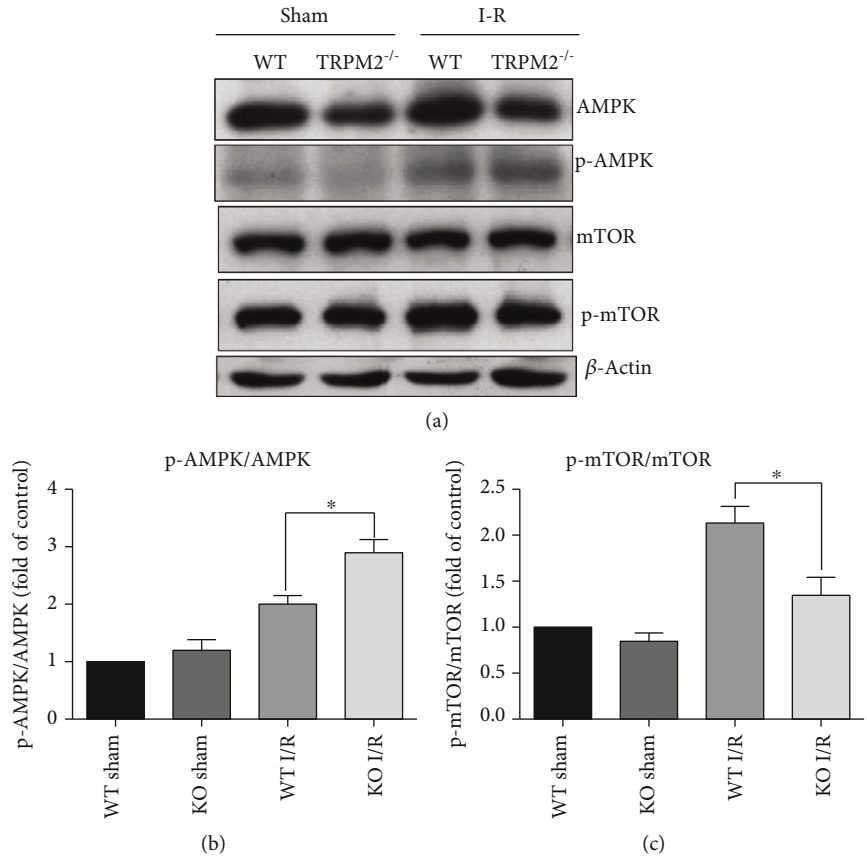

Figure 6: TRPM2 deficiency-promoted autophagy is mediated by the AMPK/mTOR pathway in I-R injury. (a) WT and TRPM2-KO mice were subjected to sham or MCAO for 1.5 h, and reperfusion was allowed for 6 h by removing the monofilament suture. Then, the mice were euthanized, and ischemic penumbra was collected for immunoblot. 3 μg of protein was sequentially immunoblotted with antibodies against AMPK, phosphorylated-AMPK (p-AMPK), mTOR and phosphorylated-mTOR (p-mTOR), and β-actin. Semiquantitative analysis of (b) p-AMPK/AMPK and (c) p-mTOR/mTOR is shown. Data was quantified as mean ± SEM from 3-4 independent experiments. $^*p < 0.05$; one-way ANOVA with post hoc Tukey test.

To further observe the dynamic autophagic flux of I-R injury *in vivo*, we injected adeno-associated virus (AAV) expressing mRFP-GFP-LC3 into the cortex of WT and TRPM2-KO mice. Fluorescent signals of both mRFP and GFP were detected in the cortical neurons from the sham and I-R groups (Figure 5(a)). Consistent with the results *in vitro*, the number of autophagosome (GFP+/mRFP+) in brain slices was similar between WT and TRPM2-KO mice (Figure 5(b)) at 1 hour of reperfusion, while at 3 hours and 6 hours of reperfusion, the autophagosome number from TRPM-KO mice was largely increased compared to that from WT mice (Figure 5(b)). These data suggested that TRPM2 deficiency reduced I-R injury through autophagy induction *in vitro* and *in vivo*.

3.3. TRPM2 Deficiency-Promoted Autophagy Is Mediated by the AMPK/mTOR Pathway to Rescue I-R Injury. A previous study reported that TRPM2 inhibited autophagy through Ca^{2+}-CAMK2 cascade-phosphorylated Beclin1 in Hela cells [16]. We examined the phosphorylation level of the Beclin1 Ser295 site and found that this site has no significant difference between ischemic WT and TRPM2-KO neurons (Figure S1), suggested that TRPM2 deficiency promoted I-R-induced autophagy is Beclin1-independent.

In addition, AMPK has been demonstrated to play a crucial role in autophagy induction in mammalian cells. AMPK could promote autophagy by phosphorylating autophagy-related proteins, such as mTOR, which induced initial phagophore formation [29]. A previous study has reported that the AMPK/mTOR pathway mediates OGD-R-induced cell injury by promoting autophagosome formation [30]. Since our above data has demonstrated that TRPM2 plays an inhibitory role in OGD-R-induced autophagy induction, we are wondering whether TRPM2 affects autophagy by regulating the AMPK/mTOR pathway. Our biochemical data revealed that the level of phosphorylated AMPK was significantly enhanced by the tMCAO treatment in WT mice (Figures 6(a) and 6(b)). Moreover, the phosphorylated AMPK was further upregulated in TRPM-KO mice compared to WT mice (Figures 6(a) and 6(b)), which indicated that TRPM2 activated by I-R injury inhibited the AMPK activation. In contrast, the level of phosphorylated mTOR was reduced in TRPM2-KO mice compared to that in WT mice after the tMCAO treatment (Figures 6(a) and 6(c)),

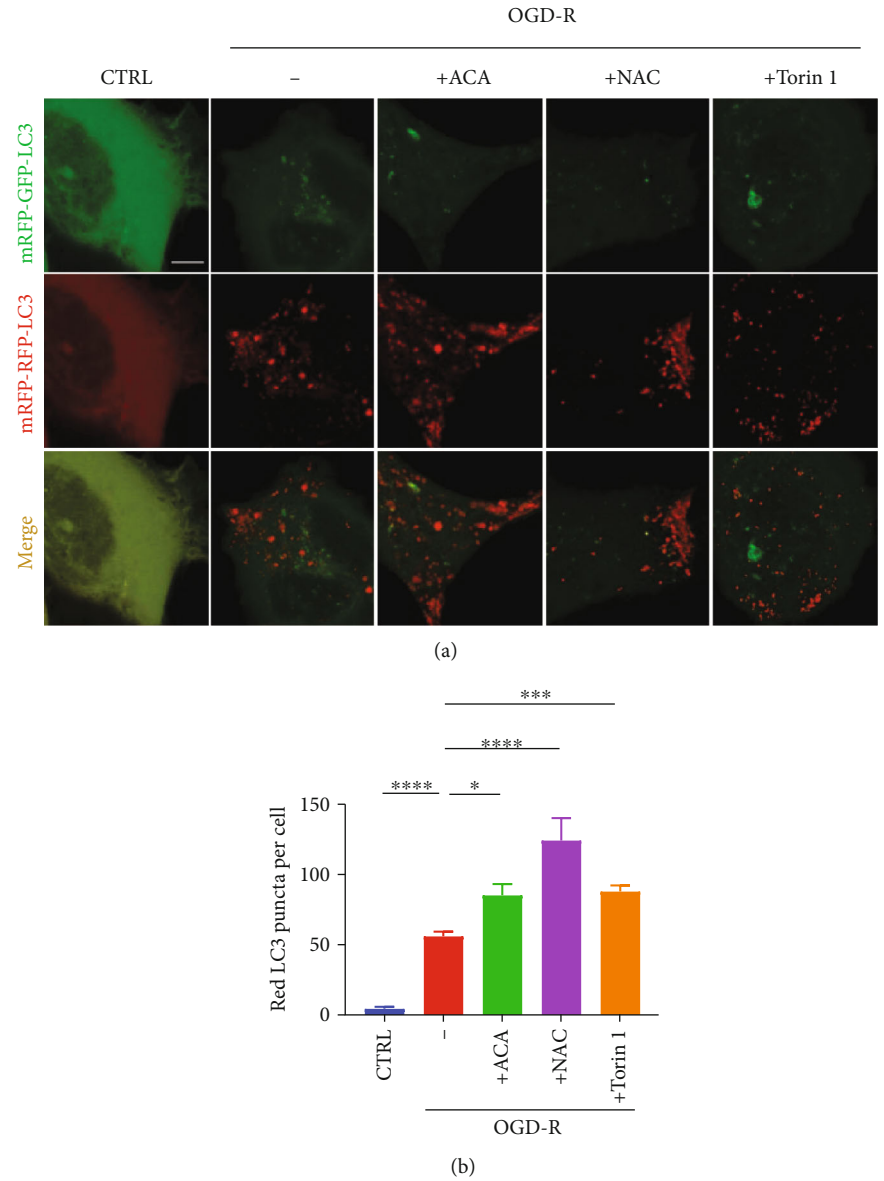

Figure 7: Inhibition of TRPM2 or mTOR enhanced autophagy induction in I-R injury. (a) SH-SY5Y cells overexpressing mRFP-GFP-LC3 were treated with OGD for 6 h and then reperfusion for 6 h with normal medium. 30 μ M ACA, 5mM NAC, or 1 μM Torin1 was added during reperfusion. Scale bar: 5 μm. (b) The average numbers of red LC3 puncta per cell in each condition were quantified. All data are represented as mean ± SEM from three independent experiments. $^{*}p < 0.05$, $^{***}p < 0.001$, and $^{****}p < 0.0001$; one-way ANOVA with post hoc Tukey test.

supporting the activation of AMPK activity in TRPM2 deficiency mice after I-R injury.

Finally, to further confirm ROS/TRPM2/mTOR pathway negatively contributed to the autophagy activity in I-R injury, we tracked the autophagy flux by transfecting mRFP-GFP-LC3 into SH-SY5Y cell. Diffused distribution of LC3 at a basal level, but OGD-R treatment increased autolysosome formation (Figure 7(a)). Interestingly, in the presence of ACA or A10 (Figure S2), two TRPM2 inhibitors, the autolysosomes were further elevated under OGD-R (Figure 7). Consistently, NAC, a synthetic precursor of glutathione (GSH) to eliminate ROS, dramatically raised the autophagy flux (Figure 7). Moreover, Torin 1, an mTOR inhibitor, also increased the autolysosome level under OGD-R condition (Figure 7). Taken together, the AMPK/mTOR pathway is responsible for TRPM2-mediated autophagy induction in I-R injury.

4. Discussion

In this study, we identified a novel signaling pathway by which TRPM2 mediated I-R injury. Our results demonstrated that OGD-R induced ROS accumulation concomitantly neuronal death, while TRPM2 deficiency attenuated OGD-R-induced neuronal death and I-R injury. Furthermore, TRPM2 deficiency reduced infarct volume and increased neurological deficit score in the tMCAO model, confirming that TRPM2 mediated I-R injury. Interestingly,

inhibition of autophagy by 3-MA or LY-294002 abolished the protective effect of TRPM2 deficiency in I-R injury. Further investigation demonstrated that TRPM2 deficiency promoted autophagy induction both *in vitro* and *in vivo*, and this process was mediated by the AMPK/mTOR pathway rather than Beclin1. Our results firstly identified that TRPM2 might impair autophagy to mediate I-R injury. This study pointed towards new therapeutic opportunities for the treatment of cerebral ischemia.

Previous studies have reported that autophagy plays a protective role in I-R injury. Promoting autophagy by urolithin A attenuated renal I-R injury through TFEB-CLEAR (Coordinated Lysosomal Expression and Regulation) pathway [31]. Autophagy protected the heart from I-R injury by attenuating reactive ROS levels and ameliorating mitochondrial dysfunction [32]. Our study revealed that autophagy plays a protective role in TRPM2 deficiency-mediated cerebral I-R injury. Autophagy is a dynamic and multistep process that includes phagophore initiation, autophagosome formation, and fusion with lysosomes for degradation [33]. Therefore, autophagy can be modulated at these steps. In the present study, we found that genetic knockout or chemically inhibition of TRPM2 further upregulates autophagosome formation under I-R *in vivo* or OGD-R treatment *in vitro*. We initially noted that a previous report demonstrated that TRPM2 activation inhibited autophagosome initiation by upregulating phosphorylation of Beclin1 (S295) in Hela cells [18]. Besides, a previous study found that Beclin1 RNAi has a protective role in cerebral I-R [14]. Unfortunately, our result showed there is no difference in phosphorylation of Beclin1 (S295) between WT and TRPM2 KO mice, indicating that TRPM2 regulated autophagy is independent of Beclin1 in cerebral I-R.

AMPK, a critical energy sensor for energy metabolism, has been demonstrated to play an important role in autophagy [34, 35]. Under OGD-R treatment or ischemia, the activation of AMPK in cortical neurons has been reported to exert neuroprotective effects [36]. To get mechanistic insight into whether AMPK is involved in TRPM2-mediated autophagy function, we examined the expression of phosphorylated AMPK levels. Consistent with the previous report, I-R increased phosphorylated AMPK level, and phosphorylated AMPK level of TRPM2 deficiency further increased compared to that of WT mice in cerebral I-R. It is well known that mTOR can be negatively regulated by AMPK in autophagy [37]. Accordingly, our results revealed that TRPM2 deficiency dramatically decreased the phosphorylation level of mTOR protein, which is consistent with the previous study [38]. In addition, our study discovered that inhibiting mTOR also elevated autophagosome formation during OGD-R treatment, further supporting the essential role of mTOR in autophagy. Therefore, we for the first time demonstrated that TRPM2 activation under I-R *in vivo* or OGD-R treatment *in vitro* impaired autophagy by downregulating the AMPK/mTOR pathway. However, the molecular mechanism of the TRPM2 channel regulating the AMPK/mTOR pathway during I-R is still unclear. Actually, in the I-R stage, TRPM2-mediated cellular Ca^{2+} and Zn^{2+} increase have been reported; besides, Ca^{2+} has been demonstrated to regulate the AMPK/mTOR pathway [39, 40]. It will be interesting to uncover the relationship between TRPM2 and AMPK/mTOR signaling pathway under I-R in the future.

5. Conclusions

In summary, we confirmed that TRPM2 deficiency reduced ROS-dependent I-R injury and OGD-R-induced neuronal death. We further uncovered that cerebral I-R injury produced ROS-activated TRPM2 channel, which inhibited autophagy induction by attenuating the AMPK/mTOR pathway rather than Beclin1. Although autophagy is a friend or foe during cerebral I-R is still debatable, our results indicated that TRPM2/AMPK/mTOR signaling pathway plays a negative role in autophagy-dependent cerebral I-R injury. Given that upregulation of autophagy is considered a useful strategy to prevent cerebral I-R injury, our findings provide new therapeutic opportunities for ischemic stroke.

Data Availability

The data used to support the findings of this study are available from the corresponding authors upon request.

Conflicts of Interest

The authors declare no conflict of interest.

Authors' Contributions

X.H., L.W., X. L., Y.Z., and M.X. performed the experiment. L.L. and F.L. drafted the paper. T.M.A. and L.H.J. discussed and revised the manuscript. F.L. and W.Y. analyzed the data and did the final approval of the version. All authors have read and agreed to the published version of the manuscript. Xupang Hu, Lijuan Wu, and Xingyu Liu contributed equally to this work.

Acknowledgments

This work was supported by grants from the Natural Science Foundation of China (31701211, 3170080636, and 8157050771), the Zhejiang Association for science and technology (CTZB-2020080127), the Public Applied Technology Research Project of Zhejiang Province (grant No. LGD21H090003), and the key research and development program of Ningxia Hui Autonomous Region (2019BFH02003).

Supplementary Materials

Figure S1:TRPM2 deficiency-upregulated autophagy is Beclin1-independent. (a) Primary cultured neurons subjected to medium alone (CTRL), 1 hour of OGD plus 3 hours of reperfusion (OGD-R) at DIV9. 3 μg of protein was sequentially immunoblotted with antibodies against Beclin1, phosphorylated-S295-Beclin1, and β-actin. (b) Normalized ratio of the phosphorylated-S295-Beclin1 and Beclin1 band intensities, determined from 3 independent experiments performed as in (a). $^{****}p < 0.0001$; NS: not significant; one-way

ANOVA with *post hoc* Tukey test. Figure S2: A10, a specific antagonist for TRPM2, accelerates autophagic flux under OGD-R treatment. (a) SH-SY5Y cells overexpressing mRFP-GFP-LC3 were treated with OGD for 6 h followed by 6 h of reperfusion. 10 μM A10 was added during reperfusion. (b) The mean number of red LC3 puncta per cell in each condition was quantified. All data are from 3 independent experiments. Error bars: SEM. $^{**}p < 0.01$, $^{****}p < 0.0001$; one-way ANOVA with post hoc Tukey test (Supplementary Material). *(Supplementary Materials)*

References

[1] G. Filomeni, D. De Zio, and F. Cecconi, "Oxidative stress and autophagy: the clash between damage and metabolic needs," *Cell Death and Differentiation*, vol. 22, no. 3, pp. 377–388, 2015.

[2] T. Hao, Y. Yang, N. Li et al., "Inflammatory mechanism of cerebral ischemia-reperfusion injury with treatment of stepharine in rats," *Phytomedicine*, vol. 79, article 153353, 2020.

[3] D. N. Granger and P. R. Kvietys, "Reperfusion injury and reactive oxygen species: the evolution of a concept," *Redox Biology*, vol. 6, pp. 524–551, 2015.

[4] R. Cursio, P. Colosetti, and J. Gugenheim, "Autophagy and liver ischemia-reperfusion injury," *BioMed Research International*, vol. 2015, Article ID 417590, 16 pages, 2015.

[5] A. L. Perraud, A. Fleig, C. A. Dunn et al., "ADP-ribose gating of the calcium-permeable LTRPC2 channel revealed by Nudix motif homology," *Nature*, vol. 411, no. 6837, pp. 595–599, 2001.

[6] A. Sumoza-Toledo and R. Penner, "TRPM2: a multifunctional ion channel for calcium signalling," *The Journal of Physiology*, vol. 589, no. 7, pp. 1515–1525, 2011.

[7] J. Jia, S. Verma, S. Nakayama et al., "Sex differences in neuroprotection provided by inhibition of TRPM2 channels following experimental stroke," *Journal of Cerebral Blood Flow and Metabolism*, vol. 31, no. 11, pp. 2160–2168, 2011.

[8] S. Verma, N. Quillinan, Y. F. Yang et al., "TRPM2 channel activation following _in vitro_ ischemia contributes to male hippocampal cell death," *Neuroscience Letters*, vol. 530, no. 1, pp. 41–46, 2012.

[9] M. Gelderblom, N. Melzer, B. Schattling et al., "Transient receptor potential melastatin subfamily member 2 cation channel regulates detrimental immune cell invasion in ischemic stroke," *Stroke*, vol. 45, no. 11, pp. 3395–3402, 2014.

[10] M. Ye, W. Yang, J. F. Ainscough et al., "TRPM2 channel deficiency prevents delayed cytosolic Zn^{2+} accumulation and CA1 pyramidal neuronal death after transient global ischemia," *Cell Death & Disease*, vol. 5, no. 11, p. e1541, 2014.

[11] I. Alim, L. Teves, R. Li, Y. Mori, and M. Tymianski, "Modulation of NMDAR subunit expression by TRPM2 channels regulates neuronal vulnerability to ischemic cell death," *The Journal of Neuroscience*, vol. 33, no. 44, pp. 17264–17277, 2013.

[12] E. Turlova, Z. P. Feng, and H. S. Sun, "The role of TRPM2 channels in neurons, glial cells and the blood-brain barrier in cerebral ischemia and hypoxia," *Acta Pharmacologica Sinica*, vol. 39, no. 5, pp. 713–721, 2018.

[13] X. Zhang, H. Yan, Y. Yuan et al., "Cerebral ischemia-reperfusion-induced autophagy protects against neuronal injury by mitochondrial clearance," *Autophagy*, vol. 9, no. 9, pp. 1321–1333, 2013.

[14] Y. Q. Zheng, J. X. Liu, X. Z. Li, L. Xu, and Y. G. Xu, "RNA interference-mediated downregulation of Beclin1 attenuates cerebral ischemic injury in rats," *Acta Pharmacologica Sinica*, vol. 30, no. 7, pp. 919–927, 2009.

[15] S. Cardaci, G. Filomeni, and M. R. Ciriolo, "Redox implications of AMPK-mediated signal transduction beyond energetic clues," *Journal of Cell Science*, vol. 125, Part 9, pp. 2115–2125, 2012.

[16] J. Kim, M. Kundu, B. Viollet, and K. L. Guan, "AMPK and mTOR regulate autophagy through direct phosphorylation of Ulk1," *Nature Cell Biology*, vol. 13, no. 2, pp. 132–141, 2011.

[17] J. K. Tripathi, A. Sharma, P. Sukumaran et al., "Oxidant sensor cation channel TRPM2 regulates neutrophil extracellular trap formation and protects against pneumoseptic bacterial infection," *FASEB J*, vol. 32, no. 12, pp. 6848–6859, 2018.

[18] Q. Wang, W. Guo, B. Hao et al., "Mechanistic study of TRPM2-Ca(2+)-CAMK2-BECN1 signaling in oxidative stress-induced autophagy inhibition," *Autophagy*, vol. 12, no. 8, pp. 1340–1354, 2016.

[19] K. Y. Zhan, P. L. Yu, C. H. Liu, J. H. Luo, and W. Yang, "Detrimental or beneficial: the role of TRPM2 in ischemia/reperfusion injury," *Acta Pharmacologica Sinica*, vol. 37, no. 1, pp. 4–12, 2016.

[20] J. Zou, J. F. Ainscough, W. Yang et al., "A differential role of macrophage TRPM2 channels in Ca^{2+} signaling and cell death in early responses to H_2O_2," *American Journal of Physiology-Cell Physiology*, vol. 305, no. 1, pp. C61–C69, 2013.

[21] Y. Fan, P. He, H. Yan et al., "Transient lack of glucose but not oxygen is involved in ischemic postconditioning-induced neuroprotection in mouse corticostriatal slices by regulating glutamate metabolism," *Circulation*, vol. 122, 2010.

[22] X. Zhang, Y. Yuan, L. Jiang et al., "Endoplasmic reticulum stress induced by tunicamycin and thapsigargin protects against transient ischemic brain injury: involvement of PARK2-dependent mitophagy," *Autophagy*, vol. 10, no. 10, pp. 1801–1813, 2014.

[23] H. Zhang, P. Yu, H. Lin et al., "The discovery of novel ACA derivatives as specific TRPM2 inhibitors that reduce ischemic injury both in vitro and in vivo," *Journal of Medicinal Chemistry*, vol. 64, no. 7, pp. 3976–3996, 2021.

[24] M. S. Keiser, Y. H. Chen, and B. L. Davidson, "Techniques for intracranial stereotaxic injections of adeno-associated viral vectors in adult mice," *Current protocols in mouse biology*, vol. 8, no. 4, p. e57, 2018.

[25] J. C. Belrose and M. F. Jackson, "TRPM2: a candidate therapeutic target for treating neurological diseases," *Acta Pharmacologica Sinica*, vol. 39, no. 5, pp. 722–732, 2018.

[26] X. Li, W. Yang, and L. H. Jiang, "Alteration in intracellular Zn^{2+} homeostasis as a result of TRPM2 channel activation contributes to ROS-induced hippocampal neuronal death," *Frontiers in Molecular Neuroscience*, vol. 10, p. 414, 2017.

[27] Q. Wang, L. Huang, and J. Yue, "Oxidative stress activates the TRPM2-Ca^{2+}-CaMKII-ROS signaling loop to induce cell death in cancer cells," *Biochimica et Biophysica Acta (BBA)-Molecular Cell Research*, vol. 1864, no. 6, pp. 957–967, 2017.

[28] S. Kimura, T. Noda, and T. Yoshimori, "Dissection of the autophagosome maturation process by a novel reporter protein, tandem fluorescent-tagged LC3," *Autophagy*, vol. 3, no. 5, pp. 452–460, 2007.

[29] D. M. Gwinn, D. B. Shackelford, D. F. Egan et al., "AMPK phosphorylation of raptor mediates a metabolic checkpoint," *Molecular Cell*, vol. 30, no. 2, pp. 214–226, 2008.

[30] H. X. Ma, F. Hou, A. L. Chen, T. T. Li, Y. F. Zhu, and Q. P. Zhao, "Mu-Xiang-You-Fang protects PC12 cells against OGD/R-induced autophagy via the AMPK/mTOR signaling pathway," *Journal of Ethnopharmacology*, vol. 252, article 112583, 2020.

[31] Y. Wang, H. Huang, Y. Jin et al., "Role of TFEB in autophagic modulation of ischemia reperfusion injury in mice kidney and protection by urolithin A," *Food and Chemical Toxicology*, vol. 131, article 110591, 2019.

[32] B. A. Miller, N. E. Hoffman, S. Merali et al., "TRPM2 Channels Protect against Cardiac Ischemia-Reperfusion Injury:," *The Journal of Biological Chemistry*, vol. 289, no. 11, pp. 7615–7629, 2014.

[33] D. J. Klionsky, K. Abdelmohsen, A. Abe et al., "Guidelines for the use and interpretation of assays for monitoring autophagy (3rd edition)," *Autophagy*, vol. 12, no. 1, pp. 1–222, 2016.

[34] R. C. Laker, J. C. Drake, R. J. Wilson et al., "Ampk phosphorylation of Ulk1 is required for targeting of mitochondria to lysosomes in exercise-induced mitophagy," *Nature Communications*, vol. 8, no. 1, p. 548, 2017.

[35] J. Ha, K. L. Guan, and J. Kim, "AMPK and autophagy in glucose/glycogen metabolism," *Molecular Aspects of Medicine*, vol. 46, pp. 46–62, 2015.

[36] V. R. Venna, J. Li, S. E. Benashski, S. Tarabishy, and L. D. McCullough, "Preconditioning induces sustained neuroprotection by downregulation of adenosine 5'-monophosphate-activated protein kinase," *Neuroscience*, vol. 201, pp. 280–287, 2012.

[37] N. Hosokawa, T. Hara, T. Kaizuka et al., "Nutrient-dependent mTORC1 association with the ULK1–Atg13–FIP200 complex required for autophagy," *Molecular Biology of the Cell*, vol. 20, no. 7, pp. 1981–1991, 2009.

[38] G. Wang, T. Wang, Y. Zhang, F. Li, B. Yu, and J. Kou, "Schizandrin protects against OGD/R-induced neuronal Injury by suppressing autophagy: involvement of the AMPK/mTOR pathway," *Molecules*, vol. 24, no. 19, p. 3624, 2019.

[39] S. G. Pfisterer, M. Mauthe, P. Codogno, and T. Proikas-Cezanne, "Ca2+/calmodulin-dependent kinase (CaMK) signaling via CaMKI and AMP-activated protein kinase contributes to the regulation of WIPI-1 at the onset of autophagy," *Molecular Pharmacology*, vol. 80, no. 6, pp. 1066–1075, 2011.

[40] B. Sun, H. Ou, F. Ren et al., "Propofol inhibited autophagy through Ca^{2+}/CaMKKβ/AMPK/mTOR pathway in OGD/R-induced neuron injury," *Molecular Medicine*, vol. 24, no. 1, p. 58, 2018.

Hindawi
Oxidative Medicine and Cellular Longevity
Volume 2021, Article ID 9949697, 16 pages
https://doi.org/10.1155/2021/9949697

Research Article

Escherichia coli Aggravates Calcium Oxalate Stone Formation via PPK1/Flagellin-Mediated Renal Oxidative Injury and Inflammation

Lingyue An,[1,2] **Weizhou Wu**,[2] **Shujue Li**,[2] **Yongchang Lai**,[2,3] **Dong Chen**,[2] **Zhican He**,[1,2] **Zhenglin Chang**,[1,2] **Peng Xu**,[2] **Yapeng Huang**,[1,2] **Min Lei**,[1,2] **Zheng Jiang**,[1,2] **Tao Zeng**,[2] **Xinyuan Sun**,[2] **Xuan Sun**,[3] **Xiaolu Duan**,[2] **and Wenqi Wu**[1,2]

[1]*Department of Urology, The Second Affiliated Hospital, Guangzhou Medical University, Guangzhou, Guangdong 510260, China*
[2]*Department of Urology, Minimally Invasive Surgery Center, Guangdong Key Laboratory of Urology, The First Affiliated Hospital of Guangzhou Medical University, Guangzhou 510230, China*
[3]*Department of Urology, Shenzhen Shockwave Lithotripsy Research Institute, The Eighth Affiliated Hospital, Sun Yat-sen University, Shenzhen, Guangdong 518033, China*

Correspondence should be addressed to Xiaolu Duan; 94302304@qq.com and Wenqi Wu; wwqwml@163.com

Received 24 March 2021; Revised 8 May 2021; Accepted 24 May 2021; Published 13 July 2021

Academic Editor: Chaoliang Tang

Escherichia coli (*E. coli*) is closely associated with the formation of kidney stones. However, the role of *E. coli* in CaOx stone formation is not well understood. We explored whether *E. coli* facilitate CaOx stone formation and its mechanism. Stone and urine cultures were reviewed from kidney stone formers. The ability of calcium oxalate monohydrate (COM) aggregation was detected to evaluate the influence of uropathogenic *E. coli*, then gel electrophoresis and nanoLC-MS/MS to detect the crystal-adhered protein. Flagellin (Flic) and polyphosphate kinase 1 (PPK1) were screened out following detection of their role on crystal aggregation, oxidative injury, and inflammation of HK-2 cell *in vitro*. By transurethral injection of wild-type, *Ppk1* mutant and *Flic* mutant strains of *E. coli* and intraperitoneally injected with glyoxylate in C57BL/6J female mice to establish an animal model. We found that *E. coli* was the most common bacterial species in patients with CaOx stone. It could enhance CaOx crystal aggregation both *in vitro* and *in vivo*. Flagellin was identified as the key molecules regulated by PPK1, and both of them could facilitate the crystal aggregation and mediated HK-2 cell oxidative injury and activated the inflammation-related NF-κB/P38 signaling pathway. Wild-type strain of *E. coli* injection significantly increased CaOx deposition and enhanced oxidative injury and inflammation-related protein expression, and this effect could be reversed by *Ppk1* or *Flic* mutation. In conclusion, *E. coli* promotes CaOx stone formation via enhancing oxidative injury and inflammation regulated by the PPK1/flagellin, which activated NF-κB/P38 pathways, providing new potential drug targets for the renal CaOx calculus precaution and treatment.

1. Introduction

Renal caliculus is a common and multifactorial disease affecting the population worldwide [1–3], which can be triggered by metabolic disorders, ethnic factors, oxidative injury, and urinary tract infections (UTIs). Approximately 80% of urinary stone contains calcium oxalate (CaOx), and the CaOx stone is the most common type, but the mechanism of its formation remains unknown [4, 5]. Infection stones, mainly composed of magnesium, ammonium, and phosphate, have been proven to be highly correlated with UTI [6]. Urease-producing bacteria (e.g., *Proteus* and *Klebsiella*) promote the formation of infection stones by changing the chemical environment of the urine [7]. Metabolic factors are usually considered to be the main etiology of CaOx stones. However, UTI is often associated with CaOx stones, and *Escherichia coli* is the most common bacterial species causing UTIs, which may be associated with the formation of kidney stones

[8, 9]. In addition, oxidative damage in renal tubular epithelial cell is currently considered to be one of the pivotal triggers for the formation of CaOx stones [10–12]. This injury provides substances for heterogeneous nucleation of CaOx crystals and enhances their adhesion to renal epithelial cells and then promotes the process of crystallization [13]. Nevertheless, the specific roles and the pivotal potential mechanism of *E. coli* in epithelial cell oxidative injury and CaOx stone formation remain to be further investigated and elucidated.

E. coli can adhere to cells with the help of virulence factors secreted by itself, which are affected by inorganic polyphosphate (polyP) and its metabolic enzymes. PolyP, whose synthesis is encoded by polyphosphate kinase 1 (PPK1), is directly correlated with mobility, biofilm development, quorum sensing, and virulence in *E. coli* [14, 15]. PPK1 is a crucial enzyme in the biosynthesis and degradation of polyP, which was the first found in *E. coli* by Kornberg [16]. *Ppk1* gene mutant strains lack toxicity-related functions, like motility, quorum sensing, exopolymer formation, and surface attachment [17]. However, the exact role of PPK1 in *E. coli*-mediated CaOx stone formation has not yet been well defined.

Thus, we hypothesized that *E. coli* could induce renal inflammation and enhances oxidative injury and then promotes CaOx formation in the kidney. The PPK1 and its downstream protein are involved in the regulation of *E. coli*-related inflammation and oxidative injury. More importantly, a previously unknown mechanism of *E. coli* promoting renal CaOx stone formation has been revealed and the conclusion provides new potential drug targets for the renal CaOx calculus precaution and treatment.

2. Materials and Methods

2.1. Stone and Urine Sample Analysis. Data of kidney stone formers treated with one-stage percutaneous nephrolithotomy between September 2016 and September 2018 were retrospectively reviewed. Patient's materials comprising stone composition, midstream urine culture (UC), and stone culture (SC) were collected to analyze the microbial spectrum of uropathogens. All stone specimens for SC were collected during operation. Briefly, stone fragments were pulverized with a sterile grinder for subsequent infrared spectroscopy analysis after an aseptic collection, which use a sterile container filled with saline.

2.2. Cell Lines and Cell Cultures. HK-2 cells, which were produced in the American Type Culture Collection (ATCC; Manassas, VA, USA), were cultured in DMEM/F-12 supplemented with 10% FBS at 37°C in a humidified atmosphere of 95% air and 5% CO_2.

2.3. Strains and Plasmids. Wild-type *E. coli* CFT073 (WT-CFT073) was purchased from ATCC (ATCC700928). DH5α, pKD46, DH5α, pKD4, and DH5α were preserved in our laboratory. All *E. coli* CFT073 strains were grown in terrific broth (TB) medium (select pepton 10 g/L, yeast extract 23.6 g/L, K_2HPO_4 9.4 g/L, and KH_2PO_4 2.2 g/L) at 37°C with shaking at 200 rpm overnight. The culture was harvested at mid-log phase ($OD_{600} = 0.5$) and centrifuged at 2,300 g for 5 min at 25°C. An equal volume of glycerol was mixed with the precipitated bacteria and stored at -80°C until needed. The remaining supernatant was sterilized through a filter (0.22 μm pore size) for the following experiments.

2.4. Construction of UPEC PPK1 and Flagellin Mutant Strains. Based on the *E. coli* CFT073 *Ppk1* and *Flic* gene sequence (GenBank Accession No. NC_004431.1), primers H1-K1, H2-K2, H3-K3, and H4-K4 were synthesized to contain homologous arms. The sequences of the primers were as follows: PPK1-F: 5′-ttgctcgccataatatccaggcagtgtcccgtgaataaaacggagtaaaaGTGCGCTCTCCTGTTCCGAC-3′ and PPK1-R 5′-tgtagtcgtaaatcgccaactgcgcccgtactttgcggcgattgccgcggAGGTGGCACTTTTCGGGGAAATG-3′. External identification of the primers is as follows: F: 5′-cccaggaacacgctatttatcc-3′, R: 5′- catctaccacacgggctatgac-3′, I-F: 5′- tctgcgttactgccttgatgat-3′, I-R: 5′-tggtggaccgcgaaatcgcaac-3′, Flic-F: 5′-atcaacaagaaccagtctgcgctgtcgagttctatcgagcgtctgtcttGAGCTGCTTCGAAGTTCCTA-3′, Flic-R: 5′-atcaggcaatttggcgttgccgtcagtctcagttaatcaggttacggcgaCATATGAATATCCTCCTTAGTTCCTATTC-3′ and external identification of the primers: F: 5′-ccaacagcctctcgctgatcactc-3′, R: 5′-cacgttgctggcaaattaccattcatgttg-3′. The PPK1-F and PPK1-R were homologous to the marginal sequence of the *Ppk1* gene. The uppercase part was homologous to the sequence at both ends of the kanamycin resistance gene. PCR technology was used to amplify the targeting gene with kanamycin resistance and then purify it. Subsequently, *E. coli* CFT073/pKD46 electrotransformation competent cells were prepared, and the electrotransformation of target fragments was completed. Briefly, *E. coli* CFT073/pKD46 was cultured with 1 M L-arabinose (final concentration of 2 mM) to an OD600 of 0.5. Bacteria was precipitated and resuspended at low temperature with 10% glycerol. The purified target fragment was added to *E. coli* CFT073/pKD46 competent cells and then subjected to an electric shock (2.5 kV, 25 μF, and 200 Ω). The transformed bacteria were grown in LB plates (containing 50 μg/mL kanamycin) at 37°C overnight. After being genetically stable, the bacteria liquid is mixed with an equal volume of glycerol as the strain, stored at -80°C for subsequent experiments. Finally, the successfully constructed *Ppk1* and *Flic* mutants were named ΔPPK1-CFT073 and ΔFlic-CFT073, respectively.

2.5. COM Crystal Preparation. COM crystals were prepared basing on the published protocols [18]. The Tris buffers were made of Tris-Base and NaCl (pH 7.40, 90 mM Tris-Base, and 10 mM NaCl). $Na_2C_2O_4$ (0.5 mM) and $CaCl_2$ (5 mM) were diluted in the Tris buffer, respectively. The mixture was incubated 20 h at 20-25°C. The COM crystals were scraped under a microscope to observe and centrifuged (2000 g, 5 min). The methanol was removed after washing the COM crystals; then, COM crystals (per 1 mg dry weight)

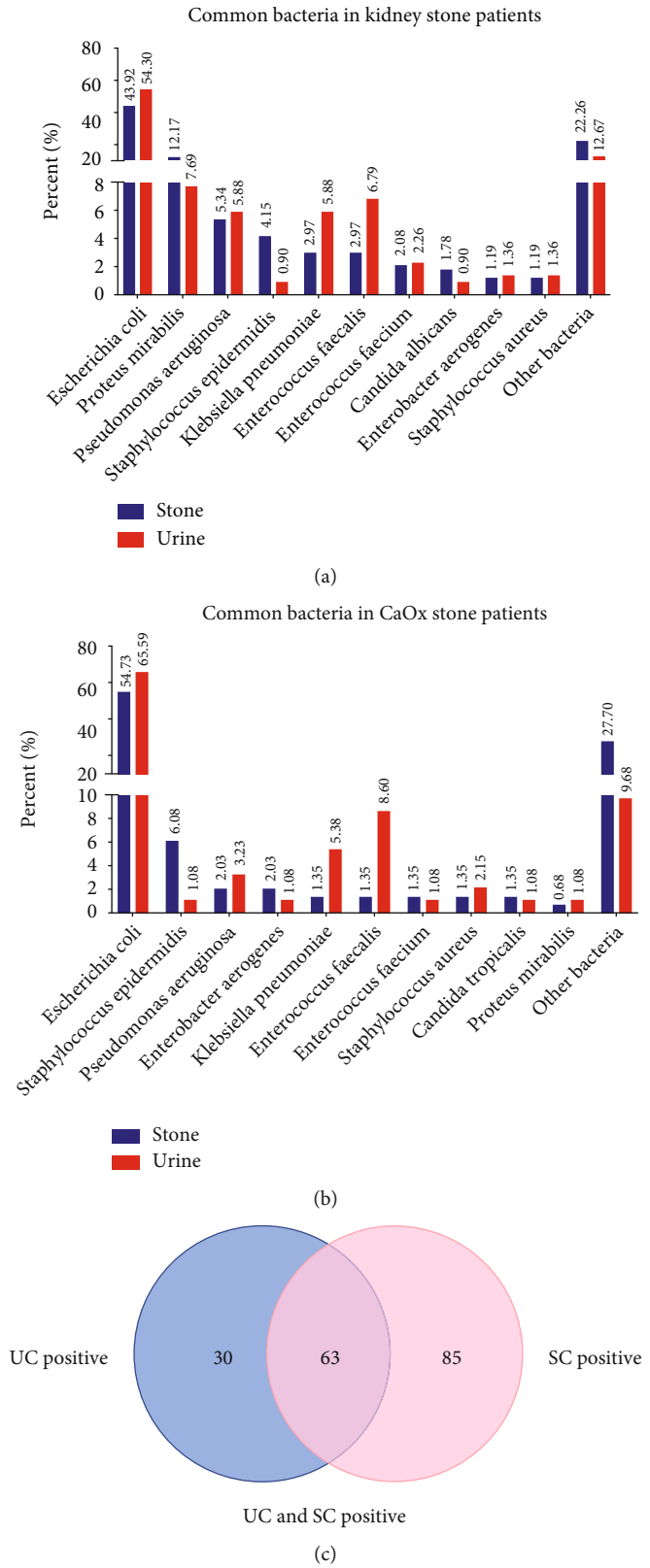

Figure 1: (a) Common bacteria in the urine and stone samples of patients with kidney stone. (b) Common bacteria in the urine and stone samples of patients with calcium oxalate stones. (c) The number of calcium oxalate stone patients with UC and SC both positive.

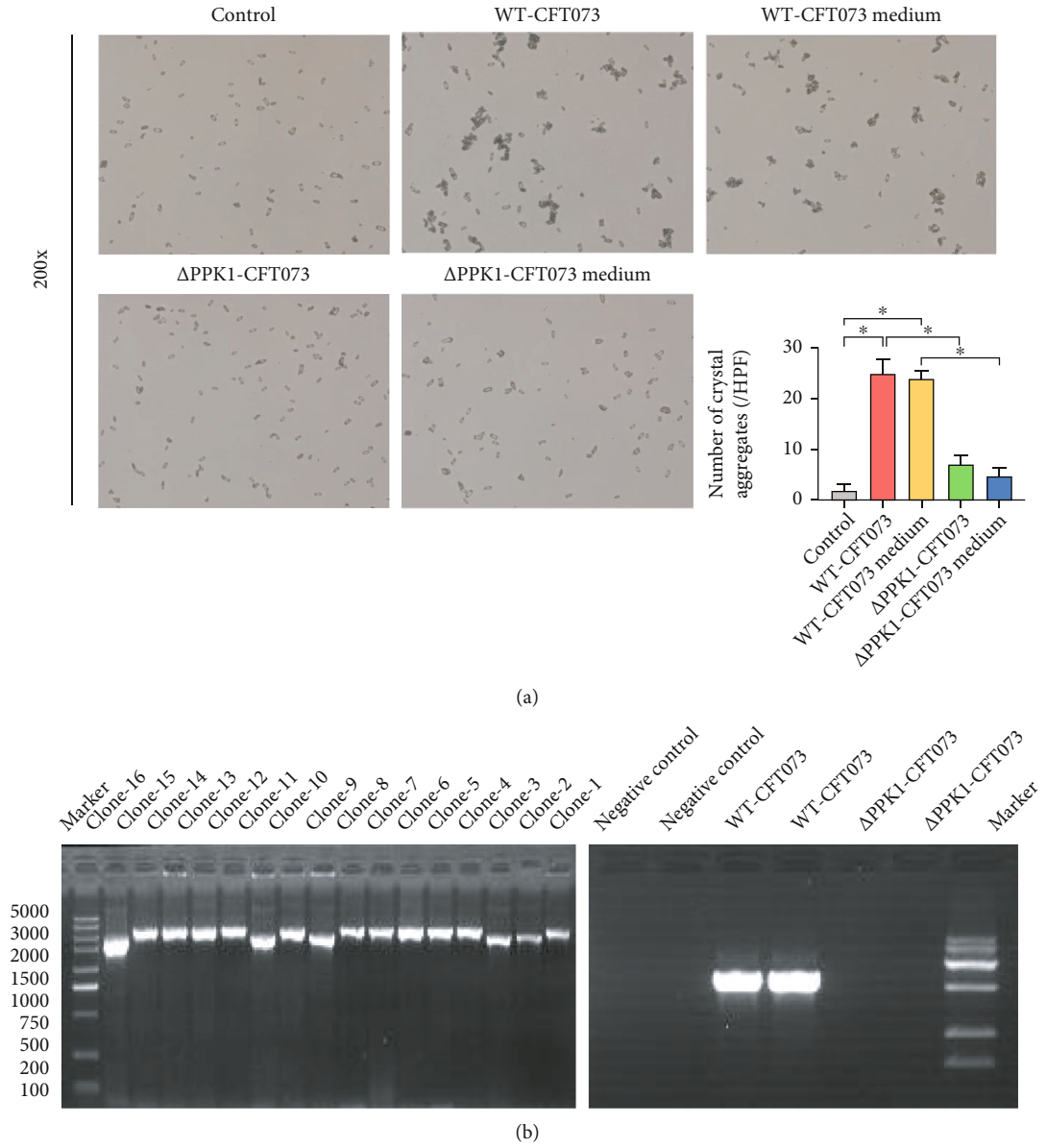

Figure 2: The aggregate effect of WT-CFT073, ΔPPK1-CFT073, and their medium on COM. (a) WT-CFT073 and its medium both promoted CaOx crystal aggregation (original magnification: ×200; the results are presented as the mean ± SEM. $^*p < 0.05$ in comparison with the corresponding group). ΔPPK1-CFT073 and its medium reduced CaOx crystal aggregation. (b) *Ppk1* knockout UPEC strain was constructed and tested by PCR. Clone 1-16: the 16 clones randomly selected on the Kana resistance plate were numbered in sequence.

were air-dried and resuspended in terilized phosphate-buffered saline (PBS).

2.6. Comparison of the Aggregation Effect of Various E. coli Strains to COM. The effects of different bacterial strains on CaOx crystal aggregation were evaluated using 10^6 CFU/mL. After coincubation with different strains of *E. coli* at 37°C for different times, CaOx crystal aggregation was evaluated as follows. The size of the COM crystals was measured from 100 random individual crystals. The average of each sample was calculated. The assembly of two or more individual COM crystals tightly combined was defined as crystal aggregation [19–21], which was counted and averaged from ten high-power fields. These experiments were performed in triplicates.

2.7. Comparison of the Aggregation Effect of Various E. coli Strains and Culture Medium to COM. To study the effect of secretion of extracellular molecules by *E. coli*, 100 μL COM crystal buffer was added to 1 mL of medium sterilized by the filter as mentioned before and coincubated at 37°C. After 1 h, crystal images were taken using a phase-contrast inverted microscope (IX-71; Olympus, Tokyo, Japan) connected to a digital camera. The estimation of COM crystal size and COM crystal aggregation numbers were mentioned before. Control experiments were performed under the same conditions as PBS.

2.8. Screening of PPK1-Regulated Differential Molecules Secreted by ΔPPK1-CFT073 and WT-CFT073 Strains. After the WT-CFT073 and ΔPPK1-CFT073 strains and culture medium (sterile filtration as mentioned before) were incubated with COM (1 mg/mL) for 12 h, they were centrifuged for 10 min (1,200 rpm, 4°C), and then, the supernatant was discarded to obtain the incubated COM crystals. After washing the COM crystal three times with cold PBS, the RIPA lysate was added to isolate the adhesive proteins on the surface of the crystals. The proteins were denatured in road buffer (2% SDS, 10% glycerol, and 62.5 mmol/L Tris-HCl; pH 6.8). SDS-polyacrylamide gel electrophoresis (PAGE; 10% acrylamide) was used to separate protein. Then, the total protein was loaded in each lane. SDS-polyacrylamide gel was stained with colloidal Coomassie brilliant blue G-250 at room temperature for 18 h after proteins were separated. Coomassie Blue de-staining solution was used to wash for 12 h. The images were visualized using an automatic gel imaging system (Bio-Rad).

2.9. In-Gel Tryptic Digestion and Differential Protein Identification by nanoLC-MS/MS. The differential proteins were extracted from SDS-polyacrylamide gels and followed an in-gel tryptic digestion. EASY-nLC II (Bruker Daltonics; Bremen, Germany) was applied to isolate the digested sample. Mass spectra were deconvoluted using Data Analysis version 4.0 SP5 (Bruker Daltonics). MASCOT 2.3 software (Matrix Science, London, UK) was used to analyze the data of MS/MS spectra, and the protein database (uniprot_Escherichia_coli_4596_20170807.fasta) was analyzed on the UniProt Library (https://www.uniprot.org/).

2.10. Effect of Different Concentrations of Flagellin Antibody on COM Aggregation. Different concentrations of flagellin antibodies were preadded to the culture medium 30 min before it was incubated with COM (1 mg/mL). CaOx crystal aggregation was evaluated as previously described.

2.11. Crystal-Cell Adhesion Assay. HK-2 cells (10^6 cells per dish) were seeded into 6 cm cell culture dishes until reaching 90% confluence (37°C, 5% CO_2 incubator). Afterwards, the cells were infected with bacteria at a ratio of 10 bacteria per host cell for 1 h. 20 $\mu g/cm^2$ COM crystals was added to the medium and maintained statically for 5 min. PBS was used to remove the nonadherent crystals for three times. COM crystal adhesion were observed under an inverted microscope and images were taken, which were counted from at least 10 randomized high-power fields per well.

2.12. ROS Measurement. The process is described in Duan et al.'s study [22]. Briefly, intracellular ROS level was evaluated by dihydroethidium (DHE) fluorescence dye. The cells were pretreated with COM and different *E. coli* strains and then incubated with DHE (Sigma-Aldrich, USA) following the instruction. Then, we removed excess DHE and captured figures with a fluorescence microscope immediately. The final results were semiquantified by ImageJ software.

2.13. Animal Experiments. All experimental procedures attached to the guidelines of the National Institutes of Health Guide for the Care and Use of Laboratory Animals. The research was approved by Guangzhou Medical University Ethics Committee (GY2019-146). 42 C57BL/6J female mice (weight 15-21 g) were purchased from Guangdong Medical Laboratory Animal Center. All mice were raised in the Animal Experimental Center of Guangzhou Medical University; the rearing condition was controlled with a 12/12 hours light/dark cycle, a temperature of 22-26°C, and humidity of 40-70%. CaOx deposits in the kidneys of mice were established by injecting glyoxylate (glyoxylic acid, GA. 80 mg/kg, and 200 μL) intraperitoneally (i.p.) for 7 days. On the first day, the mice were administered transurethral injection of bacteria to induce UTI under anesthesia (2-2.5% isoflurane induced anesthesia, followed by maintenance with 1.8-2%). The injection was repeated for 4 h as per the methods by Thai et al. [23] All mice were randomly divided into 6 groups ($n = 8$ per group): (1) normal group, (2) Ga i.p. only, (3) Ga +saline, (4) Ga i.p.+WT-CFT073, (5) Ga i.p.+△PPK1-CFT073, and (6) Ga i.p.+△Flic-CFT073. All mice were subjected to fasting for 12 h after the injecting the bacteria and then were provided food and water freely. Bilateral kidneys were removed under isoflurane anesthesia for histological examination and protein detection after 7 days.

2.14. Hematoxylin and Eosin (HE) and Pizzolato Staining to Detect the Kidney CaOx Crystals. Fixed kidney tissue samples were prepared paraffin-embedded sections (6 μm), and hematoxylin and eosin solution was used to stain the tissues. COM crystals were detected by Pizzolato staining. The histological patterns of the kidneys were observed by HE. The CaOx crystal deposition of the kidney was confirmed by polarized light optical microphotography and tissue scanner. ImageJ software was used to calculate the crystal area.

2.15. Immunohistochemistry (IHC). IHC followed a standardized process. Sections were incubated overnight at 4°C with anti-MCP1 (1 : 200 dilution, Abcam), anti-CD44 (1 : 100 dilution, Cell Signaling Technology), anti-p-P65 (1 : 200 dilution, Abcam), anti-p-P38 (1 : 200 dilution, Abcam) antibodies, anti-SOD1 (1 : 200 dilution, Proteintech), and anti-8-OHdG (1 : 200 dilution, Abcam). Subsequently, they were incubated with biotinylated horse anti-rabbit or anti-mouse antibody and avidin-biotin-peroxidase complex. The sections were dehydrated in ascending alcohol series. Finally, xylene was used to clear the sections. A polarizing microscope (CX31 Olympus, Tokyo, Japan) and tissue scanner (PathScope 4 s, DigiPath, NV, USA) were used to observe the sections. The protein expression of each antibody was calculated by ImageJ software.

2.16. Western Blot (WB). The WB followed the previous research procedure [22]. The HK-2 cells pretreated with different bacteria were lysed in RIPA buffer. The cell proteins were extracted for quantitative denaturation, and then detected by WB. SDS-polyacrylamide gel used to separate proteins and then transferred to NC membrane (Millipore). Antibodies of CD44, p-P38, P38, p-P65, and P65 were immunoblotted with an NC membrane. HRP-conjugated anti-mouse and anti-rabbit IgG (sc-2005 and sc-2004, Santa Cruz)

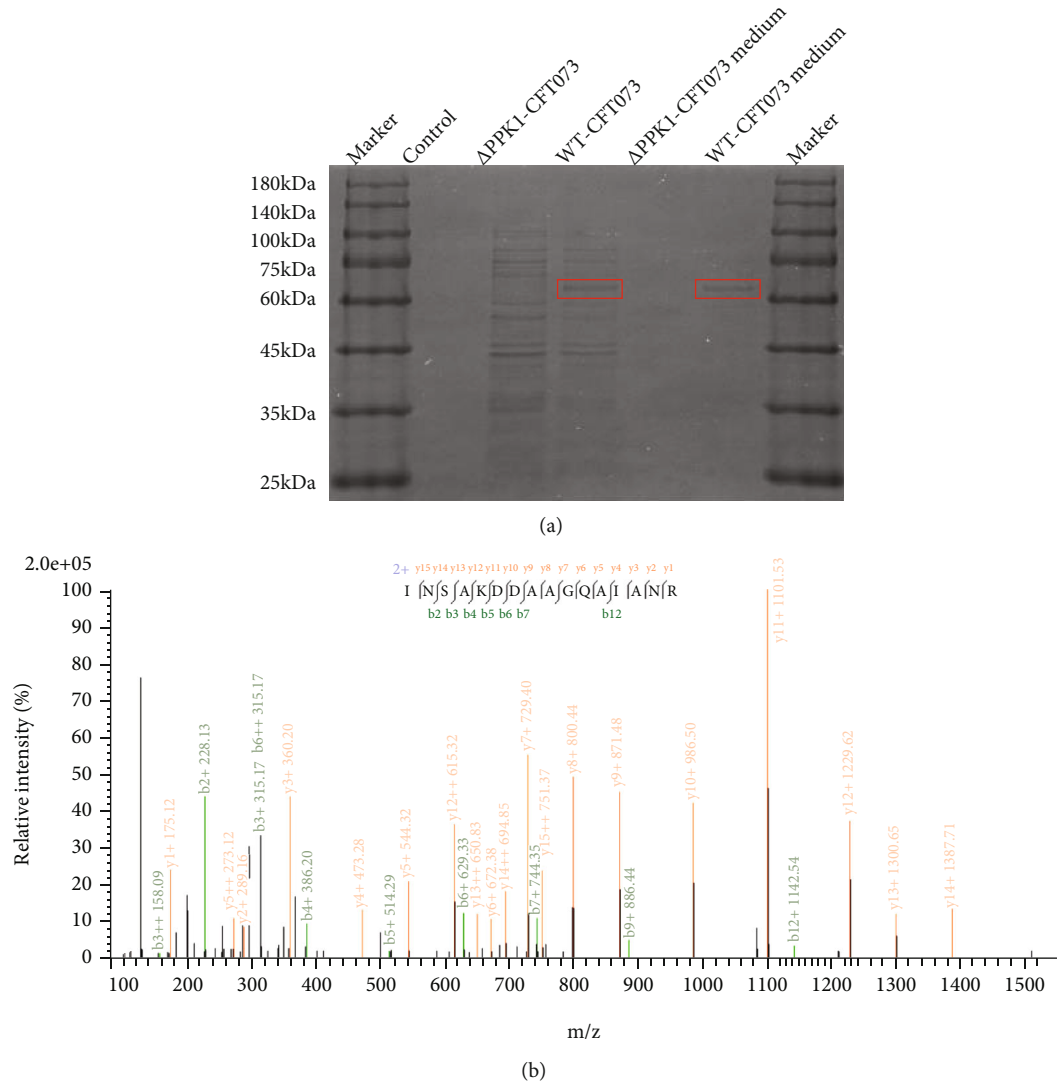

Figure 3: PPK1-regulated differential crystal aggregation relative molecules secreted by WT-CFT073 strain. (a) There existed differential protein bands with 60 kD and 75 kD between WT-CFT073 and ΔPPK1-CFT073. (b) The main differential protein is flagellin which analyzed by nanoLC-MS/MS.

are secondary antibodies. Internal control was tubulin. ImageJ software was used to quantify and normalize processing.

2.17. Statistical Analysis. Mean ± SD was used to express all data. Statistical analyses were performed utilizing GraphPad Prism (version 8.0). *t*-tests and one-way ANOVA with LSD post hoc comparisons were used to complete data analysis. $p < 0.05$ have been viewed as statistically significant on the whole analyses.

3. Results

3.1. E. coli Is the most Common Bacterial Species in Urine and Stones of Patients with CaOx Stones. In total, 1055 patients were included. SC was positive in 337 (31.94%) patients, and UC was positive in 221 (20.95%) patients. The results of bacterial culture showed that among all stone types, *E. coli* accounted for 43.92% and 54.30% of all bacteria in stones and urine, respectively (Figure 1(a)). A total of 582 patients had CaOx stones (55.17%), SC was positive in 148 (25.43%) patients, and UC was positive in 93 (15.98%) patients. The percentages of *E. coli* were 54.73% and 65.59% in stones and urine, respectively (Figure 1(b)). In addition, among the 63 CaOx stone patients with both positive US and SC (Figure 1(c)), *E. coli* was detected in 48 (76.19%) UC and 47 (74.60%) SC. The bacterial spectrum of stones and urine from these patients indicated that *E. coli* dominated in the bacterial species of stones patients' urine and stone, regardless of the type of stone.

3.2. PPK1 Mediates WT-CFT073- and Its Culture Medium-Promoted COM Crystal Aggregation. Compared to the control group, WT-CFT073 and its culture medium significantly promoted CaOx crystal aggregation. Interestingly, not only

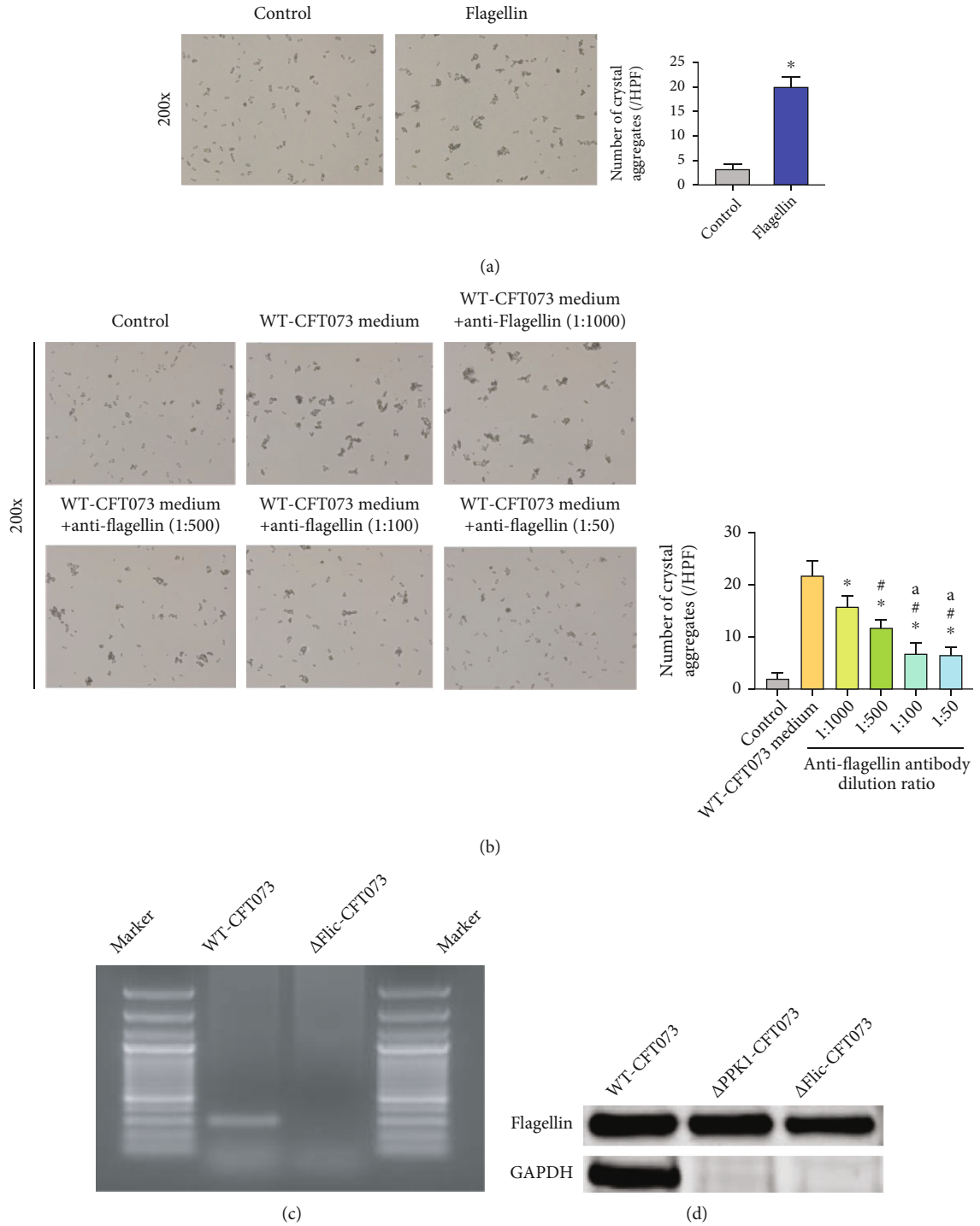

Figure 4: The aggregate effect of flagellin on COM and constructing flagellin mutant strain (ΔFlic-CFT073). (a) Flagellin showed a conspicuously aggregate ability on COM ($^{*}p < 0.05$ in comparison with the corresponding group; original magnification: ×200). (b) Anti-flagellin antibodies reduce the crystal aggregation of COM crystal compared with WT-CFT073 culture medium in a concentration dependent manner ($^{*\#a}p < 0.05$, *compare to WT-CFT073 medium group, $^{\#}$compare to 1: 1000 group, ^{a} compare to 1 : 500 group. Original magnification: ×200). (c) *Flic* knockout UPEC strain was constructed and tested by PCR. (d) Western blot showed the flagellin was decreased in ΔPPK1-CFT073 and ΔFlic-CFT073.

the WT-CFT073 strains but also its culture medium could promote COM aggregation (Figure 2(a)). These results indicated that some secretory virulence factors mediate the effect of *E. coli*-induced crystal aggregation.

The clone 2, 3, 9, 11, and 16 PCR fragments became smaller, in line with expectations, which were judged to be strain knockout *Ppk1* gene, and the *Ppk1* mutant (ΔPPK1-CFT073) was verified (Figure 2(b)). As shown in the crystal

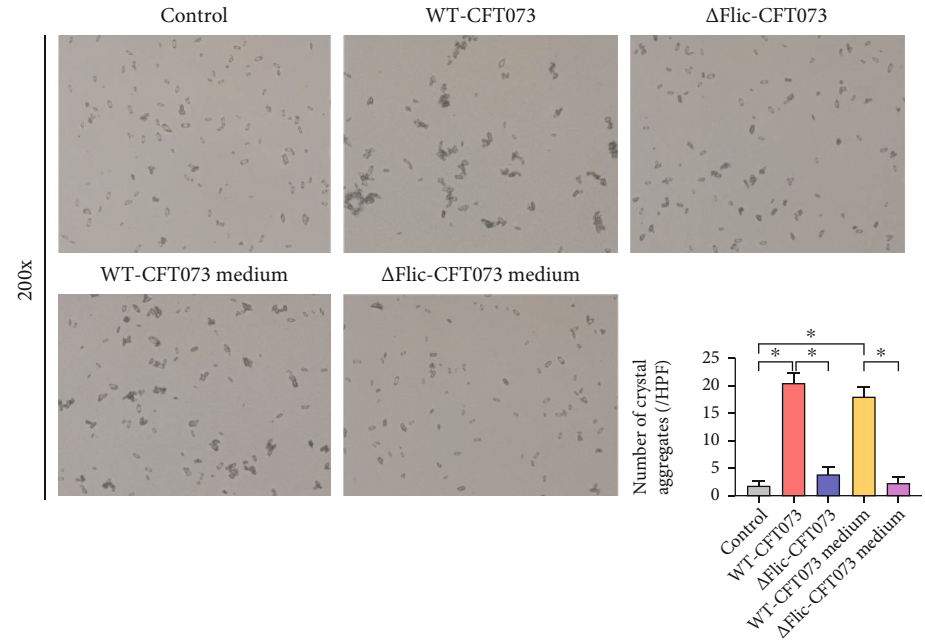

Figure 5: ΔFlic-CFT073 and its culture medium reduced CaOx crystal aggregation compared with WT-CFT073 ($^*p < 0.05$ in comparison with the corresponding group; original magnification: ×200).

aggregation assay, compared to WT-CFT073, ΔPPK1-CFT073 and its culture medium induced weaker CaOx crystal aggregation (Figure 2(a)). No differences were found between control and ΔPPK1-CFT073, as well as the culture medium of ΔPPK1-CFT073. These results suggested that PPK1 is a vital factor for the effect of *E. coli* on crystal aggregation.

3.3. Differentially Expressed Proteins Involved in Crystal Aggregation and Secreted by WT-CFT073 Strain Were Regulated by PPK1. After incubating the COM crystals with WT-CFT073, ΔPPK1-CFT073, and their respective cultures, the PPK1-regulated differential proteins related to aggregation were separated by gel electrophoresis, whereafter these proteins were identified by nanoLC-MS/MS. The differential protein bands were found to be markedly different at 60 kD and 75 kD (Figure 3(a)), and the results of Shotgun sequencing showed that the main differentially expressed protein was flagellin, which is the major component of bacterial motility organ flagellum (Figure 3(b)). These data indicated that flagellum is one of the key proteins involved in crystal aggregation regulated by PPK1.

3.4. Flagellin Mediated the Enhancing Effect of E. coli on COM Crystal Aggregation. The effect of flagellin on COM crystal aggregation was also examined. Flagellin treatment significantly increased crystal aggregation (Figure 4(a)). Pretreatment with anti-flagellin antibodies reversed the crystal aggregation induced by WT-CFT073 culture medium in a dose-dependent manner, and no differences were found between the 1 : 100 group and 1 : 50 group (Figure 4(b)). Furthermore, the ΔFlic-CFT073 strain had almost no flagellin expression (Figures 4(c) and 4(d)), and its culture medium induced less CaOx crystal aggregation compared with WT-CFT073. No differences were found between the control and ΔFlic-CFT073, as well as the culture medium of ΔFlic-CFT073 (Figure 5). These results indicated that the flagellum was indispensable for the role of *E. coli* in COM crystal aggregation.

3.5. PPK1/Flagellin Axis Was Essential for the Stimulatory Effect of E. coli on Crystal Adhesion. The amount of adhesive COM crystals in HK-2 cells and CD44 expression induced by ΔPPK1-CFT073 or ΔFlic-CFT073 strain were significantly reduced, compared with WT-CFT073 (Figures 6(a) and 6(b)). On the other hand, the adhesion of COM crystals and CD44 expression were increased by flagellin immediately after treatment (100 ng/mL flagellin-treated cells for 24 h) (Figures 6(c) and 6(d)). Using IHC, we found that an additional transurethral injection with WT-CFT073 led to higher CD44 expression than glyoxylic acid treatment alone. Particularly, the distribution of CD44 was located in the cytoplasm of renal tubular epithelial cells. In contrast, the additional transurethral injection with ΔPPK1-CFT073 or ΔFlic-CFT073 strain represented no significant effect on CD44 expression (Figure 6(e)). These *in vitro* and *in vivo* data suggest that the PPK1/flagellin axis mediates *E. coli*-induced CD44 overexpression and crystal adhesion to HK-2 cells.

3.6. E. coli-Induced CaOx Crystal Retention in Mouse Kidney Were PPK1 and Flagellin Dependent. The amount of CaOx crystals retained in mouse kidneys exhibited the same trend as CD44 expression in the corresponding group. Using polarized light optical microphotography, the crystal retention in Ga+WT-CFT073 was found to be greater than that in the Ga+saline group. HE staining showed that the renal tubules around the crystals were obviously expanded and deformed (Figure 7(a)). In addition, the CaOx crystals were mainly

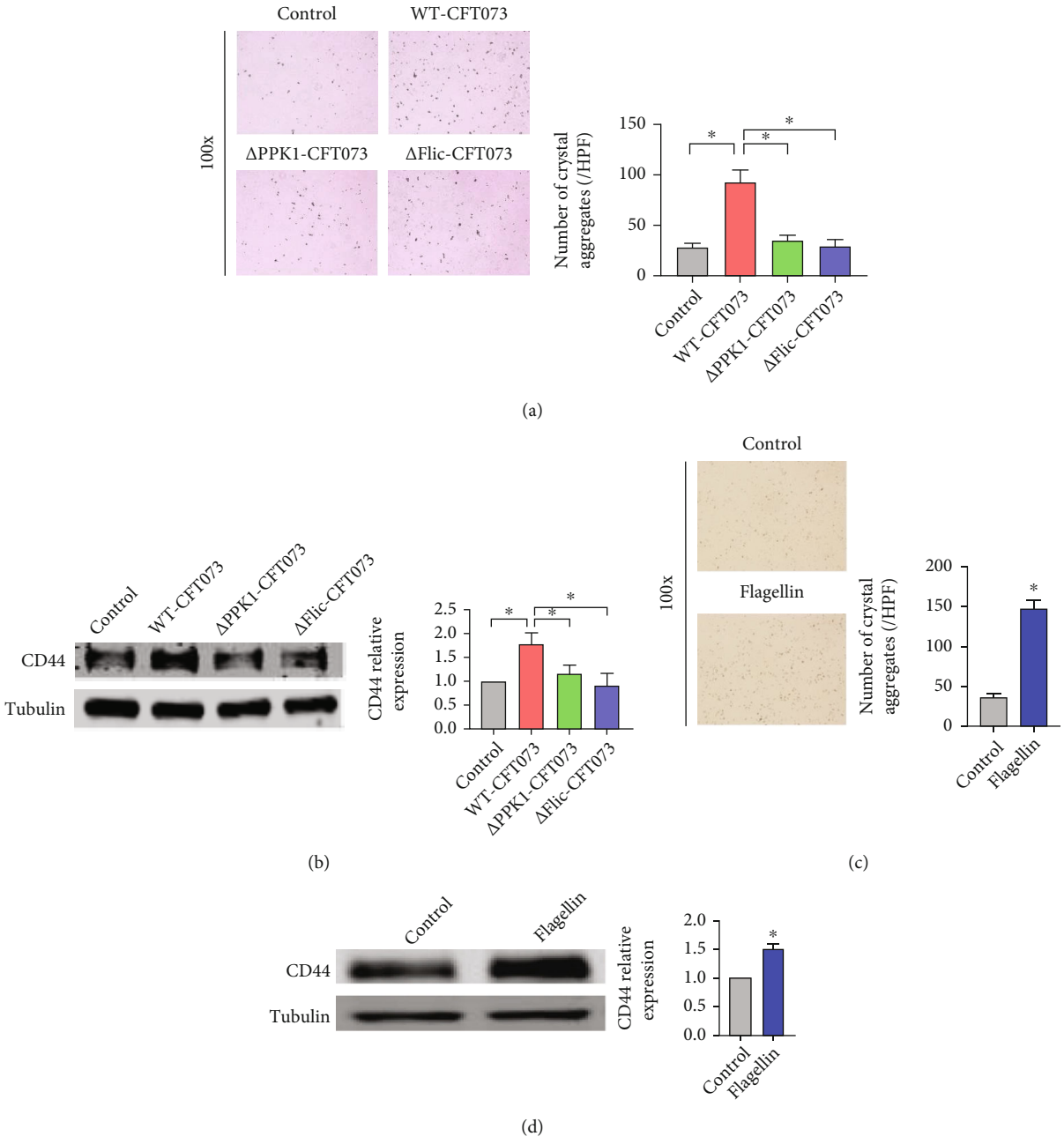

Figure 6: Continued.

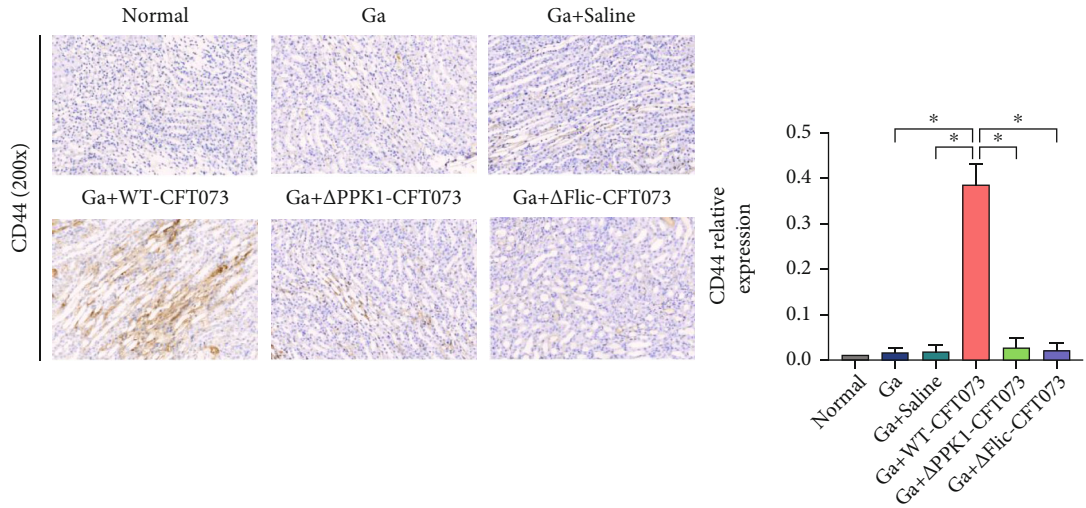

(e)

Figure 6: Flagellin is the key factor to the COM crystals adhesion *in vivo* and *in vitro*. (a) WT-CFT073-treated HK-2 showed higher adhesion COM (original magnification: ×100; $^*p < 0.05$ in comparison with the WT-CFT073 group). (b) CD44 expression was decreased in COM injured HK-2 cells by ΔPPK1-CFT073 and ΔFlic-CFT073 treated (by Western blot, tubulin was used as an internal control. $^*p < 0.05$ in comparison with the WT-CFT073 group). (c, d) The adhesion of COM crystals and the CD44 expression were increased by 100 ng/mL flagellin immediately treated ($^*p < 0.05$ in comparison with the control group). (e) CD44 expression was increased after transurethral injecting WT-CFT073 strain, but not ΔPPK1-CFT073 and ΔFlic-CFT073 strains (original magnification: ×200, $^*p < 0.05$ in comparison with the Ga+WT-CFT07 group).

located in renal cortex and medulla as observed by Pizzolato staining. In contrast to the Ga+WT-CFT073 group, the amount of CaOx crystals was less prominent in the Ga +ΔPPK1-CFT073 or Ga+ΔFlic-CFT073 group. No significant differences were observed among the Ga, Ga+saline, Ga+ΔPPK1-CFT073, and Ga+ΔFlic-CFT073 groups (Figure 7(b)). These data indicate that the PPK1/flagellin axis mediates *E. coli*-induced CaOx crystal retention *in vivo*.

3.7. E. coli-Induced Mouse Renal Oxidative Injury Regulated by PPK1/Flagellin. In the cell experiment, WT-CFT073 pretreatment clearly aggravated oxalate-induced ROS generation, which was not observed in the ΔPPK1-CFT073 and ΔFlic-CFT073 groups (Figure 8(a)). We then detected the oxidative injury markers in the mouse kidney. SOD1 expression was decreased clearly after transurethral injection of WT-CFT073 compared to ΔPPK1-CFT073 and ΔFlic-CFT073. In contrast, 8-OHdG protein (marker of oxidative damage in cellular DNA) expression increased in WT-CFT073. These increases were significantly attenuated by knockout *Ppk1* and *Flic* gene (Figure 8(b)). Together, these results suggested that wild-type *E. coli* accelerates oxalate-induced renal oxidative injury, which were reversed by knockout *Ppk1* and *Flic* genes.

3.8. PPK1/Flagellin-Mediated E. coli-Induced Mouse Renal Inflammation via Activation of NF-κB/P38 Signaling Pathway. CaOx crystal deposition in the kidney is the primary driver of tubular epithelial injury, which induces localized inflammation in the kidney. In turn, renal inflammation is a key regulator of CaOx crystal deposition. Our results showed that stimulation with 100 ng/mL flagellin significantly increased intracellular phosphorylated P38 and P65, as well as nuclear P65 expression in HK-2 cells. Exposure to the WT-CFT073 strain also induced the same change, which was PPK1 and flagellin dependent. (Figure 9(a)).

In animal experiments, the expression of MCP-1, p-P65, and p-P38 was upregulated in the kidneys of mice injected with WT-CFT073. MCP-1 was mainly located in the cytoplasm of the renal epithelial cells. Weak expression of p-P65 and p-P38 was observed in the Ga+ΔPPK1-CFT073 and Ga+ΔFlic-CFT073 groups, compared with the Ga +WT-CFT073 group. Negative expression of MCP-1, p-P65, and p-P38 was observed in the normal, Ga, and Ga +saline groups (Figure 9(b)). These results indicate that *E. coli* could activate the mouse renal inflammatory NF-κB/P38 signaling pathway, which is regulated by the PPK1/flagellin axis.

4. Discussion

Both *E. coli* and its medium promote the aggregation and adhesion of CaOx crystals in our research and that PPK1/flagellin plays a pivotal regulatory role in this process. *E. coli* enhances the renal oxidative injury and induces the renal inflammation via PPK1/flagellin expression, both of which further exacerbate the deposition of CaOx crystals in the kidney, at least, partly activating the NF-κB/P38 signaling pathway.

As the most common type of urinary tract stones, CaOx stones have a high incidence worldwide and have a high chance of recurrence after treatment. Various studies have shown that bacteria in the urinary tract are closely associated with the formation of urinary tract stones. By altering the

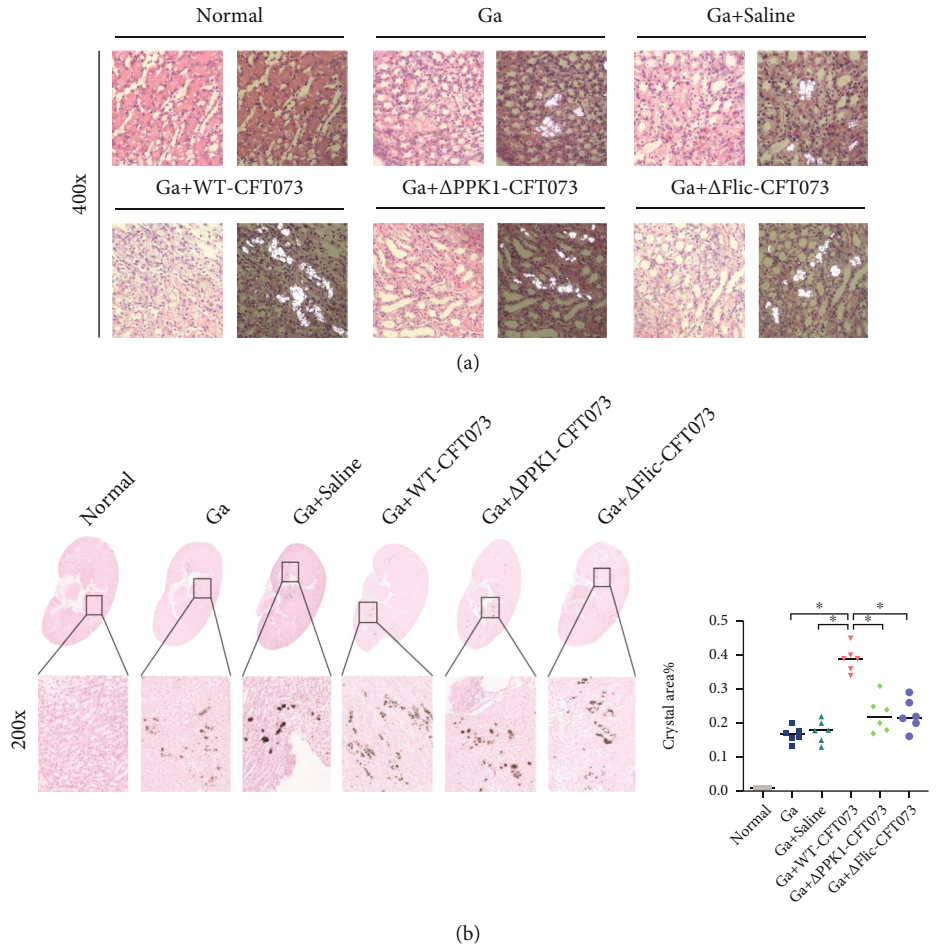

FIGURE 7: The CaOx deposition and histomorphology of mouse kidney after transurethral inject different bacteria strain. (a) HE and polarized light optical microphotography found that crystal depositions in Ga+WT-CFT073 were higher and larger; the renal tubules around crystals were obviously expanded and deformed (original magnification: ×400). (b) The Pizzolato staining (for detection of CaOx crystals) showed the area of CaOx crystals in the Ga+ΔPPK1-CFT073 and Ga+ΔFlic-CFT073 strain groups were decreased (original magnification: ×200, $^{*}p < 0.05$ in comparison with the corresponding group). Ga: glyoxylic acid.

urine composition, urease-producing bacteria (e.g., *Proteus mirabilis*) could cause the formation of infection stones. The exosomes secreted by bacteria, including proteins, polysaccharides, and lipids, could also be involved in the formation of infection stones [5, 24]. In addition to infection stones, bacteria are commonly detected in metabolic stones. Approximately 40%-80% of patients with CaOx stones have concomitant UTIs, which are generally considered to be secondary to CaOx stones rather than a causative factor for its formation [25, 26]. Our study indicated that *E. coli* is the most common bacterial species detected both in CaOx stone former's urine and stone. Additionally, *E. coli* isolated from urine and stones in the same CaOx patient had similar characteristics, like consistent antimicrobial susceptibility profiles, genotyping, phylogenetic groups, virulence, and resistance genes [27]. Instead of the dead bacteria or their fragments, only living and intact *E. coli* bacteria promote nucleation and aggregation of CaOx crystals [20]. An *in vivo* study has confirmed that injection of *E. coli* into the urinary tract of mice causes renal inflammation and promotes crystal deposition [28]. Nevertheless, none of these studies have explored the key factors and specific mechanisms by which *E. coli* promotes CaOx calculus formation, in greater detail. Intriguingly, we confirmed that even in the absence of *E. coli*, the culture medium of wild-type *E. coli* promotes the aggregation of CaOx crystals, indicating that some regulatory molecules secreted by *E. coli* may be the key factors leading to CaOx crystal aggregation *in vitro*.

The pathogenicity of bacteria is closely associated with the virulence factors. Polyphosphate (polyP) is directly linked to bacterial function. It is an inorganic salt that participates in physiological processes. In addition to storing energy, polyP also acts a regulated role in phosphate storage, metal ions chelator, alkaline ion buffering, and DNA access [14, 15]. PPK1 which was first found in *E. coli* in 1956 demonstrated the ability to participate in biosynthesis and degradation of polyP [16]. In the bacterial extracellular matrix, PPK1 is highly associated with the secretion and function of various virulence factors in bacterial resistance and is unique to UPEC [29]. Our study showed a significantly decreased COM aggregation-inducing effect *in vitro* and *in vivo* after knockout of *Ppk1* in the UPEC strain. *Ppk1* is

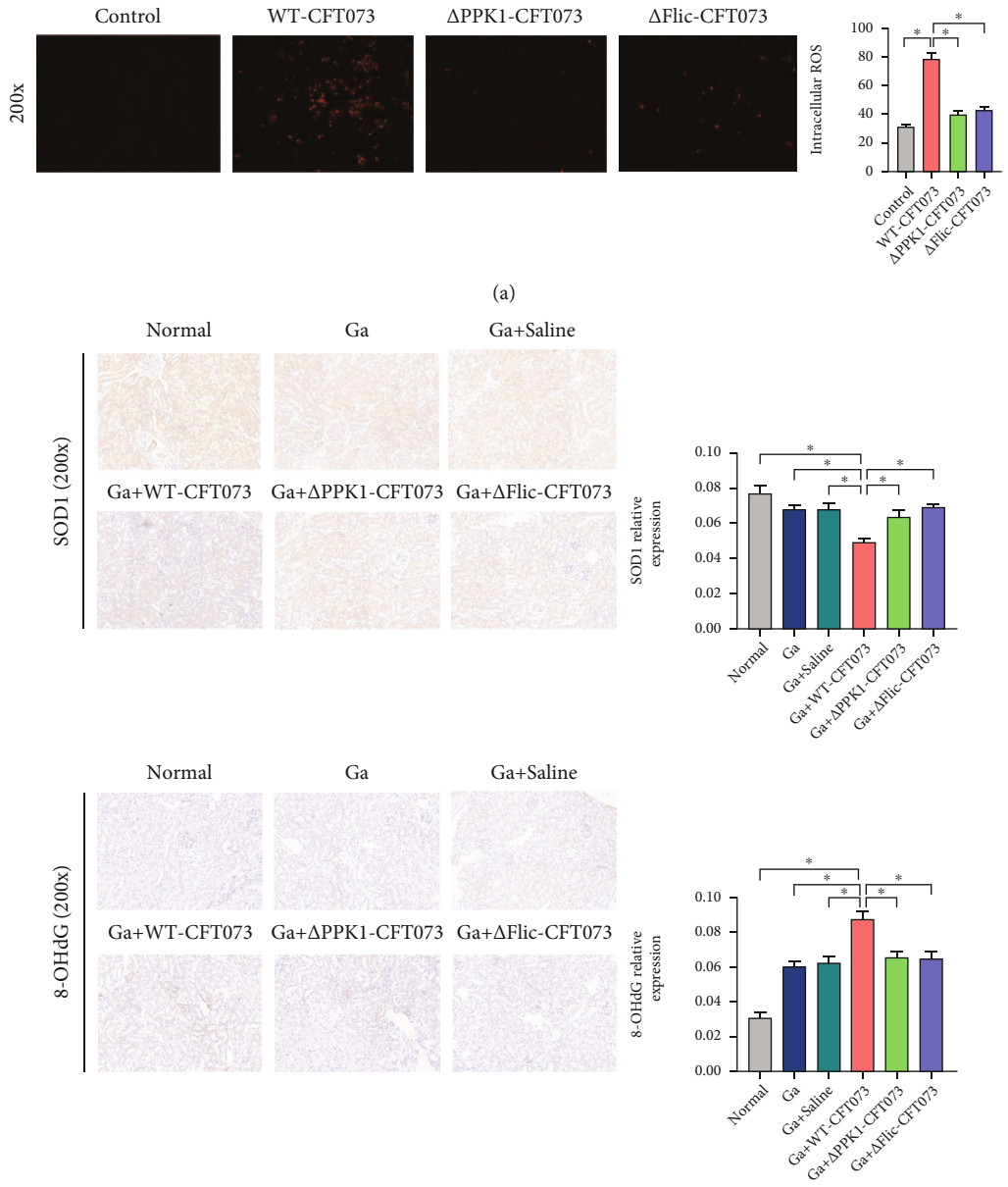

Figure 8: *E. coli*-mediated oxidative injury regulated by PPK1/flagellin. (a) HK-2 treated with WT-CFT073 were increased the intracellular ROS level (original magnification: ×200; $^*p < 0.05$ in comparison with the WT-CFT073 group). (b) SOD1 was downregulated in the Ga+WT-CFT073 group, 8-OHdG was upregulated in the Ga+WT-CFT073 group, and both proteins reversed in ΔPPK1-CFT073 and ΔFlic-CFT073 (original magnification: ×200, $^*p < 0.05$ in comparison with the WT-CFT073 group).

essential for bacteria to form biofilms, which promote stone growth and adhesion. Thus, as the biofilm-generating ability of △PPK1-CFT073 was greatly reduced, it resulted in weaker aggregation of the COM crystals. In addition, PPK1-deficient bacteria are more susceptible to environmental effects. The bacterial activity and resistance also decreased due to PPK1 deficiency. Therefore, it is reported that PPK1 may be a potential target for addressing the issue of bacterial resistance [30].

PPK1 is associated with multiple downstream factors that are secreted by bacteria. We found that flagellin is the most important crystal aggregation-related protein, associated with PPK1. It is the main component of the bacterial flagellum, which is a motor organ of bacteria that mediates swimming and mass movement, and assists in bacterial locomotion towards the host target site [31]. Flagellin is encoded by the *Flic* gene and folds into D0, D1, D2, and D3 domains in different spaces. The D1 domain could combine with the Toll-like receptor 5 in epithelial cells and monocytes, causing a strong inflammatory response [32]. *Flic* mutations lead to a significant reduction in the pathogenic capacity of bacteria [33]. In this study, flagellin was found to directly promote the aggregation of COM crystals, a finding that is also consistent with the study by Rattiyaporn et al. [34] Other

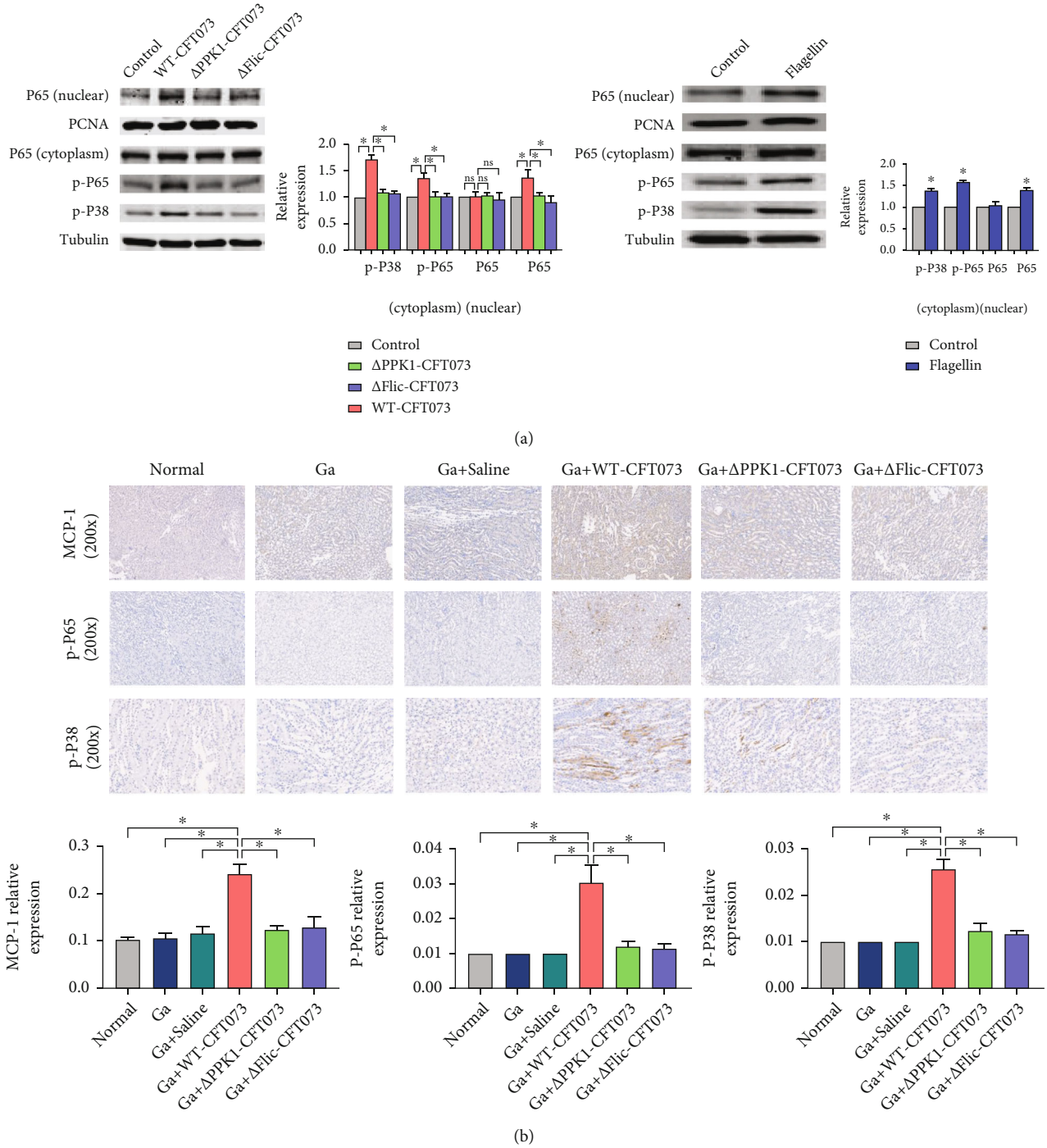

Figure 9: PPK1/flagellin may activate mouse renal inflammation via the NF-κB/P38 signaling pathway. (a) HK-2 treated with WT-CFT073 and 100 ng/mL flagellin increased the intracellular and nuclear phosphorylation of P38 and P65 (by Western blot, tubulin was used as an internal control, $^*p < 0.05$ in comparison with the WT-CFT073 group). (b) MCP-1, p-P65, and p-P38 were upregulated in the Ga+WT-CFT073 group, but not other groups. Phosphorylation of P65 and P38 were located in both the cytoplasm and nuclear of renal tubular epithelial cells (original magnification: ×200, $^*p < 0.05$ in comparison with the WT-CFT073 group).

components in *E. coli* also could aggregate COM crystals. For example, lipopolysaccharide- (LPS-) mediated negative charge on the bacterial surface may facilitate crystal aggregation, and the elongation factor Tu which is highly expressed in Outer membrane vesicles (OMVs) of UPEC also could promote the aggregation of COM crystals [34, 35]. However, their aggregation effect on COM crystals is significantly weaker than flagellin [34]. Our results validate the function of PPK1 in regulating flagellin expression and affecting the aggregation of COM crystals, indicating that flagellin is an essential factor in UPEC-induced COM crystal aggregation. In addition, the same phenomenon was observed in the

mouse model. The formation of urinary tract stones involves biomineralization, and bacterial biofilm participates in this process [36]. Flagellin can accelerate the formation of the biofilm [30]. It might have the potential to alter the crystal surface charge and thus enable the *E. coli*-induced crystal aggregation [20]. From the points discussed above, it is clear that the role of flagellin in CaOx stone formation deserves more attention, and the specific roles of flagellin in biofilm formation and CaOx stone formation are expected to be revealed in the future.

High oxalate could promote crystal adhesion and oxidative injury of renal tubular epithelial cell, which are the pivotal processes in CaOx stone formation [22, 37, 38]. Since UPEC colonized in the urinary tract induces infections that can adhere to renal tissue and cause renal tubular epithelial cell damage via the action of matrix toxic force factors [39]. Our study confirmed that *E. coli*-induced crystal adhesion to HK-2 cells was reduced after *Ppk1* or *Flic* gene mutation. Overexpression of the adhesive capacity marker CD44 induced by *E. coli* was significantly weakened both *in vitro* and *in vivo*, if *Ppk1* or *Flic* was knocked out. Interestingly, treatment of HK-2 cells with flagellin increased CD44 expression and enhanced CaOx crystal adhesion. Additionally, the oxidative injury level also reversed in the △PPK1-CFT073 and △Flic-CFT073 groups. It means the ability of *E. coli* to promote CaOx crystal adhesion to renal tubular epithelial cells and to enhance oxidative injury is partly regulated by PPK1/flagellin, which may subsequently accelerate the formation of CaOx stones.

The present study also detected *E. coli*-induced differential marker protein associated with renal inflammation in mice. It has been reported that MCP-1, expressed in normal renal epithelial cells, is one of the key factors involved in the regulation of the inflammatory response [40]. It can be upregulated by stimulation of CaOx crystals and participates in CaOx-induced renal inflammation [41]. Our results showed that *E. coli*-induced inflammation was decreased after knockout of *Ppk1* and *Flic in vitro* and *in vivo*. It has been reported that the NF-*κ*B/P38 pathway-mediated inflammatory response is associated with CaOx crystal-induced renal tubular epithelial cell damage, which increased the expression of multiple surface proteins that mediate crystal adhesion like CD44, HA, and OPN, ultimately promoting the formation of CaOx stones [12]. It has been demonstrated that flagellin in *E. coli* activates the NF-*κ*B pathway to stimulate human epithelial cells to secrete inflammatory factors [42], which is consistent with our results. In addition, our study further indicated that the NF-*κ*B/P38 pathway activated by *E. coli* is partially regulated by the PPK1/flagellin axis. Weak inflammation was observed in the △PPK1-CFT073 and △Flic-CFT073 groups. This may be related to other virulence factors secreted by *E. coli*, which are less influenced by PPK1 (like LPS) [43, 44]. However, the results of us supported LPS may not a leading element in the aggregation of CaOx crystals, which is also consistent with Rattiyaporn's study [34].

Our study did not show whether inhibition of NF-*κ*B/P38- or PPK1-related inflammation pathways could reverse or alleviate the formation of stones, and the antioxidant activity regulated by PPK1/flagellin is unknown. Nonetheless, our research partly revealed the potential mechanism by which *E. coli* promotes CaOx stone formation via PPK1/flagellin, which may explain the results of Zhong et al.'s study [27]. In addition, whether the addition of anti-inflammatory drugs and antibiotics, together with anticalculus drugs, are helpful in reducing *E. coli*-induced CaOx stone formation, is also a vital question worth addressing in the application of CaOx treatment.

5. Conclusion

In summary, we found that *E. coli* is the most common bacterial species in stone and urine of patients with CaOx. We constructed *Ppk1* knockdown strains of *E. coli*, screened and identified the PPK1-regulated downstream crystal adhesion relative molecule flagellin by mass spectrometry. The dominant function of PPK1/flagellin in promoting CaOx crystal adhesion and aggregation was confirmed. In addition, we found that the ability of △PPK1-CFT073 and △Flic-CFT073 strains to induce renal oxidative injury and inflammation was weaker than that of the WT-CFT073 strain. Meanwhile, a previously unknown, specific mechanism, by which the PPK1/flagellin/NF-*κ*B/P38 inflammation pathway is activated by *E. coli* during the CaOx calculus formation, has been revealed. Taken together, this study not only highlights the significance of UTI in the lithogenous process of CaOx stones but also provides a new direction and potential drug targets for the CaOx calculus prevention and treatment.

Data Availability

All the data supporting the results were shown in the paper can be applicable from the corresponding author.

Conflicts of Interest

The authors declare that they have no known competing financial interests or personal relationships that could have appeared to influence the work reported in this paper.

Authors' Contributions

Ling-yue An, Wei-zhou Wu, Shu-jue Li, and Yong-chang Lai contributed equally to this work.

Acknowledgments

This work was sustained in part by the National Natural Science Foundation of China (82070719, 81570633, and 81400708), Guangdong Provincial Natural Science Project (2020A151501198), Key Project of Department of Education of Guangdong Province (2018KZDXM056), Guangzhou Municipal Science and Technology Bureau (202002030042, 202002030316), Shenzhen Futian District Public Health Research Project (FTWS2020064), and Shenzhen Scientific Technology Basic Research Projects (JCYJ20170818163925018).

References

[1] I. Sorokin, C. Mamoulakis, K. Miyazawa, A. Rodgers, J. Talati, and Y. Lotan, "Epidemiology of stone disease across the world," *World Journal of Urology*, vol. 35, no. 9, pp. 1301–1320, 2017.

[2] C. D. Scales Jr., A. C. Smith, J. M. Hanley, and C. S. Saigal, "Prevalence of Kidney Stones in the United States," *European Urology*, vol. 62, no. 1, pp. 160–165, 2012.

[3] J. S. Jung, C. H. Han, and S. Bae, "Study on the prevalence and incidence of urolithiasis in Korea over the last 10 years: an analysis of National Health Insurance Data," *Investig Clin Urol.*, vol. 59, no. 6, pp. 383–391, 2018.

[4] A. Skolarikos, M. Straub, T. Knoll et al., "Metabolic Evaluation and Recurrence Prevention for Urinary Stone Patients: EAU Guidelines," *European Urology*, vol. 67, no. 4, pp. 750–763, 2015.

[5] A. P. Evan, E. M. Worcester, F. L. Coe, J. Williams Jr., and J. E. Lingeman, "Mechanisms of human kidney stone formation," *Urolithiasis.*, vol. 43, Suppl 1, pp. 19–32, 2015.

[6] K. H. Bichler, E. Eipper, K. Naber, V. Braun, R. Zimmermann, and S. Lahme, "Urinary infection stones," *International Journal of Antimicrobial Agents*, vol. 19, no. 6, pp. 488–498, 2002.

[7] E. J. Espinosa-Ortiz, B. H. Eisner, D. Lange, and R. Gerlach, "Current insights into the mechanisms and management of infection stones," *Nature Reviews Urology*, vol. 16, no. 1, pp. 35–53, 2019.

[8] D. Chen, C. Jiang, X. Liang et al., "Early and rapid prediction of postoperative infections following percutaneous nephrolithotomy in patients with complex kidney stones," *BJU International*, vol. 123, no. 6, pp. 1041–1047, 2019.

[9] G. Zanetti, S. Paparella, A. Trinchieri, D. Prezioso, F. Rocco, and K. G. Naber, "Infections and urolithiasis: current clinical evidence in prophylaxis and antibiotic therapy," *Archivio Italiano di Urologia, Andrologia*, vol. 80, no. 1, pp. 5–12, 2008.

[10] S. R. Khan, "Calcium oxalate crystal interaction with renal tubular epithelium, mechanism of crystal adhesion and its impact on stone development," *Urological Research*, vol. 23, no. 2, pp. 71–79, 1995.

[11] M. Hirose, T. Yasui, A. Okada et al., "Renal tubular epithelial cell injury and oxidative stress induce calcium oxalate crystal formation in mouse kidney," *International Journal of Urology*, vol. 17, no. 1, pp. 83–92, 2010.

[12] S. R. Khan, "Reactive oxygen species as the molecular modulators of calcium oxalate kidney stone formation: evidence from clinical and experimental investigations," *The Journal of Urology*, vol. 189, no. 3, pp. 803–811, 2013.

[13] S. R. Khan, "Is oxidative stress, a link between nephrolithiasis and obesity, hypertension, diabetes, chronic kidney disease, metabolic syndrome?," *Urological Research*, vol. 40, no. 2, pp. 95–112, 2012.

[14] M. R. Brown and A. Kornberg, "Inorganic polyphosphate in the origin and survival of species," *Proceedings of the National Academy of Sciences of the United States of America*, vol. 101, no. 46, pp. 16085–16087, 2004.

[15] M. J. Seufferheld, H. M. Alvarez, and M. E. Farias, "Role of polyphosphates in microbial adaptation to extreme environments," *Applied and Environmental Microbiology*, vol. 74, no. 19, pp. 5867–5874, 2008.

[16] A. Kornberg, S. R. Kornberg, and E. S. Simms, "Metaphosphate synthesis by an enzyme from _Escherichia coli_," *Biochimica et Biophysica Acta*, vol. 20, no. 1, pp. 215–227, 1956.

[17] L. Achbergerová and J. Nahálka, "Polyphosphate - an ancient energy source and active metabolic regulator," *Microbial Cell Factories*, vol. 10, no. 1, pp. 63–63, 2011.

[18] S. Chaiyarit, S. Mungdee, and V. Thongboonkerd, "Non-radioactive labelling of calcium oxalate crystals for investigations of crystal-cell interactions and internalization," *Analytical Method*, vol. 2, no. 10, pp. 1536–1541, 2010.

[19] S. Chutipongtanate and V. Thongboonkerd, "Red blood cell membrane fragments but not intact red blood cells promote calcium oxalate monohydrate crystal growth and aggregation," *Journal of Urology*, vol. 184, no. 2, pp. 743–749, 2010.

[20] S. Chutipongtanate, S. Sutthimethakorn, W. Chiangjong, and V. Thongboonkerd, "Bacteria can promote calcium oxalate crystal growth and aggregation," *Journal of Biological Inorganic Chemistry*, vol. 18, no. 3, pp. 299–308, 2013.

[21] G. Nichols, S. Byard, M. J. Bloxham et al., "A review of the terms agglomerate and aggregate with a recommendation for nomenclature used in powder and particle characterization," *Journal of Pharmaceutical Sciences*, vol. 91, no. 10, pp. 2103–2109, 2010.

[22] X. Duan, Z. Kong, M. Xin et al., "Autophagy inhibition attenuates hyperoxaluria-induced renal tubular oxidative injury and calcium oxalate crystal depositions in the rat kidney," *Redox Biology*, vol. 16, pp. 414–425, 2018.

[23] K. H. Thai, A. Thathireddy, and M. H. Hsieh, "Transurethral induction of mouse urinary tract infection," *Journal of Visualized Experiments Jove*, no. 42, p. e2070, 2010.

[24] R. Flannigan, W. H. Choy, B. Chew, and D. Lange, "Renal struvite stones—pathogenesis, microbiology, and management strategies," *Nature Reviews. Urology*, vol. 11, no. 6, pp. 333–341, 2014.

[25] S. R. Khan, P. A. Glenton, R. Backov, and D. R. Talham, "Presence of lipids in urine, crystals and stones: Implications for the formation of kidney stones," *Kidney International*, vol. 62, no. 6, pp. 2062–2072, 2002.

[26] L. Chen, Y. Shen, R. Jia et al., "The role of Escherichia coli form in the biomineralization of calcium oxalate crystals," *European Journal of Inorganic Chemistry*, vol. 2007, no. 20, pp. 3201–3207, 2007.

[27] F. Zhong, W. Wu, D. Chen et al., "The characteristic and relationship of Escherichia coli isolated from urine and stones in patients with calcium oxalate stones," *Urolithiasis*, vol. 17, 2021.

[28] E. Barr-Beare, V. Saxena, E. E. Hilt et al., "The Interaction between Enterobacteriaceae and Calcium Oxalate Deposits," *PLoS ONE*, vol. 10, no. 10, 2015.

[29] J. Chen, L. Su, X. Wang et al., "Polyphosphate kinase mediates antibiotic tolerance in extraintestinal pathogenic Escherichia coli PCN033," *Frontiers in Microbiology*, vol. 7, pp. 724–734, 2016.

[30] K. Ishige and T. Noguchi, "Polyphosphate:AMP Phosphotransferase and Polyphosphate:ADP Phosphotransferase Activities of Pseudomonas aeruginosa," *Biochemical & Biophysical Research Communications*, vol. 281, no. 3, pp. 821–826, 2001.

[31] Q. Duan, M. Zhou, X. Zhu et al., "The flagella of F18ab Escherichia coli is a virulence factor that contributes to infection in a IPEC-J2 cell model in vitro," *Veterinary Microbiology*, vol. 160, no. 1-2, pp. 132–140, 2012.

[32] H. Terashima, S. Kojima, and M. Homma, "Flagellar motility in bacteria structure and function of flagellar motor,"

International Review of Cell and Molecular Biology, vol. 270, pp. 39–85, 2008.

[33] R. M. Macnab, "How bacteria assemble flagella," *Annual Review of Microbiology*, vol. 57, no. 1, pp. 77–100, 2003.

[34] R. Kanlaya, O. Naruepantawart, and V. Thongboonkerd, "Flagellum is responsible for promoting effects of viable Escherichia coli on calcium oxalate crystallization, crystal growth, and crystal aggregation," *Frontiers in Microbiology*, vol. 10, 2019.

[35] P. Amimanan, R. Tavichakorntrakool, K. Fong-Ngern et al., "Elongation factor Tu on Escherichia coli isolated from urine of kidney stone patients promotes calcium oxalate crystal growth and aggregation," *Scientific Reports*, vol. 7, no. 1, p. 2953, 2017.

[36] S. Farmanesh, J. Chung, R. D. Sosa, J. H. Kwak, P. Karande, and J. D. Rimer, "Natural promoters of calcium oxalate monohydrate crystallization," *Journal of the American Chemical Society*, vol. 136, no. 36, pp. 12648–12657, 2014.

[37] Q. Z. Gan, X. Y. Sun, P. Bhadja, X. Q. Yao, and J. M. Ouyang, "Reinjury risk of nano-calcium oxalate monohydrate and calcium oxalate dihydrate crystals on injured renal epithelial cells: aggravation of crystal adhesion and aggregation," *International Journal of Nanomedicine*, vol. 11, pp. 2839–2854, 2016.

[38] H. Liu, X. Y. Sun, F. X. Wang, and J.-M. Ouyang, "Regulation on calcium oxalate crystallization and protection on HK-2 cells of tea polysaccharides with different molecular weights," *Oxidative Medicine and Cellular Longevity*, vol. 2020, Article ID 5057123, 14 pages, 2020.

[39] N. U. Rahman, M. V. Meng, and M. L. Stoller, "Infections and urinary stone disease," *Current Pharmaceutical Design*, vol. 9, no. 12, pp. 975–981, 2003.

[40] M. F. Cassini, V. R. Kakade, E. Kurtz et al., "Mcp1 Promotes Macrophage-Dependent Cyst Expansion in Autosomal Dominant Polycystic Kidney Disease," *Journal of the American Society of Nephrology*, vol. 29, no. 10, pp. 2471–2481, 2018.

[41] J. H. Cherng, Y. J. Hsu, C. C. Liu et al., "Activities of calcium-related ion channels during the formation of kidney stones in an infection-induced urolithiasis rat model. American journal of physiology," *Renal physiology*, vol. 317, no. 5, pp. F1342–F1349, 2019.

[42] N. J. Smith, C. L. Varley, I. Eardley, S. Feather, L. K. Trejdosiewicz, and J. Southgate, "Toll-like receptor responses of normal human urothelial cells to bacterial flagellin and lipopolysaccharide," *The Journal of Urology*, vol. 186, no. 3, pp. 1084–1092, 2011.

[43] Q. Ren, F. Guo, S. Tao, R. Huang, L. Ma, and P. Fu, "Flavonoid fisetin alleviates kidney inflammation and apoptosis via inhibiting Src-mediated NF-κB p65 and MAPK signaling pathways in septic AKI mice," *Biomedicine & Pharmacotherapy*, vol. 122, p. 109772, 2020.

[44] T. Djojodimedjo, D. M. Soebadi, and Soetjipto, "Escherichia coli infection induces mucosal damage and expression of proteins promoting urinary stone formation," *Urolithiasis*, vol. 41, no. 4, pp. 295–301, 2013.